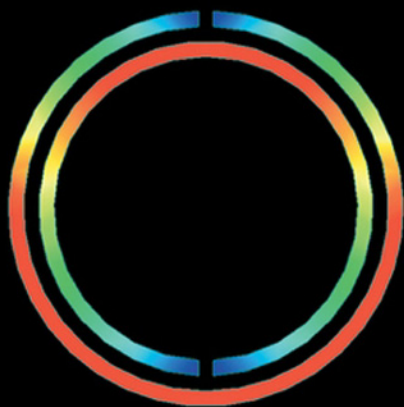


# Metamaterials with Negative Parameters

Theory, Design, and Microwave Applications



RICARDO MARQUÉS, FERRAN MARTÍN,  
and MARIO SOROLLA

# **Metamaterials with Negative Parameters**



---

THE WILEY BICENTENNIAL—KNOWLEDGE FOR GENERATIONS

---

Each generation has its unique needs and aspirations. When Charles Wiley first opened his small printing shop in lower Manhattan in 1807, it was a generation of boundless potential searching for an identity. And we were there, helping to define a new American literary tradition. Over half a century later, in the midst of the Second Industrial Revolution, it was a generation focused on building the future. Once again, we were there, supplying the critical scientific, technical, and engineering knowledge that helped frame the world. Throughout the 20th Century, and into the new millennium, nations began to reach out beyond their own borders and a new international community was born. Wiley was there, expanding its operations around the world to enable a global exchange of ideas, opinions, and know-how.

For 200 years, Wiley has been an integral part of each generation's journey, enabling the flow of information and understanding necessary to meet their needs and fulfill their aspirations. Today, bold new technologies are changing the way we live and learn. Wiley will be there, providing you the must-have knowledge you need to imagine new worlds, new possibilities, and new opportunities.

Generations come and go, but you can always count on Wiley to provide you the knowledge you need, when and where you need it!

**WILLIAM J. PESCE**  
PRESIDENT AND CHIEF EXECUTIVE OFFICER

**PETER BOOTH WILEY**  
CHAIRMAN OF THE BOARD

---

---

# Metamaterials with Negative Parameters

Theory, Design, and  
Microwave Applications

---

RICARDO MARQUÉS  
FERRAN MARTÍN  
MARIO SOROLLA



WILEY-INTERSCIENCE  
A JOHN WILEY & SONS, INC.. PUBLICATION

Copyright © 2008 by John Wiley & Sons, Inc. All rights reserved

Published by John Wiley & Sons, Inc., Hoboken, New Jersey  
Published simultaneously in Canada

No part of this publication may be reproduced, stored in a retrieval system, or transmitted in any form or by any means, electronic, mechanical, photocopying, recording, scanning, or otherwise, except as permitted under Section 107 or 108 of the 1976 United States Copyright Act, without either the prior written permission of the Publisher, or authorization through payment of the appropriate per-copy fee to the Copyright Clearance Center, Inc., 222 Rosewood Drive, Danvers, MA 01923, (978) 750-8400, fax (978) 750-4470, or on the web at [www.copyright.com](http://www.copyright.com). Requests to the Publisher for permission should be addressed to the Permissions Department, John Wiley & Sons, Inc., 111 River Street, Hoboken, NJ 07030, (201) 748-6011, fax (201) 748-6008, or online at <http://www.wiley.com/go/permission>.

**Limit of Liability/Disclaimer of Warranty:** While the publisher and author have used their best efforts in preparing this book, they make no representations or warranties with respect to the accuracy or completeness of the contents of this book and specifically disclaim any implied warranties of merchantability or fitness for a particular purpose. No warranty may be created or extended by sales representatives or written sales materials. The advice and strategies contained herein may not be suitable for your situation. You should consult with a professional where appropriate. Neither the publisher nor author shall be liable for any loss of profit or any other commercial damages, including but not limited to special, incidental, consequential, or other damages.

For general information on our other products and services or for technical support, please contact our Customer Care Department within the United States at (800) 762-2974, outside the United States at (317) 572-3993 or fax (317) 572-4002.

Wiley also publishes its books in a variety of electronic formats. Some content that appears in print may not be available in electronic formats. For more information about Wiley products, visit our web site at [www.wiley.com](http://www.wiley.com).

***Library of Congress Cataloging-in-Publication Data:***

Marqués, Ricardo, 1954-

Metamaterials with negative parameters : theory, design and microwave applications / by Ricardo Marqués, Ferran Martin, Mario Sorolla.  
p. cm.

ISBN 978-0-471-74582-2 (cloth)

1. Magnetic materials. 2. Microelectronics—Materials. I. Martin, Ferran, 1965- II. Sorolla, Mario, 1958- III. Title.

TK7871.15.M3M37 2007

620.1'1297—dc22

2007017343

Printed in the United States of America

10 9 8 7 6 5 4 3 2 1

*To our families*  
*Asunción, Ricardo Jr., Concepción and Ricardo Sr.*  
*Anna, Alba and Arnau*  
*Puri, Carolina and Viviana*  
*And also to the memory of Prof. Manuel Horno*



---

# Contents

---

<b>Preface</b>	<b>xiii</b>
<b>Acknowledgments</b>	<b>xvii</b>
<b>1 The Electrodynamics of Left-Handed Media</b>	<b>1</b>
1.1 Introduction	1
1.2 Wave Propagation in Left-Handed Media	2
1.3 Energy Density and Group Velocity	4
1.4 Negative Refraction	6
1.5 Fermat Principle	9
1.6 Other Effects in Left-Handed Media	9
1.6.1 Inverse Doppler Effect	10
1.6.2 Backward Cerenkov Radiation	10
1.6.3 Negative Goos–Hänchen Shift	12
1.7 Waves at Interfaces	13
1.7.1 Transmission and Reflection Coefficients	13
1.7.2 Surface Waves	15
1.8 Waves Through Left-Handed Slabs	16
1.8.1 Transmission and Reflection Coefficients	17
1.8.2 Guided Waves	17
1.8.3 Backward Leaky and Complex Waves	19
1.9 Slabs with $\varepsilon/\varepsilon_0 \rightarrow -1$ and $\mu/\mu_0 \rightarrow -1$	20
1.9.1 Phase Compensation and Amplification of Evanescent Modes	20
1.9.2 Perfect Tunneling	21
1.9.3 The Perfect Lens	25
1.9.4 The Perfect Lens as a Tunneling/ Matching Device	29
1.10 Losses and Dispersion	32
	<b>vii</b>



1.11	Indefinite Media	34
	Problems	35
	References	37
<b>2</b>	<b>Synthesis of Bulk Metamaterials</b>	<b>43</b>
2.1	Introduction	43
2.2	Scaling Plasmas at Microwave Frequencies	44
2.2.1	Metallic Waveguides and Plates as One- and Two-Dimensional Plasmas	44
2.2.2	Wire Media	47
2.2.3	Spatial Dispersion in Wire Media	49
2.3	Synthesis of Negative Magnetic Permeability	51
2.3.1	Analysis of the Edge-Coupled SRR	52
2.3.2	Other SRR Designs	59
2.3.2.1	The Broadside-Coupled SRR	60
2.3.2.2	The Nonbianisotropic SRR	62
2.3.2.3	The Double-Split SRR	62
2.3.2.4	Spirals	62
2.3.3	Constitutive Relationships for Bulk SRR Metamaterials	65
2.3.4	Higher-Order Resonances in SRRs	70
2.3.5	Isotropic SRRs	73
2.3.6	Scaling Down SRRs to Infrared and Optical Frequencies	75
2.4	SRR-Based Left-Handed Metamaterials	80
2.4.1	One-Dimensional SRR-Based Left-Handed Metamaterials	81
2.4.2	Two-Dimensional and Three-Dimensional SRR-Based Left-Handed Metamaterials	85
2.4.3	On the Application of the Continuous-Medium Approach to Discrete SRR-Based Left-Handed Metamaterials	87
2.4.4	The Superposition Hypothesis	88
2.4.5	On the Numerical Accuracy of the Developed Model for SRR-Based Metamaterials	90
2.5	Other Approaches to Bulk Metamaterial Design	91
2.5.1	Ferrite Metamaterials	92
2.5.2	Chiral Metamaterials	97
2.5.3	Other Proposals	102
	Appendix	107
	Problems	109
	References	114
<b>3</b>	<b>Synthesis of Metamaterials in Planar Technology</b>	<b>119</b>
3.1	Introduction	119
3.2	The Dual (Backward) Transmission Line Concept	120

3.3	Practical Implementation of Backward Transmission Lines	128
3.4	Two-Dimensional (2D) Planar Metamaterials	131
3.5	Design of Left-Handed Transmission Lines by Means of SRRs: The Resonant Type Approach	135
3.5.1	Effective Negative Permeability Transmission Lines	136
3.5.2	Left-Handed Transmission Lines in Microstrip and CPW Technologies	139
3.5.3	Size Reduction	144
3.6	Equivalent Circuit Models for SRRs Coupled to Conventional Transmission Lines	146
3.6.1	Dispersion Diagrams	151
3.6.2	Implications of the Model	151
3.7	Duality and Complementary Split Ring Resonators (CSRRs)	155
3.7.1	Electromagnetic Properties of CSRRs	156
3.7.2	Numerical Calculation and Experimental Validation	160
3.8	Synthesis of Metamaterial Transmission Lines by Using CSRRs	163
3.8.1	Negative Permittivity and Left-Handed Transmission Lines	163
3.8.2	Equivalent Circuit Models for CSRR-Loaded Transmission Lines	166
3.8.3	Parameter Extraction	170
3.8.4	Effects of Cell Geometry on Frequency Response	172
3.9	Comparison between the Circuit Models of Resonant-Type and Dual Left-Handed Lines	175
	Problems	180
	References	182
<b>4</b>	<b>Microwave Applications of Metamaterial Concepts</b>	<b>187</b>
4.1	Introduction	187
4.2	Filters and Diplexers	188
4.2.1	Stopband Filters	189
4.2.2	Planar Filters with Improved Stopband	193
4.2.3	Narrow Bandpass Filter and Diplexer Design	198
4.2.3.1	Bandpass Filters Based on Alternate Right-/Left-Handed (ARLH) Sections Implemented by Means of SRRs	199
4.2.3.2	Bandpass Filters and Diplexers Based on Alternate Right-/Left-Handed (ARLH) Sections Implemented by Means of CSRRs	203
4.2.4	CSRR-Based Bandpass Filters with Controllable Characteristics	207
4.2.4.1	Bandpass Filters Based on the Hybrid Approach: Design Methodology and Illustrative Examples	208

4.2.4.2	Other CSRR-Based Filters Implemented by Means of Right-Handed Sections	218
4.2.5	Highpass Filters and Ultrawide Bandpass Filters (UWBPFs) Implemented by Means of Resonant-Type Balanced CRLH Metamaterial Transmission Lines	225
4.2.6	Tunable Filters Based on Varactor-Loaded Split Rings Resonators (VLSRRs)	227
4.2.6.1	Topology of the VLSRR and Equivalent-Circuit Model	228
4.2.6.2	Validation of the Model	230
4.2.6.3	Some Illustrative Results: Tunable Notch Filters and Stopband Filters	230
4.3	Synthesis of Metamaterial Transmission Lines with Controllable Characteristics and Applications	233
4.3.1	Miniaturization of Microwave Components	234
4.3.2	Compact Broadband Devices	236
4.3.3	Dual-Band Components	244
4.3.4	Coupled-Line Couplers	246
4.4	Antenna Applications	252
	Problems	258
	References	260
<b>5</b>	<b>Advanced and Related Topics</b>	<b>267</b>
5.1	Introduction	267
5.2	SRR- and CSRR-Based Admittance Surfaces	268
5.2.1	Babinet Principle for a Single Split Ring Resonator	268
5.2.2	Surface Admittance Approach for SRR Planar Arrays	270
5.2.3	Babinet Principle for CSRR Planar Arrays	272
5.2.4	Behavior at Normal Incidence	273
5.2.5	Behavior at General Incidence	274
5.3	Magneto- and Electro-Inductive Waves	278
5.3.1	The Magneto-Inductive Wave Equation	279
5.3.2	Magneto-Inductive Surfaces	282
5.3.3	Electro-Inductive Waves in CSRR Arrays	284
5.3.4	Applications of Magneto- and Electro-Inductive Waves	285
5.4	Subdiffraction Imaging Devices	287
5.4.1	Some Universal Features of Subdiffraction Imaging Devices	288
5.4.2	Imaging in the Quasielectrostatic Limit: Role of Surface Plasmons	292
5.4.3	Imaging in the Quasimagnetostatic Limit: Role of Magnetostatic Surface Waves	295

5.4.4	Imaging by Resonant Impedance Surfaces: Magneto-Inductive Lenses	299
5.4.5	Canalization Devices	302
	Problems	304
	References	305
<b>Index</b>		<b>309</b>



---

# Preface

---

Discovery consists of seeing what everybody has seen and thinking what nobody has thought.

Albert Szent-Gyorgyi

Classical electromagnetism is one of the best established theories of physics. Its concepts and theorems have been shown to be useful from the atomic to the cosmological scale; and they have been more successful in surviving to the relativistic and quantum revolutions than other classical concepts. It is well known for instance that Maxwell's equations were at the very basis of relativity and that Maxwell's electromagnetic theory was the first relativistic invariant theory. Concerning quantum mechanics, classical electromagnetism still provides the best foundations—together with quantum dynamics—for atomic and solid state physics. It is only in the domain of particle physics that classical electromagnetism needs to be reformulated as quantum electrodynamics. With regard to practical applications, classical electromagnetic theory is the basis of many well-known technologies, which strongly affect our ordinary lives, from power generation to wireless communications. It seems very difficult to add something conceptually new to such well-established theories and technologies.

However, during recent years, a new expression appeared in the universe of classical electromagnetic theory: *metamaterials*. From 2000 to 2007, the number of journal and conference papers related to metamaterials has grown exponentially; there has also been a multitude of special sessions, tutorials, and scientific meetings, all around the world, devoted to this new topic. Related to *metamaterials*, other topics appeared on the scene, such as *photonic crystals*, *negative refraction*, *left-handed media*, or *cloaking*, among others. But what is the reason and meaning behind this sudden explosion in the otherwise quiet waters of electromagnetism? In fact, nothing is new from the point of view of fundamental science in metamaterials. Throughout this book, it will be shown that metamaterials can be understood by using well-known theoretical tools, such as homogenization of effective media or elementary transmission line theories. In addition, many electrical and electronic

engineers have pointed out that almost all new applications arising from metamaterial concepts can be understood by using more conventional approaches, that is, without the need to invoke these metamaterial concepts. So, what is new in metamaterials?

Physicists usually try to explain how nature works, whereas engineers try to apply this knowledge to the design of new devices and systems, useful for certain applications. In our opinion, metamaterials are placed at an intermediate position between science and engineering—for this reason they are of interest to both physicists and engineers. Metamaterials are not “materials” in the usual sense: they cannot be found in nature (by the way, this is a very common definition of metamaterials). In fact, metamaterials are artificial structures (products of human ingenuity), designed to obtain controllable electromagnetic or optical properties. This includes the possibility to synthesize artificial media with properties not found among natural materials, such as negative refraction, among others. Within this scenario, it is evident that metamaterials may open many challenging objectives of interest to physicists and scientists in general. From the technological and engineering viewpoint, the interest in metamaterials is based on the possibility of designing devices and systems with new properties or functionalities, able to open up new fields of application or to improve existing ones. Although it has been argued that certain applications of metamaterials can be analyzed through conventional approaches, the key virtue of metamaterials is in providing new design guidelines for components and systems that are missing in conventional approaches. Other applications such as subdiffraction imaging are, however, genuine products of metamaterials. This intermediate position between physics and engineering is a relevant aspect and probably one of the main novelties of metamaterials. In order to highlight this multidisciplinary nature, in our opinion it is appropriate to refer to this new topic as metamaterials science and engineering.

Most metamaterials fall in one of two categories: *photonic or electromagnetic crystals* and *effective media*. The first category corresponds to structures made of periodic micro- or nano-inclusions whose period is of the same order as the signal wavelength. Therefore, their electromagnetic properties arise mainly from periodicity. Conversely, in effective media the period is much smaller than this signal wavelength. Hence, their electromagnetic properties can be obtained from a homogenization procedure. This book is mainly devoted to the second category, specifically to those metamaterials that can be characterized by a negative effective permittivity and/or permeability.

The first chapter is devoted to the analysis of the electrodynamics of continuous media with simultaneously negative dielectric permittivity and magnetic permeability. Chapter 2 is focused on the design of bulk metamaterials made of systems of individual metallic inclusions with a strong electric and/or magnetic response near its first resonance. The third chapter develops the transmission line approach for the design of metamaterials with negative parameters, including both the nonresonant and the resonant-type approaches. Chapter 4 is devoted to the analysis of some relevant microwave applications of the concepts developed in the previous chapters. Finally, in Chapter 5, some related and/or advanced topics, such as metasurfaces, magneto-inductive waves in metamaterial structures and subdiffraction imaging devices are developed.

This book is mainly directed towards the resonant-type approach to metamaterials because, obviously, it has been strongly influenced by the personal experience of the authors. However, our aim in writing this book has been to give a complete overview of the present state-of-the-art in metamaterials theory, as well as the most relevant microwave applications of metamaterial concepts. Indeed, our purpose has been twofold: to generate curiosity and interest for this emerging field by those readers not previously involved in metamaterials science and engineering and to provide useful ideas and knowledge to scientists and engineers working in the field.

RICARDO MARQUÉS  
FERRAN MARTÍN  
MARIO SOROLLA

*Sevilla, Spain*  
*Barcelona, Spain*  
*Pamplona, Spain*  
*October 2007*





---

# Acknowledgments

---

This book is the result of an intensive research activity in the field of metamaterials, which has been carried out by the authors and the members of their respective groups. We must acknowledge all of them because without their contribution this book would never have been written.

With regard to the microwave group (Universidad de Sevilla), headed by Francisco Medina, special thanks are given to Juan Baena and Manuel Freire, who have significantly contributed to some parts of the book, including the editing of many figures. Also, special thanks are given to Francisco Medina, Francisco Mesa, Jesús Martel, and Lukas Jelinek for reading the manuscript and providing useful comments and suggestions. Finally, thanks to Rafael, Casti, Ana, Raul, Vicente, and all members of the group for providing such a friendly and stimulating environment for our research.

The members of CIMITEC (Center of Research on Metamaterials at the Universitat Autònoma de Barcelona), headed by Ferran Martín, are also acknowledged, with special emphasis given to Jordi Bonache, Joan García, Ignacio Gil, Marta Gil, and Francisco Aznar, who have been actively and exhaustively involved in this work. Special thanks are given to Marta Gil, who has helped the authors with the generation and editing of some of the figures, and to Anna Cedenilla, for being in charge of copyright issues and permissions. We would also like to mention in the list the recently incorporated members to the team: Gerard, Fito, Ferran, and Beni.

Concerning the team of the Millimeter Wave Laboratory (Universidad Pública de Navarra), headed by Mario Sorolla, the authors thank Francisco Falcone, Miguel Beruete, José A. Marcotegui, Txema Lopetegi, Mikel A. G. Laso, Jesús Illescas, Israel Arnedo, Noelia Ortiz, Eduardo Jarauta, and María Flores for their enthusiastic and creative research activities. Also, Mario Sorolla thanks Professor Manfred Thumm (FZK and University of Karlsruhe) for his support and guidance over many years in the topic of periodic structures.

The research activity presented in this book originated from several sources. At the European level, thanks are given to the European Commission (VI Framework

Programme) for funding the Network of Excellence METAMORPHOSE, to which one of the authors (Ferran Martín) belongs. Also, the authors have participated in the European Eureka project, TELEMAC, devoted to the development of metamaterial-based microwave components for communication front-ends and supported by the Spanish Ministry of Industry via PROFIT projects (headed by the SME CONATEL). At the national level, funding has been received from the Ministry of Science and Education (MEC) through several national projects. Special mention deserves the support given from MEC to the Spanish Network on Metamaterials (REME), which has been launched by the authors in collaboration with other Spanish researchers.

And last, but not least, the authors would like to express their gratitude to their respective families for their understanding and support, and for accepting the large amount of hours dedicated by the authors to the exciting field of metamaterials and to writing the present manuscript.

R. M.  
F. M.  
M. S.

# The Electrodynamics of Left-Handed Media

---

## 1.1 INTRODUCTION

Continuous media with negative parameters, that is, media with negative dielectric constant,  $\epsilon$ , or magnetic permeability,  $\mu$ , have long been known in electromagnetic theory. In fact, the Drude–Lorentz model (which is applicable to most materials) predicts regions of negative  $\epsilon$  or  $\mu$  just above each resonance, provided losses are small enough [1]. Although losses usually prevent the onset of this property in common dielectrics, media with negative  $\epsilon$  can be found in nature. The best-known examples are low-loss plasmas, and metals and semiconductors at optical and infrared frequencies (sometimes called *solid-state plasmas*). Media with negative  $\mu$  are less common in nature due to the weak magnetic interactions in most solid-state materials [2]. Only in ferrimagnetic materials are magnetic interactions strong enough (and losses small enough) to produce regions of negative magnetic permeability. Ferrites magnetized to saturation present a tensor magnetic permeability with negative elements near the ferrimagnetic resonance (which usually occurs at microwave frequencies). These materials are widely used in microwave engineering, mainly to make use of their non-reciprocity. The electrodynamics of these solid-state materials with negative  $\epsilon$  or  $\mu$  is described in many well-known textbooks [3–5], so this chapter will focus on the electrodynamics of media having *simultaneously* negative  $\epsilon$  and  $\mu$  (see, however, problems 1.1–1.3, 1.12, and 1.14).

Wave propagation in media with simultaneously negative  $\epsilon$  and  $\mu$  was discussed and analyzed in a seminal paper by Veselago [6] at the end of the 1960s. However, it was necessary to wait for more than 30 years to see the first practical realization of

such media [7], also called *left-handed* media [6,7]. This terminology will be used throughout this book.<sup>1</sup> Other terms that have been proposed for media with simultaneously negative  $\epsilon$  and  $\mu$  are *negative-refractive* media [8], *backward* media [9], *double-negative* media [10], and also *Veselago* media [11].

The propagation constant of a plane wave is given by  $k = \omega\sqrt{\epsilon\mu}$ , so it is apparent that wave propagation is not forbidden in left-handed media. Several principal questions arise from this statement:

- Does an electromagnetic wave in a left-handed medium differ in any essential way from a wave in an ordinary medium with positive  $\epsilon$  and  $\mu$ ?
- Is there any essential physical law—for instance, energy conservation—forbidding left-handed media?
- Assuming the answer to the previous question was affirmative. How to obtain a left-handed medium in practice?

In this chapter we will try to give some answers to the first and second questions above, leaving the following chapters to find the answer to the third question.

## 1.2 WAVE PROPAGATION IN LEFT-HANDED MEDIA

In order to show wave propagation in left-handed media, we will first reduce Maxwell equations to the wave equation [6]:

$$\left(\nabla^2 - \frac{n^2}{c^2} \frac{\partial^2}{\partial t^2}\right)\psi = 0, \quad (1.1)$$

where  $n$  is the refractive index,  $c$  is the velocity of light in vacuum, and  $n^2/c^2 = \epsilon\mu$ . As the squared refractive index  $n^2$  is not affected by a simultaneous change of sign in  $\epsilon$  and  $\mu$ , it is clear that low-loss left-handed media must be transparent. In view of the above equation, we can obtain the impression that solutions to equation (1.1) will remain unchanged after a simultaneous change of the signs of  $\epsilon$  and  $\mu$ . However, when Maxwell's first-order differential equations are explicitly considered,

$$\nabla \times \mathbf{E} = -j\omega\mu\mathbf{H} \quad (1.2)$$

$$\nabla \times \mathbf{H} = j\omega\epsilon\mathbf{E}, \quad (1.3)$$

it becomes apparent that these solutions are quite different. In fact, for plane-wave fields of the kind  $\mathbf{E} = \mathbf{E}_0 \exp(-j\mathbf{k} \cdot \mathbf{r} + j\omega t)$  and  $\mathbf{H} = \mathbf{H}_0 \exp(-j\mathbf{k} \cdot \mathbf{r} + j\omega t)$  (this space and time field dependence will be implicitly assumed throughout this book),

<sup>1</sup>Terms such as *right-* and *left-handed* are of common use in optics, referring to polarized light or to media having optical activity. Therefore, it will be worth noting that the use of the term *left-handed* in this book is not related to any specific polarizing property or structural handedness of the material.

the above equations reduce to

$$\mathbf{k} \times \mathbf{E} = \omega\mu\mathbf{H} \quad (1.4)$$

$$\mathbf{k} \times \mathbf{H} = -\omega\varepsilon\mathbf{E}. \quad (1.5)$$

Therefore, for positive  $\varepsilon$  and  $\mu$ ,  $\mathbf{E}$ ,  $\mathbf{H}$ , and  $\mathbf{k}$  form a right-handed orthogonal system of vectors. However, if  $\varepsilon < 0$  and  $\mu < 0$ , then equations (1.4) and (1.5) can be rewritten as

$$\mathbf{k} \times \mathbf{E} = -\omega|\mu|\mathbf{H} \quad (1.6)$$

$$\mathbf{k} \times \mathbf{H} = \omega|\varepsilon|\mathbf{E}, \quad (1.7)$$

showing that  $\mathbf{E}$ ,  $\mathbf{H}$ , and  $\mathbf{k}$  now form a *left-handed triplet*, as illustrated in Figure 1.1. In fact, this result is the original reason for the denomination of negative  $\varepsilon$  and  $\mu$  media as “left-handed” media [6].

The main physical implication of the aforementioned analysis is backward-wave propagation (for this reason, the term *backward media* has been also proposed for media with negative  $\varepsilon$  and  $\mu$  [9]). In fact, the direction of the time-averaged flux of energy is determined by the real part of the Poynting vector,

$$\mathbf{S} = \frac{1}{2}\mathbf{E} \times \mathbf{H}^*, \quad (1.8)$$

which is unaffected by a simultaneous change of sign of  $\varepsilon$  and  $\mu$ . Thus,  $\mathbf{E}$ ,  $\mathbf{H}$ , and  $\mathbf{S}$  still form a right-handed triplet in a left-handed medium. Therefore, in such media, energy and wavefronts travel in opposite directions (backward propagation). Backward-wave propagation is a well-known phenomenon that may appear in non-uniform waveguides [12,13]. However, backward-wave propagation in unbounded homogeneous isotropic media seems to be a unique property of left-handed media. As will be shown, most of the surprising unique electromagnetic properties of these media arise from this backward propagation property.

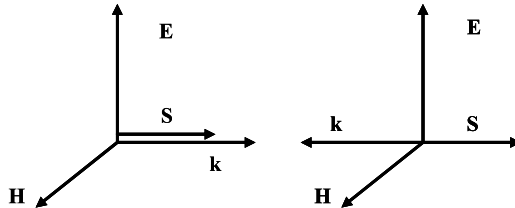


**FIGURE 1.1** Illustration of the system of vectors  $\mathbf{E}$ ,  $\mathbf{H}$ ,  $\mathbf{k}$ , and  $\mathbf{S}$  for a plane transverse electromagnetic (TEM) wave in an ordinary (left) and a left-handed (right) medium.

So far, we have neglected losses. However, losses are unavoidable in any practical material. In the following, the effect of losses in plane-wave propagation will be considered. To begin, we will consider a finite region filled by a homogeneous left-handed medium. In the steady state, and provided there are no sources inside the region, there must be some power flow into the region in order to compensate for losses. Thus, from the well-known complex Poynting theorem [14],

$$\nabla \cdot \{\mathbf{E} \times \mathbf{H}^*\} = j\omega(\mathbf{E} \cdot \mathbf{D}^* - \mathbf{B} \cdot \mathbf{H}^*), \quad (1.9)$$

it follows that

$$\operatorname{Re} \left\{ \oint \mathbf{E} \times \mathbf{H}^* \cdot \hat{\mathbf{n}} \, dS \right\} = \omega \operatorname{Im} \left\{ \int (\mu |\mathbf{H}|^2 - \varepsilon^* |\mathbf{E}|^2) dV \right\} < 0, \quad (1.10)$$

where integration is carried out over the aforementioned region. Therefore,

$$\operatorname{Im}(\varepsilon) < 0; \quad \operatorname{Im}(\mu) < 0. \quad (1.11)$$

Let us now consider a plane wave with square wavenumber  $k^2 = \omega^2 \mu \varepsilon$ , propagating in a lossy left-handed medium with  $\operatorname{Re}(\varepsilon) < 0$  and  $\operatorname{Re}(\mu) < 0$ . From expression (1.11), it follows that  $\operatorname{Im}(k^2) > 0$ . Therefore

$$\{\operatorname{Re}(k) > 0 \text{ and } \operatorname{Im}(k) > 0\} \quad \text{or} \quad \{\operatorname{Re}(k) < 0 \text{ and } \operatorname{Im}(k) < 0\}. \quad (1.12)$$

That is, waves grow in the direction of propagation of the wavefronts. This fact is in agreement with the aforementioned backward-wave propagation.

### 1.3 ENERGY DENSITY AND GROUP VELOCITY

If negative values for  $\varepsilon$  and  $\mu$  are introduced in the usual expression for the time-averaged density of energy in transparent *nondispersive* media,  $U_{\text{nd}}$ , given by

$$U_{\text{nd}} = \frac{1}{4} \{ \varepsilon |\mathbf{E}|^2 + \mu |\mathbf{H}|^2 \}, \quad (1.13)$$

they produce the nonphysical result of a negative density of energy. However, as is well known, any physical media other than vacuum must be dispersive [1], equation (1.13) being an approximation only valid for very weakly dispersive media. The correct expression for a quasimonochromatic wavepacket traveling in a dispersive

media is [2]

$$U = \frac{1}{4} \left\{ \frac{\partial(\omega\varepsilon)}{\partial\omega} |\mathbf{E}|^2 + \frac{\partial(\omega\mu)}{\partial\omega} |\mathbf{H}|^2 \right\}, \quad (1.14)$$

where the derivatives are evaluated at the central frequency of the wavepacket. Thus, the physical requirement of positive energy density implies that

$$\frac{\partial(\omega\varepsilon)}{\partial\omega} > 0 \quad \text{and} \quad \frac{\partial(\omega\mu)}{\partial\omega} > 0, \quad (1.15)$$

which are compatible with  $\varepsilon < 0$  and  $\mu < 0$  provided  $\partial\varepsilon/\partial\omega > |\varepsilon|/\omega$  and  $\partial\mu/\partial\omega > |\mu|/\omega$ . Therefore, physical left-handed media must be highly dispersive. This fact is in agreement with the low-loss Drude–Lorentz model for  $\varepsilon$  and  $\mu$ , which predicts negative values for  $\varepsilon$  and/or  $\mu$  in the highly dispersive regions just above the resonances [1]. Finally, it must be mentioned that the usual interpretation of the imaginary part of the complex Poynting theorem, which relates the flux of reactive power through a closed surface with the difference between electric and magnetic energies inside this surface [14], is not applicable to highly dispersive media, where equation (1.14) holds instead of (1.13). Thus, this interpretation is also not valid for left-handed media.

Backward-wave propagation implies opposite signs between phase and group velocities. In fact

$$\frac{\partial k^2}{\partial\omega} = 2k \frac{\partial k}{\partial\omega} \equiv 2 \frac{\omega}{v_p v_g}, \quad (1.16)$$

where  $v_p = \omega/k$  and  $v_g = \partial\omega/\partial k$  are the phase and group velocities, respectively. In addition, from  $k^2 = \omega^2 \varepsilon \mu$  and equation (1.15),

$$\frac{\partial k^2}{\partial\omega} = \omega\varepsilon \frac{\partial(\omega\mu)}{\partial\omega} + \omega\mu \frac{\partial(\omega\varepsilon)}{\partial\omega} < 0 \quad (1.17)$$

Finally, from equations (1.16) and (1.17)

$$v_p v_g < 0. \quad (1.18)$$

This property implies that wavepackets and wavefronts travel in opposite directions, and can be considered an additional proof of backward-wave propagation in physical left-handed media.



## 1.4 NEGATIVE REFRACTION

Let us now consider the refraction of an incident optical ray at the interface between ordinary ( $\epsilon > 0$  and  $\mu > 0$ ) and left-handed media. Boundary conditions impose continuity of the tangential components of the wavevector along the interface. Thus, from the aforesaid backward propagation in the left-handed region, it immediately follows that, unlike in ordinary refraction, the angles of incidence and refraction must have opposite signs. This effect is illustrated in Figure 1.2.

From the aforementioned continuity of the tangential components of the wavevectors of the incident and refracted rays, it follows that (Fig. 1.2)

$$\frac{\sin \theta_i}{\sin \theta_r} = \frac{-|\mathbf{k}_2|}{|\mathbf{k}_1|} \equiv \frac{n_2}{n_1} < 0, \quad (1.19)$$

which is the well-known Snell's law. In this expression,  $n_1$  and  $n_2$  are the refractive indices of the ordinary and left-handed media, respectively. Assuming  $n_1 > 0$ , from equation (1.19) it follows that  $n_2 < 0$ . That is, the sign of the square root in the refractive index definition must be chosen to be negative [6]:

$$n \equiv -c\sqrt{\epsilon\mu} < 0. \quad (1.20)$$

For this reason, left-handed media are also referred to as *negative refractive index* or *negative refractive* media.

Geometrical optics of systems containing left-handed media is dominated by this last property. By tracing the paths of optical rays through conventional lenses made of left-handed media, it can be shown that concave lenses become convergent and

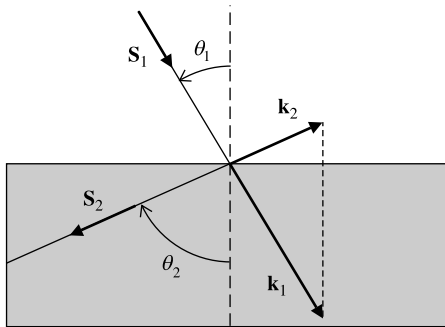


**FIGURE 1.2** Graphic demonstration of the negative refraction between ordinary (subscript 1, top) and left-handed (subscript 2, gray area) media. Poynting and wavevectors for each media are labeled as  $\mathbf{S}_1$ ,  $\mathbf{S}_2$ ,  $\mathbf{k}_1$ , and  $\mathbf{k}_2$ , respectively. Negative refraction arises from the continuity of the components of the wavevectors,  $\mathbf{k}_1$  and  $\mathbf{k}_2$ , parallel to the interface, and from the fact that rays propagate along the direction of energy flow. That is, they must be parallel to the Poynting vectors  $\mathbf{S}_1$  and  $\mathbf{S}_2$ .

convex lenses become divergent, thus reversing the behavior of lenses made from ordinary media [6]. However, the most interesting effect that can be deduced from the geometrical optics of left-handed media is probably the focusing of energy coming from a point source by a left-handed slab [6]. This effect is illustrated in Figure 1.3. For paraxial rays

$$|n| = \frac{|\sin \theta_1|}{|\sin \theta_2|} \simeq \frac{|\tan \theta_1|}{|\tan \theta_2|} = \frac{a'}{a} = \frac{b'}{b}, \quad (1.21)$$

where  $n$  is the refractive index of the left-handed slab relative to the surrounding medium. Therefore, as is illustrated in Figure 1.3, electromagnetic energy coming from the point source is focused at two points, one inside and the other outside the left-handed slab, the latter at a distance

$$x = a + a' + b' + b = d + \frac{d}{|n|} \quad (1.22)$$

from the source, where  $d$  is the width of the slab. If  $n = -1$  the aforementioned effect is not restricted to paraxial rays, because in this case  $|\theta_1| = |\theta_2|$  for any angle of incidence. In fact, when  $n = -1$ , all rays coming from the source are focused at two points, inside and outside the slab, the latter being at a distance  $2d$  from the source. We will return later to this interesting situation.

The above discussion mainly followed the earlier work of Veselago [6]. More recently, negative refraction at the interface between ordinary and left-handed media has been criticized on the basis of the highly dispersive nature of left-handed media [15]. In spite of these criticisms, negative refraction in left-handed media seems now to be well established. In fact, both theoretical calculations [16,17] and experiments [18–22] have confirmed Veselago's predictions. The reader interested in this specific topic can consult the aforementioned references for a more complete discussion.

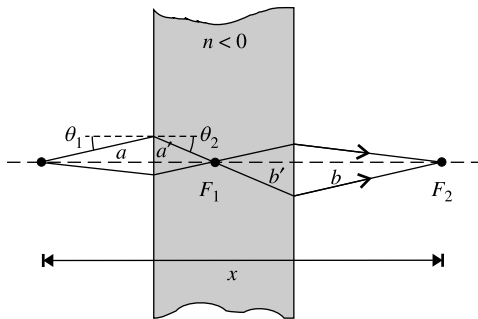


**FIGURE 1.3** Graphic illustration of the focusing of paraxial rays coming from a point source by a left-handed slab. Light focuses at two points,  $F_1$  and  $F_2$ , inside and outside the slab.

A brief discussion about the meaning and scope of the term *negative refraction* is of interest at this point. In the frame of this section, negative refraction and negative refractive index are equivalent. That is, the incident and refracted beams always lie at the same side of the normal, and Snell's law (1.19) is satisfied with a negative refractive index that does not depend on the angle of incidence. In this *strong* sense, negative refraction seems to be a unique property of isotropic left-handed media. In a less restrictive sense, negative refraction can also be understood as the simple situation where an incident and a refracted beam both lie at the same side of the normal, for a particular angle of incidence. However, it may be worth mentioning that, in this *weak* sense, negative refraction can appear in many physical systems that may not include left-handed media, nor even media with negative parameters. As an illustration of this statement, Figure 1.4 shows the negative refraction of the extraordinary ray at the interface between an ordinary isotropic medium and an hypothetical uniaxial medium with  $\varepsilon_{\perp} > \varepsilon_{\parallel}$ . The isofrequency ellipsoids,  $\omega(\mathbf{k}) = \text{constant}$ , for the isotropic and the uniaxial media are shown for a specific orientation of the optical axis. For this specific orientation, and for the considered specific angle of incidence, the group velocity  $\nabla_{\mathbf{k}}(\omega)$  corresponding to the wavevector of the refracted ray forms a negative angle with the normal (in spite of the fact that the corresponding wavevector  $\mathbf{k}_r$  makes a positive angle with the normal). Because the direction of the refracted ray is determined by the group velocity, the refracted ray forms a negative angle with the normal. However, unlike negative refraction in left-handed media, negative refraction in uniaxial media only occurs for very specific orientations of the optical axis, and for very specific angles of incidence and polarizations of the incident light. A more restrictive concept is *all-angle negative refraction* [23]. This means that a negative refraction in the aforementioned *weak* sense is observed for all angles of incidence. All-angle negative refraction, with a refractive index depending on the angle of incidence, has been reported in uniaxial media with negative permittivity or permeability along the optical axis [9] (see problem 1.8). Generalized refraction laws at the interface

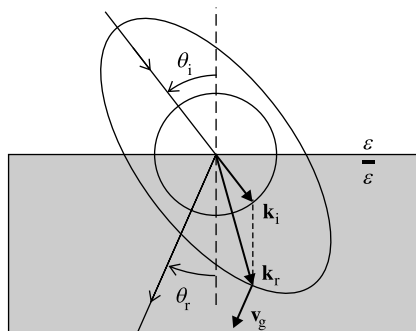


**FIGURE 1.4** Graphic demonstration of the negative refraction of the extraordinary ray at the interface between an isotropic and an uniaxial medium. The isofrequency surfaces for both media are shown, and the wavevector and the group velocity of the refracted ray are graphically obtained from these surfaces. The reported negative refraction only occurs for very specific angles of incidence and polarizations.

between anisotropic media with negative parameters are analyzed in detail in [24]. Finally, it may be worth mentioning that negative refraction has been also reported in strongly modulated photonic crystals for some specific frequency bands [25].

## 1.5 FERMAT PRINCIPLE

As is shown in many textbooks, Snell's law can be deduced from the variational Fermat principle, and vice versa. The variational Fermat principle states that the optical length of the path followed by light between two fixed points, A and B, is an extremum. The optical length is defined as the physical length multiplied by the refractive index of the material. Therefore, the Fermat principle is stated as

$$\delta L = 0, \quad \text{where} \quad L = \int_A^B n \, dl. \quad (1.23)$$

Because Snell's law (1.19) still holds for left-handed media, the Fermat principle will also hold for systems containing left-handed media, provided the appropriate definition for  $n$  (1.20) is taken in equation (1.23) [8]. It may be worth mentioning that, according to this statement of the Fermat principle, the optical length of the actual path chosen by light is not necessarily a minimum when left-handed media are present. In fact, it may even be negative or null. It also becomes apparent that the time taken by light to travel between two points is not related to the optical length through the usual formula for ordinary weakly dispersive media, that is  $t \neq L/c$ . Therefore, the path followed by light in optical systems containing left-handed media is not necessarily the shortest in time [8].

From the definition of  $L$  (1.23), it follows that the optical length between two points, A and B, on a given optical ray is proportional to the phase advance between such points:  $\Delta\phi = -k\overline{AB} = -n(\omega/c)\overline{AB} = -(\omega/c)L$ . It is of interest to evaluate the optical length between the source and the focuses,  $F_1$  and  $F_2$ , in the experiment shown in Figure 1.3 for the particular case of  $n = -1$ . It follows immediately that the optical length between the source and the focus is exactly zero for all rays (not only for paraxial rays). Thus, all the rays coming from the source are recovered at the focus with exactly the same phase as at the source. Nevertheless, because the reflection coefficient for each ray depends on the angle of incidence, the intensity of the rays is not reproduced at the focus. However, if  $\varepsilon/\varepsilon_0 \rightarrow -1$  and  $\mu/\mu_0 \rightarrow -1$ , the wave impedance of the slab becomes equal to that of free space, and the reflection coefficient vanishes for all rays. In such a case, it can be shown that the electromagnetic field at the source is exactly reproduced at the focus [26]. We will return later to this point.

## 1.6 OTHER EFFECTS IN LEFT-HANDED MEDIA

Backward-wave propagation in left-handed media also has implications in other well-known physical effects related to electromagnetic wave propagation. The following text considers some of them.

### 1.6.1 Inverse Doppler Effect

When a moving receiver detects the radiation coming from a source at rest in a uniform medium, the detected frequency of the radiation depends on the relative velocity of the emitter and the receiver. This is the well-known Doppler effect. If this relative velocity is much smaller than the velocity of light, a nonrelativistic analysis suffices to describe such an effect. The qualitative analysis is quite simple for ordinary ( $n > 0$ ) media, and can be found in many textbooks. If the receiver moves towards the source, wavefronts and receiver move in opposite directions. Therefore, the frequency seen by the receiver will be higher than the frequency measured by an observer at rest. However, if the medium is a left-handed material, wave propagation is backward, and wavefronts move towards the source. Therefore, both the receiver and the wavefronts move in the same direction, and the frequency measured at the receiver is smaller than the frequency measured by an observer at rest.

A straightforward calculation shows that the aforementioned frequency shifts are given by

$$\Delta\omega = \pm \omega_0 \frac{v}{v_p}, \quad (1.24)$$

where  $\omega_0$  is the frequency of the radiation emitted by the source,  $v$  is the velocity at which the receiver moves *towards* the source,  $v_p$  the phase velocity of light in the medium, and the  $\pm$  sign applies to ordinary/left-handed media. Equation (1.24) can be written in a more compact form as [6]

$$\Delta\omega = \omega_0 \frac{nv}{c}, \quad (1.25)$$

where  $n$  is the refractive index of the medium and  $c$  the velocity of light in free space. In equation (1.25),  $\Delta\omega$  is the difference between the frequency detected at the receiver and the frequency of oscillation of the source. For  $n < 0$ , the frequency shift becomes negative for positive  $v$  (receiver moving towards the source), as it was qualitatively shown at the beginning of this section. Interestingly, from equation (1.17), it directly follows that  $d|k|/d\omega < 0$  in left-handed media. Thus, a negative frequency shift results in an increase of  $|k|$ . Therefore, a shift towards shorter wavelengths is seen when the receiver approaches the source, both in ordinary and left-handed media.

### 1.6.2 Backward Cerenkov Radiation

Cerenkov radiation occurs when a charged particle enters an ordinary medium at a velocity higher than the velocity of light in such a medium. If the deceleration of this particle is not too high, its velocity can be considered approximately constant over many wave periods. Then, as is illustrated in Figure 1.5a, the spherical wavefronts radiated by this particle become *delayed* with regard to the particle motion,

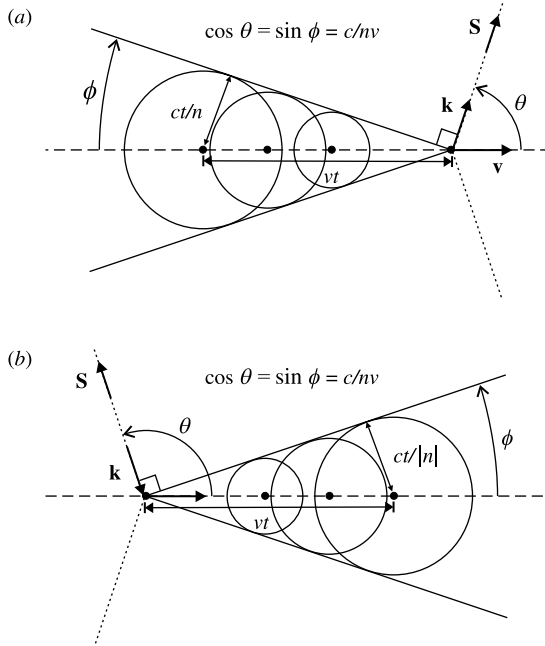


**FIGURE 1.5** Illustration of the formation of Cerenkov shock waves: (a) in an ordinary medium, and (b) in a left-handed medium. In (a) the spherical wavefronts move outwards from the source at a velocity  $c/n$ . In (b) the spherical wavefronts move inwards to the source at a velocity  $c/|n|$ .

thus giving rise to a *shock wave* [1], which travels forward, making an angle  $\theta$  with the particle velocity. This angle is given by

$$\cos \theta = \frac{c}{nv}, \tag{1.26}$$

where  $c/n$  is the velocity of light in the medium and  $v$  the velocity of the particle.

If the medium has a negative refractive index, wave propagation is backward, and the spherical wavefronts corresponding to each frequency harmonic of the radiation move inwards to the source, at a velocity  $c/|n(\omega)|$ . Therefore, each wavefront collapses at the advanced position of the particle shown in Figure 1.5b. Thus, the resulting shock wave travels backward at an obtuse angle from the particle motion. This angle is still given by equation (1.26) [6], as is illustrated in the figure.

In practice, any left-handed medium must be highly dispersive, the left-handed behavior being restricted to some frequency range. Because the particle radiates at all frequencies, the Cerenkov radiation spectra must show wavefronts moving in both forward and backward directions [27].

### 1.6.3 Negative Goos–Hänchen Shift

When a plane wave is incident from a medium of refractive index  $n = n_1$  onto the plane interface of another medium with  $n = n_2$ , where  $|n_2| < |n_1|$ , there is a critical angle  $\sin \theta_c = |n_2/n_1|$ , beyond which total reflection onto medium 1 occurs. However, fields penetrate into medium 2 by a small distance, forming a nonuniform plane wave that is evanescent in the direction normal to the interface and propagative along the interface. Power associated with this plane wave flows parallel to the interface in the forward direction for ordinary media and in the backward direction for left-handed media. Thus, when a beam of finite extent is incident from medium 1 to medium 2, the reflected beam experiences a finite lateral shift  $\Delta$ , as a consequence of the aforementioned energy flow in medium 2. This effect is illustrated in Figure 1.6. As energy flow is parallel to wavefront propagation, the Goos–Hänchen shift must be positive in ordinary media. However, if medium 2 is a left-handed medium, energy flow and wavefront propagation are antiparallel. Therefore, the Goos–Hänchen shift must be negative in such media, as is illustrated in Figure 1.6*b*.

The Goos–Hänchen shift  $\Delta$  can be calculated by expanding the incident beam in plane waves, and studying the reflection of these waves at the interface. If the angular spectrum of the beam is not too wide, and the angle of incidence is sufficiently away from the critical and grazing angles, the Goos–Hänchen shift is given by [28]

$$\Delta = \frac{\partial \phi_r}{\partial k_{\parallel}}, \quad (1.27)$$

where  $\phi_r$  is the phase of the reflection coefficient and  $k$  is the component of the wavevector parallel to the interface (for lossless left-handed media  $|r| = 1$ , and  $\phi_r = -j \ln r$ ). The Goos–Hänchen effect in left-handed media has been analyzed in detail in [29–32]. In [33], giant Goos–Hänchen shifts due to the excitation of surface waves have been reported for stratified media including left-handed layers. In all these calculations, the sign of the Goos–Hänchen shift agrees with the predictions of Figure 1.6.

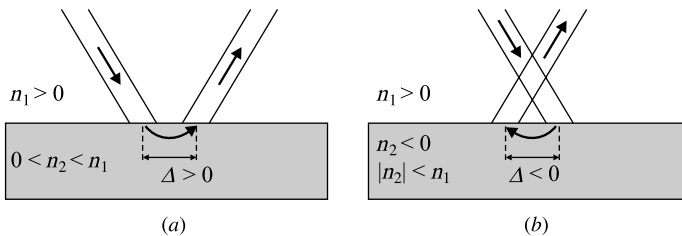


**FIGURE 1.6** Illustration of the Goos–Hänchen effect in (a) ordinary media and (b) left-handed media.

## 1.7 WAVES AT INTERFACES

So far, our analysis has been developed in the frame of the geometrical optics approximation, although with some general considerations regarding electromagnetic wave analysis. In this section we will describe in more detail the electromagnetic interactions at the interface between a left-handed medium and an ordinary medium. We will consider s-polarized waves, so that electromagnetic fields are transverse electric (or TE) along the normal to the interface (these waves are also called *longitudinal section electric*, or LSE, waves). The analysis of p-polarized (*transverse magnetic*, TM, or *longitudinal section magnetic*, LSM) waves is quite similar, and the main results can be deduced from the results for s-polarized waves by means of a duality transformation [14] (see Problem 1.7). In this and the following section we will consider transparent lossless media. Thus, unless explicitly specified, losses will be neglected, so that  $\varepsilon$  and  $\mu$  will be real quantities. This approximation, although nonphysical, is useful when losses can be considered small and propagative effects dominate.

### 1.7.1 Transmission and Reflection Coefficients

Transmission and reflection coefficients at the interface between an ordinary medium and a left-handed medium can be found using standard electromagnetic techniques. In this section we will follow the transverse transmission matrix [34] method. For this purpose, plane waves at both sides of a plane interface will be decomposed into propagative positive (+) and negative (-) waves, with a common wavevector component parallel to the interface (the  $k_z$  component in Fig. 1.7). For the plane

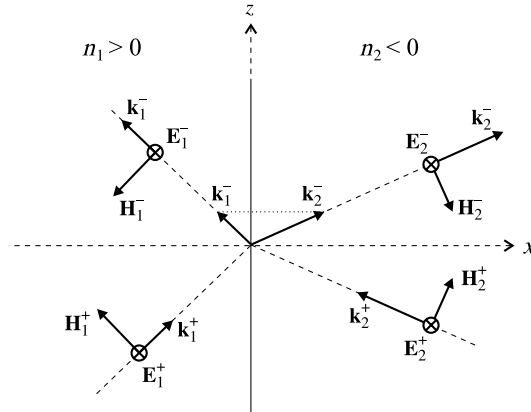


**FIGURE 1.7** Definition of positive and negative waves for the determination of the transverse transmission matrix at the interface between an ordinary medium and a left-handed medium. Note that backward propagation in the left-handed medium has been taken into account in the definition of positive and negative waves.



interface shown in Figure 1.7, and for the considered s-polarized waves,

$$E_i \equiv E_{y,i} = E_i^+ + E_i^-, \quad (1.28)$$

where subindex  $i = 1$  ( $i = 2$ ) stands for the fields at the left-(right-)hand side of the interface (at  $x = 0$ ). Positive waves are defined as those waves carrying energy along the positive axis perpendicular to the interface. Thus, if the interface is perpendicular to the  $x$ -axis, as in Figure 1.7, the field dependence of positive and negative waves can be summarized as

$$E_i^\pm \equiv E_{y,i}^\pm \propto \exp(\mp jk_{x,i}x - jk_zz + j\omega t), \quad (1.29)$$

where  $k_z$  is the common wavevector component parallel to the interface. According to backward propagation, in the left-handed half space,  $k_{x,2} = \sqrt{\omega^2 \varepsilon_2 \mu_2 - k_z^2}$  must be chosen with  $\text{Re}(k_{x,2}) < 0$ . For ordinary media  $k_{x,1}$  must be chosen with  $\text{Re}(k_{x,1}) > 0$ , as usual.

A key magnitude in our analysis is the wave impedance of each medium,  $Z_i$ , which is defined as the ratio between the transverse (to  $x$ ) components of the electric and magnetic fields for positive waves propagating in such media. For the considered TE waves, a straightforward calculation leads to the result [1,34]

$$Z_i \equiv \frac{E_i^+}{H_{z,i}^+} = \frac{\omega \mu_i}{k_{x,i}}, \quad (1.30)$$

where  $E_i^+ \equiv E_{y,i}^+$  is the electric field component of the positive wave. As both  $\mu_2$  and  $k_{x,2}$  are negative in the left-handed medium, the impedance (1.30) is positive, as is required for passive media.

After expanding the transverse electric and magnetic fields at the left ( $i = 1$ ) and the right ( $i = 2$ ) sides of the interface into positive and negative waves ( $E_i = E_i^+ + E_i^-$  and  $H_{z,i} = H_{z,i}^+ + H_{z,i}^- = (E_i^+ - E_i^-)/Z_i$ ), and after imposing the continuity of the these field components at the interface, the transverse transmission matrix is determined as

$$\begin{pmatrix} E_1^+ \\ E_1^- \end{pmatrix} \equiv \bar{T} \cdot \begin{pmatrix} E_2^+ \\ E_2^- \end{pmatrix} = \frac{1}{2Z_2} \begin{pmatrix} Z_2 + Z_1 & Z_2 - Z_1 \\ Z_2 - Z_1 & Z_2 + Z_1 \end{pmatrix} \cdot \begin{pmatrix} E_2^+ \\ E_2^- \end{pmatrix}. \quad (1.31)$$

From this result, the transmission,  $t$ , and reflection,  $r$ , coefficients are readily obtained by taking  $E_1^+ = 1$ ,  $E_1^- = r$ ,  $E_2^+ = t$ ,  $E_2^- = 0$ ; that is,

$$\begin{pmatrix} 1 \\ r \end{pmatrix} = \frac{1}{2Z_2} \begin{pmatrix} Z_2 + Z_1 & Z_2 - Z_1 \\ Z_2 - Z_1 & Z_2 + Z_1 \end{pmatrix} \cdot \begin{pmatrix} t \\ 0 \end{pmatrix}, \quad (1.32)$$

or

$$t = \frac{2Z_2}{Z_2 + Z_1} \quad \text{and} \quad r = \frac{Z_2 - Z_1}{Z_2 + Z_1}. \quad (1.33)$$

For the particular case of  $Z_2 = Z_1$ , from equations (1.33) it follows that  $t = 1$  and  $r = 0$ . That is, the left-handed medium is perfectly matched with the ordinary medium. From equations (1.30) it follows that this is the case for any angle of incidence if  $\varepsilon_2/\varepsilon_1 \rightarrow -1$  and  $\mu_2/\mu_1 \rightarrow -1$ .

Equations (1.33) are also valid when losses in the left-handed half space are taken into account. If, according to backward-wave propagation, we choose  $\text{Re}(k_{x,2}) < 0$  in equation (1.29), from equation (1.12) it follows that  $\text{Im}(k_{x,2}) < 0$ . Therefore, positive waves carry energy and attenuate along the positive  $x$ -axis, as is required from energy conservation. Substitution of these values of  $k_{x,2}$  in equations (1.30) and (1.33) gives the correct values for the transmission and reflection coefficients. Equations (1.33) are also valid for the total reflection case (i.e., when  $k_z^2 > \omega^2 \varepsilon_2 \mu_2$ ), provided  $k_{x,2}$  is chosen as  $k_{x,2} = -j\alpha$ ,  $\alpha = +\sqrt{k_z^2 - \omega^2 \varepsilon_2 \mu_2}$ . In this case,  $Z_2$  (1.30) is imaginary, and  $t$  and  $r$  become complex, with  $|r| = 1$ , as is required from energy conservation.

### 1.7.2 Surface Waves

Surface waves along the interface between two different media must decay at both sides of the interface. Therefore, imaginary values of  $k_{x,i}$  should be considered. From the definitions of the previous section, it follows that

$$k_{x,i} = -j\alpha_i \quad \text{and} \quad \alpha_i = +\sqrt{k_z^2 - \omega^2 \mu_i \varepsilon_i}, \quad (1.34)$$

in both ordinary and left-handed media. Therefore, positive waves in equation (1.29) will decay along the positive  $x$ -axis in both media. On the other hand, in order to obtain imaginary values of  $k_{x,i}$ , it must be that

$$k_z^2 > k_1^2, k_2^2, \quad (1.35)$$

where  $k_1$  and  $k_2$  are the wavevectors in the unbounded ordinary and left-handed media, respectively ( $k_i^2 = \omega^2 \varepsilon_i \mu_i$ ). With these definitions, surface waves correspond to solutions of the following implicit equation (see also equation (1.31):

$$\begin{pmatrix} 0 \\ E_1^- \end{pmatrix} = \frac{1}{2Z_2} \begin{pmatrix} Z_2 + Z_1 & Z_2 - Z_1 \\ Z_2 - Z_1 & Z_2 + Z_1 \end{pmatrix} \cdot \begin{pmatrix} E_2^+ \\ 0 \end{pmatrix}. \quad (1.36)$$

This equation has nontrivial solutions if  $Z_2 + Z_1 = 0$ . According to equations (1.30) and (1.34),  $Z_1$  and  $Z_2$  are both imaginary and have opposite signs in ordinary and left-handed media. Therefore, solutions to equation (1.36) can exist at the interface between these media, provided that expression (1.35) is satisfied. The general condition for the existence of such solutions is

$$k_z^2 = \frac{\mu_2^2 k_1^2 - \mu_1^2 k_2^2}{\mu_2^2 - \mu_1^2} > k_1^2, k_2^2, \quad (1.37)$$

which is also the dispersion relation for s-polarized (or TE, or LSE) surface waves. As both  $\varepsilon_2$  and  $\mu_2$  strongly depend on frequency (see Section 1.3), the frequency dependence of  $k_z(\omega)$  will depend on the specific characteristics of the left-handed medium. Dispersion curves for surface waves at the interface between free space and left-handed media have been investigated in [35,36] for some realistic frequency dependences of  $\varepsilon_2$  and  $\mu_2$ . It may be worth mentioning that similar surface waves (sometimes called surface plasmons) are guided along the interface between ordinary media and media with negative  $\varepsilon$  (see Problem 1.3). Surface waves can also be guided along the interfaces between ordinary and negative  $\mu$  media, and at the interface between a medium with negative  $\varepsilon$  and other with negative  $\mu$  [38].

Let us now consider again the limit  $\varepsilon_2/\varepsilon_1 \rightarrow -1$  and  $\mu_2/\mu_1 \rightarrow -1$ . In this limit, the above dispersion relation becomes degenerate, being satisfied for any value of  $k_z > k_1 = |k_2|$ . Thus, in this limit, the bandwidth is zero and the density of states becomes infinite. This behavior is quite similar to that of surface plasmons at the surface of an ideal plasma in the quasistatic limit (see Problems 1.2 and 1.3). However, unlike for surface plasmons, the degeneracy of the considered surface waves is complete, not being restricted to the quasistatic limit (i.e., to  $k_z \gg k_1 = |k_2|$ ).

Finally, due to the particular form of the transverse transmission matrix in equations (1.31) and (1.36), mathematical solutions corresponding to nonphysical surface waves growing to infinity at both sides of the interface show the same dispersion relation (1.37) as the aforementioned physical surface waves. Such solutions, although nonphysical for an isolated interface, will play an important role in the perfect lens configuration, as will be shown in the following.

## 1.8 WAVES THROUGH LEFT-HANDED SLABS

In this section, transmission and guidance of electromagnetic waves through left-handed slabs will be analyzed. The method of analysis will be a straightforward extension of the transverse transmission matrix technique of the previous section. The same method can be applied to the analysis of transmission and guidance of waves through multilayered structures.

### 1.8.1 Transmission and Reflection Coefficients

The transmission matrix for a left-handed slab of width  $d$  is obtained by simply cascading the transmission matrices for each interface (1.31) and for the left-handed medium in between,

$$\begin{pmatrix} E_1^+ \\ E_1^- \end{pmatrix} = \frac{1}{4Z_2Z_3} \begin{pmatrix} Z_2 + Z_1 & Z_2 - Z_1 \\ Z_2 - Z_1 & Z_2 + Z_1 \end{pmatrix} \cdot \begin{pmatrix} e^{jk_{x,2}d} & 0 \\ 0 & e^{-jk_{x,2}d} \end{pmatrix} \cdot \begin{pmatrix} Z_3 + Z_2 & Z_3 - Z_2 \\ Z_3 - Z_2 & Z_3 + Z_2 \end{pmatrix} \cdot \begin{pmatrix} E_3^+ \\ E_3^- \end{pmatrix}, \quad (1.38)$$

where, using the same notation as in equation (1.31), we have considered s-polarized waves. In equation (1.38)  $k_{x,2} = -\sqrt{\omega^2\mu_2\varepsilon_2 - k_z^2} < 0$  is the  $x$ -component of the propagation constant for positive waves inside the slab, and subscripts 1, 2, and 3 stand for the left-handed medium (2) and for the media at the left- and the right-hand sides of the slab (1 and 3).  $Z_i$  are the wave impedances (1.30), and electric fields are evaluated just on the left ( $E_1^\pm$ ) and on the right ( $E_3^\pm$ ) interfaces of the slab. All waves inside and outside the slab have a common propagation vector,  $k_z$ , parallel to the slab interface, which determines the angle of incidence  $\sin \theta_i = k_z/k_1$ .

In the following, media 1 and 3 will be considered identical, so that  $Z_3 = Z_1$ . In this case, the transmission and reflection coefficients,  $t$  and  $r$ , are obtained from equation (1.38) by taking  $E_1^+ = 1$ ,  $E_1^- = r$ ,  $E_3^+ = t$ ,  $E_3^- = 0$ . After a straightforward calculation, the following expressions arise:

$$t = \frac{2Z_1Z_2}{j(Z_1^2 + Z_2^2) \sin(k_{x,2}d) + 2Z_1Z_2 \cos(k_{x,2}d)} \quad (1.39)$$

and

$$r = \frac{Z_2^2 - Z_1^2}{Z_2^2 + Z_1^2 - 2jZ_1Z_2 \cot(k_{x,2}d)}. \quad (1.40)$$

Note that  $k_{x,2} < 0$ , so the phase advance through the slab is positive for small values of  $k_{x,2}d$ , which corresponds to the propagation of a backward wave inside the slab.

### 1.8.2 Guided Waves

Waves guided along the slab correspond to the poles of the reflection coefficient (1.40) that may appear for imaginary values of  $k_{x,1}$ . In such cases, according to our previous definitions,  $k_{x,1} = -j\alpha_1$ , with  $\alpha_1 = \sqrt{k_z^2 - \omega^2\varepsilon_1\mu_1} > 0$ . Therefore,

surface waves correspond to solutions of the implicit equation

$$Z_2^2 + Z_1^2 - 2jZ_1Z_2 \cot(k_{x,2}d) = 0, \quad \text{with } Z_1 = j\frac{\omega\mu_1}{\alpha_1}, \quad (1.41)$$

with the additional condition  $k_z > k_1$ , so that electromagnetic energy decays at both sides of the slab. Two cases may arise in equation (1.41), depending on whether  $k_{x,2}$  is real or imaginary. If  $k_z < k_2 = \omega\sqrt{\epsilon_2\mu_2}$ ,  $k_{x,2}$  is real and fields inside the slab have a trigonometric dependence, so that they are *volume waves*. In that case equation (1.41) reduces to

$$\frac{\mu_2\alpha_1}{\mu_1 k_{x,2}} - \frac{\mu_1 k_{x,2}}{\mu_2\alpha_1} + 2 \cot(k_{x,2}d) = 0, \quad (1.42)$$

which, taking into account the trigonometric relation  $2 \cot(2x) = \cot x - \tan x$ , can be written as

$$\left( \frac{\mu_2\alpha_1}{\mu_1 k_{x,2}} \tan(k_{x,2}d/2) + 1 \right) \left( \frac{\mu_1 k_{x,2}}{\mu_2\alpha_1} \tan(k_{x,2}d/2) - 1 \right) = 0, \quad (1.43)$$

which is the implicit dispersion relation for guided volume waves. In equation (1.43) the two branches, corresponding to symmetric and antisymmetric modes, are explicitly shown. As can be seen from the above dispersion relations, volume waves in the left-handed slabs do not substantially differ from guided volume waves in ordinary dielectric slabs [34]; waves inside the slab can be seen as the composition of two propagating TEM waves, which suffer total reflection at the slab interfaces. Therefore energy flow is backward inside the left-handed slab and forward outside the slab, the whole wave being forward or backward depending on the structural parameters of the waveguide.

If  $k_z > k_2 = \omega\sqrt{\epsilon_2\mu_2}$ , electromagnetic fields show an exponential decay inside the slab, and the guided waves become *surface waves*. They correspond to the coupling between the surface waves generated at each slab interface (see Section 1.7.2). Therefore, when  $d \rightarrow \infty$ , these waves should converge to the surface waves found in Section 1.7.2. For these surface waves, both  $Z_1$  and  $Z_2$  are imaginary and  $\cot(k_{x,2}d)$  becomes a hyperbolic function. Thus, equation (1.41) reduces to

$$\frac{\mu_2\alpha_1}{\mu_1\alpha_2} + \frac{\mu_1\alpha_2}{\mu_2\alpha_1} + 2 \coth(\alpha_2d) = 0, \quad (1.44)$$

which, taking into account the relation  $2 \coth(2x) = \coth x + \tanh x$ , can be written as

$$\left( \frac{\mu_2\alpha_1}{\mu_1\alpha_2} \tanh(\alpha_2d/2) + 1 \right) \left( \frac{\mu_1\alpha_2}{\mu_2\alpha_1} \tanh(\alpha_2d/2) + 1 \right) = 0, \quad (1.45)$$

where the two branches, corresponding to symmetric and antisymmetric modes, can be appreciated. The specific dependence of  $k_z$  on frequency will depend on the specific dependence of  $\varepsilon$  and  $\mu$  on  $\omega$ . Surface and volume guided waves in left-handed slabs, also including metallic ground shields, have been analyzed in [37–43]. Finally, it would be worth mentioning that resonant modes in other geometries distinct from planar ones, such as spherical or cylindrical, have been also studied (see, for instance, [44–47], and references therein).

### 1.8.3 Backward Leaky and Complex Waves

As in any open guiding system, most of the electromagnetic modes guided by a left-handed slab leak power to the surrounding space [13,34]. These waves correspond to the poles of the reflection coefficient (1.40) that may appear for complex values of  $k_{x,1}$ .

Leaky modes in a left-handed slab have been analyzed in [48]. In the following we will consider, without loss of generality, a leaky wave with field dependence  $\exp(-jk_z z + j\omega t)$ , and  $\text{Re}(k_z) > 0$ . The wavenumber of such a leaky mode should satisfy  $\text{Re}(k_z) < k_1 \equiv \omega\sqrt{\varepsilon_1\mu_1}$ , so that power leaks at an angle  $\cos\theta = \text{Re}(k_z)/k_1$  from the slab (Fig. 1.8). Inside the left-handed slab, power flow is backward, but in the surrounding medium, outside the slab, power flows in the forward direction. Therefore, for the analyzed leaky mode, power always leaks *backward* with regard to the main stream of guided power, inside the slab. For this reason, such leaky modes have been called *backward leaky modes* [48].

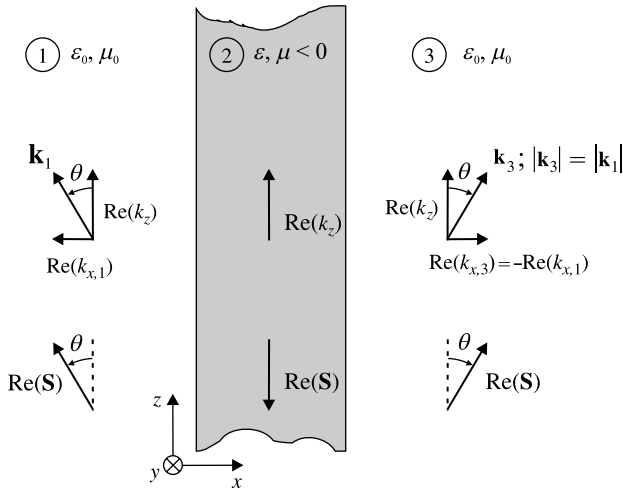


**FIGURE 1.8** Illustration of the wavevectors and power flows in a backward leaky mode guided by a left-handed slab.  $\text{Re}(k_z)$  is the mode phase vector, and  $\text{Re}(\mathbf{S})$  shows the power flux inside and outside the slab. The angle of leakage is determined by  $\cos\theta = \text{Re}(k_z)/k_1$ .

Physical leaky modes can be excited by sources at the onset of a semi-infinite guiding system. In such a configuration, power is guided along the waveguide, from the source to its end. Considering Figure 1.8, this means that the source must be located at the top of the figure. Therefore, it must be that  $\text{Im}(k_z) > 0$ , so that the leaky wave attenuates towards the lower end of the slab. On both sides of the slab the field dependence must be of the kind  $\exp(\mp jk_x x - k_z z + j\omega t)$ . On the other hand, boundary conditions impose that  $k_z^2 + k_x^2 = k_1^2$ , so that, for small attenuating constants,

$$k_1^2 \simeq \{\text{Re}(k_z)\}^2 + \{\text{Re}(k_x)\}^2 \quad (1.46)$$

$$0 = \text{Re}(k_z)\text{Im}(k_z) + \text{Re}(k_x)\text{Im}(k_x). \quad (1.47)$$

The first equation defines the leakage angle mentioned at the beginning of this section. The second determines the sign of  $\text{Im}(k_x)$  as follows: at the left-hand side of the slab, power must flow to the left, so that  $\text{Re}(k_z) > 0$  and  $\text{Re}(k_x) < 0$ . Moreover,  $\text{Im}(k_z) > 0$ , as has already been mentioned. Therefore, it must be that  $\text{Im}(k_x) > 0$ , so that backward leaky waves are attenuated in the transverse direction. This result is somewhat unexpected, as leaky modes in ordinary guiding systems are usually unbounded modes, whose amplitude grows to infinity in the transverse direction [34,49]. This unusual behavior of leaky modes in left-handed slabs is a direct consequence of the reported backward leakage of power [48], and recalls the behavior of the complex modes that may appear in some very inhomogeneous wave-guiding systems [13]. Backward leakage of power in a circuit analogous to an open left-handed waveguide has been experimentally reported in [50].

## 1.9 SLABS WITH $\varepsilon/\varepsilon_0 \rightarrow -1$ AND $\mu/\mu_0 \rightarrow -1$

As has already been mentioned, many striking properties of left-handed media arise in the limit when  $\varepsilon$  and  $\mu$  become equal in magnitude, but opposite in sign, as in those of the surrounding medium. In this section we will analyze these properties in detail. For simplicity, the surrounding medium is considered free space.

### 1.9.1 Phase Compensation and Amplification of Evanescent Modes

If  $\varepsilon/\varepsilon_0 \rightarrow -1$  and  $\mu/\mu_0 \rightarrow -1$ , the left-handed wave impedances (1.30) of the left-handed medium become identical to that of free space for any propagative wave, and for any angle of incidence. Therefore, for any angle of incidence, the transmission matrix at each slab interface (1.31) reduces to unity. Thus, the slab is perfectly matched to free space. Even more interesting, because wave propagation is backward inside the left-handed slab, the phase advance inside the slab is positive, and can be exactly compensated by the phase advance outside the slab (which must be negative). A straightforward calculation shows that this compensation actually happens—for

any angle of incidence—when the distance between the input and output planes is  $2d$ , where  $d$  is the slab width. In fact, this last property is a direct consequence of the zero optical length between the input and output planes already mentioned in Section 1.5

Let us now consider the incidence of evanescent waves on the slab. In this case, after substitution in equations (1.30), (1.39), and (1.40) (with  $k_{x,1} = k_{x,2} = -j\alpha$ ;  $\alpha = +\sqrt{k_z^2 - \varepsilon_0\mu_0}$ ), it is readily shown that

$$t = e^{\alpha d} \quad \text{and} \quad r = 0. \quad (1.48)$$

Thus, evanescent plane waves are *amplified* inside the left-handed slab by a factor that is just the attenuation constant at the input. Because evanescent modes do not carry energy, this amplification, although striking, is not forbidden by energy conservation. Interestingly, when the input and output planes are separated by a distance  $2d$ , the amplitude of any incident evanescent wave is recovered at the output. Thus, for this specific location of the input and output planes, both propagating and evanescent waves are recovered without change at the output.

Phase compensation and amplification of evanescent modes is not a unique property of left-handed slabs. After attention was first drawn to this effect by Pendry [26], it was also shown in a pair of consecutive slabs with only negative  $\varepsilon$  and  $\mu$  [51,52] and, for some specific polarizations and planes of incidence, in some anisotropic slabs with negative parameters [53]. It has also been shown in a pair of coupled resonant surfaces [54]. Some of these results have been summarized in a *generalized perfect lens theorem* [55].

### 1.9.2 Perfect Tunneling

As is well known, when a wave is incident from a medium of refractive index  $n = n_1$  onto the plane interface of another medium of  $n = n_2$ , where  $|n_2| < |n_1|$ , there is a critical angle  $\theta_c = \sin^{-1}|n_2/n_1|$  beyond which total reflection onto medium 1 occurs. However, if medium 2 is substituted by a slab of finite thickness, and the slab is not too thick, some amount of energy can tunnel through medium 2 onto the medium behind the slab. For ordinary media, the power tunneled through the slab is always smaller than the incident power, so there is also some reflected power. This tunneling of power is due to the coupling of evanescent waves generated at both sides of the slab. Thus, because a left-handed slab can restore the amplitude of evanescent waves (as was shown in the previous section), it can be guessed that tunneling through left-handed slabs can be very significant. In fact, as will be shown in this section, under some circumstances such tunneling of power can be so high that all the incident power will flow through the slab. This “perfect tunneling” effect will be analyzed in this section.

Instead of analyzing incidence in free space, a different but fully equivalent system will be analyzed. This system is shown in Figure 1.9, and consists of a rectangular waveguide that includes a section filled with a left-handed medium with  $\varepsilon/\varepsilon_0 \rightarrow -1$  and



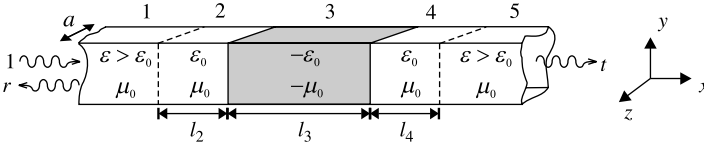


**FIGURE 1.9** Illustration of a device designed to study perfect tunneling and amplification of evanescent waves in a waveguide. The device consists of five consecutive waveguides with the same cross-section. Input and output waveguides (1 and 5) are above cutoff. Waveguides 2 to 4 are below cutoff. Waveguides 2 and 4 are empty. Waveguide 3 is filled with an isotropic left-handed medium with  $\varepsilon = -\varepsilon_0$ ,  $\mu = -\mu_0$ , and  $l_3 = l_2 + l_4$ .

$\mu/\mu_0 \rightarrow -1$ . As is well known [1,34], the fundamental mode in a rectangular waveguide is the  $\text{TE}_{1,0}$  mode, which corresponds to the composition of two propagating s-polarized plane waves ( $\mathbf{E} = E_y \hat{\mathbf{y}}$ ), which are reflected by the lateral sidewalls of the waveguide, giving rise to a stationary wave in the transverse direction and a propagating wave along the waveguide axis:  $E_y \propto \sin(\pi z/a) \exp(-jk_x x + j\omega t)$ . This mode is propagative/evanescent if the waveguide width is larger/smaller than a half-wavelength ( $a \geq \pi/k$ , where  $k = \omega/\sqrt{\mu\varepsilon}$ ). Therefore, evanescent plane waves are generated in sections 2 to 4 of Figure 1.9 if  $a < \pi/k_0$ , where  $k_0 = \omega\sqrt{\mu_0\varepsilon_0}$ . In order to excite this evanescent mode, we can simply place at the input a waveguide filled by a high-permittivity dielectric, supporting a propagative  $\text{TE}_{1,0}$  mode incident on section 2 (if the cross-sections of both waveguides are identical, no other modes will be generated at the interface [34]). It can be easily realized that such a system is equivalent to the incidence of two identical s-polarized waves coming from a semi-infinite medium (medium 1) onto a slab formed by media 2 to 4, and with a semi-infinite medium (medium 5) at the end of the system. The angle of incidence is  $\theta = \sin^{-1}\{\pi/(ka)\}$ , where  $k^2 = \omega^2\varepsilon\mu_0$ , and incidence by an angle higher than the critical angle corresponds to the excitation of evanescent modes at waveguide sections 2 to 4 of Figure 1.9. Thus, a system such as that shown in this figure is fully equivalent, from an analysis standpoint, to a composite slab made of media 2 to 4, sandwiched between two semi-infinite media (1 and 5). However, the system of Figure 1.9 is easier to implement for an experimental verification of tunneling effects.

Let us now analyze the behavior of the device. When a propagative  $\text{TE}_{1,0}$  mode is incident from waveguide 1, evanescent  $\text{TE}_{1,0}$  modes are generated in waveguides 2 to 4 and, eventually, some power may tunnel to waveguide 5. Following our previous analysis, transmission and reflection coefficients can be obtained from the implicit equation

$$\begin{pmatrix} 1 \\ r \end{pmatrix} = \frac{1}{2Z_2} \begin{pmatrix} Z_2 + Z_1 & Z_2 - Z_1 \\ Z_2 - Z_1 & Z_2 + Z_1 \end{pmatrix} \cdot \begin{pmatrix} e^{\alpha_2 l_2} & 0 \\ 0 & e^{-\alpha_2 l_2} \end{pmatrix} \\ \cdot \frac{1}{2Z_3} \begin{pmatrix} Z_3 + Z_2 & Z_3 - Z_2 \\ Z_3 - Z_2 & Z_3 + Z_2 \end{pmatrix} \cdot \begin{pmatrix} e^{\alpha_3 l_3} & 0 \\ 0 & e^{-\alpha_3 l_3} \end{pmatrix}$$

$$\begin{aligned} & \cdot \frac{1}{2Z_4} \begin{pmatrix} Z_2 + Z_3 & Z_2 - Z_3 \\ Z_2 - Z_3 & Z_2 + Z_3 \end{pmatrix} \cdot \begin{pmatrix} e^{\alpha_2 l_4} & 0 \\ 0 & e^{-\alpha_2 l_4} \end{pmatrix} \\ & \cdot \frac{1}{2Z_1} \begin{pmatrix} Z_1 + Z_2 & Z_1 - Z_2 \\ Z_1 - Z_2 & Z_1 + Z_2 \end{pmatrix} \cdot \begin{pmatrix} t \\ 0 \end{pmatrix}, \end{aligned} \quad (1.49)$$

where  $\alpha_i$  are the attenuation constants of the TE<sub>1,0</sub> mode in waveguides 2, 3, and 4 ( $\alpha_i = +\sqrt{(\pi/a)^2 - \omega^2 \mu_i \varepsilon_i}$ ), and  $Z_i$  are the wave impedances (1.30) for each mode, with  $k_{x,i} = -j\alpha_i$ ,

$$Z_i = j \frac{\omega \mu_i}{\alpha_i}; \quad i = 2, 3, 4. \quad (1.50)$$

In the limit  $\varepsilon/\varepsilon_0 \rightarrow -1$  and  $\mu/\mu_0 \rightarrow -1$ ,  $Z_3 = -Z_2$ , and we obtain

$$t = 1 \text{ and } r = 0, \quad \text{for } l_2 + l_4 = l_3. \quad (1.51)$$

That is, total transmission is obtained for the appropriate waveguide lengths. This total transmission is not a Fabry–Perot resonance, because all waves between the input and the output are evanescent. It is a perfect tunneling of power between input and output [56].

Interestingly, the condition for perfect tunneling coincides with the condition for focusing (1.22) when  $n = -1$ , and with the condition for amplitude and phase restoration (see Sections 1.4 and 1.9.1). In fact, if  $l_2 + l_4 \neq l_3$ , the amount of power tunneled through the device decreases. This effect is illustrated in Figure 1.10, where the

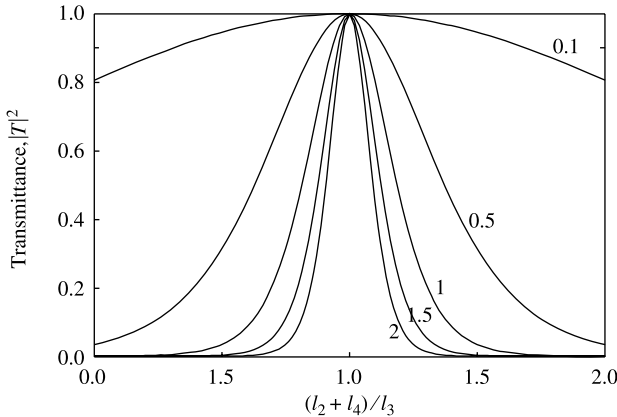


**FIGURE 1.10** Transmitted power through the device of Figure 1.9 versus the ratio  $(l_2 + l_4)/l_3$  for several values of  $l_3/\lambda_0$  (values given close to the lines). The waveguide width is  $a = 0.8 \lambda_0/2$ . The dielectric constant of sections 1 and 5 is  $\varepsilon = 2\varepsilon_0$ . (Source: Reprinted with permission from [56]; copyright 2005 by the American Physical Society.)

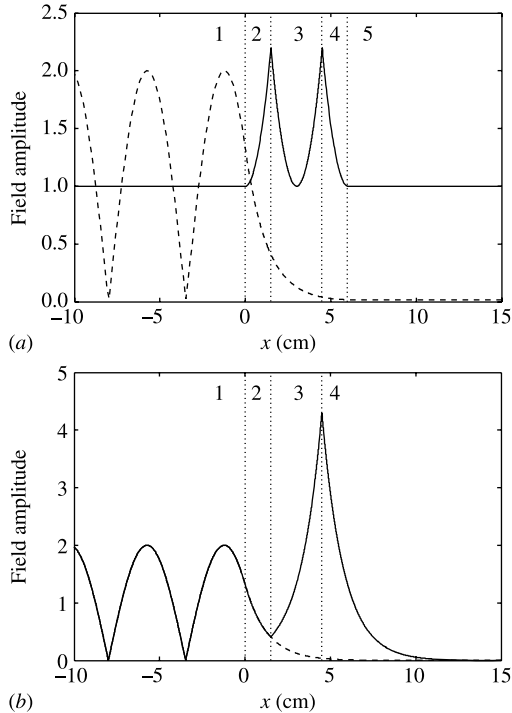


**FIGURE 1.11** Field amplitude distribution inside the structure of Figure 1.9. (a) Perfect tunneling when  $l_3 = l_2 + l_4$ . (b) Field amplitude when the last transition is eliminated ( $l_4 \rightarrow \infty$ ). Dashed lines show the amplitude when waveguide 3 is empty. Geometrical dimensions are  $a = 24$  mm,  $l_2 = l_4 = 15$  mm,  $l_3 = 30$  mm, and the operating frequency is 5 GHz. The dielectric constant of sections 1 and 5 is  $\epsilon = 2\epsilon_0$ . (Source: Reprinted with permission from [56]; copyright 2005 by the American Physical Society.)

fraction of power tunneled through the device is shown as a function of  $(l_2 + l_4)/l_3$ . The sensitivity of the device to the normalized length of the left-handed slab  $l_3/\lambda_0$  ( $\lambda_0$  is the free-space wavelength at the frequency of operation) can also be observed. As can be expected, this sensitivity is higher for larger slabs.

In order to clarify the relation between perfect tunneling and amplification of evanescent waves, it is illustrative to analyze field amplitudes along the device of Figure 1.9 for the perfect tunneling configuration, and when the output waveguide is eliminated ( $l_4 \rightarrow \infty$ ).<sup>2</sup> Both amplitudes are shown in Figure 1.11. Amplification of the evanescent wave inside the left-handed medium can be clearly appreciated in Figure 1.11b. The restoration of the mode amplitude at a distance  $2l_3$  from the input can also be appreciated in this figure. However, the pattern for the wave amplitude is quite different in the perfect tunneling configuration (Fig. 1.11a). The reason

<sup>2</sup>Such amplitudes can be obtained from the amplitudes at the input by cascading the appropriate transmission matrices between the input and the plane of interest.

for this is that single evanescent modes do not carry power, and perfect tunneling implies a maximum of power transmission. To obtain this transmission peak, the composition of two symmetrical evanescent modes decaying at opposite directions is necessary. This leads to the amplitude pattern shown in Figure 1.11a.

Perfect tunneling of power through waveguides filled by metamaterials with negative parameters was proposed and demonstrated in [56], where an experimental verification of this effect was also provided. Photon tunneling through a left-handed slab in free space was analyzed in [57].

### 1.9.3 The Perfect Lens

The perfect lens is one of the most fascinating devices that can be designed by using the striking optical properties of left-handed materials. This configuration was first proposed by Pendry in his seminal paper of 2000 [26]. In this paper Pendry showed how the amplitude of evanescent waves can be restored by a left-handed slab, and how using this property, a perfect lens overcoming the diffraction limit for the resolution of conventional lenses can be designed.

Before showing how the properties of left-handed slabs can be used to improve lens resolution, the limitations imposed by Fourier optics to the resolution of a lens will be described in detail. Following [26], we will consider an infinitesimal dipole of frequency  $\omega$  in front of a lens. The electric field produced by this dipole can be expanded in some two-dimensional Fourier integral of plane waves (spatial Fourier harmonics),

$$\mathbf{E}_p(x, y, z) = \int_{-\infty}^{\infty} dk_y \int_{-\infty}^{\infty} dk_z \mathbf{E}(k_y, k_z) \exp(-jk_x x - jk_y y - jk_z z + j\omega t), \quad (1.52)$$

where  $k_x = \sqrt{\omega^2 \varepsilon_0 \mu_0 - k_y^2 - k_z^2}$ . The response of any optical system to this excitation can be obtained by analyzing the scattering of each plane wave of (1.52), and then adding up for all the scattered waves. However, optical systems are usually only sensitive to propagating waves, that is, to waves with real values of  $k_x$  (the  $x$ -axis is assumed to be the axis of the system). Evanescent waves are usually strongly attenuated and do not reach the image. Therefore, even for the best manufactured lens, the resolution at the image is limited by the truncation of the expansion (1.52) to

$$\mathbf{E}_p(x, y, z) \simeq \int_{-k_{\max}}^{k_{\max}} dk_y \int_{-k_{\max}}^{k_{\max}} dk_z \mathbf{E}(k_y, k_z) \exp(-jk_x x - jk_y y - jk_z z + j\omega t), \quad (1.53)$$

where  $k_{\max} = k_0 = \omega \sqrt{\varepsilon_0 \mu_0}$ . Equation (1.53) gives the *effective* source seen by the optical system. Therefore, from a well-known rule of Fourier analysis, it immediately follows that the aforementioned infinitesimal dipole is restored at the image with a resolution  $\Delta$  not better than a wavelength ( $\Delta \geq 2\pi/k_0 = \lambda_0$ ).

The above analysis is based on the assumption that any lens or optical system will lose all the information contained in the evanescent Fourier harmonics of the source

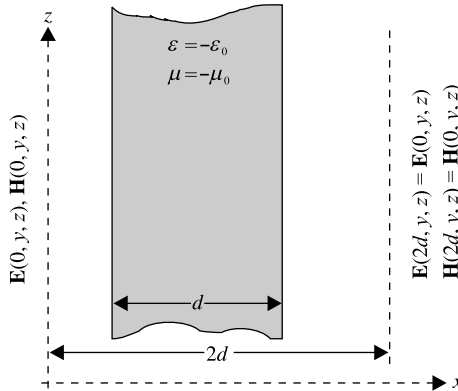


**FIGURE 1.12** Illustration of the perfect lens proposed in [26]. The fields at  $x = 0$  ( $\mathbf{E}(0, y, z)$  and  $\mathbf{H}(0, y, z)$ ) are exactly reproduced at  $x = 2d$ :  $\mathbf{E}(0, y, z) = \mathbf{E}(2d, y, z)$  and  $\mathbf{H}(0, y, z) = \mathbf{H}(2d, y, z)$ , provided there are no sources between the planes  $x = 0$  and  $x = 2d$ .

field expansion (1.52). However, we have already seen how a left-handed slab of width  $d$ , and  $\varepsilon/\varepsilon_0 \rightarrow -1$ ,  $\mu/\mu_0 \rightarrow -1$  can restore the amplitude and phase of any incident plane wave at a distance  $2d$  from the input, both for propagative and evanescent waves. Therefore, it is the whole field at the source (1.52) that is restored at  $x = 2d$ , not the truncated expansion (1.53). That is, left-handed slabs in the limit  $\varepsilon/\varepsilon_0 \rightarrow -1$  and  $\mu/\mu_0 \rightarrow -1$  behave as perfect lenses, translating the whole field distribution on a plane at the left side of the slab to another plane at the right side of the slab, as is shown in Figure 1.12.

It is illustrative to analyze the role of surface waves in the restoration of the evanescent Fourier harmonics at the image plane. Figure 1.13 shows the amplitude pattern for one of these evanescent Fourier harmonics between  $x = 0$  and  $x = 2d$ . The physical and nonphysical surface waves mentioned at the end of Section 1.7.2 can be easily recognized in the amplitude curves of Figure 1.13. Therefore, the restoration of an evanescent Fourier harmonic in the perfect lens is due to the excitation of a physical surface wave at the right interface of the slab. This physical surface wave couples with the evanescent fields generated at the source through the excitation of a nonphysical (see the end of Section 1.7.2) surface wave<sup>3</sup> at the left interface of the slab. It may be worth mentioning that this field pattern does not imply that an actual surface wave is generated at the slab. In fact, it can be easily realized that equation (1.45) has no solutions for  $\varepsilon/\varepsilon_0 = \mu/\mu_0 = -1$  (except for the trivial case of  $d \rightarrow \infty$ ). In fact, the generation of such slab surface waves would be undesirable, because it would imply a disproportionate contribution of the corresponding Fourier harmonic to the image.

<sup>3</sup>The denomination “nonphysical” indicates that these waves do not satisfy physical boundary conditions at infinity when they are considered in an unbounded system (they monotonically grow at both sides of the interface). However, the presence of additional boundary conditions, as in Figure 1.13, allows for its excitation.

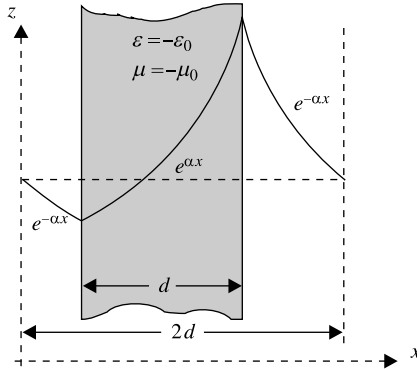


**FIGURE 1.13** Amplitude pattern for an evanescent Fourier harmonic of the perfect lens shown in Figure 1.12. The amplitude follows the curves  $\exp(\pm\alpha x)$ , where  $\alpha(k_y, k_z) = \sqrt{k_y^2 + k_z^2 - \omega^2 \varepsilon_0 \mu_0}$ .

Some considerations should be made at this point. First of all, as has already been mentioned, restoration of evanescent Fourier harmonics at  $x = 2d$  implies the amplification of such Fourier harmonics inside the slab (Fig. 1.13). As we approach the back interface of the slab, the density of energy stored by these evanescent waves grows by the exponential factor  $\exp[2\alpha(d - \delta)]$ , where  $\delta$  is the distance to the interface. In the limit  $|k_z|, |k_y| \rightarrow \infty$ , we have  $\alpha(k_y, k_z) = \sqrt{k_x^2 + k_y^2 - \omega^2 \varepsilon_0 \mu_0} \rightarrow \infty$ , and the density of energy grows to infinity at the slab interface. Therefore, the perfect lens implies a nonphysical divergence of energy [58]. Although we will return to this point later (see Section 1.10) it should be mentioned here that this apparent paradox disappears if lossy slabs are considered [59–61]. An additional effect of losses is to limit the resolution of the perfect lens. Lossy left-handed slab lenses can still improve the value of  $k_{\max}$  ( $k_{\max} > \omega\sqrt{\varepsilon_0\mu_0}$ ) in equation (1.53), but leaving it finite (see Section 1.10 for a complete discussion on this point). Therefore, it will be more appropriate to speak about lossy left-handed superlenses, which approach Pendry’s perfect lens when losses approach to zero.

Other considerations of interest arise from the comparison between the Veselago lens (see Fig. 1.3) and Pendry’s perfect lens. For this purpose we will consider the image of a point source created by both lenses. A Veselago lens, with  $n < 0$  but  $\varepsilon/\varepsilon_0, \mu/\mu_0 \neq -1$ , will be considered first. It is a nonconventional geometrical optics system, where electromagnetic energy coming from a point source is focused into a three-dimensional spot beyond the lens, of radius not smaller than a half wavelength (this behavior is sketched in Fig. 1.14a). Therefore, superresolution is not present in the Veselago lens. Let us now consider Pendry’s perfect lens. In this device, the fields at  $x = 0$ , where the source is placed, are exactly reproduced at  $x = 2d$  (see Fig. 1.12). Therefore, from the uniqueness theorem [14], it immediately follows that the source fields in the  $x$ -interval  $[0, \infty)$  are exactly reproduced beyond the lens in the  $x$ -interval  $[2d, \infty)$ . However, nothing ensures that the source

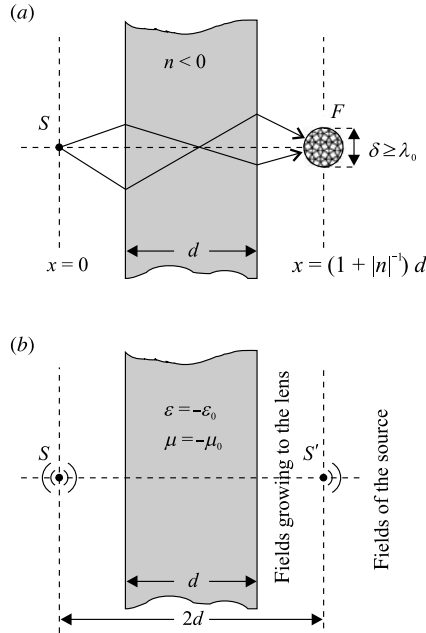


**FIGURE 1.14** Illustration of the behavior of the Veselago (a) and Pendry (b) lenses. In the Veselago lens the energy coming from a point source,  $S$ , is focused onto a spot at the focus,  $F$ , at a distance  $d + d/|n|$  from the source. The size of this spot is not smaller than a wavelength. In Pendry's perfect lens, a virtual image,  $S'$ , of a point source,  $S$ , is created at a distance  $2d$  from  $S$ . However, fields at  $x < 2d$  grow exponentially towards the lens, so there is no focusing of energy at any point.

fields for  $x < 0$  will be reproduced at  $x < 2d$ . In fact, this will be impossible, as the presence of the source implies a field divergence at  $x = 0$  that is not present at  $x = 2d$  [62]. Intuitively, it can be guessed from the amplitude pattern of Figure 1.13 that fields must grow from the image plane to the lens, regardless of behavior near the source (such behavior is sketched in Fig. 1.14b). In fact, this behavior has been confirmed by analysis [63] and experiment [64]. Therefore, Pendry's perfect lens does not focus the energy coming from a point source into any spot in three-dimensional space. Nevertheless, it still produces a two-dimensional spot on the image plane ( $x = 2d$ ), of a size that can be much smaller than a square wavelength. Therefore, Pendry's perfect lens produces two-dimensional superresolution in the image plane, but not superfocusing of energy in three-dimensional space<sup>4</sup>. This characteristic of the perfect lens (and similar devices) imposes severe limitations to its applicability for subsurface heating or burning devices. It also imposes restrictions on its usefulness

<sup>4</sup>Such three-dimensional superfocusing will be contrary to the well-known uncertainty principle, as has already been noted in [65] and [66]. It should also be mentioned that any practical lens must be lossy, and that the behavior of lossy Pendry's superlenses approaches that of Veselago lenses when the ratio  $d/\lambda_0$  increases (see Section 1.10).

in imaging devices, at least if the distance between the source and the lens is unknown. In fact, because the electromagnetic field intensity has a monotonic decay at the back side of the lens, the location of an unknown source can hardly be recovered from the analysis of the field distribution at the back side of the lens (see [63] for a complete discussion, with examples, of this point).

Experimental confirmation of subdiffraction imaging in Pendry's perfect lens has been reported in [64], and the effects of an input or output medium other than free space have been investigated in [67] (see Problem 1.13). Superresolution similar to that produced by a left-handed perfect lens, but in the quasistatic limit, can be obtained by using slabs with only negative  $\varepsilon$  (such as silver plates at optical frequencies) [26,68–71] (see Problem 1.14). It can be also obtained in magnetized ferrite slabs [72] and in pair-coupled magnetoinductive surfaces [73].

#### 1.9.4 The Perfect Lens as a Tunneling/Matching Device

In the previous section, the field created by a source placed in front of a perfect lens was studied. In this section we will address the problem of image detection in such devices. A key point in the behavior of Pendry's perfect lens is that most of the information reaching the image plane is carried by evanescent electromagnetic waves (the aforementioned evanescent Fourier harmonics). As is well known, a single evanescent electromagnetic wave does not carry power (for this reason the amplification of evanescent Fourier harmonics inside the lens does not violate energy conservation). However, any measurement of the image should imply the transmission of some amount of power from the source to the detector. Power transmission by evanescent waves is known in physics as *tunneling*. Therefore, seen from the detector, a *perfect lens* is a kind of tunneling device. For a single electromagnetic mode, tunneling of power was analyzed in Section 1.9.2. For a summation of evanescent waves (the aforementioned evanescent Fourier harmonics), the basic mechanism should be essentially the same: Some *new* evanescent waves are generated at the output in addition to the evanescent Fourier harmonics generated by the source. It is the composition of all these waves that allows for power transmission. The aforementioned *new* evanescent waves generated at the output are not present *before* the detector is placed at the output. Therefore, the image detection process substantially affects the field distribution along the system formed by the source and the lens. These kind of devices, where fields depends on both the input and the output, have long been considered by electrical engineers. Some of these devices—those that maximize power flow—are usually called *matching* devices. Thus, from this standpoint, the perfect lens can also be considered a matching device [66,74].

In the following we will analyze the image detection process in detail. As usual, we will consider a system formed by the perfect lens, an input antenna (the source  $S$ ), and an output antenna (the detector  $D$ ). Two waveguides are connected to the input and output antennas (for simplicity both waveguides will be assumed identical, with characteristic impedance  $Z_0$ ). The image is obtained by scanning the detector behind the lens, as a map of the transmission coefficient between the source and the detector. The whole system is illustrated in Figure 1.15. The computation of the transmission



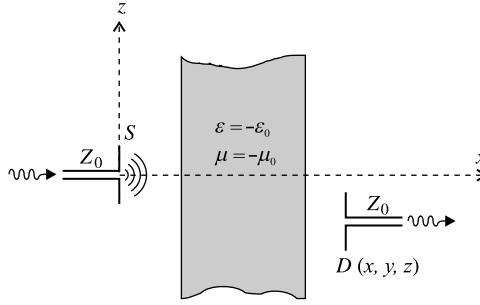


**FIGURE 1.15** Experimental setup for the detection of images created by a left-handed perfect lens. The source  $S$  is placed at a fixed distance from the left-handed slab, and the detector  $D$  is scanned behind the slab. The transmission coefficient between  $S$  and  $D$  is measured.

coefficient is a standard problem of electromagnetic theory, which can be solved if the impedance matrix  $Z_{ij}$  of the system formed by the antennas and the lens is known. The resulting expression is [75]

$$t = \frac{2Z_{12}Z_0}{(Z_{11} + Z_0)(Z_{22} + Z_0) - Z_{12}^2}, \quad (1.54)$$

where  $Z_{ij}$  are the elements of the impedance matrix of the system formed by the two antennas and the left-handed slab, and  $Z_0$  is the characteristic impedance of the input/output waveguides. If superresolution has to be detected, the size of the input and output antennas has to be smaller than the free-space wavelength, which would also make the real part of  $Z_{ij}$  (the radiation resistance) negligible with respect to its imaginary part [14]; in other words,  $Z_{ij} \simeq jX_{ij}$ , where  $X_{ij}$  is the reactance matrix of the system<sup>5</sup>. Moreover, because the perfect lens perfectly matches any source to free space,  $X_{11}$  and  $X_{22}$  can be approximated by the reactances of the input and output antennas in free space. The off-diagonal term,  $X_{12}$ , accounts for the mutual reactance between the antennas, which is strongly affected by the presence of the lens. Therefore,

$$t \approx \frac{2jX_{12}Z_0}{(jX_{11} + Z_0)(jX_{22} + Z_0) + X_{12}^2}. \quad (1.55)$$

If one of the self-reactances dominates over the remaining ones, the first term in the denominator of (1.55) dominates over the second, and

$$t \propto X_{12}. \quad (1.56)$$

<sup>5</sup>Throughout this section we will consider lossless antennas. Loading the antennas with a resistance has consequences that will not be analyzed here. See [63] for an analysis of this particular scenario.

That is, the transmission coefficient is simply proportional to the mutual reactance,  $X_{12}$ , which usually provides a good measure of the field in the absence of the output. This case may correspond to a small electric dipole antenna at the output (in such a case,  $|X_{22}| \gg |X_{21}|, |X_{11}|$ ). It may also occur when the output antenna is a small magnetic loop (in such a case, usually,  $|X_{11}| \gg |X_{21}|, |X_{11}|$ , [63]). Therefore, if small electric or magnetic probes are used as detectors, the transmission coefficient through the device can give a correct measurement of the field created by the source at the back side of the lens. This result can be expected from the physics of the experiment; in both cases the field generated by the currents at the output antenna should be very small, and should not substantially affect either the current at the input antenna or the field distribution behind the lens. As was shown in [64], when such a small probe is used for field measurements at the back side of the lens, the maximum of transmission is obtained just at the back interface of the lens, in agreement with the behavior outlined in Figure 1.14.

However, if the self-reactances of the input and output antennas are the same ( $X_{11} = X_{22} = X$ ), which may correspond to a detector identical to the source, then

$$t \approx \frac{2jX_{12}Z_0}{X_{12}^2 - X^2 + Z_0^2 + 2jXZ_0}. \quad (1.57)$$

The values of  $t$ , as a function of  $X_{12}$  and  $X$ , are plotted in Figure 1.16. Except for very small values of  $X$ , the maximum is achieved for  $X_{12} \approx X$ , and in such a case it is also the case that  $|t| \approx 1$ . Because both antennas are identical and the lens reproduces the field of the source at the image plane, the condition  $X_{12} \approx X$  is fulfilled when the detector is placed at the theoretical location of the image, at a distance  $2d$  from the source. Therefore, if the source and the detector are identical, and the detector is

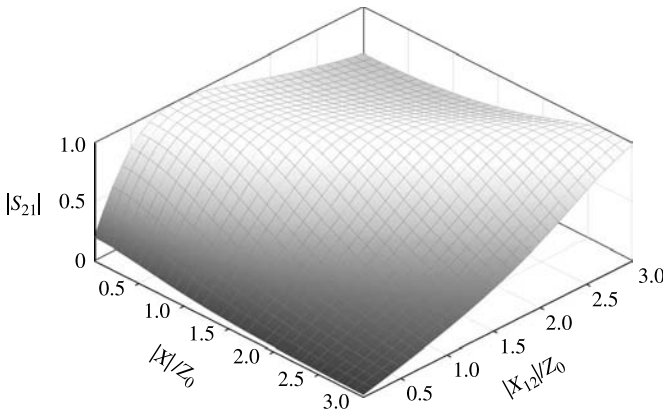


**FIGURE 1.16** Plot of the modulus of the transmission coefficient  $t = S_{21}$  (1.57) as a function of the modulus of the reactances  $X_{11} = X_{22} = X$  and  $X_{21}$  (Source: Reprinted with permission from [63]; copyright 2005 by the American Physical Society.)

placed at the theoretical location of the image (i.e., at a distance  $2d$  from the source), the perfect lens behaves as a perfect tunneling (or perfect matching) device, giving a maximum of power transmission at the theoretical location of the image (i.e., at the point marked as  $S'$  in Fig. 1.14). If the antennas are not identical, but none can be considered a small probe (in the sense defined in the previous paragraph), the location and magnitude of the maximum transmission will vary. This tunneling effect in metamaterial perfect lenses and similar devices has been analyzed in detail in [63]. The experimental confirmation of such an effect has been shown in a device similar to Pendry's super-lens [73] (see also Chapter 5).

Two main conclusions arise from the above analysis. The first is that for field measurements at the back side of a metamaterial super-lens, care must be taken in order to avoid artifacts coming from the matching/tunneling capabilities of such devices. The second is that, in some circumstances, it may be possible to take advantage of such a tunneling effect in order to obtain additional information from the image. For instance, if the shape and characteristics of the source are known, it is possible to design an appropriate detector in order to determine the source location in three-dimensional space from measurements of the transmission coefficient behind the lens.

## 1.10 LOSSES AND DISPERSION

After the first seminal papers showing propagation in left-handed media, it was claimed that losses and dispersion will destroy many of the previously reported effects. Specifically, negative refraction [15] and super-resolution in Pendry's perfect lens [58] were criticized. The analysis of the refraction of a Gaussian beam at the interface between an ordinary and a left-handed medium showed, without doubt, that negative refraction occurs in such a situation [16,17], thus confirming the Veselago analysis [6]. Of more interest are the effects of losses on the perfect lens proposed by Pendry [26]. This effect was analyzed in [59–61] among others, leading to similar conclusions. In the following we will briefly examine this aspect.

In order to develop the analysis, it is convenient to rewrite the transmission coefficient (1.39) as

$$t = \frac{4Z}{(1+Z)^2 \exp(jk_{x,2}d) - (1-Z)^2 \exp(-jk_{x,2}d)}, \quad (1.58)$$

where  $Z = Z_2/Z_1$ . If  $\varepsilon/\varepsilon_0 \rightarrow -1$  and  $\mu/\mu_0 \rightarrow -1$ , from our definitions of positive waves<sup>6</sup> and from equation (1.30), it follows that  $Z = 1$  if  $k_{x,2} = -|k_{x,2}|$  is real, and  $Z = -1$  if  $k_{x,2} = -j\alpha$  is imaginary. Therefore  $t \rightarrow \exp(j|k_{x,2}|d)$  for propagative waves and  $t \rightarrow \exp(\alpha d)$  for evanescent waves. In both cases, the phase and amplitude

<sup>6</sup>According to our definitions (see Fig. 1.7 as well as Section 1.7 and equation 1.12), in the left-handed slab, propagation is backward and positive waves are defined with  $\text{Re}(k_{x,2}) < 0$  and/or  $\text{Im}(k_{x,2}) < 0$ . In ordinary media, positive waves are defined with  $\text{Re}(k_{x,2}) > 0$  and/or  $\text{Im}(k_{x,2}) < 0$ , as usual.

of the incident waves change along the slab just by the amount necessary to produce Fourier harmonics restoration at a distance  $2d$  from any source (see Section 1.9.3). Let us now introduce a small amount of losses in the left-handed slab, so that  $\varepsilon \rightarrow -\varepsilon_0(1 + j\delta_\varepsilon)$  and  $\mu \rightarrow -\mu_0(1 + j\delta_\mu)$ . Let us also suppose that  $k_z \gg k_0$ , so that  $k_{x,2} = -j\alpha \simeq -j|k_z|$ . In such limit, taking into account equation (1.30), we obtain

$$t \rightarrow \frac{4}{4 \exp(-|k_z|d) - \delta_\mu^2 \exp(|k_z|d)}. \quad (1.59)$$

Therefore, for high values of  $k_z$  it is still  $t \simeq \exp(|k_z|d) \simeq \exp(\alpha d)$  provided  $\delta_\mu^2 \exp(|k_z|d) < 4 \exp(-|k_z|d)$ , or

$$|k_z|d \lesssim \ln\left(\frac{2}{\delta_\mu}\right). \quad (1.60)$$

However, if the above condition is not fulfilled, then  $t \sim \exp(-|k_z|d)$ , and evanescent waves are not amplified inside the left-handed slab. A similar (dual) result holds for  $p$ -polarized (or TM) modes.

Regarding the analysis of Section 1.9.3, the above results imply that, in general, a lossy left-handed slab with  $\varepsilon/\varepsilon_0 \rightarrow -(1 + j\delta_\varepsilon)$  and  $\mu/\mu_0 \rightarrow -(1 + j\delta_\mu)$  will *see* the effective source (1.53) with

$$k_{\max} \approx \frac{1}{d} \ln\left(\frac{2}{\delta}\right); \quad \delta = \max(\delta_\varepsilon, \delta_\mu), \quad (1.61)$$

so that the source is *seen* at the image with a resolution  $\Delta$  given by

$$\frac{\Delta}{d} \gtrsim \frac{2\pi}{k_{\max}d} = 2\pi \left\{ \ln\left(\frac{2}{\delta}\right) \right\}^{-1}. \quad (1.62)$$

It is worth noting that the wavelength of the incident radiation does not appear in equation (1.62), only the losses and thickness limit the resolution of the device.

An interesting consequence of the above results is that losses prevent the divergence of energy mentioned in section 1.9.3. In fact, because Fourier harmonics are only restored upto some finite value of  $|k_z| = k_{\max}$ , the energy divergence associated with the harmonics in the limit  $|k_z| \rightarrow \infty$  disappears. However, this regularization takes place at the cost of a loss in resolution. Thus, the lossy perfect lens is, in fact, a *super-lens*, with a resolution limited by equation (1.62). As the free-space wavelength is not present in equation (1.62), the resolution of such a lens may still overcome the diffraction limit ( $\Delta \lesssim \lambda_0$ ). However, the logarithmic dependence on  $1/\delta$  of  $\Delta/d$  strongly limits this effect. In fact, even in the best dielectrics,  $\delta_\varepsilon$  is not

much smaller than  $10^{-3}$ . Therefore, as a consequence of equation (1.62), super-resolution can only be present in left-handed slabs with a width of only a fraction of the wavelength. Thus, in practice, any left-handed super-lens is a near-field device whose effectiveness should be measured with regard to other near-field microscopy devices [76]. In order to reduce the limitations caused by losses in the super-lens performance, multilayer lenses formed by alternating layers of ordinary and left-handed media have been proposed [77,78]. Such devices provide a larger distance between the source and the image, but not a larger distance between the source and the left interface of the lens.

The above analysis can easily be extended to variations in the real part of  $\varepsilon$  and  $\mu$ :  $\varepsilon \rightarrow -\varepsilon_0(1 + \delta_\varepsilon)$  and  $\mu \rightarrow -\mu_0(1 + \delta_\mu)$  [59]. The results are quite similar to those reported in the previous paragraph. The main difference is that these small variations of  $\varepsilon$  or  $\mu$  may allow for the excitation of slab guided waves (see Section 1.8.2) for some values of the transverse wavenumber. In such cases, very high values of the transmission coefficient are obtained for the corresponding spatial Fourier harmonic [59], which may distort the image. As left-handed metamaterials are highly dispersive media, this effect may appear for sources emitting radiation pulses of finite duration.

The effect of the finite duration of RF pulses in the focusing of rays in the Veselago lens was also analyzed in [61]. The main conclusion is that, for the effective focusing of a ray, the pulse duration should be longer than the time taken by light to travel between the source and the focus along such a ray.

## 1.11 INDEFINITE MEDIA

Upto now, we have focused our attention on isotropic left-handed media. However, most present realizations of such media are in fact highly anisotropic, showing a left-handed behavior only for very specific polarizations and directions of propagation. These structures (some of them will be described in detail in the following chapters of this book) are easier to manufacture than isotropic left-handed media, while keeping many of their interesting properties. Therefore, they are of great practical interest. Many of them can be described by means of symmetric and simultaneously diagonalizable permittivity,  $\bar{\varepsilon}$ , and permeability,  $\bar{\mu}$ , tensors with some negative eigenvalues. These media have been called *indefinite* media [53], a denomination that emphasizes that not all the eigenvalues of the constitutive tensors have the same sign. In this section, wave propagation in indefinite media will be briefly discussed. This discussion will mainly follow the analysis in [53].

In order to simplify the analysis, we will choose a system of reference such that both  $\bar{\varepsilon}$  and  $\bar{\mu}$  are diagonal:

$$\bar{\varepsilon} = \begin{pmatrix} \varepsilon_x & 0 & 0 \\ 0 & \varepsilon_y & 0 \\ 0 & 0 & \varepsilon_z \end{pmatrix}; \quad \bar{\mu} = \begin{pmatrix} \mu_x & 0 & 0 \\ 0 & \mu_y & 0 \\ 0 & 0 & \mu_z \end{pmatrix}. \quad (1.63)$$

Because the dispersion relation for plane waves of generic polarization propagating in such a medium may be rather complicated, we will focus our attention on some particular cases of interest. In particular we will consider the very important case of TE waves polarized along a main axis of  $\bar{\varepsilon}$  and  $\bar{\mu}$ . As in the previous sections we will choose, without loss of generality,  $\mathbf{E} = E \hat{\mathbf{y}}$ . The dispersion relation for such waves is [53]

$$\omega^2 = \frac{k_z^2}{\varepsilon_y \mu_x} + \frac{k_x^2}{\varepsilon_y \mu_z} \quad (1.64)$$

(the dispersion relation for TM waves is the dual one). Taking  $\omega$  as a parameter, equation (1.64) defines the isofrequency curves in the  $(k_z, k_x)$  plane. These curves may be ellipses or hyperbolae, depending on the signs of  $\varepsilon_y \mu_x$  and  $\varepsilon_y \mu_z$ . It may be worth mentioning that, because left-handed media are highly dispersive, the constitutive parameters in equations (1.63) and (1.64) are usually frequency dependent. Therefore, in practical indefinite media, the shape of these curves may change from hyperbolic to elliptic, and vice versa, depending on frequency.

The direction of propagation of optical rays and energy is defined by the group velocity  $\mathbf{v}_g = \nabla_{\mathbf{k}} \omega(\mathbf{k})$ . From equation (1.64) it is readily found that

$$\mathbf{v}_g = \frac{1}{\omega} \left( \frac{k_x}{\varepsilon_y \mu_z}, 0, \frac{k_z}{\varepsilon_y \mu_x} \right). \quad (1.65)$$

The angle between group and phase ( $\mathbf{v}_p = \mathbf{k}\omega/k^2$ ) velocities is defined by

$$\mathbf{v}_p \cdot \mathbf{v}_g = \frac{1}{k^2} \left( \frac{k_x^2}{\varepsilon_y \mu_z} + \frac{k_z^2}{\varepsilon_y \mu_x} \right), \quad (1.66)$$

which generalizes equation (1.18). The laws for the refraction of optical rays at the interface of an indefinite media can be deduced from equation (1.64) by imposing the continuity of the tangential component of the wavevector  $\mathbf{k}$  at the interface, and using equation (1.66) to draw the rays in the indefinite media [24] (see Fig. 1.4 and Problem 1.8). Equation (1.64) is also useful for analyzing the propagation of TE modes in rectangular waveguides filled with indefinite media [79], or the amplification of TE evanescent modes by slabs made of such media [53].

## PROBLEMS

- 1.1. Quasistatic plasmonic resonance of a sphere.** Find the polarization of a sphere of permeability  $\varepsilon < 0$  in the presence of a uniform quasielectrostatic field. Assume a plasmonic type of frequency dependence  $\varepsilon = \varepsilon_0(1 - \omega_p^2/\omega^2)$ , and find the frequency of oscillation of quasistatic polarization modes.

- 1.2. Quasistatic surface plasmons.** Show that Laplace's equation at the interface between two media, 1 and 2, has bounded propagative solutions along such interface provided  $\varepsilon_1 = -\varepsilon_2$ . These solutions are usually called quasistatic surface plasmons [3].
- 1.3. Full-wave surface plasmons–polaritons.** Find the dispersion relation for TM surface waves at the interface between two media with  $\varepsilon_1 > 0$  and  $\varepsilon_2 < 0$ . Show that these solutions converge to the aforementioned surface plasmons (see Problem 1.2) in the limit  $k \rightarrow \infty$ . For small values of  $k$ , these waves have a different dispersion relation and are sometimes called *surface polaritons*. See [3] for a deeper discussion on surface plasmons–polaritons.
- 1.4. Energy flow of a plane wave in a left-handed medium.** Show that equation (1.14) ensures that the density of energy ( $U$ ) and the energy flux (the Poynting vector  $\mathbf{S}$ ) of a plane wave in a lossless left-handed medium are related through  $\mathbf{S} = \mathbf{v}_g U$ .
- 1.5. Left-handed concave and convex lenses.** Show that a concave (convex) lens made of a left-handed metamaterial becomes convergent (divergent). These lenses were analyzed in [6].
- 1.6. Refraction of nonparaxial rays by a left-handed slab.** Study the refraction of nonparaxial rays coming from a point source by a left-handed slab, and find the distance from the source at which these rays refocus. Show that this distance reduces to equation (1.22) for paraxial rays.
- 1.7. Dispersion relation for p-polarized surface waves.** Find the dispersion relation for p-polarized (or TM, or LSM) surface waves at the interface between a left-handed medium and free space. Show that it is deduced from equation (1.37) by the duality transformations  $\varepsilon \rightarrow \mu$ ,  $\mu \rightarrow \varepsilon$ ,  $\mathbf{E} \rightarrow \mathbf{H}$ ,  $\mathbf{H} \rightarrow -\mathbf{E}$  (see [14]).
- 1.8. All-angle negative refraction by an indefinite uniaxial dielectric.** Study the refraction of plane waves at the interface between free space and a uniaxial dielectric with  $\mu = \mu_0$ ,  $\varepsilon_{\parallel} < 0$  and  $\varepsilon_{\perp} = \varepsilon_0$ . Show that *all-angle negative refraction* occurs for p-polarized (TM) waves when the optical axis is perpendicular to the interface. Similar systems have been analyzed in [9,24].
- 1.9. Energy flow in surface waves.** Show that in the surface waves (1.37), power flows in the backward direction inside the left-handed material, and in the forward direction in free space. Discuss, in terms of the constitutive parameters, if the whole surface wave is forward or backward.
- 1.10. Small resonators made with left-handed media.** Study the resonant modes of a one-dimensional cavity made of two consecutive slabs of ordinary and left-handed media, placed between two parallel metallic plates. Show that the condition for the resonance of TEM waves does not depend on the distance between the plates, but on the relative width of the slabs. This and other similar resonators and waveguides have been proposed in [47].

- 1.11. Modes in parallel-plate waveguides partially filled by a left-handed slab.** Find, making use of the transverse transmission matrix technique, the dispersion relation for TE and TM modes in parallel plate waveguides partially filled by a left-handed slab. This and other similar waveguides have been analyzed in [38].
- 1.12. Phase compensation in single negative slabs.** Show that all-angle phase compensation and amplification of evanescent waves also occurs in two consecutive slabs with  $0 < \varepsilon_2 = -\varepsilon_1$  and  $0 > \mu_2 = -\mu_1$ , provided the widths of both slabs are identical. Draw a plot of the amplitude of electromagnetic waves inside this system for the different aforementioned effects. See [52] for a deeper discussion on the properties of a pair of consecutive single negative slabs.
- 1.13. Asymmetric perfect lens.** Find the transmission coefficient through a left-handed slab with  $\varepsilon = -\varepsilon_0$  and  $\mu = -\mu_0$  sandwiched between free space and a semi-infinite medium with  $0 < \varepsilon \neq \varepsilon_0$  and  $0 < \mu \neq \mu_0$ . This system is sometimes called an asymmetric perfect lens [67].
- 1.14. Near-field near-perfect lens made with a medium with  $\varepsilon = -\varepsilon_0$ .** Find the transmission coefficient for evanescent quasiolelectrostatic waves (i.e., solutions to Laplace's equation of the kind  $\phi(\mathbf{r}) = \phi_0 \exp(-j\mathbf{k} \cdot \mathbf{r})$ ) through a slab with  $\varepsilon = -\varepsilon_0$  and  $\mu = \mu_0$ . Show that this slab behaves as a near-field near-perfect lens for the quasiolelectrostatic field. A deeper discussion of this proposal can be found in [26] and in [68–71], among others.
- 1.15. TE anticutoff waveguide made with an indefinite uniaxial medium.** Find the dispersion relation for the fundamental  $TE_{1,0}$  mode in a rectangular waveguide filled with a uniaxial indefinite medium with  $\varepsilon = \varepsilon_0$ ,  $\mu_x = \mu_y = \mu_0$ ,  $\mu_z < 0$  (see Fig. 1.9 for the axis definition). Show that this mode has an anticutoff behavior; that is, it is propagative below certain cutoff frequency and evanescent above this frequency. This device has been studied and experimentally demonstrated in [79].
- 1.16. TM anticutoff waveguide made with an indefinite uniaxial medium.** Find the dispersion relation for the fundamental  $TM_{1,1}$  mode in a rectangular waveguide filled with a uniaxial indefinite medium with  $\mu = \mu_0$ ,  $\varepsilon_x = \varepsilon_0$ ,  $\varepsilon_y = \varepsilon_z < 0$  (see Fig. 1.9 for the axis definition). Show that this mode has an anticutoff behavior; that is, it is propagative below a certain cutoff frequency and evanescent above this frequency. This device has been studied and experimentally demonstrated in [80].

## REFERENCES

1. J. D. Jackson *Classical Electrodynamics*. Wiley, New York, 1999 (3rd ed.).
2. L. D. Landau, E. M. Lifshitz, and L. P. Pitaevskii *Electrodynamics of Continuous Media*. Pergamon, New York, 1984.



3. H. Raether *Excitation of Plasmons and Interband Transitions by Electrons*. Springer, Berlin, 1980.
4. M. S. Sodha and N. C. Shrivastava *Microwave Propagation in Ferrimagnetics*. Plenum Press, New York, 1981.
5. A. G. Gurevich and G. A. Melkov *Magnetization Oscillations and Waves*. CRC Press, Boca Raton, Florida, 1996.
6. V. G. Veselago "The electrodynamics of substances with simultaneously negative values of  $\epsilon$  and  $\mu$ ." *Sov. Phys. Usp.*, vol. 47, pp. 509–514, 1968.
7. D. R. Smith, W. J. Padilla, D. C. Vier, S. C. Nemat-Nasser, and S. Schultz "Composite medium with simultaneously negative permeability and permittivity." *Phys. Rev. Lett.*, vol. 84, pp. 4184–4187, 2000.
8. V. G. Veselago "Formulating Fermat's principle for light travelling in negative refraction materials." *Physics–Uspekhi*, vol. 45, pp. 1097–1099, 2002.
9. I. V. Lindell, S. A. Tretyakov, K. I. Nikoskinen, and S. Ilvonen "BW-media with negative parameters, capable of supporting backward waves." *Microwave Opt. Tech. Lett.*, vol. 31, pp. 129–133, 2001.
10. R. W. Ziolkowski and E. Heynman "Wave propagation in media having negative permeability and permittivity." *Phys. Rev. E*, vol. 64, paper 056625, 2001.
11. A. Sihvola "Electromagnetic emergence in metamaterials." In *Advances in Electromagnetics of Complex Media and Metamaterials*, S. Zouhdi, A. Sihvola, M. Arsalane Eds., NATO Science Series: II: Mathematics, Physics, and Chemistry, vol. 89, pp. 1–17, Kluwer Academic Publishers, Dordrecht, 2003.
12. S. Ramo, J. R. Whinnery, and T. Van-Duzer *Fields and Waves in Communication Electronics*. John Wiley, New York, 1965.
13. M. Mrozowski *Guided Electromagnetic Waves. Properties and Analysis*. Research Studies Press (Taunton, UK) and John Wiley (New York), 1997.
14. R. F. Harrington *Time-harmonic Electromagnetic Fields*. McGraw-Hill, New York, 1961.
15. P. M. Valanju, R. M. Walser, and A. P. Valanju "Wave refraction in negative-index media: Always positive and very inhomogeneous." *Phys. Rev. Lett.*, vol. 88, paper 187401, 2002.
16. D. R. Smith, D. Schurig, and J. B. Pendry "Negative refraction of modulated electromagnetic waves." *Appl. Phys. Lett.*, vol. 81, pp. 2713–2715, 2002.
17. S. Foteinopoulou, E. N. Economou, and C. M. Soukoulis "Refraction in media with a negative refractive index." *Phys. Rev. Lett.*, vol. 90, paper 107402, 2003.
18. R. A. Shelby, D. R. Smith, and S. Schultz "Experimental verification of a negative index of refraction." *Science*, vol. 292, pp. 77–79, 2001.
19. C. G. Parazzoli, R. B. McGregor, K. Li, B. E. C. Kontenbah, and M. Tlianian "Experimental verification and simulation of negative index of refraction using Snell's law." *Phys. Rev. Lett.*, vol. 90, paper 107401, 2003.
20. K. Li, S. J. McLean, R. B. Gregor, C. G. Parazzoli, and M. H. Tanielian "Free-space focused-beam characterization of left-handed materials." *Appl. Phys. Lett.*, vol. 82, pp. 2535–2537, 2003.
21. A. A. Houck, J. B. Brock, and I. L. Chuang "Experimental observations of a left-handed material that obeys Snell's law." *Phys. Rev. Lett.*, vol. 90, paper 137401, 2003.

22. D. Felbacq and A. Moreau, "Direct evidence of negative refraction at media with negative  $\varepsilon$  and  $\mu$ ." *J. Opt. A: Pure and Appl. Opt.*, vol. 5, pp. L9–L11, 2003.
23. C. Luo, S. G. Johnson, and J. B. Pendry "All-angle negative refraction without negative effective index." *Phys. Rev. B*, vol. 65, 201104(R), 2002.
24. T. Gregorczyk, M. Nikku, X. Chen, B.-I. Wu, and J. A. Kong "Refraction laws for anisotropic media and their application to left-handed metamaterials." *IEEE Trans. Microwave Theory Tech.*, vol. 53, pp. 1443–1450, 2005.
25. M. Notomi "Theory of light propagation in strongly modulated photonic crystals: Refractionlike behavior in the vicinity of the photonic band gap." *Phys. Rev. B*, vol. 62, pp. 10696–10705, 2000.
26. J. B. Pendry "Negative refraction makes perfect lens." *Phys. Rev. Lett.*, vol. 85, pp. 3966–3969, 2000.
27. J. Lu, T. M. Gregorczyk, Y. Zhang, J. Pacheco, B. Wu, J. A. Kong, and M. Chen "Cerenkov radiation in materials with negative permittivity and permeability." *Opt. Express*, vol. 11, pp. 723–734, 2003.
28. K. Artmann "Berechnung der Seitenversetzung des totalreflektierten strahles." *Ann. Phys. Lpz.*, vol. 2, pp. 87–102, 1948.
29. J. A. Kong, B. I. Wu, and Y. Zhang "Lateral displacement of a Gaussian beam reflected from a grounded slab with negative permittivity and permeability." *Appl. Phys. Lett.*, vol. 80 pp. 2084–2086, 2002.
30. P. R. Bermann "Goos-Hänchen shift in negative refractive media." *Phys. Rev. E*, vol. 66, paper 067603, 2002.
31. R. W. Ziolkowski "Pulsed and CW Gaussian beam interactions with double negative metamaterial slabs." *Opt. Express*, vol. 11, pp. 662–681, 2003.
32. A. Lakhtakia "On planewave remittances and Goos-Hänchen shifts of planar slabs with negative real permittivity and permeability." *Electromagnetics*, vol. 23, pp. 71–75, 2002.
33. I. V. Shadrivov, A. A. Zharov, and Y. S. Kivshar "Giant Goos-Hänchen effect at the refraction from left-handed metamaterials." *Appl. Phys. Lett.*, vol. 83, pp. 2713–2715, 2003.
34. R. E. Collin *Field Theory of Guided Waves*. IEEE Press, New York, 1990 (2nd. ed.).
35. R. Ruppin "Surface polaritons of a left-handed medium." *Phys. Lett. A*, vol. 277, pp. 61–64, 2000.
36. S. A. Darmanyan, M. Neviere, and A. A. Zakhidov "Surface modes at the interface of conventional and left-handed media." *Opt. Commun.*, vol. 225, pp. 233–240, 2003.
37. R. Ruppin "Surface polaritons of a left-handed material slab." *J. Phys.: Cond. Matter*, vol. 13, pp. 1811–1818, 2001.
38. A. Alu and N. Engheta "Guided modes in a waveguide filled with a pair of single negative (SNG), double negative (DNG), and/or double positive (DPS) layers." *IEEE Trans. Microwave Theory Tech.*, vol. 52, pp. 199–210, 2004.
39. H. Cory and A. Burger "Surface-wave propagation along a metamaterial slab." *Microwave Opt. Tech. Lett.*, vol. 38, pp. 392–395, 2003.
40. B.-I. Wu, T. M. Gregorczyk, Y. Zhang, and J. A. Kong "Guided modes with imaginary transverse wave-number in a slab waveguide with negative permittivity and permeability." *J. Appl. Phys.*, vol. 93, pp. 9386–9388, 2003.

41. I. W. Shadrivov, A. A. Sukhorukov, and Y. S. Kivshar "Guided waves in negative refractive index waveguides." *Phys. Rev. E*, vol. 67, paper 057602, 2003.
42. I. S. Nefedov and S. A. Tretyakov "Waveguide containing a backward-wave slab." *Radio Sci.*, vol. 38, pp. 1101–1109, 2003.
43. P. Baccarelli, P. Burghignoli, F. Frezza, A. Galli, P. Lampariello, G. Lovat, and S. Paulotto "Fundamental modal properties of surface waves on metamaterial grounded slabs." *IEEE Trans. Microwave Theory Tech.*, vol. 53, pp. 1431–1442, 2005.
44. R. Ruppin "Extinction properties of a sphere with negative permittivity and permeability." *Solid State Commun.*, vol. 116, pp. 411–415, 2000.
45. V. Kuzmiak and A. A. Maradudin "Scattering properties of a cylinder fabricated from a left-handed material." *Phys. Rev. B*, vol. 66, paper 045116, 2002.
46. R. Ruppin "Surface polaritons and extinction properties of a left-handed material cylinder." *J. Phys.: Cond. Matter*, vol. 16, pp. 5991–5998, 2004.
47. N. Engheta and R. W. Ziolkowski "A positive future for double-negative metamaterials." *IEEE Trans. Microwave Theory Tech.*, vol. 53, pp. 1535–1556, 2005.
48. P. Baccarelli, P. Burghignoli, F. Frezza, A. Galli, P. Lampariello, G. Lovat, and S. Paulotto "Effects of leaky-wave propagation in metamaterial grounded slabs excited by a dipole source." *IEEE Trans. Microwave Theory Tech.*, vol. 53, pp. 32–44, 2005.
49. T. Tamir and A. A. Oliner "Guided complex waves. Part I: Fileds at an interface. Part II: Relation to radiation patterns." *Proc. Inst. Elec. Eng.*, vol. 110, pp. 310–334, 1963.
50. A. Grbic and G. Eleftheriades "Experimental verification of backward-wave radiation from a negative refractive index metamaterial." *J. Appl. Phys.*, vol. 92, pp. 5930–5935, 2002.
51. D. R. Fedkin and A. Ron "Effective left-handed (negative index) composite material." *Appl. Phys. Lett.*, vol. 81, pp. 1753–1755, 2002.
52. A. Alu and N. Engheta "Pairing an epsilon-negative slab with a mu-negative slab: resonance, tunneling and transparency." *IEEE Trans. Antennas Propag.*, vol. 51, pp. 2558–2571, 2003.
53. D. R. Smith and D. Schurig "Electromagnetic wave propagation in media with indefinite permittivity and permeability tensors." *Phys. Rev. Lett.*, vol. 90, paper 077405, 2003.
54. S. Maslowski, S. Tretyakov, and P. Alitalo "Near-field enhancement and imaging in double planar polariton-resonant structures." *J. Appl. Phys.*, vol. 96, pp. 1293–1300, 2004.
55. J. B. Pendry and S. A. Ramakrishna "Focusing light using negative refraction." *J. Phys.: Cond. Matter*, vol. 15, pp. 6345–6364, 2003.
56. J. D. Baena, L. Jelinek, R. Marqués, and F. Medina "Near-perfect tunneling and amplification of evanescent electromagnetic waves in a waveguide filled by a metamaterial: Theory and experiments." *Phys. Rev. B*, vol. 72, paper 075116, 2005.
57. Z. M. Zhang and C. J. Fu "Unusual photon tunneling in the presence of a layer with a negative refractive index." *Appl. Phys. Lett.*, vol. 80, pp. 1097–1099, 2002.
58. N. Garcia and M. Nieto-Vesperinas "Left-handed materials do not make perfect lens." *Phys. Rev. Lett.*, vol. 88, paper 207403, 2002.
59. D. R. Smith, D. Schurig, M. Rosenbluth, and S. Schultz "Limitations on subdiffraction imaging with a negative refractive index slab." *Appl. Phys. Lett.*, vol. 82, pp. 1506–1508, 2003.
60. R. Merlin "Analytical solution of the almost-perfect-lens problem." *Appl. Phys. Lett.*, vol. 84, pp. 1290–1292, 2004.

61. R. Marques and J. Baena “Effect of losses and dispersion on the focusing properties of left-handed media.” *Microwave Opt. Tech. Lett.*, vol. 41, pp. 290–294, 2004.
62. G. Tayeb and S. Enoch “Perfect lenses made with left-handed materials: Alices mirror?” *J. Opt. Soc. Am.*, vol. 21, pp. 1417–1423, 2004.
63. F. Mesa, R. Marques, M. Freire, and J. D. Baena “Three dimensional super-resolution in metamaterial slab lenses.” *Phys. Rev. B*, vol. 72, paper 235117, 2005.
64. A. Grbic and G. Eleftheriades “Overcoming diffraction limit with a planar left-handed transmission line lens.” *Phys. Rev. Lett.*, vol. 92, paper 117403, 2004.
65. J. M. Williams “Some problems with negative refraction.” *Phys. Rev. Lett.*, vol. 87, paper 249703, 2001.
66. V. G. Veselago “Some remarks regarding electrodynamics of materials with negative refraction.” *Appl. Phys. B*, vol. 81, pp. 403–407, 2005.
67. S. A. Ramakrishna, J. B. Pendry, D. R. Smith, D. Schurig, and S. Schultz “The asymmetric lossy near-perfect lens.” *J. Mod. Opt.*, vol. 49, pp. 1747–1762, 2002.
68. J. T. Shen and P. M. Platzman “Near field imaging with negative dielectric constant lenses.” *Appl. Phys. Lett.*, vol. 80, pp. 3286–3288, 2002.
69. N. Fang and X. Zhang “Imaging properties of a metamaterial superlens.” *Appl. Phys. Lett.*, pp. 161–163, 2003.
70. N. Fang, H. Lee, C. Sun, and X. Zhang “Sub-diffraction-limited optical imaging with a silver superlens.” *Science*, vol. 308, pp. 534–537, 2005.
71. R. J. Blaikie and D. O. S. Melville “Imaging through planar silver lenses in the optical near field.” *J. Opt. A*, vol. 7, pp. S176–S183, 2005.
72. R. Marques, F. Mesa, and F. Medina “Near-field enhanced imaging by a metamaterial magnetized ferrite slab.” *Appl. Phys. Lett.*, vol. 86, paper 023505, 2005.
73. M. J. Freire and R. Marques “Planar magnetoinductive lens for three dimensional subwavelength imaging.” *Appl. Phys. Lett.*, vol. 86, paper 183505, 2005.
74. V. Veselago “Superlens as a matching device.” <http://xxx.lanl.gov/ftp/cond-mat/papers/0501/0501438.pdf>
75. D. M. Pozar *Microwave Engineering* Addison-Wesley, Reading, MA, 1993.
76. M. Nieto-Vesperinas “Problem of image superresolution with a negative—refractive—index slab.” *J. Opt. Soc. Am. A*, vol. 21, pp. 491–498, 2004.
77. E. Shamonina, V. A. Kalinin, K. H. Ringhofer, and L. Solymar “Imaging, compression and Poynting vector streamlines with negative permittivity materials.” *Electron. Lett.*, vol. 37, pp. 1243–1244, 2001.
78. S. A. Ramakrishna, J. B. Pendry, M. C. K. Wiltshire, and W. J. Stewart “Imaging the near field.” *J. Mod. Opt.*, vol. 50, pp. 1419–1430, 2003.
79. S. Hrabar, J. Bartolic, and Z. Sipus “Waveguide miniaturization using uniaxial negative permeability metamaterial.” *IEEE Trans. Antennas Propag.*, vol. 53, pp. 110–119, 2005.
80. J. Esteban, C. Camacho-Peñalosa, J. E. Page, T. M. Martin-Guerrero, and E. Marquez-Segura “Simulation of negative permittivity and negative permeability by means of evanescent waveguide modes—theory and experiment.” *IEEE Trans. Microwave Theory Tech.*, vol. 53, pp. 1506–1514, 2005.



# Synthesis of Bulk Metamaterials

---

## 2.1 INTRODUCTION

This chapter is devoted to the design of bulk metamaterials with negative parameters. By *bulk metamaterials* we mean discrete media made of a combination of *unit cells* of small electrical size at the frequencies of interest. It will be assumed that the constitutive parameters of such media can be deduced from the unit cell polarizabilities by an appropriate homogenization procedure. This approach is, in fact, a direct translation of the methods used in solid-state physics for the characterization of natural substances. Bulk metamaterials, as they have been defined here, substantially differ from photonic or electromagnetic crystals. In fact, the electromagnetic properties of bulk metamaterials arise, in essence from the electromagnetic properties of its constitutive elements. Periodicity usually plays a secondary role in bulk metamaterials.

After the seminal works of Walter Rotman [1], John Pendry [2,3], and David Smith and his co-workers [4], a standard procedure was established for the design of bulk artificial media with negative parameters at microwave frequencies. This standard procedure makes use of a system of metallic wires and/or plates to obtain the negative dielectric permittivity. A system of split ring resonators (SRRs) is used to obtain the negative magnetic permeability. This standard approach will be developed through the main part of this chapter, in Sections 2.2 to 2.5. The homogenization of systems of metallic wires and plates is described in Section 2.2. In the last part of this section, the key issue of spatial dispersion in wire media is introduced. Section 2.3 is devoted to the synthesis of negative permeability media using SRRs. A physical model for these elements, based on equivalent *LC* circuits, is developed. Then, Lorentz local field theory is applied to the homogenization of SRR media. Some advanced topics, such as higher-order SRR resonances, the design of isotropic SRRs, or the behavior of SRRs at infrared and optical frequencies, will be addressed in the last part of this Section. The synthesis of left-handed metamaterials using a

superposition of the aforementioned negative permittivity and negative permeability configurations will be developed in Section 2.4. Some key issues of this approach, such as the limits of the homogenization procedure in discrete left-handed metamaterials, and the justification of the superposition hypothesis underlying this procedure, will be addressed at the end of the section. Finally, in the last section of this chapter, other proposals for the design of bulk metamaterials with negative parameters are described and analyzed.

It must be mentioned here that there is also an alternative and widely used approach for the design of metamaterials at microwave frequencies. This approach was introduced simultaneously by Iyer and Eleftheriades [5], Caloz et al. [6], and Oliner [7]. It may be classified as a *nonresonant circuit analysis approach*. Such an approach substantially differs from the bulk media approach, because only circuit-like interactions between the nearest-neighbors elements of the system are considered. It also makes it possible to avoid the resonant behavior inherent in bulk design approaches. This *circuit analysis approach* will be described in the next chapter. The relation between such an approach and the analysis developed in this chapter, as well as the analysis of SRR-loaded transmission lines in the frame of the circuit analysis approach, will be developed in Chapter 3.

## 2.2 SCALING PLASMAS AT MICROWAVE FREQUENCIES

The simulation of plasmas at microwave frequencies became an active field of research during the 1960s, mainly aimed at the simulation of radio-communications with spaceships during transit through the ionosphere. In a paper that became a classic, Walter Rotmann studied the modeling of dilute plasmas—with plasma frequencies in the microwave range—by systems of metallic wires or plates [1]. Many years later, the same problem was addressed from a different standpoint by John Pendry [2]. Because lossless plasmas exhibit a negative effective permittivity below plasma frequency, these works opened the way to the design of artificial media with negative dielectric permittivity. Such an approach will be developed in this section. We will start with the simpler analysis of hollow metallic waveguides and plates, which simulate one- and two-dimensional plasmas, respectively. Wire media will then be analyzed.

### 2.2.1 Metallic Waveguides and Plates as One- and Two-Dimensional Plasmas

Let us consider a hollow rectangular metallic waveguide. The propagation constant corresponding to the fundamental  $TE_{10}$  mode is given by

$$k^2 = \omega^2 \epsilon_0 \mu_0 \left( 1 - \frac{\omega_c^2}{\omega^2} \right), \quad (2.1)$$

where  $\omega_c$  is the cutoff frequency of the waveguide. This dispersion relation is identical to that of an ideal plasma provided the cutoff frequency  $\omega_c$  is substituted by the plasma frequency  $\omega_p$ . This identity suggests that a rectangular waveguide can be seen—to some extent—as a one-dimensional plasma [8] with an effective dielectric constant of

$$\varepsilon_{\text{eff}} = \varepsilon_0 \left( 1 - \frac{\omega_c^2}{\omega^2} \right). \quad (2.2)$$

This equivalence is supported by analysis of the wave impedance corresponding to the considered mode [9,10],

$$Z = \frac{\omega \mu_0}{k}. \quad (2.3)$$

In fact, if we assume that the continuous media relations

$$k^2 = \omega^2 \varepsilon_{\text{eff}} \mu_{\text{eff}} \quad \text{and} \quad Z^2 = \frac{\mu_{\text{eff}}}{\varepsilon_{\text{eff}}}, \quad (2.4)$$

are simultaneously satisfied with  $k$  and  $Z$  given by equations (2.1) and (2.3), the effective dielectric constant (2.2) is deduced, as well as  $\mu_{\text{eff}} = \mu_0$ . Additional computations show that the proper relation between the effective polarization and the averaged electric field also holds (see Problem 2.1). Therefore, the proposed equivalence between rectangular waveguides and one-dimensional ideal plasmas is also supported by the averaging of the electromagnetic quantities. In fact, because the previous discussion is not restricted to rectangular waveguides, this equivalence can be extended to any hollow waveguide supporting TE modes. In particular, in square waveguides the fundamental modes  $\text{TE}_{10}$  and  $\text{TE}_{01}$  are degenerated. Therefore, a bunch of square waveguides such as those shown in Figure 2.1 will behave as a one-dimensional plasma for TE wave polarization.<sup>1</sup>

The above results can easily be extended to the simulation of two-dimensional plasmas by a system of parallel metallic plates [1] such as that shown in Figure 2.1. When this structure is illuminated by a plane wave polarized with the electric field parallel to the plates, and with a wavevector also parallel to them (so that the incident magnetic field is perpendicular to the plates) the  $\text{TE}_{10}$  mode is excited in the system.<sup>2</sup> Such a  $\text{TE}_{10}$  mode has a propagation constant inside the system of plates as given by equation (2.1), and an impedance given by equation (2.3). Therefore, from equation (2.4), the system of plates can be characterized by the effective dielectric

<sup>1</sup>It may be worth mentioning that a similar equivalence between waveguides supporting TM modes and ideal magnetic plasmas can be stated (see Problem 2.2 and [11])

<sup>2</sup>In fact, higher-order modes are also excited. However, it is usually supposed that only the  $\text{TE}_{10}$  mode has a significant penetration inside the system, so that the effect of higher-order modes can be accounted for as a boundary condition at the interface.



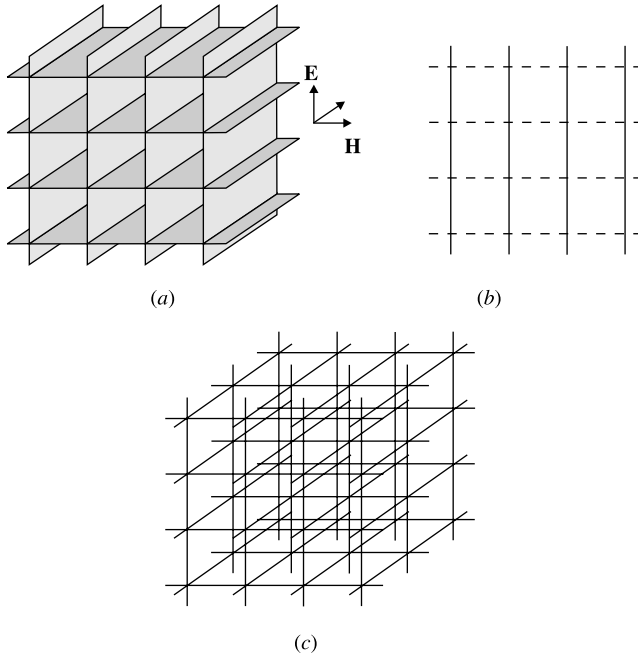


**FIGURE 2.1** Illustration of the development of one-, two-, and three-dimensional artificial plasma designs by using square waveguides, metallic plates, and wires. (a) A bunch of square metallic waveguides behaves as a one-dimensional plasma (with a plasma frequency equal to the cutoff frequency of the waveguides). (b) The horizontal conducting walls, which do not affect the field distribution in (a), are suppressed in order to obtain a two-dimensional design (front view). (c) The metallic boundaries of (a) are substituted by a regular mesh of wires in order to achieve an isotropic three-dimensional artificial plasma.

constant (2.2), and the effective magnetic permeability  $\mu_{\text{eff}} = \mu_0$ . Such effective constants correspond to an ideal plasma with plasma frequency  $\omega_p = \omega_c = c\pi/a$ , where  $c$  is the velocity of light in free space, and  $a$  is the distance between the plates. Because, for the  $\text{TE}_{10}$  mode, the average component of the magnetic field along the direction of propagation vanishes, the average fields inside the system of parallel plates ( $\langle \mathbf{E} \rangle$  and  $\langle \mathbf{H} \rangle$ ) form a TEM wave, with  $\langle \mathbf{E} \rangle$  parallel and  $\langle \mathbf{H} \rangle$  perpendicular to the plates. It can also be shown (see Problem 2.1) that the average electric polarization  $\mathbf{P}$  inside the structure is related to the averaged electric field by

$$\mathbf{P} = -\varepsilon_0 \frac{\omega_c^2}{\omega^2} \langle \mathbf{E} \rangle, \quad (2.5)$$

which corresponds to the effective dielectric constant (2.2). In summary, the system of parallel plates shown in Figure 2.1 behaves as a two-dimensional ideal plasma with plasma frequency  $\omega_p = c\pi/a$ . However, it should be kept in mind that this equivalence is restricted to waves polarized with the electric field parallel to the plates.

### 2.2.2 Wire Media

The designs described in Section 2.2.1 are simple and can be easily analyzed and manufactured. However, they are restricted to propagation in one or two dimensions, and to waves with the proper polarization. It can be guessed that a cubic mesh of conducting wires can provide the generalization of the above concepts to a three-dimensional structure. This concept is illustrated in Figure 2.1. If the period of the wire mesh is smaller than the free-space wavelength, it should be approximately equivalent to the bunch of waveguides shown in Figure 2.1*a*. Moreover, because the considered wire mesh is isotropic at large scales, it can be guessed that such system will behave as an isotropic artificial plasma for all wave polarizations and directions of propagation (at least in the long wavelength limit). The plasma frequency of such artificial plasma should be close to the cutoff frequency of the waveguide bunch  $\omega_p \sim c\pi/a$ .

A more accurate determination of  $\omega_p$  comes from the analysis of the equivalent transmission line for the wire medium. Let us consider a TEM transmission line loaded by metallic posts, as shown in Figure 2.2. This transmission line is useful for modelling the propagation of TEM waves along the wire media of Figure 2.1, provided the electromagnetic field is polarized with the electric field parallel to a set of wires. The per unit length series inductance of the parallel plate transmission line is  $L_s/a = \mu_0$ , where the per unit length shunt capacitance is  $C/a = \epsilon_0$ . In the circuit model for the transmission line of Figure 2.2, the effect of the wires can be modeled by periodically loading this transmission line with the shunt inductances associated with each metallic post. We can estimate this shunt inductance as [2]

$$L \simeq \frac{\mu_0 a}{2\pi} \ln(a/r), \quad (2.6)$$

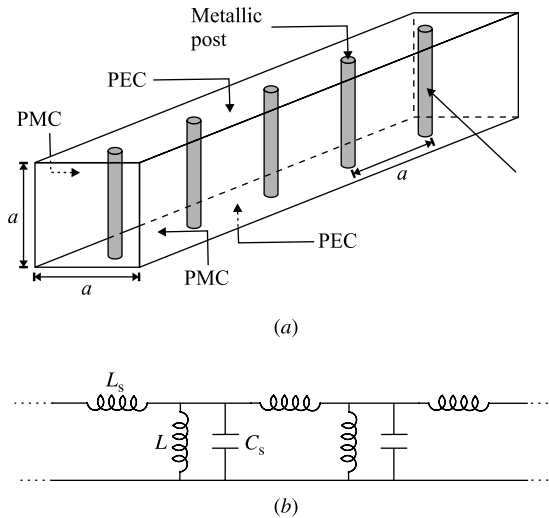


**FIGURE 2.2** Illustration of the transmission line model for wire media. (a) Equivalent transmission line (PEC: perfect electric conductor; PMC: perfect magnetic conductor). (b) Circuit model for the equivalent transmission line,  $L_s = \mu_0 a$ ,  $C = \epsilon_0 a$ .

where  $r$  is the wire radius. In this expression, the effect of the remaining wires has been taken into account by imposing that the magnetic field created by a single wire is shielded by its nearest neighbors at a distance  $a$  from the considered wire (otherwise, this inductance will become infinite). From standard transmission line theory it follows that the phase propagation along the wire-loaded transmission line of Figure 2.2 is given by

$$k^2 = \frac{\omega^2}{a^2} (L + L_s)C = \omega^2 \mu_0 \varepsilon_0 \left( 1 - \frac{2\pi}{\omega^2 \mu_0 \varepsilon_0 a^2 \ln(a/r)} \right), \quad (2.7)$$

provided the periodicity  $a$  can be considered small with regard to wavelength. By comparing this expression with the corresponding one for an ideal plasma, the following value is obtained for the plasma frequency of the wire media:

$$\omega_p^2 = \frac{2\pi}{\mu_0 \varepsilon_0 a^2 \ln(a/r)}. \quad (2.8)$$

This value coincides with the result reported in [2]. More accurate calculations [14], lead to the result

$$\omega_p^2 = \frac{2\pi}{\mu_0 \varepsilon_0 a^2 [\ln\{a/(2\pi r)\} + 0.5275]}. \quad (2.9)$$

The reported theory on the homogenization of wire media cannot be accepted without some criticism. In fact, except for extremely thin wires, the above expression implies that propagation of electromagnetic waves is only possible at frequencies with an associated free-space wavelength of the same order as the period of the structure. Nevertheless, near the plasma frequency, the internal wavelength is very large, so the assumption of an electrically small periodicity along the line can still be considered valid. However, as frequency increases, the internal wavelength soon becomes similar to the period. Needless to say, below the plasma frequency, the penetration length of evanescent waves also soon becomes of the same order as the period. Therefore, except for a small region around the plasma frequency, the reported homogenization seems to be against the most basic assumption of any homogenization theory: The scale of variation of the averaged field should be much larger than the period. Nevertheless, in metamaterial analysis, the above expression is widely used without too much care about its frequency range of validity. This use is ordinarily justified by the fact that, when other elements (*split ring resonators* for instance) are added to the wires, waves with an internal wavelength much larger than the period can propagate in the metamaterial. This argument leads, however, to the superposition problem, which will be addressed in Section 2.4.4. Ultimately, it is the agreement between theory and experiments that justifies the homogenization.

### 2.2.3 Spatial Dispersion in Wire Media

The analysis reported in the previous section is valid for TEM waves propagating along a set of wires, and polarized with the electric field parallel to another set of wires (see Fig. 2.1c). From this result, and from the isotropy at large scales of the structure, we could assume that the results of such an analysis are generalizable to any TEM wave. That is, the system of wires could be described as an ideal isotropic plasma with a plasma frequency given by equation (2.8). However, as will be shown in the following, this assumption is not always justified.

To begin, we will consider the more simple system made of a set of periodic parallel infinite wires, as shown in Figure 2.3. For homogenized TEM waves propagating perpendicular to the wires and polarized with the magnetic field also perpendicular to the wires, this medium behaves as an ideal plasma with plasma frequency given by equation (2.8). For waves with orthogonal polarization, the medium is transparent with  $\varepsilon = \varepsilon_0$ . Also, for TEM waves of any polarization propagating along the wires, the medium is transparent with  $\varepsilon = \varepsilon_0$  (for thin wires). However, it has been shown [12] that these facts do not mean that the wire medium could be characterized as an uniaxial dielectric with  $\varepsilon_x = \varepsilon_y = \varepsilon_0$  and  $\varepsilon_z = \varepsilon_0(1 - \omega_p^2/\omega^2)$ .

The effective permittivity tensor of the artificial medium shown in Figure 2.3 can be obtained from the analysis of the propagation of TM-to- $z$  electromagnetic waves through such medium (TE-to- $z$  waves do not see the wires, thus being TEM waves with propagation constant  $k_0 = \omega\sqrt{\varepsilon_0\mu_0}$ ). The fields of such TM waves are fully determined by the electric field component  $E_z$ , which should satisfy Helmholtz's equation

$$\left\{ \frac{\partial}{\partial x^2} + \frac{\partial}{\partial y^2} + \gamma^2 \right\} E_z = 0, \quad (2.10)$$

where  $\gamma^2 = k_0^2 - k_z^2$  (with  $k_0^2 = \omega^2\varepsilon_0\mu_0$ ), and  $k_z$  is the wavevector along the wires' axis. Boundary conditions impose that  $E_z = 0$  on the wires. Solutions to this

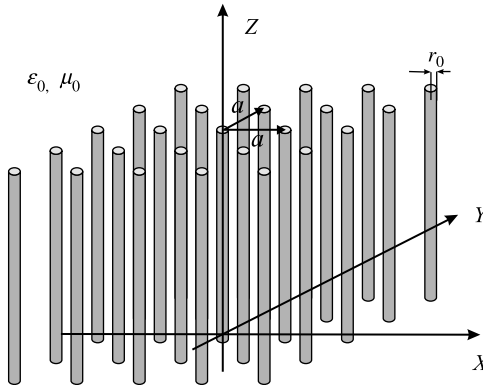


FIGURE 2.3 A system of perfectly conducting infinite parallel wires.

system of equations only depend on the eigenvalue  $\gamma^2$ , so the transverse dependence of the fields is not affected by  $k_z$  and  $\omega$  independently, but by the combination of both  $\gamma^2 = k_0^2 - k_z^2$ . The eigenvalue  $\gamma$  can be identified with the free-space wavevector,  $k_0$ , corresponding to a TM wave with  $k_z = 0$ ;  $\gamma^2 = k_0^2(k_x, k_y, 0)$ . Therefore, the dispersion relation for the considered TM waves must satisfy

$$\gamma^2 \equiv k_0^2(k_x, k_y, k_z) - k_z^2 = k_0^2(k_x, k_y, 0), \quad (2.11)$$

for any value of  $k_z$ . The dispersion relation for such TM waves with  $k_z = 0$ , is known, having the plasma-like form

$$k_x^2 + k_y^2 = k_0^2(k_x, k_y, 0) - k_p^2, \quad (2.12)$$

where  $k_p = \omega_p \sqrt{\varepsilon_0 \mu_0}$  is the free-space wavevector corresponding to the plasma frequency  $\omega_p$ . From this result, the dispersion relation for TM waves with  $k_z \neq 0$  is obtained by substitution of equation (2.11) into (2.12):

$$k^2 \equiv k_x^2 + k_y^2 + k_z^2 = k_0^2 - k_p^2. \quad (2.13)$$

This result is not compatible with the uniaxial permittivity tensor previously assumed (see Problem 2.3). However, if the uniaxial permittivity tensor [12]

$$\varepsilon_x = \varepsilon_y = \varepsilon_0, \quad \varepsilon_z(\omega, k_z) = \varepsilon_0 \left( 1 - \frac{k_p^2}{k_0^2 - k_z^2} \right); \quad k_p^2 = \omega_p^2 \varepsilon_0 \mu_0 \quad (2.14)$$

is assumed for the parallel wire medium, then the dispersion relation (2.13) is obtained (see Problem 2.3). Thus, we can conclude that the considered wire medium behaves as a uniaxial dielectric with the permittivity tensor (2.14). This result shows that spatial dispersion, expressed in the dependence on  $k_z$  of the permittivity tensor (2.14), plays an important role in the characterization of wire media, even in the very large wavelength limit. Such a result may be expected, because the *unit cell* of the considered parallel-wire medium has an infinite extent along the  $z$ -axis, and spatial dispersion is expected to appear when the unit cell size is not small with regard to the wavelength [13].

The above result raises an important question on the homogenization of wire media: to what extent spatial dispersion should be considered in the analysis of wire meshes? This question has been answered in [14]. The main result reported there is that the connected configuration shown in Figure 2.1c actually behaves as an ideal plasma, supporting homogenized TEM waves with the dispersion relation (2.1), and with an effective plasma frequency given by equation (2.9). However, a regular mesh of nonconnected wires shows strong spatial dispersion in the long wavelength limit, similar to that reported for the parallel-wire media.

### 2.3 SYNTHESIS OF NEGATIVE MAGNETIC PERMEABILITY

In 1852, Wilhem Weber formulated the first theory of diamagnetism, discovered by Faraday some years before. He assumed the existence of closed circuits at the molecular scale, and invoked Faraday's law to prove that currents would be induced in these circuits when they were under the effect of an external time-varying magnetic field. As the secondary magnetic flux created by such currents would be opposite to that created by the external field, this mechanism would explain the diamagnetism reported by Faraday [15]. In fact, it is easily shown that the magnetic polarizability of a lossless conducting ring along its axis (namely the  $z$ -axis) is given by

$$m_z = \alpha_{zz}^{\text{mm}} B_z^{\text{ext}} \quad \text{and} \quad \alpha_{zz}^{\text{mm}} = -\frac{\pi^2 r^4}{L}, \quad (2.15)$$

where  $\alpha_{zz}^{\text{mm}}$  is the polarizability,<sup>3</sup>  $B_z^{\text{ext}}$  is the  $z$ -component of the applied magnetic field,  $r$  is the radius of the ring, and  $L$  the self-inductance of the ring. However, the diamagnetic effect associated with a closed metallic ring is not strong enough to produce negative values for  $\mu$ . In fact, the self-inductance of a perfect conducting ring can be efficiently calculated as [13]

$$L = \mu_0 r \left[ \ln \left( \frac{16r}{d} \right) - 2 \right], \quad (2.16)$$

where  $d$  is the diameter of the wire. This expression gives  $L \geq \mu_0 r$  for any realistic  $r/d$  ratio. Thus,  $\mu_0 |\alpha_{zz}^{\text{mm}}| \leq \pi^2 r^3$ . Therefore, the magnetic susceptibility of an arrangement of rings (which can be estimated as  $\chi_m \sim \mu_0 \alpha_{zz}^{\text{mm}} / V$ , where  $V \gtrsim (2r)^3$  is the volume per ring) is  $|\chi| \lesssim \pi^2 / 8 \sim 1$ . That is, it does not seem possible to obtain an effective negative  $\mu$  from any arrangement of closed metallic rings.

The magnetic polarizability of a closed metallic loop can be easily enhanced by loading the loop with a capacitor. This configuration, proposed by Schelkunoff [16], provides the following expression for  $\alpha_{zz}^{\text{mm}}$ :

$$\alpha_{zz}^{\text{mm}} = \frac{\pi^2 r^4}{L} \left( \frac{\omega_0^2}{\omega^2} - 1 \right)^{-1}, \quad (2.17)$$

where  $\omega_0 = 1/\sqrt{LC}$  is the resonant frequency of the LC circuit formed by the loop and the capacitor. This expression shows that, just above the frequency of resonance, the polarizability becomes negative and very large. Therefore, it is expected that a regular array of capacitively loaded metallic loops will show a negative magnetic

<sup>3</sup>The repeated sub-index  $zz$  indicates that it is due to a force directed along the  $z$ -axis, and produces an effect along the same axis. The repeated super-index  $mm$  indicates that the external force is magnetic, and that the effect is also magnetic.

permeability just above the frequency of resonance of the loops. However, this configuration may be difficult to manufacture at microwave and higher frequencies, a fact that is crucial if we are interested in the design of effective media that may involve hundreds or, perhaps, thousands of elements. This difficulty is solved at microwave frequencies if the lumped capacitance is substituted by a distributed one. This modification of Shelkunoff's proposal leads to the split ring resonator (SRR) proposed by Pendry in [3]. Using this design it is possible to manufacture large series of small loops, of very high and negative magnetic polarizability, by using standard planar photo-etching techniques. The analysis of Pendry's SRR and related geometries is the main purpose of this section. This analysis will account for the main properties of these elements, providing accurate analytical design formulas useful for the design of SRR-based metamaterials.

In the last part of this section some related topics will be addressed. Such topics include the design of isotropic SRRs useful for isotropic metamaterial design, as well as the behavior of split ring resonators when they are scaled down in order to obtain a resonant magnetic response at infrared and optical frequencies.

### 2.3.1 Analysis of the Edge-Coupled SRR

The SRR (in the following, "edge-coupled SRR", or EC-SRR), as it was initially proposed by Pendry [3], consists of two concentric metallic split rings, printed on a microwave dielectric circuit board (Fig. 2.4). When it is excited by a time-varying external magnetic field directed along the  $z$ -axis, the cuts on each ring (which are placed on opposite sides of the EC-SRR) force the electric current to flow from one ring to another across the slots between them, taking the form of a strong displacement current. The slots between the rings therefore behave as a distributed capacitance, and the whole EC-SRR has the equivalent circuit shown in Figure 2.5*b*, where  $L$  is the EC-SRR self-inductance and  $C$  is the capacitance associated with each EC-SRR half. This capacitance is  $C = \pi r C_{\text{pul}}$ , where  $r$  is the mean radius of the EC-SRR ( $r = r_{\text{ext}} - c - d/2$ ), and  $C_{\text{pul}}$  is the per unit length capacitance along the slot between the rings. The total capacitance of this circuit is the series connection of

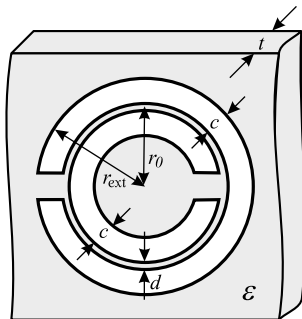


**FIGURE 2.4** The edge-coupled split ring resonator (EC-SRR). Metallizations are in white and dielectric substrate in gray.

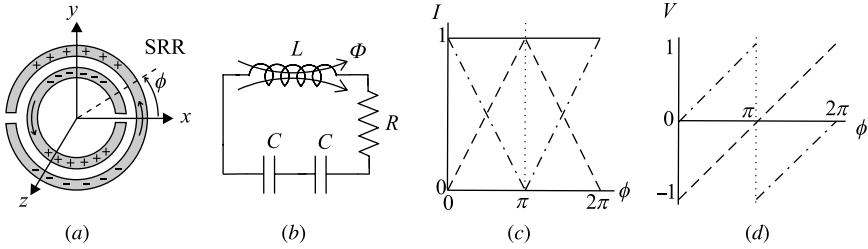


**FIGURE 2.5** Quasistatic circuit model for the EC-SRR. (a) Sketch of the resonator. (b) Equivalent circuit for the determination of the frequency of resonance, where  $C$  is the capacitance across the slots on the upper and lower halves of the EC-SRR:  $C = \pi r C_{\text{pul}}$ . (c) Plots of the angular dependence of currents on the inner ring (dashed line), on the outer ring (dash-dotted line), and of the total current on both rings (solid line). (d) Plots of the angular dependence of the voltage on the inner ring (dashed line) and on the outer ring (dash-dotted line).

the capacitances of both EC-SRR halves, that is  $C/2$ . Thus, neglecting losses, the equation for the total current  $I$  on the circuit is given by

$$\left( \frac{2}{j\omega C} + j\omega L \right) I = \Sigma, \quad (2.18)$$

where  $\Sigma$  is the external excitation. The reported circuit model was first proposed in [17]. It is valid as long as the perimeter of the ring can be considered small with regard to a half-wavelength, and the capacitance associated with the cuts on each ring can be neglected. Under such assumptions, the currents on each ring must vanish at the cuts, and the angular dependence of the currents on each ring can be assumed to be linear (so that the total current on both rings is constant). Such assumptions also imply that the voltage across the slots is constant in both EC-SRR halves (see Fig. 2.5c and d for a detailed illustration of these hypotheses). A more detailed circuit model, which takes into account the gap capacitance and includes a transmission-line model for the slot between the rings has been reported in [18]. It has been shown that such a model converges to the previous model when the capacitance of the cuts on each ring is neglected, and the electrical length of the EC-SRR is small [18]. As both approximations are usually fulfilled for any practical EC-SRR design, the more simple model developed above will be assumed valid throughout this book. The frequency of resonance,  $\omega_0$ , of the EC-SRR can be obtained from the proposed model by solving equation (2.18) for  $\Sigma = 0$ . This leads to

$$\omega_0^2 = \frac{2}{LC} = \frac{2}{\pi r C_{\text{pul}} L}. \quad (2.19)$$

As has already been mentioned, near-resonance current lines flow across the slot between the rings as displacement current lines. Thus, the EC-SRR self-inductance,



$L$ , can be modeled as the inductance of an average ring of radius  $r$  (the mean radius of the ring) and width  $c$  (the width of each ring) [17]. The analysis in [18] leads to the same conclusion: The self-inductance  $L$  in equation (2.19) must be the average of the inductances of both rings (without the gaps). In [19], approximate expressions for the average inductance  $L$ , based on a variational calculation, are provided. Closed expressions for the per unit length capacitances between the rings can be found in many microwave handbooks (see, for instance, [20]). Such explicit expressions for  $L$  and  $C_{\text{pul}}$  are given in the Appendix.

If the EC-SRR is excited by an external magnetic field, the excitation in equation (2.18) is  $\Sigma = -j\omega\Phi_{\text{ext}}$ , where  $\Phi_{\text{ext}}$  is the external magnetic flux across the EC-SRR. The equation for the total current becomes

$$I = \frac{\Phi_{\text{ext}}}{L} \left( \frac{\omega_0^2}{\omega^2} - 1 \right)^{-1}. \quad (2.20)$$

As has been shown, the EC-SRR essentially behaves as a capacitively loaded conducting loop. It therefore exhibits a resonant magnetic polarizability  $\alpha_{zz}^{\text{mm}}$ , given by equation (2.17).

A careful consideration of the behavior of the EC-SRR shows that, near the resonance, the particle reacts to an external magnetic field not only as a strong magnetic dipole, but also as a strong electric dipole. In fact, when the EC-SRR is excited at resonance, charges in the upper half of the EC-SRR must be the images of charges at its lower half, as sketched in Figure 2.5a. Two parallel electric dipoles directed along the  $y$ -axis are generated at each EC-SRR half. From the well-known Onsager symmetry principle [21], it directly follows that the EC-SRR resonance can also be excited by an external electric field directed along the  $y$ -axis of Figure 2.5a. In both cases, a strong magnetic dipole along the  $z$ -axis, and a strong electric dipole along the  $y$ -axis, are simultaneously excited. Moreover, the EC-SRR exhibits some nonresonant electric polarizabilities along the  $x$ - and  $y$ -axis, which can be approximated by those of a metallic disk of radius  $r_{\text{ext}} = r + d/2 + c$  [10]. All these results can be summarized by the following set of equations [19]:

$$m_z = \alpha_{zz}^{\text{mm}} B_z^{\text{ext}} - \alpha_{yz}^{\text{em}} E_y^{\text{ext}} \quad (2.21)$$

$$p_y = \alpha_{yy}^{\text{ee}} E_y^{\text{ext}} + \alpha_{yz}^{\text{em}} B_z^{\text{ext}} \quad (2.22)$$

$$p_x = \alpha_{xx}^{\text{ee}} E_x^{\text{ext}} \quad (2.23)$$

where the symmetry of the cross-polarizabilities derived from the Onsager symmetry principle [21,22], ( $\alpha_{yz}^{\text{em}} = -\alpha_{zy}^{\text{me}}$ ) has been explicitly introduced.

The EC-SRR magnetic polarizability is directly obtained from equation (2.20) by taking into account that the dipolar magnetic moment of the ring is  $m_z = \pi r^2 I$ ,

and  $\Phi_{\text{ext}} = \pi r^2 B_z^{\text{ext}}$ ; that is,

$$m_z = \frac{\pi^2 r^4}{L} \left( \frac{\omega_0^2}{\omega^2} - 1 \right)^{-1} B_z^{\text{ext}}, \quad (2.24)$$

a result that coincides with equation (2.17). The electric dipole induced by the external field component  $B_z^{\text{ext}}$  can be computed as

$$p_y = 2 \int_0^\pi p_r r \sin \phi \, d\phi = 4rp_r, \quad (2.25)$$

where  $p_r$  is the radial per unit length electric dipole created along the slot between the rings in the upper half of the EC-SRR ( $y > 0$  in Fig. 2.5a). This quantity can be written as  $p_r = qd_{\text{eff}}$ , where  $q$  is the per unit length charge on the outer ring (the charge on the inner ring must be equal in magnitude and of opposite sign), and  $d_{\text{eff}}$  some effective distance  $d_{\text{eff}} \simeq c + d$ . That is,

$$p_r = qd_{\text{eff}} = C_{\text{pul}} V d_{\text{eff}}, \quad (2.26)$$

where  $V$  is the voltage difference across the slot between the outer and the inner rings, which is a constant in the considered approximation (Fig. 2.5d). This voltage can be calculated from  $2V = \oint \mathbf{E} \cdot d\mathbf{l}$ , where the field integral is taken along a path going on the rings, and passing from one ring to another across the slots. From Faraday's law,  $2V = -j\omega(LI + \Phi_{\text{ext}})$ . Therefore, taking into account equations (2.25) and (2.26),

$$p_y = -2j\omega r C_{\text{pul}} d_{\text{eff}} (LI + \Phi_{\text{ext}}), \quad (2.27)$$

and taking into account equation (2.20) and  $\Phi_{\text{ext}} = \pi r^2 B_z^{\text{ext}}$ ,

$$p_y = -2j\pi r^3 d_{\text{eff}} C_{\text{pul}} \frac{\omega_0^2}{\omega} \left( \frac{\omega_0^2}{\omega^2} - 1 \right)^{-1} B_z^{\text{ext}}. \quad (2.28)$$

Let us now consider the behavior of the EC-SRR under an electric excitation. The external excitation  $\Sigma$  is now the series connection of the external voltage across the capacitors formed by the upper and the lower EC-SRR halves. This external voltage can be estimated as two times the average voltage created by the external field through each EC-SRR half.

$$\Sigma = 2\langle V^{\text{ext}} \rangle = \frac{2}{\pi} \int_0^\pi E_y^{\text{ext}} d_{\text{eff}} \sin \phi \, d\phi = \frac{4}{\pi} d_{\text{eff}} E_y^{\text{ext}}. \quad (2.29)$$

By substitution in equation (2.18), the total current in the EC-SRR is found to be

$$I = j \frac{4d_{\text{eff}}}{\pi\omega L} \left( \frac{\omega_0^2}{\omega^2} - 1 \right)^{-1} E_y^{\text{ext}}. \quad (2.30)$$

This current creates a magnetic moment  $m_z = \pi r^2 I$ , which, taking into account equation (2.19), can be written as<sup>4</sup>

$$m_z = 2j\pi r^3 d_{\text{eff}} C_{\text{pul}} \frac{\omega_0^2}{\omega} \left( \frac{\omega_0^2}{\omega^2} - 1 \right)^{-1} E_y^{\text{ext}}. \quad (2.31)$$

Moreover, when the EC-SRR is under this excitation, the resonant current generated around the rings must also create an electric moment, due to the radial polarization (2.26) along the slots. It is easier to obtain the per unit length charge on the outer ring from the current on this ring, and from charge conservation,

$$j\omega q = -\frac{1}{r} \frac{dI_{\text{out}}}{d\phi}, \quad (2.32)$$

where  $I_{\text{out}}$  is the current on the outer ring. As, according to the model sketched in Figure 2.5, the dependence of  $I_{\text{out}}$  on  $\phi$  is linear, and  $I_{\text{out}}$  takes a maximum  $I_{\text{out}} = I$  at  $\phi = 0$ , and a minimum  $I_{\text{out}} = 0$  at  $\phi = \pi$ , the derivative in equation (2.32) can be evaluated as  $dI_{\text{out}}/d\phi = -I/\pi$ . Therefore, taking into account equation (2.30),

$$q = \frac{I}{j\omega\pi r} = \frac{4d_{\text{eff}}}{\pi^2\omega^2 r L} \left( \frac{\omega_0^2}{\omega^2} - 1 \right)^{-1} E_y^{\text{ext}}. \quad (2.33)$$

The total electric dipole associated with the EC-SRR is evaluated by substitution in equations (2.25) and (2.26). Taking into account equation (2.19), this electric dipole can be written as

$$p_y = 4d_{\text{eff}}^2 r^2 C_{\text{pul}}^2 L \left( \frac{\omega_0^2}{\omega} \right)^2 \left( \frac{\omega_0^2}{\omega^2} - 1 \right)^{-1} E_y^{\text{ext}}. \quad (2.34)$$

Finally, the EC-SRR must show a nonresonant electric polarizability in the plane of the rings, which can be approximated as the electric polarizability of a metallic disk of the same size as the EC-SRR. This polarizability is

<sup>4</sup>Note that the symmetry of the cross-polarizabilities assumed in equations (2.21) and (2.22) is fulfilled.

$\alpha = \varepsilon_0 16r_{\text{ext}}^3/3$ , where  $r_{\text{ext}} = r + 2c + d$  [10]. In summary, the polarizabilities of the EC-SRR are as follows:<sup>5</sup>

$$\alpha_{zz}^{\text{mm}} = \frac{\pi^2 r^4}{L} \left( \frac{\omega_0^2}{\omega^2} - 1 \right)^{-1} \quad (2.35)$$

$$\alpha_{xx}^{\text{ee}} = \varepsilon_0 \frac{16}{3} r_{\text{ext}}^3 \quad (2.36)$$

$$\alpha_{yz}^{\text{em}} = -\alpha_{zy}^{\text{me}} = -2j\pi r^3 d_{\text{eff}} C_{\text{pul}} \frac{\omega_0^2}{\omega} \left( \frac{\omega_0^2}{\omega^2} - 1 \right)^{-1} \quad (2.37)$$

$$\alpha_{yy}^{\text{ee}} = \varepsilon_0 \frac{16}{3} r_{\text{ext}}^3 + 4d_{\text{eff}}^2 r^2 C_{\text{pul}}^2 L \left( \frac{\omega_0^2}{\omega} \right)^2 \left( \frac{\omega_0^2}{\omega^2} - 1 \right)^{-1}. \quad (2.38)$$

In such equations the effect of the polarization charges induced in the dielectric substrate has been neglected. However, they should affect the electric polarizabilities. If the substrate is thin ( $t \ll d$ ), it can be assumed that the polarization charges induced on each side of the dielectric substrate cancel each other. Therefore, the electric dipole (2.26) is mainly due to the free charge alone, and the above expressions are approximately valid. However, for thick substrates, it is the overall (free and polarization) charge that contributes in equation (2.26). In such a case it can be more appropriate to use the *in vacuo* per unit length capacitance between the rings,  $C_{\text{pul}}^0$ , instead of  $C_{\text{pul}}$  in equation (2.26).<sup>6</sup> Moreover, it is also more appropriate to use

$$\Sigma = 2\langle V^{\text{ext}} \rangle = \frac{C_{\text{pul}}^0}{C_{\text{pul}}} \frac{2}{\pi} \int_0^\pi E_y^{\text{ext}} d_{\text{eff}} \sin \phi \, d\phi = \frac{C_{\text{pul}}^0}{C_{\text{pul}}} \frac{4}{\pi} d_{\text{eff}} E_y^{\text{ext}}, \quad (2.39)$$

instead of equation (2.29).<sup>7</sup> All these changes are accounted for by simply substituting  $C_{\text{pul}}$  with  $C_{\text{pul}}^0$  in equations (2.35) to (2.38) [17,19] (of course, equation (2.19) should not be changed).

From equations (2.35) to (2.38) it follows an interesting property of the resonant part of the polarizabilities  $\alpha_{zz}^{\text{mm}}$ ,  $\alpha_{yz}^{\text{em}}$ , and  $\alpha_{yy}^{\text{mm}}$ , that is,

$$\alpha_{zz}^{\text{mm}} \left( \alpha_{yy}^{\text{ee}} - \varepsilon_0 \frac{16}{3} r_{\text{ext}}^3 \right) = -(\alpha_{yz}^{\text{em}})^2. \quad (2.40)$$

<sup>5</sup>The value for  $\alpha_{yy}^{\text{ee}}$  slightly differs from the value reported in [17]. We are in debt to Dr Juan Baena and Dr Lukas Jelinek for bringing this mistake to our attention.

<sup>6</sup>In other words, the total (free plus polarization) charge  $q^0 = C_{\text{pul}}^0/C_{\text{pul}}q$  is used instead of the free charge  $q$ .

<sup>7</sup>The reason for this choice is that the voltage induced by an external electric field  $E^{\text{ext}}$  in a capacitor partially filled by a dielectric is approximately given by  $C^0/C E^{\text{ext}}d$ , where  $d$  is the distance between the plates. An additional reason is that this choice guarantees that the cross-polarizabilities satisfy the Onsager symmetry:  $\alpha_{yz}^{\text{em}} = -\alpha_{zy}^{\text{me}}$ .

In fact, this property is quite general and comes from the quasistatic nature of the first EC-SRR resonance, and in particular from the possibility of modeling this resonance, by an  $LC$  circuit.

Up to now, we have considered a lossless EC-SRR. However, as was already mentioned in Chapter 1, losses play an important role in the characterization of metamaterials. As SRRs are resonant elements, it can be expected that metamaterial losses will be mainly associated with ohmic losses in the SRRs. These losses can easily be taken into account by considering the AC resistance of the SRRs, which can be estimated as [19]

$$R = \begin{cases} \frac{2\pi r_0}{ch\sigma} & \text{if } h/2 < \delta, \\ \frac{\pi r_0}{c\delta\sigma} & \text{otherwise,} \end{cases} \quad (2.41)$$

where  $h$  is the metal thickness,  $\sigma$  is the conductivity of the metallic strips, and  $\delta$  is the skin depth. The introduction of this resistance in the above analysis leads to the substitution

$$L \rightarrow \hat{L} = L + \frac{R}{j\omega}. \quad (2.42)$$

Such a substitution must be made through equations (2.35) to (2.38) (as well as in equations (2.52) and (2.53) in the next section). It implies that the frequency of resonance (2.19) must also be substituted by the function

$$\hat{\omega}_0^2(\omega) = \frac{2}{\hat{L}C} = \frac{2}{\pi r C_{\text{pul}} \hat{L}}. \quad (2.43)$$

A straightforward calculation leads to

$$\left(\frac{\hat{\omega}_0^2}{\omega^2} - 1\right)^{-1} = (\hat{\omega}_0^2)^{-1} \frac{\omega^2 \hat{\omega}_0^2}{\omega_0^2 - \omega^2 + j\omega\gamma}, \quad (2.44)$$

where  $\gamma = R/L$ . After the substitutions  $L \rightarrow \hat{L}$  and  $\omega_0 \rightarrow \hat{\omega}_0$  in equations, (2.35) to (2.38), and taking into account equation (2.44) as well as the relation  $\hat{L}\hat{\omega}_0^2 = L\omega_0^2$ , the polarizabilities for a lossy EC-SRR take the form

$$\alpha_{zz}^{\text{mm}} = \frac{\pi^2 r^4}{L} \left( \frac{\omega^2}{\omega_0^2 - \omega^2 + j\omega\gamma} \right), \quad (2.45)$$

$$\alpha_{xx}^{\text{ee}} = \varepsilon_0 \frac{16}{3} r_{\text{ext}}^3, \quad (2.46)$$

$$\alpha_{yz}^{\text{em}} = -\alpha_{zy}^{\text{me}} = -2j\pi r^3 d_{\text{eff}} C_{\text{pul}} \frac{\omega_0^2}{\omega} \left( \frac{\omega^2}{\omega_0^2 - \omega^2 + j\omega\gamma} \right), \quad (2.47)$$

and

$$\alpha_{yy}^{\text{ee}} = \varepsilon_0 \frac{16}{3} r_{\text{ext}}^3 + 4d_{\text{eff}}^2 r^2 C_{\text{pul}}^2 L \left( \frac{\omega_0^2}{\omega} \right)^2 \left( \frac{\omega^2}{\omega_0^2 - \omega^2 + j\omega\gamma} \right). \quad (2.48)$$

These equations have a quite familiar form, showing the typical Lorentzian form near the resonance. However, they are not causal for high values of  $\omega$ , due to the presence of powers of  $\omega$  in the numerator. Nevertheless, this fact has no importance, because the behavior of the polarizabilities at high frequencies is actually determined by higher-order resonances, which are not accounted for in equations (2.45) to (2.48).

The frequency of resonance of an EC-SRR can be measured by placing the EC-SRR inside a rectangular waveguide and measuring the transmission coefficient, which must show a sharp dip at the EC-SRR resonance [19]. These experiments systematically show an agreement with the circuit model developed in this section within a few percent of error. The presence of cross-polarization effects in the EC-SRR was experimentally checked in [23] (and previously in [24]) by measuring the transmission coefficient through a waveguide loaded with an EC-SRR placed at different orientations inside the waveguide (Fig. 2.6). As can be seen, the aforementioned dip in the transmission coefficient appears or not depending on the particle orientation. Only in orientation 4 of Figure 2.6 is there neither magnetic flux across the EC-SRR, nor an electric field component along the  $y$ -axis of the particle. According to equations (2.35) to (2.38), it is only for this orientation that the resonance should not appear, as can be seen in the figure.

The reported expressions for the EC-SRR polarizabilities in equations (2.35) to (2.38) can be used for the computation of the effective permeability and permittivity of artificial magnetic media made from periodic or nonperiodic arrangements of EC-SRRs. According to the above set of equations, an electric permittivity tensor and a magnetic susceptibility tensor do not suffice for the complete characterization of these media. They are, in general, bianisotropic, and a cross-polarization tensor must also be included for their complete characterization.

### 2.3.2 Other SRR Designs

In the previous section, the EC-SRR originally proposed by Pendry [3] was analyzed. It was shown that this element may produce a strong magnetic polarizability near its resonance. Because the EC-SRR is electrically small at resonance, and it can be easily and reliably manufactured by using standard photo-etching techniques, its usefulness for the design of magnetic metamaterials is apparent. However, some properties of the EC-SRR, such as bianisotropy, may be the origin of unwanted effects in the metamaterial. Moreover, the EC-SRR electrical size, although small, cannot be reduced in practice to values much smaller than  $\lambda/10$ , where  $\lambda$  is the free-space wavelength. This limitation comes from the edge-coupling of the metallic rings forming the EC-SRR. This fact implies a logarithmic dependence with the inverse of the distance between the rings,  $d$ , for the per unit length capacitance  $C_{\text{pul}}$ . Thus,  $C_{\text{pul}}$  cannot be increased too much by reducing  $d$  (at least for practical values of  $d$ ). Therefore, the frequency of

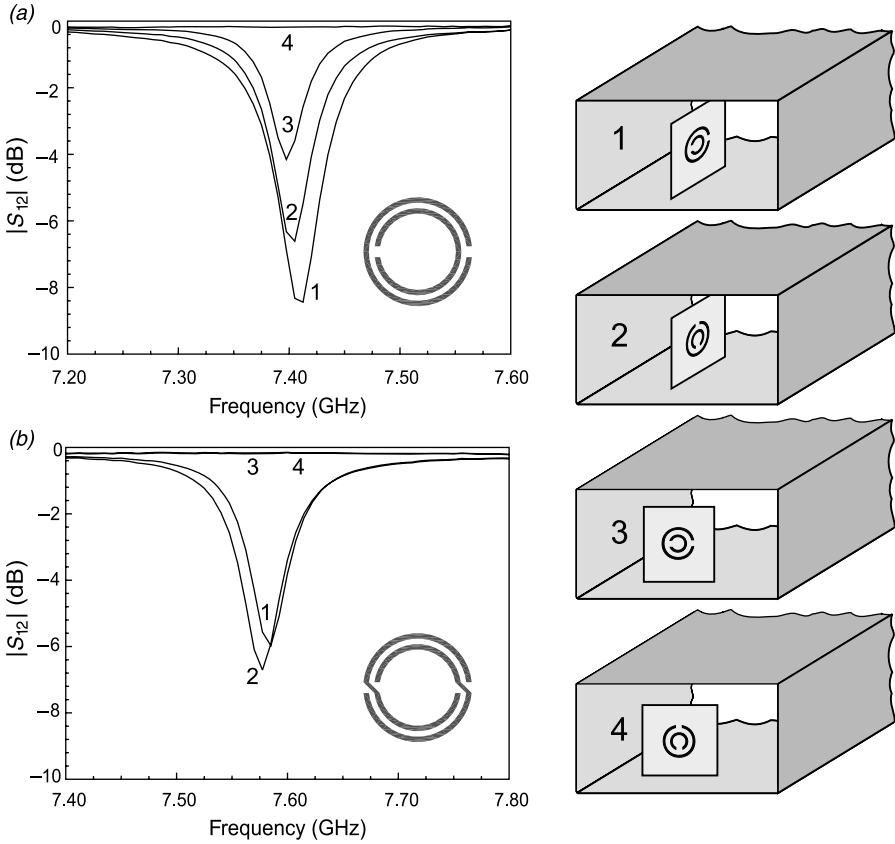


**FIGURE 2.6** (a) Experimental determination of the frequency of resonance, and demonstration of cross-polarization effects in the EC-SRR. Position 1: electric and magnetic excitation. Position 2: magnetic excitation only. Position 3: Electric excitation only. Position 4: no excitation. (b) Behavior of the nonbianisotropic SRR (NB-SRR) under the same excitations. The absence of electric excitation (3 and 4) shows the absence of cross-polarization effects. (Source: Reprinted with permission from [23]; copyright 2005 by the IEEE.)

resonance (2.19) cannot be made too small. Such limitations can be overcome by means of small modifications of the EC-SRR design. This section is devoted to a brief description of such alternatives.

**2.3.2.1 The Broadside-Coupled SRR** The broadside-coupled SRR (BC-SRR) was proposed in [17] in order to avoid the EC-SRR bianisotropy. It has the additional advantage of a potentially much smaller electrical size [19]. The BC-SRR is shown in Figure 2.7. The main modification with regard to the EC-SRR is that both rings are printed at both sides of the dielectric board, so that the per unit length capacitance  $C_{pul}$  is the capacitance of the broadside-coupled strips. This modification does not substantially affect the behavior of the resonator. Therefore, the equivalent circuit

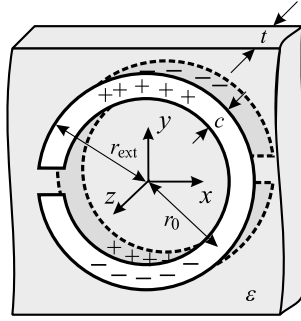


FIGURE 2.7 Broadside-coupled split ring resonator (BC-SRR).

for the BC-SRR, as well as the current and voltage distributions, are the same as for the EC-SRR (Fig. 2.5*b–d*). As in the EC-SRR, near the resonance, charges in the upper half of the BC-SRR are the images of charges in the lower half. However, as is sketched in Figure 2.7, this charge distribution does not result in a net electric dipole. Thus, the BC-SRR is nonbianisotropic. The same conclusion is obtained from symmetry considerations: The BC-SRR has inversion symmetry with regard to the center of both rings. Therefore, any second-order pseudo-tensor characterizing the resonator (for instance, the cross-polarizability tensor) must vanish.

From the above considerations, it turns out that the BC-SRR polarizabilities are summarized by the following set of equations [19]:

$$m_z = \alpha_{zz}^{\text{mm}} B_z^{\text{ext}} \quad (2.49)$$

$$p_y = \alpha_{yy}^{\text{ee}} E_y^{\text{ext}} \quad (2.50)$$

$$p_x = \alpha_{xx}^{\text{ee}} E_x^{\text{ext}} \quad (2.51)$$

where

$$\alpha_{zz}^{\text{mm}} = \frac{\pi^2 r^4}{L} \left( \frac{\omega_0^2}{\omega^2} - 1 \right)^{-1} \quad (2.52)$$

and

$$\alpha_{xx}^{\text{ee}} = \alpha_{yy}^{\text{ee}} = \varepsilon_0 \frac{16}{3} r_{\text{ext}}^2, \quad (2.53)$$

where  $\omega_0$  is the frequency of resonance, which can still be obtained from equation (2.19). However,  $C_{\text{pul}}$  in equation (2.19) is now the per unit length capacitance between the broadside-coupled rings forming the BC-SRR (closed expressions for this parameter are given in the Appendix).

The per unit length capacitance for the BC-SRR approximately corresponds to a parallel plate capacitor. Therefore, it has a linear dependence with the inverse of



the width  $t$  of the dielectric substrate. Thus, the frequency of resonance varies as the square root of  $t$ . It also varies as the inverse of the square root of the dielectric permittivity of the substrate. Both properties imply that the electrical size at resonance of the BC-SRR can be made potentially much smaller than for the EC-SRR. In order to achieve such a goal, thin substrates of high permittivity can be used. This behavior is illustrated in Figure 2.8, where the electrical sizes at resonance of EC- and BC-SRRs of similar characteristics are compared.

**2.3.2.2 The Nonbianisotropic SRR** The nonbianisotropic SRR (NB-SRR) was initially proposed in [25] in order to avoid EC-SRR bianisotropy while keeping a uniplanar design. This structure is shown in Figure 2.9. It can be easily observed that the equivalent circuit, as well as the frequency of resonance of this element, should be the same as for an EC-SRR with similar dimensions. However, the NB-SRR, like the BC-SRR, has inversion symmetry with regard to its center. Therefore, the NB-SRR polarizabilities are formally given by the same set of equations as the BC-SRR (2.49–2.53). The frequency of resonance is given by equation (2.19), with  $C_{\text{pul}}$  being the same as for the EC-SRR. An experimental demonstration of the absence of cross-polarization effects in the NB-SRR is shown in Figure 2.6.

**2.3.2.3 The Double-Split SRR** An alternative way to obtain inversion symmetry, thus overcoming bianisotropy, is by introducing additional cuts in the EC-SRR design. The double-split SRR (2-SRR) [25] shown in Figure 2.10 is an example of this strategy. The equivalent circuit for the 2-SRR is also shown in Figure 2.10. As the capacitances in this equivalent circuit are  $C = \pi r C_{\text{pul}}/2$ , the total capacitance of the circuit is four times smaller than for the conventional EC-SRR. Therefore, the frequency of resonance of the 2-SRR is twice the frequency of resonance of an EC-SRR or NB-SRR of the same size and shape:

$$\omega_0[2\text{-SRR}] = 2\omega_0[\text{EC-SRR}] = 2\omega_0[\text{NB-SRR}]. \quad (2.54)$$

Because it implies a larger electrical size at resonance, this property is a clear disadvantage of the 2-SRR. However, the high symmetry of the 2-SRR will make this design very useful for the development of isotropic negative magnetic permeability media (see Section 2.3.5). As the 2-SRR is a nonbianisotropic design, the 2-SRR polarizabilities are still formally given by equations (2.49) to (2.53).

**2.3.2.4 Spirals** Spirals are well-known resonators in planar microwave circuitry. Their usefulness for the design of negative magnetic permeability and left-handed media was shown in [26]. As an example, we will analyze the two-turns spiral resonator (2-SR) shown in Figure 2.11. A quasistatic analysis of this configuration leads to the equivalent circuit, and to the current and voltage distributions shown in the figure. This design also provides a strong magnetic dipole at resonance, thus being useful for metamaterial design. From the equivalent circuit of Figure 2.11, it

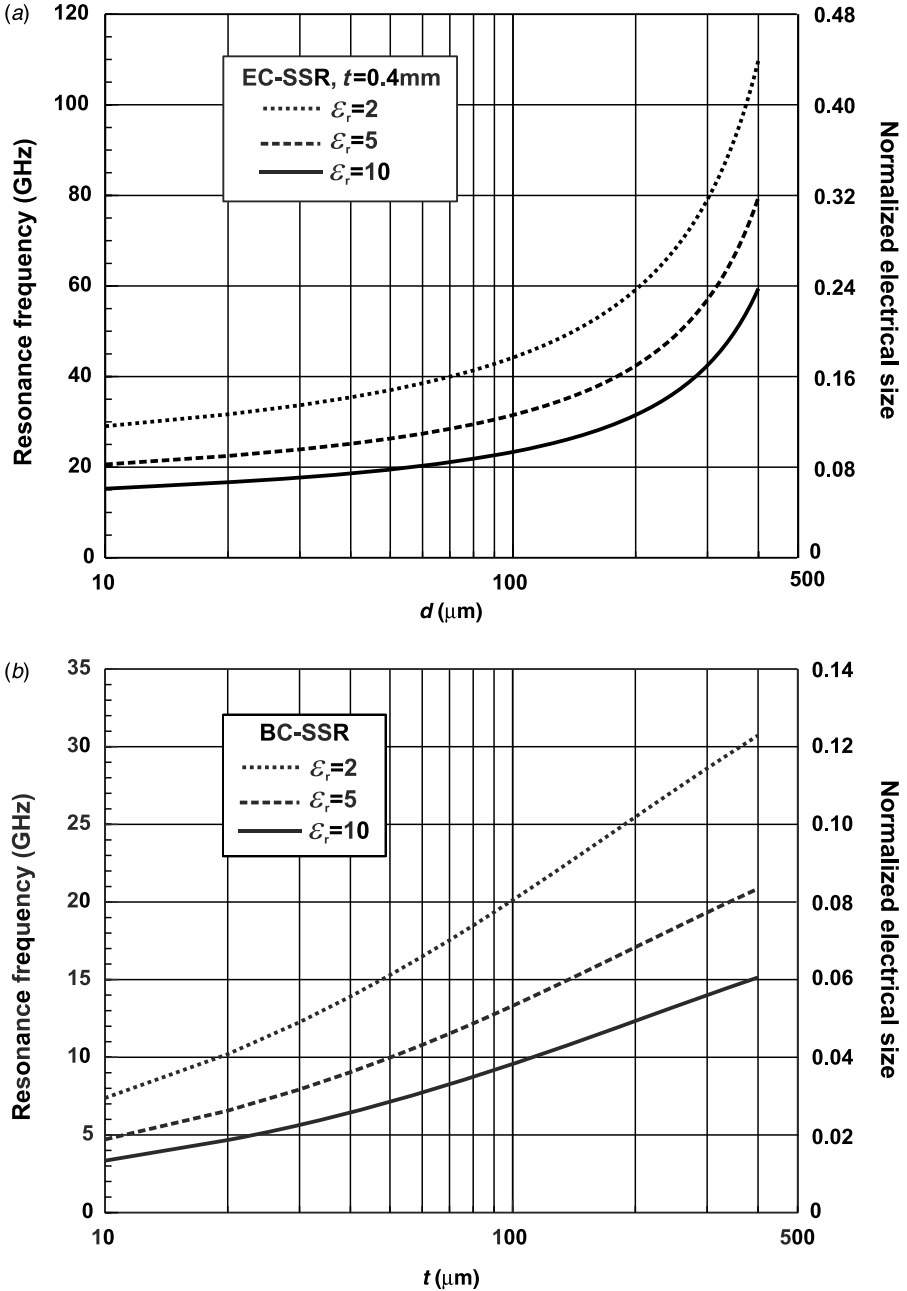


**FIGURE 2.8** Frequency of resonance and normalized electrical size ( $2r_{\text{ext}}/\lambda$ ) for several EC-SRRs (a) and BC-SRRs (b) with the same external radius  $r_{\text{ext}} = 0.6\text{mm}$  and ring width  $c = 0.2\text{mm}$ , printed on several dielectric substrates. (Source: Reprinted with permission from [19]; copyright 2003, IEEE.)

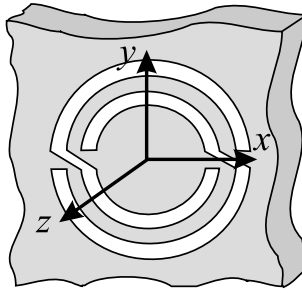


**FIGURE 2.9** Nonbianisotropic split ring resonator (NB-SRR). Metallizations are in white and dielectric substrate in gray.

follows that the frequency of resonance of the 2-SR must be half the frequency of resonance of the EC-SRR—or the NB-SRR—of the same size and shape:

$$\omega_0[2\text{-SR}] = \frac{1}{2} \omega_0[\text{EC-SRR}] = \frac{1}{2} \omega_0[\text{NB-SRR}]. \quad (2.55)$$

This property is a clear advantage, as it implies a smaller electrical size at resonance. The electrical size can still be reduced by increasing the number of turns [26] (see Problem 2.4).

Relations (2.54) and (2.55) have been experimentally checked. Table 2.1 shows an example of such results [25].

From the current and charge distributions on the 2-SR at resonance (Fig. 2.11) it can be guessed that this design will be also nonbianisotropic. However, this conclusion comes only from the quasistatic analysis and not from the symmetries of the element. In practice, any 2-SR design must imply long strips (of length  $\sim 4\pi r$ , where  $r$  is the mean radius of the 2-SR). These strips may be long with regard to the half-wavelength at resonance. Thus, the reported quasistatic analysis, although accurate enough for the determination of the frequencies of resonance, may not give accurate results for the polarizabilities. As a consequence, the 2-SR always

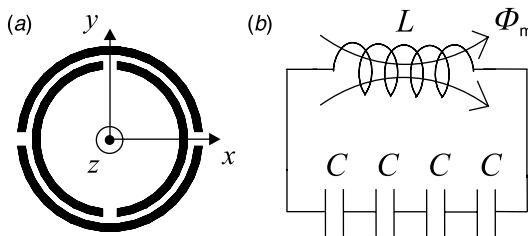


**FIGURE 2.10** Sketch of a double-split SRR (a) and its equivalent circuit (b). The four capacitances  $C$  of the equivalent circuit correspond to the capacitances across the four slots between the rings  $C = \pi r C_{\text{pul}}/2$ .

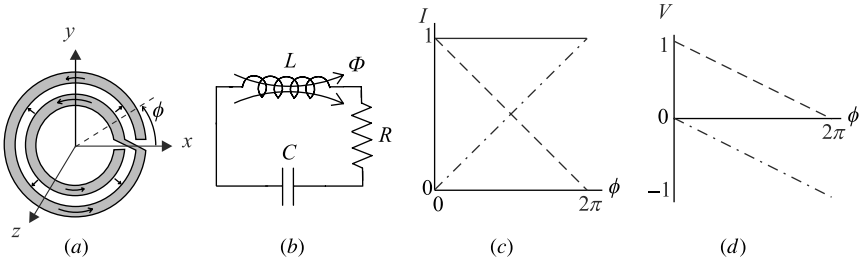


**FIGURE 2.11** (a) Sketch of a two-turns spiral resonator (2-SR). (b) Equivalent circuit for the determination of the frequency of resonance, where  $C$  is the capacitance across the slot between the rings:  $C = 2\pi r C_{\text{pul}}$ . (c) Angular dependence of current along the inner (dashed line) and outer (dot-dashed line) strips. (d) Voltage along the inner (dashed line) and outer (dot-dashed line) strips. Such distributions (c and d) imply a constant voltage across the slot and a total current (the sum of currents on both strips) constant with  $\phi$  (solid line in (c)).

presents some degree of bianisotropy, although smaller than for the EC-SRR [27]. This result shows the importance of symmetry in order to avoid bianisotropy: Only designs invariant by inversion, or by other appropriate symmetry, are completely free of this effect.

**2.3.3 Constitutive Relationships for Bulk SRR Metamaterials**

The effective constitutive parameters of bulk SRR media can be found from the polarizabilities obtained in previous sections. There are many possible periodic or nonperiodic combinations of SRRs that provide an effective medium. In fact, the only necessary condition is that the size of the unit cell must be much smaller than the internal wavelength. In this section, a cubic periodic arrangement of coplanar SRRs will be considered in order to illustrate the general procedure. The resulting artificial medium, which is illustrated in Figure 2.12, is strongly anisotropic. Moreover, due to the presence of cross-polarizabilities in the SRRs (see Section 2.3.1), the resulting medium is also bianisotropic. Therefore, the most general linear constitutive relationships must

**TABLE 2.1 Comparison Between the Resonance Frequency Provided by Experiment (exp) and Theory (th) for an SRR, a 2-SRR, and a 2-SR of Similar Dimensions Printed on the Same Substrates**

	$f_0^{\text{exp}}$ (GHz)	$f_0^{\text{th}}$ (GHz)
SRR	5.03	5.06
2-SSR	10.31	10.13
2-SR	2.66	2.53

The external radius of the three particles is 2.54mm, the width of the strips is of 0.19mm and its separation 0.17mm. The substrate is 0.49mm thick with a permittivity of  $2.43\epsilon_0$  [25].

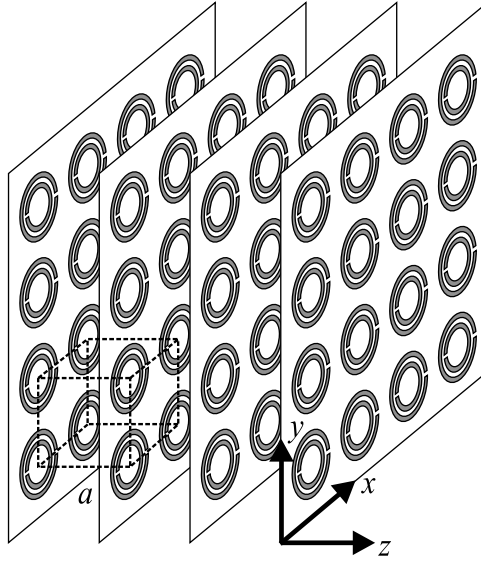


**FIGURE 2.12** Artificial magnetic medium made of a cubic three-dimensional array of SRRs (EC-SRRs in the figure).

be considered [22]:

$$\mathbf{D} \equiv \varepsilon_0 \mathbf{E} + \mathbf{P} = \varepsilon_0(1 + \bar{\bar{\chi}}_e) \cdot \mathbf{E} + j\sqrt{\varepsilon_0\mu_0} \bar{\bar{\kappa}} \cdot \mathbf{H} \quad (2.56)$$

$$\mathbf{B} \equiv \mu_0(\mathbf{H} + \mathbf{M}) = -j\sqrt{\varepsilon_0\mu_0} (\bar{\bar{\kappa}})^T \cdot \mathbf{E} + \mu_0(1 + \bar{\bar{\chi}}_m) \cdot \mathbf{H}, \quad (2.57)$$

where  $\mathbf{P}$  and  $\mathbf{M}$  are the polarization and magnetization vectors,  $(\cdot)^T$  indicates the transpose, and  $\bar{\bar{\chi}}_e$ ,  $\bar{\bar{\chi}}_m$ , and  $\bar{\bar{\kappa}}$  are the electric, magnetic, and magnetoelectric susceptibility tensors, which are related to the permittivity and permeability tensors through

$$\bar{\bar{\varepsilon}} = \varepsilon_0(1 + \bar{\bar{\chi}}_e); \quad \bar{\bar{\mu}} = \mu_0(1 + \bar{\bar{\chi}}_m). \quad (2.58)$$

In equations (2.56) and (2.57), the symmetry properties of the generalized susceptibilities [21], derived from the Onsager principle, have been explicitly included. These symmetries also imply that  $\bar{\bar{\chi}}_e$  and  $\bar{\bar{\chi}}_m$  must be symmetric tensors, so that the whole medium is bianisotropic and reciprocal [22].

The simplest approach for the computation of the constitutive tensors  $\bar{\bar{\chi}}_e$ ,  $\bar{\bar{\chi}}_m$ , and  $\bar{\bar{\kappa}}$  is to ignore couplings between adjacent elements. In such an approach, each susceptibility is simply the corresponding polarizability, divided by the volume of the unit cell. In this *zero-order* approach, we obtain

$$\bar{\bar{\chi}}_e = \frac{1}{\varepsilon_0 a^3} \bar{\bar{\alpha}}^{ee}, \quad \bar{\bar{\chi}}_m = \mu_0 \frac{1}{a^3} \bar{\bar{\alpha}}^{mm}, \quad \text{and} \quad \bar{\bar{\kappa}} = -j\sqrt{\frac{\mu_0}{\varepsilon_0}} \frac{1}{a^3} \bar{\bar{\alpha}}^{em}, \quad (2.59)$$

where  $\bar{\alpha}^{ee}$ ,  $\bar{\alpha}^{mm}$ , and  $\bar{\alpha}^{em}$  are the polarizability tensors of the SRRs, and  $a$  is the lattice parameter. For the artificial medium of Figure 2.12, only the susceptibilities

$$\begin{aligned}\chi_{e,xx} &= \frac{1}{\varepsilon_0 a^3} \alpha_{xx}^{ee}; & \chi_{e,yy} &= \frac{1}{\varepsilon_0 a^3} \alpha_{yy}^{ee}; & \chi_{m,zz} &= \frac{\mu_0}{a^3} \alpha_{zz}^{mm}; \\ \kappa_{yz} &= -j \sqrt{\frac{\mu_0}{\varepsilon_0}} \frac{1}{a^3} \alpha_{yz}^{em}\end{aligned}\quad (2.60)$$

are different from zero.

A better approximation, which takes into account the coupling between elements in a rather simple way, makes use of the well-known Lorentz local field theory (see [9], for instance). For a cubic array, this approximation considers that each element is excited by a local electric field  $\mathbf{E}_{\text{loc}} = \mathbf{E} + \mathbf{P}/3\varepsilon_0$ , and by a local magnetic field  $\mathbf{H}_{\text{loc}} = \mathbf{H} + \mathbf{M}/3$  (or, equivalently,  $\mathbf{B}_{\text{loc}} \equiv \mu_0 \mathbf{H}_{\text{loc}} = \mathbf{B} - (2/3)\mu_0 \mathbf{M}$ ). When this approach is applied to the coupled electric and magnetic polarizations,  $P_y$  and  $M_z$ , it leads to the equations

$$M_z = \frac{1}{a^3} \left\{ \mu_0 \alpha_{zz}^{mm} \left( H_z + \frac{M_z}{3} \right) - \alpha_{yz}^{em} \left( E_y + \frac{P_y}{3\varepsilon_0} \right) \right\}, \quad (2.61)$$

$$P_y = \frac{1}{a^3} \left\{ \alpha_{yy}^{ee} \left( E_y + \frac{P_y}{3\varepsilon_0} \right) + \mu_0 \alpha_{yz}^{em} \left( H_z + \frac{M_z}{3} \right) \right\}. \quad (2.62)$$

At this point it may be convenient to rewrite expressions (2.45) to (2.48) in the form

$$\alpha_{zz}^{mm} = \alpha_m X^{-1}; \quad \alpha_m = \frac{\pi^2 r^4}{L} \quad (2.63)$$

$$\alpha_{xx}^{ee} = \alpha_0; \quad \alpha_0 = \varepsilon_0 \frac{16}{3} r_{\text{ext}}^3 \quad (2.64)$$

$$\alpha_{yz}^{em} = -\alpha_{zy}^{me} = \alpha_{em} X^{-1}; \quad \alpha_{em} = -2j\pi r^3 d_{\text{eff}} C_{\text{pul}} \frac{\omega_0^2}{\omega} \quad (2.65)$$

$$\alpha_{yy}^{ee} = \alpha_0 + \alpha_e X^{-1}; \quad \alpha_e = 4d_{\text{eff}}^2 r^2 C_{\text{pul}}^2 L \left( \frac{\omega_0^2}{\omega} \right)^2, \quad (2.66)$$

where

$$X = (\omega_0^2/\omega^2 - 1 + j\gamma/\omega). \quad (2.67)$$

With such definitions, equation (2.40) takes the form

$$\alpha_m \alpha_e = -\alpha_{em}^2. \quad (2.68)$$

The next step is to solve equations (2.61) and (2.62) for  $P_y$  and  $M_z$ . After a cumbersome but straightforward calculation, and taking equation (2.68) into account, it is found that

$$P_y = \frac{1}{\Delta} \left\{ \Lambda E_y + \frac{\mu_0 \alpha_{em}}{a^3} H_z \right\} \quad (2.69)$$

and

$$M_z = \frac{1}{\Delta} \left\{ -\frac{\alpha_{em}}{a^3} E_y + K \frac{\mu_0 \alpha_m}{a^3} H_z \right\}, \quad (2.70)$$

where

$$\Delta = K \left\{ \frac{\omega_0^2}{\omega^2} - \left( 1 + \frac{\alpha_e}{3K\epsilon_0 a^3} + \frac{\mu_0 \alpha_m}{3a^3} \right) + j \frac{\gamma}{\omega} \right\}, \quad (2.71)$$

$$\Lambda = \frac{\alpha_0}{a^3} \left\{ \frac{\omega_0^2}{\omega^2} - \left( 1 - \frac{\alpha_e}{\alpha_0} + \frac{\mu_0 \alpha_m}{3a^3} \right) + j \frac{\gamma}{\omega} \right\}, \quad (2.72)$$

and

$$K = 1 - \frac{\alpha_0}{3\epsilon_0 a^3} = 1 - \frac{16r_{\text{ext}}^3}{9a^3}. \quad (2.73)$$

Finally, from the above equations it directly follows that

$$\chi_{e,yy} = \frac{\Lambda}{\epsilon_0 \Delta}; \quad \chi_{m,zz} = \frac{K \mu_0 \alpha_m}{\Delta a^3}; \quad \kappa_{yz} = -j \sqrt{\frac{\mu_0}{\epsilon_0}} \frac{\alpha_{em}}{\Delta a^3}. \quad (2.74)$$

The main difference between these results and equation (2.60) is a variation of the frequency of resonance, from  $\omega_0$  to  $\omega_1$ , given by

$$\omega_1^2 = \omega_0^2 \left( 1 + \frac{\alpha_e}{3K\epsilon_0 a^3} + \frac{\mu_0 \alpha_m}{3a^3} \right)^{-1}. \quad (2.75)$$

Bianisotropy has relevant effects in wave propagation through the considered SRR media. The general dispersion relation for plane waves of arbitrary polarization is rather complicated<sup>8</sup>, so we will only consider some specific examples. Plane waves propagating along the  $x$ -axis of Figure 2.12, with the electric field polarized along the  $y$ -axis (plane waves with the orthogonal polarization see a medium with  $\epsilon = \epsilon_0$

<sup>8</sup>An implicit expression for this dispersion relation can be found in [28].

and  $\mu = \mu_0$ ) are TEM waves with the dispersion relation [17]

$$k_x = \omega \sqrt{\mu_{zz} \epsilon_{yy} - \mu_0 \epsilon_0 \kappa_{yz}^2}. \quad (2.76)$$

However, plane waves propagating in the  $y$  direction with the electric field parallel to the  $x$ -axis are TM waves with the  $\mathbf{E}$  field elliptically polarized in the  $x$ - $z$  plane. The dispersion relation for such waves is

$$k = \omega \sqrt{\epsilon_{yy} \mu_{\text{eff}}} \quad \text{and} \quad \mu_{\text{eff}} = \mu_{xx} - \epsilon_0 \mu_0 \frac{\kappa_{yx}^2}{\epsilon_{yy}} \quad (2.77)$$

(see Problems 2.7 and 2.9).

The constitutive parameters for the considered medium when the EC-SRRs are substituted with nonbianisotropic inclusions (such as BC-SRRs or NB-SRRs) can be obtained from the above expressions by taking  $\alpha_{\text{em}}, \alpha_e = 0$ . It is apparent that bianisotropy disappears in such media, which can be included into the category of *indefinite* media [29], already analyzed in Chapter 1.

The behavior of the relevant constitutive parameters in a typical cubic array (Fig. 2.12) of EC-SRRs and BC-SRRs is illustrated in Figure 2.13 and Figure 2.14, respectively. Lorentz local field theory is used for the computation of the constitutive parameters in both cases. Because the EC-SRR medium is bianisotropic, there are four relevant parameters in Figure 2.13: magnetic permeability  $\mu_{zz}$ , magneto-electric susceptibility  $\kappa_{yz}$ , and the dielectric permittivities

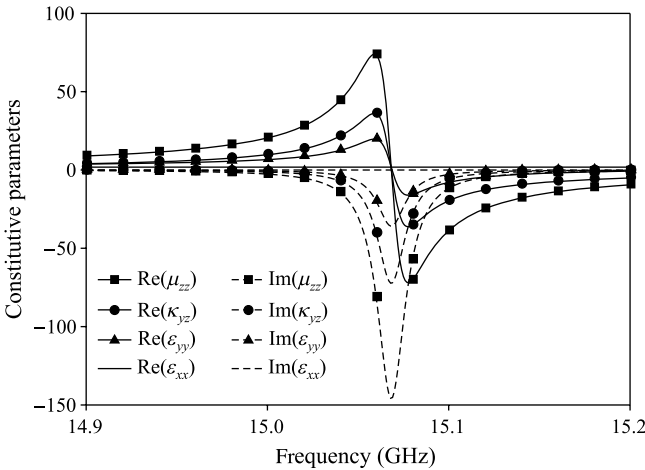


**FIGURE 2.13** Constitutive parameters of the cubic array of Figure 2.12. The Lorentz approximation (2.74) was used for the modeling of the coupling between elements. The Medium parameters are  $r_{\text{ext}} = 1.24$  mm,  $c = 0.2$  mm,  $d = 0.1$  mm, and  $\epsilon = \epsilon_0$ . The metal is copper with a thickness of  $35 \mu\text{m}$ . Periodicity is  $a = 2.5$  mm.



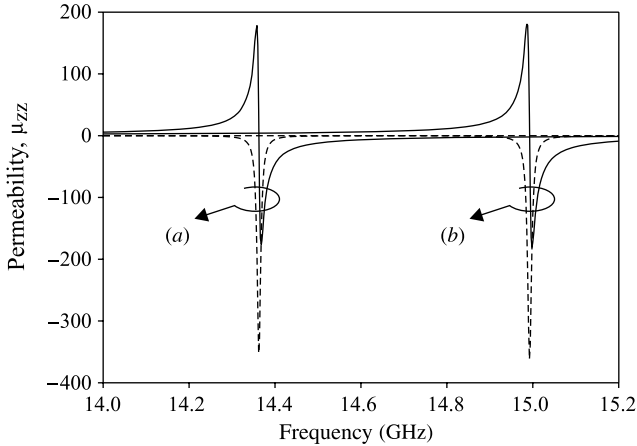


**FIGURE 2.14** Real (solid lines) and imaginary (dashed lines) parts of the constitutive parameters of the cubic array of Figure 2.12 when BC-SRRs are used as basic elements. The medium parameters are  $r_{\text{ext}} = 1.24 \text{ mm}$ ,  $c = 0.2 \text{ mm}$ ,  $t = 0.3 \text{ mm}$ , and  $\epsilon = \epsilon_0$ . The metal is copper with a thickness of  $35 \mu\text{m}$ . Periodicity is  $a = 2.5 \text{ mm}$ . (a) Lorenz approximation (2.74). (b) Zero-order approximation (2.59).

$\epsilon_{yy}$  and  $\epsilon_{xx}$ . Except for this last quantity, all the remaining constitutive parameters show a resonant behavior, and take negative values above the resonance. Unlike the EC-SRR medium, the BC-SRR medium is not bianisotropic (see Section 2.3.2). Therefore, only two parameters are relevant for this structure: the magnetic permeability  $\mu_{zz}$ , and the dielectric permittivities  $\epsilon_{yy} = \epsilon_{xx}$ . Moreover, only one of these quantities—the magnetic permeability  $\mu_{zz}$ —is resonant, taking negative values above the resonance. In order to evaluate the importance of the different homogenization procedures for SRR media, the magnetic permeability for the BC-SRR medium obtained from the zero-order approach (2.60) is also shown in Figure 2.14. Except for a small shift in the frequency of resonance, the results are quite similar. Therefore, we can conclude that the zero-order approach is useful, at least as a rough approximation, for SRR media characterization.

### 2.3.4 Higher-Order Resonances in SRRs

So far, only the first resonance of the SRRs has been analyzed. For such resonance it was shown that the total current excited on the SRR is almost uniform; so that the whole SRR behaves as a small closed loop of uniform current, with a strong associated magnetic moment. As was shown, such resonance can be modeled by an  $LC$  circuit model, whose  $L$  and  $C$  values can be extracted from the SRR geometry. For this reason, the first SRR resonance has been named the *quasistatic resonance* [30]. SRRs also exhibit higher-order resonances that can be excited at higher frequencies. The analysis of such resonances is of interest because they can affect the behavior of the metamaterial at high frequencies. They can be also useful for the design of

some microwave devices [31]. Distributed circuit models to describe SRR higher-order resonances, based on the assumption that almost all the electric field lines go across the slots between the rings, have been recently proposed [18]. From such circuit models, as well as from experiments and simulations [30], it follows that strongly nonuniform total currents are excited on the SRR at higher-order resonances. Therefore, such resonances will be referred to as *dynamic resonances*.

It is illustrative to compare the behavior of higher-order resonances in an SRR presenting cross-polarization effects (for instance the EC-SRR of Fig. 2.5), and in an SRR with inversion symmetry, where such effects are not present (for instance the BC-SRR of Fig. 2.7 or the NB-SRR of Fig. 2.9). This analysis has been developed in detail in [30] on the basis of numerical simulations and experiments. In this section we will briefly describe the main conclusions of such an analysis.

Let us first consider resonators with inversion symmetry, namely the BC-SRR or the NB-SRR. As both rings forming the structure are identical, it is expected that SRR resonances will appear as a consequence of the splitting of the resonances of a single ring. Therefore, the number of resonances in a given frequency interval for the NB- and the BC-SRR should be approximately twice the number of resonances of its constitutive single rings inside such an interval. The analysis of Section 2.3.1 (specifically, the analysis of the current distribution shown in Fig. 2.5c) can be easily extended to the quasistatic resonances of the BC- or the NB-SRR of Figures 2.7 and 2.9, respectively. From such an analysis it follows that the current distribution of these resonances must be *antisymmetric*. That is, the surface current on a given point,  $(x, y)$ , of a ring, namely ring A,  $\mathbf{J}_{s,A}(x, y)$ , has the same amplitude but opposite sign as the surface current on the other ring, namely ring B, at the opposite point:  $\mathbf{J}_{s,A}(x, y) = -\mathbf{J}_{s,B}(-x, -y)$ . In fact, this property is directly related to the inversion symmetry of NB- and BC-SRRs. Therefore, it can be extended to higher-order resonances, which can be classified as *symmetric* (with  $\mathbf{J}_{s,A}(x, y) = \mathbf{J}_{s,B}(-x, -y)$ ) and *antisymmetric* (with  $\mathbf{J}_{s,A}(x, y) = -\mathbf{J}_{s,B}(-x, -y)$ ). Thus, it is expected that each single-ring resonance will split into two NB- or BC-SRR resonances, one symmetric and the other anti-symmetric. This behavior is illustrated in Figure 2.15, where the splitting of the single-ring resonances in the symmetric and anti-symmetric NB-SRR resonances is shown. It follows directly from this classification (and from the definitions of the electric and magnetic dipolar moments) that the symmetric resonances cannot produce any magnetic dipolar moment, whereas the antisymmetric ones (which have a symmetric charge distribution) cannot produce any electric dipolar moment. A particular case of this last property is demonstrated by the well-known behavior of the first (quasistatic) antisymmetric resonance for the considered NB- and BC-SRRs; it is essentially a *magnetic* resonance, which does not present cross-polarization effects (see Section 2.3.2). From the above schema, it follows that the second NB- and BC-SRR resonances are symmetric and *electric* (there is no magnetic dipolar moment associated with such resonance).

The onset of the resonances for the conventional EC-SRR is quite different. Because the rings forming the particle are not identical, its individual frequencies

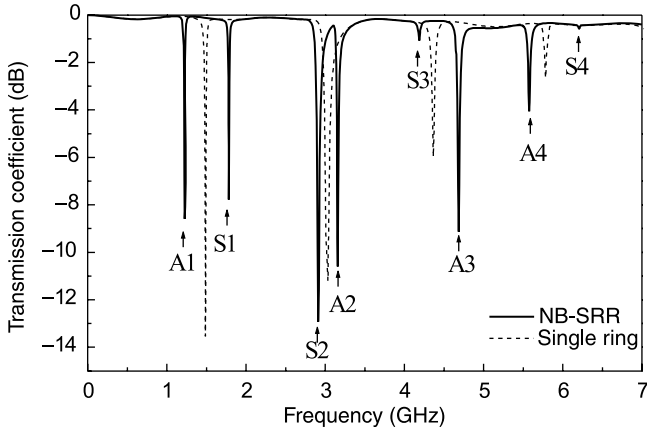


**FIGURE 2.15** Resonances of an NB-SRR. The resonances appear as dips in the transmission coefficient of a microstrip line coupled to the NB-SRR. The NB-SRR resonances are labeled as “symmetric” (S) and “antisymmetric” (A) according to the classification in the text. The resonances of one of the rings making the NB-SRR are also shown. The NB-SRR parameters are external radius  $r_{\text{ext}} = 6.217$  mm, strip width  $c = 0.56$  mm, width separation  $d = 0.37$  mm. The substrate parameters are thickness  $h = 0.49$  mm, dielectric constant  $\varepsilon = 2.43\varepsilon_0$ . (Source: Reprinted with permission from [30]; copyright 2005, American Institute of Physics.)

of resonance must be different. When they are strongly coupled to form an EC-SRR, the frequencies of resonance of each ring will change as a consequence of the coupling. Thus, the final number of these resonances in a given frequency interval will remain constant; that is, it will be roughly the same as for the system of two decoupled rings. The stronger the coupling, the wider the difference between the EC-SRR resonances and those of its constitutive rings. From the above considerations, it directly follows that the classification of symmetric and antisymmetric does not hold for the EC-SRR resonances. Instead, as is illustrated in Figure 2.16, higher-order EC-SRR resonances resemble more the individual resonances of the individual rings forming the structure. Thus, bianisotropic effects can be present, in principle, in all resonances. However, it has been experimentally found that the second resonance of the EC-SRR does not present cross-polarization effects [30]. That is, it has only an associated electric dipolar moment, without any detectable additional magnetic dipolar moment. We do not have, for the moment, any theoretical explanation for this remarkable fact.

As has already been mentioned, higher-order SRR resonances may have effects on the behavior of SRR-based metamaterials. In particular, the second resonance may strongly affect the behavior of such metamaterials if the coupling between the rings forming the SRRs is weak. In such a case, the first and the second resonances appear closely spaced. Because the second resonance produces a strong electric dipole, a dielectric permittivity higher than expected may appear around such a resonance. This region of unexpectedly high electric permittivity may overlap with

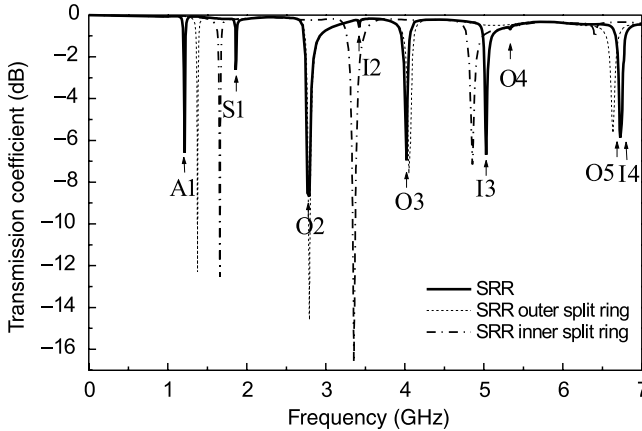


**FIGURE 2.16** Resonances of an EC-SRR determined as in Figure 2.15. The EC-SRR and substrate parameters are the same as in Figure 2.15. Only the first and second resonances can be identified as approximately symmetric or anti-symmetric. Higher-order resonances are similar to those of the outer (O) or inner (I) isolated rings. (*Source:* Reprinted with permission from [30]; copyright 2005, American Institute of Physics.)

the region of negative magnetic permeability, above the first SRR resonance. Conversely, if both SRR rings are strongly coupled, the second SRR resonance will appear far away from the first one. It will then produce a frequency band of high positive/negative dielectric permittivity neatly separated from the negative permeability frequency band. This effect can be useful for some applications [31].

### 2.3.5 Isotropic SRRs

Small magnetic resonators showing a purely magnetic and isotropic response are of great interest for the design of isotropic magnetic metamaterials. It is clear that the magnetic response of any planar SRR, as those analyzed in the previous sections, must be highly anisotropic. In addition, depending on its specific topology, an SRR may also be bianisotropic; that is, it can show both magnetic and electric response at the same resonance. The first attempt to obtain an isotropic SRR design was reported in [32]. In this work, two SRRs of cylindrical shape were attached in order to obtain a composite SRR configuration, which was shown to be isotropic in two dimensions. Unfortunately, it was not possible to generalize this approach to obtain an isotropic three-dimensional configuration. A different approach to the same problem was reported in [33] and [34]. In these works, cubic arrays of SRRs and *Omega* resonators [35] were proposed in order to obtain a composite isotropic magnetic resonator. However, it has been shown [36] that couplings between adjacent elements can destroy the isotropic response of such arrangements.

A systematic approach to the design of isotropic SRR composites must start from the group theory of symmetry transformations in periodic systems [36]. It will be

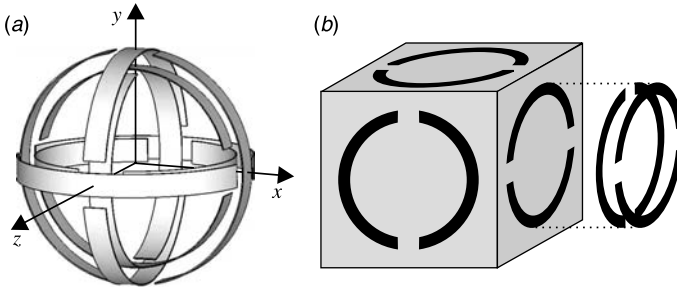


**FIGURE 2.17** Two isotropic composite SRR resonators belonging to the  $T_h$  symmetry group. Both resonators show a purely magnetic response at the first resonance. (Source: Reprinted with permission from [36]; copyright 2006, American Institute of Physics.)

assumed, as usual, that the electromagnetic response of the composite is accurately described by some linear polarizabilities, which form some second-order tensors or pseudotensors. It is well known [21] that there are 32 symmetry groups for periodical systems, which can be classified in seven systems. It is also well known that only the symmetry groups of the cubic system reduce the second-order tensors to scalars, thus imposing an isotropic behavior. Moreover, if cross-polarizabilities must be forbidden, inversion symmetry must be included in such groups. This reduces the possible symmetry groups to only two: the  $O_h$  and  $T_h$  groups in Schönflies notation [36]. The  $O_h$  group includes all the symmetry rotations of the cube, and the inversion. It has the highest symmetry, including 48 symmetry operations. In [37], a resonant magnetic structure showing this symmetry was proposed for magnetic metamaterial design.<sup>9</sup>

The  $T_h$  group is generated by the rotations of symmetry of the tetrahedron and the inversion. It has 24 operations of symmetry, thus imposing lower symmetry constraints than the  $O_h$  group. This fact results in potentially simpler designs. As an example, two isotropic magnetic resonators pertaining to the  $T_h$  symmetry group are shown in Figure 2.17 [36]. The structure shown in Figure 2.17a is a modification of the SRR composite previously proposed in [32]. It is the composition of three 2-SRRs (see Section 2.3.2) of cylindrical shape. This last structure shows two orthogonal symmetry planes (the  $x = 0$  and the  $y = 0$  planes in Fig. 2.10), which behave as virtual perfectly conducting planes at resonance. Therefore, the inclusion of two additional 2-SRRs at these planes (as in Fig. 2.17a) will not affect the behavior of the former 2-SRR when it is illuminated by an orthogonal external magnetic field  $\mathbf{B}_{\text{ext}} = B_{\text{ext}}\hat{\mathbf{z}}$ . Thus, by superposition, the whole structure must exhibit an isotropic and purely magnetic response. The frequency of resonance of the composite must be the same as for each individual 2-SRR (2.54), which is twice that of an EC-SRR of the same size and characteristics. However, this is not a big problem in that the broadside coupling between the rings allows for very high interring capacitances.

<sup>9</sup>In fact, for left-handed metamaterial design, since the proposed structure also included a regular array of wires.

An other example of an isotropic magnetic resonator belonging to the  $T_h$  group of symmetry is the structure shown in Figure 2.17*b*. This is a composite of six two-split BC-SRRs (the structure shown in Fig. 2.7, with an additional symmetric cut on each ring). This composite also belongs to the  $T_h$  symmetry group. Thus, it will also show an isotropic and purely magnetic response [36].

### 2.3.6 Scaling Down SRRs to Infrared and Optical Frequencies

After the demonstration of negative permeability in the microwave range [4], there has been a continuous effort for pushing up the frequency of operation of magnetic metamaterials to terahertz and optical frequencies. A rather obvious strategy in this regard is to take advantage of the linearity of electromagnetism and scaling down the size of the well-known metallic SRR, so that its frequency of operation is pushed up [38,39]. However, the application of this procedure has a limit, because, when frequency increases, metals cannot be characterized as near-perfect conductors, as was assumed in Section 2.3.1. From terahertz to ultraviolet frequencies, most metals can be characterized by the well-known Drude complex permittivity,

$$\hat{\epsilon} = \epsilon_0 \left( 1 - \frac{\omega_p^2}{\omega(\omega - jf_c)} \right), \quad (2.78)$$

where  $\omega_p$  is the plasma frequency, and  $f_c$  is the collision frequency of the electrons. The effects of this new metal characterization on the SRR frequency of resonance and polarizability will be considered throughout this section.

Before analyzing the behavior of an SRR, we will consider the more simple case of a single metallic ring (Fig. 2.18*a*). We will consider, for simplicity, a metallic ring of mean radius  $r$ , made with a cylindrical wire of diameter  $d$  and cross-section  $S = \pi(d/2)^2$ . For good conductors  $f_p = \omega_p/2\pi$  is in the ultraviolet range (several

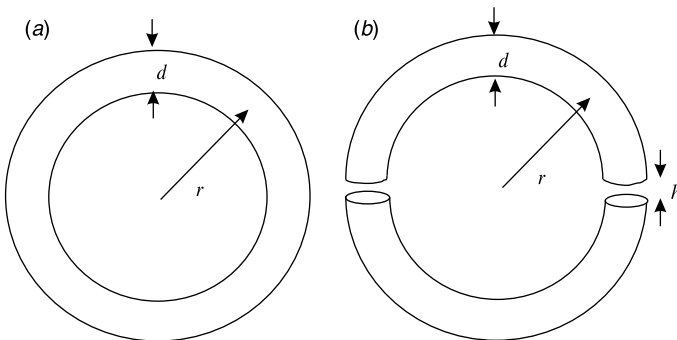


**FIGURE 2.18** (a) Closed metallic ring and (b) the simplest split-ring configuration with inversion symmetry.

thousands of terahertz), and  $f_c$  is between 10 THz and 100 THz. Therefore, roughly speaking,  $\omega_p \sim 10^2 f_c$ . At infrared and optical frequencies,  $\omega$  is still smaller than  $\omega_p$ , say  $\omega \lesssim 0.1 \omega_p$ . Therefore, at such frequencies and below,  $|\hat{\epsilon}| \gg \epsilon_0$ , and equation (2.78) can be approximated as

$$\hat{\epsilon} \simeq -\epsilon_0 \frac{\omega_p^2}{\omega(\omega - jf_c)}. \quad (2.79)$$

From the continuity of the normal component of  $j\omega\hat{\epsilon}\mathbf{E}$  at the metal–air interface, it directly follows that  $\mathbf{n} \cdot \mathbf{E}_r \approx 0$ , where  $\mathbf{E}_r$  is the electric field inside the ring, and  $\mathbf{n}$  is the unit vector normal to the ring boundary. Thus, the electric lines of force are strongly confined inside the wire, forming closed loops along the ring. Therefore, it makes sense to define a *total* current inside the ring as

$$I_t = j\omega\hat{\epsilon}E_r S, \quad (2.80)$$

where  $E_r$  is the magnitude of the electric field inside the ring. This current includes both ohmic and displacement currents, and is approximately uniform along the ring due to the aforementioned confinement effect. Therefore, it is still possible to define the ring magnetic inductance,  $L_m$ , as usual, that is,

$$L_m \equiv \frac{\Phi(I_t)}{I_t}, \quad (2.81)$$

where  $\Phi(I_t)$  is the magnetic flux across the ring. Because the magnetic flux is related to the total current through Ampère's law,  $L_m$  is still approximately given by equation (2.16). In fact, a small correction must be included in equation (2.16) in order to take into account the magnetic energy stored inside the wire, which cannot be neglected for nonperfect conductors. Assuming a uniform distribution of the current inside the ring, the final expression for  $L_m$  is [13]

$$L_m = \mu_0 r \left[ \ln \left( \frac{16d}{r} \right) - \frac{7}{4} \right]. \quad (2.82)$$

Taking into account equations (2.79) and (2.80), the electromotive force around the ring  $\mathcal{E} = \oint \mathbf{E} d\mathbf{l} \simeq 2\pi r E_r$  can be written as

$$\mathcal{E} \simeq (R + j\omega L_k) I_t, \quad (2.83)$$

where  $R$  is the resistance of the ring

$$R = \frac{2\pi r f_c}{S\omega_p^2 \epsilon_0}, \quad (2.84)$$

and  $L_k$  is a magnitude with dimensions of inductance given by

$$L_k = \frac{2\pi r}{S\omega_p^2 \epsilon_0}. \quad (2.85)$$

This inductance can be interpreted as being due to the kinetic energy of the electrons [40]. Putting all this together, the final equation for the current  $I_t$  on the ring is given by

$$\{R + j\omega(L_m + L_k)\}I_t = -j\omega\Phi_{\text{ext}}, \quad (2.86)$$

where  $\Phi_{\text{ext}}$  is the external magnetic flux across the ring. Therefore, as long as  $|\hat{\epsilon}| \gg \epsilon_0$  (which is satisfied if  $\omega \lesssim 0.1\omega_p$ ), the only effect of scaling down the ring is the onset of the additional inductance  $L_k$ . From equations (2.82) and (2.85) it follows that [41]

$$\frac{L_m}{L_k} \approx \frac{2\pi S}{\lambda_p^2}, \quad (2.87)$$

where  $\lambda_p = 2\pi c/\omega_p$  is the ‘‘plasma wavelength’’, that is, the free-space wavelength at the plasma frequency.

Let us now consider what happens when some capacitive gaps are added to the closed ring of Figure 2.18, in order to obtain a resonant behavior. The simplest resonant configuration having inversion symmetry (in order to avoid cross-polarization effects) is shown in Figure 2.18*b*.<sup>10</sup> However, the present analysis is not restricted to such a configuration, and more complicated geometries can be considered, including the SRRs reported in Sections 2.3.1 and 2.3.2. We will assume, as in the preceding paragraph, that  $|\hat{\epsilon}| \gg \epsilon_0$ , so that equation (2.79) holds. If the gaps are sufficiently narrow, the electric field lines of force are still confined inside the ring, passing across the gaps from one half ring to the other. Moreover, from the continuity of the normal component of  $j\omega\hat{\epsilon}\mathbf{E}$  at the gap boundaries, it directly follows that the total current  $I_t$  is still uniform along the ring and gaps.<sup>11</sup> Also, because the

<sup>10</sup>This configuration was proposed and analyzed in [40].

<sup>11</sup>This behavior is quite similar to the behavior of the magnetic flux through the arms and between the poles of an electromagnet, as described in many elementary textbooks of electricity and magnetism (see, e.g., [42]).



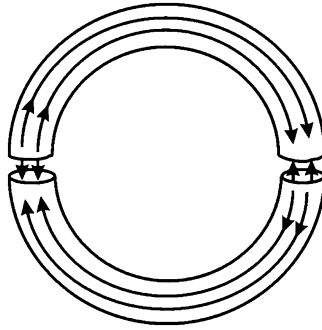


**FIGURE 2.19** Schematic illustration of the behavior of the electric field lines inside the resonator of Figure 2.18b.

permittivity inside the metal is essentially real and negative, the continuity of  $\hat{\epsilon}\mathbf{E}$  implies that the sign of the electric field lines is reversed in the gaps, as is shown in Figure 2.19.

Provided the aforementioned hypotheses are fulfilled, the equation for the total current in the resonator of Figure 2.18b is given as

$$\left(R + j\omega(L_m + L_k) + \frac{1}{j\omega C}\right)I_t = -j\omega\Phi_{\text{ext}}, \quad (2.88)$$

where  $C$  is the total capacitance provided by the series connection of the gaps (i.e.,  $C = C_g/2$ , where  $C_g$  is the capacitance of each gap). From equation (2.88), the total current, as well as the associated magnetic moment  $m = \pi r^2 I_t$ , can be obtained. Finally, the magnetic polarizability of the ring is obtained as

$$\alpha_{zz}^{\text{mm}} = \alpha_0 \left( \frac{\omega^2}{\omega_0^2 - \omega^2 + j\omega\gamma} \right) \quad \text{and} \quad \alpha_0 = \frac{\pi^2 r^4}{L_m + L_k}, \quad (2.89)$$

where  $\omega_0$  is the frequency of resonance,

$$\omega_0 = \sqrt{\frac{1}{(L_m + L_k)C}}, \quad (2.90)$$

and

$$\gamma = \frac{R}{L_m + L_k}. \quad (2.91)$$

Such expressions are, in fact, quite similar to equation (2.45). The only difference with equation (2.45) is the presence of the kinetic inductance  $L_k$ . Therefore, we can conclude that the analysis developed throughout the previous sections is still

valid at optical and infrared frequencies, provided the presence of the kinetic inductance (2.85) is taken into account. The main restriction for the validity of such an analysis is that the condition  $|\hat{\epsilon}| \gg \epsilon_0$  must hold at the considered frequency.

Let us now consider the behavior of the SRR polarizability when the resonator is scaled down in order to increase its frequency of resonance. Because, according to equation (2.85),  $L_k$  scales as  $1/r$ , for small SRR sizes it dominates over  $L_m$ , which scales as  $r$ . Therefore, for sufficiently small ring sizes,  $L_k \gg L_m$ , and the frequency of resonance (2.90) saturates [40] to the value

$$\omega_0 = \sqrt{\frac{1}{L_k C}} \quad (2.92)$$

which does not depend on SRR size. Also the loss factor saturates to

$$\gamma_s = \frac{R}{L_k} = f_c. \quad (2.93)$$

Finally, the amplitude of the magnetic polarizability scales down as

$$\alpha_0 \rightarrow \frac{\pi^2 r^4}{L_k} = \omega_p^2 \epsilon_0 r^3 S. \quad (2.94)$$

Let us consider, as in previous paragraphs, a cubic array of SRRs of lattice constant  $a$ . As was discussed in Section 2.3.3, the magnetic susceptibility  $\chi_{zz}$  can be approximated as  $\chi_{zz} \approx \mu_0 \alpha_{zz}^{\text{mm}} / a^3$ . Thus, from the previous considerations, it follows that, for sufficiently small SRR sizes, this susceptibility behaves as

$$\chi_{zz} \approx \chi_0 \left( \frac{\omega^2}{\omega_s^2 - \omega^2 + j\omega\gamma_s} \right) \quad \text{and} \quad \chi_0 = \mu_0 \frac{\alpha_0}{a^3} \sim (2\pi)^2 \left( \frac{r}{a} \right)^3 \frac{S}{\lambda_p^2}. \quad (2.95)$$

This expression shows that, when the structure is scaled down in the optical range, the amplitude of the magnetic susceptibility also scales down as the square of SRR size (see also Problem 2.11).<sup>12</sup> The above discussion shows that scaling down SRR media in order to achieve a negative magnetic permeability at infrared and optical frequencies has two main limitations: saturation of frequency of resonance and decrease of the magnetic response. Such effects appear when the key parameter  $S/\lambda_p^2$  becomes small, which, according to equation (2.87), makes the kinetic inductance dominant over the magnetic one.

Recently, kinetic inductance of conductors has been invoked in order to develop nano-inductors at optical frequencies [43]. According to our previous discussion, a

<sup>12</sup>In the RF and microwave range, however, because  $L_m$  scales down as  $r$ , the amplitude  $\chi_0$  does not vary substantially when the structure is scaled down.

metallic wire of length  $l$  and section  $S$  has a kinetic inductance that is given by a direct generalization of equation (2.85); that is,

$$L_k = \frac{l}{S\omega_p^2\epsilon_0}. \quad (2.96)$$

Therefore, it can be considered as a nanoinductor with the above inductance. In fact, any nanocircuit is composed of some closed loops of current, and in order to apply Kirchoff's laws, the magnetic inductance of every loop should be much smaller than the inductance of each inductor in the circuit. For instance, the SRR of Figure 2.18*b* can be considered a nanocircuit formed by two nanoinductors (the wires) and two nanocapacitors (the gaps), provided its magnetic inductance  $L_m$  is much smaller than the kinetic inductance  $L_k$ . From equation (2.87) it follows that this condition is satisfied if

$$S/\lambda_p^2 \ll 1. \quad (2.97)$$

In fact, it can be easily realized that the same condition must hold for any closed loop of any hypothetical nanocircuit. Therefore, equation (2.97) seems to be a necessary condition for the applicability of the nanoinductor concept.

Higher-order SRR resonances in the optical range are dynamic plasmonic resonances. Closed metallic rings made of metallic wires resonate when the ring perimeter is equal to a wavelength of one of the plasmons that can be excited along the wire [44]. From this result it can be guessed that  $n$ -cuts SRRs will resonate when each piece of wire forming the SRR is a multiple of a half-wavelength of a plasmon propagating along the wire. Such resonances can also generate electric and magnetic dipoles, so their analysis (either to avoid, or to take advantage of them) may also be important for SRR characterization at infrared and optical frequencies. Such analysis is, however, beyond the scope of this book.

## 2.4 SRR-BASED LEFT-HANDED METAMATERIALS

The first artificial left-handed medium, designed by David Smith and co-workers [4], came only one year after Pendry's proposal for SRR-based artificial negative magnetic permeability media [3]. Smith's first design was a combination of wires (which provide the negative permittivity) and SRRs (which provide the negative permeability) [4]. Soon after, negative refraction in left-handed media was experimentally demonstrated [45], using a very similar design. Since then, wires and/or metallic plates assembled with SRRs have been the most popular combination for left-handed metamaterial design. Through this section, the main characteristics of these proposals will be described in detail. Other proposals will be analyzed in Section 2.5.

### 2.4.1 One-Dimensional SRR-Based Left-Handed Metamaterials

The first practical realization of a left-handed metamaterial [4] was, in fact, a one-dimensional realization. The reported structure is shown in Figure 2.20. It consists of an array of metallic wires and EC-SRRs placed between two parallel metallic plates. The structure was illuminated by a plane wave polarized with the electric field parallel to the wires, and the magnetic field perpendicular to the EC-SRRs, so that the parallel metallic plates simulate an infinite periodic medium along the wire axis. In a previous experiment, propagation through a structure as in Figure 2.20, but without the wires, was checked. A stopband was observed in this last structure near the frequency of resonance of the SRRs (solid line in Fig. 2.21). This stopband is consistent with the negative magnetic permeability associated with the SRRs. When wires were introduced, the aforementioned stopband switched to a passband (dashed lines in Fig. 2.21). Because the frequency of the experiment was well below the plasma frequency of the system of wires, the aforementioned passband is consistent with the combination of the negative permittivity of the wire system (see Section 2.2.2) and the negative permeability of the SRR system. Therefore, it was the first experimental observation of electromagnetic propagation through a left-handed medium. Backward-wave propagation was tested by computing the dispersion relation by electromagnetic simulation. The results of such simulations, as well as the dispersion relations obtained from the theory reported in this chapter (see Sections 2.2.2 and 2.3.3), are shown in Figure 2.22. The slight mismatch between the negative- $\mu$  stopband and the left-handed passband comes from the bianisotropy of the EC-SRR system [17] (see Problem 2.8).

The structure of Figure 2.20 only shows a left-handed behavior for a specific polarization and direction of propagation of the electromagnetic field. Therefore, it can be considered a one-dimensional metamaterial, showing negative effective permittivity along the wires, and—neglecting bianisotropy—negative permeability along the SRR

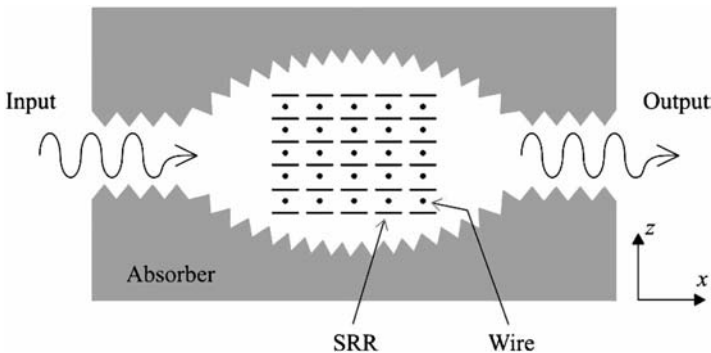


**FIGURE 2.20** Sketch of Smith's experiment (top view). The relative location of wires and SRRs is illustrated. The whole system is placed between two (upper and bottom) metallic plates, and simulates an infinite medium along the wire axis. The orientation of the EC-SRRs with regard to the  $x$ - $y$ - $z$  axes is the same as in Figure 2.12.

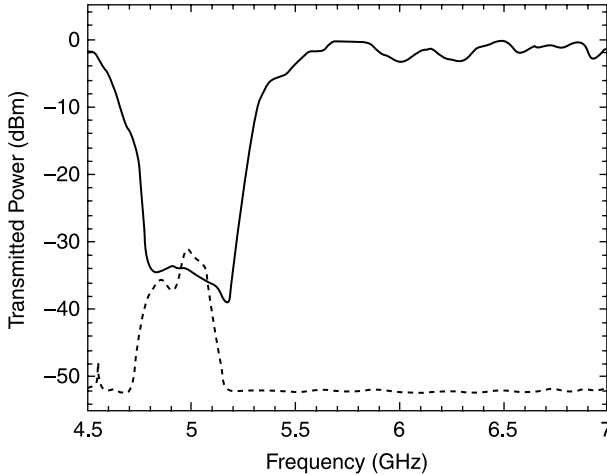


**FIGURE 2.21** Transmission coefficient through the structure proposed in [4] (see Fig. 2.20) when only SRRs are present (solid line), and when wires and SRRs are present (dashed line). (Source: Reprinted with permission from [4]; copyright 2000, by the American Physical Society.)

axis. If the wire rows are substituted with metallic plates, a more simple one-dimensional structure is obtained [46]. Such a structure is shown in Figure 2.23. It is made of a single row of SRRs placed inside a cutoff square waveguide, along its middle E-plane. In such a configuration, the effective negative permittivity (2.2) is provided by the cutoff waveguide and the effective negative permeability by the SRRs:  $\mu_{\text{eff}} = \mu_0(1 + \chi_{m,zz})$ , with  $\chi_{m,zz}$  given by equation (2.74). The left-handed passband measured in the device of Figure 2.23 is shown in Figure 2.24. Backward-wave propagation along this device has been experimentally demonstrated in [48]. As in the structure reported in [4], bianisotropic effects are also present in the structure of Figure 2.23. These effects can be eliminated if BC-SRRs are used instead of EC-SRRs [50]. This last structure provides an easy way of simulating propagation in left-handed metamaterials. It will be extensively used in Section 2.4.5 to check the accuracy of the models proposed in this chapter for SRR-based metamaterials.

It will be illustrative to mention here that the results reported in Figures 2.23 and 2.24 can also be interpreted in terms of a cutoff waveguide filled by an uniaxial medium with negative permeability along the SRR axis [47,48]. This interpretation models the structure of Figure 2.23 as a waveguide filled by a uniaxial anisotropic magnetic medium with  $\mu_{xx} = \mu_{yy} = \mu_0$  and  $\mu_{zz}$  obtained from equation (2.74).<sup>13</sup> From Maxwell's equations, it is deduced that the dispersion relation for such

<sup>13</sup>Bianisotropy, as well as the small correction to  $\epsilon_{yy}$  due to the nonresonant electric polarizability of the SRRs, are neglected in this analysis. However, they can be easily included in the model.

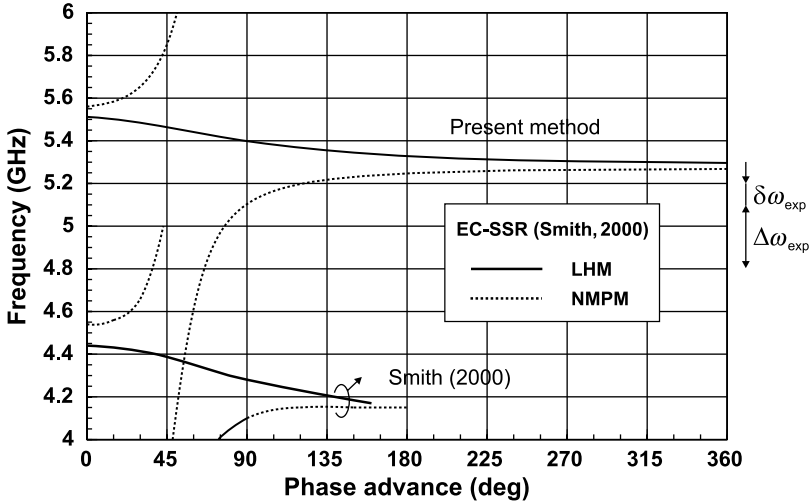


**FIGURE 2.22** Phase advance ( $ka$ ) as a function of frequency for the SRR medium of Figure 2.20 without wires (dotted lines), and phase advance for the SRR and wire left-handed medium of Figure 2.20 (solid line). The experimental (see Fig. 2.21) left-handed passband  $\Delta\omega$ , as well as the experimental stopband  $\Delta\omega + \delta\omega$ , are also shown in the figure. The SRR dimensions are  $c = 0.8$  mm,  $d = 0.2$  mm,  $r_{\text{int}} = r - d/2 - c = 1.5$  mm, and  $t = 0.216$  mm. The relative dielectric permittivity of the circuit board is  $\epsilon_r = 3.4$ , and the lattice constant  $a = 8.0$  mm. (Source: Reprinted with permission from [19]; copyright 2003, IEEE.)

a waveguide is given by

$$k^2 = \omega^2 \mu_{zz} \epsilon_0 \left( 1 - \frac{\omega_c^2}{\omega^2} \right) = \omega^2 \epsilon_{\text{eff}} \mu_{\text{eff}}, \quad (2.98)$$

where  $\omega_c$  is the cutoff frequency of the hollow waveguide. This dispersion relation is exactly the same dispersion relation that is deduced from the analysis in the previous paragraph. Therefore, both models are fully equivalent, leading to the same dispersion relation. In our opinion this fact does not mean that the interpretation previously developed in this section is erroneous.<sup>14</sup> It only shows that, in order to obtain a left-handed behavior by loading a waveguide below cutoff with magnetic resonators, such resonators must interact with the transverse components of the magnetic field and not with the longitudinal components of such a field. This behavior can be obtained from SRRs, or from a hypothetical uniaxial magnetic medium.<sup>15</sup>

<sup>14</sup>See author's reply to [47] for a deeper discussion on this point.

<sup>15</sup>There are at least two more interesting interpretations of the results reported in [46]. The first was proposed by Belov [49], and considers the SRR-loaded waveguide as equivalent to a system of magnetic scatterers (the SRRs) propagating a wave that is stationary in the  $z$ -direction (with  $k_z = \pm \pi/a$ , where  $a$  is the width of the waveguide). Another possible interpretation considers the results reported in [46] as the composition of two magnetostatic waves in an infinite SRR medium (see Problem 2.10) with  $k_z = \pm \pi/a$ ,  $k_y = 0$  and  $k_x$  given by equation (2.167) (see Problem 2.10). It can be easily shown that for  $\pi/a \ll k_0 \equiv \omega\sqrt{\epsilon_0\mu_0}$ , the value of  $k_x$  obtained from equation (2.167) coincides with equation (2.98).

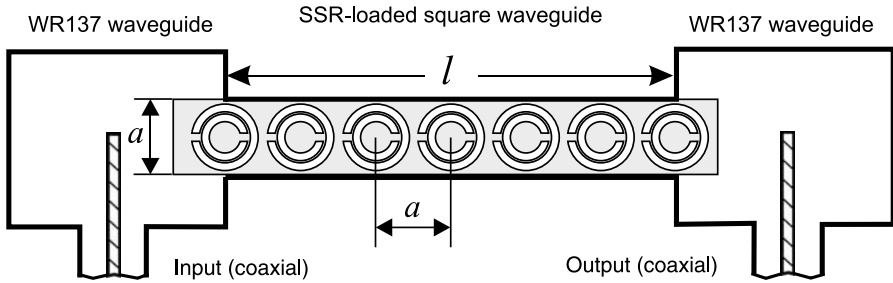


**FIGURE 2.23** Sketch of the one-dimensional left-handed medium simulation experiment in [46]. [Source: Reprinted with permission from [46]; copyright 2002, American Physical Society.]

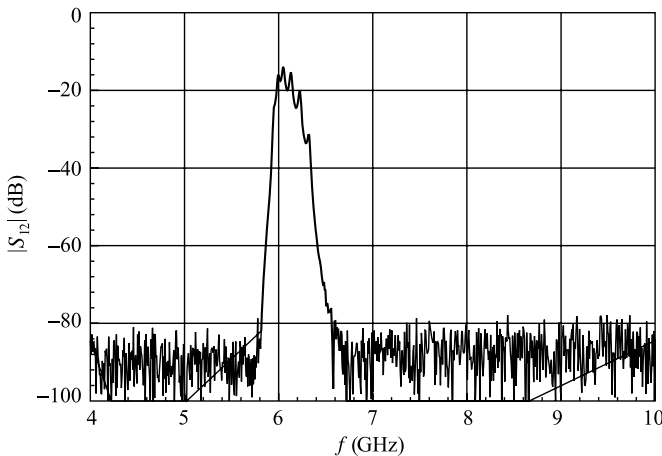


**FIGURE 2.24** Transmission coefficient through the structure of Figure 2.23. (Source: Reprinted with permission from [46]; copyright 2002, American Physical Society.)

From the dispersion relation (2.98)—whatever the physical interpretation of such an equation—it is deduced that, if the hollow waveguide is above cutoff, the left-handed passband associated with the negative magnetic permeability becomes a stopband. This effect has been shown experimentally in [51]. In such an experiment, two hollow waveguides—one above and the other below cutoff—were loaded by equispaced BC-SRR rows. The resulting transmission is shown in Figure 2.25, where it can be clearly seen how the left-handed passband of the narrow waveguide becomes a stopband in the wider waveguide. The mismatch between both bands, near the BC-SRR resonance, can be explained by the high losses and anomalous dispersion at such frequencies. The behavior shown in Figure 2.25 can be considered as the counterpart, in waveguide configurations, of the passbands and stopbands of Figure 2.21.

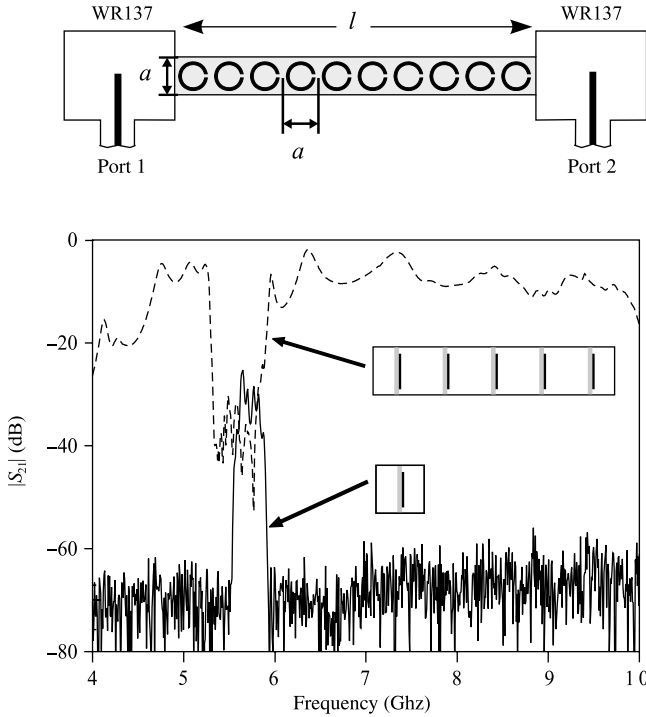


**FIGURE 2.25** Transmission coefficient through the BC-SRR loaded waveguides sketched in the figure. The narrow waveguide cross-section was  $6 \times 6 \text{ mm}^2$ , and the wide waveguide cross-section was  $30 \times 6 \text{ mm}^2$ . The periodicity is  $a = 6 \text{ mm}$ . The BC-SRR parameters are  $r_{\text{ext}} = 2.28$  and  $c = 0.5 \text{ mm}$ . The substrate parameters are  $\epsilon = 2.43\epsilon_0$  and thickness  $t = 0.49 \text{ mm}$ . The metallization was in copper with a thickness  $h = 35 \mu\text{m}$ . (Source: Reprinted with permission from [51]; copyright 2003, IEEE.)

### 2.4.2 Two-Dimensional and Three-Dimensional SRR-Based Left-Handed Metamaterials

The structures reported in the previous section exhibit a left-handed behavior for a specific direction of propagation, and for a specific polarization of the electromagnetic wave. Therefore, they are not suitable for the demonstration of negative refraction at the interface with an ordinary medium. For this purpose, a two-dimensional isotropic left-handed medium is necessary. Such a medium was designed and manufactured soon after the first demonstration of a left-handed medium [52]. It was a modification of the earlier design of [4], consisting of an orthogonal arrangement of dielectric circuit boards with EC-SRRs and metallic strips printed on each side, as is shown in Figure 2.26. The whole array is placed between two horizontal metallic plates connected to the strips, so that an infinite structure is simulated along the  $z$ -axis. As in the structure of Figure 2.20, the negative permittivity comes from the metallic strips, and the negative permeability from the SRRs. However, the whole structure is



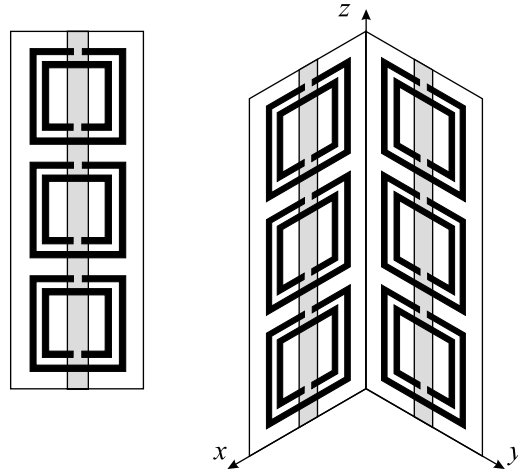


**FIGURE 2.26** The basic unit of the two-dimensional left-handed metamaterial reported in [52] (left). The metallic strips (gray) and the EC-SRRs (black) are printed on opposite sides of the dielectric substrate. The metamaterial was made from a two-dimensional periodic array along the  $x$ - and  $y$ -directions of such basic units (right). The whole system was placed between two conducting plates parallel to the  $x$ - $y$  plane that simulates an infinite medium in the  $z$ -direction.

now isotropic in two dimensions.<sup>16</sup> Using the reported structure, negative refraction at the interface between ordinary and left-handed media was first demonstrated [45]. It is instructive to note that, in Figure 2.26, metallic strips are placed along the symmetry planes of the SRRs. Such planes behave as virtually perfect electric conductors at resonance, a fact that minimizes the strip-SRR interaction (we will return to this point later, in Section 2.4.4).

An alternative design for two-dimensional isotropic left-handed metamaterials was proposed in [50]. It consists of metallic plates and BC-SRRs arranged and illuminated as is shown in Figure 2.27. As in previous designs, the negative permeability comes from the SRRs. However, in the present design, negative permeability comes from the parallel metallic plates (see Section 2.2.1). Because its fabrication only involves a single printed circuit board, this design is more simple to manufacture than the previous one. Moreover, the use of BC-SRRs ensures that cross-polarization effects are not present along the structure. Negative refraction using the two-dimensional left-handed structure of Figure 2.27 was experimentally demonstrated in [53].

Compared with two-dimensional structures, the development of practical isotropic left-handed media in three dimensions is still a challenging issue. In principle, a three-dimensional cubic array of connected wires could provide negative permittivity (see Section 2.2.2), whereas magnetic permeability could come from a cubic arrangement

<sup>16</sup>In fact, regarding the analysis in Section 2.3.3, this structure must be biisotropic in two dimensions (see Problem 2.9). However, for the structure proposed in [52] this effect is small except near the resonance, and can be neglected in a first-order approximation.

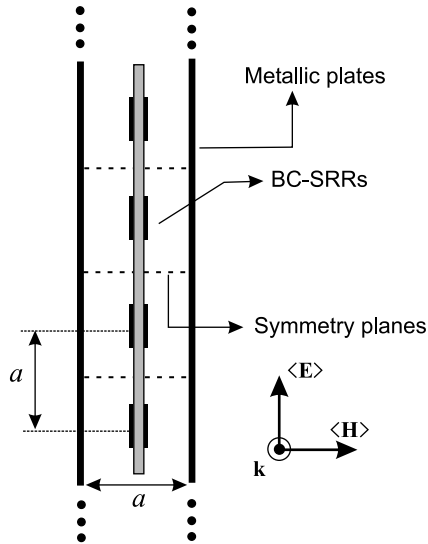


**FIGURE 2.27** Sketch (front view) of the two-dimensional isotropic left-handed metamaterial proposed in [50]. A square array of BC-SRRs is printed on a dielectric board, placed between two parallel metallic plates.

of any of the isotropic SRRs reported in Section 2.3.5. However, practical technological limitations to this procedure may be enormous. First, isotropic SRRs are rather sophisticated structures, much more difficult to manufacture than planar SRRs. Then, the number of SRRs involved in a three-dimensional design grows as  $l^3$ , where  $l$  is the typical length of the structure. Finally, to assembly all the elements is not a trivial task. Moreover, once backward-wave propagation and negative refraction in left-handed media has been demonstrated using one- and two-dimensional structures, the scientific interest in three-dimensional structures decays. However, these designs may still be of interest for many practical applications, such as three-dimensional lenses or coats. In [37] an isotropic three-dimensional left-handed metamaterial design was proposed and validated by numerical simulations. Other similar designs, using a cubic network of metallic wires in combination with different isotropic SRRs, such as those shown in Figure 2.17, can be envisaged.

### 2.4.3 On the Application of the Continuous-Medium Approach to Discrete SRR-Based Left-Handed Metamaterials

The continuous-medium approach for the description of electromagnetic properties of a discrete medium always involves an averaging—or homogenization—procedure. This homogenization only has sense if the variation of the *average field* is small at the scale of the constitutive elements of the medium. This condition is usually expressed as follows: The size of the elements must be small as compared with the wavelength of the host medium,  $\lambda_h$ , at the frequency of operation. Stated in this

form, the above condition is approximately satisfied by the reported SRR-based metamaterials. In fact, in all the experiments reported along the previous section, the unit cell size was  $\sim\lambda_h/10$ . However, the aforementioned condition cannot be accepted without discussion. All left-handed metamaterials analyzed in this section are resonant structures, whose wavevector varies from 0 to  $\infty$  in a small frequency band (see, e.g., Fig. 2.22). Therefore, the internal wavelength of the metamaterial  $\lambda_i = 2\pi/k$  varies from very large to very small values in the operation band. Because it is the internal wavelength that determines the scale of variations of the averaged field, we conclude that the size of the metamaterial elements must be much smaller than  $\lambda_i$  in order to justify the homogenization. It is apparent that this condition cannot be fulfilled in the whole left-handed passband. In particular (Fig. 2.22), it cannot be fulfilled at the lower frequencies of this passband, where  $\lambda_i \rightarrow 0$  (in fact, all the values of the phase advance outside the first Brillouin zone, i.e., higher than  $\pi$ , have no physical meaning—they were only computed in order to determine the passband predicted by the model). Therefore, for the lowest frequencies of the passband the discrete nature of the metamaterial must be taken into account. That is, the metamaterial should be explicitly analyzed as a three-dimensional periodic structure. Of course, the smaller the electrical size of the elements is (in terms of the host medium wavelength), the smaller is such a frequency region.

Conversely, at the upper frequencies inside the passband,  $\lambda_i \rightarrow \infty$ , and the homogenization makes sense regardless of the size of the elements. Therefore, it can be concluded that the continuous medium approach in left-handed metamaterials is valid at the high-frequency region of the passband, and becomes more and more inaccurate as the frequency approaches the lower limit of the passband.

#### 2.4.4 The Superposition Hypothesis

There is another important issue that has to be discussed in relation to the accuracy of the continuous-medium approach, as it has been applied in most of the reported contributions to left-handed metamaterials. In fact, all left-handed metamaterials described in this section (and in all the reported references), are the superposition of two systems, one of them exhibiting negative permittivity and the other showing negative permeability. It was assumed without discussion that the electric and magnetic susceptibilities of the resulting media are the superposition of the electric and magnetic susceptibilities of the aforementioned isolated systems. Because the elements of both systems are placed very close in the metamaterial, and therefore they can interact, this assumption is not apparent at all.

This topic was discussed in [54], where it was shown that a system of parallel wires placed in a host medium with negative permeability cannot propagate electromagnetic waves. This result could be expected from the expression for the inductance of the wires (2.6): When the permeability of the surrounding medium is negative, such inductance also becomes negative, thus destroying the negative permittivity provided by the wires. From such a result, it was concluded in [54] that the superposition of a system of wires and a system of SRRs cannot be seen, in general, as a medium with simultaneously negative permittivity and permeability. The argument in [54]

becomes even more apparent if we consider the structure shown in Figure 2.23 (or in Fig. 2.27). It can be easily shown [47] that electromagnetic waves cannot propagate along a waveguide filled by an isotropic medium of negative permeability.

The meaning and validity of the superposition hypothesis for left-handed media based on SRRs and wires or plates was further discussed in [55] and in the author's reply to [47]. It is important to recall that the continuous-medium approach only accounts for the behavior of the average field, and not for the field behavior at the much smaller scale of the metamaterial elements. At this scale, the short-range quasiolestatic and quasimagnetostatic interactions between the metamaterial elements determine the coupling between them. Therefore, the relative disposition of such elements is crucial for the accuracy of the aforementioned superposition hypothesis. Systems providing negative permittivity and negative permeability should be placed in such a way that the interaction between its elements through its quasistatic fields is minimized. This is actually the case in Figure 2.20, where the magnetic flux created by a wire on its nearest SRRs vanishes, so that the wire's inductance is not affected by the SRRs. This is also the case in Figure 2.26, where the metallic strips are placed in the plane of symmetry of the SRRs, which behave as a virtual perfect conductor (see Section 2.4.2). In fact, it has been shown that if the SRRs of Figure 2.20 are placed along the wire rows (where magnetic interaction has a maximum), and not between these rows, as in the actual experiment, the left-handed behavior disappears [56] (both configurations are illustrated in Fig. 2.28).

Regarding the structures where negative permittivity comes from metallic waveguides or plates—as in Figures 2.23 and 2.27—in order to obtain a left-handed behavior, the SRRs must interact with the transverse magnetic field, but not with the longitudinal magnetic field of the structure. Note that the transverse component of the magnetic field, after averaging, produce the *macroscopic* magnetic component of the left-handed wave. However, due to the symmetry of such devices, the average longitudinal magnetic field component vanishes. That is, in order to achieve a left-handed behavior for the average wave, the magnetic resonators must interact with the macroscopic field components, and not with the *microscopic* ones.

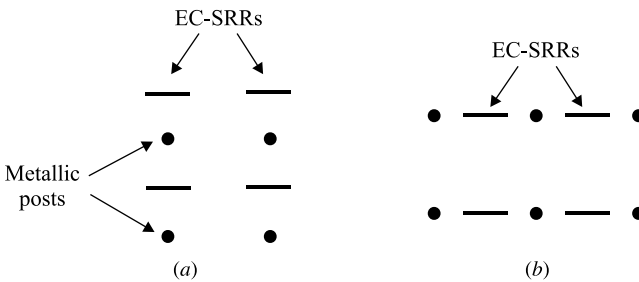


**FIGURE 2.28** (a) Sketch (top view) of the configuration of Figure 2.20, where a left-handed behavior was observed at some frequency range [4]. (b) Sketch (top view) of a configuration in which there is no wave propagation at the same frequencies [56].

In summary, it can be concluded that, in general, a superposition of two systems, one of them providing negative permittivity and the other providing negative permeability, does not make a left-handed medium. However, there are some clever relative dispositions of the elements of both systems for which the aforementioned superposition hypothesis is fulfilled, and the left-handed behavior is achieved. Ultimately, it is the agreement with the experiments that provides the final proof of the superposition hypothesis for a given design.

#### 2.4.5 On the Numerical Accuracy of the Developed Model for SRR-Based Metamaterials

The numerical accuracy of the reported theory for the computation of the constitutive parameters of left-handed metamaterials has already been illustrated in Figure 2.22, where it was compared with simulations and experimental results. It has also been experimentally tested in [51]. In this paper a BC-SRR loaded cutoff waveguide, similar to that shown in Figure 2.23, was used in order to experimentally check the theoretical model (the only difference with Fig. 2.23 was that BC-SRRs instead of EC-SRRs were used). Electromagnetic propagation through three similar devices of different lengths, with 10, 20, and 30 consecutive BC-SRRs, was studied. In particular, the time delay and the attenuation were measured. From these results, the slow-wave factor  $c/v_g$  (where  $v_g$  is the group velocity) and the attenuation constant of the metamaterial were extracted in a quite direct way (see [51] for more details). Theoretical and experimental results for a particular structure are shown in Figures 2.29 and 2.30. The slow-wave factor can be directly related to the phase constant,  $k$ , through  $v_g = |\partial\omega/\partial k|$ . Therefore, its measurement can be considered equivalent to a measurement of the dispersion relation

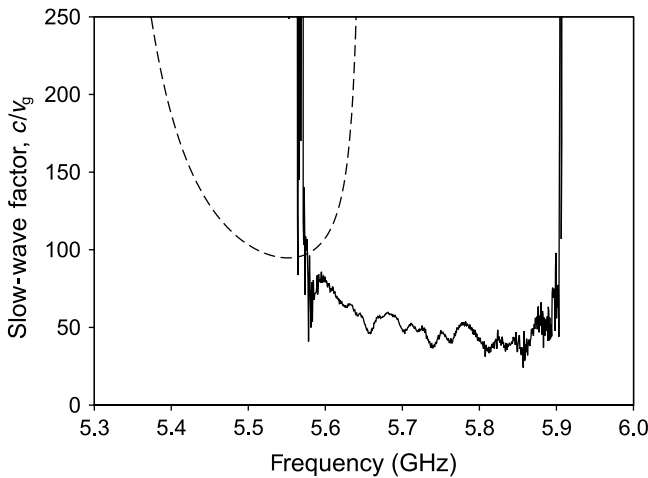


**FIGURE 2.29** Theoretical and experimental values for the slow-wave factor along the narrow BC-SRR loaded waveguide of Figure 2.25. Waveguide and BC-SRR characteristics are as in Figure 2.25. (Source: Data reproduced with permission from [51]; copyright 2003, IEEE.)

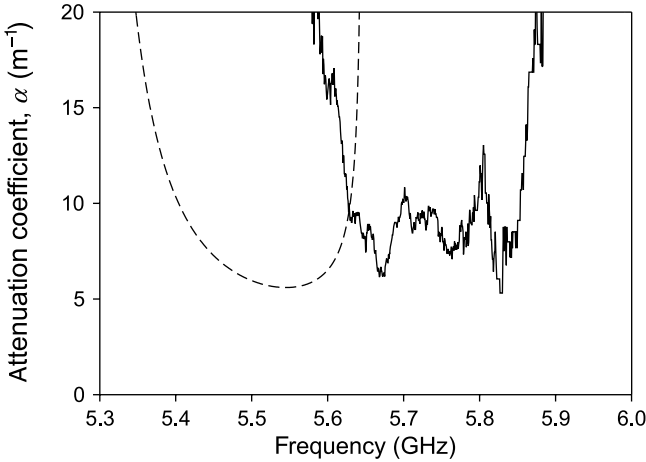


**FIGURE 2.30** Theoretical and experimental values for the attenuation factor along the narrow BC-SRR loaded waveguide of Figure 2.25. (Source: Data reproduced with permission from [51]; copyright 2003, IEEE.)

$\omega(k)$  of the metamaterial. On the other hand, the measurement of the phase and attenuation constants in the considered structure corresponds to the measurement of these quantities on a typical SRR-based left-handed metamaterial (see Sections 2.4.1 and 2.4.2). Therefore, such measurements can be considered to be a good test for the accuracy of the model developed in this chapter. It is clear from the figures that the model provides a good qualitative picture of the metamaterial behavior, reproducing the passband width and location with only a few percent of error. Attenuation also seems to be approximately predicted. The main disagreement is in the slow-wave factor, that is, in the slope of the dispersion relation  $\omega(k)$ . This fact can be related to a drawback in the application of the continuous-medium approach to a discrete metamaterial with a periodicity not smaller than  $\lambda/10$ . In fact, as has already been discussed in Section 2.4.3, for the lower frequencies of the passband, the internal wavelength becomes very small, and the discrete nature of the metamaterial cannot be ignored. It can be guessed that for smaller periodicities this drawback could be overcome.

In summary, it can be concluded that the reported theory not only provides physical insight on the qualitative behavior of left-handed SRR-based metamaterials, but also reasonable quantitative results (only limited by general considerations about the validity of the homogenization procedures). This is a remarkable fact, because the developed theory is analytical and, therefore, much more simple to implement than standard electromagnetic simulation techniques.

## 2.5 OTHER APPROACHES TO BULK METAMATERIAL DESIGN

There are two main approaches for metamaterial design at microwave frequencies. One of them was developed in the previous section. The other, introduced

simultaneously in [5] to [7], will be described in detail in the next chapter. Apart from these two main approaches, there are many other interesting proposals that can be also considered as bulk metamaterial designs (as they were defined at the beginning of this chapter). Some of them are described in this section.

### 2.5.1 Ferrite Metamaterials

There are two main groups of materials in nature showing negative permittivity or permeability and small losses. One of them comprises semiconductors and metals at infrared and optical frequencies. As has already been mentioned, metals and semiconductors are accurately described by permittivity (2.78). At frequencies between the collision frequency of the electrons  $f_c$  and the plasma frequency  $f_p$ , this dielectric constant becomes approximately real and negative. For this reason, such materials are sometimes referred as *solid-state plasmas*. The other group corresponds to saturated ferrimagnetic materials (ferrites), which have long been used in microwave technology, and show negative magnetic permeability near the ferrimagnetic resonance. Unfortunately, both groups present these interesting properties at quite different frequency bands, which prevents their combination in designing left-handed metamaterials.<sup>17</sup>

Before proceed with the description of ferrite-based left-handed metamaterials, we will briefly describe the main characteristics of microwave propagation in ferrites.<sup>18</sup> Ferrites, when magnetized to saturation by an external DC magnetic field  $\mathbf{H}_0$ , acquire a resonant anisotropic magnetic permeability. Low-loss cubic ferrites, such as yttrium iron garnets (YIG), are accurately described by the well-known Polder permeability tensor<sup>19</sup> [58,59]

$$\bar{\bar{\mu}} = \mu_0 \begin{pmatrix} \bar{\mu}_t & 0 \\ 0 & \mu_z \end{pmatrix} = \mu_0 \begin{pmatrix} \mu & j\kappa & 0 \\ -j\kappa & \mu & 0 \\ 0 & 0 & 1 \end{pmatrix}, \quad (2.99)$$

where the external magnetic field is assumed along the  $z$ -axis ( $\mathbf{H}_0 = H_0 \hat{\mathbf{z}}$ ) and

$$\mu = 1 + \frac{\omega_M \omega_H}{\omega_H^2 - \omega^2} \quad (2.100)$$

and

$$\kappa = \frac{\omega \omega_M}{\omega_H^2 - \omega^2}, \quad (2.101)$$

<sup>17</sup>Recently, the use of superconductors has been proposed to overcome this difficulty [57].

<sup>18</sup>See, for a more detailed analysis, [58,59].

<sup>19</sup>In such ferrites the only source of anisotropy is the DC field  $\mathbf{H}_0$ . Other ferrites with lower symmetry, such as hexagonal ferrites, are described by a similar tensor, which takes into account the intrinsic anisotropy of the material.

where  $\omega_H$  is the ferrimagnetic resonance frequency given by

$$\omega_H = \gamma H_0 \quad (2.102)$$

and

$$\omega_M = 4\pi\gamma M_s, \quad (2.103)$$

where  $M_s$  is the saturation magnetization of the ferrite, and  $\gamma$  is the gyromagnetic ratio  $\gamma = 1.76 \times 10^7$  rad/sec Oe (c.g.s. units).<sup>20</sup> It may be worth noting here that the Polder tensor (2.99) is not symmetric. Therefore, ferrites are nonreciprocal media, and many practical applications of ferrites in microwave technology come from such nonreciprocity. In fact, the Polder tensor becomes transposed if the sign of the biasing magnetic field  $H_0$  is reversed. This fact can be expected from the general properties of generalized susceptances in magnetized media [21]. A generalized reciprocity theorem for ferrite media was given in [60].

It is clear from equation (2.99) that for  $\omega > \omega_H$ ,  $\kappa$  becomes negative and that, for  $\omega_H < \omega < \sqrt{\omega_H(\omega_H + \omega_M)}$ ,  $\mu$  also becomes negative. Therefore, ferrites exhibit negative permeability in a significant frequency range near the ferrimagnetic resonance. Regarding plane-wave propagation, the solution to the Maxwell equations with the tensor permeability (2.99) gives four solutions for the wavevector. For propagation along the biasing field  $\mathbf{H}_0$ , such solutions are circularly polarized plane waves. These waves have different phase constants for the different polarizations, given by

$$k^\pm = \pm \omega \sqrt{\varepsilon \mu_{\text{eff}}^\pm}, \quad (2.104)$$

where  $\varepsilon$  is the dielectric constant of the ferrite, and  $\mu_{\text{eff}}^\pm$  is an *effective magnetic permeability* given by the two eigenvalues of  $\bar{\bar{\mu}}_t$ ,

$$\mu_{\text{eff}}^\pm = \mu_0(\mu \pm \kappa), \quad (2.105)$$

where the “+” sign stands for the right-handed circularly polarized (RCP) wave and the “−” sign for the left-handed circularly polarized (LCP) wave<sup>21</sup> with regard to the direction of the biasing field  $\mathbf{H}_0$ . From equation (2.105), it is deduced that there is a region of negative  $\mu_{\text{eff}}^+$  for

$$\omega_H < \omega < \omega_H + \omega_M. \quad (2.106)$$

<sup>20</sup>The reported expression for the Polder tensor neglects losses. Expressions including losses may be found in many textbooks, as, for instance, in [58] or [59].

<sup>21</sup>Here, left- and right-handed refer only to the polarization, and do not imply any backward behavior.



In this frequency range, the RCP wave sees a negative effective permeability, and becomes evanescent.

For plane waves propagating in a direction orthogonal to the biasing field  $\mathbf{H}_0$ , there are two kind of solutions to Maxwell's equations. One of them is an ordinary TEM plane wave polarized with the magnetic field parallel to  $\mathbf{H}_0$  and  $k = \pm \omega \sqrt{\varepsilon \mu_0}$ . The other is an *extraordinary* TE plane wave, with the electric field parallel to  $\mathbf{H}_0$  and the  $\mathbf{H}$  field elliptically polarized in the plane orthogonal to  $\mathbf{H}_0$ . The dispersion relation for the extraordinary wave is

$$k = \pm \omega \sqrt{\varepsilon \mu_{\text{eff}}}, \quad (2.107)$$

where

$$\mu_{\text{eff}} = \mu_0 \frac{\mu^2 - \kappa^2}{\mu}. \quad (2.108)$$

From equation (2.108), a negative effective permeability stopband is deduced for extraordinary waves in the frequency range

$$\sqrt{\omega_H(\omega_H + \omega_M)} < \omega < \omega_H + \omega_M. \quad (2.109)$$

In the neighborhoods of current sources, at distances much smaller than the wavelength, magnetic fields are quasimagnetostatic. Such quasimagnetostatic fields obey Ampère's law.<sup>22</sup> Therefore, in source-free regions, they are irrotational, and can be expressed as the gradient of a scalar magnetic potential  $\psi_m$ :

$$\mathbf{H} = -\nabla \psi_m. \quad (2.110)$$

Source-free solutions for such quasistatic magnetic potential with the permeability tensor (2.99) leads to the magnetostatic wave equation [59]

$$\nabla \cdot \bar{\bar{\mu}} = \cdot \nabla \psi_m = \left\{ \mu \left( \frac{\partial^2}{\partial x^2} + \frac{\partial^2}{\partial y^2} \right) + \frac{\partial^2}{\partial z^2} \right\} \psi_m = 0. \quad (2.111)$$

It is interesting to note that the cross-term  $\kappa$  does not appear in the magnetostatic wave equation.<sup>23</sup> Therefore, for the quasimagnetostatic field, the ferrite appears as an uniaxial magnetic medium with  $\mu_{\perp} = \mu_0 \mu$  and  $\mu_{\parallel} = \mu_0$ . Such an effective medium

<sup>22</sup>In other words, electric displacement current can be neglected.

<sup>23</sup>However, for finite systems, it usually appears in the boundary conditions.

shows a negative transverse permeability in the range

$$\omega_H < \omega < \sqrt{\omega_H(\omega_H + \omega_M)}. \quad (2.112)$$

Among the many similarities between ferrites and solid-state plasmas is the excitation of magnetostatic surface waves (MSSWs), similar to surface plasmons. Such MSSWs appears in ferrite–metal and ferrite–air interfaces, for external magnetization parallel to the interface (see Problems 2.12–2.14). MSSWs are unidirectional waves, which propagate only in the direction defined by the cross-product  $\mathbf{H}_0 \times \mathbf{n}$ , where  $\mathbf{n}$  is the outward normal to the ferrite. Depending on the boundary conditions, such MSSWs can also be excited in ferrite slabs, in all the frequency range

$$\sqrt{\omega_H(\omega_H + \omega_M)} < \omega < \omega_H + \omega_M. \quad (2.113)$$

In addition to MSSWs, ferrite slabs can also support magnetostatic volume waves (MSVWs), with a trigonometric field dependence inside the ferrite. The range of excitation of MSVWs coincides with the range of negative  $\mu$  (2.112), and for magnetization parallel to the slab and propagation parallel to  $\mathbf{H}_0$ , they are backward-waves. Backward MSSWs can also appear for some specific boundary conditions.<sup>24</sup> Like surface plasmons, magnetostatic waves are slow waves with  $k \gg k_0 = \omega\sqrt{\mu_0\epsilon_0}$ . In such waves, energy is mainly associated with the magnetic field, which can be accurately determined from the magnetostatic wave equation (2.111).

The above paragraphs show the large variety of phenomena that may appear in ferrite media, including regions of effective negative permeability, and backward-wave propagation. This variety is even higher in waveguide configurations [61]. All these properties strongly suggest the usefulness of ferrites for designing micro-structured metamaterials, with novel electromagnetic properties. Regarding left-handed metamaterials, there is an interesting precedent for the results reported in [46] using ferrite-loaded waveguides. In a paper published in 1955 [62], Thompson reported backward-wave propagation in a below-cutoff waveguide, filled with a ferrite magnetized along the waveguide axis. The physical interpretation of this effect relies on the effective negative permeability (2.105) seen for right-handed circularly polarized (RCP) waves in the frequency range (2.106). This effective negative permeability, when combined with the effective negative permittivity (2.2) provided by the below-cutoff waveguide, produces the typical left-handed behavior: backward-wave propagation below the cutoff frequency of the hollow waveguide. Note that, according to equation (2.99), the permeability of the ferrite along the waveguide axis is undoubtedly positive ( $\mu_z = 1$ ). Therefore, only the transverse effective polarizability is negative inside the waveguide. Such simultaneously positive/negative axial/transverse permeability explains, according to the discussion in Sections 2.4.1 and 2.4.4, the observed effect. Therefore, although there was obviously not any reference to left-handed media in [62], the reported structure can be

<sup>24</sup>Specifically, when there is a metallic plate at some distance from the ferrite interface [58].

interpreted as a one-dimensional left-handed metamaterial. More recently, the same anticutoff behavior has been demonstrated in ferrite-filled rectangular waveguides with transverse magnetization [63]. In this case, the effective negative magnetic polarizability (for the appropriate wave polarization) is provided by equation (2.108).

The substitution by a ferrite of the SRRs in the first Smith's proposal for left-handed metamaterial design (Fig. 2.20) has also been considered [64]. The proposed structure is the same as in Figure 2.3, with the space between the wires filled by a homogeneous ferrite, magnetized in the direction parallel to the wires. According to the previous analysis, a plane wave incident in the plane perpendicular to the wires, and with the electric field polarized parallel to the wires (and to the external magnetization) will see an effective permeability given by equation (2.108). This effective permeability is negative in the frequency range given in equation (2.109). Thus, when combined with the negative permittivity provided by the wire system, it will produce a left-handed metamaterial in a such frequency range, at least for the considered field polarization. The proposal has the additional advantages of isotropy in the transverse plane, and tunability by a proper adjustment of the external magnetization. However, such a proposal presents an important drawback. It can be easily realized that, for the considered excitation, the magnetic field in the direction parallel to the wires vanishes. Therefore, only the magnetic permeability in the plane perpendicular to the wires affects the field behavior. Assuming that this permeability can be approximated by the scalar permeability (2.108), the behavior of the structure will be identical to that of a system of wires immersed in a homogeneous medium with such permeability. It has also been shown [54] (see Section 2.4.4) that such system does not behave as a left-handed metamaterial. To circumvent this drawback, the first proposal in [64] was modified, so that the wires were surrounded with a dielectric cladding [65]. This cladding strongly affects the wire inductance (2.6), such that it remains positive.

As was mentioned at the beginning of this section, metals and semiconductors behave as solid-state plasmas, presenting a permittivity whose real part is negative at frequencies below the plasma frequency (which is usually located between the infrared and the ultraviolet frequency ranges). However, at microwave frequencies—where the ferrimagnetic resonance of known ferrites is located—the imaginary part of the permittivity of metals and semiconductors dominates over the real part. This fact seems to prevent the design of left-handed composites by taking advantage of the simultaneously negative real parts of the permeability and permittivity of ferrites and solid-state plasmas. Recently, the use of superconductors has been proposed to overcome this difficulty [57]. The proposed structure consists of a set of stacked ferromagnetic<sup>25</sup> and superconducting very thin layers. Magnetization is in the direction parallel to the layers. Normal incidence of plane waves polarized with the magnetic field perpendicular to the external magnetization is considered. For these waves, the ferromagnetic layers present the effective permeability (2.108), which is negative in the frequency range of expression (2.109). Superconducting layers are thinner than

<sup>25</sup>Results in [57] were reported for insulating ferromagnetic layers, with a behavior similar to those of ferromagnetic layers.

the penetration depth at the frequency of operation, and present a permittivity that is mostly real and negative. Thus, the resulting structure is quite similar to a stratified system of stacked  $\varepsilon$ -negative and  $\mu$ -negative layers. The properties of such a system were analyzed in [66] (see also Chapter 1). For thin layers and normal incidence, it behaves as a one-dimensional left-handed medium, with a permeability and a permittivity that are the average of the permeabilities and permittivities of the layers. In [57], experimental results supporting this interpretation were provided.

Results reported in this section show the possibilities of ferrites magnetized to saturation as constituent elements of left-handed metamaterials. Magnetized ferrites have the drawbacks of being highly anisotropic, fragile, and expensive. They also need an external magnet, which may prevent many technological applications. However, they have the key advantage of tunability by a proper adjustment of the external biasing field. Because most bulk metamaterials are resonant devices, with a narrow frequency band of operation, such tunability can be a crucial advantage.

### 2.5.2 Chiral Metamaterials

Optical activity in natural materials is known in physics from the former analysis of Arago and Biot, in the early 19th century. After Pasteur's studies on the crystal structure of optically active materials, it became apparent that optical activity is closely related to handedness or *chirality*. As has already been mentioned in Section 2.3.2, if the constituents of a material are not invariant by inversion (that is, if they have some handedness), cross-polarization effects can be expected in the material. Therefore, isotropic optically active media can be considered as a particular case of the wider category of bianisotropic media. In fact, the constitutive relations for an isotropic and optically active medium are quite similar to equations (2.56) and (2.57):

$$\mathbf{D} = \varepsilon \mathbf{E} + j\sqrt{\varepsilon_0\mu_0} \kappa \mathbf{H}; \quad \varepsilon = \varepsilon_0(1 + \chi_e) \quad (2.114)$$

$$\mathbf{B} = -j\sqrt{\varepsilon_0\mu_0} \kappa \mathbf{E} + \mu \mathbf{H}; \quad \mu = \mu_0(1 + \chi_m), \quad (2.115)$$

where  $\chi_e$ ,  $\chi_m$ , and  $\kappa$  are the electric, magnetic, and magnetoelectric susceptibilities, respectively. For lossless media, these quantities are real numbers [22].

The term *chiral media* is usually restricted to artificial materials that replicate natural optical activity at microwave frequencies [22]. The first systematic experiments on chiral media were reported by Lindmann between 1914 and 1920 [67]. Lindmann placed several hundreds of small helices made of copper wire inside cotton balls, and then put these balls, randomly orientated, inside a cardboard box. When these boxes were illuminated by a linearly polarized electromagnetic wave (of a frequency between 1 and 3 GHz), the rotation of the plane of polarization after crossing the box was clearly observed. This rotation changed sign when the handedness of the helices was reversed, and disappeared when a *racemic* (balanced) mixture of helices of both handedness was put into the box. Other inclusions also

producing chirality were later proposed in [68] to [70].<sup>26</sup> Because all these inclusions show a resonant behavior, strong values of the susceptibilities  $\chi_e$ ,  $\chi_m$ , and  $\kappa$  can be expected around the resonance. Thus, causality constraints suggest that regions of simultaneously strong and negative dielectric and magnetic susceptibilities should appear just above the resonance. In fact, negative refraction from artificial chiral inclusions has been proposed either for chiral mixtures [71,72] or for racemic mixtures of such elements [73].

Plane waves in biisotropic chiral media are TEM circularly polarized waves, with square wavevectors [22]

$$k^2 = k_0^2(\sqrt{\mu_r \epsilon_r} \pm \kappa)^2; \quad \epsilon_r = \epsilon/\epsilon_0, \quad \mu_r = \mu/\mu_0, \quad (2.116)$$

where  $k_0 = \omega\sqrt{\mu_0\epsilon_0}$  is the wavevector in free space, and the sign of the square roots is chosen positive by convention (in fact, a change in this sign will not affect the equation). The four roots of equation (2.116) give the four RCP and LCP waves propagating in the positive and negative directions, respectively. The TEM wave impedance for all these waves is the same [22]:

$$\eta = \sqrt{\frac{\mu}{\epsilon}}. \quad (2.117)$$

In general, chiral media present forbidden frequency bands for plane-wave propagation at those frequencies where  $\epsilon$  and  $\mu$  have opposite sign. At such frequencies, the propagation constant (2.116) becomes complex, and the plane wave becomes a nonpropagating “complex wave”.<sup>27</sup> The same condition holds for racemic mixtures of chiral particles. However, in this case, the wavevector  $k = \omega\sqrt{\epsilon\mu}$  becomes imaginary and the plane wave is evanescent in the forbidden frequency region. Only media with  $\epsilon\mu > 0$  at all frequencies do not present forbidden frequency bands. This condition is fulfilled when  $\chi_e = \chi_m$  for all frequencies. In such a case, the wave impedance (2.117) coincides with that of free space.<sup>28</sup>

The conditions for backward-wave propagation—and therefore for negative refraction—in chiral media have been analyzed in [72]. They can be deduced from the condition

$$\mathbf{k} \cdot \mathbf{S} < 0, \quad (2.118)$$

<sup>26</sup>As has already been mentioned, any resonant inclusion without inversion symmetry must show some degree of cross-polarizability, leading to a bianisotropic medium. Chiral inclusions can be considered as a particular case of the former inclusions, showing resonant electric, magnetic, and cross-polarizabilities along the same direction.

<sup>27</sup>Complex waves are plane waves that presents a complex propagation constant even if the media is lossless. They can appear in bi(iso/aniso)tropic media, as well as in some complex guiding systems [61].

<sup>28</sup>However, except for normal incidence, this does not mean that there will not be reflected waves at the interface between free space and such a chiral medium. The reason for this behavior is the different values taken by the wavevectors in free space and in the chiral medium.

where  $\mathbf{k}$  is the wavevector and  $\mathbf{S}$  is the real part of the Poynting vector for the plane wave. From this equation, cumbersome but straightforward calculations lead to the following general condition [72]:

$$\sqrt{\varepsilon_r \mu_r} \pm \kappa < 0, \quad (2.119)$$

where the negative sign of the square root has to be chosen if  $\varepsilon_r$  and  $\mu_r$  are both negative. According to equation (2.119), if  $\kappa^2 < |\varepsilon_r \mu_r|$  then both solutions of equation (2.116) show negative refraction when both  $\varepsilon_r$  and  $\mu_r$  are negative. However, if  $\kappa^2 > |\varepsilon_r \mu_r|$ , only one of the solutions of equation (2.116) can be a backward wave and therefore will experience negative refraction at the interface with ordinary media.

Concerning racemic mixtures, it is well known that they present backward-wave propagation when  $\varepsilon < 0$  and  $\mu < 0$  simultaneously.

In order to obtain a better understanding of the behavior of artificial chiral media, we will analyze the quasiplanar inclusion proposed in [74] and shown in Figure 2.31. It is a slight modification of the two-turns spiral resonator shown in Figure 2.11. This modification is enough to provide a chiral behavior, while maintaining the equivalent circuit shown in Figure 2.11. In particular, the frequency of resonance is still given by

$$\omega_0 = 1/\sqrt{LC}; \quad C = 2\pi r C_{\text{pul}}, \quad (2.120)$$

where  $L$  is the ring inductance (2.152),  $C_{\text{pul}}$  is the per unit length capacitance between the rings (2.161), and  $r$  the mean radius of the inclusion. However, unlike the planar spiral of Figure 2.11, the quasiplanar helix of Figure 2.31 presents quasistatic cross-polarizations. Such cross-polarizations can be obtained from an analysis similar to that reported in Section 2.3.1. For lossless inclusions, the result is

$$m_z = \alpha_{zz}^{\text{mm}} B_z^{\text{ext}} - \alpha_{zz}^{\text{em}} E_z^{\text{ext}} \quad (2.121)$$

and

$$p_z = \alpha_{zz}^{\text{ee}} E_z^{\text{ext}} + \alpha_{zz}^{\text{em}} B_z^{\text{ext}}, \quad (2.122)$$

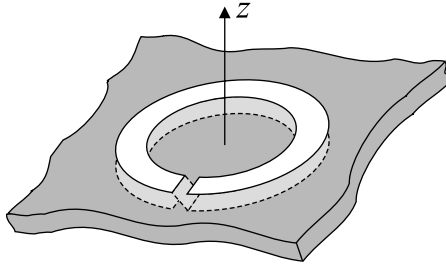


FIGURE 2.31 Quasiplanar chiral resonator.

where the polarizabilities are given by

$$\alpha_{zz}^{\text{mm}} = \frac{\pi^2 r^4}{L} \left( \frac{\omega_0^2}{\omega^2} - 1 \right)^{-1}, \quad (2.123)$$

$$\alpha_{zz}^{\text{em}} = \pm j \pi r^2 t C_0 \frac{\omega_0^2}{\omega} \left( \frac{\omega_0^2}{\omega} - 1 \right)^{-1}, \quad (2.124)$$

and

$$\alpha_{zz}^{\text{ee}} = t^2 C_0^2 L \frac{\omega_0^4}{\omega^2} \left( \frac{\omega_0^2}{\omega^2} - 1 \right)^{-1}, \quad (2.125)$$

where  $C_0$  is the *in vacuo* capacitance between the rings ( $C_0 \sim \varepsilon_0/\varepsilon C$ ), and the sign in equation (2.124) depends on the helicity of the element. These expressions are, in fact, very similar to equation (2.35) to (2.38), and the presence of the *in vacuo* capacitance  $C_0$  is justified as in the footnote of Section 2.3.1. An interesting property of the above polarizabilities is that

$$\alpha_{zz}^{\text{mm}} \alpha_{zz}^{\text{ee}} = -(\alpha_{zz}^{\text{em}})^2. \quad (2.126)$$

This property is very similar to equation (2.40). It is quite general, being shared by many chiral inclusions, and comes from its *LC* resonant nature (see Problem 2.15). In addition to these resonant polarizabilities, the particle also shows some non-resonant quasistatic polarizabilities  $\alpha_{xx}^{\text{ee}}$  and  $\alpha_{yy}^{\text{ee}}$ , which can be estimated as (see Section 2.3.1)

$$\alpha_{xx}^{\text{ee}} = \alpha_{yy}^{\text{ee}} = \varepsilon_0 \frac{16}{3} r_{\text{ext}}^3, \quad (2.127)$$

where  $r_{\text{ext}}$  is the external radius of the particle. Therefore, for a random arrangement of particles, the average *isotropic* polarizabilities per particle are

$$\langle \alpha^{\text{mm}} \rangle = \frac{1}{3} \alpha_{zz}^{\text{mm}}, \quad (2.128)$$

$$\langle \alpha^{\text{em}} \rangle = \pm \frac{1}{3} \alpha_{zz}^{\text{em}}, \quad (2.129)$$

and

$$\langle \alpha^{\text{ee}} \rangle = \frac{1}{3} \alpha_{zz}^{\text{ee}} + \frac{2}{3} \alpha_{xx}^{\text{ee}} \quad (2.130)$$

In order to develop an *ab initio* analysis of a random arrangement of the considered inclusions, we will assume a zero-order homogenization:<sup>29</sup>

$$\chi_e = \frac{1}{\varepsilon_0} N \langle \alpha^{ee} \rangle; \quad \chi_m = \mu_0 N \langle \alpha^{mm} \rangle; \quad \kappa = \pm j \sqrt{\frac{\mu_0}{\varepsilon_0}} N \langle \alpha^{em} \rangle, \quad (2.131)$$

where  $N$  is the number of inclusions per unit volume. If the medium is made from a balanced (or *racemic*) mixture of elements, it will be isotropic with  $\kappa = 0$ .

The electric susceptibility  $\chi_e$  can be expanded into two terms, one resonant and other nonresonant:

$$\chi_e = \chi_e^{nr} + \chi_e^r; \quad \chi_e^{nr} = \frac{32N}{9\varepsilon_0} r_{\text{ext}}^3; \quad \chi_e^r = \frac{1}{3\varepsilon_0} N \alpha_{zz}^{ee}. \quad (2.132)$$

From equation (2.131) it follows that a property quite similar to equation (2.126) also holds for the resonant susceptibilities:

$$\chi_e^r \chi_m = \kappa^2. \quad (2.133)$$

Near the resonance, where  $\chi_e^r$  takes very high values, the nonresonant susceptibility is much smaller than the resonant one.<sup>30</sup> Therefore, the above inequality becomes

$$\chi_e \chi_m \approx \kappa^2. \quad (2.134)$$

As has already been shown, media with  $\chi_e \approx \chi_m$  minimize the forbidden frequency bands. From equation (2.134), such a condition also implies that

$$\chi_m \approx \chi_e \approx |\kappa|. \quad (2.135)$$

The corresponding condition for the resonant polarizabilities (2.123) to (2.125) is

$$c^2 \alpha_{zz}^{ee} = \alpha_{zz}^{mm} = \pm j c \alpha_{zz}^{em}; \quad c = \frac{1}{\sqrt{\varepsilon_0 \mu_0}}, \quad (2.136)$$

<sup>29</sup>We know from Section 2.3.3 that this simple homogenization can give a good qualitative picture of the behavior of the system. A careful calculation (not included) shows that a similar behavior is obtained if Lorentz local field theory is applied.

<sup>30</sup>This condition is not too restrictive in practice. For instance, if the ratio between the external diameter of the particle and the average distance between particles is 2/3, the resulting nonresonant susceptibility is  $\chi_e^{nr} = 0.13$ .



which is compatible with equation (2.126). Taking into account equation (2.134), condition (2.119) can be rewritten as

$$1 + \chi_e + \chi_m < 0. \quad (2.137)$$

Let us consider the particular case when equation (2.135) and (2.136) are fulfilled. In such a case the forbidden frequency band is minimized, and backward-wave propagation occurs for

$$\chi_e \approx \chi_m \lesssim -0.5. \quad (2.138)$$

In this region,  $\kappa > \varepsilon_r \mu_r$  and, therefore, only one of the solutions of equation (2.116) exhibits negative refraction.

At frequencies where  $\chi_e \approx \chi_m \approx -0.5$ ,  $k \approx 0$  for the corresponding wave. Therefore, at such frequencies there is power transmission (or nonzero group velocity) with very small (or even zero) phase velocity. This behavior recalls that of the balanced right/left-handed structures (analyzed in Chapter 3).

For racemic dilute mixtures of the same chiral particles, backward-wave propagation is present in the frequency range

$$\chi_e \approx \chi_m \lesssim -1, \quad (2.139)$$

and the aforementioned balanced behavior occurs for  $\chi_e \approx \chi_m \approx -1$ . Therefore, the frequency band for backward-wave propagation is wider in biisotropic mixtures than in racemic ones. The price to pay for this bandwidth enhancement is that only one of the two circular polarizations shows this behavior in the reported biisotropic mixtures.

Negative refractive metamaterial design from random (chiral or racemic) mixtures of chiral inclusions is advantageous because left-handedness comes from only one kind of element. Regarding the quasiplanar chiral inclusion analyzed in this section, its main advantage is the reliability and reproducibility that can be obtained from standard photoetching manufacturing techniques. Other works dealing with the application of chirality to left-handed media design have stressed the usefulness of a mixture of a chiral medium operating far from the resonance and a resonant dielectric medium [75]. Finally, the specific situation when  $\varepsilon/\varepsilon_0 = \mu/\mu_0 = 0$  but  $\kappa \neq 0$ , so-called *chiral nihility*, has been analyzed in [76].

### 2.5.3 Other Proposals

In this section we will briefly describe some alternative designs to bulk left-handed metamaterials. Because a description of all such alternatives would be impossible (and the number of such proposals steadily increase with time), this description will be necessarily incomplete.

An interesting alternative for the design of left-handed metamaterials at microwave frequencies has recently been proposed in [78] and [79]. This proposal starts from the consideration of a system of spheres embedded in a dielectric matrix. The problem of the homogenization of an array of dielectric or magnetic spheres inside a homogeneous host matrix has long been known. If the size of the spheres is small compared with the wavelength in both the host medium and the spheres, the array behaves as a homogeneous medium with intermediate values of  $\epsilon$  and  $\mu$  [77]. However, if the size of the spheres is of the same order as the internal wavelength, they may present resonances at some specific frequencies (such resonances are sometimes referred to as *Mie* resonances). If the wavelength in the host medium is still larger than the size of the spheres, then the array can be seen as a homogeneous medium, with a resonant permittivity or permeability that, eventually, may be negative above the resonances [78,79]. In order to achieve this behavior, at least one of the constitutive parameters of the spheres,  $\epsilon_s$  and/or  $\mu_s$ , must be much higher than the corresponding constitutive parameter of the host medium  $\epsilon_h$  and/or  $\mu_h$ :

$$\frac{\epsilon_s}{\epsilon_h} \gg 1 \quad \text{and/or} \quad \frac{\mu_s}{\mu_h} \gg 1. \quad (2.140)$$

The problem of the homogenization of a system of spheres embedded in a host medium satisfying (2.140) was studied by Lewin [80] in 1947. Lewin provided closed expressions for the constitutive parameters of the homogenized medium, which were subsequently utilized in [78] and [79] for their analysis.

Starting from Lewin's results, Holloway et al. [78] analyzed a hypothetical composite medium made of magnetodielectric spherical particles embedded in a host medium, with  $\epsilon_h \ll \epsilon_s$  and  $\mu_h \ll \mu_s$ . They found that, for  $\epsilon_s$  and  $\mu_s$  high enough, the homogenized medium shows a frequency band of simultaneously negative  $\epsilon$  and  $\mu$ . However, isotropic media showing simultaneously very high electric permittivity and magnetic permeability are not known for microwaves. In fact, even isotropic media with very high magnetic permeability are not known for microwaves. However, ferroelectric or ceramic media with very high dielectric constants are available in such a frequency range. Vendik and Gashinova [79] considered this specific case, that is,  $\epsilon_s \gg \epsilon_h$ ,  $\mu_s = \mu_h = \mu_0$ . Dielectric resonators made with small inclusions of high dielectric constant, such as the spheres proposed in [79], are well known in microwave technology. They are usually analyzed by assuming "magnetic wall" boundary conditions around the resonator,<sup>31</sup> that is, assuming the following conditions at the sphere's boundary:

$$\mathbf{n} \cdot \mathbf{E}_s \simeq 0; \quad \mathbf{n} \times \mathbf{H}_s \simeq 0; \quad (2.141)$$

where  $\mathbf{n}$  is the normal to the interface, and  $\mathbf{E}_s, \mathbf{H}_s$  are the fields inside the sphere. From this approach it follows that the field distribution inside the spheres corresponds

<sup>31</sup>This assumption can be justified from the fact that the reflection coefficient at the boundary between a medium of high permittivity and a medium of low permittivity is approximately +1, the same as for a magnetic wall [81].

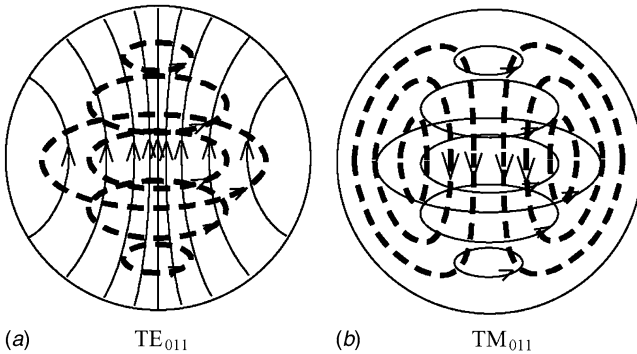


**FIGURE 2.32** Sketch of the magnetic (solid lines) and electric (dashed lines) fields inside a spherical cavity in a perfect magnetic conductor, for the two first resonances. (a)  $TE_{011}$  first resonance. (b)  $TM_{011}$  second resonance. (Source: Reprinted with permission from [79]; copyright 2003, IEEE.)

approximately to that of a spherical cavity in a perfect magnetic conductor. This problem is dual to that of a spherical cavity inside a perfect electric conductor, a well-known problem of classical electromagnetism [82]. Figure 2.32 shows the electric and magnetic field inside the high-permittivity spheres proposed in [79], obtained from the aforementioned magnetic wall approximation. It becomes apparent from such a figure that the first resonance ( $TE_{011}$  resonance) is associated with a magnetic dipole, arising from the circulation of the electric displacement current. The second resonance ( $TM_{011}$ ) is associated with an electric dipole arising from the continuity of the tangential electric field at the sphere's boundary. Around such resonances, the aforementioned dipoles must show the universal causal behavior, which ensures that they are positive/negative (regarding the external excitation) below/above the resonance. Starting from this result, Vendik and Gashinova [79] proposed a composite left-handed medium made of two sets of high-permittivity dielectric spheres of different radii, embedded in a dielectric matrix. The radius of each set is chosen so that the first and the second Mie resonances are excited at each set of spheres at the same frequency. Therefore, according to causality requirements, just above this specific frequency the permittivity and the permeability of the effective medium must be negative. Numerical finite difference time domain (FDTD) simulations supporting this conclusion were reported in [79].

The aforementioned proposal is conceptually simple, and has the additional advantage of being intrinsically isotropic. The main disadvantage of such a design seems to be the small bandwidth, about a 1% in the analyzed structures [79]. A limitation of this proposal comes from the fact that, the higher the  $\epsilon_s$ , the smaller the interaction between the fields internal and external to the spheres (in the limit  $\epsilon_s \rightarrow \infty$ , the spheres behave as perfect conducting spheres).

Negative-permittivity media made from systems of metallic wires or plates present an important drawback for small absolute values of  $\epsilon$ , such as those needed for the design of super-lenses and other devices of practical interest. In fact, according to equations (2.2)

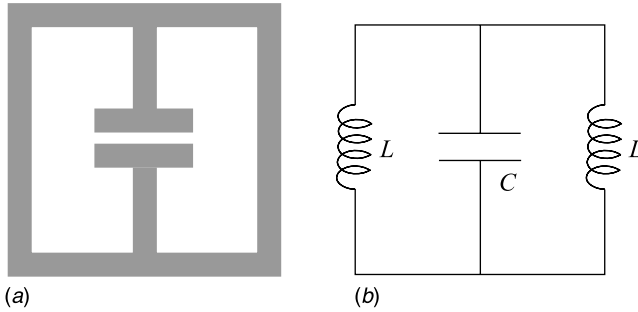


**FIGURE 2.33** (a) Electric coupled-field resonator proposed in [83] for negative permittivity metamaterial design; (b) Equivalent circuit.

and (2.8), the wire spacing must be of the same order as a half-wavelength in order to obtain values of  $\epsilon/\epsilon_0 \sim -1$ . Therefore, the continuous-medium approach can be hardly justified for such values of  $\epsilon$  (see Section 2.4.3). In order to overcome this difficulty, a modification of the SRR concept has been proposed in [83]. The proposed structure, two symmetric closed inductive loops connected to a common capacitor, is shown in Figure 2.33a. The equivalent circuit is shown in Figure 2.33b. At resonance, the magnetic moment associated with currents in both loops cancels, only the electric dipole associated with the capacitor remaining. According to causality requirements, the electric polarizability must be large and negative just above the resonance, thus providing the required behavior for negative-permittivity metamaterial design. By properly adjusting the resonator parameters (by slight modifications of the basic design [83]) the electrical size of the resonator can be made small enough to overcome the aforementioned drawback of wire media. In [83], numerical calculations supporting the above discussion are reported. In our opinion, the main inconvenience of this proposal may be the excitation of unwanted magnetoinductive waves (see Chapter 5) due to the magnetic coupling between adjacent resonators.

It was shown in Section 2.2.1 that a hollow metallic waveguide operating in the fundamental  $TE_{10}$  mode behaves as a one-dimensional ideal plasma, with plasma frequency equal to the cutoff frequency of the waveguide. Let us now consider a rectangular waveguide operating at the first TM mode, that is, the  $TM_{11}$  mode. The propagation constant is still given by equation (2.1); however, the wave impedance is now given by

$$Z = \frac{k}{\omega \epsilon_0}, \quad (2.142)$$

instead of equation (2.3). Therefore, from the same rationale as in Section 2.2.1, it follows that the waveguide behaves now as a *magnetic plasma* with effective dielectric constant

$$\mu_{\text{eff}} = \mu_0 \left( 1 - \frac{\omega_c^2}{\omega^2} \right), \quad (2.143)$$

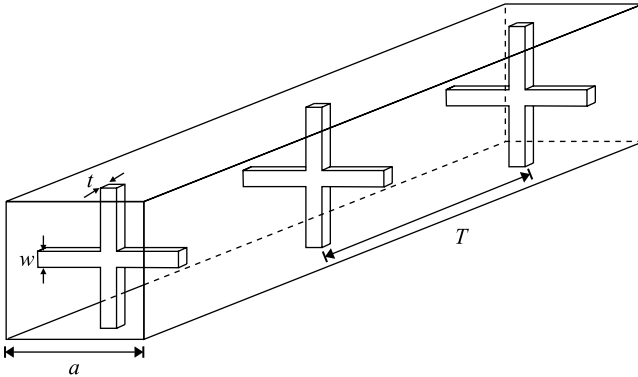


**FIGURE 2.34** Simulation of a one-dimensional left-handed medium by a below-cutoff TM hollow waveguide, filled by a system of crossed wires [11].

and effective dielectric constant  $\epsilon_{\text{eff}} = \epsilon_0$ . This concept was proposed and demonstrated by Esteban et al. [11] by filling a below-cutoff square waveguide with a two-dimensional wire medium of effective negative dielectric constant given by equation (2.2).<sup>32</sup> The proposed structure is shown in Figure 2.34. The propagation constant for TM modes is given by [11]

$$k^2 = \omega^2 \epsilon_0 \mu_0 \left(1 - \frac{\omega_c^2}{\omega^2}\right) \left(1 - \frac{\omega_p^2}{\omega^2}\right), \quad (2.144)$$

where  $\omega_c$  is the cutoff frequency of the TM mode of the hollow waveguide, and  $\omega_p$  the plasma frequency of the wire system. It can be easily realized that propagation is backward for  $\omega < \omega_c$ ,  $\omega_p$  (which correspond to the left-handed passband) and forward for  $\omega > \omega_c$ ,  $\omega_p$ . For  $\omega_c < \omega < \omega_p$  (or  $\omega_c > \omega > \omega_p$ ) there is a stopband of negative  $\epsilon$  (or  $\mu$ ). A key advantage of this proposal over other one-dimensional left-handed media waveguide simulations (see Section 2.4.1) is a wider bandwidth, as well as smaller losses due to the absence of resonances in the system. The case with  $\omega_c = \omega_p$  is of interest because no stopband appears. The reported behavior is quite similar to the behavior of the composite left-/right-handed transmission lines [5–7], which will be analyzed in detail in the next chapter. In fact, the proposal of Esteban et al. [11] can be seen as the waveguide counterpart of the aforementioned proposals.

To end this section we will devote some words to the synthesis of left-handed metamaterials at optical frequencies. Because negative permittivity is already present at such frequencies in many metals, the main challenge seems to be how to obtain negative permeability. That materials do not show a magnetic response

<sup>32</sup>In fact, the analysis in [11] models the system as a hollow waveguide filled with a uniaxial dielectric medium with  $\epsilon_{\perp} < 0$  and  $\epsilon_{\parallel} = \epsilon_0$  (see Problem 1.16 of Chapter 1).

at optical frequencies has been almost a dogma in optics for many years. The reason usually invoked to support this statement is that optical frequencies are of the same order as natural frequencies of oscillation of electrons in atoms and molecules. Therefore, it seems impossible to obtain closed loops of atomic currents—and therefore magnetization—at such frequencies [13]. More recently, many attempts have been made in order to obtain a nonvanishing magnetic response at infrared and optical frequencies from artificial atoms, such as SRRs [39] and other nanofabricated plasmonic structures [84,85], which can also be modeled as  $LC$  resonant circuits [86]. However, the measured magnetic response of such structures was always much smaller than those obtained from similar structures at microwave frequencies. This result is in agreement with the considerations already made in Section 2.3.6.

## APPENDIX

In this appendix, accurate quasianalytical expressions for the inductances and per unit length capacitances used in Section 2.3 will be provided. To begin, the self-inductance of a ring of mean radius  $r$  and width  $c$  will be obtained. Let us assume a uniform current  $I$  on the ring. As there is no field and/or current dependence on the azimuthal coordinate, the magnetic energy can be computed as

$$U_M = \pi \int_0^\infty r A_\phi J_{s,\phi} dr, \quad (2.145)$$

where  $A_\phi$  is the azimuthal component of the vector magnetic potential. Integrating by parts and using  $B_z = r^{-1} \partial_r (r A_\phi)$ , where  $B_z$  is the  $z$  component of the magnetostatic field, and  $\partial_r$  the partial derivative with respect to  $r$ , it is found that

$$U_M = \pi \int_0^\infty r B_z I(r) dr, \quad (2.146)$$

where  $I(r)$  is defined by

$$I(r) = \int_r^\infty J_{s,\phi}(r') dr', \quad (2.147)$$

and  $J_{s,\phi}$  is the azimuthal surface current density on the ring.

Because the currents are restricted to the  $z = 0$  plane,  $B_z$  can be derived from a scalar magnetic potential,  $\psi(r, z)$ :  $B_z = -\mu_0 \partial_z \psi$ . This scalar magnetic potential must satisfy Laplace's equation,  $\partial_z^2 \psi + r^{-1} \partial_r (r \partial_r \psi) = 0$ , subjected to the following boundary conditions:  $\partial_z \psi(r, 0^+) = \partial_z \psi(r, 0^-)$ ;  $I(r) = \psi(r, 0^+) - \psi(r, 0^-)$  and

$\psi(\infty, z) \equiv \psi(r, \infty) = 0$ . Taking the Fourier–Bessel transform, which is defined as

$$\tilde{F}(k) = \int_0^\infty r J_0(kr) F(r) dr, \quad (2.148)$$

the above problem is analytically solved for  $\tilde{\psi}(k, z)$ , which is found to be

$$\tilde{\psi}(k, z) = \pm \frac{1}{2} \tilde{I}(k) e^{\mp kz}, \quad (2.149)$$

where the upper (lower) sign stands for  $z > 0$  ( $z < 0$ ).

After introducing  $B_z = -\mu_0 \partial_z \psi$  into equation (2.146), using equations (2.148) and (2.149), and making use of the Parseval theorem as well as the relation  $L = 2U_M/I^2$ , the SRR inductance is obtained as

$$L = \frac{\mu_0 \pi^2}{I^2} \int_0^\infty [\tilde{I}(k)]^2 k^2 dk. \quad (2.150)$$

For practical computations, a constant value for  $J_{s,\phi}$  has been assumed on the ring, that is,

$$J_{s,\phi} = \begin{cases} I/c & \text{for } r - c/2 < r' < r + c/2 \\ 0 & \text{otherwise.} \end{cases} \quad (2.151)$$

Introducing this expression into equation (2.147), after some algebraic manipulations, the SRR inductance can be obtained as the following integral:

$$\frac{L}{\mu_0} = \frac{\pi^3}{4c^2} \int_0^\infty \frac{1}{k^2} (b\mathcal{B}(kb) - a\mathcal{B}(ka))^2 dk, \quad (2.152)$$

where  $a = r - c/2$ ,  $b = r + c/2$  and function  $\mathcal{B}(x)$  is defined as

$$\mathcal{B}(x) = S_0(x)J_1(x) - S_1(x)J_0(x), \quad (2.153)$$

with  $S_n$  and  $J_n$  being the  $n$ th order Struve and Bessel functions respectively. This integral can be easily calculated in a computer, giving an accurate evaluation of the SRR inductance [19].

Regarding the per unit length capacitances for the EC-SRR and the BC-SRR, they can be directly obtained from well-known microwave circuit design formulas. For the EC-SRR, from Table 2.7 and equation (2.4) of [20], it is directly obtained that

$$C_{\text{pul}}/\varepsilon_0 = \varepsilon_e F(k), \quad (2.154)$$

where

$$\varepsilon_e = 1 + \frac{\varepsilon - \varepsilon_0}{2\varepsilon_0} \frac{F(k)}{F(k_1)} \quad (2.155)$$

$$k = a/b; \quad a = d/2; \quad b = d/2 + c \quad (2.156)$$

$$k_1 = \frac{\sinh(\pi a/2t)}{\sinh(\pi b/2t)} \quad (2.157)$$

$$F(k) = \frac{1}{\pi} \ln \left( 2 \frac{1 + \sqrt{k'}}{1 - \sqrt{k'}} \right) \quad (2.158)$$

if  $0 \leq k \leq 0.7$ , and

$$F(k) = \pi \left\{ \ln \left( 2 \frac{1 + \sqrt{k}}{1 - \sqrt{k}} \right) \right\}^{-1} \quad (2.159)$$

if  $0.7 \leq k \leq 1$ , where

$$k' = \sqrt{1 - k^2}. \quad (2.160)$$

For the BC-SRR, from Table 2.6 of [20], it directly follows that

$$C_{\text{pul}}/\varepsilon_0 = \frac{1}{2} \varepsilon_e \left\{ \frac{2c}{t} + 1.393 + 0.667 \ln \left( \frac{2c}{t} + 1.444 \right) \right\} \quad (2.161)$$

where

$$\varepsilon_e = \frac{\varepsilon + \varepsilon_0}{2\varepsilon_0} + \frac{\varepsilon - \varepsilon_0}{2\varepsilon_0} \left( 1 + \frac{6t}{c} \right)^{-1}. \quad (2.162)$$

## PROBLEMS

**2.1. Polarizability of a waveguide.** Define the average polarization of a rectangular waveguide that supports the fundamental  $\text{TE}_{10}$  mode as

$$\mathbf{P} = \frac{1}{j\omega S_w} \oint \mathbf{J}_s \, dl, \quad (2.163)$$

where  $\mathbf{J}_s$  is the surface current on the waveguide walls,  $S_w$  the surface of the waveguide cross-section, and the integral is over the boundary of the



waveguide section. Show that this average polarization is related to the average electric field in the waveguide cross-section by equation (2.5).

**2.2. TM waveguides as artificial magnetic plasmas.** Show, following the same procedure as in Section 2.2.1, that a waveguide operating in a TM mode can be seen as an artificial magnetic plasma with an effective dielectric constant  $\epsilon_{\text{eff}} = \epsilon_0$  and an effective permeability  $\mu_{\text{eff}} = \mu_0(1 - \omega_c^2/\omega^2)$ , where  $\omega_c$  is the cutoff frequency of the TM mode.

**2.3. Spatial dispersion in wire media.** Show that a uniaxial medium with permittivity tensor  $\epsilon_x = \epsilon_y = \epsilon_0$  and  $\epsilon_z(\omega) = \epsilon_0(1 - \omega_p^2/\omega^2)$  gives the following dispersion relation for TM (to  $z$ ) waves:

$$k_x^2 + k_y^2 = \frac{\epsilon_z(\omega)}{\epsilon_0}(k_0^2 - k_z^2). \tag{2.164}$$

Show that if  $\epsilon_z$  is given by equation (2.14), then the dispersion relation (2.13) is obtained.

**2.4. Three-turns spirals as metamaterial elements.** Consider the resonator shown in Figure 2.35. Derive an equivalent circuit for the determination of the frequency of resonance of this element. Using this equivalent circuit show that the frequency of resonance,  $f$ , of this element is related to the frequency of resonance  $f_{2\text{SR}}$  of the two-turns spiral (Fig. 2.11) of the same mean radius, strip width, and slot width through  $f \simeq f_{2\text{SR}}/\sqrt{2}$ . Derive an expression for the magnetic polarizability of such an element (see [26]).

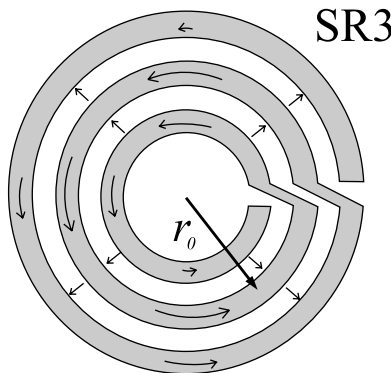


**FIGURE 2.35** Sketch of a three-turns spiral resonator. Metallizations are in gray, and the arrows show the direction of the ohmic and displacement currents at resonance.

**2.5. Nonbianisotropic two-turns spirals.** Consider the metamaterial element shown in Figure 2.36. It can be easily realized that it presents inversion symmetry, so that its cross-polarizabilities must vanish. Derive an equivalent circuit

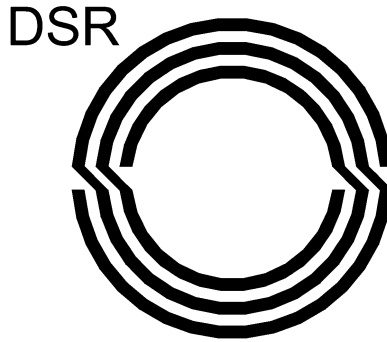


**FIGURE 2.36** Sketch of a nonbianisotropic spiral resonator. Note the presence of two non-connected metallizations.

for this element. Using this equivalent circuit, show that the frequency of resonance,  $f$ , of this element is related to the frequency of resonance,  $f_{2SR}$ , of the two-turns spiral (Fig. 2.11) of the same mean radius, strip width, and slot width through  $f = \sqrt{2}f_{2SR}$ . Derive an expression for the magnetic polarizability of such element.

- 2.6. Open EC-SRR.** Consider the configuration shown in Figure 2.37. Derive an equivalent circuit for this configuration. Using this equivalent circuit show that this element is equivalent to a short circuit at a frequency that is a half of the frequency of resonance of the EC-SRR of similar design. This configuration is useful for microwave filter design (see [87]).

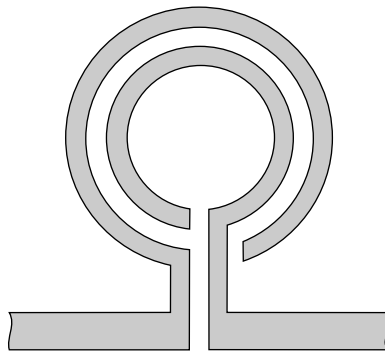


**FIGURE 2.37** Open split rings resonator.

- 2.7. Dispersion relation for plane TEM waves in SRR media.** Consider the SRR media shown in Figure 2.12, with EC-SRRs as elementary constituents. Using the model reported in Section 2.3.3, show that the dispersion relation for electromagnetic plane waves propagating along the  $x$ -axis and polarized with the

magnetic field parallel to the  $z$ -axis is

$$k_x = \omega \sqrt{\mu_{zz} \varepsilon_{yy} - \mu_0 \varepsilon_0 k_{yz}^2}. \quad (2.165)$$

**2.8. Effects of bianisotropy on the dispersion relation of a left-handed medium.**

Using expression (2.76), and assuming the superposition hypothesis for the left-handed composite of wires and SRRs reported in [4], find the width of the mismatch between the negative- $\mu$  stopband and the left-handed passband of Figure 2.22.

**2.9. TM plane waves in SRR media.** Consider the SRR media shown in Figure 2.12, with EC-SRRs as elementary constituents. Show that plane waves propagating along the  $y$ -axis and polarized with the magnetic field along the  $z$ -axis are TM waves, with the electric field elliptically polarized in the  $x$ - $y$  plane. Show that the dispersion relation for such waves is

$$k = \omega \sqrt{\varepsilon_{yy} \mu_{\text{eff}}}; \quad \mu_{\text{eff}} = \mu_{xx} - \varepsilon_0 \mu_0 \frac{\kappa_{yx}^2}{\varepsilon_{yy}}. \quad (2.166)$$

**2.10. Magnetostatic waves in SRR media.** Consider the SRR medium shown in Figure 2.12, with BC-SRRs as elementary constituents. Consider a quasimagnetostatic field,  $\mathbf{H} = -\nabla \psi_m$ , where  $\psi_m$  is the magnetostatic potential.

- Show that magnetostatic waves with the dispersion relation

$$k_x^2 + k_y^2 + \frac{\mu_{zz}}{\mu_0} k_z^2 = 0 \quad (2.167)$$

can propagate through the metamaterial in the region of  $\mu_{zz} < 0$ .

- Study the propagation of magnetostatic modes in a slab of the SRR medium of width  $d$ . Consider the two cases, with the SRRs in the plane of the slab, and with the SRRs orthogonal to the plane of the slab.

These waves can be considered analogous to the well-known magnetostatic waves in ferrites [58,59] (see also Section 2.5.1). As happens in ferrites, such magnetostatic approximation is only valid in the limit  $k \gg k_0 \equiv \omega_0 \sqrt{\varepsilon_0 \mu_0}$ .

**2.11. Magnetic susceptibility of a nano-SRR media at near-optical frequencies.**

Consider a cubic network of SRRs such as that shown in Figure 2.12, with elementary constituents such as those shown in Figure 2.18*b*. Show that, if losses are small, the magnetic susceptibility along the ring axis is approximately given by

$$\chi_m \approx \frac{\omega_m^2}{\omega_0^2 - \omega^2 + j\omega\gamma}, \quad (2.168)$$

where

$$\omega_m^2 = \mu_0 \frac{\pi^2 r \omega_0^2}{8K^3(L_m + L_k)}, \tag{2.169}$$

$$\omega_0 = \frac{1}{\sqrt{(L_m + L_k)C}}, \quad \gamma = \frac{R}{L_m + L_c} \ll \omega, \omega_0, \tag{2.170}$$

and  $K$  is the dimensionless ratio  $a/2r$ .

Show that, when  $L_k > L_m$ , the maximum value of  $|\Re(\chi_m)|$  is

$$|\Re(\chi_m)|_{\max} \approx \frac{\pi^3}{8K^3} \frac{\omega_0}{f_c} \left( \frac{S}{\lambda_p^2} \right)^2, \tag{2.171}$$

where  $S$  is the wire section.

**2.12. Magnetostatic surface modes in a saturated ferrite I.** Show that the magnetostatic wave equation (2.111) has bounded propagative solutions at the interface between a magnetized ferrite and a perfect conductor for  $\omega = \omega_H + \omega_M$ . These surface magnetostatic waves have the following characteristics: static magnetization  $\mathbf{H}_0$  parallel to the surface and propagation along the direction defined by  $\mathbf{H}_0 \times \mathbf{n}$ , where  $\mathbf{n}$  is the outgoing normal to the ferrite interface. As in quasistatic surface plasmons (see Chapter 1), the dispersion equation for such waves is degenerate (any wavevector is excited at the aforementioned frequency).

**2.13. Magnetostatic surface modes in a saturated ferrite II.** Show that the magnetostatic wave equation (2.111) has bounded propagative solutions at the interface between a magnetized ferrite and free space similar to those analyzed

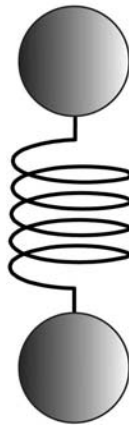


**FIGURE 2.38** A chiral inclusion made of two metallic balls, connected by a solenoid.

in the previous problem. Show that the frequency of excitation of such MSSWs is  $\omega = \omega_H + \frac{1}{2}\omega_M$ .

- 2.14. Magnetostatic surface modes in a saturated ferrite III.** Find, from Maxwell equations, the dispersion equation without approximations for the MSSWs analyzed in the previous problem (see [58] for more information).
- 2.15. Quasistatic analysis of a chiral inclusion.** Consider the chiral inclusion of Figure 2.38. Using elementary formulas for the self-inductance of a solenoid, and for the capacitance between two metallic balls [9], find closed expressions for the polarizabilities of the inclusion.

## REFERENCES

1. W. Rotman "Plasma simulation by artificial dielectrics and parallel-plate media." *IRE Trans. Antennas Propag.*, vol. 10, pp. 82–95, 1962.
2. J. B. Pendry, A. J. Holden, W. J. Stewart, and I. Youngs "Extremely low frequency plasmons in metallic mesostructures." *Phys. Rev. Lett.*, vol. 76, pp. 4773–4776, 1996.
3. J. B. Pendry, A. J. Holden, D. J. Robbins, and W. J. Stewart "Magnetism from conductors and enhanced nonlinear phenomena." *IEEE Trans. Microwave Theory Tech.*, vol. 47, pp. 2075–2084, 1999.
4. D. R. Smith, W. J. Padilla, D. C. Vier, S. C. Nemat-Nasser, and S. Schultz "Composite medium with simultaneously negative permeability and permittivity." *Phys. Rev. Lett.*, vol. 84, pp. 4184–4187, 2000.
5. A. K. Iyer, and G. Eleftheriades "Negative refractive index metamaterials supporting 2-D waves." *Proc. IEEE-MTT Int. Symp.*, vol. 2, pp. 412–415, Seattle, WA, 2002.
6. C. Caloz, H. Okabe, H. Iwai, and T. Itoh "Transmission line approach of left-handed metamaterials." *Proc. USNC/URSI Nat. Radio Sci. Meeting*, pp. 39, San Antonio, TX, 2002.
7. A. A. Oliner "A periodic-structure negative-refractive index medium without resonant elements." *Proc. USNC/URSI Nat. Radio Sci. Meeting*, pp. 41, San Antonio, TX, 2002.
8. R. Marqués, J. Martel, F. Mesa, and F. Medina "Left-handed-media simulation and transmission of EM waves in subwavelength split-ring-resonator-loaded metallic waveguides." *Phys. Rev. Lett.*, vol. 9, paper 183901, 2002.
9. J. D. Jackson *Classical Electrodynamics*. Wiley, New York, 1999 (3rd. ed.).
10. R. E. Collin *Field Theory of Guided Waves*, IEEE Press, New York, 1990 (2nd. ed.).
11. J. Esteban, C. Camacho-Peñalosa, J. E. Page, T. M. Martin-Guerrero, and E. Marquez-Segura "Simulation of negative permittivity and negative permeability by means of evanescent waveguide modes—theory and experiment." *IEEE Trans. Microwave Theory Tech.*, vol. 53, pp. 1506–1514, 2005.
12. P. A. Belov, R. Marqués, S. I. Maslowski, I. S. Nefedov, M. Silveirinha, C. R. Simovski, and S. A. Tretyakov "Strong spatial dispersion in wire media in the very large wavelength limit." *Phys. Rev. Lett.*, vol. 67, paper 113103, 2003.
13. L. D. Landau, E. M. Lifshitz, and L. P. Pitaevskii *Electrodynamics of Continuous Media* Pergamon, New York, 1984.

14. M. G. Silveirinha, and C. Fernandes “Homogenization of 3-D-connected and nonconnected wire metamaterial.” *IEEE Trans. Antennas and Propag.*, vol. 53, pp. 1418–1430, 2005.
15. W. Weber “On the relationship of the science of the diamagnetism with the sciences of magnetism and electricity.” *Ann. Phys.*, vol. 87, pp. 145–189, 1852.
16. S. A. Shelkunoff, and H. T. Friis *Antennas. Theory and Practice*, Wiley, New York, 1966 (3rd. ed.).
17. R. Marqués, F. Medina and R. Rafii-El-Idrissi “Role of bi-anisotropy in negative permeability and left handed metamaterials.” *Phys. Rev. B*, vol. 65, paper 144441, 2002.
18. M. Shamonin, E. Shamonina, V. Kalinin, and L. Solymar “Resonant frequencies of a split-ring resonator: analytical solutions and numerical simulations.” *Microwave Opt. Tech. Lett.*, vol. 44, pp. 133–137, 2005.
19. R. Marqués, F. Mesa, J. Martel, and F. Medina “Comparative analysis of edge and broadside coupled split ring resonators for metamaterial design. Theory and experiment.” *IEEE Trans. Antennas Propag.*, vol. 51, pp. 2572–2581, 2003.
20. I. Bahland P. Bhartia, *Microwave Solid State Circuit Design*, Wiley, New York, 1988.
21. L. D. Landau and E. M. Lifshitz *Statistical Physics*. Pergamon Press, Oxford, England, 1980 (3rd ed.).
22. I. V. Lindell, A. H. Sihvola, S. A. Tretyakov, and A. J. Viitanen *Electromagnetic Waves in Chiral and Bi-isotropic Media*. Artech House, Norwood, MA, 1994.
23. J. D. Baena, J. Bonache, F. Martín, R. Marqués, F. Falcone, T. Lopetegi, M. A. G. Laso, J. García-García, I. Gil, M. Flores, and M. Sorolla “Equivalent circuit models for split rings resonators and complementary split rings resonators coupled to planar transmission lines.” *IEEE Trans. Microwave Theory Tech.*, vol. 53, pp. 1451–1461, 2005.
24. P. Gay-Balmaz, and O. J. F. Martín “Electromagnetic resonances in individual and coupled split ring resonators.” *J. Appl. Phys.* vol. 92, pp. 2929–36, 2002. (See also R. Marqués, F. Medina, R. Rafii-El-Idrissi “Comment to electromagnetic resonances in individual and coupled split ring resonators.” *J. Appl. Phys.*, vol. 94, p. 2770, 2003.)
25. R. Marqués, J. D. Baena, J. Martel, F. Medina, F. Falcone, M. Sorolla, and F. Martín “Novel small resonant electromagnetic particles for metamaterial and filter design.” *Proc. ICEAA'03*, pp. 439–442, Torino, Italy, 2003.
26. J. D. Baena, R. Marqués, F. Medina, and J. Martel “Artificial magnetic metamaterial design by using spiral resonators.” *Phys. Rev. B*, vol. 69, paper 014402, 2004.
27. J. D. Baena. Private communication.
28. X. Xu, B. Quan, Ch. Gu, and L. Wang “Bianisotropic response of microfabricated metamaterials in the terahertz region.” *J. Opt. Soc. Am. B*, vol. 23, pp. 1174–1180, 2006.
29. D. R. Smith, and D. Schurig “Electromagnetic wave propagation in media with indefinite permittivity and permeability tensors.” *Phys. Rev. Lett.*, vol. 90, paper 077405, 2003.
30. J. García-García, F. Martín, J. D. Baena, R. Marqués, and L. Jelinek “On the resonances and polarizabilities of split ring resonators.” *J. Appl. Phys.*, vol. 98, paper 033103, 2005.
31. C. A. Fernandes, R. Marqués, and M. Silveirinha “Transmission in rectangular waveguides periodically loaded with SRRs: simulation and measurement.” *Proc. of the European Microwave Assoc.* vol. 2, pp. 66–70, 2006.
32. Ph. Gay-Balmaz and O. J. F. Martín “Efficient isotropic magnetic resonator.” *Appl. Phys. Lett.*, vol. 81, pp. 939–941, 2002.

33. C. R. Simovski, and B. Sauviac "Towards creating isotropic microwave composites with negative refraction." *Radio Sci.*, vol. 39, pp. RS2014, 2004.
34. C. R. Simovski and S. He "Frequency range and explicit expressions for negative permittivity and permeability for an isotropic medium formed by a lattice of perfectly conducting  $\Omega$  particles." *Phys. Lett. A*, vol. 311, pp. 254–263, 2003.
35. M. M. I. Saadoun and N. Engheta "A reciprocal phase shifter using a novel pseudo-chiral or  $\Omega$  medium." *Microwave Opt. Tech. Lett.*, vol. 5, pp. 184–188, April 1992.
36. J. D. Baena, L. Jelinek, R. Marqués, and J. Zehentner "Electrically small isotropic three-dimensional magnetic resonators for metamaterial design." *Appl. Phys. Lett.*, vol. 88, pp. 134108, (2006).
37. Th. Koschny, L. Zhang, and C. M. Soukoulis "Isotropic three-dimensional left-handed metamaterials." *Phys. Rev. B*, vol. 71, paper 121103, 2005.
38. T. J. Yen, W. J. Padilla, N. Fang, D. C. Vier, D. R. Smith, J. B. Pendry, D. N. Basov, and X. Zhang "Terahertz magnetic response from artificial materials." *Science*, vol. 303, pp. 1494–1496, 2004.
39. S. Linden, C. Enkrich, M. Wegener, J. Zhou, T. Koschny, and C. M. Soukoulis "Magnetic response of metamaterials at 100 terahertz." *Science*, vol. 306, pp. 1351–1353, 2004.
40. J. Zhou, Th. Koschny, M. Kafesaki, E. N. Economou, J. B. Pendry, and C. M. Soukoulis "Saturation of the magnetic response of split ring resonators at optical frequencies." *Phys. Rev. Lett.*, vol. 95, paper 223902, 2005.
41. R. Marqués and M. J. Freire "On the usefulness of split ring resonators for magnetic metamaterial design at infrared and optical frequencies." *Proc. 13th IEEE Mediterranean Electrochemical Conference (MELECON 2006)*, May 16–19, 2006, Benalmádena (Málaga), Spain, pp. 122–124.
42. J. R. Reitz, F. J. Milford, and R. W. Christy *Foundations of Electromagnetic Theory*. Addison-Wesley, Reading, MA, (4th ed.).
43. N. Engheta, A. Salandrino, and A. Alù "Circuit elements at optical frequencies: nano-inductors, nanocapacitors, and nanoresistors." *Phys. Rev. Lett.*, vol. 95, paper 095504, 2005.
44. J. Aizpurua, P. Hanarp, D. S. Sutherland, M. Kall, G. W. Bryant, and F. J. Garcia de Abajo "Optical properties of gold nanorings." *Phys. Rev. Lett.*, vol. 90, paper 057401, 2003.
45. R. A. Shelby, D. R. Smith, and S. Schultz "Experimental verification of a negative index of refraction." *Science*, vol. 292, pp. 77–79, 2001.
46. R. Marqués, J. Martel, F. Mesa, and F. Medina "Left-handed-media simulation and transmission of EM waves in subwavelength split-ring-resonator-loaded metallic waveguides." *Phys. Rev. Lett.*, vol. 89, paper 183901, 2002.
47. I. G. Kondrat'ev and A. I. Smirnov "Comments on left-handed media simulation and transmission of EM waves in subwavelength split-ring-resonator-loaded metallic waveguides." *Phys. Rev. Lett.*, vol. 91, paper 2494011, 2003. See also authors reply.
48. S. Hrabar, J. Bartolic, and Z. Sipus "Waveguide miniaturization using uniaxial negative permeability metamaterial." *IEEE Trans. Antennas Propag.*, vol. 53, pp. 110–119, 2005.
49. P. A. Belov and C. R. Simovski "Subwavelength metallic waveguides loaded by uniaxial resonant scatterers." *Phys. Rev. E*, vol. 72, paper 036681, 2005.

50. R. Marqués, J. Martel, F. Mesa, and F. Medina “A new 2-D isotropic left-handed metamaterial design: theory and experiment.” *Microwave Opt. Tech. Lett.*, vol. 35, pp. 405–408, 2002.
51. J. D. Baena, R. Marqués, J. Martel, and F. Medina “Experimental results on metamaterial simulation using SRR-loaded waveguides.” *Proc. IEEE-AP/S Int. Symp. on Antennas and Propagation*, pp. 106–109, 2003.
52. R. A. Shelby, D. R. Smith, S. C. Nemat-Nasser, and S. Schultz “Microwave transmission through a two-dimensional, isotropic, left-handed metamaterial.” *Appl. Phys. Lett.*, vol. 78, pp. 489–491, 2001.
53. S. Hrabar, Z. Sipus, and J. Bartolic “Experimental verification of negative index of refraction by lateral beam displacement.” *Proc. 2004 URSI-EMT Symp.*, pp. 373–375, Pisa, Italy, 2004.
54. A. L. Pokrovsky and A. L. Efros “Electrodynamics of photonic crystals and the problem of left-handed metaterials.” *Phys. Rev. Lett.*, vol. 89, paper 093901, 2002.
55. R. Marques and D. R. Smith “Comments to Electrodynamics of photonic crystals and the problem of left-handed metamaterials.” *Phys. Rev. Lett.*, vol. 92, paper 059401, 2004.
56. D. R. Smith, W. Padilla, D. Vier, R. Shelby, S. Nemat-Nasser, N. Kroll, and S. Schultz, in *Proc. NATO-ASI Conf. on Photonic Crystals and Light Localization in the 21st Century*. June 18–30 2002, Heraclion, Crete (Greece). Edited by C. M. Soukoulis. Kluwer Academic, Dordrecht, 2001, p. 351.
57. A. Pimenov, A. Loidl, P. Przyslupsky, and B. Dabrowski “Negative refraction in ferromagnetic-superconductor superlattices.” *Phys. Rev. Lett.*, vol. 95, paper 247009, 2005.
58. M. S. Sodha and N. C. Shrivastava *Microwave Propagation in Ferrimagnetics*. Plenum Press, New York, 1981.
59. A. G. Gurevich and G. A. Melkov *Magnetization Oscillations and Waves*. CRC Press, Boca Raton, Florida, 1996.
60. R. F. Harrington and A. T. Villeneuve “Reciprocity relationships for gyrotropic media.” *IRE Trans. Microwave Theory Tech.*, vol. 6, pp. 308–310, 1958.
61. M. Mrozowski *Guided Electromagnetic Waves. Properties and Analysis*. Research Studies Press, Taunton, UK and Wiley, New York, 1997.
62. G. H. B. Thompson “Unusual waveguide characteristics associated with the apparent negative permeability obtainable in ferrites.” *Nature*, vol. 175, pp. 1135–1136, 1955. (Authors want to thank Prof. Laszlo Solymar for bringing this paper to their attention.)
63. A. Dechant and M. Okoniewski “Broadband double negative material from ferrite-loaded metallic waveguides.” *Electron. Lett.*, vol. 42, pp. 4–5, 2006.
64. G. Dewar “Candidates for  $\mu < 0$ ,  $\varepsilon < 0$  nanostructure.” *Int. J. Modern Phys. B*, vol. 15, pp. 3258–3265, 2001.
65. G. Dewar “A thin wire array and magnetic host structure with  $n < 1$ .” *J. Appl. Phys.*, vol. 97, paper 10Q101, 2005.
66. A. Alu and N. Engheta “Pairing an epsilon-negative slab with a mu-negative slab: resonance, tunneling and transparency.” *IEEE Trans. Antennas Propag.*, vol. 51, pp. 2558–2571, 2003.
67. K. F. Lindmann “Rotation polarisation of electromagnetic waves generated by the isotropic system of spiral resonators.” *Annalen der Physik*, vol. 63, pp. 621–644, 1920.
68. A. J. Bahr and K. R. Clausing “An approximate model for artificial chiral material.” *IEEE Trans. Microwave Theory Tech.*, vol. 42, pp. 1592–1599, 1994.



69. F. Mariotte, S. A. Tretyakov, and B. Sauviac "Isotropic chiral composite modelling: comparison between analytical, numerical and experimental results." *Microwave Opt. Tech. Lett.*, vol. 7, pp. 861–864, 1994.
70. S. A. Tretyakov, F. Mariotte, C. R. Simovski, and T. G. Kharina "Analytical antenna model for chiral scatterers: Comparison with numerical and experimental data." *IEEE Trans. Microwave Theory Tech.*, vol. 44, pp. 1006–1014, 1996.
71. S. A. Tretyakov, A. Sihvola, and L. Jylh "Backward-wave regime and negative refraction in chiral composites." *Photonics and Nanostruct. Fund. Appl.*, vol. 3, pp. 107–115, 2005.
72. T. G. Mackay "Plane waves with negative phase velocity in isotropic chiral mediums." *Microwave Opt. Tech. Lett.*, vol. 45, pp. 120–121, 2005.
73. S. A. Tretyakov *Analytical Modelling in Applied Electromagnetics*. Artech House, Norwood, MA, 2003.
74. R. Marqués, L. Jelinek, and F. Mesa "Negative refraction from quasi-planar chiral inclusions." *Microwave Opt. Tech. Lett.*, vol. 49, pp. 2006–2009, 2006.
75. J. B. Pendry "A chiral route to negative refraction." *Science*, vol. 306, pp. 1353–1355, 2004.
76. S. A. Tretyakov, I. Nefedov, A. Sihvola, S. Maslowski, and C. Simowski "Waves and energy in chiral nihility." *J. Electromagnetic Waves and Appl.*, vol. 5, pp. 695–706, 2003.
77. A. Sihvola *Electromagnetic Mixing Formulas and Applications*. IEE Press, London, UK, 1999.
78. C. L. Holloway, E. F. Kuester, J. Baker-Jarvis, and P. A. Kabos "Double negative (DNG) composite medium composed of magnetodielectric spherical particles embedded in a matrix." *IEEE Trans. Antennas Propag.*, vol. 51, pp. 2596–2603, 2003.
79. O. G. Vendik and M. S. Gashinova "Artificial double negative (DNG) media composed by two different dielectric sphere lattices embedded in a dielectric matrix." *Proc. 34th European Microwave Conf.*, vol. 3, pp. 1209–1212, Amsterdam, 2004.
80. L. Lewin "The electrical constants of a material loaded with spherical particles." *Proc. IEE*, vol. 94, pp. 65–68, 1947.
81. D. M. Pozar *Microwave Engineering*. Addison-Wesley, Reading, MA, 1993.
82. R. F. Harrington *Time-Harmonic Electromagnetic Fields*. McGraw-Hill, New York, 1961.
83. D. Schurig, J. J. Mock, and D. R. Smith "Electric-field-coupled resonators for negative permittivity metamaterials." *Appl. Phys. Lett.*, vol. 88, paper 041109, 2006.
84. V. M. Shalaev, W. Cai, U. K. Chettiar, H. K. Yuan, A. K. Sarychev, V. P. Drachev, and A. V. Kildishev "Negative index of refraction in optical metamaterials." *Opt. Lett.*, vol. 30, pp. 3356–3358, 2005.
85. A. N. Grigorenko, A. K. Geim, H. F. Gleeson, Y. Zhang, A. A. Frisov, I. Y. Khrushchev, and J. Petrovic "Nanofabricated media with negative permeability at visible frequencies." *Nature*, vol. 438, pp. 335–338, 2005.
86. A. N. Lagarkov and A. K. Sarychev "Electromagnetic properties of composites containing elongated conducting inclusions." *Phys. Rev. B*, vol. 53, pp. 6381–6336, 1996.
87. J. Martel, R. Marqués, F. Falcone, J. Baena, F. Medina, F. Martín, and M. Sorolla "A new LC series element for compact band-pass filter design." *IEEE Microwave Wirel. Comp. Lett.*, vol. 14, pp. 210–212, 2004.

# Synthesis of Metamaterials in Planar Technology

---

## 3.1 INTRODUCTION

This chapter is focused on the synthesis of left-handed and single negative structures in planar technology. Essentially, one-dimensional propagating structures, that is, metamaterial transmission lines, will be considered, although a subsection will also be dedicated to the implementation of planar two-dimensional left-handed media. Regarding the synthesis of metamaterial transmission lines, most of the chapter will be devoted to the resonant-type approach, where the formerly constitutive particles for the implementation of bulk left-handed structures, that is, the SRRs, are used in combination with other elements. A resonant particle that is the dual version of the SRR, which is useful for the implementation of negative-permittivity media in planar technology will also be introduced in this chapter, that is, the complementary split rings resonator (CSRR). The lumped-element equivalent circuit models for left-handed and single negative transmission lines loaded with both SRRs and CSRRs will be presented, analysed, and discussed. These models are fundamental for the design of microwave components based on SRRs and CSRRs, as will be shown in Chapter 4.

This book predominantly reflects the results of the research activities carried out by the authors and their respective groups in the field of metamaterials. These activities have been mainly oriented towards the resonant-type approach, and the authors have pioneered the synthesis and applications of metamaterial transmission lines based on SRRs, CSRRs, and related topologies. However, chronologically, there was an earlier approach to the design of metamaterials in planar technology, namely that based on the dual transmission line concept. This approach, initially proposed by Iyer et al. [1], Oliner [2] and Caloz et al. [3], has reached a level of maturity

that has led to many prospective engineering applications in the field of microwaves. Therefore, the first sections of this chapter will be devoted to a brief introduction of this approach. Applications of both approaches (dual transmission line and resonant-type approaches) will be discussed in Chapter 4.

### 3.2 THE DUAL (BACKWARD) TRANSMISSION LINE CONCEPT

The concept of backward waves to describe propagating waves with antiparallel phase and group velocities is not new (several textbooks have dealt with and described this subject [4,5]). Conceptually, backward waves can be generated by feeding a ladder network with alternating shunt-connected inductors and series capacitors (Fig. 3.1). Such a network is the dual version of the equivalent-circuit model of a conventional lossless planar transmission line with forward (as opposed to backward) wave propagation (see also Fig. 3.1). The analysis of the propagation characteristics of the structures shown in Figure 3.1 can be realized from the theory of periodic structures [6], where it is assumed that the structure is either infinite or it is matched to the ports. From this analysis, the phase constant,<sup>1</sup>  $\beta$ , and the characteristic (or Bloch) impedance,<sup>2</sup>  $Z_B$ , of the transmission media can be inferred according to

$$\cos \beta l = 1 + \frac{Z_s(\omega)}{Z_p(\omega)} \quad (3.1)$$

$$Z_B = \sqrt{Z_s(\omega)[Z_s(\omega) + 2Z_p(\omega)]}, \quad (3.2)$$

where  $Z_s$  and  $Z_p$  are the series and shunt impedances of the basic cell of the structure, described by its T-circuit model, and  $l$  is the period. Application of expressions (3.1) and (3.2) to the circuits of Figure 3.1 leads to the following expressions [the sub-indices  $L$  and  $R$  are used to distinguish between the left-handed (backward wave)

<sup>1</sup>The phase constant is usually designated by  $\beta$  in circuit theory, whereas in the previous chapters it has been designated by  $k$ , which is the usual convention to express the dispersion relation in continuous media.

<sup>2</sup>The characteristic impedance of a transmission line is the relation between voltage and current for a single propagating wave at any position of the line. In periodic structures (either infinite or matched to the ports) the relation between voltage and current for the Bloch waves is usually called Bloch impedance. For finite periodic structures not matched to the ports, both incident (energy flow from the input to the output port) and reflected (energy flow in the opposite direction) waves necessarily arise. For either propagating wave (incident or reflected), expression (3.2) provides the relation between voltage and current. This impedance is usually called image impedance, as it is the load impedance required to see identical input impedance. Nevertheless, we will not distinguish between image and Bloch impedances, and we will call the impedance given by expression (3.2) Bloch impedance or, even, characteristic impedance. Indeed the image or Bloch impedance play exactly the same role as the characteristic impedance in conventional lines.

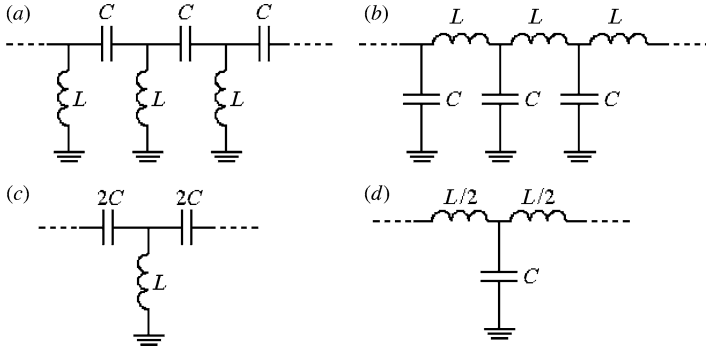


**FIGURE 3.1** Equivalent circuit model of backward (a) and forward (b) transmission lines. The T-circuit models of the basic cell structures are also indicated in (c) and (d).

and right-handed (forward wave) structures]:

$$\cos \beta_R l = 1 - \frac{LC}{2} \omega^2 \quad (3.3)$$

$$Z_{BR} = \sqrt{\frac{L}{C} \left( 1 - \frac{\omega^2}{\omega_{cR}^2} \right)} \quad (3.4)$$

$$\cos \beta_L l = 1 - \frac{1}{2LC\omega^2} \quad (3.5)$$

$$Z_{BL} = \sqrt{\frac{L}{C} \left( 1 - \frac{\omega_{cL}^2}{\omega^2} \right)} \quad (3.6)$$

where  $\omega_{cR} = 2/(LC)^{1/2}$  and  $\omega_{cL} = 1/2(LC)^{1/2}$  are angular cutoff frequencies for the forward and backward wave transmission line structures, respectively. The dispersion diagram as well as the dependence of  $Z_B$  on frequency are depicted in Figure 3.2. Transmission is limited to those frequency intervals that make the phase constant and the characteristic impedance to be real numbers. It is worth mentioning that frequency dispersion is present in both structures. Even though the circuit of Figure 3.1*b* models an ideal lossless forward transmission line, where dispersion is absent, in fact this circuit is only valid for frequencies satisfying  $\omega \ll \omega_{cR}$ , that is, in the long wavelength limit (corresponding to those frequencies where the wavelength for guided waves satisfies,  $\lambda_g \gg l$ ).<sup>3</sup> To correctly model an ideal lossless transmission line at higher frequencies, we simply need to reduce the period of the structure, and, accordingly, the per-section inductance and capacitance of the line,  $L$  and  $C$ , with the result of a higher cutoff frequency. Thus, the circuit of Figure 3.1*b* can properly describe

<sup>3</sup> $\lambda_g$  has been called the internal wavelength and was designated  $\lambda_i$  in the previous chapter (see Section 2.4.3).

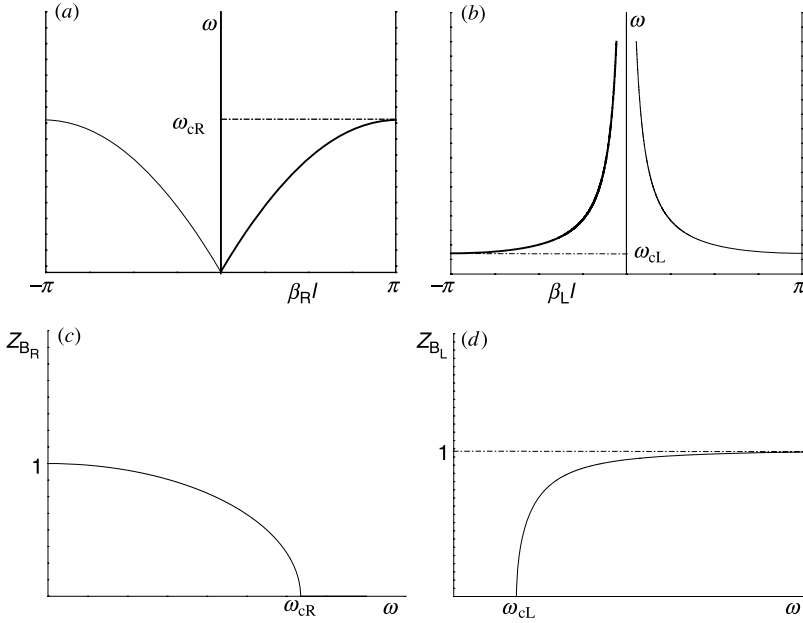


**FIGURE 3.2** Typical dispersion diagram of forward (a) and backward (b) transmission line models. The dependence of the normalized ( $Z_B/Z_{lw}$ ) Bloch impedance with frequency is shown in (c) and (d) for the forward and backward lines, respectively.

ideal transmission lines without dispersion. To this end we simply need to select the period such that the long wavelength limit approximation holds. Under this approximation, expressions (3.3) and (3.4) lead us to the following well-known expressions:

$$\beta_R = \omega\sqrt{L'C'} \quad (3.7)$$

and

$$Z_{BR} = \sqrt{\frac{L'}{C'}} \equiv Z_{lw}, \quad (3.8)$$

where  $L'$  and  $C'$  are the per-unit length inductance and capacitance of the transmission line (in expression 3.8,  $L'$  and  $C'$  can be replaced by  $L$  and  $C$  with no effect). From (3.7), we can obtain the phase and group velocities of the forward transmission line. These velocities are given by:

$$v_{pR} = \frac{\omega}{\beta_R} = \frac{1}{\sqrt{L'C'}} = \frac{l}{\sqrt{LC}} \quad (3.9)$$

$$v_{gR} = \left(\frac{\partial\beta_R}{\partial\omega}\right)^{-1} = v_{pR} \quad (3.10)$$

and they are both positive and constant.

Conversely, the backward-wave structure of Figure 3.1a is dispersive even in the long wavelength limit. In order to identify this structure as an effective propagating medium (i.e., one-dimensional metamaterial), operation under this approximation is required.<sup>4</sup> However, regardless of the operating frequency within the transmission band, the structure supports backward waves and, for this reason, it is a left-handed transmission line. In order to properly identify effective constitutive parameters,  $\mu_{\text{eff}}$  and  $\epsilon_{\text{eff}}$ , the long wavelength approximation is necessary. However, many circuit applications of these left-handed lines are based on left-handedness, rather than on the effective medium properties, and operation under this approximation is not a due. Nevertheless, for coherence and simplicity, the phase constant, the characteristic impedance, as well as the phase and group velocities are derived under the long wavelength limit ( $\omega \gg \omega_{\text{cL}}$ ). The following results are obtained:

$$\beta_{\text{L}}l = -\frac{1}{\omega\sqrt{LC}} \quad (3.11)$$

$$Z_{\text{BL}} = \sqrt{\frac{L}{C}} \equiv Z_{\text{lw}} \quad (3.12)$$

$$v_{\text{pL}} = \frac{\omega}{\beta_{\text{L}}} = -\omega^2 l \sqrt{LC} < 0 \quad (3.13)$$

$$v_{\text{gL}} = \left(\frac{\partial\beta_{\text{L}}}{\partial\omega}\right)^{-1} = +\omega^2 l \sqrt{LC} > 0 \quad (3.14)$$

and the phase and group velocities have opposite signs. From a mathematical point of view, in the dispersion diagrams for the forward and backward lines depicted in Figure 3.2, and obtained from expressions (3.3) and (3.5), the sign of  $\beta$  can be either positive or negative. This ambiguity comes from the two possible directions of energy flow, namely from left to right or vice versa. If we adopt the usual convention of energy flow from left to right, then the sign of the phase constant is determined by choosing that portion of the curves that provide a positive group velocity (bold lines in Fig. 3.2a and b). From this, it is clear that for the forward transmission line,  $\beta$  and  $v_{\text{p}}$  are both positive, whereas these magnitudes are negative for the backward transmission line. In both cases,  $v_{\text{g}}$  is positive, as one expects, on account of the codirectionality between power flow and group velocity.

In the backward and forward transmission lines depicted in Figure 3.1, it is possible to identify effective constitutive parameters. To this end, we should take into account that transverse electromagnetic (TEM) mode propagation in planar transmission media and plane wave propagation in isotropic and homogeneous dielectrics are described by identical equations (telegraphist's equation) provided the following

<sup>4</sup>This aspect was discussed in Section 2.4.3.

mapping holds:

$$Z'_s(\omega) = j\omega\mu_{\text{eff}} \quad (3.15)$$

$$Y'_p(\omega) = j\omega\varepsilon_{\text{eff}} \quad (3.16)$$

where  $Z'_s$  and  $Y'_p$  are the series impedance and shunt admittance per unit length. Thus, for the forward line, the effective permittivity and permeability are constant and they are given by

$$\varepsilon_{\text{eff}} = C/l \quad (3.17)$$

and

$$\mu_{\text{eff}} = L/l, \quad (3.18)$$

whereas for the backward transmission line, the constitutive parameters are

$$\varepsilon_{\text{eff}} = -\frac{1}{\omega^2 Ll} \quad (3.19)$$

and

$$\mu_{\text{eff}} = -\frac{1}{\omega^2 Cl}, \quad (3.20)$$

and they are both negative, a sufficient condition to obtain left-handed wave propagation.

From a practical point of view, in order to implement a dual (or backward) transmission line, a host line (microstrip or CPW, among others) is required. The host line thus introduces parasitic elements that in general may not be negligible, and they should be taken into account to accurately describe the propagation characteristics of the lines. As will be shown later, these structures may exhibit left-handed or right-handed wave propagation, depending on the frequency interval, and, for these reason, they have been termed as composite right-/left-handed (CRLH) transmission lines [7]. The equivalent circuit model of these structures is depicted in Figure 3.3. For clarity, we have renamed the reactive elements of the dual transmission line as  $C_L$  and  $L_L$ , and  $C_R$  and  $L_R$  correspond to the per-section capacitance and inductance of the host line. By using expressions (3.1) and (3.2), the dispersion relation as well as the characteristic impedance of the CRLH transmission line can be inferred, namely:

$$\cos \beta l = 1 - \frac{\omega^2}{2\omega_R^2} \left(1 - \frac{\omega_s^2}{\omega^2}\right) \left(1 - \frac{\omega_p^2}{\omega^2}\right) \quad (3.21)$$

$$Z_B = \sqrt{\frac{L_R \left(1 - \frac{\omega_s^2}{\omega^2}\right)}{C_R \left(1 - \frac{\omega_p^2}{\omega^2}\right)} - \frac{L_R^2 \omega^2}{4} \left(1 - \frac{\omega_s^2}{\omega^2}\right)^2} \quad (3.22)$$

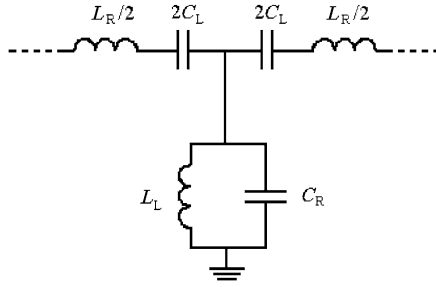


**FIGURE 3.3** Equivalent circuit model (basic cell) of the CRLH transmission line.

where the following variables

$$\omega_R = \frac{1}{\sqrt{L_R C_R}} \quad (3.23)$$

$$\omega_L = \frac{1}{\sqrt{L_L C_L}} \quad (3.24)$$

and the series and shunt resonance frequencies

$$\omega_s = \frac{1}{\sqrt{L_R C_L}} \quad (3.25)$$

$$\omega_p = \frac{1}{\sqrt{L_L C_R}} \quad (3.26)$$

have been introduced to simplify the mathematical formulas. Expressions (3.21 and 3.22) are depicted in Figure 3.4. Two propagating regions, separated by a gap at the spectral origin, can be distinguished. In the lowest frequency region the parameters of the dual transmission line,  $C_L$  and  $L_L$ , are dominant, and wave propagation is backward. This situation is reversed above the stopband, where the parasitic reactances of the host line make the structure behave as a right-handed line. Indeed, at high frequencies, the CRLH transmission line tends to behave as a purely right-handed (PRH) line. Conversely, in the lower limit of the first allowed band, the CRLH structure exhibits the characteristics of a purely left-handed (PLH)—or dual—transmission line. The gap limits are given by the frequencies satisfying

$$\omega_{G1} = \min(\omega_s, \omega_p) \quad (3.27)$$

$$\omega_{G2} = \max(\omega_s, \omega_p). \quad (3.28)$$

In the long wavelength limit, expression (3.21) is rewritten as

$$\beta = \frac{s(\omega)}{l} \sqrt{\frac{\omega^2}{\omega_R^2} \left(1 - \frac{\omega_s^2}{\omega^2}\right) \left(1 - \frac{\omega_p^2}{\omega^2}\right)}, \quad (3.29)$$



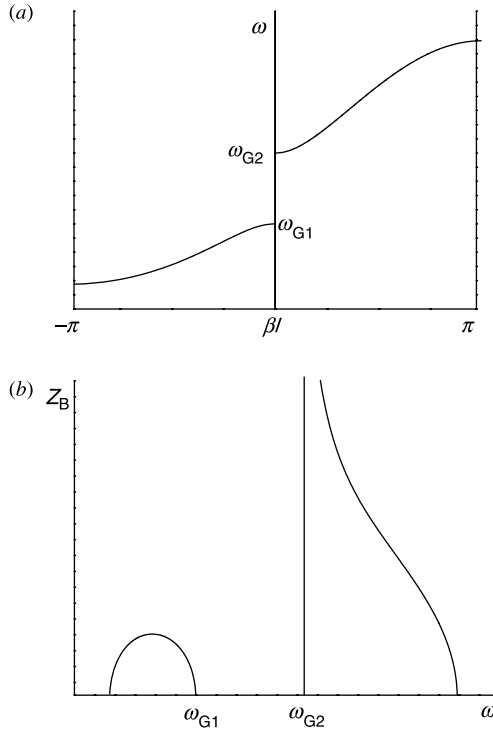


**FIGURE 3.4** Typical dispersion diagram (a) and variation of Bloch impedance with frequency (b) in a CRLH transmission line model. In this example,  $\omega_s < \omega_p$ .

where  $s(\omega)$  is the following sign function:

$$s(\omega) = \begin{cases} -1 & \text{if } \omega < \min(\omega_s, \omega_p) \\ +1 & \text{if } \omega > \max(\omega_s, \omega_p). \end{cases} \quad (3.30)$$

From the phase constant (equation 3.29), the phase and group velocities can be easily inferred, these velocities being of opposite sign in the left-handed band and both being positive in the right-handed band.

With regard to the constitutive parameters for the CRLH transmission line, they can be inferred as previously indicated, that is,

$$\epsilon_{\text{eff}} = \frac{C_R}{l} - \frac{1}{\omega^2 L_L l} \quad (3.31)$$

and

$$\mu_{\text{eff}} = \frac{L_R}{l} - \frac{1}{\omega^2 C_L l}, \quad (3.32)$$

and they can be positive or negative, depending on the frequency range.

One particular case of interest is the so-called balanced CRLH line, which corresponds to the situation where the series and shunt resonances are identical, namely  $\omega_s = \omega_p = \omega_0$  [8]. In this case, there is not a forbidden band between the left-handed and right-handed allowed bands; in other words, the change between backward and forward wave behavior is continuous. Concerning the characteristic impedance, it reaches its maximum at  $\omega_0$  (the transition frequency), where

$$Z_B = \sqrt{\frac{L_R}{C_R}} = \sqrt{\frac{L_L}{C_L}}, \quad (3.33)$$

and the characteristic impedance decreases as frequency increases or decreases from  $\omega_0$ . At the limits of the allowed propagation interval (which contains both the left-handed and right-handed frequency bands) the characteristic impedance nulls, and beyond this limits, it takes imaginary values. Figure 3.5 depicts the dispersion diagram and the variation of line impedance with frequency. In contrast, the characteristic impedance dependence on frequency is more complicated for the unbalanced case (see Fig. 3.4). If we consider that  $\omega_s < \omega_p$  (which is the situation considered in Fig. 3.4), the characteristic impedance is zero at the lower limit of the left-handed interval, it increases as frequency increases, reaches a maximum, and then decreases

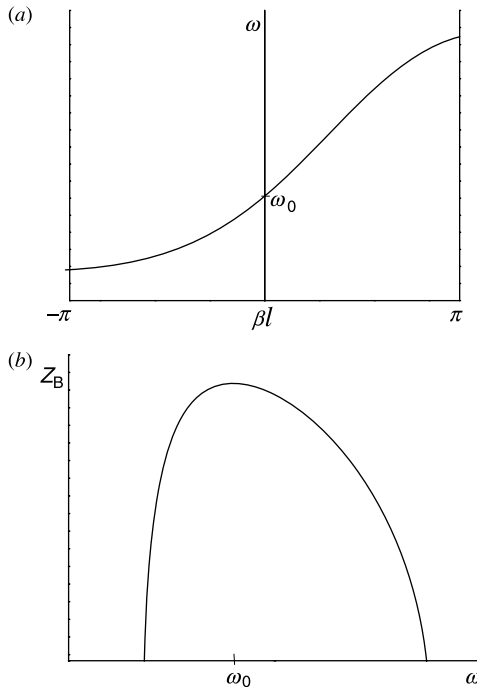


**FIGURE 3.5** Typical dispersion diagram (a) and variation of Bloch impedance with frequency (b) in a balanced CRLH transmission line.

towards zero, at  $\omega_s$ , the upper limit of the left-handed band. In the right-handed band, the impedance exhibits a pole at  $\omega_p$  (the lower frequency limit), it decreases as frequency increases, and it nulls at the higher cutoff frequency of the right-handed band. However, the behavior changes if  $\omega_s > \omega_p$ ; in this case, the impedance goes from zero up to infinity in the left-handed passband, and it nulls at the edges of the right-handed band.

From the point of view of the characteristic impedance, the balanced CRLH transmission line is interesting because in the vicinity of the transition frequency,  $Z_B$  is not very dependent on frequency, and it allows for broadband matching, as compared to the unbalanced case, where the characteristic impedance is much more sensitive to frequency. On the other hand, the balanced case exhibits another important difference as compared to the unbalanced CRLH transmission line. Namely, at the transition frequency, where the phase velocity exhibits a pole, the phase shift<sup>5</sup> is zero, and the group velocity differs from zero. In other words, at this frequency, wave propagation is possible ( $v_g \neq 0$ ) with  $\beta = 0$ . The phase origin of the balanced CRLH line thus takes place at  $\omega_o$ . When frequency is decreased below  $\omega_o$ , the phase becomes positive and it increases progressively; conversely, when frequency increases from  $\omega_o$ , the phase increases in magnitude but with negative sign (as occurs in conventional transmission lines). Regarding the behavior of wavelength for guided waves,  $\lambda_g$ , in the balanced CRLH transmission line, this reaches its maximum (infinity) at  $\omega_o$ , and  $\lambda_g$  decreases as frequency increases or decreases from  $\omega_o$ . Indeed, for the unbalanced case, the guided wavelength also increases when frequency approaches the spectral gap. However, at the edges of the gap the group velocity is zero, the line impedance takes extreme values, and signal propagation is not allowed.

### 3.3 PRACTICAL IMPLEMENTATION OF BACKWARD TRANSMISSION LINES

As has been indicated in the previous section, the practical implementation of a dual transmission line requires a host medium. As consequence, the description of the whole structure by means of a lumped element model includes not only the series capacitor and the shunt inductor, but also the elements of the host line, namely the per-section inductance and capacitance. Depending on the frequency region, propagation is backward (or left-handed) or forward (or right-handed) and the line behaves as a CRLH transmission medium. Thus, rather than the implementation of backward (or purely left-handed) lines, which is not possible in practice, the main concern is the design and fabrication of CRLH transmission lines. These lines can be considered one-dimensional metamaterials belonging to the category of structures based on the dual transmission line approach. Another type of one-dimensional metamaterial is that based on the resonant-type approach, where a host line is loaded with SRRs, or other related topologies. The design of left-handed transmission lines based on SRRs will be discussed in Section 3.5.

<sup>5</sup>Notice that by phase shift we refer to the phase of the transmission coefficient, which is of opposite sign to the phase constant.

Returning to the CRLH lines, in principle, the host propagating medium can be any type of planar transmission line, such as microstrip, strip line or coplanar waveguide (CPW) structures. For the reactive elements (series capacitor and shunt inductor) necessary to achieve a CRLH line, two possibilities arise, namely the use of lumped (typically *surface mount technology*) elements, or, alternatively, distributed components. In this context, distributed components means planar elements that are electrically small, that is, with a size smaller than  $\lambda_g$ . Typically, these planar elements are termed semi-lumped, because their size cannot be as small as those of lumped elements. However, the key point for the synthesis of metamaterials, that is, effectively homogeneous materials, is to make use of electrically small constitutive elements, or *particles*. Thus, it is important to reduce the size of the semi-lumped components as much as possible. The advantage of lumped elements is their size; however, lumped elements can operate only in a limited frequency range (typically below 5–6 GHz) due to parasitic effects that cause self-resonance to appear. Moreover, it is difficult to achieve the required electrical characteristics by using lumped elements, because their values are restricted to those provided by the manufacturers. Finally, the use of lumped elements is more expensive; soldering is necessary (it causes additional losses) and it goes against the full integration of microwave components. Hence, semi-lumped elements are preferred.

Two main host lines have been considered for the synthesis of metamaterial transmission lines based on the dual (or backward) transmission line concept: the microstrip structure and the coplanar waveguide configuration. The former was proposed by Caloz et al. in 2002 [9], and subsequently used in many applications. The implementation of a CRLH structure by means of a CPW configuration was due to the group of Eleftheriades [10], who used the structure to demonstrate the occurrence of backward-wave radiation in the fast-wave region of the dispersion diagram. The microstrip structure proposed by Caloz consists of a periodic arrangement of series interdigital capacitors alternated with grounded (through metallic vias) stubs, which act as shunt-connected inductors (see Fig. 3.6). The interdigital capacitors are described by the series capacitance  $C_L$  in the circuit of Figure 3.3, whereas  $L_L$  models the grounded stubs. The other reactive elements  $C_R$  and  $L_R$  correspond to the line capacitance and inductance, respectively. As this book is mainly focused on the resonant-type approach of metamaterials, we will not discuss the detailed procedure to generate the layout, or to extract the electrical parameters from it [8]. Nevertheless, we have included in Figure 3.7 the frequency responses (measured, simulated through electromagnetic solvers and by means of circuit simulation) of a

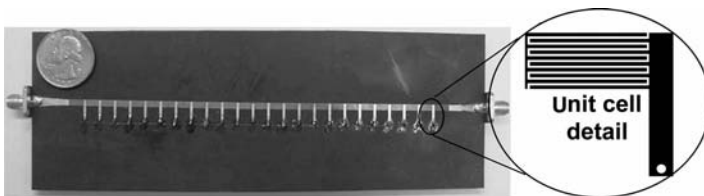


**FIGURE 3.6** Microstrip CRLH transmission line implemented by means of shunt-connected grounded stubs and interdigital capacitors. (*Source*: Photo courtesy of C. Caloz.)

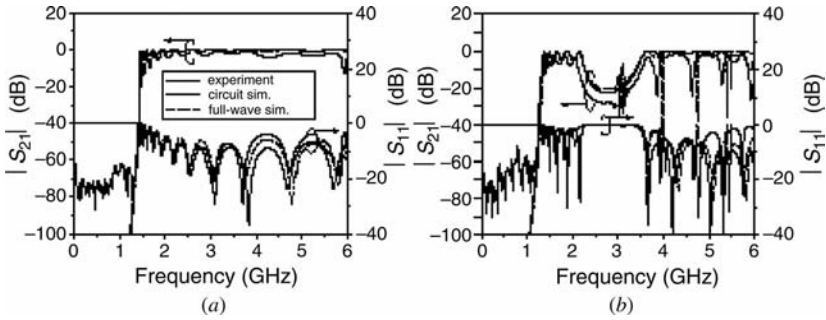


**FIGURE 3.7** Typical frequency responses for nine-cell balanced (a) and seven-cell unbalanced (b) CRLH transmission lines of the type depicted in Figure 3.6. (Source: Reprinted with permission from [8]; copyright 2006, John Wiley & Sons.)

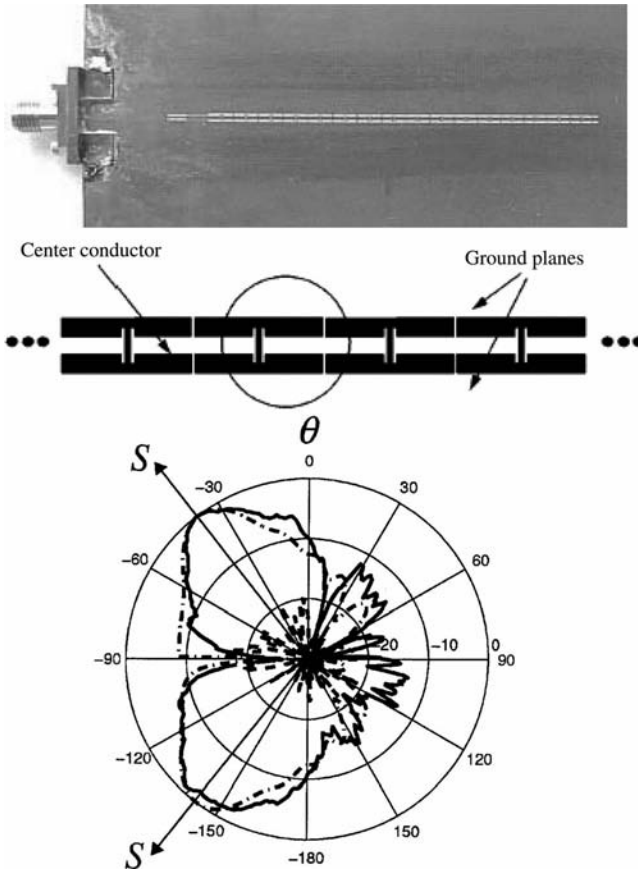


**FIGURE 3.8** CPW CRLH transmission line leaky wave antenna (a). The detail of the structure and the radiation diagram are depicted in (b) and (c), respectively. (Source: Reprinted with permission from [10]; copyright 2002, American Institute of Physics.)

nine-cell balanced structure and a seven-cell unbalanced design. The transition frequency is  $f_o = 3.9$  GHz in the balanced structure, which does not exhibit the stopband. However, this stopband can be appreciated (separating the left-handed and right-handed frequency bands) in the unbalanced structure.

In the CPW configuration, the shunt inductors can be implemented by means of connecting strips between the central strip and ground planes. The series capacitors can be implemented through interdigital geometries, or by means of series gaps. The latter are more simple, but the achievable capacitance values are much smaller. The Eleftheriades Group at the University of Toronto (Canada) presented a realization of a left-handed line fabricated in CPW technology by using series gaps and shunt strips (see Fig. 3.8) [10]. This line was used as a leaky wave antenna, where the operating frequency was set in the fast-wave region of the spectrum, where the structure may radiate. The most relevant aspect of this structure is that, unlike ordinary leaky wave antennas, which exhibit forward radiation, this line exhibits backward radiation. This effect has been explained as being due to the propagation of backward leaky waves in the structure (see Section 1.8.3), and this can be considered as the signature of left-handed wave propagation in the radiating element. This aspect will be discussed in more detail in Chapter 4.

### 3.4 TWO-DIMENSIONAL (2D) PLANAR METAMATERIALS

In this section, the authors simply want to point out that the extension of the previous transmission line, that is, planar one-dimensional (1D), metamaterials to 2D metamaterials is straightforward, rather than providing a network analysis of such 2D structures. This has been done by others and is explained in [8] and [11]. Indeed, the first 2D metamaterial was synthesized by the group of David Smith in 2001 by etching SRRs and strips in multiple dielectric slabs orthogonally oriented [12] (see Fig. 2.26). Although the structure was utilized to demonstrate negative refraction, it was a bulk structure, rather than planar. In planar technology, the first 2D structure was proposed by the group of Eleftheriades [13], who experimentally demonstrated for the first time the occurrence of near-field focusing [14]. The structure consisted of a 2D  $L-C$  loaded transmission line (see Fig. 3.9), where the capacitances were implemented by means of chip capacitors surface-mounted between gaps etched in the grid lines between lattice nodes, and the inductances were realized through chip inductors embedded into holes drilled at the node positions. The possibility of overcoming the diffraction limit in a planar lens made of a 2D  $L-C$  loaded periodic lattice [15], which was placed between two 2D grids made of conventional microstrip lines, was also experimentally demonstrated (Fig. 3.10). In Figure 3.10 are also depicted the measured vertical electric field detected in the structure (0.8 mm above the surface), as well as the measured vertical electric field at the image, which is compared to the theoretical limit corresponding to a continuous medium. The amplification of evanescent waves and subdiffraction imaging are both demonstrated.

Alternatively, the possibility of implementing a 2D left-handed structure avoiding the use of lumped elements has also been demonstrated [16]. The structure was first proposed by Sievenpiper [17] for the realization of high-impedance surfaces.

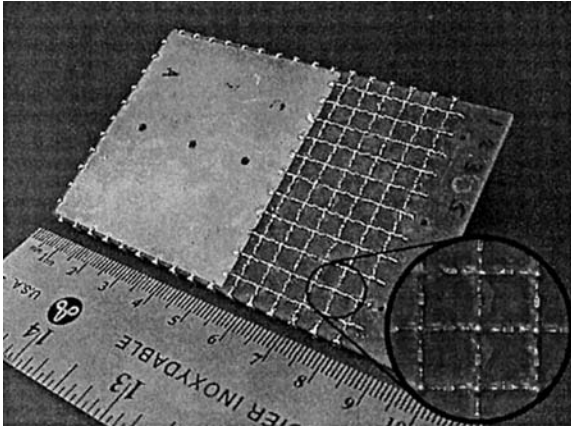


**FIGURE 3.9** Two-dimensional metamaterial consisting of a grid of transmission lines loaded with series capacitors and shunt-connected inductors. (Source: Reprinted with permission from [13]; copyright 2002, IEEE.)

It consists of a mushroom structure (Fig. 3.11), which can be described by a CRLH transmission line model in two dimensions (Fig. 3.12).<sup>6</sup> The series capacitances ( $C_L$ ) are implemented by means of the slots present between neighboring patches, whereas vias are responsible for the shunt inductance ( $L_L$ ) necessary to obtain left-handedness. In the structure, the caps are used to enhance the weak capacitance couplings between adjacent patches. The other elements of the circuit model ( $C_R$  and  $L_R$ ) are provided by the capacitance and inductance of the transmission line formed by the ground plane and metal patches. The typical dispersion diagram for a periodic structure based on the unit cell of Figure 3.12 is depicted in Figure 3.13 (see details for calculation and parameters in [16]) for the balanced and unbalanced cases. As occurs in the 1D case, backward and forward wave transmission arise in different frequency intervals, separated by a gap in the unbalanced case, and with a continuous transition under balance conditions. The dispersion diagram for the structure of Figure 3.11 has been also obtained by Sanada et al. [16] from full wave (FEM) simulation (Fig. 3.14). Similar characteristics as those of Figure 3.13 are observed. However, the fundamental mode of the structure is mixed left-handed/right-handed, because, as argued in [16], the structure is opened and the left-handed mode couples with the TM air mode (in a closed stripline structure a purely left-handed mode has been found [16]). On the other hand, there is also a degenerate right-handed TE mode not accounted for in the circuit model. The fact that the left-handed mode is shifted towards higher frequencies when the caps are not present is indicative of the influence of the caps on the series capacitance  $C_L$ .

Although this chapter is focused on planar structures, proposals of three-dimensional structures based on the transmission line approach of metamaterials have also been done (see for instance [18] and [19]).

<sup>6</sup>This circuit model also describes the unit cell of those structures depicted in Figures 3.9 and 3.10.

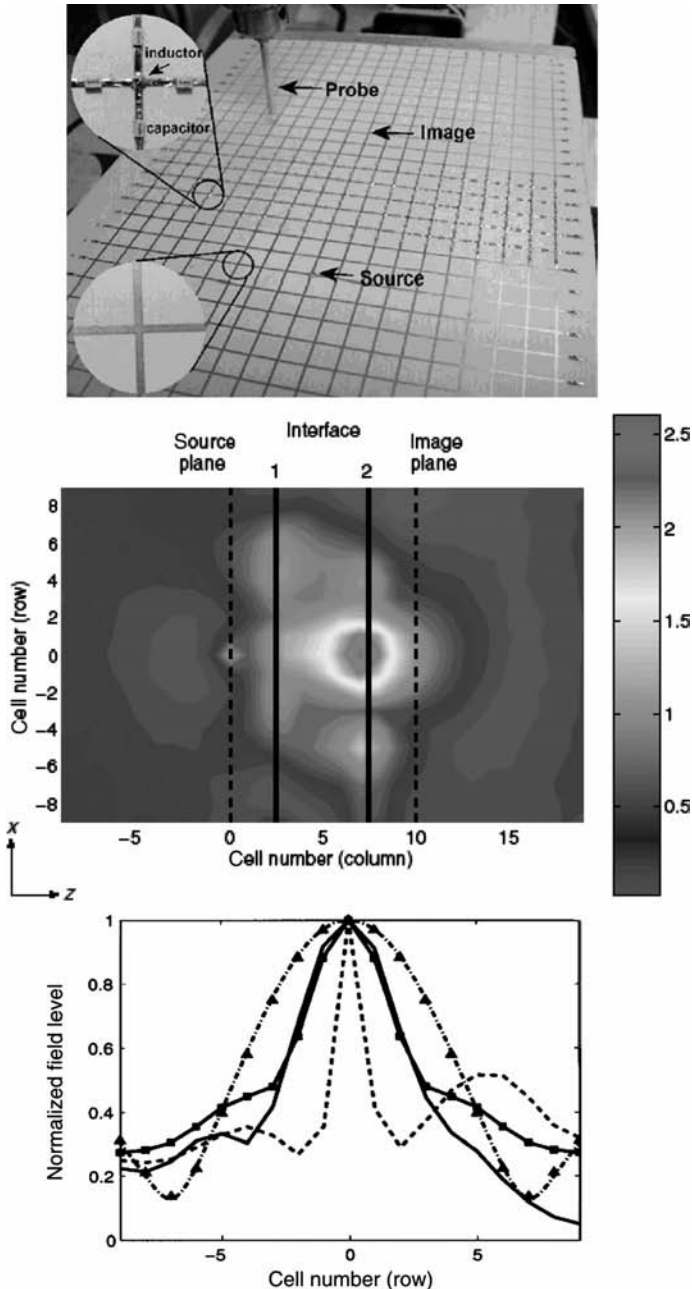


**FIGURE 3.10** Left-handed planar transmission line lens (a), measured vertical electric field detected 0.8 mm above the surface of the entire structure at 1.057 GHz (b), and measured vertical electric field at the image plane in solid line (c). For comparison, (c) also illustrates the electric field at the source plane (dashed curve), and the theoretical diffraction-limited pattern in a continuous medium (dash-dotted curve). (Source: Reprinted with permission from [15]; copyright 2004, American Physical Society.)



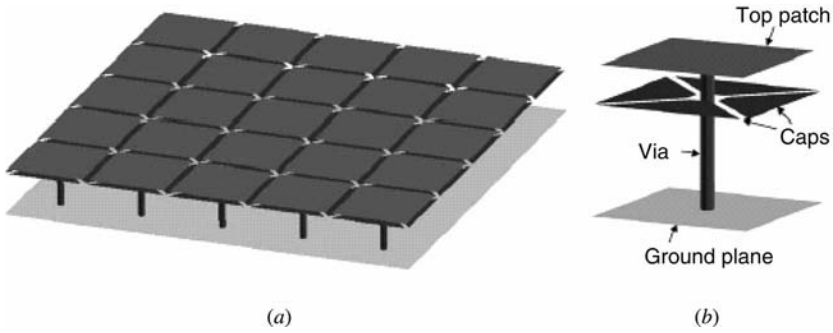


**FIGURE 3.11** General view of the 2D CRLH structure based on the mushroom configuration (a) and unit cell (b). (Source: Reprinted with permission from [16]; copyright 2004, IEEE.)

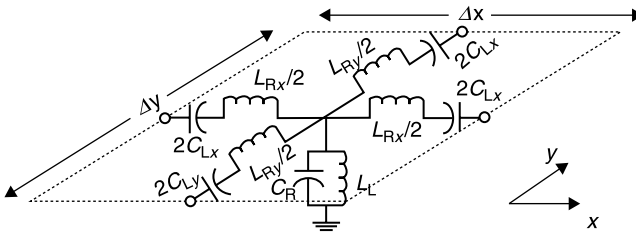


**FIGURE 3.12** Equivalent circuit model of the unit cell of the structure shown in Figure 3.11. (Source: Reprinted with permission from [16]; copyright 2004, IEEE.)

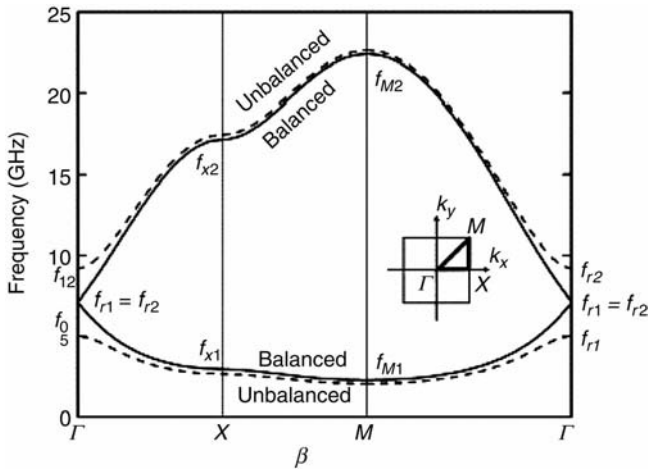


**FIGURE 3.13** Typical dispersion diagram for a 2D periodic structure composed of the unit cells described by the circuit of Figure 3.12. (Source: Reprinted with permission from [16]; copyright 2004, IEEE.)

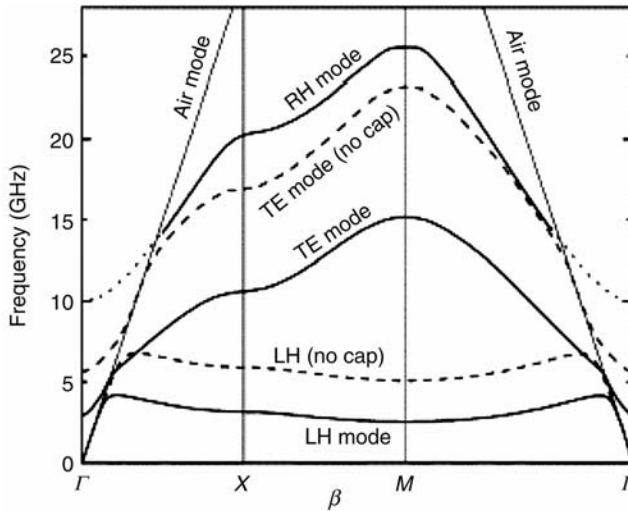


**FIGURE 3.14** Typical dispersion diagram inferred from full wave (FEM) simulation and corresponding to the structure depicted in Figure 3.11. (Source: Reprinted with permission from [16]; copyright 2004, IEEE.)

### 3.5 DESIGN OF LEFT-HANDED TRANSMISSION LINES BY MEANS OF SRRs: THE RESONANT TYPE APPROACH

In the preceding sections of this chapter, it has been demonstrated that the dual transmission line concept can be used for the synthesis of planar left-handed transmission lines in both microstrip and coplanar waveguide technologies. The negative effective permeability and permittivity values are provided by the series (capacitive) and shunt (inductive) impedances, respectively, loading the line. In fact, these impedances are not purely capacitive and inductive, because the host transmission line introduces extra reactances of opposite sign (that is, series inductance and shunt capacitance) and their effects increase with frequency, with the result of a CRLH behavior that limits the bandwidth of the left-handed transmission band. Therefore, the backward transmission lines of the previous sections have a limited bandwidth, and they exhibit forward transmission above the left-handed band.

The synthesis of left-handed transmission lines by properly etching SRRs in the host line is also possible [20]. In contrast to the dual transmission line approach, we can term this approach the *resonant-type approach*, because resonators (SRRs) are utilized as loading elements.<sup>7</sup> The authors would like to emphasize at this point that this designation (resonant-type approach) merely indicates that subwavelength resonators are used. As will be shown later, the transmission characteristics of both approaches (dual transmission line and resonant-type approach) are qualitatively very similar. In other

<sup>7</sup>Alternatively, resonant-type metamaterial transmission lines can be implemented by using complementary split rings resonators (CSRRs). These particles will be introduced in Section 3.7.

words, resonant-type metamaterial transmission lines also exhibit a composite right-/left-handed (CRLH) behavior. Indeed, as for dual transmission lines, it is also possible to design resonant-type balanced structures, with the absence of the stopband between the left-handed and right-handed bands. Differences between the dual and resonant-type approach concern their descriptions through equivalent circuit models. These models are not identical, but they are similar. A comparison between both models and with the transmission line model of bulk SRR-based metamaterials will be carried out later in this chapter (Section 3.9).

The natural host lines for the implementation of SRR-based left-handed metamaterials in one dimension are the microstrip line and the coplanar waveguide, among others. SRRs provide the negative effective permeability. However, to achieve backward-wave propagation, further microstructuring is necessary, in order to obtain the required negative effective permittivity. In coplanar waveguide technology, a possible solution is that proposed by Eleftheriades and co-workers [10], namely, the periodic connection of metallic strips between the central strip and the ground planes. As has been discussed previously, these connecting wires act as shunt inductors and, hence, they provide a negative value of the effective permittivity up to a cutoff (or plasma) frequency that depends on the period of the structure, on the width of the shunt-connecting strips (which is intimately related to the inductance value) and on the per-unit cell capacitance of the line. In microstrip technology, grounded stubs can be used to implement the negative permittivity, as reported by the group of Professor Itoh at the University of California at Los Angeles (UCLA) [9]. Alternatively, the implementation of metallic vias between the conductor strip and the ground plane at periodic positions arises as a possible solution where lateral metallization (to etch the stubs) is avoided [21]. This is of interest, because SRRs must necessarily be etched in the upper substrate side in close proximity to the conductor strip to achieve high line-to-SRRs magnetic coupling. Therefore the lack of stubs is preferred. Let us now consider in more detail the implementation of microstrip and CPW transmission lines simply loaded with SRRs (that is, 1D negative permeability media). After this, the design of left-handed microstrip and CPW transmission lines will be discussed in detail.

### 3.5.1 Effective Negative Permeability Transmission Lines

In order to load a CPW transmission line with SRRs, and thus obtain a negative effective permeability medium, it is necessary to etch the rings at the appropriate locations, that is, in such a way that the magnetic field generated by the current flowing through the line exhibits a significant component in the axial direction of the rings. Under these conditions, the rings will be properly excited and the overall structure will be expected to behave as an effective medium with negative-valued permeability in a certain band above the resonance frequency of the SRRs.<sup>8</sup> This means that the SRRs must be etched in the slot region. However, they can be etched either at the upper metal level, or in the back substrate side (provided there is no ground metallization at that side of

<sup>8</sup>Although not explicitly indicated, by resonance frequency of the SRRs the authors refer to the first one (quasistatic resonance). This applies to the whole chapter.

the substrate). In the former case, we may call the structure a uniplanar transmission line, but in the latter case it seems appropriate to talk in terms of a bi-metal implementation [22]. The uniplanar structure is more simple, as no back-side etching is required. However, it exhibits two drawbacks. First, wide slots are required to accommodate the SRRs; this has a direct influence on the characteristic impedance of the host line, which is expected to be high when compared to the usual impedance of  $50\Omega$  required to obtain low insertion losses<sup>9</sup> in the allowed frequency bands. On the other hand, line-to-rings magnetic coupling is expected to be relatively weak provided the magnetic field flowing through the rings is only a few percent of the overall magnetic flux generated by the host line (details on this structure including its behavior are given in [22]).

The preferred solution to obtain high line-to-rings coupling and low insertion losses in the allowed band<sup>10</sup> (that is, in that region where  $\epsilon_{\text{eff}}$  and  $\mu_{\text{eff}}$  are both positive) is the bimetal structure. Figure 3.15 depicts, the layout corresponding to a bimetal implementation as well as the simulated and measured frequency responses. Because SRRs are etched in this case in the back substrate side, the lateral dimensions of the host line (etched in the upper metal level) are no longer influenced by the presence of the rings, and line matching is easily achieved. Moreover, as long as the substrate is thin enough, the magnetic flux generated by the current flowing through the line can efficiently penetrate the SRRs and hence a high magnetic coupling between line and rings is expected. A stopband appears in the vicinity of  $f_o = 7.7\text{GHz}$ , the resonance frequency of the SRRs (their dimensions are indicated in the caption of the figure and they have been calculated following [23] and Chapter 2 to obtain such resonance frequency). In fact, the forbidden band extends above and below  $f_o$ . This stopband can be interpreted as a consequence of the properties of the structure, which behaves as a 1D effective medium with negative magnetic permeability in a narrow band above resonance and with high positive permeability in a narrow band below resonance,<sup>11</sup> which causes a strong mismatch at the feeding port of the line. In Figure 3.15, it can be perfectly appreciated that no ripple is present in the allowed band, which is indicative of a good matching. Indeed, outside the forbidden band, the signal does not see the presence of the rings and it is propagated between the input and output ports of the structure. A current diagram of the structure for two different frequencies (that is, within the stopband and below) is depicted in Figure 3.16. At 2 GHz, the signal propagates and SRRs are not excited. However, at 7.7 GHz, SRR excitation is very visible and the injected power is returned back

<sup>9</sup>In two-port networks it is usual to describe the transmission and reflection levels of the feeding signals by means of the insertion ( $IL$ ) and return ( $RL$ ) losses, respectively, where  $IL = 20 \log|S_{21}|$  and  $RL = 20 \log|S_{11}|$ .

<sup>10</sup>To efficiently use these negative permeability lines as small-sized stopband structures, it is necessary to reduce transmission band losses as small as possible. This application will be discussed in detail in the next chapter.

<sup>11</sup>Simultaneous positive or negative values of  $\epsilon_{\text{eff}}$  and  $\mu_{\text{eff}}$  are necessary but not sufficient conditions for signal propagation. This is very clear to the light of Figure 3.2, where signal propagation is limited to a certain region of the electromagnetic spectrum.

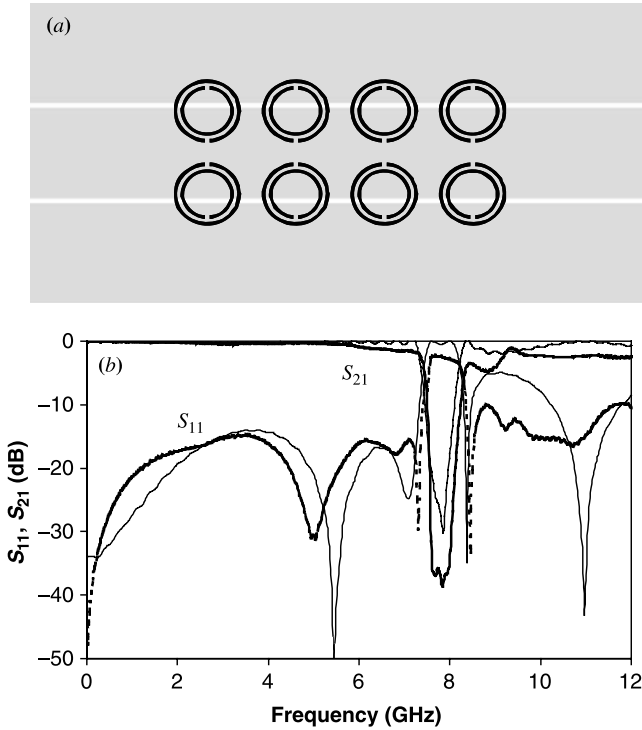


**FIGURE 3.15** Layout (a) and simulated (thin line) and measured (bold line) frequency response (b) of the bi-metal SRR loaded CPW structure. SRRs, etched in the back side of the substrate, are depicted in black, whereas the upper metal level is depicted in gray. Ring dimensions have been determined following [23] to obtain a resonance frequency of  $f_o = 7.7$  GHz, where ring width and separation are  $c = d = 0.2$  mm and the radius of the inner ring is  $r = 1.3$  mm. The distance  $l$  between adjacent rings is 5 mm. Lateral CPW dimensions have been calculated to obtain a  $50\Omega$  characteristic impedance. The parameters used in the simulation are those of the Arlon 250-LX-0193-43-11 substrate ( $\epsilon_r = 2.43$ , thickness  $h = 0.49$  mm). (Source: Reprinted with permission from [22]; copyright 2004, John Wiley & Sons.)

to the source. It is interesting to notice that four ring pairs suffice to obtain a rejection level in the vicinity of 40 dB (Fig. 3.15).

In microstrip technology only one possibility arises, that is, the rings should be etched as close as possible to the line in order to obtain high magnetic coupling. In fact, in order to enhance this coupling, square-shaped or rectangular SRRs are preferred in this case. This way, the magnetic flux lines penetrate the SRR's area more efficiently. Figure 3.17 depicts the layout and simulated frequency response of a  $50\Omega$  microstrip transmission line loaded with square-shaped SRRs. Significant attenuation in the stopband is also achieved in this case, this band extending up and down the resonant frequency of SRRs.

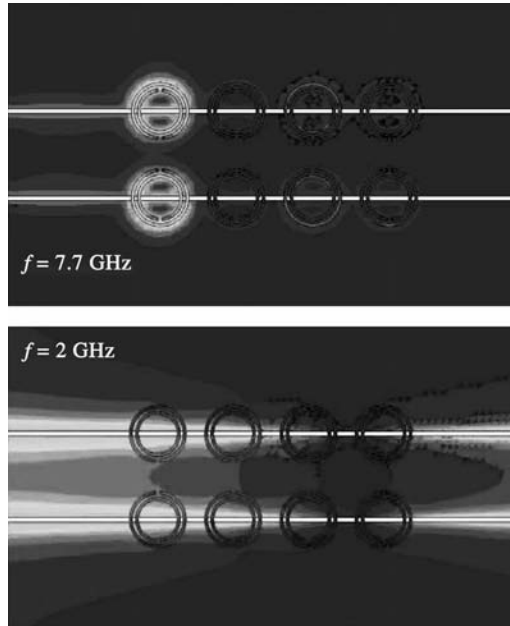


**FIGURE 3.16** Current diagrams for the bimetal structure of Figure 3.15, obtained by means of *CST Microwave Studio*, at two different frequencies.

### 3.5.2 Left-Handed Transmission Lines in Microstrip and CPW Technologies

The first left-handed transmission line implemented by means of SRRs was proposed by Martín et al. [20]. The structure was a coplanar waveguide with SRRs etched in the back substrate side, underneath the slots, and signal-to-ground metallic connections (strips) periodically located above the SRRs, as shown in Figure 3.18. In fact, this structure is identical to that shown in Figure 3.15, except for the presence of the shunt strips. These strips act as shunt-connected inductors, and hence they make the structure behave as an effective medium with negative dielectric permittivity, up to a frequency (plasma or cutoff frequency,  $f_c$ ) that depends on the period and width of the shunt strips. Therefore, as long as  $f_c$  is set above the resonance frequency of the SRRs, a region exists where both the effective dielectric permittivity and magnetic permeability (the latter provided by the rings) are both simultaneously negative. According to our previous words, this occurs in a narrow band above the resonance frequency of the SRRs. Signal propagation in this band is thus allowed, but with backward waves (that is, with negative phase velocity). The measured frequency response of this structure is also depicted in Figure 3.18. This result confirms that the stopband behavior obtained when the shunt strips are not present switches to a passband in the SRR-loaded CPW with shunt strips. Moreover, there is a visible displacement towards positive frequencies in the passband, relative to the onset of the

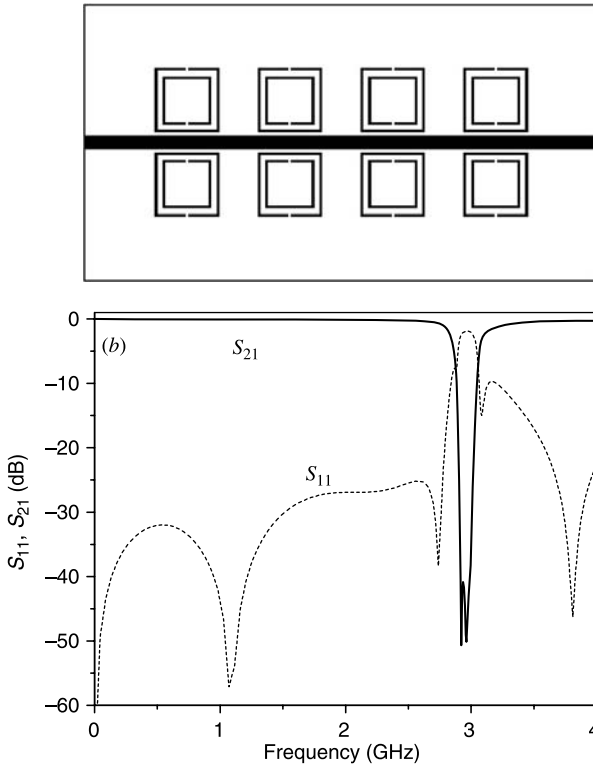


**FIGURE 3.17** Layout (a) and simulated frequency response (b) of a  $50\ \Omega$  microstrip line loaded with square-shaped SRRs. The structure has been implemented in the Rogers RO3010 substrate (thickness  $h = 1.27$  mm, dielectric constant  $\epsilon_r = 10.2$ ). Dimensions: ring width and separation  $c = 0.2$  mm and  $d = 0.4$  mm, respectively, ring side (external) 5 mm, line width  $W = 1.2$  mm, and distance between adjacent rings 3 mm.

stopband in Figure 3.15. This is an expected result on account of the fact that the negative effective permeability, necessary to obtain a band with negative wave propagation, arises at the resonant frequency of the SRRs.<sup>12</sup> In contrast, the stopband in the negative-permeability CPW (that is, without shunt-connecting strips) extends below the resonance frequency of the SRRs.

An interesting aspect of the structure shown in Figure 3.18 is the fact that the relative position and orientation of the SRRs with regard to the shunt strips is relevant in order to optimize the insertion losses in the allowed band. Namely, it has been found that by aligning the slits of the SRRs with the wire shorts, an optimum result in terms of in-band losses is obtained. An explanation of this is given in [24], and it has also been given in Section 2.4.4, where the validity of the superposition principle in bulk

<sup>12</sup>In fact, the left-handed band begins slightly above the resonance frequency of the SRRs, as will be shown later.

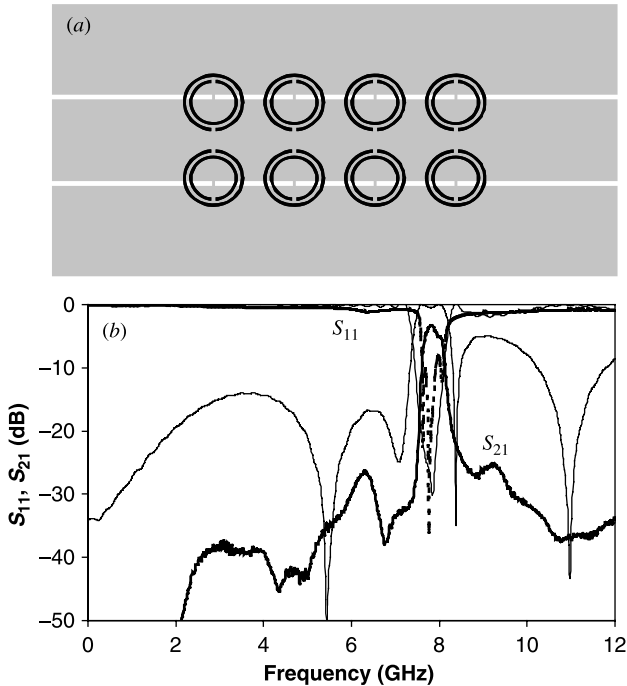


**FIGURE 3.18** Layout (a) and simulated (thin line) and measured (bold line) frequency response (b) of the left-handed SRR-based line. SRR dimensions and separation as well as lateral dimensions of the CPW structure are identical to those of Figure 3.15. Wire width is 0.2 mm. (Source: Reprinted with permission from [20]; copyright 2003, American Institute of Physics.)

media composed of wires and SRRs was discussed. Essentially, thanks to this alignment, no interference between the SRRs and the shunt strips takes place, because at the SRR resonance there is a virtual electric wall along the orthogonal plane to the rings containing the slits. Hence, if the relative orientation of the shunt strips and the rings causes the strips to be contained in this imaginary plane, then such interaction is minimized, this being a necessary condition for generating a 1D effective medium where both permeability and permittivity are negative.

In CPW technology, it is also possible to design left-handed structures with multiple transmission bands. To this end, the buried CPW concept is invoked, where the metal level containing the ground planes and the central conductor strip is surrounded by a dielectric on top and bottom [24]. This allows SRRs to be etched in two separated metal layers (on both sides of the substrate), which is of interest in tailoring the frequency response of the structure, that is, to achieve two separated left-handed allowed bands (if the rings etched at opposite sides are tuned at different frequencies), or to widen the bandwidth (provided the SRRs are tuned at closer frequencies). This structure can be considered as the parallel combination of two SRR-loaded CPW



transmission media, where the host CPW is shared. This explains the presence of two transmission bands, which can be partially overlapped to produce a single transmission band with improved bandwidth. To illustrate these ideas, two buried CPW structures are provided, one with the top and bottom SRRs tuned at closed frequencies (Fig. 3.19), and the other designed to provide separated narrow pass-bands (Fig. 3.20). The simulated and measured frequency responses for these structures are also depicted in Figures 3.19 and 3.20. The slight frequency shift between simulations and experiments is due to some discrepancy between the dimensions of the fabricated rings and the nominal values. This may also cause the degradation of

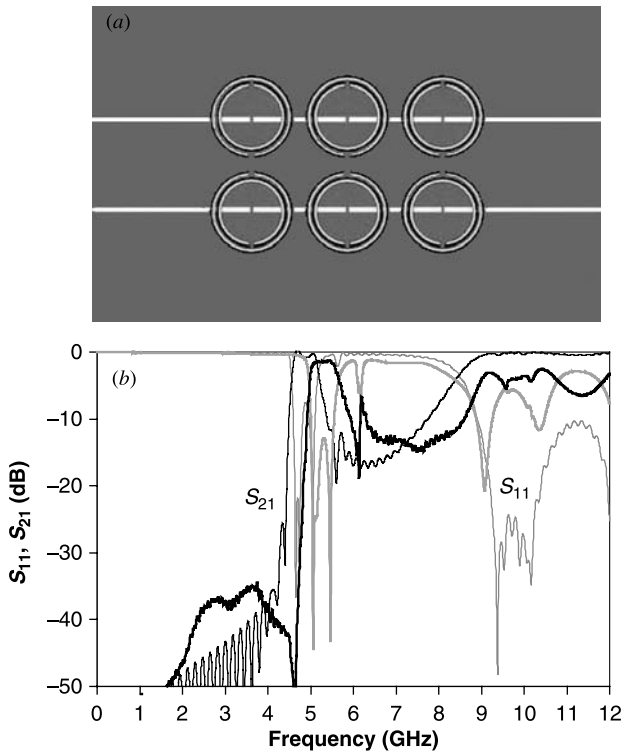


**FIGURE 3.19** Layout (a) and frequency response (b) of the left-handed buried CPW structure with closely tuned SRRs. Measured results are depicted as bold lines, and simulations are depicted as thin lines. To better distinguish, measured return losses have been depicted in gray. Geometrical parameters are  $c = d = 0.2$  mm, inner radius for the top and bottom rings  $r = 1.9$  mm and  $r = 2.0$  mm, respectively (the parameters of the *Arlon 250-LX0193-43-11* substrate have been considered:  $\epsilon_r = 2.43$ , thickness  $h = 0.49$  mm). With these dimensions, the nominal resonant frequencies for the top/bottom rings are in the vicinity of 5 GHz. The width of connecting wires (0.2 mm) guarantees a plasma frequency beyond the resonant frequency of SRRs. Slot and strip widths ( $G = 0.3$  mm,  $W = 5.5$  mm) correspond to a  $50 \Omega$  line. Simulations have been carried out using *CST Microwave Studio*. (Source: Reprinted with permission from [24]; copyright 2004, IEEE.)

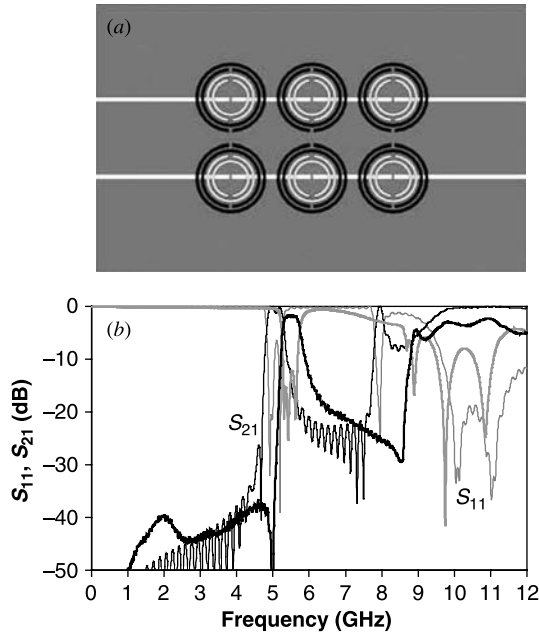


**FIGURE 3.20** Layout (a) and frequency response (b) of the left-handed buried CPW structure with two separated transmission bands. Measured results are depicted as bold lines, and simulations are depicted as thin lines. To better distinguish, measured return losses have been depicted in gray. The inner radius of SRRs etched in the top metal level has been set to  $r = 1.2$  mm, and other geometric parameters are identical to those given in Figure 3.19. (Source: Reprinted with permission from [24]; copyright 2004, IEEE.)

the second passband for the structure of Figure 3.20, which is too close to the plasma frequency of the CPW structure loaded with shunt strips. Nevertheless, the presence of two allowed bands confirms that the device can be viewed as two separated left-handed structures parallel connected, and it explains bandwidth widening when the two sets of rings are closely tuned. The high-frequency selectivity and low level of losses (allowed band) measured in both structures ( $< 1.5$  dB) is remarkable.

In microstrip technology, it has previously been anticipated that the combination of SRRs (etched as close as possible to the conductor strip to enhance magnetic coupling) and via holes is appropriate for the synthesis of left-handed structures in one dimension [21]. The metallic vias emulate shunt-connected inductors and provide the required negative permittivity, whereas SRRs are responsible for the negative effective permeability. In Figure 3.21, it is depicted a left-handed line with these elements (the measured and simulated frequency responses are also depicted). Again, as expected, a passband behavior has been obtained, the allowed band extending over a narrow region above the resonance frequency of the SRRs. In this case the geometry of the rings has been chosen to be square-shaped to enhance magnetic coupling between the line and the rings, as has previously been commented.

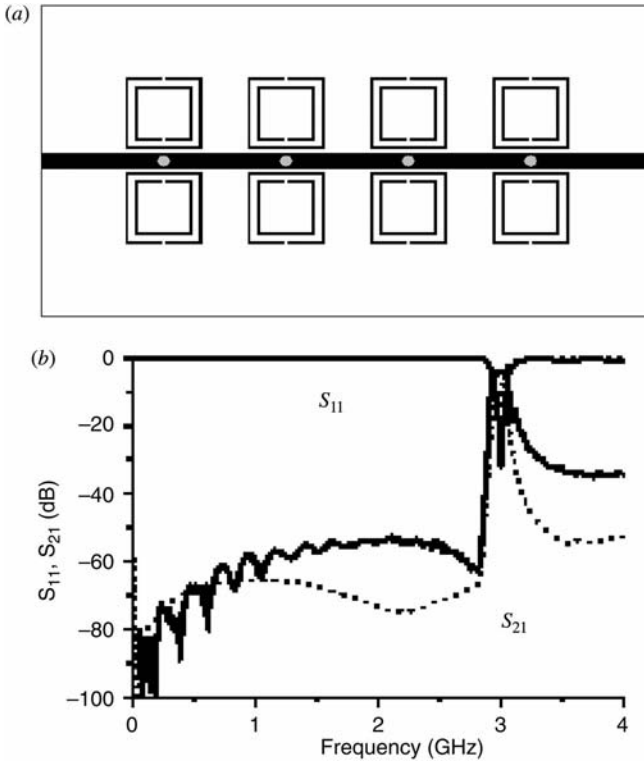


**FIGURE 3.21** Layout (a) and simulated (dashed line) and measured (solid line) (b) frequency response for the microstrip left-handed line implemented by means of square-shaped SRRs and metallic vias. Substrate and dimensions are as in Figure 3.17. (Source: Reprinted with permission from [21]; copyright 2005, IEEE.)

### 3.5.3 Size Reduction

In the previous implementations of metamaterial transmission lines based on SRRs, dimensions were relatively small on account of the small electrical size of the SRRs. For instance, in the left-handed CPW structure shown in Figure 3.18, the length, excluding access lines, is as small as  $l \approx \lambda/2$ ,  $\lambda$  being the wavelength corresponding to a 50  $\Omega$  line implemented onto a identical substrate at SRR resonance.<sup>13</sup> To reduce the size of SRR-based structures, it is necessary to decrease the electrical size of SRRs, and to this end it is imperative to reduce the space between the rings and/or to narrow their width. The effect is a shift of the resonance frequency of the SRRs to lower values and hence an improvement of their electrical size. However, in practice, due to the limited lateral resolution of standard fabrication systems (typically in the vicinity of 100  $\mu\text{m}$  for chemical etching or drilling machines on conventional microwave

<sup>13</sup>Notice that  $\lambda \neq \lambda_g$  (see Section 3.2).

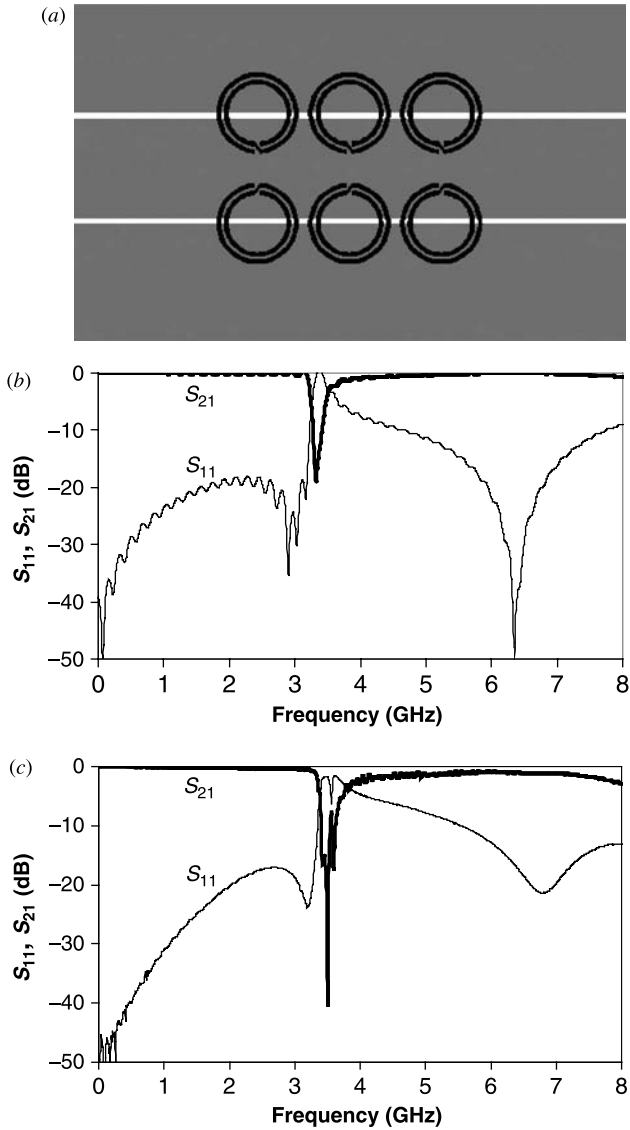


**FIGURE 3.22** Layout (a), simulated (b), and measured (c) frequency response of the negative-permeability CPW structure loaded with SRs. SRs, etched in the back side of the substrate, are depicted in black, and the upper metal level is depicted in gray. SR dimensions and separation are roughly the same as those of Figure 3.15. Lateral CPW dimensions have been calculated to obtain a  $50\text{-}\Omega$  characteristic impedance. (Source: Reprinted with permission from [27]; copyright 2004, John Wiley & Sons.)

substrates), it is difficult to drive SRR dimensions (external diameter) below one-tenth of a wavelength at resonance (this being indeed an optimistic prospect).

To further reduce the size of the devices and circuits, alternative topologies for the resonators may be more convenient. As has already been pointed out in Chapter 2 (Section 2.3), the BC-SRR, where one ring is placed above the other, allows for higher levels of miniaturization [25]. This is possible because, thanks to the broad side coupling (which can be enhanced by simply reducing the width of the inter-ring dielectric), the equivalent capacitance of the structure is increased. Another possibility is to replace the SRRs with spiral resonators (SRs) [26,27]. By etching them onto the same substrate, the electrical size of a two-turn SR is roughly half the electrical size of an SRR, provided dimensions are identical. To illustrate this, Figure 3.22 depicts a negative-permeability CPW transmission line loaded with two-turn SRs, together with the simulated and the measured frequency responses. The dimensions of the SRs are very similar to those of the SRRs of Figure 3.15. Again, a stopband behavior related to the negative effective permeability provided by the SRs is obtained. However, the forbidden band arises in the vicinity of 3.5 GHz, which is approximately half the frequency of the central frequency for the forbidden band depicted in Figure 3.15. Obviously, by increasing the number of turns of the spirals, it is possible to further decrease their electrical size. However, this makes ohmic losses significant for practical applications, unless high-temperature superconductors (HTS) are used [28]. It is worth mentioning that the combination of SRs and shunt strips to achieve a left-handed transmission band has been considered by the authors, but poor frequency responses as compared to those of Figures 3.18–3.21 have been obtained. It is believed that the reason for this degradation is the lack of symmetry of the SR with regard to the plane of the shunt strips, which may cause a nonnegligible interaction between SRs and strips.

### 3.6 EQUIVALENT CIRCUIT MODELS FOR SRRs COUPLED TO CONVENTIONAL TRANSMISSION LINES

In the previous chapter, it was demonstrated that SRRs can be modeled by an  $LC$  resonant tank that can be externally driven by a time-varying magnetic field applied in the axial direction. The equivalent capacitance is the series connection of the edge capacitance corresponding to the lower and upper halves of the structure, and the equivalent inductance is given by the inductance of a closed ring with the same width of each individual ring and average SRR radius. For the alternative topologies of the SRR presented in Chapter 2, similar equivalent circuits arise. All of them can be reduced to a simple parallel  $LC$  tank, as for the SRRs. However, in order to design metamaterial transmission lines based on SRRs, equivalent circuit models for these lines are necessary. These models should describe the host transmission line, the resonators (SRR or other resonators), and their coupling. It was indicated in the previous chapter that the basic SRR topology exhibits cross-polarization effects. This means that SRRs can be magnetically and/or electrically excited if the rings are properly oriented. However, it has been verified that magnetic coupling is the dominant

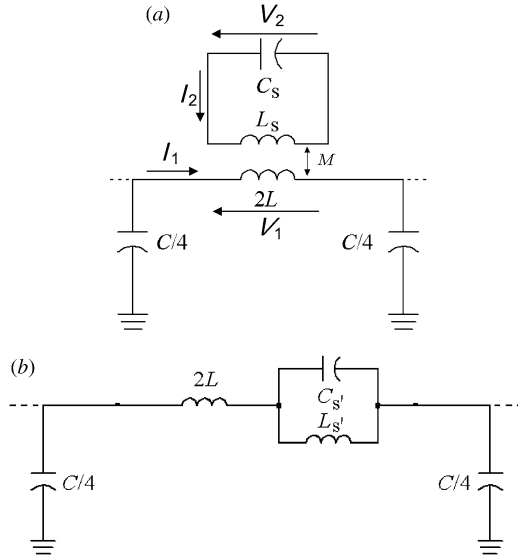


**FIGURE 3.23** Lumped element equivalent  $\pi$ -circuit model of the SRR loaded negative-permeability transmission lines (a), and circuit model that results after transformation of the series branch (b).

coupling mechanisms in SRRs. Therefore cross-polarization effects can be ignored in a first-order approximation (this assumption is strictly valid for NB-SRRs and other nonbianisotropic configurations under a uniform field excitation).

Due to the small electrical dimensions of SRRs at resonance, the structures (CPW or microstrip loaded lines) can be described by means of lumped element equivalent circuits. The proposed equivalent circuit model (basic cell) for the SRR loaded transmission line (of Figs 3.15 and 3.17) is shown in Figure 3.23a [22].  $L$  and  $C$  are the per-section inductance and capacitance of the line, and SRRs are modeled as resonant tanks (with inductance  $L_s$  and capacitance  $C_s$ ) magnetically coupled to the line through a mutual inductance,<sup>14</sup>  $M$ . For the SRR-loaded CPW, this mutual inductance can be inferred from the fraction,  $f$ , of the slot area occupied by the rings, according to

$$M = 2L \cdot f, \tag{3.34}$$

whereas for the microstrip structure it is difficult to accurately determine  $M$  and it is considered a fitting parameter. Neither losses (ohmic and dielectric) nor inter-resonator coupling have been considered in this model.<sup>15</sup> The equivalent impedance

<sup>14</sup>In the circuit models of Figure 3.23, the presence of a virtual magnetic wall at the middle plane of the lines of Figures 3.15 and 3.17 has been taken into account, so that only one of the SRRs loading each section of the line is included in the model.

<sup>15</sup>Coupling between adjacent SRRs is only significant in closely spaced square or rectangular SRRs. Such coupling is the origin of magnetoinductive waves in chains of SRRs, and it will be considered in the last chapter. However, it can be neglected in modeling the structures considered in this chapter.

of the series branch can be simplified to that shown in the circuit of Figure 3.23*b*, which is formally identical to the series impedance corresponding to a left-handed transmission line (in that region where the total series impedance is capacitive). To demonstrate this, the voltage–current equations for the transformer are first derived (in this analysis, to gain further insight on the effect of losses, a series resistance,  $R_s$ , will be included in the  $LC$  tank modeling the SRRs). These equations are

$$V_1(\omega) = j\omega 2LI_1(\omega) + j\omega MI_2(\omega) \quad (3.35)$$

and

$$-I_2(\omega)Z_a(\omega) = j\omega MI_1(\omega) + j\omega L_s I_2(\omega), \quad (3.36)$$

where the variables refer to the circuit of Figure 3.23*a*, and  $Z_a$  is the series connection of the equivalent capacitance of the SRR,  $C_s$ , and  $R_s$ , namely:

$$Z_a(\omega) = \frac{1 + j\omega R_s C_s}{j\omega C_s}. \quad (3.37)$$

By isolating  $I_2$  in equation (3.36), and substituting it into equation (3.35), we directly obtain the series impedance of the line:

$$Z_s(\omega) = j2\omega L + \omega^2 M^2 \left\{ \frac{j\omega C_s}{(1 - \omega^2 L_s C_s) + j\omega R_s C_s} \right\}. \quad (3.38)$$

This impedance is equivalent to the series connection of an inductor (with inductance  $2L$ ) and a parallel  $RLC$  tank, provided the following conditions are satisfied:

$$L'_s = \omega_0^2 M^2 C_s \quad (3.39)$$

$$C'_s = L_s / \omega_0^2 M^2 \quad (3.40)$$

$$R' = \omega_0^2 M^2 / R_s, \quad (3.41)$$

where  $\omega_0 = (C_s L_s)^{-1/2} = (C'_s L'_s)^{-1/2}$  is the resonance frequency of the SRRs. Therefore, the equivalent circuit model of Figure 3.23*a* can be simplified to that shown in Figure 3.23*b* (where  $R'$  has not been included for coherence).

For the left-handed structures shown in Figures 3.18 and 3.21, where either a shunt-connected strip or a metallic via has been introduced (compared to the negative-permeability structures), the equivalent circuit model is identical to that shown in Figure 3.23*a* (or to the simplified version of Fig. 3.23*b*), but with the addition of a shunt-connected inductance that models the signal to ground strips (CPW configuration) or the vias (microstrip structures). This circuit is depicted in Figure 3.24. The value of the shunt inductance,  $L_p$ , can be inferred from the simulated frequency response of the host line with SRRs removed, where the plasma frequency is given by the resonator composed by  $C$  and  $L_p$  [20].

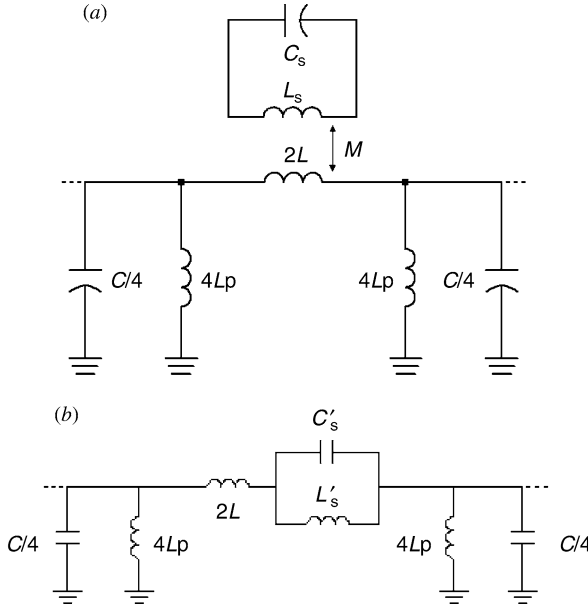


**FIGURE 3.24** Lumped element equivalent  $\pi$ -circuit model of the SRR loaded left-handed transmission lines (a), and circuit model that results after transformation of the series branch (b).

A comparison between the frequency responses measured on the CPW metamaterial structures and those obtained through electrical simulation of the equivalent circuit models (with  $L_s$  and  $C_s$  obtained from the expressions in the Appendix of Chapter 2) is depicted in Figure 3.25 [29]. Reasonable agreement between model and experiment results, if one takes into account that losses are neglected and the electrical parameters of the equivalent circuit model are all estimated, rather than used as fitting parameters.

It is worth mentioning that the model of Figure 3.24 also predicts a forward-wave transmission band above the left-handed region (CRLH behavior). As for the transmission lines loaded with series capacitances and shunt inductances studied in Section 3.2, at high enough frequencies the parameters of the host line become dominant and signal propagation is forward. The shunt impedance changes its sign at the resonance frequency of the tank formed by  $L_p$  and  $C$ :

$$\omega_p = \frac{1}{\sqrt{CL_p}}. \tag{3.42}$$

The series reactance is negative in the left-handed band and it switches to a positive value (that is, inductive) at the following angular frequency:

$$\omega_s = \sqrt{\frac{1}{2C'_s L} + \frac{1}{L'_s C'_s}}. \tag{3.43}$$



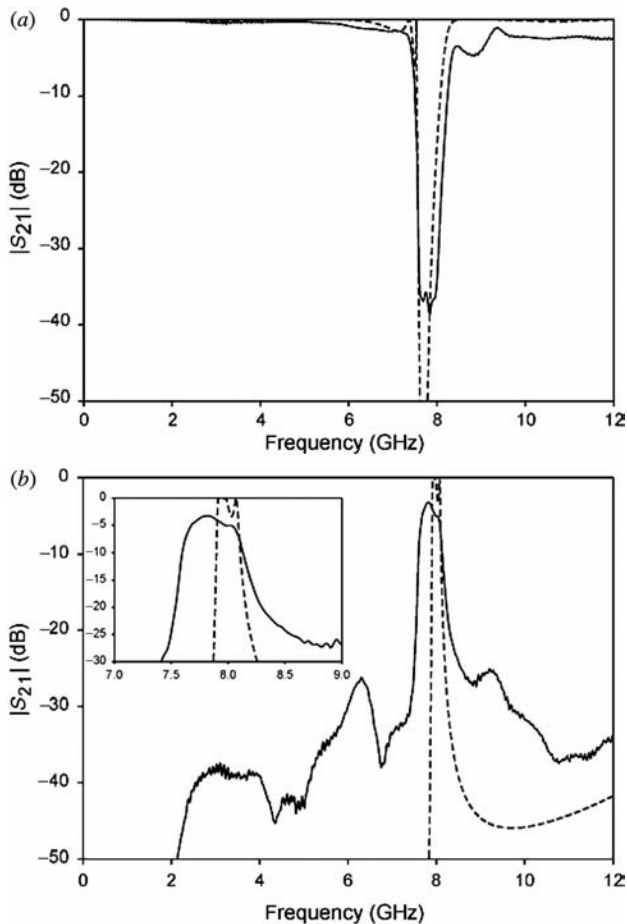


**FIGURE 3.25** Comparison between the measured insertion losses (solid line) and those inferred from the equivalent circuit models (dashed line) for the negative permeability structure of Figure 3.15 (a) and for the left-handed structure of Fig. 3.18 (b). (Source: Reprinted with permission from [29]; copyright 2005, IEEE.)

Thus, the limits of the stopband present between the left-handed and right-handed regions are given by expressions (3.27) and (3.28), with  $\omega_p$  and  $\omega_s$  given by expressions (3.42) (a) and (3.43) (b). Usually, these left-handed lines based on SRRs are designed with  $\omega_p > \omega_s$ . In other words, the cutoff (plasma) frequency related to the presence of the shunt strips or vias is set significantly above the resonance frequency of the SRRs (which is close to  $\omega_s$  in practical implementations). The special case where  $\omega_p = \omega_s$  collapses the gap and provides the balanced SRR-loaded left-handed transmission line.<sup>16</sup>

<sup>16</sup>Practical realizations of balanced CRLH resonant-type metamaterial transmission lines implemented by using complementary split rings resonators (CSRRs) will be presented later in this chapter.

In the structures presented in Figures 3.18–3.21, the interest was to achieve a backward wave band. Nevertheless, the gap and the right-handed band above it can be clearly appreciated in Figures 3.19 and 3.20 (in Figs 3.18 and 3.21 the horizontal scale is limited to show only the backward transmission band).

### 3.6.1 Dispersion Diagrams

For the equivalent  $\pi$ -circuit models obtained for the negative permeability and left-handed transmission lines based on SRRs or other related topologies, the dispersion diagram is also given by expression (3.1).  $Z_s(\omega)$  and  $Z_p(\omega)$  are the series and shunt impedances of the  $\pi$ -circuit models. By applying (3.1) to the circuits shown in Figures 3.23 and 3.24, we obtain

$$\cos(\beta l) = 1 - \frac{LC\omega^2}{2} + \frac{C/C'_s}{4\left(1 - \frac{\omega_0^2}{\omega^2}\right)} \quad (3.44)$$

$$\cos(\beta l) = 1 - \frac{1}{2}LC\omega^2 \left(1 - \frac{\omega_p^2}{\omega^2}\right) \left(1 - \frac{1}{2LC'_s\omega^2\left(1 - \frac{\omega_0^2}{\omega^2}\right)}\right), \quad (3.45)$$

with  $\omega_p$  given by equation (3.42). These expressions have been evaluated by using the electrical parameters corresponding to the structures depicted in Figures 3.15 and 3.18, and they are represented in a reduced Brillouin diagram in Figure 3.26. For comparison purposes, in this figure there are also represented the dispersion diagrams that have been obtained from the  $S$ -parameters computed by electromagnetic simulation of a single unit cell, according to the following expression [6]:

$$\cos \phi = \frac{A + D}{2}, \quad (3.46)$$

where  $A$  and  $D$  are the diagonal elements of the ABCD matrix, which are related to  $S$ -parameters through well-known expressions [30]. As expected, a stopband appears in the vicinity of the resonant frequency of the SRRs for the negative permeability structure, whereas this stopband is switched to a bandpass behavior with antiparallel phase and group velocities for the left-handed structure.<sup>17</sup>

### 3.6.2 Implications of the Model

Let us now analyze in more detail the transmission properties of SRR-based left-handed transmission lines. These structures are by nature frequency-selective

<sup>17</sup>The portion of the dispersion diagram of the left-handed line corresponding to the right-handed band has not been represented in the figure.

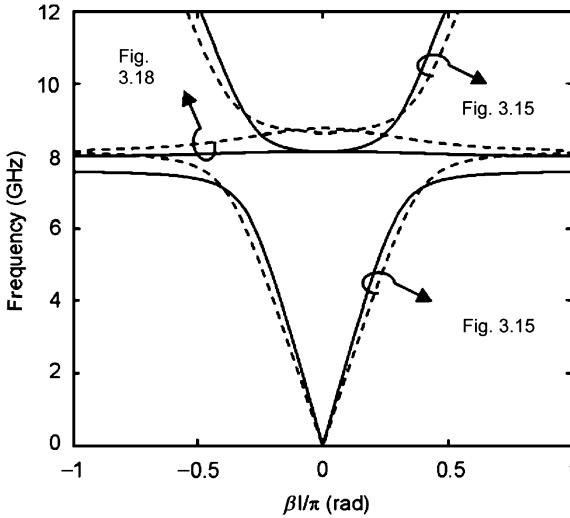


**FIGURE 3.26** Theoretical (solid lines) and simulated (dashed lines) dispersion diagram for the infinite periodic SRR-CPW structures with unit cells identical to those shown in Figures 3.15 and 3.18. (Source: Reprinted with permission from [29]; copyright 2005, IEEE.)

devices that exhibit a bandpass behavior. In Chapter 4, the use of SRR-based structures for the implementation of planar microwave filters will be discussed exhaustively, and it will be shown that it is possible to design compact and high-performance filters with controllable characteristics. However, before this discussion, it is necessary to point out the main relevant characteristics of metamaterial transmission lines based on SRRs. This will provide us with interesting information, which will be helpful in order to predict the potentiality of SRR-based devices as filtering structures and to envisage other possible circuit applications. For the analysis that we want to carry out, the frequency dependence of the Bloch impedance of the structure will provide us with valuable information. In reference to the  $\pi$ -circuit model of Figure 3.24b, the Bloch impedance is given by the following expression [6]:

$$Z_B(\omega) = \sqrt{\frac{Z_s(\omega)Z_p(\omega)/2}{1 + \frac{Z_s(\omega)}{2Z_p(\omega)}}}, \quad (3.47)$$

where  $Z_s$  and  $Z_p$  are the series and shunt impedances of the  $\pi$ -circuit, respectively. The allowed band for backward-wave propagation in the structures occurs in that region where the Bloch impedance,  $Z_B$ , and the phase constant,  $\phi = \beta l$ , given by expression (3.1) are both real numbers. From equation (3.1), the limits of this interval

are given by the following conditions:<sup>18</sup>

$$Z_s(\omega) = 0 \quad (3.48)$$

where  $\phi = 0$  and  $Z_B = 0$ , and

$$Z_s(\omega) = -2Z_p(\omega), \quad (3.49)$$

where  $\phi = -\pi$  and  $Z_B = \infty$ . Expression (3.48) leads to the upper limit of the left-handed band, namely

$$f_H = \frac{1}{2\pi} \sqrt{\frac{1}{2C'_s L} + \frac{1}{L'_s C'_s}}, \quad (3.50)$$

and the lower limit can be inferred from equation (3.49):

$$f_L = \frac{1}{2\pi} \sqrt{\frac{1}{C'_s(2L + 8L_p)} + \frac{1}{L'_s C'_s}}. \quad (3.51)$$

To obtain expression (3.51), it has been assumed that the shunt reactance is dominated by  $L_p$ , that is,  $C$  has been neglected. This approximation is reasonable as long as  $\omega_p \gg \omega_s$ , and it simplifies expression (3.51). In the interval delimited by the previous frequencies ( $f_L$  and  $f_H$ ), the sign of the series,  $Z_s(\omega)$ , and shunt,  $Z_p(\omega)$ , impedances is negative and positive, respectively. With the signs of these reactances, the structure formally behaves as a dual transmission line; that is, it admits backward waves. It is interesting to mention at this point that, as was previously anticipated, the onset of left-handed wave propagation does not exactly coincide with the resonance frequency of the SRRs,  $f_o$ , despite the fact that these resonant elements provide the negative value of  $\mu_{\text{eff}}$  just above this frequency. Indeed, at  $f_o$  the series branch of the  $\pi$ -circuit model opens and the signal is completely reflected (transmission zero).<sup>19</sup>

According to equations (3.50) and (3.51), the left-handed bandwidth depends on the values of the electrical parameters of the equivalent circuit model. As low as  $L$  is compared to  $L_p$  and  $L'_s$ , the wider the bandwidth can be. However, this is not the conventional 3dB bandwidth of filters, delimited by those frequencies where insertion losses drop to 3dB. The left-handed bandwidth, delimited by  $f_L$  and  $f_H$ , must be understood as that region of the spectrum where the phase constant,  $\beta$ , is real and

<sup>18</sup>At that frequency where  $Z_p(\omega) = \infty$  (expression 3.42) the phase shift per cell is also  $\phi = 0$ , whereas  $Z_B = \infty$ . This frequency is the lower limit of the forward wave band. Above this frequency, the signs of the series and shunt reactance are positive and negative, respectively.

<sup>19</sup>Under ideal conditions (lossless line and SRRs).

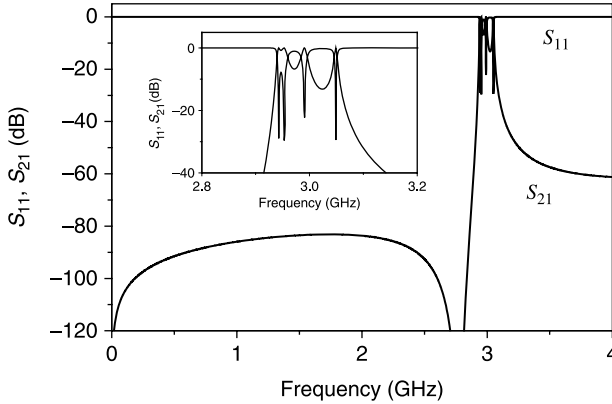


**FIGURE 3.27** Electrical response of the circuit of Figure 3.24, with the parameters corresponding to the four-stage left-handed structure of Figure 3.21.

negative, regardless of the transmission coefficient. In fact, at  $f_L$  and  $f_H$  the impedance mismatch between the source, the load, and the line is maximum, because the Bloch impedance takes extreme values at these frequencies. Thus the 3 dB bandwidth is lower than the left-handed bandwidth. However, the frequency response within the left-handed band is not only controlled by impedance matching, but also by phase matching. In other words, total transmission not only occurs when the Bloch impedance coincides with the reference impedance of the ports<sup>20</sup> (usually  $50 \Omega$ ), but also when the electrical length of the structure is a multiple of  $\pi$ . The latter condition (phase-matching) takes place at  $N - 1$  different frequencies ( $N$  being the number of device stages) satisfying the following rule (relative to expression 3.45):

$$\phi_i = \frac{\pi}{N} i \quad (3.52)$$

where  $0 < i < N$ . Hence, the number of transmission peaks equals the number of basic cells,<sup>21</sup>  $N$ . As  $N$  increases, the transmission peaks spread out towards the limits given by expressions (3.50) and (3.51). The effect is an enhancement of the 3 dB bandwidth. By using the electrical parameters corresponding to the model that describes the left-handed microstrip line of Figure 3.21, the electrical response has been obtained (Fig. 3.27). The transmission peaks are clearly visible, although in measurement these peaks are obscured by losses, and they do not emerge (see Fig. 3.21). In practice, as a first-order approximation and provided that the number of cells is not very small, it can be assumed that the left-handed and 3 dB bandwidths coincide.

We have mentioned in the preceding paragraph that the left-handed bandwidth depends on the relative value of  $L$  as compared to  $L_p$  and  $L'_s$ . In practice, the line

<sup>20</sup>This occurs at a single frequency.

<sup>21</sup>Unless one of the frequencies given by expression (3.52) coincides with that frequency where impedance matching is satisfied.

inductance cannot be driven to very low values (as this would require very wide conductor strips). On the other hand, the inductance of the shunt metallic strips or vias cannot be increased too much, because the plasma frequency, determined by the resonator formed by this inductance and the line capacitance, must remain beyond the SRR resonance. For these reasons, it is not simple in practice to design wide-band left-handed transmission lines by combining SRRs and shunt-connected strips (or vias). However, the reason, rather than being related to the quality factor of the SRRs, is due to the difficulty of satisfying the requirements for wide allowable bands by using the structures under study. In Chapter 4, it will be shown that, by introducing additional elements to the structures, it is possible to achieve very wide-band left-handed transmission lines and that these 1D metamaterials can be applied to the design of planar microwave filters with controllable characteristics.

A relevant characteristic of the left-handed transmission lines based on SRRs is the presence of a transmission zero at the resonance frequency of SRRs (as has been previously indicated). This transmission zero is not present in the  $LC$  loaded dual (or CRLH) structures<sup>22</sup> considered in Section 3.2. Due to this transmission zero, the lower band edge of the left-handed band can be made sharp. To this end,  $L_p$  must be increased, although this degrades frequency selectivity in the upper edge of the band, because the cutoff (plasma) frequency related to the presence of the vias decreases. Nevertheless, for reasonable values of the electrical parameters of the model, that is, for implementable device geometries, typically the lower band edge is sharp, whereas frequency selectivity at the upper band is smooth, as can be appreciated in Figure 3.21. In Chapter 4, it will be shown that by alternating SRR/strip (or via) stages with basic cells consisting of the combination of SRRs with capacitive gaps (that is, right-handed stages), it is possible to improve frequency selectivity at the upper band edge.

To end this section, we would like to mention that, apart from the frequency-selective properties of SRR-based devices (which are of interest for microwave filter design), it has been shown that the Bloch impedance and the phase shift per cell vary over a wide margin within the allowed band. This points out the potential of these structures in those applications where the control of impedance and phase is of interest, as occurs in most microwave circuits. As will be studied in the next chapter of this book, many applications, where miniaturization is a key aspect, will be derived from this fact.

### 3.7 DUALITY AND COMPLEMENTARY SPLIT RING RESONATORS (CSRRs)

In this section, the concept of complementary split ring resonators (CSRRs) is introduced as an alternative to the design of metamaterials based on resonant elements, providing an effective negative permittivity, rather than permeability [31]. By invoking the concepts of duality and complementarity [32–34], the CSRR can be derived

<sup>22</sup>In fact, the transmission zero for  $LC$  loaded lines is at the origin.

from the SRR structure in a straightforward way. This particle, which in planar technology can be defined as the *negative image* of the SRR, exhibits an electromagnetic behavior that is almost the *dual* of that of the SRR. Specifically, a negative effective permittivity can be expected for any CSRR-based medium, whereas a negative- $\mu$  behavior arises in an equivalent SRR-based system.

### 3.7.1 Electromagnetic Properties of CSRRs

The electromagnetic properties of SRRs have been already analyzed in Chapter 2. This analysis shows that SRRs behave as an  $LC$  resonator that can be excited by an external magnetic flux, exhibiting a strong diamagnetism above their first resonance. SRRs also exhibit cross-polarization effects (magnetolectric coupling) [25], so that excitation by a properly polarized time-varying external electric field is also possible. Figure 3.28 again reproduces the basic topology of the SRR, as well as the equivalent circuit model, for comparison purposes. In this diagram,  $C_o$  indicates the total capacitance between the rings, that is,  $C_o = 2\pi r_o C_{\text{pul}}$ , where  $C_{\text{pul}}$  is the per-unit-length edge capacitance. The resonance frequency of the SRR is given by  $f_o = (L_s C_s)^{-1/2} / 2\pi$ , where  $C_s$  is the series capacitance of the upper and lower halves of the SRR, that is,  $C_s = C_o/4$ . The inductance,  $L_s$ , can be approximated by that of a single ring with *averaged* radius  $r_o$  and width  $c$  [25,29].

As is well known, the complementary of a planar metallic structure is obtained by replacing the metal parts of the original structure with apertures, and the apertures

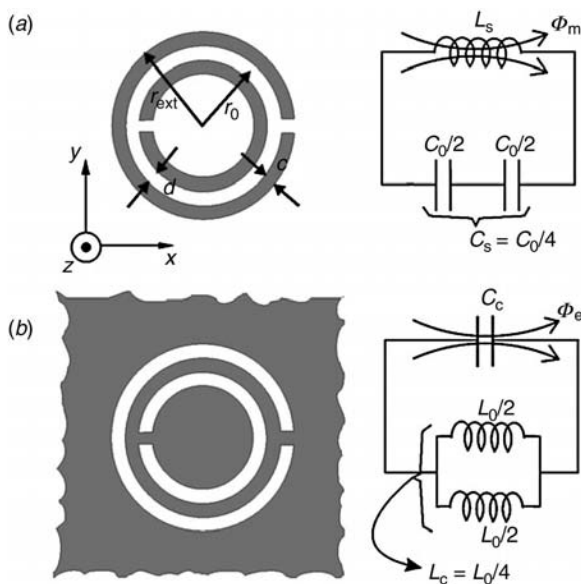


**FIGURE 3.28** Topologies of the SRR (a) and CSRR (b), and their equivalent circuit models (ohmic losses can be taken into account by including a series resistance in the model). Gray zones represent the metallization. (Source: Reprinted with permission from [29]; copyright 2005, IEEE.)

with metal plates [32]. Due to symmetry considerations, it can be demonstrated that, if the thickness of the metal plate is zero, and its conductivity is infinity (perfect electric conductor), then the apertures behave as perfect magnetic conductors. In that case the original structure and its complementary are effectively dual, and if the field  $F = (E, H)$  is a solution for the original structure, its dual  $F'$  defined by

$$F' = (E', H') = (-\sqrt{\mu/\varepsilon} \cdot H, \sqrt{\varepsilon/\mu} \cdot E), \quad (3.53)$$

is the solution for the complementary structure [33]. Thus, under these ideal conditions, a perfectly dual behavior is expected for the complementary screen of the SRR. Thus, whereas the SRR can be mainly considered as a resonant magnetic dipole that can be excited by an axial magnetic field, the CSRR (also depicted in Fig. 3.28) essentially behaves as an electric dipole (with the same frequency of resonance) that can be excited by an axial electric field. In a more rigorous analysis, the cross-polarization effects in the SRR [25], discussed in Chapter 2, should be considered and extended also to the CSRR. Thus, this last element will also exhibit a resonant magnetic polarizability along its  $y$ -axis (see Fig. 3.28) and, therefore, its main resonance can be also excited by an external magnetic field applied along this direction [29].

Rigorously speaking, due to the continuity of the tangential/normal components of the electric/magnetic fields in the CSRR plane,  $F'$  in equation (3.53) is the solution on one side of this plane, and  $-F'$  on the other side. With regard to the CSRR polarizabilities, this means that the sign of such polarizabilities changes from one side to another. Therefore, the net electric and magnetic dipoles on the CSRR must vanish, a result that can be also deduced from the fact that electric currents confined in a plane cannot produce any net normal/tangential electric/magnetic polarization. However, when the CSRR is seen from one side, the aforementioned effective polarizabilities arise.

The intrinsic circuit model for the CSRR (dual of the SRR model) is shown in Figure 3.28. In this circuit [29], the inductance  $L_s$  of the SRR model is substituted by the capacitance,  $C_c$ , of a disk of radius  $r_o - c/2$  surrounded by a ground plane at a distance  $c$  of its edge. Conversely, the series connection of the two capacitances  $C_o/2$  in the SRR model is substituted by the parallel combination of the two inductances connecting the inner disk to the ground. Each inductance is given by  $L_o/2$ , where  $L_o = 2\pi r_o L_{\text{pul}}$  and  $L_{\text{pul}}$  is the per-unit-length inductance of the CPWs connecting the inner disk to the ground. For infinitely thin perfect conducting screens, and in the absence of any dielectric substrate, it directly follows from duality that the parameters of the circuit models for the SRRs and the CSRRs are related by  $C_c = 4(\varepsilon_o/\mu_o)L_s$  and  $C_o = 4(\varepsilon_o/\mu_o)L_o$ . The factor of 4 appearing in these relations is deduced from the different symmetry properties of the electric and magnetic fields of both elements, as is sketched in Figure 3.29. From the above relations it is easily deduced that the frequency of resonance of both structures is the same, as is expected from duality.

It has already been mentioned that the behavior of SRRs and CSRRs is strictly dual for perfectly conducting and infinitely thin metallic screens placed in vacuum. However, deviations from duality—which may give rise to a shift in



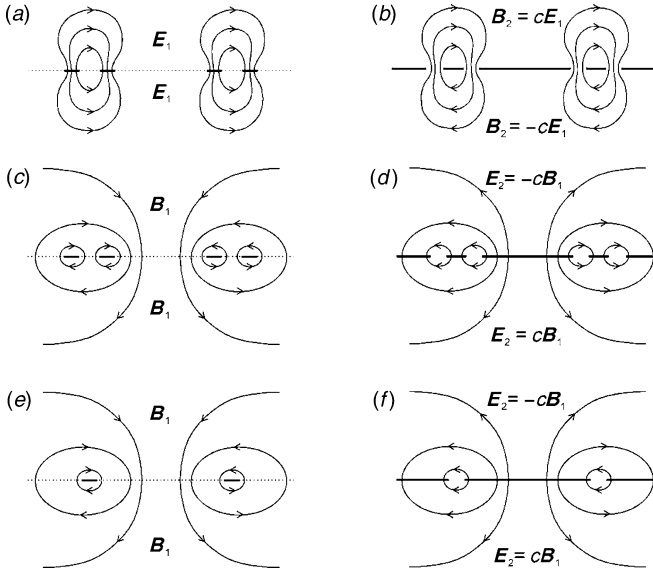


**FIGURE 3.29** Sketch of the electric and magnetic field lines in the SRR (left) and the CSRR (right). (a) Electric field lines in the SRR at resonance. (b) Magnetic field lines in the dual CSRR. (c, d) Magnetic and electric field lines in the SRR and the CSRR, respectively. (e) Magnetic induction field in the equivalent ring inductance used for the computation of  $L_s$  in the SRR [31]. (f) Electric field in the dual equivalent capacitor proposed for the computation of  $C_c$  for the CSRR. (Source: Reprinted with permission from [29]; copyright 2005, IEEE.)

the frequencies of resonance—arise from losses, the finite width of metallizations, and the presence of a dielectric substrate. The latter is expected to be the main cause of deviations from duality. This fact is due to the variations of the elements of the CSRR circuit model,  $C_c$  and  $L_o$ , from the values extracted from the SRR circuit model parameters  $C_o$  and  $L_s$  by duality ( $C_c = 4(\epsilon_o/\mu_o)L_s$  and  $C_o = 4(\epsilon_o/\mu_o)L_o$ ). As is sketched in Figure 3.30, these variations arise directly from the presence of a dielectric substrate, which affects  $C_c$  and  $C_o$  but leaves  $L_s$  and  $L_o$  unaltered. Analytical expressions for  $L_s$  and  $C_o$  in the SRR when a dielectric substrate is present were provided in Chapter 2 [23]. As we have already mentioned, the capacitance  $C_c$  in Figure 3.29 is that corresponding to a metallic disk of radius  $r_o - c/2$  surrounded by a ground plane at a distance  $c$ . An analytical approximate expression for  $C_c$  when a dielectric substrate is present (see Fig. 3.31) has been derived in reference [29]. The final expression is

$$C_c = \frac{\pi^3 \epsilon_0}{c^2} \int_0^{+\infty} dk \frac{[bB(kb) - aB(ka)]^2}{k^2} \left[ \frac{1}{2} \left( 1 + \frac{\epsilon}{\epsilon_0} \tan h(kh) \right) \right], \quad (3.54)$$

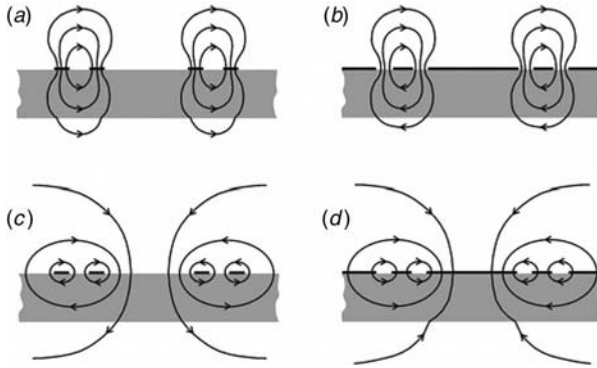


**FIGURE 3.30** Sketch of the electric (a) and magnetic (c) field lines of an SRR on a dielectric substrate. The magnetic (b) and electric (d) lines of a similar CSRR on the same dielectric substrate are also sketched. (Source: Reprinted with permission from [29]; copyright 2005, IEEE.)

where  $a$ ,  $b$ , and  $h$  are geometrical variables defined in Fig. 3.31 and function  $B$  is defined as

$$B(x) = S_0(x)J_1(x) - S_1(x)J_0(x), \tag{3.55}$$

with  $S_n$  and  $J_n$  being the  $n$ th-order Struve and Bessel functions. The inductance  $L_o$  in Fig. 3.28 is that corresponding to a circular CPW structure of length  $2\pi r_o$ , strip width  $d$ , and slot width  $c$ . The design formulas given in [35] for the per-unit-length CPW inductance provide enough accuracy and have been used in all numerical computations of the next subsection.

The previous analysis can be easily extended to the complementary version of other planar topologies derived from the basic geometry of the SRR, such as the NB-SRR, the 2-SRR (double-slit SRR) and the SR. The equivalent circuit models for such complementary particles are depicted in Figure 3.32, jointly with the

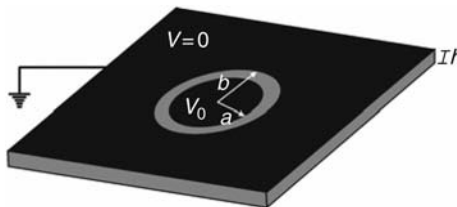


**FIGURE 3.31** The capacitance of the CSRR is approximately equal to that corresponding to a metallic disk of radius  $a = r_o - c/2$  surrounded by a ground plane at a distance  $b - a = c$ ,  $r_o$  being the averaged radius of the CSRR and  $c$  the width of the slots in this. The dielectric substrate is characterized by its permittivity  $\epsilon$  and thickness  $h$ . (Source: Reprinted with permission from [29]; copyright 2005, IEEE.)

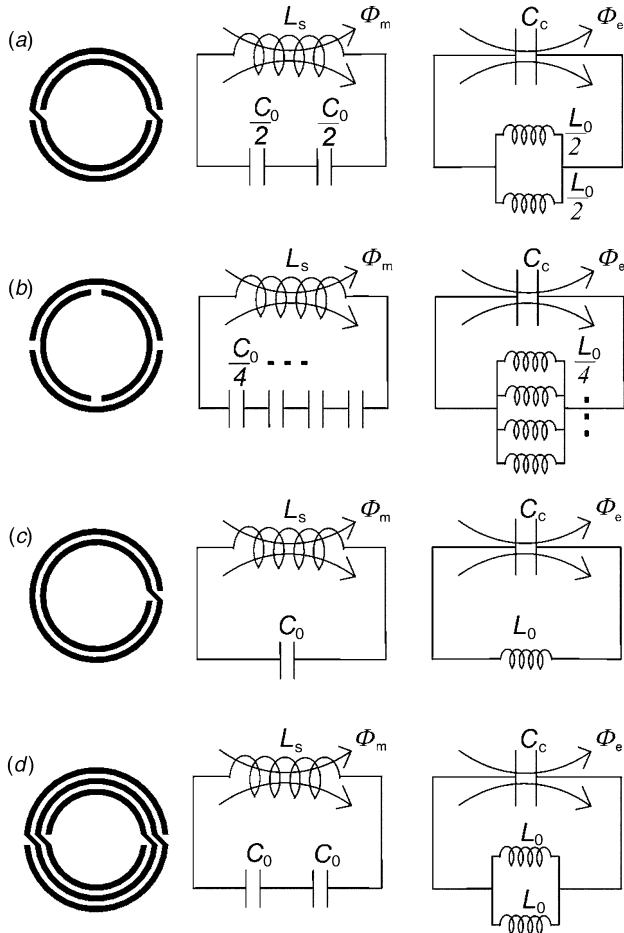


**FIGURE 3.32** Topologies corresponding to (a) the nonbianisotropic SRR (NB-SRR), (b) the double-slit SRR (2-SRR), (c) the spiral resonator (SR), and (d) the double SR (DSR). The equivalent circuits for these topologies are depicted in the second column, and the circuit models for the complementary counterparts are represented in the third column. (Source: Reprinted with permission from [29]; copyright 2005, IEEE.)

equivalent circuits of the noncomplementary counterparts, which are reproduced here for comparison purposes.

### 3.7.2 Numerical Calculation and Experimental Validation

The effect of the dielectric substrate on the relative shift between the resonance frequency of CSRRs and SRRs of identical dimensions is shown in Figure 3.33. As expected, there is no difference for the two limiting values of a zero- and an infinite substrate thickness. However, significant differences in the values of the frequency of

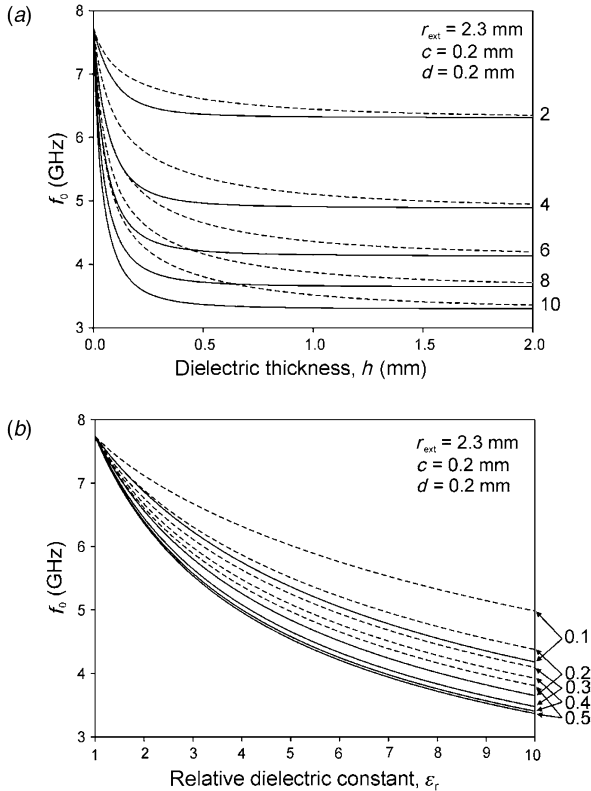


**FIGURE 3.33** Numerical calculations showing the dependence of the resonance frequency of SRRs (solid lines) and CSRRs (dashed lines) on the substrate parameters. (a) Dependence on the dielectric thickness for different values of the relative permittivity of the substrate (shown at right). (b) Dependence on the value of the relative dielectric constant, for different substrate thickness (in mm). (Source: Reprinted with permission from [29]; copyright 2005, IEEE.)

resonance for both elements can be observed for intermediate thickness. Obviously, these differences increase with the dielectric constant of the substrate (see also Fig. 3.33). In order to experimentally verify the accuracy of the proposed circuit models for the CSRR and derived geometries, a set of these resonators with different topologies were etched on a metallized microwave substrate and its frequencies of resonance were measured. Their dual counterparts were also manufactured and measured for completeness. The resonance frequencies were obtained from the transmission coefficient,  $S_{21}$ , measured in a rectangular waveguide, properly loaded with the corresponding element [29]. The waveguide was excited in the fundamental  $TE_{01}$  mode, and connected to an *Agilent 8510* network analyzer. The SRRs or derived geometries were placed in the central  $E$ -plane, so that they were excited by the magnetic field perpendicular to the element plane. Their dual counterparts were etched in the top wall of the waveguide, being excited by the electric field perpendicular to the

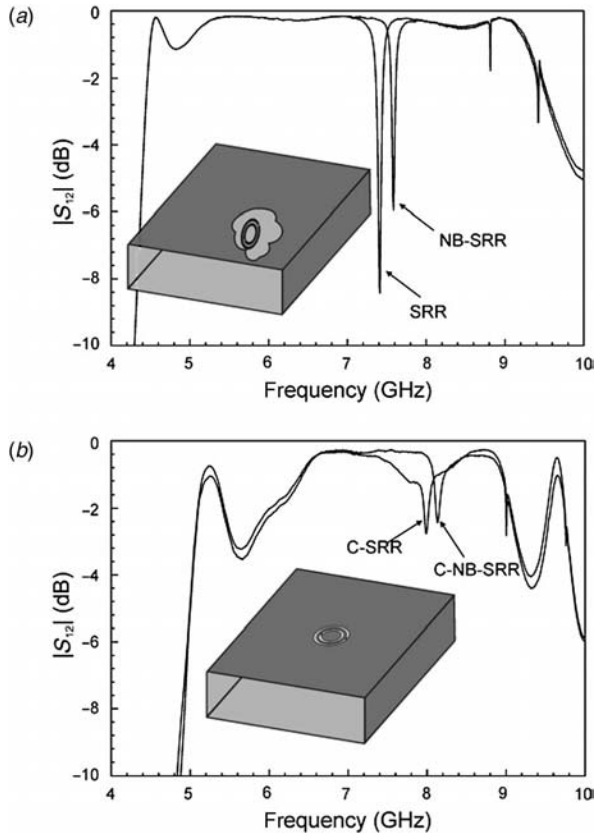


**FIGURE 3.34** Frequency response obtained in a rectangular waveguide loaded with SRRs and NB-SRRs, as well as their dual counterparts (C-SRR and C-NB-SRR). The method of excitation is sketched in the insets of the Figures. The element parameters are those of Table 3.1. (Source: Reprinted with permission from [29]; copyright 2005, IEEE.)

element plane. Figure 3.34 shows the transmission coefficients for an SRR and an NB-SRR with identical geometrical parameters, as well as the same coefficients for their duals (CSRR and C-NB-SRR). The SRR and the NB-SRR have the same frequency of resonance (the small shift can be attributed to tolerances in the manufacturing process). The same can be said for their complementary elements. Finally, the frequencies of resonance for different configurations, measured by following the method illustrated in Figure 3.34, are shown in Table 3.1 [29]. The theoretical values shown in this table were obtained from the proposed circuit models with  $C_c$  calculated from equation (3.54),  $L_o$  from the design formulas in [35] and  $C_s$ ,  $L_s$  from the expressions in the Appendix of Chapter 2. As can be seen, a reasonable agreement between theory and experiment is obtained. It is remarkable that the CSRRs always resonate at frequencies slightly higher than those of the SRRs. This effect is sharper for the higher dielectric constants.

**TABLE 3.1 Measured and Theoretical Values for the Frequency of Resonance**

	Conventional		Complementary	
	$f_0^{\text{th}}$ (GHz)	$f_0^{\text{exp}}$ (GHz)	$f_0^{\text{th}}$ (GHz)	$f_0^{\text{exp}}$ (GHz)
SRR <sup>a</sup>	7.17	7.40	7.49	8.00
NB-SRR <sup>a</sup>	7.17	7.56	7.49	8.14
DSR <sup>a</sup>	5.07	5.05	5.30	5.49
2-SR <sup>a</sup>	3.59	3.78	3.75	4.07
SRR <sup>b</sup>	3.33	3.40	3.56	3.77
2-SRR <sup>b</sup>	6.66	6.77	7.12	7.41

The resonators are printed on a substrate with thickness  $h = 0.49$  mm and relative permittivity  $\epsilon_r = 2.43$ . The parameters of rings, named in Figure 3.28, are <sup>(a)</sup>  $r_o = 1.7$  mm,  $c = d = 0.2$  mm; <sup>(b)</sup>  $r_o = 3.55$  mm,  $c = d = 0.3$  mm.

### 3.8 SYNTHESIS OF METAMATERIAL TRANSMISSION LINES BY USING CSRRs

In this section, it is demonstrated that CSRRs can be used for the design of metamaterial transmission lines. From duality, it follows that whereas the dominant mode of excitation of SRRs is by applying an axial time-varying magnetic field, for CSRRs the main driving mechanism is electric coupling, and a significant component of the electric field parallel to the axis of the rings is required. Thus, by etching the CSRRs in the ground plane (in close proximity to the conductor strip), or in the conductor strip (provided there is space enough for this purpose), the required conditions for CSRR excitation are fulfilled in most common transmission lines (microstrip, CPW, and so on).

#### 3.8.1 Negative Permittivity and Left-Handed Transmission Lines

The natural (although not exclusive) host transmission line for the implementation of one-dimensional metamaterials using CSRRs is the microstrip configuration. By etching the complementary rings in the ground plane, under the signal strip, a significant component of the electric line field results parallel to the rings' axis, as desired. Figure 3.35 illustrates such structure, where 4 CSRRs are etched in the ground plane (relevant dimensions are indicated in the caption). The simulated and measured frequency responses for this device are also depicted in Figure 3.35. Due to the negative effective permittivity in the vicinity of CSRR's resonance, the signal is inhibited in a narrow band.

In order to synthesize a left-handed medium, additional elements able to provide the required negative effective permeability must be introduced to the structure. It was shown in the beginning of this chapter that the negative effective permeability can be achieved by etching series capacitive gaps in the host line. These gaps make the structure behave as a magnetic plasma, with negative valued permeability up to a frequency that depends on the resonator formed by the gap capacitance and the

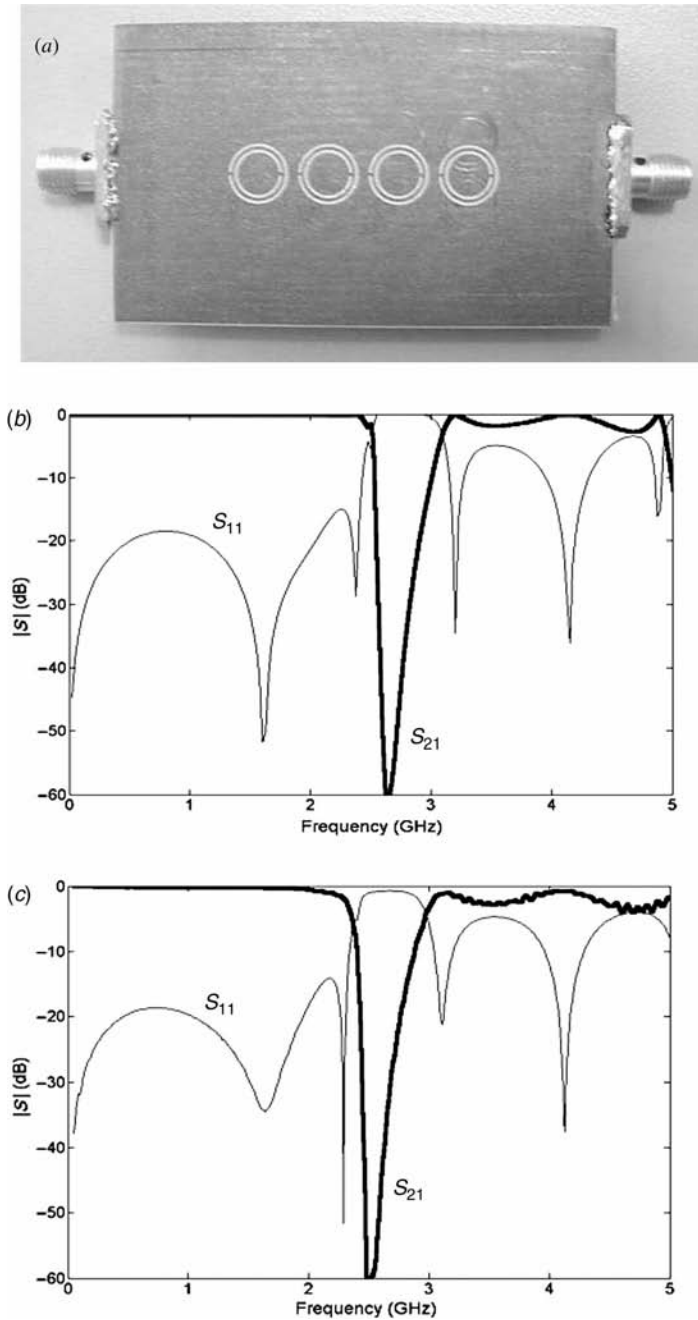


**FIGURE 3.35** Bottom face (ground plane) of a microstrip structure loaded with CSRRs (a), simulated (b) and measured (c) frequency responses. CSRR dimensions are  $c = d = 0.3$  mm, and the radius of the inner ring is  $r = 2.1$  mm. The period of the structure is 7 mm. The substrate used is the commercially available Rogers RO3010 ( $\epsilon_r = 10.2$ , thickness  $h = 1.27$  mm). (Source: Reprinted with permission from [31]; copyright 2004, IEEE.)

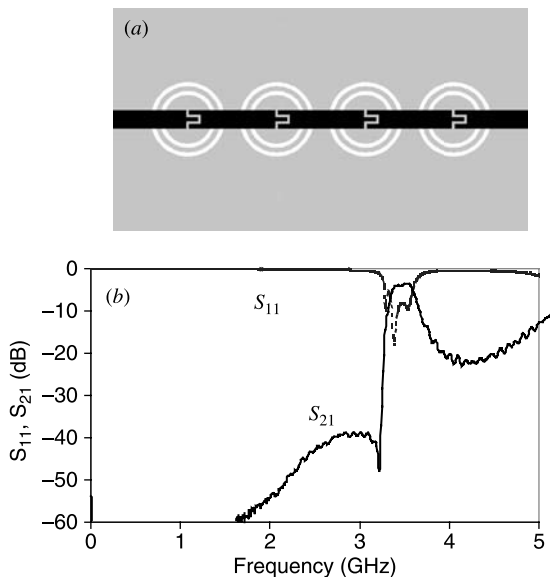


**FIGURE 3.36** Layout of a left-handed microstrip structure based on CSRRs (a) and measured frequency response (b). The period of the device, the strip width and gap spacing are  $l = 6\text{ mm}$ ,  $W = 1.2\text{ mm}$  and  $l_g = 0.2\text{ mm}$ , respectively. The dimensions of CSRRs have been determined to obtain a resonant frequency of  $f_o = 3.5\text{ GHz}$ , that is,  $c = d = 0.3\text{ mm}$  and the internal radius of the inner ring is  $r = 1.6\text{ mm}$  (the parameters of the Rogers RO3010 substrate have been considered, namely, dielectric constant  $\epsilon_r = 10.2$ , thickness  $h = 1.27\text{ mm}$ ).

per-section inductance of the line. Hence, to design a left-handed metamaterial by combining CSRRs and gaps, it is necessary to design the structure such that the plasma frequency extends beyond the resonance frequency of the CSRRs. By taking this into account, a region where negative effective permeability and permittivity coexist is expected. Figure 3.36 illustrates a left-handed microstrip line as well as its measured frequency response. A passband with negative wave propagation arises. As occurs in SRR-based left-handed transmission lines, a sharp cutoff in the lower band edge and a soft upper transition band are visible. The reasons for this behavior are discussed in the following subsection, where the equivalent circuit models of these structures are inferred.

We have indicated that the usual host line for the design of CSRR-based 1D planar metamaterials is the microstrip line. However, it does not mean that CPWs and other planar transmission lines should be ruled out. Indeed, by using CPWs, the lateral dimensions necessary to achieve a matched line are not univocally determined, and hence, the central strip can be made wide enough to provide the required space to etch the CSRRs on it. This way, the ground plane can be preserved from being etched, which is of interest in certain applications.<sup>23</sup> On the other hand, the

<sup>23</sup>For instance, if the substrate is sustained by a metallic holder.



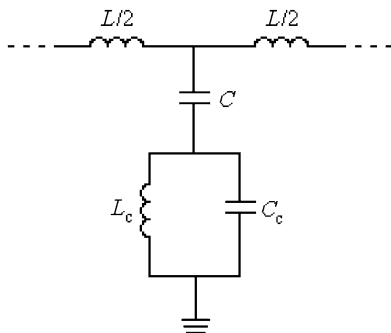


**FIGURE 3.37** Equivalent circuit model of a negative-permittivity line consisting of a transmission line loaded with CSRRs.

etching of CSRRs in the signal strip of microstrip lines is possible in applications where low-impedance transmission line sections are required (as will also be shown in the next chapter).

### 3.8.2 Equivalent Circuit Models for CSRR-Loaded Transmission Lines

Because CSRRs are mainly excited by the electric field induced by the line, this coupling can be modeled by series connecting the line capacitance to the CSRRs, which are modeled as parallel  $LC$  tanks, as has been shown previously. According to this, the proposed lumped element equivalent circuit model for the CSRR-loaded transmission line is that depicted in Figure 3.37, where  $L$  and  $C$  are the per-section inductance and capacitance of the line, and  $L_c$  and  $C_c$  model the CSRR. For the structure loaded with CSRRs and series gaps (left-handed medium), the lumped element equivalent circuit model is identical, but with the addition of a capacitance,  $C_g$ , to account for the series gaps (see Fig. 3.38).<sup>24</sup> In fact, for these models to be valid, the CSRRs should be relatively close. Otherwise, a significant portion of the line would lie outside the region occupied by the CSRRs and the approximation of the coupling capacitance by the line capacitance would not be correct [36].<sup>25</sup>

For an infinitely periodic structure composed by cascading the T-circuit models of Figures 3.37 and 3.38, the dispersion relation and Bloch impedance are given by expressions (3.1) and (3.2), respectively. The dispersion relations for both the negative permittivity and left-handed transmission lines inferred from the corresponding lumped element circuit models are depicted in reduced Brillouin diagrams in Figure 3.39 (these diagrams have been obtained by using the electrical parameters

<sup>24</sup>It must be mentioned that with the series gaps etched above the position of the CSRRs,  $C$  accounts for the line capacitance and the fringing capacitance. As will be shown later,  $C$  may change substantially when the gaps are present.

<sup>25</sup>A more accurate model for CSRR/gap loaded transmission lines, which includes line effects between adjacent CSRRs (substantially spaced CSRRs), as well as inter-resonator coupling (tiny spaced CSRRs), has been proposed in [36]. See also Problem 3.8.

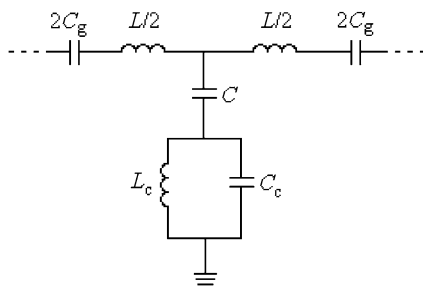


**FIGURE 3.38** Equivalent circuit model of a left-handed line consisting of a transmission line loaded with CSRRs and series gaps.

corresponding to the microstrip structures of Figs 3.35 and 3.36). The features are similar to those of Figure 3.26, corresponding to negative permeability and left-handed media, respectively, implemented through SRRs. For comparison, the dispersion relation inferred from the simulated  $S$ -parameters of the unit cell is also depicted in the diagrams. The slight discrepancies are mainly due to fabrication-related tolerances. These diagrams point out the left-handed nature of the line loaded with CSRRs and series gaps, as well as the stopband behavior of the structure without the presence of the gaps, which is related to the negative effective permittivity associated with the CSRRs.

Let us now focus on the analysis of the transmission properties of CSRR left-handed transmission lines to the light of the equivalent circuit model. The structure

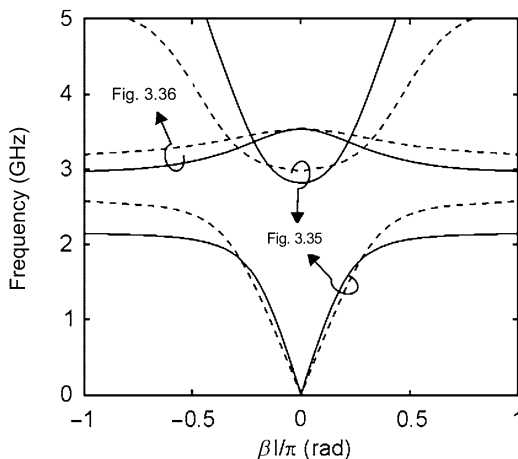


**FIGURE 3.39** Theoretical (solid lines) and simulated (dashed lines) dispersion diagram for the infinite CSRR–microstrip structures with unit cells identical to those shown in Figures 3.35 and 3.36. The mismatch between the stop- and passbands is due to the different dimensions of the CSRRs in Figures 3.35 and 3.36. (Source: Reprinted with permission from [29]; copyright 2005, IEEE.)

supports propagating waves in the frequency interval where  $\phi$  is a real number. Analysis of expression (3.1) indicates that this occurs in the region delimited by the following frequencies (it has been assumed that the series impedance of the equivalent circuit model is dominated by  $C_g$  and, hence,  $L$  has been neglected in the analysis)<sup>26</sup>:

$$f_L = \frac{1}{2\pi} \frac{1}{\sqrt{L_c \left( C_c + \frac{4}{\frac{1}{C_g} + \frac{4}{C}} \right)}} \quad (3.56)$$

$$f_H = \frac{1}{2\pi\sqrt{L_c C_c}}, \quad (3.57)$$

where the subindexes simply make reference to the lower and higher frequency of the interval. At these frequencies, both the phase and Bloch impedance take extreme values; that is,  $Z_B \rightarrow \infty$  and  $\phi = 0$  at  $f_H$ , whereas  $Z_B = 0\Omega$  and  $\phi = -\pi$  at  $f_L$ . Obviously, these results are valid under the assumption of negligible losses.

Inspection of the circuit of Figure 3.38 also reveals that there is a transmission zero at a frequency given by

$$f_z = \frac{1}{2\pi\sqrt{L_c(C + C_c)}}. \quad (3.58)$$

As long as  $C \leq 4C_g$ ,  $f_z$  and  $f_L$  are very close, and the structure exhibits a very sharp cutoff in the lower edge of the left-handed allowed band, regardless of the number of stages. As for the left-handed structure based on SRR, the number of transmission peaks (losses neglected) coincides with the number of stages. One of these transmission peaks arises as a consequence of impedance matching (that is, for that frequency that makes the Bloch impedance equal to  $Z_B = 50\Omega$ ), and the others are due to phase matching, the exact location of them being given by those frequencies for which the phase variation satisfies the rule given in expression (3.52).

Following expressions (3.56) and (3.57), to design left-handed transmission lines with relatively wide allowed bands, it is necessary that the gap capacitance as well as the capacitance of the line is high, as compared to the equivalent capacitance of the CSRRs. By using the following electrical parameters, that is,  $C_g = 0.50\text{pF}$ ,  $C = 3.12\text{pF}$ ,  $L_c = 0.93\text{nH}$ , and  $C_c = 2.81\text{pF}$ , the simulated electrical response of the equivalent T-circuit model (10-stage device) shown in Figure 3.38 can be inferred (Fig. 3.40). A left-handed microstrip structure with these electrical parameters has been synthesized (Fig. 3.40). The geometry of the structure has been obtained

<sup>26</sup>This approximation is valid if the series resonance (i.e., the resonance frequency of the  $C_g$  and  $L$  combination) is substantially higher than the resonance frequency of the CSRRs (expression 3.57).

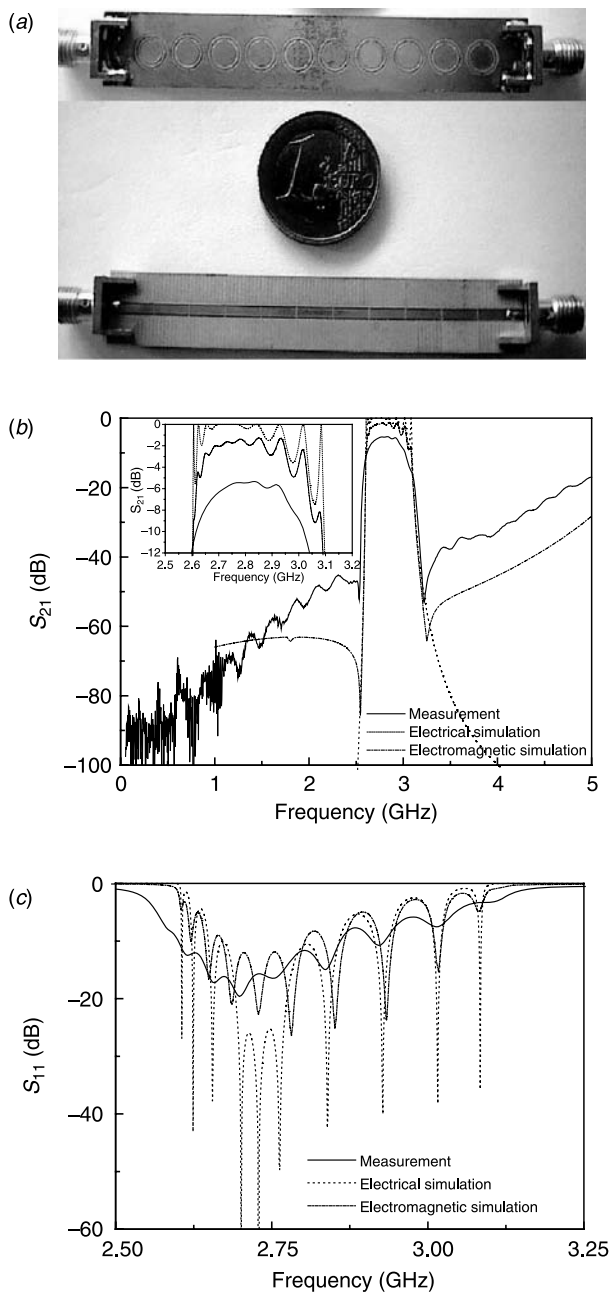


**FIGURE 3.40** Fabricated 10-stage prototype device (a), insertion losses (b), and return losses (c). The period is  $l=6.4$  mm, gap spacing  $g = 0.2$  mm, and strip width  $W = 1.69$  mm. The dimensions of the CSRRs are  $c_{in} = 0.472$  mm,  $c_{out} = 0.391$  mm,  $d = 0.149$  mm, and  $r_{ext} = 2.972$  mm. In (a) top and bottom views are shown. The device has been fabricated on the Rogers RO3010 substrate (dielectric constant  $\epsilon_r = 10.2$ , thickness  $h = 1.27$  mm,  $\tan \delta = 0.0023$ ). (Source: Reprinted with permission from [37]; copyright 2006, John Wiley & Sons.)

according to the procedure described in [37]. The simulated and measured frequency responses of this structure are also shown in Figure 3.40. Obviously, the transmission peaks are obscured in the measurement due to conductor and dielectric losses. Nevertheless, these results point out the validity of the lumped element model and show that left-handed structures with moderate left-handed bandwidth can be implemented by using CSRRs.

### 3.8.3 Parameter Extraction

To further verify the validity of the lumped element circuit models of the CSRR-loaded lines, a method to extract the electrical parameters from either electromagnetic simulation or measurement has been proposed [38]. As will be shown at the end of this section, the agreement between measurement and electrical simulation of the circuit models with extracted parameters is excellent. Indeed, the technique includes the determination of the unloaded  $Q$  factor of the CSRRs. Hence, it is necessary to account for CSRR losses by adding a parallel resistance,  $R$ , to the models (Fig. 3.41).

In a first-order approximation, losses can be neglected and two characteristic frequencies can be identified: the frequency that nulls the shunt impedance (transmission zero frequency,  $f_z$ , given by expression 3.58) and the frequency that nulls the shunt admittance (which obviously coincides with the intrinsic resonant frequency of the CSRR,  $f_o$ , or  $f_H$  according to expression 3.57). These frequencies can be experimentally determined, or they can be obtained through full-wave

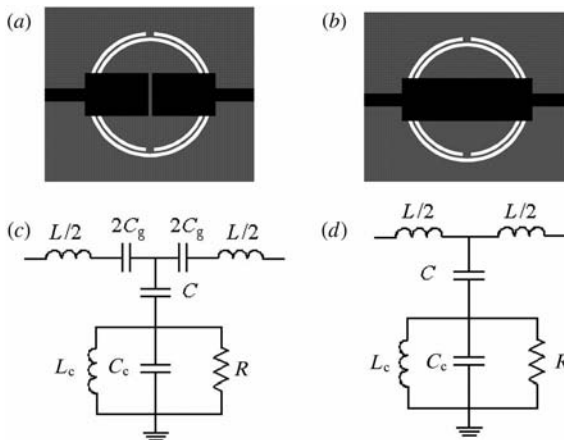


**FIGURE 3.41** Topologies of the considered left-handed (a) and negative-permittivity (b) cells, and their equivalent circuit models including losses (c) and (d), respectively. CSRR dimensions are (in reference to Fig. 3.28)  $c = 0.3$  mm,  $d = 0.19$  mm,  $r_{\text{ext}} = 5.65$  mm, gap separation and width are 0.30 mm and 3.85 mm, respectively, and the width of the access lines is 1.15 mm. Substrate characteristics correspond to the Rogers RO3010 substrate: dielectric constant  $\epsilon_r = 10.2$ , thickness  $h = 1.27$  mm and  $\tan \delta = 0.0023$ . (Source: Reprinted with permission from [38]; copyright 2006, IEEE.)

electromagnetic simulation. At  $f_z$  a notch in the transmission coefficient is expected and this frequency can be measured accurately. To obtain  $f_o$ , a representation of the transmission coefficient on a Smith Chart is required. At this frequency the shunt path to ground is opened, and the input impedance seen from the ports is solely formed by the series elements of the structure and the resistance of the opposite port ( $50 \Omega$ ). Therefore,  $f_o$  is given by the intersection between the measured (or simulated)  $S_{11}$  curve and the unit normalized resistance circle. From this result we can also obtain the impedance of the series elements at that frequency. This directly gives the value of  $L$  for negative-permittivity lines. For left-handed lines,  $L$  can be independently estimated from a transmission line calculator, whereas  $C_g$  can be determined by adjusting its value to fit the impedance inferred from simulation or experiment. Alternatively, to determine  $L$  and  $C_g$  in a left-handed line, a negative permittivity line can be fabricated, identical to the left-handed line except for the absence of the gap. By applying the technique to the structure without the series gap,  $L$  can be univocally determined. It can then be corrected to account for the presence of the gap, and we can adjust  $C_g$  as mentioned before.

Expressions (3.57) and (3.58) are dependent on three parameters. Therefore, the element values of the CSRR and the coupling capacitance cannot be directly obtained. To this end, an additional condition is needed. This can be obtained from the dispersion relation for the Bloch modes (3.1). At the angular frequency,  $\omega_{\pi/2}$ , where the phase of the transmission coefficient (which is a measurable quantity) is  $\phi(S_{21}) = \pi/2$ , the phase constant is  $\beta l = \pi/2$ . Following expression (3.1), we have

$$Z_s(\omega_{\pi/2}) = -Z_p(\omega_{\pi/2}). \quad (3.59)$$

Thus, from equations (3.57), (3.58), and (3.59), we can determine the three reactive element values that contribute to the shunt impedance. To determine  $R$ , this parameter is swept until electrical simulations of the circuit model and measured frequency responses agree. In practice, this parameter is determined with good accuracy from the transmission coefficient of the negative-permittivity structure, because the rejection level is very sensitive to this parameter. From this, the unloaded  $Q$  factor is given by  $Q = R\omega_o C_c$ .

The method has been applied to the negative-permittivity and left-handed cells depicted in Figure 3.41 (substrate characteristics and dimensions are indicated in the caption). The electrical parameters have been obtained by applying the method to the measured frequency responses (Fig. 3.42), and they are represented in Table 3.2. By using these electrical parameters, the electrical simulation of the structures can be inferred. The results are also depicted in Figure 3.42 for easy comparison. Very good agreement between measurements and electrical simulation has been obtained. This confirms the validity of the circuit model of CSRR-loaded transmission lines. The slight discrepancy between measurements and electromagnetic simulation is attributed to fabrication-related tolerances. For more details on the parameter extraction technique see [38].

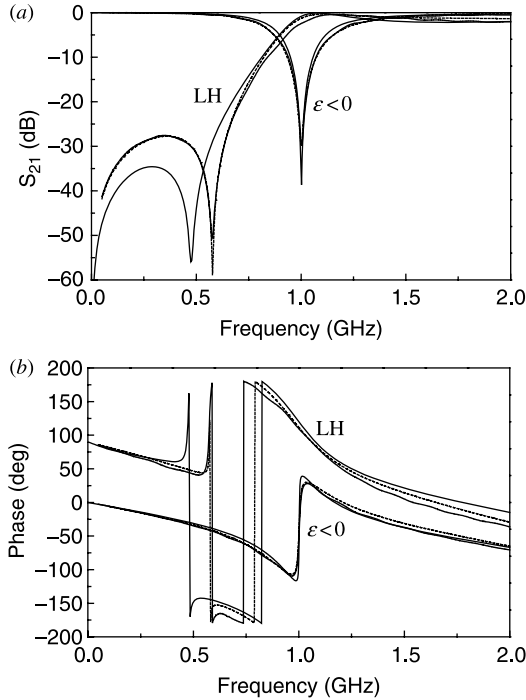


**FIGURE 3.42** Magnitude (a) and phase (b) of the transmission coefficient for the structures shown in Figure 3.41. Measurement, electromagnetic simulation, and electrical simulation, are depicted in bold, thin, and dashed lines, respectively. (Source: Reprinted with permission from [38]; copyright 2006, IEEE.)

A similar parameter-extraction technique can be applied to SRR-loaded transmission lines, by considering the circuit models depicted in Figures 3.23b and 3.24b. However, this would not directly provide the electrical parameters of the SRRs, but  $L'_s$  and  $C'_s$ . To determine  $L_s$  and  $C_s$  the value of  $M$  is needed, and it is difficult to accurately obtain such a parameter (in particular in the microstrip configuration). Nevertheless, parameter extraction for the models of Figures 3.23b and 3.24b can be of interest in certain applications, and follows a similar procedure to that described above for CSRR-loaded lines.

### 3.8.4 Effects of Cell Geometry on Frequency Response

In this subsection, the effects of varying gap separation, substrate thickness and the width of the host transmission line are analyzed and interpreted in the framework of the proposed circuit model. Figure 3.43 presents three frequency responses corresponding to different gap separations. As gap decreases, the upper band edge is not substantially altered. However, the lower band edge is clearly displaced towards lower values, resulting in a wider allowed band. This effect can be explained by expressions (3.56) and (3.57). The upper edge of the band only depends on the

**TABLE 3.2** Extracted Element Parameters for the Structures Shown in Figure 3.41<sup>a</sup>

	$C_g$ (pF)	$L$ (nH)	$C$ (pF)	$C_c$ (pF)	$L_c$ (nH)	$R$ (k $\Omega$ )
LH cell	1.27	4.96	19.58	4.01	3.22	1.39
$\epsilon < 0$ cell	–	5.08	4.43	4.06	2.98	1.39

<sup>a</sup>Notice that the value of  $C$  in the left-handed cell is much larger than in the negative permeability cell. The gap should be modeled by the series capacitance and fringing capacitances in a  $\pi$ -model configuration. Through  $\pi$ - $T$  transformation, the effects of the line and fringing capacitances can be grouped in a single capacitance,  $C$ , whose value can be substantially much larger than the addition of the individual components. This has been verified by the authors in other microstrip left-handed structures based on CSRRs and series gaps.

parameters of the resonant tank that models the CSRRs. Therefore, we do not expect a modification of the upper fall-off, because gap width reduction does not affect the intrinsic resonant frequency of the CSRRs. However, the lower edge depends on  $C_g$  and this capacitance increases as gap separation decreases. This explains the shift of the band onset towards lower frequencies when gap separation is decreased. In view of these results, the left-handed band of these structures can be widened by tailoring gap separation.

Bandwidth also depends on the height of the substrate. The results are depicted in Figure 3.44. The thinner the substrate is, the wider the bandwidth is. However, in this case, both band edges are shifted to expand the left-handed band. The upper band edge is moved towards higher frequencies because, the thinner the dielectric is, the

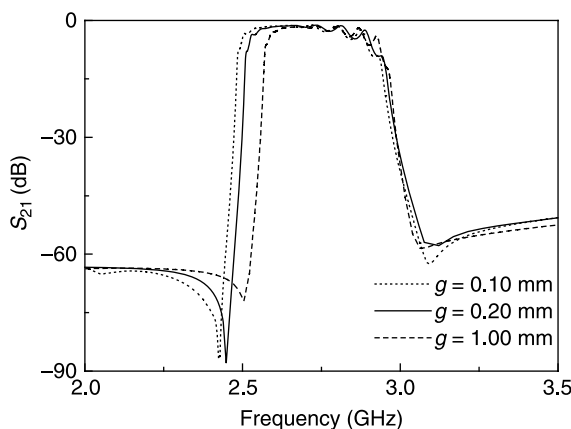


**FIGURE 3.43** Simulated insertion losses for a 10-stage device with different values of gap distance,  $g$ , obtained by means of agilent momentum. The dimensions are: period  $l = 6.4$  mm, strip width  $W = 1.69$  mm. The dimensions of the CSRRs are  $c_{in} = 0.472$  mm,  $c_{out} = 0.391$  mm,  $d = 0.149$  mm and  $r_{ext} = 2.972$  mm. The parameters of the Rogers RO3010 substrate have been considered ( $\epsilon_r = 10.2$ ;  $h = 1.27$  mm). (Source: Reprinted with permission from [37]; copyright 2006, John Wiley & Sons.)



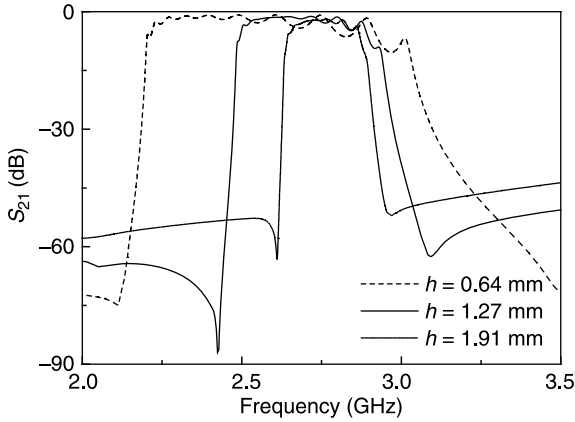


**FIGURE 3.44** Simulated insertion losses for a 10-stage device with different values of substrate height,  $h$ , obtained by means of agilent momentum. The dimensions are period  $l = 6.4$  mm, gap spacing  $g = 0.2$  mm, strip width  $W = 1.69$  mm. The dimensions of the CSRRs are  $c_{in} = 0.472$  mm,  $c_{out} = 0.391$  mm,  $d = 0.149$  mm, and  $r_{ext} = 2.972$  mm. The parameters of the Rogers RO3010 substrate, except thickness, which is the varying parameter, have been considered ( $\epsilon_r = 10.2$ ). (Source: Reprinted with permission from [37]; copyright 2006, John Wiley & Sons.)

higher the resonant frequency of the CSRRs [29], and hence  $f_H$ , becomes. On the other hand, as substrate height is reduced, the coupling capacitance  $C$  is augmented, this having the effect of reducing  $f_L$  (in spite of the fact that  $C_g$  is slightly reduced).

Finally, the effects of varying line width are presented. This modifies both  $C_g$  and  $C$ , and it may slightly affect the resonance frequency of the CSRRs through the influence of the upper metallic strip on  $L_c$  and  $C_c$ . We expect a variation of the lower band edge towards lower frequencies when line width is widened (because both  $C$  and  $C_g$  are expected to increase), and a small (although probably nonnegligible) shift in the upper transition band. This behavior has been verified by electromagnetic simulation (Fig. 3.45).

According to the results shown in this section, it is clear that 1D left-handed structures with moderate bandwidths based on CSRRs can be designed. To enhance bandwidth, thin substrates are preferred, as this favors the possibility of moving away  $f_L$  and  $f_H$ . As long as bandwidth, out-of-band rejection (mainly dependent on the number of stages), and in-band losses can be controlled, these structures can be applied to the synthesis of frequency-selective structures of compact dimensions. Also, these structures can be of interest for the design of artificial transmission lines, where impedance and phase shift can be independently (within certain limits) controlled over wide margins, without the need to manipulate line width and length (as occurs in conventional transmission lines). This has many potential applications, as will be shown in the next chapter.

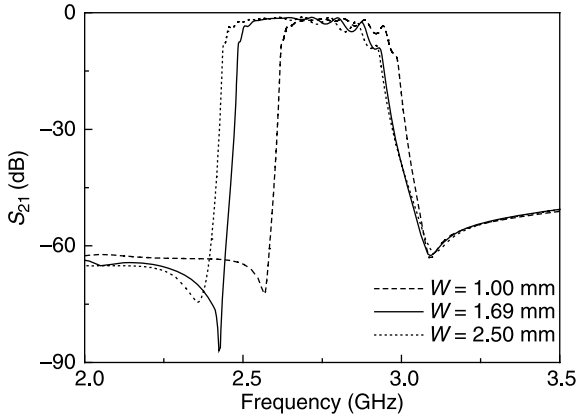


**FIGURE 3.45** Simulated insertion losses for a 10-stage device with different values of strip width,  $W$ , obtained by means of agilent momentum. The dimensions are period  $l=6.4$  mm, gap spacing  $g=0.2$  mm. The dimensions of the CSRRs are  $c_{in}=0.472$  mm,  $c_{out}=0.391$  mm,  $d=0.149$  mm, and  $r_{ext}=2.972$  mm. The parameters of the Rogers RO3010 substrate have been considered ( $\epsilon_r=10.2$ ;  $h=1.27$  mm). (Source: Reprinted with permission from [37]; copyright 2006, John Wiley & Sons.)

### 3.9 COMPARISON BETWEEN THE CIRCUIT MODELS OF RESONANT-TYPE AND DUAL LEFT-HANDED LINES

At the beginning of Section 3.5, it was pointed out that resonant-type and dual<sup>27</sup> transmission lines exhibit similar behavior. In particular, it was mentioned that, as in dual transmission lines, there is also a forward wave band at high frequencies in resonant-type structures. Indeed, in the preceding sections devoted to the synthesis and analysis of SRR- and CSRR-loaded transmission lines, the main interest was on demonstrating the occurrence of left-handedness, and on interpreting this in terms of circuit analysis. However, inspection of the circuit model (unit cell) of a host line loaded with series capacitors and shunt inductors (Fig. 3.3) and those circuits describing the unit cells of SRR loaded (Fig. 3.24) and CSRR loaded (Fig. 3.38) left-handed lines, indicates that similar characteristics may be expected in all cases (obviously with certain singularities that will be highlighted).

Let us start by comparing the circuit of Figure 3.38 (CSRR-loaded left-handed line) to that of Figure 3.3 (dual transmission line). The single difference between

<sup>27</sup>Along this section, by dual line the authors mean a host line loaded with series capacitors and shunt inductors. A composite right-/left-handed behavior arises in such lines, due to the effect of the parasitic elements of the host line. These lines are usually called composite right-/left-handed (CRLH) lines (as was pointed out previously). However, this CRLH behavior is not exclusive to this type of lines. It is also present in resonant-type (i.e., loaded with SRRs or CSRRs) left-handed lines. For this reason we use the term dual to designate  $C-L$  loaded lines.

these circuits is the presence of the coupling capacitance,  $C$ , in the circuit of Figure 3.38. The direct consequence of this is the presence of a transmission zero to the left-hand side of the backward wave band.<sup>28</sup> In the limit of very high coupling ( $C \rightarrow \infty$ ) the transmission zero shifts to the origin and both models tend to be identical. In practice the capacitance  $C$  can be enhanced by decreasing the substrate height (in microstrip configuration). Thus, we may conclude by mentioning that CSRR-loaded left-handed lines implemented in very narrow microstrip substrates can be described by a circuit model that is formally identical to that of the dual transmission line in the region of interest.

Another key aspect to highlight is the composite right-/left-handed (CRLH) behavior of CSRR-loaded lines [39,40]. The origin of such behavior in dual transmission lines was studied in detail in Section 3.2. According to the model of Figure 3.38, this behavior is also expected in CSRR-loaded left-handed lines, because above the resonance frequency of the series resonator (formed by  $L$  and  $C_g$ ), the series impedance is positive (inductive), whereas the shunt admittance is dominated by  $C_c$ . Indeed, balanced CSRR structures can be achieved by merely forcing the series ( $\omega_s = (LC_g)^{-1/2}$ ) and shunt ( $\omega_p = (L_c C_c)^{-1/2}$ ) resonances to be identical.<sup>29</sup> This possibility is demonstrated in Figure 3.46, which depicts the dispersion diagram of a balanced CRLH CSRR-loaded transmission line cell (also included in the figure). As can be seen, the structure is almost balanced (that is, there is a quasi-continuous transition between the left handed and right handed bands).<sup>30</sup> The measured and simulated frequency responses of the cell, also depicted in Figure 3.46, exhibit a very broad transmission band, which is due to the absence of gap between the backward and forward regions.<sup>31</sup> According to these results, it is very clear that CRLH and balanced CRLH transmission lines can be achieved by loading the host line with CSRRs. Also, it is clear that broadband metamaterial transmission lines can be achieved by means of the resonant-type approach. It is interesting to analyze the dependence of the characteristic impedance on frequency for the CRLH CSRR-loaded line. From expression (3.2) and the circuit of Figure 3.38 (including all the circuit parameters), the following expression is obtained (Problem 3.3):

$$Z_B = \sqrt{\frac{L}{C_c} \frac{\left(1 - \frac{\omega_s^2}{\omega^2}\right)}{\left(1 - \frac{\omega_p^2}{\omega^2}\right)} - \frac{L^2 \omega^2}{4} \left(1 - \frac{\omega_s^2}{\omega^2}\right)^2 + \frac{L}{C} \left(1 - \frac{\omega_s^2}{\omega^2}\right)}. \quad (3.60)$$

<sup>28</sup>This transmission zero is of interest for the design of planar filters based on CSRR left-handed lines, as will be discussed in Chapter 4.

<sup>29</sup>The shunt resonance frequency is the frequency that nulls the shunt admittance and it coincides with the intrinsic resonance frequency of the CSRRs. It also coincides with the upper limit of the left-handed band in unbalanced structures (expression 3.57).

<sup>30</sup>Perfect balance is difficult to achieve in practice. Nevertheless, for the structure of Figure 3.46, a continuous transition between the left-handed and right bands is visible in the frequency response.

<sup>31</sup>The measured and simulated (through EM software) frequency responses are wider than that predicted by the circuit model. The reason for this is the inability of the model to properly describe the structure at high frequencies, as is discussed in [39,40].

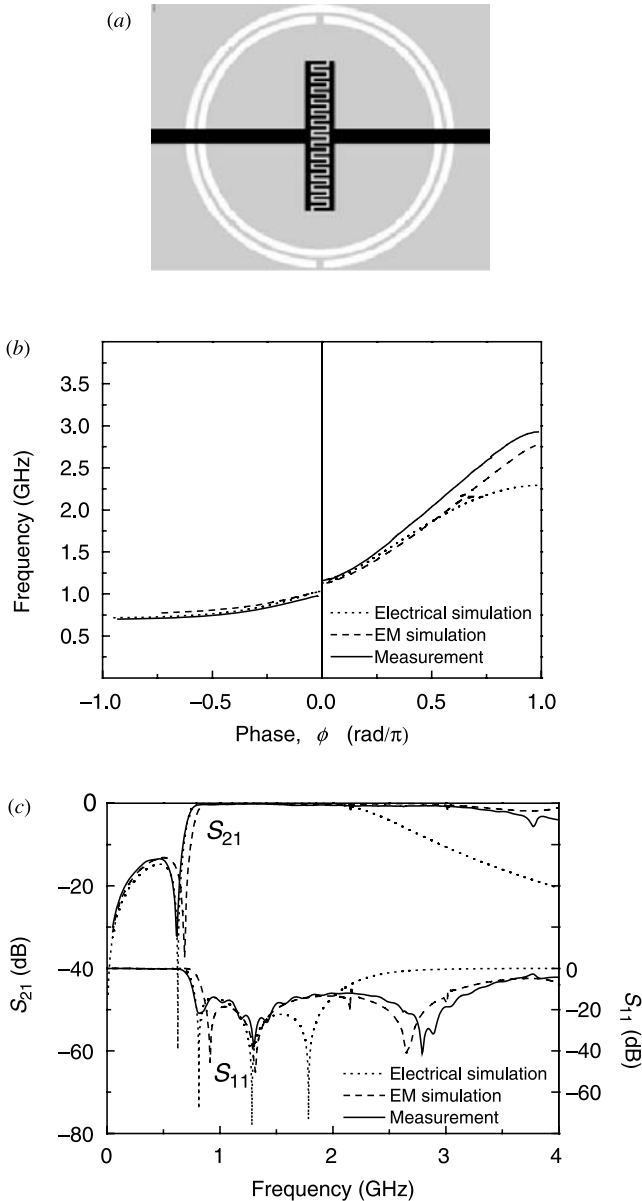


**FIGURE 3.46** Balanced CRLH cell based on a microstrip line loaded with CSRRs (a), dispersion diagram (b) and frequency response (c). The structure has been implemented in the Rogers RO3010 substrate with dielectric constant  $\epsilon_r = 10.2$  and thickness  $h = 1.27$  mm. Dimensions are line width  $W = 0.8$  mm, external radius of the outer ring  $r = 7.3$  mm, ring width  $c = 0.4$  mm, and ring separation  $d = 0.2$  mm; the interdigital capacitor, formed by 28 fingers separated by 0.16 mm, has been used to achieve the required capacitance value. (Source: Reprinted with permission from [39]; copyright 2007, IEEE.)

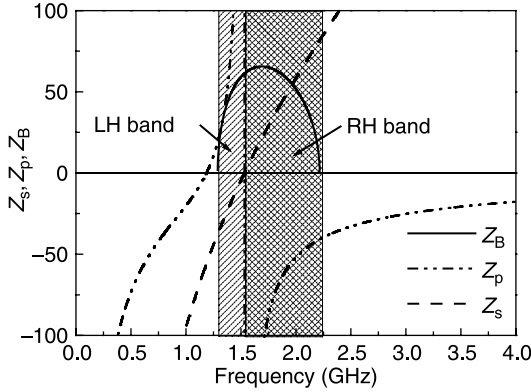


**FIGURE 3.47** Representation of the series,  $Z_s$ , shunt,  $Z_p$ , and characteristic impedance,  $Z_B$ , for a CRLH transmission line corresponding to the model of a balanced CSRR-based structure. Electrical parameters are  $L = 45$  nH,  $C_g = 0.48$  pF,  $C = 10$  pF,  $C_c = 3$  pF,  $L_c = 3$  pF. The depicted values of  $Z_s$  and  $Z_p$  are the reactances. The transition frequency has been set to  $f_o = 1.5$  GHz. (Source: Reprinted with permission from [39]; copyright 2007, IEEE.)

For the balanced case  $\omega_s = \omega_p = \omega_o$ , and the previous expression simplifies to

$$Z_B = \sqrt{\frac{L}{C_c} - \frac{L^2 \omega^2}{4} \left(1 - \frac{\omega_o^2}{\omega^2}\right)^2 + \frac{L}{C} \left(1 - \frac{\omega_o^2}{\omega^2}\right)}. \quad (3.61)$$

This expression is very similar to equation (3.22). The difference is the presence of the last term in the square root of equation (3.61). As for the balanced dual transmission line, the characteristic impedance is null at the extremes of the allowed band, and it varies continuously in between. However, in resonant-type balanced lines loaded with CSRRs, the impedance is maximum above the transition frequency,  $f_o$  (see Problem 3.3). Nevertheless, the impedance variation in the vicinity of the transition frequency is smooth and this is interesting to preserve matching in a wide band. The variation of  $Z_p$ ,  $Z_s$  and  $Z_B$  with frequency for the transmission line model of Figure 3.38 in the balanced case is depicted in Figure 3.47.

With regard to the lumped element model of SRR-loaded left-handed lines (Fig. 3.24b), this can also be considered an extension of the dual transmission line model of Figure 3.3. Both models are identical in the limiting case of  $L'_s \rightarrow \infty$ . However, in practice, it is not possible to achieve high values of  $L'_s$ , because  $M$  is limited and  $C_s$  cannot be made very large (see expression 3.39). In other words, the transmission zero cannot be easily driven to the origin. This is obvious, because this transmission zero directly coincides with the resonance frequency of the SRRs, which is identical to the resonance frequency of the parallel tank

formed by  $L'_s$  and  $C'_s$ . It has already been pointed out in Section 3.6 the CRLH behavior of transmission lines loaded with SRRs and shunt inductors (strips or vias). For SRR-loaded lines, it is also possible to balance these lines. To this end, the structure must be tailored in order to have identical shunt (expression 3.42) and series (expression 3.43) resonance frequencies.

According to the previous comments, dual and resonant-type metamaterial transmission lines are conceptually very similar. The narrow band behavior usually exhibited by SRR- or CSRR-based left-handed lines is not something intrinsic to the approach, but rather due to the difficulty of tailoring the geometry of the lines (resonators and other elements) to the required values to achieve wide left-handed bands. This narrow-band behavior also occurs (though less accentuated) in fully planar dual transmission lines. To obtain wide left-handed bands, lumped elements may be used. Alternatively, to synthesize broad transmission bands, balanced lines can be implemented. These balanced lines are also convenient to ensure impedance matching in a wide band, although, obviously, this band includes a backward and a forward region. The balance condition can also be forced in resonant-type CRLH transmission lines. Hence, it is potentially possible to achieve broadband characteristics by using SRR- and CSRR-loaded lines. In other words, broadband characteristics are not exclusive of the dual transmission line approach.

To end this chapter we would like to compare the lumped element model of SRR-loaded left-handed transmission lines (Fig. 3.24) with the transmission line model of bulk left-handed structures consisting of a combination of SRRs and metallic posts (see Fig. 2.20). This model was described in [41], and it coincides with the model depicted in Figure 3.24*b*. In such a model, the posts are accounted for by means of shunt inductors, whereas SRRs and their magnetic excitation by the incident field are appropriately described by means of series-connected parallel  $LC$  resonators. It was shown in [41] that through the transmission line model depicted in Figure 3.24*b*,<sup>32</sup> the effective permeability and permittivity, as derived from expressions (3.15) and (3.16), coincide with the effective permittivity and permeability of the SRR/wire medium, reported in [42]:

$$\varepsilon_{\text{eff}} = 1 - \frac{\omega_p}{\omega^2} \quad (3.62)$$

$$\mu_{\text{eff}} = 1 - \frac{F \omega_0^2}{\omega^2 - \omega_0^2 - j\omega\Gamma}, \quad (3.63)$$

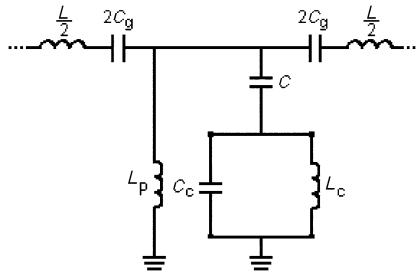
where  $\omega_p$  is the plasma frequency of the wire medium,  $\omega_0$  is the resonance frequency of the SRRs,  $F$  is the fractional area occupied by the SRRs in the unit cell, and  $\Gamma$  is the dissipation factor, which depends on the conductor losses in the SRRs. It is interesting to highlight that by modeling the SRR-loaded

<sup>32</sup>In the transmission line model of the SRR/wire medium considered in [41], losses have been included by means of a resistance, disposed in parallel with the resonant tank describing the SRR.

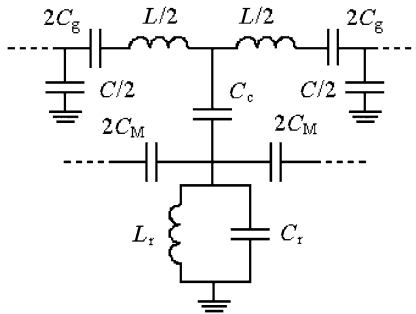
left-handed line by means of the circuit of Figure 3.24a, where the lumped elements have a very clear physical interpretation, we finally obtain (through transformation 3.35–3.41) a circuit model (Fig. 3.24b) that is identical to that circuit needed to obtain the effective electromagnetic parameters ( $\epsilon_{\text{eff}}$  and  $\mu_{\text{eff}}$ ) of the SRR/wire medium. This means that the bulk SRR/wire media and the planar SRR-loaded left-handed lines are equivalent structures, because they are described by identical transmission line circuit models. Thus, the models of Figure 3.24 and the transformation equations (3.35–3.41) between them bridge the gap between the bulk and transmission line approaches for the analysis of SRR-based left-handed metamaterials.

## PROBLEMS

- 3.1. Equivalence between plane wave propagation in homogeneous dielectrics and TEM wave propagation in transmission lines.** Demonstrate the equivalence between plane wave propagation in homogeneous isotropic dielectrics and TEM wave propagation in transmission lines given by expressions (3.15) and (3.16), and use it to obtain the effective permittivity and permeability of ideal lossless conventional, dual, and CRLH transmission lines.
- 3.2. Phase constant of a CRLH line.** Obtain the phase constant of a CRLH transmission line in the long wavelength limit (expression 3.29) by expanding expression (3.21) in a Taylor series.
- 3.3. Analysis of the CSRR-based left-handed lines by including the effects of the line inductance.** The CSRR-based left-handed transmission line is described by the lumped element model represented in Figure 3.38. In this model, the series inductance of the line has been neglected. This can be done provided (a) the right-handed band is significantly separated from the left-handed band and (b) the interest is only focused on the left-handed transmission band. However, in a general case, it may be of interest to exploit the composite right-/left-handed behavior of such lines. In this case the complete circuit model (with  $L$  included) must be considered. From this model, obtain the expressions for the characteristic impedance and phase constant. Simplify these expressions for the balance condition and determine in this case where the characteristic impedance reaches its maximum.
- 3.4. Hybrid model of left-handed lines based on CSRRs.** The following circuit model corresponds to the hybrid approach of a left-handed transmission line (basic cell), because it describes a transmission line loaded with both CSRRs (modeled by  $C_c$  and  $L_c$ ) and shunt inductors ( $L_p$ ). The series capacitances  $C_g$  are responsible for the negative effective permeability of the line, as occurs in the dual transmission line and resonant-type approach. For this model, obtain the different transmission regions indicating if propagation is backward or forward.



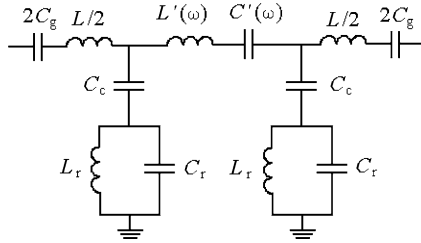
- 3.5. Repeat the previous problem, excluding the capacitance  $C_c$ .
- 3.6. **CRLH lines based on SRRs.** For the circuit model given in Figure 3.24b, the dispersion relation has been analytically obtained (expression 3.45). Derive this expression and demonstrate that above the left-handed pass band, there exists a forward wave transmission band. Obtain the conditions that are necessary to suppress the frequency gap between the left-handed and right-handed bands (balance condition).
- 3.7. **Relationship between SRR and CSRR parameters.** Demonstrate that for infinitely thin perfect conducting screens, and in the absence of any dielectric substrate, the parameters of the circuit models for the SRRs and the CSRRs (Fig. 3.28) are related by  $C_c = 4(\epsilon_o/\mu_o)L_s$  and  $C_o = 4(\epsilon_o/\mu_o)L_o$ .
- 3.8. **CSRR-based left-handed lines with inter-resonator coupling.** A generalization of the equivalent circuit model of a left-handed transmission line implemented by means of CSRRs is given as follows [36]:



This model takes into account not only the presence of the CSRRs coupled to the host line, but also inter-resonator coupling (important in tiny spaced square-shaped or rectangular CSRRs), which is modeled by means of the mutual capacitances  $C_M$ . Moreover, this model accounts for those situations where the distance between adjacent resonators is significant (negligible coupling) and the capacitance of the host line corresponding to the regions where CSRRs are not present,  $C$ , must be considered. Assuming that CSRRs are closely spaced ( $C$  negligible), but coupling between



adjacent resonators is small, demonstrate that the previous model can be transformed to the following:



where  $L'(\omega)$  and  $C'(\omega)$  are frequency-dependent inductance and capacitance, respectively, related to the second and first term of the following impedance:

$$Z_{eq} = \frac{1}{j\omega C_g} \frac{[1 - L_r(C_C + 2C_M + C_r)\omega^2][L_r(C_C + C_r)\omega^2 - 1]}{LL_r^2 C_C^2 C_M \omega^6 + [1 - L_r(C_C + 2C_M + C_r)\omega^2][L_r(C_C + C_r)\omega^2 - 1] - L_r^2 C_C^2 C_M \omega^4 / C_g} + j\omega L \frac{\omega C_g [1 - L_r(C_C + 2C_M + C_r)\omega^2][L_r(C_C + C_r)\omega^2 - 1]}{LL_r^2 C_C^2 C_M C_g \omega^7 + \omega C_g [1 - L_r(C_C + 2C_M + C_r)\omega^2][L_r(C_C + C_r)\omega^2 - 1] - L_r^2 C_C^2 C_M \omega^5}$$

## REFERENCES

1. A. K. Iyer and G. V. Eleftheriades “Negative refractive index metamaterials supporting 2-D waves.” *IEEE-MTT Int’l Microwave Symp.*, vol. 2, Seattle, WA, pp. 412–415, June 2002.
2. A. A. Oliner “A periodic-structure negative-refractive-index medium without resonant elements.” *URSI Digest, IEEE-AP-S USNC/URSI National Radio Science Meeting*, San Antonio, TX, pp. 41, June 2002.
3. C. Caloz and T. Itoh “Application of the transmission line theory of left-handed (LH) materials to the realization of a microstrip LH transmission line.” *Proc. IEEE-AP-S USNC/URSI National Radio Science Meeting*, vol. 2, San Antonio, TX, pp. 412–415, June 2002.
4. S. Ramo, J. R. Whinnery, and T. Van Duzer, *Fields and Waves in Communication Electronics*. Wiley, New York, 1994.
5. J. A. Kong *Electromagnetic Wave Theory*. EMW Pub., 2000.
6. D. M. Pozar *Microwave Engineering*. Addison-Wesley, Reading, MA, 1993.
7. C. Caloz and T. Itoh “Novel microwave devices and structures based on the transmission line approach of metamaterials.” *IEEE-MTT Int’l Microwave Symp.*, vol. 1, Philadelphia, pp. 195–198, June 2003.

8. C. Caloz and T. Itoh *Electromagnetic Metamaterials: Transmission Line Theory and Microwave Applications*. Wiley, Hoboken, NJ, 2006.
9. C. Caloz, H. Okabe, T. Iwai, and T. Itoh "Transmission line approach of left handed materials." *USNC/URSI National Radio Science Meeting*, San Antonio, TX, vol. 1, pp. 39, June 2002.
10. A. Grbic and G. V. Eleftheriades "Experimental verification of backward wave radiation from a negative refractive index metamaterial." *J. Appl. Phys.*, vol. 92, pp. 5930–5935, November 2002.
11. G. V. Eleftheriades and K. G. Balmain *Negative Refraction Metamaterials: Fundamental Principles and Applications*. Wiley, Hoboken, NJ, 2005.
12. R. Shelby, D. R. Smith, and S. Schultz "Experimental verification of a negative index of refraction." *Science*, vol. 292, pp. 77, 2001.
13. G. V. Eleftheriades, A. K. Iyer, and P. C. Kremer "Planar negative refractive index media using periodically L-C loaded transmission lines." *IEEE Trans. Microwave Theory Tech.*, vol. 50, pp. 2702–2712, December 2002.
14. A. K. Iyer, P. C. Kremer, and G. V. Eleftheriades "Experimental and theoretical verification of focusing in a large, periodically loaded transmission line negative refractive index metamaterial." *Opt. Express*, vol. 11, pp. 696–708, April 2003.
15. A. Grbic and G. V. Eleftheriades "Overcoming the diffraction limit with a planar left handed transmission line lens." *Phys. Rev. Lett.*, vol. 92, paper 117403, March 2004.
16. A. Sanada, C. Caloz, and T. Itoh "Planar distributed structures with negative refractive index." *IEEE Trans. Microwave Theory Tech.*, vol. 52, pp. 1252–1263, April 2004.
17. D. Sievenpiper, L. Zhang, R. F. J. Broas, N. G. Alexopolous, and E. Yablonovitch "High-impedance electromagnetic surfaces with a forbidden frequency band." *IEEE Trans. Microwave Theory Tech.*, vol. 47, pp. 2059–2074, November 1999.
18. A. Grbic and G. V. Eleftheriades "An isotropic three-dimensional negative refractive index transmission line metamaterial." *J. Appl. Phys.*, vol. 98, paper 043106, August 2005.
19. W. J. R. Hofer, P. P. M. So, D. Thompson, and M. Tentzeris "Topology and design of wide band 3D metamaterials made of periodically loaded transmission line arrays." *IEEE MTT Int. Microwave Symposium Digest*, pp. 313–316, Long Beach, CA, June 2005.
20. F. Martín, F. Falcone, J. Bonache, R. Marqués, and M. Sorolla "Split ring resonator based left handed coplanar waveguide." *Appl. Phys. Lett.*, vol. 83, pp. 4652–4654, December 2003.
21. I. Gil, J. Bonache, J. García-García, F. Falcone, and F. Martín "Metamaterials in microstrip technology for filter applications." *Proc. APS-URSI*, Washington, July 2005.
22. F. Falcone, F. Martín, J. Bonache, R. Marqués, and M. Sorolla "Coplanar waveguide structures loaded with split ring resonators." *Microwave Opt. Tech. Lett.*, vol. 40, pp. 3–6, January 2004.
23. R. Marqués, F. Mesa, J. Martel, and F. Medina "Comparative analysis of edge and broad-side couple split ring resonators for metamaterial design. Theory and experiment." *IEEE Trans. Antennas Propag.*, vol. 51, pp. 2572–2582, October 2003.
24. F. Falcone, F. Martín, J. Bonache, R. Marqués, T. Lopetegi, and M. Sorolla "Left handed coplanar waveguide band pass filters based on bi-layer split ring resonators." *IEEE Microwave Wirel. Comp. Lett.*, vol. 14, pp. 10–12, January 2004.

25. R. Marqués, F. Medina, and R. Rafii-El-Idrissi "Role of bianisotropy in negative permeability and left handed metamaterials." *Phys. Rev. B*, vol. 65, paper 144440, April 2002.
26. J. D. Baena, R. Marqués, and F. Medina "Artificial magnetic metamaterial design by using spiral resonators." *Phys. Rev. B*, vol. 69, paper 14402 (2004).
27. F. Falcone, F. Martín, J. Bonache, M. A. G. Laso, J. García-García, J. D. Baena, R. Marqués, and M. Sorolla "Stop band and band pass characteristics in coplanar waveguides coupled to spiral resonators." *IEEE Microwave Opt. Tech. Lett.*, vol. 42, pp. 386–388, September 2004.
28. G. Zhang, F. Huang, and M. J. Lancaster "Superconducting spiral filters with quasi-elliptic characteristic for radio astronomy." *IEEE Trans. Microwave Theory Tech.*, vol. 53, pp. 947–951, March 2005.
29. J. D. Baena, J. Bonache, F. Martín, R. Marqués, F. Falcone, T. Lopetegi, M. A. G. Laso, J. García, I. Gil, and M. Sorolla "Equivalent circuit models for split ring resonators and complementary split rings resonators coupled to planar transmission lines." *IEEE Trans. Microwave Theory Tech.*, vol. 53, pp. 1451–1461, April 2005.
30. B. C. Wadell *Transmission Line Design Handbook*. Artech House, Norwood, MA, 1991.
31. F. Falcone, T. Lopetegi, J. D. Baena, R. Marqués, F. Martín, and M. Sorolla "Effective negative- $\epsilon$  stop-band microstrip lines based on complementary split ring resonators." *IEEE Microwave Wirel. Comp. Lett.*, vol. 14, pp. 280–282, June 2004.
32. H. G. Booker "Slot aerials and their relation to complementary wire aerials (Babinet's principle)." *J. IEE*, vol. 93, pt. III–A, no. 4, pp. 620–626, March–May 1946.
33. G. A. Deschamps "Impedance properties of complementary multiterminal planar structures." *IRE Trans. Antennas Propag.*, vol. AP–7, pp. 371–378, December 1959.
34. W. J. Getsinger "Circuit duals on planar transmission media." *1983 IEEE MTT-S International Microwave Symposium*, Boston, May–June 1983, pp. 154–156.
35. I. Bahl and P. Bhartia *Microwave Solid State Circuit Design*. Wiley, New York, 1988.
36. I. Gil, J. Bonache, M. Gil, J. García-García, F. Martín, and R. Marqués "Accurate circuit analysis of resonant type left handed transmission lines with inter-resonator's coupling." *J. Appl. Phys.*, vol. 100, paper 074908-1-10, October 2006.
37. M. Gil, J. Bonache, I. Gil, J. García-García, and F. Martín "On the transmission properties of left handed microstrip lines implemented by complementary split rings resonators." *Int. Numerical Modelling: Electronic Networks, Devices and Fields*, vol. 19, pp. 87–103, 2006.
38. J. Bonache, M. Gil, I. Gil, J. Garcia-García, and F. Martín "On the electrical characteristics of complementary metamaterial resonators." *IEEE Microwave Wirel. Comp. Lett.*, vol. 16, pp. 543–545, October 2006.
39. M. Gil, J. Bonache, J. Selga, J. García-García, and F. Martín "Broadband resonant type metamaterial transmission lines." *IEEE Microwave Wirel. Comp. Lett.*, vol. 17, pp. 97–99, February 2007.
40. I. Gil, J. Bonache, M. Gil, J. García-García, and F. Martín "On the left handed and right handed transmission properties of microstrip lines loaded with complementary split rings resonators." *IEEE Microwave Opt. Tech. Lett.*, vol. 48, pp. 2508–2511, December 2006.

41. G. V. Eleftheriades, O. Siddiqui, and A. Iyer "Transmission line models for negative refractive index media and associated implementations without excess resonators." *IEEE Microwave Wirel. Comp. Lett.*, vol. 13, pp. 51–53, February 2003.
42. D. R. Smith and N. Kroll "Negative refractive index in left handed materials." *Phys. Rev. Lett.*, vol. 85, pp. 2933–2936, October 2000.



# Microwave Applications of Metamaterial Concepts

---

## 4.1 INTRODUCTION

The main aim of this chapter is to highlight the potential of metamaterials and metamaterial-based structures for the synthesis and design of new microwave devices and subsystems. Improved performance and novel functionalities, due to the unique and controllable electromagnetic properties of these structures, as well as device miniaturization, because of the small electrical size of their constitutive elements, are the main areas where metamaterial concepts may produce a major impact. In the following subsections, several applications of metamaterials will be considered and exhaustively analyzed. Although this textbook is mostly oriented towards the resonant-type approach of metamaterials, the authors wish to provide a wide overview of metamaterial applications, including representative achievements of other authors. Hence, several applications will be illustrated through implementations based on the dual transmission line concept.

As metamaterials are frequency-selective structures by nature, their application to the design of compact microwave filters and diplexers seems to be straightforward. Thus, the first subsection of this chapter is focused on the design of microwave filters. Because such devices require resonant elements, the preferred (although not exclusive) approach for the synthesis of filters and diplexers based on one-dimensional (1D) metamaterials is the resonant-type approach. It will be shown in Section 4.2 that SRRs and CSRRs are useful *particles* for the synthesis of narrow-band and wide-bandpass filters (also including bandpass filters for ultrawide-band—UWB—applications). A systematic methodology for the design of planar filters subject to specifications will be presented. Finally, reconfigurable filters based on varactor-loaded metamaterials will also be included in this section.

Probably the most outstanding property of metamaterial transmission lines is the controllability of the electrical characteristics. This includes the dispersion diagram<sup>1</sup> as well as the characteristic impedance of such artificial lines. Owing to this control, it is possible to design components with superior performance compared to conventional implementations (such as enhanced bandwidth devices), components based on new functionalities (such as dual band components), or microwave devices with small dimensions. In such devices, the conventional transmission lines and stubs are substituted by *metalines*, resulting in *metacircuits* with smaller dimensions and/or improved performance. These metamaterial based components will be discussed and studied in Section 4.3. It will also be shown in this section that coupled lines based on metamaterials are useful to improve the performance/dimensions of coupled-line couplers.

Radiated wave applications, due to the unusual dispersion diagram of left-handed or CRLH metamaterial transmission lines, will also be considered in this chapter. It will be shown that these structures may produce backfire (analogous to reversed Cerenkov radiation in left-handed media [1]) to endfire radiation, including the possibility of electronically scanning the radiation angle by tuning through varactor diodes. Implementations based on both the dual transmission line concept and the resonant-type approach will be provided.

## 4.2 FILTERS AND DIPLEXERS

It was shown in Chapter 3 that transmission lines simply loaded with SRRs or CSRRs are able to inhibit signal propagation in a narrow band in the vicinity of resonance [2,3]. This was interpreted as being due to the negative effective permeability or permittivity of such 1D artificial transmission media. It was also demonstrated that this behavior can be switched to a passband by merely introducing additional elements to the structures. Thus, in SRR-loaded lines, an allowed band with backward-wave propagation can be generated by introducing shunt-connected strips or vias [4]. These elements provide the required negative effective permittivity up to a frequency (plasma frequency) that can be tailored through their dimensions and separation. As long as this frequency is set beyond the resonance frequency of the SRRs, a frequency region where both electromagnetic parameters (permeability and permittivity) are negative arises, and hence a left-handed band. In artificial lines loaded with CSRRs, the additional elements must provide a negative-valued effective permeability (because the negative permittivity is obtained by means of the CSRRs), and this is achieved by etching series gaps to the line (as discussed in Chapter 3). The result is also a narrow band with negative wave propagation [5].

<sup>1</sup>In general, the dispersion characteristics in conventional transmission lines depend on both the substrate and line dimensions (width). However, it is not possible to tailor these characteristics as desired to achieve certain requirements. In metamaterial transmission lines, the dispersion diagram is determined by the characteristics of the host line and loading elements. This major number of line parameters makes it possible to engineer such artificial lines in order to obtain the required characteristics (within certain limits). For this reason, the design of microwave components based on these artificial transmission lines can be called *dispersion engineering*.

In spite of their small dimensions, these structures have serious drawbacks for their practical applications as stopband or bandpass filters. The single negative SRR- or CSRR-loaded lines exhibit highly selective stopbands with a rejection level depending on the number of stages [2]. However, it is difficult to control the width of the forbidden band. This depends on the distance between adjacent resonators, because interresonator coupling enhances this gap. However, in practice, this coupling is very limited, and no substantial control on device gap width is achieved by this means. As bandpass structures, the double-negative artificial lines considered in Chapter 3 also exhibit some limitations. Namely, the typical frequency responses measured on these left-handed lines are very selective at the lower edge of the band, due to the presence of a transmission zero, but the transition band is smooth at the upper band edge [4,5]. The frequency response is thus asymmetric, and the first spurious band may lie close to the passband of interest. On the other hand, bandwidth cannot be easily controlled and it is difficult to achieve wide bands. Depending on the applications, the left-handed transmission lines studied in Chapter 3 may suffice. However, in other applications, bandwidths beyond those that may be achievable by means of the cited structures, or frequency responses with wide stopbands, to mention some typical needs, may be required. The purpose of this section is to study how the structures presented in Chapter 3 can be modified in order to obtain compact filters based on SRRs or CSRRs with improved performance. As will be shown, it is possible to design both stopband and bandpass filters with small dimensions and electrical characteristics comparable to or superior than those that may be obtained by means of conventional distributed approaches. In the next subsection, the implementation of stopband filters with controllable gap width is considered. After that, the implementation of bandpass filters will be analyzed. The preferred strategies to generate both narrow and wide bands will be discussed, including a design methodology based on the generalized bandpass filter network. Also included in this study will be the implementation of microwave diplexers based on CSRRs. The section devoted to filters will end with a subsection focused on reconfigurable metamaterial transmission lines and their application to tunable filters.

### 4.2.1 Stopband Filters

Stopband filters are typically of interest in microwave engineering for the suppression of undesired responses or for the elimination of interfering signals. As has been indicated previously, single negative transmission lines based on SRRs or CSRRs are rejection band structures that produce reasonable suppression levels with small dimensions. This is so because the elemental cell is very effective in inhibiting signal propagation and is electrically small. However, for certain applications, the forbidden bands required are wider than those achievable by cascading several SRR or CSRR stages. To overcome this limitation, we may take advantage of the high reflectivity of the particles considered, and cascade several resonators tuned at different frequencies over the frequency interval of interest. To this end, we may simply scale up and down the dimensions of the SRRs (or CSRRs), or simply increase or decrease their radius. Following this idea, it is possible to substantially enhance the



width of the forbidden band. This has been driven to practice in both microstrip and coplanar waveguide technologies by using SRRs and CSRRs [6–8]. Figure 4.1 shows a multiple-tuned SRR-loaded CPW structure with five ring pairs. Tuning has been implemented in this case by increasing the inner radius of the SRRs in 0.05 mm step increments and leaving  $c$  and  $d$  unaltered (as compared to the SRR geometry of Fig. 3.15). The simulated and measured frequency responses, depicted in Figure 4.1, show that the rejected band broadens towards lower frequencies. This is expected, because an increment of  $r$  has the effect of decreasing the resonant frequency of the SRRs. The pronounced cutoff at either side of the gap and the absence of significant insertion losses in the pass band is noteworthy. This is important in using SRRs for the elimination of undesired frequencies in CPW circuits.

The application of the multituning concept to SRR-loaded microstrip lines is also possible. In this case, square-shaped SRRs are preferred in order to enhance magnetic coupling between line and rings [7]. Figure 4.2 shows a possible implementation of such a multituned structure. The host line is designed to exhibit a  $50\ \Omega$  impedance, and the SRR dimensions, indicated in the caption, have been varied by scaling up and down the geometry. The result is a wide stopband of approximately 1 GHz

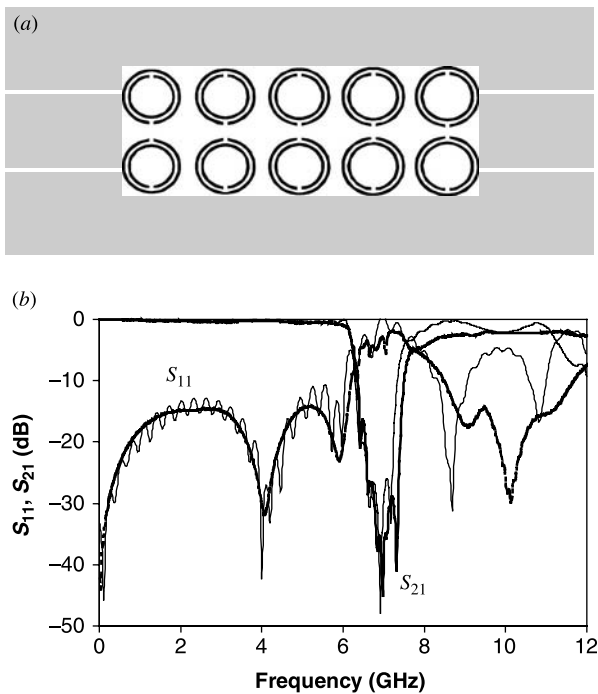


**FIGURE 4.1** Layout (a), simulated (thin line), and measured (bold line) frequency responses (b) of the multituned SRR-CPW stopband filter. The length of the active region is 4 cm. The dimensions of the smallest SRRs are  $c = d = 0.2$  mm, internal radius  $r = 1.3$  mm. For the other SRRs,  $r$  has been incremented in 0.05 mm steps, and  $c$  and  $d$  have been left unaltered. (Source: Reprinted with permission from [6]; copyright 2003, IEEE.)

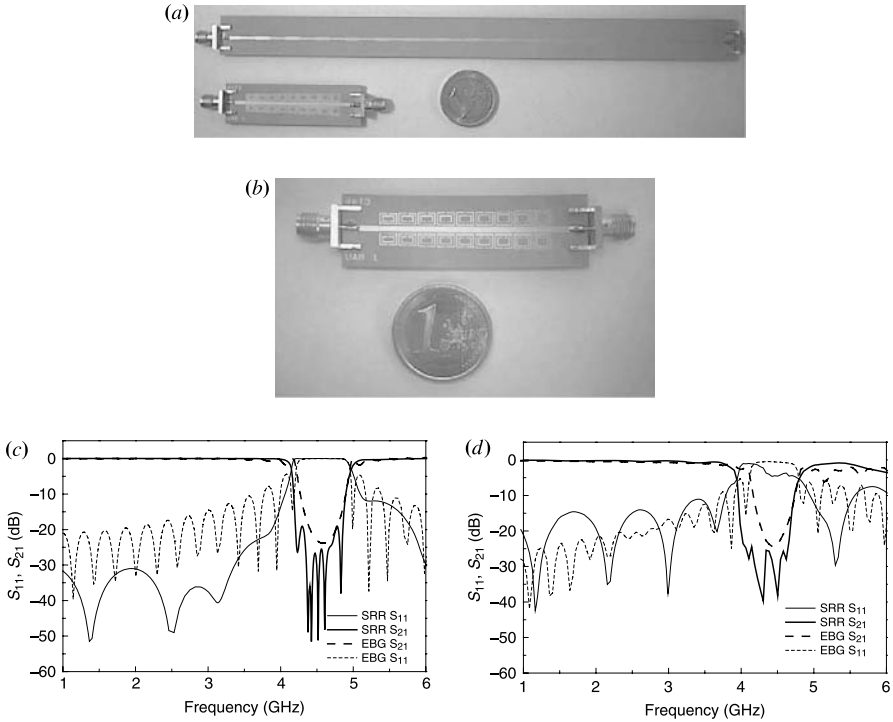


**FIGURE 4.2** Multi-tuned SRR-based microstrip stopband filter compared to an EBG implemented by varying the strip width of a microstrip line (a). Zoom view of the SRR-based structure (b), simulated frequency responses (c), and measured frequency responses (d). The separation between concentric rings and their width are  $c = d = 0.3$  mm for all SRRs. The larger SRRs have an external edge (in the direction orthogonal to the line) of  $l_o = 3.55$  mm, and the smaller rings,  $l_o = 2.7$  mm (tuning has been applied to this parameter). For all SRRs, the external edge in the direction of the line is  $l_1 = 4.1$  mm. Finally, the strip line width is  $W = 1.17$  mm and the distance to SRRs (outer edges) is 0.3 mm. The total length of the device is 39.3 mm, which corresponds to approximately  $1.6\lambda$  ( $\lambda$  being the signal wavelength at the central frequency of the forbidden band). The structures have been fabricated on the Rogers RO3010 substrate ( $\epsilon_r = 10.2$ ,  $h = 1.27$  mm). (Source: Reprinted with permission from [7]; copyright 2005, John Wiley & Sons.)

centered at 4.5 GHz, as can be seen in the simulated and measured frequency responses, shown in Figure 4.2c and d. For comparison purposes, also included in this figure is an electromagnetic bandgap (EBG)<sup>2</sup> transmission line, which has been designed to produce comparable rejection and gap width. The required

<sup>2</sup>EBGs are periodic structures able to inhibit signal propagation at certain frequencies and/or directions [9,10]. They can be three-, two- or one-dimensional structures, and one particular case for the latter category corresponds to EBG transmission lines, where typically the ground plane [11] or the conductor strip [12] are periodically microstructured to achieve the required properties (for instance by drilling holes in the ground plane [13], or by periodically modulating line width and hence line impedance [12,14–17]).

number of stages in the EBG structure (with linewidth modulation) is much higher. Because the period of the EBG structure scales with frequency (namely, it must be set to half the signal wavelength at the central frequency of the stopband), the resulting dimensions are huge. Therefore, compared to EBG transmission lines, the approach introduced in this chapter, and based on SRRs, seems to be more effective not only in terms of miniaturization but also to achieve superior performance [7].

As elements able to generate a negative effective permittivity, CSRRs are also expected to produce controllable stopbands when etched in planar transmission lines and tuned at different frequencies [8]. Examples of such structures implemented in microstrip and CPW technology are depicted in Figures 4.3 and 4.4, respectively. For the CSRR-loaded microstrip line (Fig. 4.3), rectangular-shaped CSRRs are etched in the ground plane under the conductor strip, where a significant component of the electric field in the axial direction of the rings is present. This is necessary to achieve high electric coupling between line and CSRRs, which is in turn of interest to obtain high levels of rejection in the forbidden band. As in the previous illustrative examples, the host line must be matched to the ports to minimize insertion losses in the allowed band. The relevant dimensions of the structure are indicated in the caption. The measured frequency response of this structure, which is also depicted in Figure 4.3, reveals that rejection above 20 dB can be achieved within a 25% fractional band. For the CPW structure of Figure 4.4, similar levels of rejection can be achieved. In this case, however, the relative gap width is narrower, because a smaller number of CSRRs has been used. The reason is that CSRRs have been

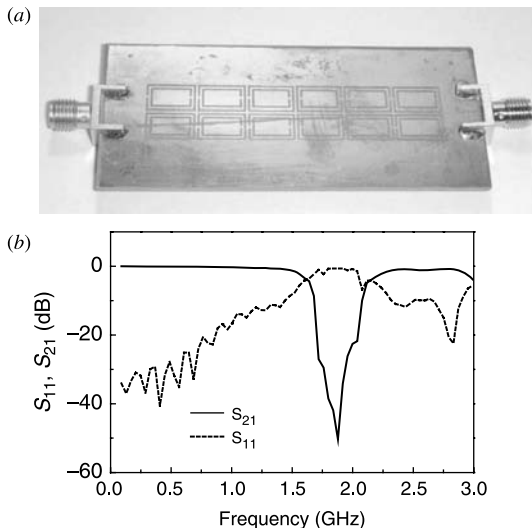


**FIGURE 4.3** 50- $\Omega$  microstrip line with square-shaped CSRR etched in the ground plane (a) and measured frequency response (b).  $c = d = 0.4$  mm and the external edges of the CSRRs have been tuned in the vicinity of  $9.4 \text{ mm} \times 5.8 \text{ mm}$ . The structure has been fabricated on the Rogers RO3010 substrate ( $\epsilon_r = 10.2$ ,  $h = 1.27$  mm). (Source: Reprinted with permission from [8]; copyright 2005, IEEE.)

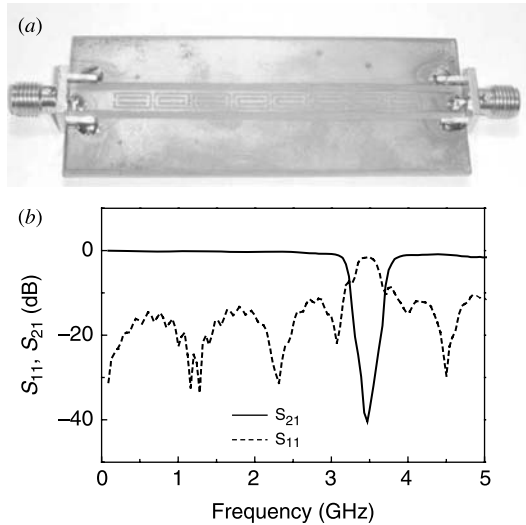


**FIGURE 4.4** CPW stopband structure with CSRRs etched in the central strip (a), and measured frequency response (b). Ring dimensions are  $c = d = 0.4$  mm and external edges are tuned in the vicinity of  $6.6 \text{ mm} \times 3.6 \text{ mm}$ . The structure has been fabricated on the Rogers RO3010 substrate ( $\epsilon_r = 10.2$ ,  $h = 1.27$  mm). (Source: Reprinted with permission from [8]; copyright 2005, IEEE.)

etched in the central strip. This represents the optimum procedure to save layout area, because the ground planes are maintained unaltered. This idea can find practical application, as will be explained later.

To summarize, it has been shown that it is possible to implement quasiperiodic artificial transmission lines, loaded with SRRs or CSRRs, where, due to their capability to inhibit signal propagation within a limited frequency interval, rejection bands with controllable gap width can be generated. The most relevant characteristic of these structures is their size, which can be made small on account of the subwavelength nature of the constitutive elements (SRRs or CSRRs). This size can be optimized by using other topologies discussed in Chapter 2, such as the BC-SRR, the SR, and so on. In the next subsection, the application of these concepts to improve the frequency response of conventional distributed filters (through the suppression of undesired spurious bands) is explored.

#### 4.2.2 Planar Filters with Improved Stopband

The presence of spurious bands is an important limitation of microwave filters implemented by means of distributed elements [18]. These undesired frequency bands can seriously degrade filter performance and may be critical in certain applications that require huge rejection bandwidths. Unfortunately, for most filter implementations the first spurious band is relatively close to the frequency region of interest. For example, in coupled line bandpass filters, the first spurious band appears at the first harmonic of the central frequency ( $2f_0$ ), and it is a consequence

of the different phase velocities of the even and odd modes supported by the coupled lines. In capacitively (gap) or inductively coupled resonator bandpass filters, an undesired band is also inherently present at  $2f_o$  due to the resonance condition at this frequency. Finally, the stopband in stepped-impedance lowpass filters is limited by the presence of the first spurious band, which is typically too close to the cutoff frequency. The rejection of these undesired frequency bands has been a subject of interest for filter designers for years. Traditional techniques include the use of half-wavelength short-circuit stubs, chip capacitors or cascaded stopband filters. However, these techniques are either narrow band, increase device area, or introduce significant insertion losses. In coupled-line filters, several approaches based on modified structures, aimed at obtaining equal modal phase velocities, have been proposed as a means to improve out-of-band filter performance [19–22]. These approaches are very effective, but they are also very specific (that is, for application in parallel coupled-line filters).

Based on the concept of EBGs [9,10], numerous works have been devoted to the suppression of harmonics in a wide variety of microwave circuits, including passives [12,17,23] and actives [24]. Apart from this versatility, EBGs can be integrated within the device active region, thus avoiding the need to cascade additional stages [12,17,23]. This is an important property for optimizing final layout area. Although effective, frequency selectivity in EBG structures is based on their periodicity (Bragg effect), and several stages are required (typically 6 or 7) to obtain significant rejection levels. As the EBG period scales with wavelength (Bragg condition), the required dimensions of the structure might be too big for certain applications (in particular at moderate or low frequencies). Moreover, EBGs do not provide an easy way to control gap width [25]. Nevertheless, EBG structures have been successfully applied to the elimination of multiple spurious bands in microstrip bandpass filters, with measured rejection levels above 30dB up to  $5f_o$  [23].

An alternative to the previously cited approaches for the elimination of spurious frequency bands in distributed filters is the use of SRRs or CSRRs. Their small electrical size, rejection efficiency, and versatility (stopband filters based on these particles have been demonstrated in both microstrip and CPW technology [6,8]) make these elements very attractive to achieve effective spurious suppression with minimum area increase. Such a possibility is explored in this subsection. The main advantage of the approach, as with EBGs, is the fact that SRRs and CSRRs can be etched within the active region of the devices. Namely, it is not necessary to cascade the SRRs or the CSRRs at the input or output access lines. This represents an optimum design in terms of area saving. To illustrate the efficiency of SRRs and CSRRs for the elimination of spurious bands and their versatility, several illustrative examples are provided. The first one is a parallel coupled-line bandpass filter implemented in microstrip technology [8]. The layout of the device, a third-order Butterworth bandpass filter with a central frequency of  $f_o = 2.4$  GHz and 10% fractional bandwidth, is depicted in Figure 4.5. Rectangular SRRs are etched adjacent to the coupled lines in order to reject the first and second spurious bands. The multiple tuning procedure explained in the previous subsection has been used, although final SRR geometries have been determined by means of an optimization

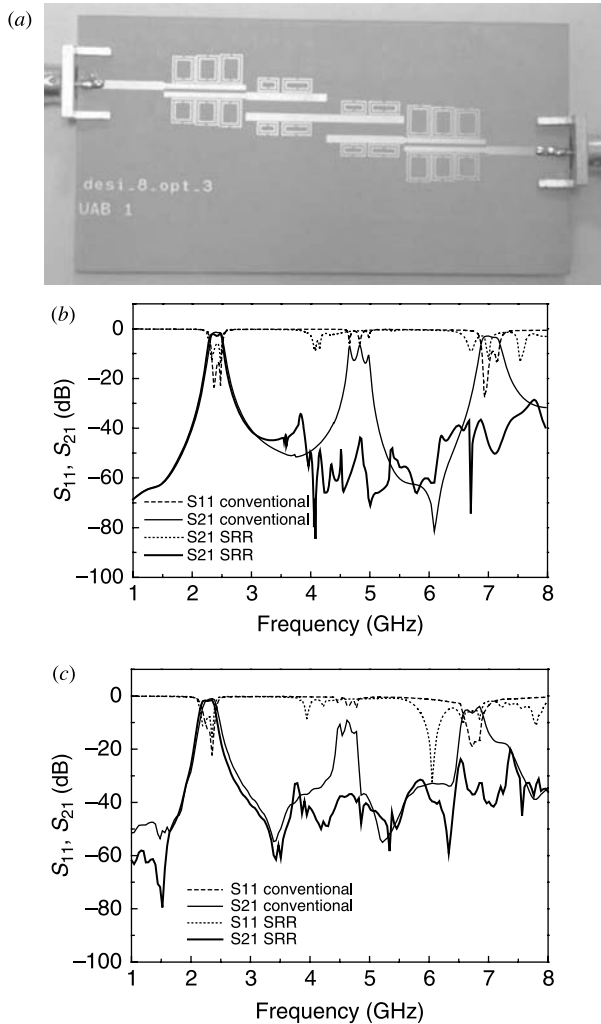


**FIGURE 4.5** (a) SRR coupled-line microstrip bandpass filter. (b) Simulated frequency response compared to that obtained in the device without rings. (c) Measured frequency responses. The device has been fabricated on the Rogers RO3010 substrate (thickness  $h = 1.27$  mm, dielectric constant  $\epsilon_r = 10.2$ ) by means of a standard photo/mask etching technique. (Source: Reprinted with permission from [8]; copyright 2005, IEEE.)

algorithm (integrated within the Agilent momentum software). The smaller rings (etched in the central stages) are responsible for the rejection of the second spurious band, whereas the first undesired band is rejected by the action of the larger SRRs, which are allocated in the first and fourth filter stages. The simulated and measured frequency responses of this device are represented in Figure 4.5 *b* and *c*. In comparison to a conventional device, the first spurious band is rejected with attenuation levels

near 40 dBs, and insertion losses in the second spurious band are clearly below  $-20$  dBs. This efficiency can be attributed to the significant number of SRR pairs distributed along the device, which is possible by virtue of their small electrical size. It is also worth mentioning that the use of square or rectangular SRRs enhances magnetic coupling between line and rings (as has been explained), and this allows for further rejection levels, as compared to circular SRRs [26,27].

In Figure 4.6, a coupled-line bandpass filter fabricated in CPW technology is depicted [8]. In this device (a third-order Butterworth, 10% fractional bandwidth,

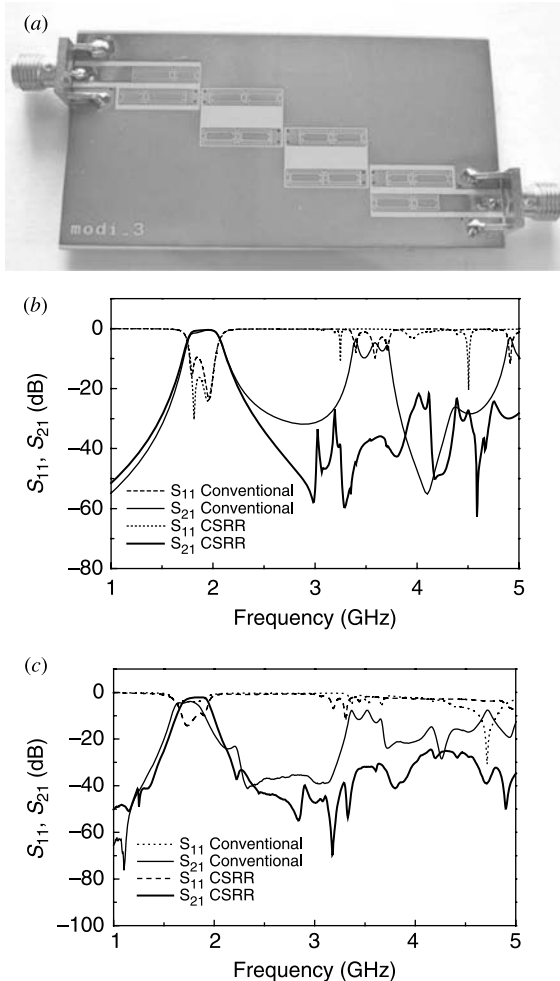


**FIGURE 4.6** (a) CSRR coupled-line bandpass filter in CPW technology. (b) Simulated frequency response compared to that obtained in the device without rings. (c) Measured frequency responses. The device has been fabricated on the Rogers RO3010 substrate (thickness  $h = 1.27$  mm, dielectric constant  $\epsilon_r = 10.2$ ). (Source: Reprinted with permission from [8]; copyright 2005, IEEE.)

central frequency  $f_0 = 1.8$  GHz), square-shaped CSRRs are etched in the coupled lines with the aim of eliminating the first and second harmonic bands. According to the frequency response, also shown in Figure 4.6, suppression levels above 20dBs up to 5GHz are achieved, and the passband is scarcely affected. This points out the efficiency of the technique, this time with CSRRs etched in the conductor strips. Compared with CPW coupled-line filters with SRRs etched in the back substrate side (not shown), the structure of Figure 4.6 is more effective for spurious suppression. In addition, the back substrate side is left unaltered, except by the presence of the via bridges that are required in these types of structures to avoid the generation of parasitic modes [28]. In fact, this structure (Fig. 4.6) is very interesting, because the CSRRs are etched in the strips of the coupled lines; that is no lateral microstructuring is added to the device. Therefore this is a very interesting solution for the elimination of undesired bands in terms of area saving.

Following this idea, CSRRs may also be etched in the active region of other planar filters, such as stepped-impedance lowpass filters, in order to eliminate the first harmonic band [29]. The topology of these filters is very suitable for this purpose because it presents low-impedance transmission line sections, which are wide and may provide the necessary space for CSRR etching. To illustrate this, the layout of a stepped-impedance lowpass filter with spurious suppression is depicted in Figure 4.7. Circular CSRRs have been etched in the low-impedance sections, with the result of significant attenuation of the first harmonic band. Again, no area is added to the device because the resonators are etched in the metallic strips of the filter.

In the reported examples, the passband of interest is not substantially affected by the presence of the SRRs or CSRRs. This is an important aspect to highlight and it is related to the relatively high  $Q$  factor of the resonators. In other words, the signal *ignores* the presence of the rings, unless its frequency is very close to the nominal resonant frequency of the SRRs (or CSRRs). These are tuned in the vicinity of the first (or second) spurious band and hence the frequency response in the operating band is not substantially altered.<sup>3</sup> Miniaturization (due to subwavelength operation of SRRs and CSRRs), high levels of rejection, and the possibility of controlling gap width by fine tuning, are key aspects that make this technique very promising for the elimination of undesired bands in microwave filters. Moreover, the technique can be applied to a wide variety of structures (including CPW and microstrip transmission lines) and filter types.

<sup>3</sup>In fact the presence of SRRs or CSRRs in the active region of the filters may affect somewhat the electrical characteristics of the structures. Specifically, it has been found that the presence of SRRs and CSRRs in the parallel coupled-line filters of Figures 4.5 and 4.6, respectively, slightly modifies the phase characteristics of the coupled-line sections (as compared to the structures without SRRs or CSRRs). Therefore, it is necessary to recalculate dimensions to preserve central filter frequency and bandwidth (the procedure is explained in [8]). However, rather than, being a disadvantage, this is useful to reduce final device dimensions (5% and 10% for the filters of Figures 4.5 and 4.6, respectively).



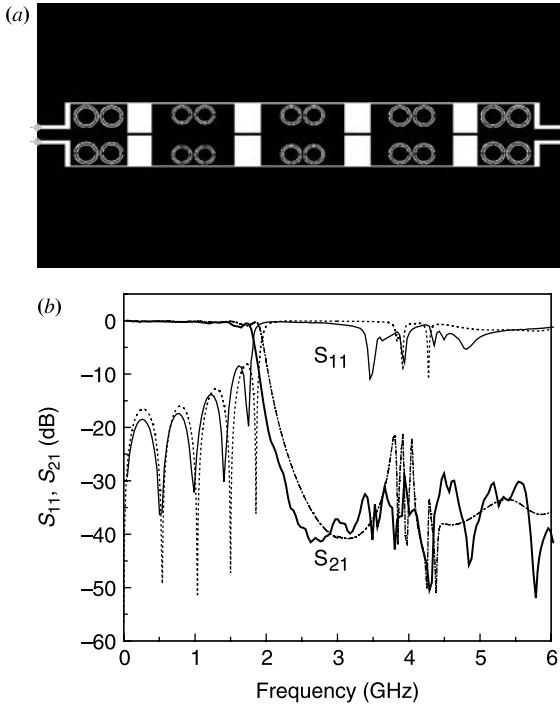


**FIGURE 4.7** (a) Layout of the CSRR-based stepped-impedance lowpass filter drawn to scale. Total device length, including 50- $\Omega$  access lines, is 94 mm; (b) Simulated (dashed lines) and measured (solid lines) frequency response for the CSRR stepped-impedance lowpass filter. The device has been fabricated on the Rogers RO3010 substrate (thickness  $h = 1.27$  mm, dielectric constant  $\epsilon_r = 10.2$ ). (Source: Reprinted with permission from [29].)

### 4.2.3 Narrow Bandpass Filter and Diplexer Design

It has been indicated previously that left-handed transmission lines consisting of a combination of SRRs with shunt-connected strips (or vias), or CSRRs with series gaps, exhibit an abrupt transition band at the lower edge, but poor frequency selectivity at the upper edge of the band. A transmission zero present below and close to the left-handed allowed band explains the sudden change in the transmission coefficient prior to this band. However, the upper band limit is determined by that frequency where the series impedance switches from capacitive to inductive behavior (for SRR-based left-handed lines) or the shunt impedance switches from inductive to capacitive behavior (for CSRRs lines).<sup>4</sup> This change is gradual rather than abrupt and this is the reason for the soft transition that is typically measured above the

<sup>4</sup>Indeed, the left-handed transmission band can also be truncated at the upper edge by a change in the sign of the shunt and series impedance for SRR and CSRR loaded lines, respectively. However, unbalanced resonant-type left-handed lines are usually designed with the resonance frequency of the branch not dependent on the SRRs or CSRRs well beyond SRRs' or CSRRs' resonance.

passband. One possibility to improve frequency selectivity at the upper edge of the band is to alternate left-handed transmission line sections with artificial right-handed sections. The latter, which consist of SRRs combined with gaps, or CSRRs combined with shunt-connected strips, exhibit a transmission zero above the passband. Therefore, by overlapping the passbands of both stages, it is potentially possible to achieve roughly symmetric and highly frequency-selective devices. Let us explore this possibility.

#### 4.2.3.1 Bandpass Filters Based on Alternate Right-/Left-Handed (ARLH) Sections Implemented by Means of SRRs

A representative and illustrative structure of the alternate right-/left-handed (ARLH) concept<sup>5</sup> implemented by means of SRRs is depicted in Figure 4.8 [30]. It consists of a CPW transmission line loaded with three SRR pair sections. The central stage is a right-handed SRR/gap section, and it is sandwiched between two SRR/strip (i.e., left-handed) stages. The outer stages are described by the  $\pi$  lumped-element circuits of Figure 3.24, and the central stage is modeled by the circuits shown in Figure 4.9 ( $C_g$  is the capacitance of the series gap). An analysis of this latter circuit indicates that signal propagation is allowed for those frequencies providing a real value of  $\beta$ , according to the following expression:

$$\cos(\beta l) = 1 + \frac{C}{2C_g} - \frac{LC\omega^2}{2} + \frac{C\omega}{4} \frac{L'_s/C'_s}{\omega L'_s - \frac{1}{\omega C'_s}}. \quad (4.1)$$

Equation (4.1) corresponds to the dispersion relation of an infinitely long periodic structure composed of a cascade of elemental cells. Although the number of cells is in fact limited (a single SRR/gap stage sandwiched between two SRR/strip cells is used in the structure of Fig. 4.8), equation (4.1) provides valuable information, because it confirms that the SRR/gap combination supports propagating modes in a narrowband below SRR resonance. Moreover, inspection of equation (4.1) reveals that the series impedance rapidly changes from a highly inductive to a highly capacitive behavior at resonance, with the result of a sharp cutoff at that frequency. This has been verified by full-wave electromagnetic simulation of the central SRR/gap stage alone (the commercial software Agilent momentum has been used). The result is visible in

<sup>5</sup>Notice that the ARLH concept is different than the composite right-/left-handed (CRLH) concept introduced in Chapter 3. Namely, the CRLH concept expresses the composite (left- and right-handed) nature of both dual and resonant-type metamaterial transmission lines. The expression ARLH is used to designate the combination of left-handed and right-handed sections in the same structure. Although the left-handed sections exhibit a CRLH behavior, the right-handed band of such sections is not used. In ARLH structures, the alternance of right- and left-handed sections is not actually necessary. The relevant advantages of such structures are due to the combination of left- and right-handed sections. However the term *combined right-/left-handed* has been avoided, because its acronym coincides with that of the composite right-/left-handed concept. Moreover, in the illustrative examples provided, the right- and left-handed sections do in fact alternate.

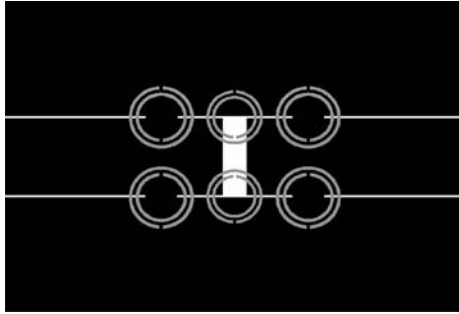


**FIGURE 4.8** Layout of the strip/gap SRR-CPW structure. For the smaller SRRs the inner radius has been set to  $r = 1.39$  mm, and for the rings located at the edges of the structure,  $r = 1.52$  mm. In all cases,  $c = d = 0.2$  mm. The strip width is  $w_w = 2.16$  mm and the gap length is  $l_g = 1.6$  mm. With these dimensions, the shunt-connected inductance and series capacitances take the values  $L_p = 115.76$  pH and  $C_g = 96.84$  fF, respectively. The lateral dimensions of the host CPW are  $W = 5.4$  mm,  $G = 0.16$  mm. The central strip is wide in order to avoid SRR-pair overlapping. The length of the active region of the device (i.e., excluding access lines and connectors) is 14.4 mm. The Arlon 250-LX-0193-43-11 substrate was used, that is, dielectric constant  $\epsilon_r = 2.43$ , thickness  $h = 0.49$  mm. (Source: Reprinted with permission from [30]; copyright 2004, IEEE.)

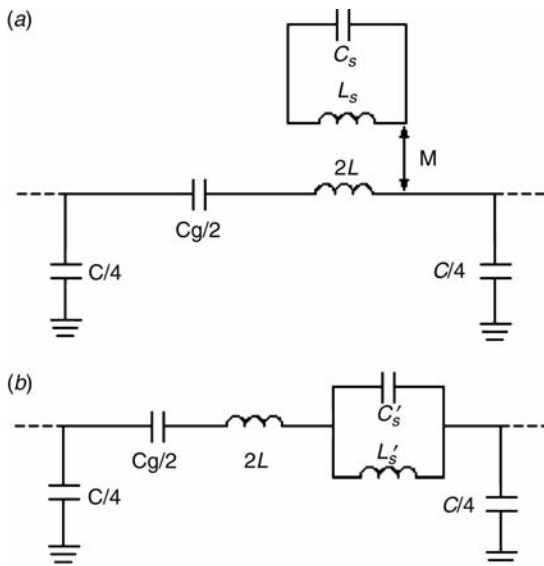


**FIGURE 4.9** Lumped-element equivalent circuit for the gap-SRR stage (a) and simplified model with the series branch replaced by its equivalent impedance (b).  $C_g$  is the capacitance of the series gap.

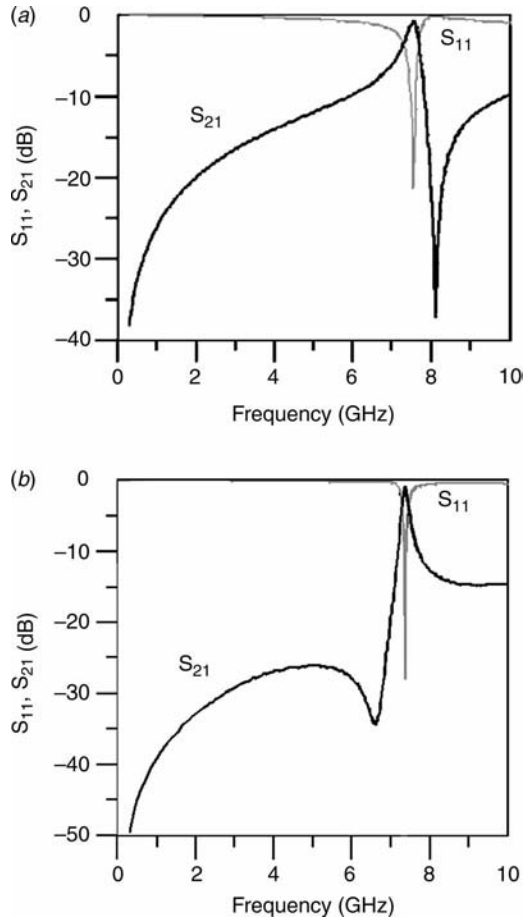


**FIGURE 4.10** Simulated frequency responses for individual SRRs/gap (a) and SRRs/strip (b) cells.

Figure 4.10, where, for comparison purposes, the frequency response of an individual SRR/strip stage is also depicted. In both cases, the parameters of the Arlon 250-LX-0193-43-11 substrate were considered; that is, dielectric constant  $\epsilon_r = 2.43$ , thickness  $h = 0.49$  mm. Because in the allowed band the series impedance is inductive and the shunt impedance is capacitive, it follows that signal propagation is forward and hence the SRR/gap combination is a right-handed cell.

The different locations of the passband for the left-handed and right-handed stages relative to the resonant frequency of the rings explains the smaller dimensions of the central SRRs. The dimensions of the SRRs and other relevant dimensions of the filter are given in the caption of Figure 4.8. With these SRR geometries, the resonance frequencies for the central and external SRRs (according to the model reported in Chapter 2 and also given in [31]) are  $f_o = 7.22$  GHz and  $f_o = 6.64$  GHz,

respectively.<sup>6</sup> Hence, the passband of the structure is expected to lie within this frequency interval. The strip and gap geometries have been determined to obtain shunt inductances and a series capacitance able to obscure the effects of line capacitance and line inductance in the region of interest (i.e., within the passband) for the outer and central stages, respectively. Filter size is approximately three times smaller than the wavelength at the central frequency of the filter.

The simulated and measured frequency responses of the designed structure are depicted in Figure 4.11. There is a reasonable agreement between simulation and experiment. The slight discrepancies in the region of interest are attributed to fabrication-related tolerances.<sup>7</sup> In agreement with the analysis based on the equivalent circuit model, a passband is obtained between the resonant frequencies of the central and outer rings. The sharp transition band obtained at either edge of the allowed band is noticeable, with more than 30 dB fall in 0.5 GHz and peak rejection levels of 60 dBs and near 40 dBs at 6 GHz and 7.7 GHz, respectively.

Another illustrative example of the ARLH transmission line concept is an S-band filter (central frequency  $f_0 = 2.4$  GHz), where the number of cells has been reduced to two [32]. Namely, a single SRR/strip cell has been cascaded with an SRR/gap combination (Fig. 4.12). The length of the active device region is 22.5 mm, that is, five times smaller than the signal wavelength at 2.4 GHz. The simulated and measured frequency responses of this device are depicted in Figure 4.13. In spite of the reduced number of stages (*only* two), frequency selectivity is good, with measured rejection levels better than 50 dBs at the left of the pass band and above 30 dB up to approximately 4 GHz. The upper transition band edge is very sharp with 60 dB fall in 0.4 GHz, and an average slope of 125 dB/GHz has been measured at the lower band edge.

The potentiality of ARLH transmission lines in terms of filter miniaturization is pointed out by comparing the designed S-band filter with a conventional microstrip coupled-line bandpass filter with similar performance (an identical substrate is considered to validate the comparison). The layout of this filter is also depicted in Figure 4.12. The simulated frequency response of the coupled-line bandpass filter is depicted in Figure 4.13a (this device has not been fabricated). To obtain similar slopes in the transition bands, it has been necessary to design a three-stage conventional filter (Chebyshev response) with a length (excluding the access lines) of 63.6 mm, that is, roughly three times longer than the active region of the ARLH SRR-based prototype.<sup>8</sup> The authors would like to highlight the absolute coincidence of the simulated frequency responses in the pass band for both implementations (Fig. 4.13a). This indicates that in-band losses in the ARLH SRR filter are related

<sup>6</sup>Due to the presence of the CPW structure at the other side of the substrate, these resonance frequencies do not exactly coincide with those inferred from full-wave electromagnetic simulation (Fig. 4.10).

<sup>7</sup>It has been demonstrated by simulation that variations of ring dimensions of less than 1% around the design values are enough to degrade in-band losses. This explains the measured in-band losses (4 dB) not being as good as those obtained by electromagnetic simulation, and also the slight frequency shift between simulation and measurement.

<sup>8</sup>The performance of the ARLH SRR-based filter in terms of frequency selectivity is superior. Therefore, at least a four-stage coupled-line filter is necessary to improve the frequency response obtained in the SRR-based filter.

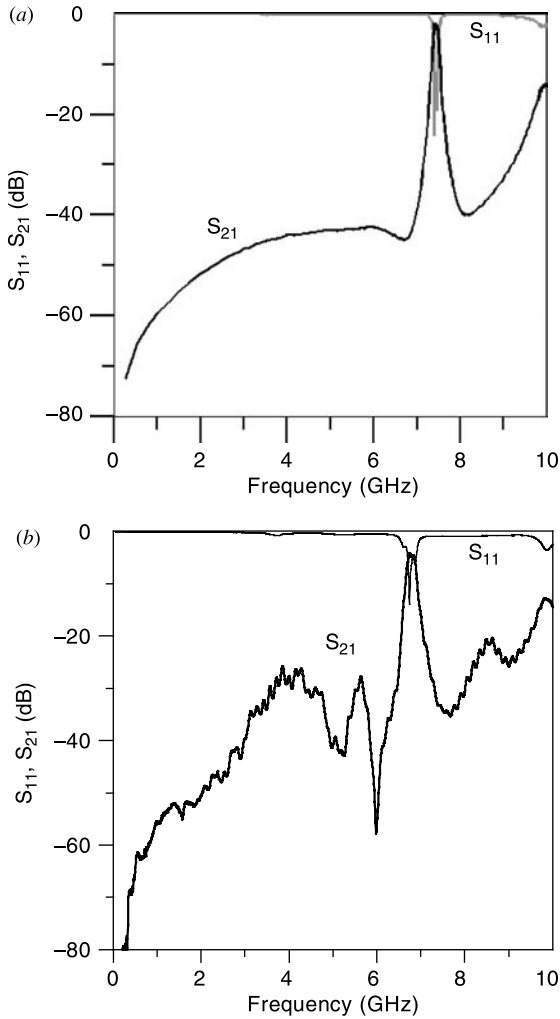


**FIGURE 4.11** Simulated (a) and measured (b) frequency responses for the fabricated C-band filter of Figure 4.8. (Source: Reprinted with permission from [30]; copyright 2004, IEEE.)

to the finite  $Q$  factor of the resonators, rather than to an improper design (although it has been observed that in-band losses are very dependent on variations of ring dimensions around the design values). These results clearly suggest the possibilities of the ARLH concept in reducing filter dimensions in planar technology.

**4.2.3.2 Bandpass Filters and Diplexers Based on Alternate Right-/Left-Handed (ARLH) Sections Implemented by Means of CSRRs** ARLH transmission lines properly designed to act as narrow bandpass filters can also be implemented by means of CSRRs. As expected, the left-handed stages consist of

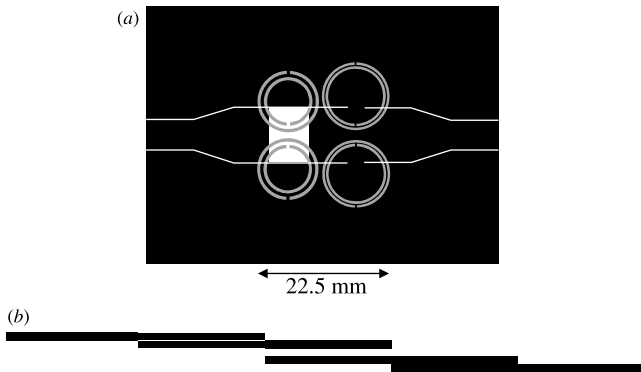


**FIGURE 4.12** (a) Layout of the fabricated S-band filter drawn to scale. The dimensions of the SRR pairs corresponding to the strip and gap stages are  $r = 5.2$  mm,  $c = 0.44$  mm, and  $d = 0.22$  mm, and  $r = 4.1$  mm,  $c = d = 0.55$  mm, respectively. Strip and gap dimensions have been set to  $w_w = 2.8$  mm and  $l_g = 6.6$  mm, respectively. With these geometries, the equivalent inductance and capacitance of the strip and gap have been estimated to be  $L_p = 183$  pH and  $C_g = 147$  fF, respectively (as for the C-band filter of Fig. 4.8, the parameters of the Arlon 250-LX-0193-43-11 substrate have been considered). Finally, the host CPW is a  $50\ \Omega$  line with a wide strip ( $W = 10$  mm) in order to accommodate the rings. As the separation between ground planes is wider than the dimensions of the connectors in use, it has been necessary to cascade taper transitions at the input and output ports to allow for connector insertion. The length of the active device region is 22.5 mm. (b) Layout of a conventional microstrip parallel coupled-line bandpass filter with comparable performance. (Source: Reprinted with permission from [32]; copyright 2005, John Wiley & Sons.)

CSRRs combined with series gaps, whereas CSRRs combined with shunt stubs are used for the forward sections [33]. The lumped-element equivalent circuit model for the CSRR/gap stage was presented in Chapter 3 (Fig. 3.38). The equivalent circuit model for the right-handed CSRR/stub cell is depicted in Figure 4.14.  $L$  and  $C$  are the inductance and capacitance of the line, respectively, and  $L_p$  models the inductance of the shunt stubs. As in Chapter 3, CSRRs are modeled as resonant tanks electrically coupled to the line through the capacitance  $C$ . The circuit model corresponding to the CSRR/stub stage is valid as long as CSRRs are electrically small (as in Chapter 3, coupling between neighbor CSRRs is neglected). The dispersion relation corresponding to an infinitely long structure composed of the unit cells depicted in Figure 4.14 is given by

$$\cos(\beta l) = 1 + \frac{L\omega^2 \left[ L_p + \frac{L_c}{1 - L_c C_c \omega^2} \right] - \frac{L}{C}}{2 \left( \frac{L_c L_p \omega^2}{1 - L_c C_c \omega^2} - \frac{L_p}{C} \right)}. \quad (4.2)$$

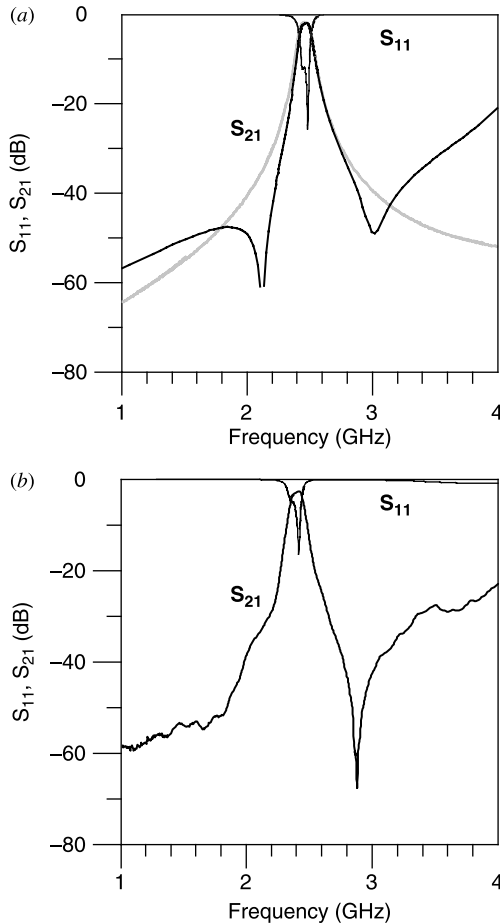


**FIGURE 4.13** Simulated (a) and measured (b) frequency responses for the fabricated S-band filter. Insertion losses (simulated) for the conventional three-stage coupled-line bandpass filter are depicted in gray. (Source: Reprinted with permission from [32]; copyright 2005, John Wiley & Sons.)

Signal propagation is only allowed in that region where the phase constant is real. For this, it is necessary that the shunt reactance is negative. This occurs in a narrow band to the left of  $f_s$ , the frequency that nulls the shunt impedance.<sup>9</sup>

By combining CSRR/gap stages with CSRR/stub unit cells, it is possible to synthesize narrow passbands with transmission zeros at both band edges. As was done in SRR-based ARLH transmission line filters, it is necessary to design the CSRR of the right-handed and left-handed stages to exhibit the transmission zeros at different

<sup>9</sup>If the inductance  $L_p$  were not present, the shunt impedance would be negative from the origin up to  $f_s$ . Thus, the inductance  $L_p$  is introduced to generate a limited forward band.



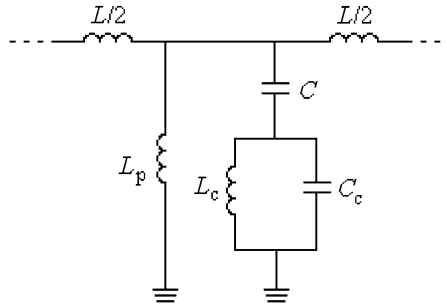


**FIGURE 4.14** Equivalent T-circuit model for the CSRR/stub cell.

frequencies, and to design either filter stage with identical central frequency. Illustrative examples of narrow microstrip bandpass filters based on ARLH lines implemented by means of CSRRs are given in [33].

These ARLH transmission-line bandpass filters can be applied to the synthesis of microwave diplexers [34]. A diplexer is a three-port device that is used at the input stage of communication transceiver front-ends to separate the receiver (Rx) and transmitter (Tx) channel signals. To this end, a Rx and a Tx filter is required. A possible configuration for the diplexer is that shown in Figure 4.15, where the Rx and Tx filters are cascaded at the output ports of a Y-junction. The main relevant parameters representative of diplexer performance are in-band losses for the Tx and Rx channels (which should be as small as possible) and Rx/Tx isolation (which should be high to avoid interfering signals between the Rx and Tx channels). A prototype device operative in the 2.4–3.0 GHz frequency band is depicted in Figure 4.16a. The Tx and Rx filters (implemented by means of CSRR-based ARLH microstrip lines<sup>10</sup>) have been designed to provide passbands centered at 2.4 GHz and 3.0 GHz, respectively, with absolute bandwidths of 0.25 GHz (namely 10.3% and 8% fractional bandwidths for transmission and reception). Figure 4.16b depicts the measured transmission coefficient for the Tx and Rx filters (i.e.,  $S_{21}$  and  $S_{31}$ , respectively), as

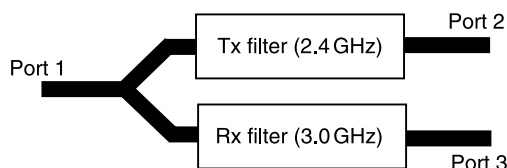


**FIGURE 4.15** Structure of the diplexer.

<sup>10</sup>Notice that in the right-handed sections of the Rx and Tx filters, two CSRRs are used. The reason for this is the moderate bandwidth (rather than narrow) of either filter. To achieve such bandwidths, it is necessary to implement unit cells also with moderate 3 dB bandwidths. For the forward sections, this is more easily achieved by using two CSRRs, rather than only one.

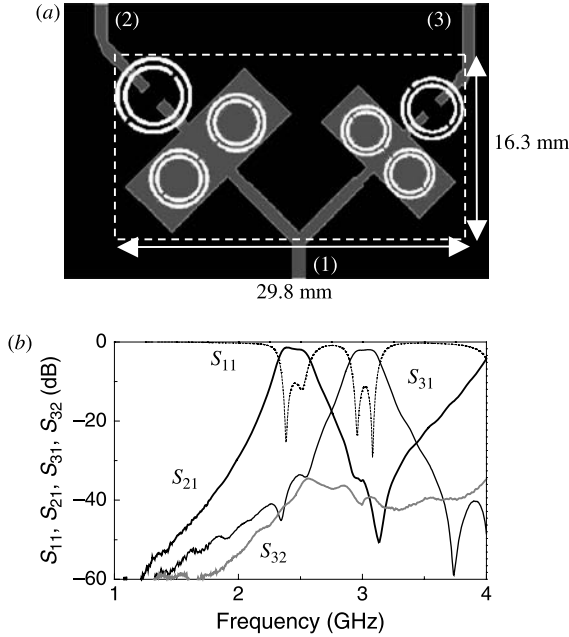


**FIGURE 4.16** (a) Topology of the fabricated ARLH microstrip line diplexer and (b) the measured frequency response. The upper metal level is depicted in gray, and the lower metal is drawn in black. Gap spacing is 1.33 mm and 1.67 mm for the Rx and Tx filters, respectively, and the shunt strip dimensions are 4.54 mm  $\times$  11.9 mm and 5.70 mm  $\times$  14.48 mm. External CSRR radii are 2.18 mm, 2.73 mm, 2.56 mm, and 3.27 mm for the Rx (1st stage), Rx (2nd stage), Tx (1st stage), and Tx (2nd stage), respectively. The structure has been implemented in the Rogers RO3010 substrate (thickness  $h = 1.27$  mm, dielectric constant  $\epsilon_r = 10.2$ ). (Source: Reprinted with permission from [34].)

well as the measured Rx/Tx isolation ( $S_{32}$ ). In-band losses lower than 2 dB are measured for either filter, and return losses (also represented in Fig. 4.16b) are better than 10 dB. The frequency response of the filters is quite symmetric and the measured isolation between ports 2 and 3 is in the vicinity of 40 dB. Remarkable also are the dimensions of the diplexer (see the region indicated in Fig. 4.16a), which are as small as 29.8 mm  $\times$  16.3 mm (namely  $0.63\lambda \times 0.34\lambda$ ,  $\lambda$  being the signal wavelength at the Tx frequency) thanks to the compact resonators used.

#### 4.2.4 CSRR-Based Bandpass Filters with Controllable Characteristics

In this section, a methodology for the design of bandpass filters with controllable characteristics in microstrip technology is proposed. It is based on cascading filter stages consisting of a combination of CSRRs, series capacitive gaps, and grounded stubs. By this means we achieve the necessary flexibility to simultaneously obtain quite symmetric frequency responses, controllable bandwidths, and compact

dimensions. Compact dimensions and symmetric frequency responses were obtained by means of the ARLH concept proposed in the previous subsection. However, the synthesis of bandpass filters with controllable bandwidth (over wide margins) was not considered. It will be shown in this section that by means of the proposed approach we can obtain wide- and even ultrawideband (UWB) frequency responses. Moreover, by sacrificing periodicity, it is possible to synthesize standard frequency response filters (Butterworth, Chebyshev, and so on), as will be shown later. Another interesting aspect to highlight is that the basic cell of the structure exhibits a transmission zero above the pass band of interest. This transmission zero can be tailored to some extent and hence it can be useful to improve the out-of-band performance of the filters through suppression of undesired harmonic bands. We will also consider in this section alternative topologies for the basic cell, where the series gaps are replaced with transmission line sections. Although in this case wave propagation is forward, we can also take the benefit of the small dimensions of the resonators (CSRRs) to achieve compact designs. It will be shown that this latter strategy is powerful for the synthesis of UWB response filters.

#### **4.2.4.1 Bandpass Filters Based on the Hybrid Approach: Design Methodology and Illustrative Examples**

The CSRR-based microstrip filters proposed in this section are planar structures that can be modeled by the circuit of Figure 4.17a, which consists of a cascade of admittance inverters (with normalized admittance  $J = 1$ ) alternating with shunt-connected resonators tuned at the central frequency of the filter band,  $f_0$  [35,36]. This circuit is inferred from the lowpass filter prototype by the well-known frequency and element transformations that can be found in any microwave textbook [18] or in monographs devoted to microwave filters [35,36].<sup>11</sup> By properly designing the shunt resonators, the synthesis of standard frequency approximations is potentially possible. Infact, the transformation from the lowpass filter prototype leads to the structure of Figure 4.17b, with parallel  $LC$  resonant tanks. Thus, as long as the resonator's admittances fit those of the  $LC$  tanks (which depend on the  $L$  and  $C$  values inferred from circuit transformation), the targeted approximation (Butterworth, Chebyshev, and so on) is achievable. Generally speaking, in planar circuit technology, the resonators can be implemented either by means of a distributed approach, or by using planar semi-lumped elements. Therefore, the ideal case of perfect fitting at all frequencies is not possible, and the admittances of the  $LC$  resonators can only be approximated near resonance. This is the conventional procedure for the design of filters with limited bandwidth, and this will be the case considered in this section.

The elemental cell of the proposed CSRR-based filters is depicted in Figure 4.18 [37]. This consists of a CSRR etched in the ground plane (underneath the conductor strip), combined with two series gaps and two shunt-connected metallic strips (stubs), which are grounded by means of vias. The equivalent-circuit model of this basic cell is also shown in Figure 4.18. CSRRs are modeled by means of an  $LC$  resonant tank

<sup>11</sup>Alternatively, bandpass filters can be synthesized by cascading impedance inverters and series-connected resonators.

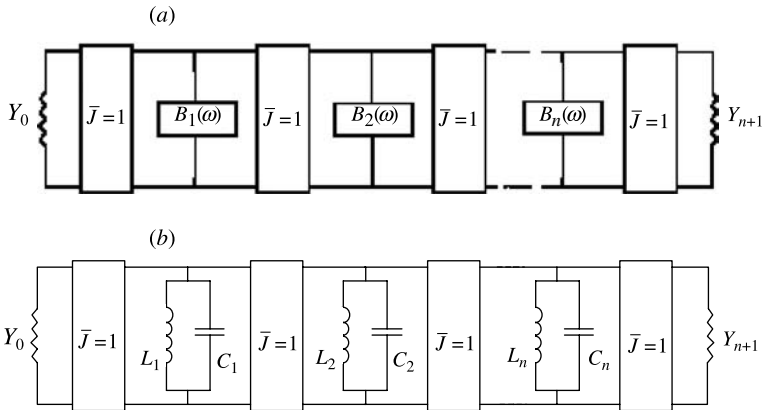


**FIGURE 4.17** Generalized bandpass filter network with admittance inverters and shunt resonators (a). In (b) the resonators are LC resonant tanks.

( $L_c$  and  $C_c$ ), and their coupling to the line is described by means of the capacitance  $C$ , which depends on the portion of the inter-metallic region between the series gaps that lies face-to-face with the metal inside the inner slot of the CSRR. The grounded stubs are modeled by means of a shunt inductance,  $L_p$ , and  $C_g$  accounts for the series gaps. The elements of the basic cell, including the CSRR, are electrically small, this being a necessary condition to properly describe the cell by means of the proposed lumped-

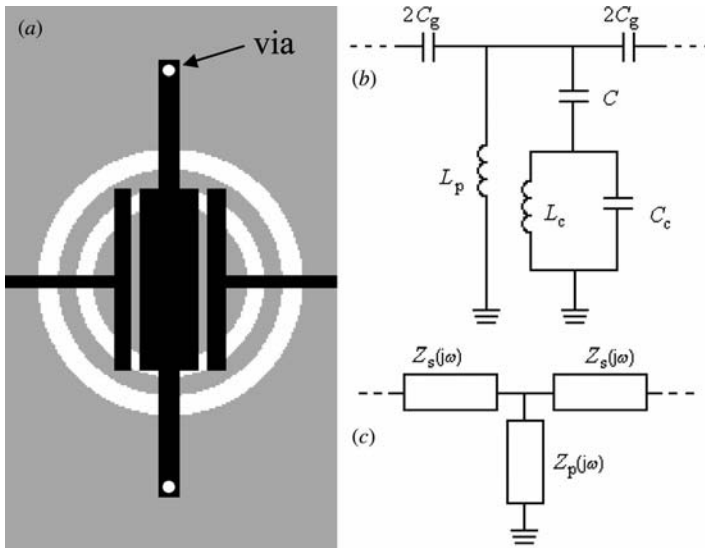


**FIGURE 4.18** (a) Basic cell of the proposed filters, (b) the equivalent-circuit model, and (c) The T-model of the elemental cell. The upper metallization is depicted in black, and the bottom metal regions are depicted in gray.

element equivalent circuit. The series inductance of the line is neglected in this study, as was done in Chapter 3 in the modeling of microstrip lines loaded with CSRRs and series gaps. Indeed, the basic cell shown in Figure 4.18 is inspired by the elemental cell of the left-handed microstrip line depicted in Figure 3.36. The introduction of the shunt-connected stubs in the structure is a consequence of the need to improve the upper transition band of the filter. However, the introduction of such elements represents an additional degree of freedom that is relevant not only to improve frequency selectivity, but also to ease the design and to improve the out-of-band rejection of the filter, as will be shown later.

Inspection to the circuit of Figure 4.18b reveals that the electrical model of the proposed unit cell is a combination of the dual transmission-line model and the resonant-type model. Therefore, this model can be called the *hybrid model*, and the methodology based on the left-handed unit cells depicted in Figure 4.18a can be identified as the *hybrid approach* [38]. Another key advantage of the structure of Figure 4.18 is related to the admittance inverter. Because the characteristic admittance of the inverters is unity (Fig. 4.17), the inverters merely act as  $90^\circ$  transmission lines. However, because gap capacitances are present in the structures, they can be used to obtain the desired phase shift, without the need to physically cascade  $90^\circ$  transmission lines between the resonators, something relevant to device miniaturization.<sup>12</sup>

The design methodology of the filters consists in determining the electrical parameters of the equivalent-circuit model for either filter section (provided the filter is not periodic) from given specifications (central frequency, fractional bandwidth, and filter order), and also the synthesis of the layout of the structure. Let us first consider the first aspect. In the circuit of Figure 4.17b, the central filter frequency,  $f_o$ , is determined by the resonance frequency of the shunt  $LC$  tank, which nulls its admittance. However, this is not exactly the case for the filter implemented by cascading the elemental cells depicted in Figure 4.18, because the resonators and admittance inverters are intermixed. Specifically,  $f_o$ , neither coincides with the intrinsic resonance of the CSRRs, nor does it null  $Y_p(\omega) = Z_p^{-1}(\omega)$ . Nevertheless, at  $f_o$ , the phase shift and transmission coefficient between the input and output ports of the basic cell should be  $\phi = 90^\circ$  and  $|S_{21}| = 1$ , respectively. This means that at  $f_o$  the image impedance (or Bloch impedance for a periodic structure),  $Z_B$ , should coincide with the reference impedance of the ports, which is usually set to  $Z_o = 50 \Omega$ . If we now consider that the circuit of Figure 4.18b can be described by means of its T-circuit model, with series impedance  $Z_s$  and shunt impedance  $Z_p$  (Fig. 4.18c), and we take into account that the phase shift and image impedance for this circuit are given by expressions (3.1) (with  $\phi = \beta l$ ) and (3.2), respectively, the previous conditions lead us to  $Z_s = -jZ_o$  and  $Z_p = jZ_o$ . In fact, the dual solution ( $Z_s = jZ_o$  and  $Z_p = -jZ_o$ ) also satisfies the previous conditions on phase shift and impedance matching, but this solution is not compatible with the circuit of Figure 4.18b, because the series impedance of this circuit is capacitive.

<sup>12</sup>Nevertheless, in other filter implementations that will be analyzed later, such admittance inverters will be implemented by means of transmission line sections.

Consequently, at the central filter frequency, the series reactance is negative (capacitive), and the shunt reactance (corresponding to the parallel combination of  $L_p$  and the impedance of the CSRRs coupled to the line) is positive and, hence, inductive. According to the signs of these reactances, the filter structure composed of the elemental cells depicted in Figure 4.18 supports backward waves and behaves as a left-handed transmission line. To determine the element values for the circuit of Figure 4.18b, the series and shunt impedances have to be set to  $Z_s = -jZ_o$  and  $Z_p = jZ_o$ , respectively, at  $f_o$ . This does not univocally determine the element values for the shunt impedance. These values are also determined by the 3 dB bandwidth of the resonators,

$$\Delta = \frac{\omega_2 - \omega_1}{\omega_o} \quad (4.3)$$

(where  $\omega_o$ ,  $\omega_1$ , and  $\omega_2$  are the central—angular—frequency and 3 dB frequencies, respectively), and by the transmission zero, which occurs at that frequency where the shunt impedance reduces to zero, namely

$$f_z = \frac{1}{2\pi\sqrt{L_c(C_c + C)}} \quad (4.4)$$

For an  $LC$  parallel resonant tank, with inductance and capacitance  $L_{eq}$  and  $C_{eq}$ , respectively, we have

$$\Delta = \frac{2}{Z_o} \sqrt{\frac{L_{eq}}{C_{eq}}} \quad (4.5)$$

If we consider the filter structure of Figure 4.17b, where the  $L$  and  $C$  values come from the low-pass filter prototype by frequency and element transformation according to [35]:

$$C_{eq} = \left[ \frac{1}{FWB \cdot \omega_o \cdot Z_o} \right] g_i \quad (4.6)$$

$$L_{eq} = \frac{1}{\omega_o^2 C_{eq}} \quad (4.7)$$

and expressions (4.6) and (4.7) are introduced in equation (4.5), the following expression for resonator bandwidths results:

$$\Delta_i = \frac{2FWB}{g_i} \quad (4.8)$$

where the  $g_i$  factors are the element values of the lowpass filter prototype (which depend on the specific filter approximation and can be inferred from published tables) and  $\Delta_i$  is the 3 dB bandwidth of the resonators. According to expression (4.8),  $\Delta_i$  is proportional to the fractional bandwidth,  $FBW$ , and hence it is determined from the required bandwidth of the filter. Obviously,  $\Delta_i$  is also dependent on  $g_i$ , and it is therefore determined by the type of response and order. Once  $\Delta_i$  are known, we can force the frequencies  $\omega_1$  and  $\omega_2$  to be equidistant from the central filter frequency. At these frequencies, under the assumption that  $Z_s(\omega)$  does not substantially vary along the passband, the shunt impedance of the unit cell becomes  $Z_p = jZ_0/2$  and infinity, respectively (see Problem 4.1), and, as has been previously indicated,  $Z_p = jZ_0$  at  $\omega_0$ . These conditions can be expressed as

$$\frac{L_p L_c \omega_1^3 (C + C_c) - L_p \omega_1}{L_c \omega_1^2 (C + C_c) - C \omega_1^2 L_p (L_c C_c \omega_1^2 - 1) - 1} = \frac{Z_0}{2} \quad (4.9)$$

$$L_c \omega_2^2 (C + C_c) - C \omega_2^2 L_p (L_c C_c \omega_2^2 - 1) - 1 = 0 \quad (4.10)$$

$$\frac{L_p L_c \omega_0^3 (C + C_c) - L_p \omega_0}{L_c \omega_0^2 (C + C_c) - C \omega_0^2 L_p (L_c C_c \omega_0^2 - 1) - 1} = Z_0. \quad (4.11)$$

The previous approximation (which is valid for narrow and moderate bandwidths) leads us to simple analytical expressions (equations (4.9) and (4.10)). If this approximation is not applied, then the conditions arising from the 3 dB frequencies are not mathematically simple. Solution of equations (4.9)–(4.11) and (4.4) leads us to the parameters of the shunt reactance, and the series capacitance is given by

$$C_g = \frac{1}{2Z_0 \omega_0}. \quad (4.12)$$

The criterion to set the transmission zero frequency,  $f_z$ , obeys a compromise between the need to obtain a sharp transition in the upper band edge, and the convenience to separate the spurious responses as much as possible from the passband of interest, and thus optimize the out-of-band performance of the filter. Namely, a narrow spurious band above the passband of interest arises, unless  $f_z$  is properly set. This spurious response is due to the presence of a parasitic half-wavelength resonator coupled by the series capacitances (gaps) of the unit cells. By adjusting  $f_z$  to the position of the frequency parasitic, this spurious response can be minimized, and the filter frequency response can be significantly improved. However, the position of the spurious response is not known *a priori*. So the transmission zero frequency must be set to a certain tentative value, for instance  $f_z = 2f_0$ , which is expected to lie in the vicinity of the spurious band.<sup>13</sup> From the previous equations, the parameters of Figure 4.18b are

<sup>13</sup>There is no physical reason that justifies this choice. However, in practice, the typical electrical sizes of CSRRs makes the spurious band appear in the vicinity of the first harmonic of the central filter frequency. This is not something absolute, but it has been corroborated by several examples. Nevertheless, the location of the spurious band can be estimated from the distance between the series gaps of adjacent cells.

inferred, and the topology of each filter cell (Fig. 4.18a) is obtained. The model described in [39] can be used to obtain an initial guess for CSRR dimensions (the validity of the model is subject to conditions that do not exactly apply in the considered filter cells [39]). The coupling capacitance,  $C$ , can be adjusted by partially removing the metal delimited by the CSRR contour. The length and width of the grounded metal strips (stubs) can be determined from independent full-wave electromagnetic simulations carried out in microstrip transmission lines loaded with these elements, or by using standard formulas [18]. A similar procedure can be used to determine the geometry of the series capacitances. From this initial layout, the frequency response of the complete filter is then simulated by means of a full-wave electromagnetic solver, thus making visible the position of the spurious band. To eliminate this band,  $f_z$  must be forced to coincide with the center of the spurious band, and the model parameters must be recalculated. To determine the final layout, cell dimensions should be adjusted (starting from the seeding topology) in order to fit as closely as possible the electrical response obtained from the latter model parameters. In practice this is simple, because cell bandwidth is mainly controlled by  $L_p$  and  $C$  (provided  $f_z$  and  $f_o$  are distant enough). Therefore, stub dimensions and the etched area inside the CSRRs can be adjusted to match the required bandwidth, and the transmission zero frequency can be tailored by scaling the CSRR dimensions.

Let us now consider two illustrative examples of bandpass filters designed by following this approach. The first example is a bandpass filter based on a periodic repetition of the basic cell. The second example is a bandpass filter where periodicity is sacrificed in favor of the synthesis of a standard (Chebyshev) frequency response. In both cases, significant levels of miniaturization are achieved, as compared to conventional distributed implementations, as will be shown later. The specifications of the periodic filter are as follows: order 3, central frequency  $f_o = 1$  GHz and fractional bandwidth  $FBW = 10\%$ . This filter does not obey any standard approximation, therefore we cannot directly determine  $g_i$  from tabulated values, as is usual. Obviously, due to periodicity, all resonators must have the same  $\Delta$ , and accordingly the same  $g$ . To obtain the value of  $g$ , an order-3 low-pass filter prototype with identical element values has been considered, and it has been forced to exhibit the 3 dB cutoff at the normalized  $\omega = 1$  rad/s angular frequency. From this,  $g = 1.521$  is obtained; hence the 3 dB bandwidth of the resonators,  $\Delta$ , is perfectly determined. From the previously explained procedure, the element values of the equivalent circuit model have been obtained. They are identical for the three filter cells and are depicted in Table 4.1. Layout dimensions for the basic cell are indicated in Figure 4.19 (the parameters of the Rogers RO3010 substrate have been used; thickness  $h = 1.27$  mm, dielectric constant  $\epsilon_r = 10.2$ ).

**TABLE 4.1** Element Values of the Equivalent-Circuit Model for the Filter of Figure 4.20

$C_g$ (pF)	$L_p$ (nH)	$C$ (pF)	$C_c$ (pF)	$L_c$ (nH)
1.59	1.33	12.33	21.7	0.23



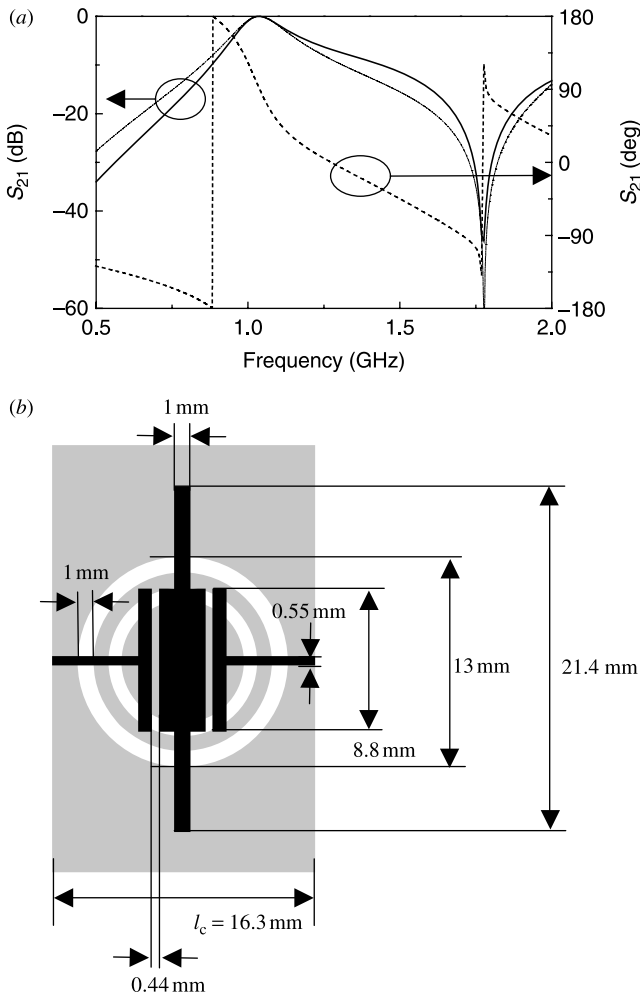


**FIGURE 4.19** Simulated frequency response (amplitude and phase) corresponding to the basic filter cell of Figure 4.18a. The insertion losses obtained by electrical simulation of the equivalent circuit model are also depicted (thin line). Dimensions are indicated in (b). The positive phase ( $+90^\circ$ ) of  $S_{21}$ , obtained at  $f_0$ , clearly points out the left, handed nature of the structure. (Source: Reprinted with permission from [37]; copyright 2006, IEEE.)

The simulated (using Agilent momentum) frequency response (amplitude and phase) of the single-cell structure is represented in Figure 4.19 and compared to that obtained from the electrical simulation (insertion losses only) of the equivalent-circuit model (with the parameters indicated in Table 4.1). A reasonable fit between the electrical and the electromagnetic simulations has been obtained. The simulated and measured insertion and return losses for the fabricated three-stage filter are depicted in Figure 4.20. Thanks to the transmission zero, the frequency response is

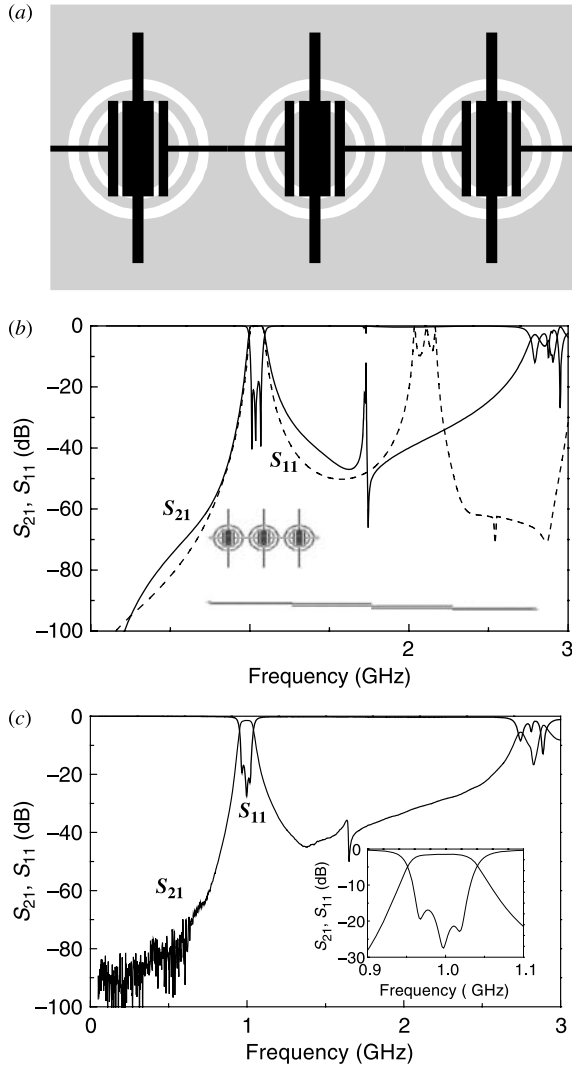


**FIGURE 4.20** Layout of the fabricated periodic filter (a), and simulated (b) and measured (c) insertion and return losses. Total device length excluding access lines is 4.56 cm. In (b), the simulated insertion losses for a conventional order-3 coupled-line filter with similar performance are depicted (dashed line). (Source: Reprinted with permission from [37]; copyright 2006, IEEE.)

spurious free up to approximately  $3f_0$  (this transmission zero is clearly visible in Fig. 4.19, where it is not obscured by parasitic resonances, as only one stage has been considered in that figure). In-band insertion and return losses are good (i.e.,  $IL < 1.5$  dB and  $RL > 17$  dB), and frequency selectivity at both band edges is high, with near-symmetric transition bands. The measured fractional bandwidth

is  $FBW = 8\%$ , which coincides to a good approximation with the nominal value (the discrepancy is due to the narrow band approximation related to the nonideal admittance inverters used). Cell dimensions (length) are small compared with signal wavelength at  $f_o$  (i.e.,  $l_c \sim \lambda/7$ ). Further miniaturization can be achieved with the penalty of critical (smaller) dimensions being closer to the limits imposed by the fabrication technology ( $\sim 100 \mu\text{m}$ ). To avoid problems related to fabrication tolerances, critical dimensions substantially larger than  $100 \mu\text{m}$  have been considered in this design, with the result of a moderately small cell size. Figure 4.20b also includes the simulated frequency response (insertion losses) obtained on a conventional microstrip coupled-line bandpass filter with similar performance (layout comparison is shown in the inset of Fig. 4.20b). As compared to the conventional response, where a spurious band is present at  $2f_o$ , the CSRR-based prototype device filter exhibits near-40 dB rejection at that frequency, and the device length, excluding access lines, is 2.4 times shorter. Obviously, the size of the conventional device can be partially improved by folding the coupled half-wavelength resonators in a U-shape. However, the resonator's length cannot be reduced in contrast to our basic cells, where the limits of miniaturization are given by technological constraints, rather than by the signal frequency. This prototype device, published in [37], is the first left-handed transmission line based on CSRRs (hybrid approach) used for the design of a bandpass filter following a methodology able to provide the element values of the equivalent-circuit model.

The nonperiodic structure is a third-order Chebyshev bandpass filter with 0.3 dB ripple and 9% fractional bandwidth, centered at  $f_o = 2.5$  GHz. In this case, filter stages are not identical on account of the different element values,  $g_i$ , of the low-pass filter prototype. These have been inferred from table values corresponding to the considered ripple and, from expression (4.8), the 3 dB bandwidth,  $\Delta_i$ , for each resonator has been obtained. From these values, circuit parameters for either filter section have been calculated by means of expressions (4.9)–(4.11) and (4.4), and the seeding filter layout has been inferred as explained before. By forcing the position of the transmission zeros at the convenient values, element parameters have been recalculated (see Table 4.2) and the optimized filter layout has been inferred as explained previously (see Fig. 4.21). In this case, two transmission zeros at 4 GHz and 5 GHz have been considered to reject the spurious band. This prototype device has been fabricated on a Rogers RO3010 substrate with dielectric constant  $\epsilon_r = 10.2$ , but thinner dielectric layer (i.e.,  $h = 0.635$  mm). The measured frequency response is also depicted in Figure 4.21 and compared to that obtained from the

**TABLE 4.2** Element Values for the Equivalent-Circuit Model of the Filter of Figure 4.21

Filter Cell	$C_g$ (pF)	$L_p$ (nH)	$C$ (pF)	$C_c$ (pF)	$L_c$ (nH)
1	0.63	0.49	6.11	20.50	0.059
2	0.63	0.67	3.77	1.03	0.217
3	0.63	0.49	6.11	20.50	0.059

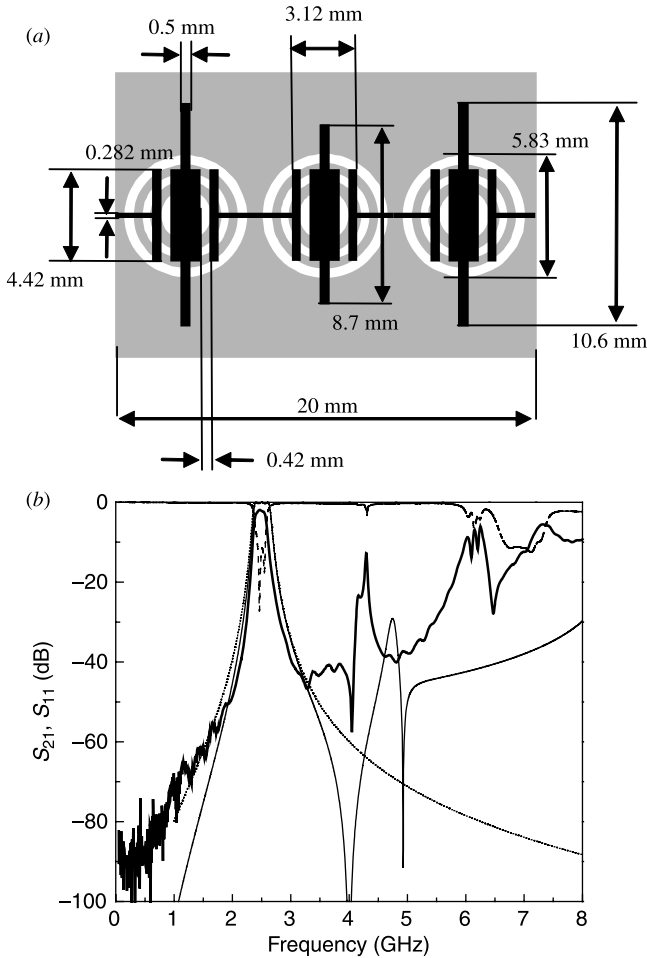


**FIGURE 4.21** Layout and relevant dimensions of the nonperiodic CSRR-based Chebyshev bandpass filter (a) and measured insertion (bold solid line) and return (bold dashed line) losses (b). The insertion losses obtained from circuit simulation of the equivalent circuit model of the filter (thin line) and from the low-pass filter prototype transformation (dotted line) are also depicted for comparison. (Source: Reprinted with permission from [37]; copyright 2006 IEEE.)

equivalent circuit model (by electrical simulation using *Agilent ADS*). It has also been compared to the simulated frequency response inferred on the circuit model obtained by frequency and element transformation from the lowpass filter prototype. Very good agreement between the electrical simulation of the equivalent-circuit model of the filter and the circuit that results from transformation of the lowpass filter prototype has been found in the region of interest. This indicates that the lumped-element model of Figure 4.18b can model, to a very good approximation, any standard approximation inferred from the lowpass filter prototype. The slight discrepancy

between the measured filter fractional bandwidth  $FBW = 7\%$  and the nominal value has been explained before with reference to the previous periodic filter implementation. Moreover, it has to be taken into account that losses have been neglected in the electrical simulations. Measured in-band insertion and return losses are  $IL = 1.9$  dBs and  $RL > 13$  dB, respectively. Finally the authors want to highlight again the small dimensions of the device, with a length, excluding access lines, of  $l = 2\lambda/5$  ( $\lambda$  being the signal wavelength at the central filter frequency). As compared to conventional distributed approaches, the design methodology presented in this section makes it possible to simultaneously achieve small dimensions, low losses, high-frequency selectivity, and good out-of-band performance.

#### 4.2.4.2 Other CSRR-Based Filters Implemented by Means of Right-Handed

**Sections** In the bandpass filters reported in Section 4.2.4.1, the elemental cell is described by a T-circuit model where the series impedance is capacitive and the shunt impedance is inductive (positive reactance) in the passband of interest (hence the structure behaves as a left-handed transmission line section). The design methodology for such bandpass filters, which allows for the synthesis of bandpass filters subject to given specifications and/or standard approximations, is based on the generalized bandpass filter network depicted in Figure 4.17. Indeed, the elemental cell depicted in Figure 4.18 is a particular case, among other possible solutions, for the physical implementation of such a network. The phase shift per cell is positive in the region of interest, instead of being negative, as occurs in other filter unit cells where the shunt resonators are coupled through  $90^\circ$  (actually  $-90^\circ$ ) transmission lines acting as admittance inverters.<sup>14</sup> This is just one of the alternative solutions for the synthesis of CSRR-based bandpass filters, where the characteristic impedance of the  $90^\circ$  line must be set to  $50 \Omega$  in order to obtain the desired electrical characteristics [40]. Another possibility is to replace such transmission line sections by transmission lines merely acting as coupling inductances [41].

Let us now analyze the synthesis of bandpass filters implemented by means of CSRR/stub resonators<sup>15</sup> coupled by means of  $\lambda/4$  (or  $90^\circ$ ) lines. The topology of the basic cell is depicted in Figure 4.22, where rectangular CSRRs have been considered (the shape of the rings is not critical).<sup>16</sup> The equivalent-circuit model is also depicted in this figure. It is identical to that shown in Figure 4.18b, but with the series capacitances replaced by  $\lambda/8$  lines with  $50 \Omega$  characteristic impedance. By cascading such filter sections, the resulting structure can be described by the generalized bandpass filter network shown in Figure 4.17. The admittance inverter ( $\lambda/4$  lines) and the shunt resonator (formed by the parallel combination of the grounded stubs and the capacitively coupled, through  $C$ , CSRRs) can be perfectly identified. The design equations are similar to those reported in Section 4.2.4.1,

<sup>14</sup>The positive phase shift per cell (phase of  $S_{21}$ ) in the structure of Figure 4.18 (see Fig. 4.19a) corresponds to a negative phase constant in the region of interest (left-handed passband).

<sup>15</sup>By CSRR/stub resonators the authors mean those shunt resonators of the elemental unit cell of the hybrid approach, namely, consisting of a CSRR (coupled to the line through a capacitance  $C$ ) combined with a shunt stub.

<sup>16</sup>In the topology of Figure 4.22, only one grounded stub is considered. Obviously, two stubs are also possible, the circuit model of the unit cell being identical.

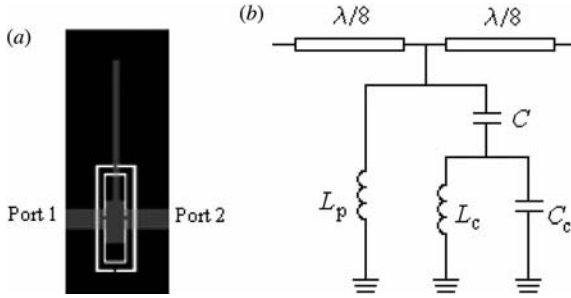


**FIGURE 4.22** Layout of the CSRR/stub resonator (a) and equivalent circuit model (b). The impedance inverter is obtained by means of two  $\lambda/8$  transmission line sections (which form a  $90^\circ$  line when several stages are cascaded to form a filter).

but they are not identical. Namely, the 3 dB bandwidth of each resonator is given by expression (4.8). To univocally determine the four electrical parameters of the equivalent circuit model, four independent equations are required. One of such equations is given by the transmission zero frequency (expression 4.4). Two further equations arise by forcing insertion loss to be  $IL = 3$  dB at  $\omega_1$  and  $\omega_2$ , where these angular frequencies are obtained from expression (4.3) and (4.8), subject to the additional constraint of being equidistant from  $\omega_0$ . This gives

$$\frac{L_p L_c \omega_1^3 (C + C_c) - L_p \omega_1}{L_c \omega_1^2 (C + C_c) - C \omega_1^2 L_p (L_c C_c \omega_1^2 - 1) - 1} = \frac{Z_0}{2} \quad (4.13)$$

and

$$\frac{L_p L_c \omega_2^3 (C + C_c) - L_p \omega_2}{L_c \omega_2^2 (C + C_c) - C \omega_2^2 L_p (L_c C_c \omega_2^2 - 1) - 1} = -\frac{Z_0}{2}. \quad (4.14)$$

Finally, the fourth equation arises by forcing the shunt impedance to be infinity at the central filter frequency. This gives

$$L_c \omega_0^2 (C + C_c) - C \omega_0^2 L_p (L_c C_c \omega_0^2 - 1) - 1 = 0. \quad (14.15)$$

With these model equations, the equivalent circuit as well as the layout of the filtering structure can be inferred (the procedure explained before can be also applied).

One prototype device example is discussed in the following steps in order to highlight the potential of this approach. Specifically, an ultrawide bandpass filter<sup>17</sup> (UWBPF) has been designed with the following specifications:  $FBW = 90\%$ ,  $f_0 = 6.8$  GHz, order  $N = 3$  [40]. The layout that has been obtained after optimization is

<sup>17</sup>UWBPFs are defined as those filters covering a bandwidth of more than 1 GHz or larger than 20%. Nevertheless, ultrawideband (UWB) communication systems are restricted to fulfill the requirements of the mask supplied by the Federal Communication Commission (FCC) in February 2002 to regulate such systems. This mask extends from 3.1 GHz up to 10.6 GHz. Therefore, to avoid interfering signals, filters roughly covering this bandwidth are of interest. Usually such filters are called UWBPFs. Obviously, they satisfy the above definition, but these UWBPFs do not represent the exclusive definition of the term.

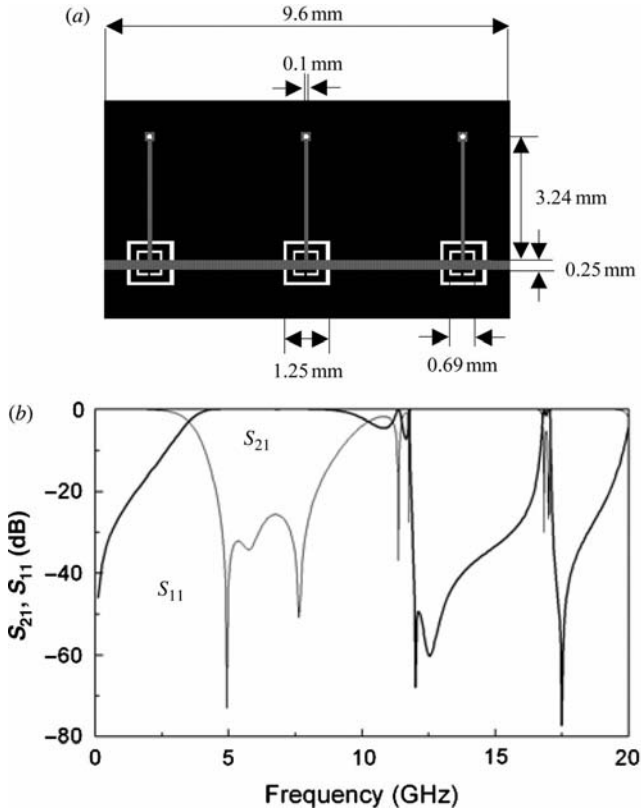


**FIGURE 4.23** Layout of the CSRR-based filter implemented by means of CSRR/stub resonators and  $90^\circ$  impedance inverters (a) and simulated insertion and return losses (b). (Source: Reprinted with permission from [40]; copyright 2005, John Wiley & Sons.)

depicted in Figure 4.23 (the relevant dimensions are indicated). The parameters of the Rogers RO3010 substrate (dielectric constant  $\epsilon = 10.2$ , thickness  $h = 127 \mu\text{m}$ , have been considered). The simulated frequency response of this structure (obtained by means of Agilent momentum) is also represented in Figure 4.23. The frequency parasitic related to the presence of an undesired inductive coupled half-wavelength resonator can be appreciated very close to the upper edge of the band. There is also an additional narrow band at 17 GHz, which is due to a second-order resonance of the CSRRs. To suppress these bands, two properly tuned CSRRs are etched at the filter output. The layout of the final filter and the simulated frequency response are depicted in Figure 4.24a. The *FBW* that results from the simulated frequency response is slightly lower than the nominal value. This is expected on account of the limited frequency range of the admittance inverters, but this effect could be compensated by over-dimensioning the *FBW*. In order to ease fabrication, a prototype device scaled down in frequency has been fabricated on a Rogers RO3010 substrate with identical dielectric constant ( $\epsilon = 10.2$ ), but thicker dielectric layer

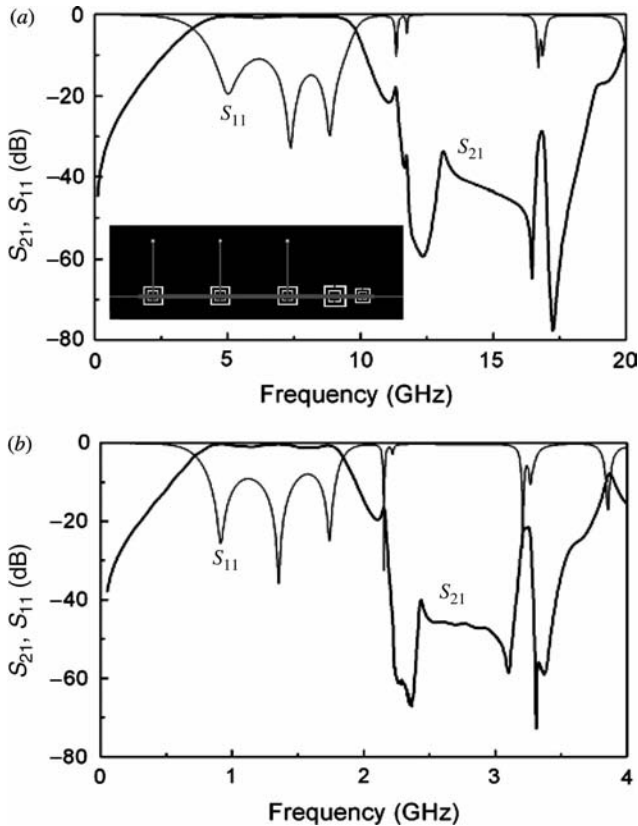


**FIGURE 4.24** Layout and simulated frequency response for the CSRR-based UWB filter with improved stopband (a) and measured frequency response of the fabricated UWBPF scaled down in frequency (scaled up in dimensions) by a factor of 5 (b). (Source: Reprinted with permission from [40]; copyright 2005, John Wiley & Sons.)

( $h = 635 \mu\text{m}$ ). Lateral filter dimensions have been scaled by the same factor as the thickness, so that the lower dimensions are not so critical. The measured frequency response is depicted in Figure 4.24b. Good agreement between simulation (original layout of Fig. 4.24a) and measurements has been obtained. The measured fractional bandwidth is  $FBW = 87\%$ , in-band losses (optimum value) are  $IL = 0.3 \text{ dB}$ , with 1 dB ripple, and return losses are in the vicinity of  $RL = 10 \text{ dB}$ . The authors would also like to highlight that the first spurious band arises at approximately  $3f_0$ . Therefore, the out-of-band filter behavior is quite satisfactory, with rejection levels above 40 dB between 2.2 GHz and 3.2 GHz and above 20 dB up to 3.7 GHz. Obviously, frequency selectivity at the lower transition band can be improved by increasing the number of stages. To illustrate this, an eighth-order prototype-device periodic filter is depicted in Figure 4.25 (the Rogers RO3010 substrate with  $\epsilon_r = 10.2$ ,  $h = 1.27 \text{ mm}$  was used) [42]. The device exhibits a bandwidth covering the



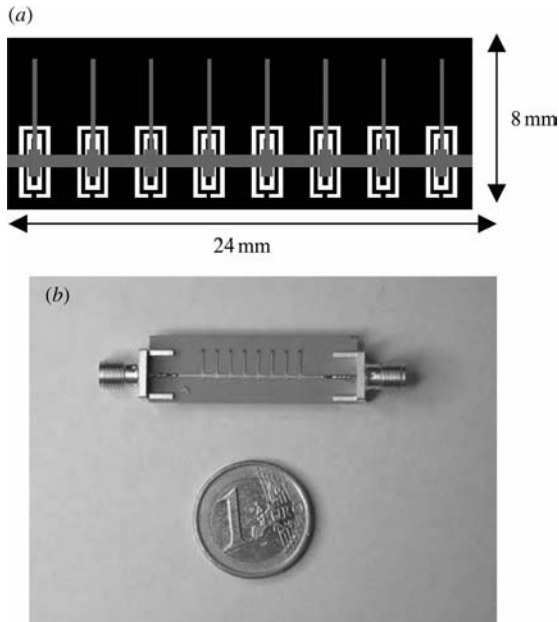


**FIGURE 4.25** Layout (a) and photograph (b) of the fabricated eight-stage UWBPF. Relevant dimensions are indicated. (Source: Reprinted with permission from [42]; Springer Science and Business Media.)

standard band for UWB applications, namely from 3.1 GHz up to 10.6 GHz. The simulated and measured frequency responses for this structure are shown in Figure 4.26. Good out-of-band performance is obtained, return losses in the allowed band are reasonable, and insertion losses are better than 2.4 dB. These results indicate that by using CSRRs, it is possible to design very wide bandpass filters with good out-of-band performance and small dimensions, something not easily achievable simultaneously.

Concerning the design of bandpass filters based on CSRR/stub resonators coupled through transmission-line sections acting as series inductive elements, the topology of the basic cell and its lumped-element equivalent-circuit model are both depicted in Figure 4.27 [41].<sup>18</sup> In contrast to the previous filters, where the characteristic impedance of the  $90^\circ$  lines was always set to  $50 \Omega$ , this impedance (and hence line width) is now an adjustable parameter that is used to achieve the required inductance value. To determine the circuit elements, we again appeal to the generalized bandpass filter network. At the central filter frequency,  $f_o$ , the phase shift between adjacent stages is  $\phi = -90^\circ$  and the image impedance is given by the reference impedance of the ports,  $Z_o$ . If these conditions are applied to the T-circuit model of Figure 4.27b, the series

<sup>18</sup>Notice that the topology and circuit model of these cells are identical to those of the right-handed stages of the ARLH filters discussed in Section 4.2.3.2.

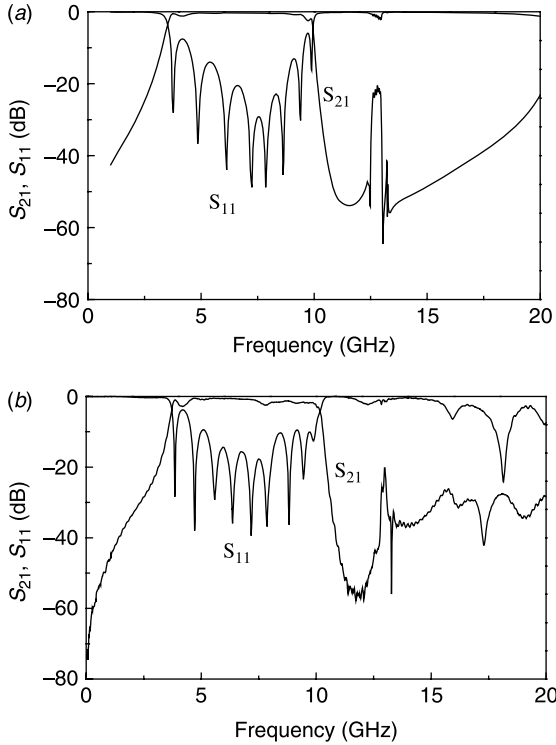


**FIGURE 4.26** Simulated (a) and measured (b) frequency responses for the filter of Figure 4.25. (Source: Reprinted with permission from [42]; Springer Science and Business Media.)

and shunt impedances at  $f_o$  are given by  $Z_s = jZ_o$  and  $Z_p = -jZ_o$ , respectively. Note that the signs of these impedance are the opposite to those of Section 4.2.4.1. From these impedance values, the line inductance is given by

$$L = \frac{2Z_o}{\omega_o}, \tag{4.16}$$

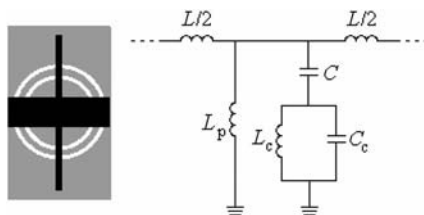


**FIGURE 4.27** Topology of the basic cell for the filters based on inductive coupling, and equivalent circuit model.

and the following condition for the elements of the shunt reactance must hold:

$$\frac{L_p \omega_0 - L_p L_c \omega_0^3 (C + C_c)}{L_c \omega_0^2 (C + C_c) - C \omega_0^2 L_p (L_c C_c \omega_0^2 - 1) - 1} = Z_0 \quad (4.17)$$

The three additional equations required to univocally determine the element values are given by the transmission zero frequency (equation 4.4) and by the 3 dB frequencies,  $\omega_1$  and  $\omega_2$ , of the T-circuit model. At these frequencies the shunt impedance becomes  $Z_p = -jZ_0/2$  and infinity, respectively. Therefore,

$$\frac{L_p \omega_1 - L_p L_c \omega_1^3 (C + C_c)}{L_c \omega_1^2 (C + C_c) - C \omega_1^2 L_p (L_c C_c \omega_1^2 - 1) - 1} = \frac{Z_0}{2} \quad (4.18)$$

and

$$L_c \omega_2^2 (C + C_c) - C \omega_2^2 L_p (L_c C_c \omega_2^2 - 1) - 1 = 0, \quad (4.19)$$

and  $\omega_1$  and  $\omega_2$  are determined from equations (4.3) and (4.8). These equations are very similar to those reported in Section 4.2.4.1. However, the fact that the shunt impedance is capacitive in the region of interest, makes the sign of expression (4.18) to be opposite to that of equation (4.9). The design procedure for these filters is very similar to that explained in the previous subsection. To determine the width of the transmission-line sections between adjacent resonators, the line inductance is forced to take the value given by expression (4.16). This inductance is identical for all the filter stages. However, because filter section lengths may not be identical (due to the variable CSRR size of the different stages), slightly narrower lines are required in those sections with smaller etched rings.

A prototype-device bandpass filter representative of this latter approach is given in Figure 4.28 [41], together with the required specifications (further details on the synthesis of this filter can be found in [41]). To achieve the required 3 dB bandwidths for either resonator section, it has been necessary to use double-slit CSRRs (2-CSRRs), and it has also been necessary to etch two 2-CSRRs pairs at the input and output stages of the filter. The simulated and measured frequency responses of the device, also depicted in Figure 4.28, show that the target specifications are satisfied. The measured central frequency and fractional bandwidth are  $f_0 = 3.8$  GHz and 31.2%, respectively. Measured in-band losses are below 1 dB between 3.36 GHz and 4.15 GHz, with an optimum value of 0.7 dB at  $f_0$ . Return losses better than 15 dB have been obtained between 3.37 GHz and 4.27 GHz. Finally, the out-of-band filter performance is good, with 40 dB rejection at the desired frequency regions. The size of the filter, excluding access lines, is as small as 30 mm  $\times$  16 mm.

The bandpass filters studied in this section can be described by the network representation depicted in Figure 4.17, consisting of a cascade of shunt resonators and admittance inverters. However, bandpass responses can also be synthesized by cascading series resonators and impedance inverters. As open split rings resonators (OSRRs; see Chapter 2 and Problem 2.6) are modeled as series resonant tanks [43], bandpass filters based on these particles can also be designed. The design

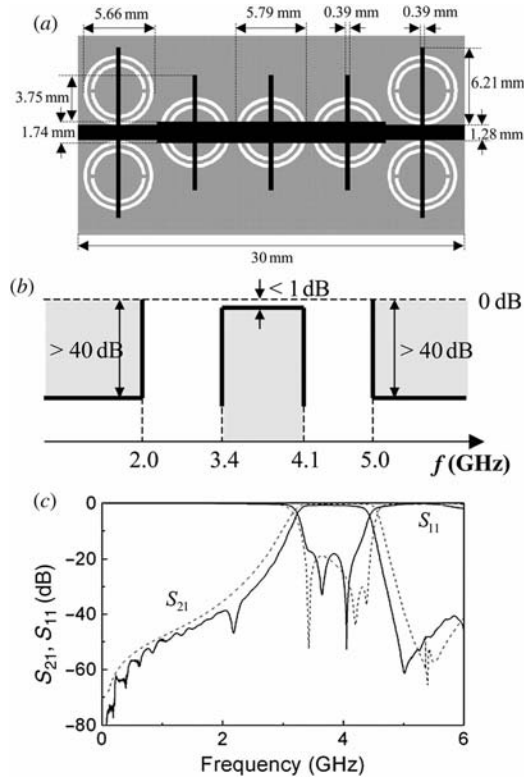


**FIGURE 4.28** (a) Layout of a filter implemented by means of 2-CSRR/stub resonators coupled through inductive transmission lines, and relevant dimensions. (b) Target specifications (insertion loss) for the filter prototype (gray regions represent forbidden loci). (c) Simulated (dashed line) and measured (solid line) insertion and return losses for the fabricated prototype filter. For the external 2-CSRRs, rings slot and separation are 0.29 mm, and for the 2nd, 3rd and 4th stages, these are 0.30 mm. The device has been fabricated on a Rogers RO3010 substrate with dielectric constant  $\epsilon_r = 10.2$  and thickness  $h = 1.27$  mm. (Source: Reprinted with permission from [41]; copyright 2005, John Wiley & Sons.)

methodology is very similar to that corresponding to CSRR/stub shunt resonators coupled through  $90^\circ$  transmission lines and, hence, it is not reproduced here (details of such filters can be found in [44]).

#### 4.2.5 Highpass Filters and Ultrawide Bandpass Filters (UWBPFs) Implemented by Means of Resonant-Type Balanced CRLH Metamaterial Transmission Lines

It was pointed out in Chapter 3 that left-handed lines implemented by means of SRRs or CSRRs exhibit a CRLH behavior, and that by properly designing such lines it is possible to collapse the gap between the left-handed and right-handed bands

(balanced design). Balanced CRLH lines exhibit typically broad bandwidths that are useful for the synthesis of highpass filters (HPFs) or ultrawide bandpass filters (UWBPFs). In microwave engineering the difference between an HPF and a UWBPF is subtle. Namely, a microwave HPF implemented in planar technology does not in fact exhibit an unlimited (i.e., extending up to infinity) band above the cutoff frequency. Thus, microwave HPFs are indeed bandpass filters with a very wide band and a controllable cutoff frequency at the lower band edge. In other words, the difference between an HPF and a UWBPF is merely the fact that in these latter filters, both the upper and lower cutoff frequencies are controllable, and in HPFs the upper limit of the band is not a target specification. With these comments in mind, it is clear that balanced CRLH CSRR-based unit cells such as those depicted in Figure 3.46 are useful for the synthesis of HPFs. They exhibit a huge transmission band above the cutoff, and frequency selectivity is good due to the presence of a transmission zero. Moreover, rejection below cutoff can be controlled by the number of stages of the structure. To illustrate this possibility, a prototype-device HPF consisting of three stages, identical to that depicted in Figure 3.46 has been fabricated and characterized (Fig. 4.29) [45]. For comparison, also depicted in this figure are the simulated frequency responses of two- and four-stage devices. As has been indicated, rejection below cutoff is controlled by the number of cells.

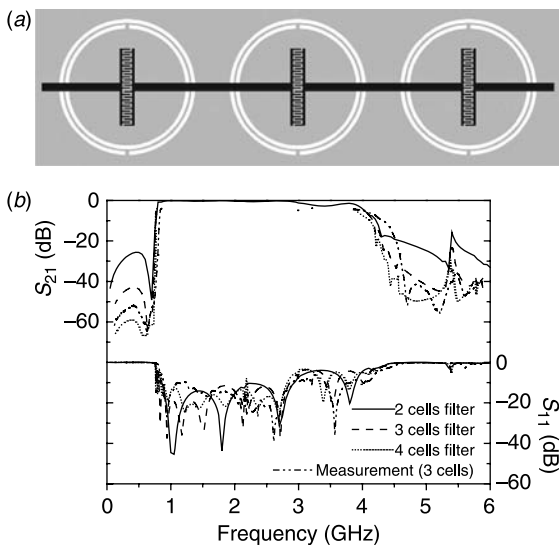


**FIGURE 4.29** Layout of the microstrip filter formed by three balanced CRLH CSRR-based cells (a) and measured frequency response (b). In (b) are also depicted the simulated insertion and return losses for two-, three-, and four-stage device filters. The metallic parts are depicted in black in the top layer and in gray in the bottom layer. Dimensions are: total length  $l = 55$  mm, line width  $W = 0.8$  mm, external radius of the outer rings  $r = 7.3$  mm, ring width  $c = 0.4$  mm and ring separation  $d = 0.2$  mm; the interdigital capacitors are formed by 28 fingers separated by 0.16 mm. (Source: Reprinted with permission from [45]; copyright 2007, IEEE.)

For the measured three-stage device filter, rejection below cutoff is better than 50 dB, and in-band insertion and return losses are good up to 3 GHz.

To synthesize a UWBPf by using the previous structures, it is necessary to include additional elements able to limit the transmission band. These elements can also be multituned CSRRs (see Section 4.2.1), acting as negative-permittivity particles and designed to achieve the upper filter cutoff at the required frequency. In Figure 4.30 a UWBPf is depicted roughly covering the mask supplied by the Federal Communication Commission (FCC) to regulate ultrawideband (UWB) communication systems (3.1–10.6 GHz). In this filter, the CSRRs introduced to control the upper stopband are etched inside those CSRRs that are used to synthesize the balanced CRLH structure. Moreover, additional CSRs (complementary spiral resonators) can be seen cascaded to the input and output ports. These latter elements are introduced to demonstrate that it is possible to provide a transmission zero within the allowed band, this being of interest for the rejection of potential interfering signals, such as WLAN, among others<sup>19</sup> [46,47]. The simulated and measured frequency responses of this filter are depicted in Figure 4.30b.<sup>20</sup> As expected, a notch in the vicinity of 5 GHz results due to the presence of the CSRs. The measured bandwidth roughly coincides with that given by the FCC (discrepancy between measurement and simulation is attributed to fabrication-related tolerances). Other UWBPfs based on a combination of CSRRs and SRRs covering the FCC mask have been proposed [48]. Broadband filters based on balanced dual transmission lines can be found in [49].

#### 4.2.6 Tunable Filters Based on Varactor-Loaded Split Rings Resonators (VLSRRs)

Reconfigurable (tunable) devices are required in modern communications systems that need to adapt to changing operating conditions. Among these devices, filters are probably the microwave components where most efforts have been devoted towards finding solutions providing accurate control of their electrical characteristics and tunability over wide ranges. Tunable filters are based on electronically controllable components such as varactor diodes or RF-MEMS (microelectromechanical switches), among others, where a variable capacitance is used to tailor device characteristics. Varactor diodes and RF-MEMS have been applied to the design of tunable devices, such as filters and other microwave components, based on conventional configurations [50]. The possibility of designing tunable filters and resonators by means of active electromagnetic bandgaps (EBGs) [51] has also been demonstrated based on varactor diodes. In this section, it is demonstrated that tunable filters can be implemented by using resonant-type metamaterial transmission lines loaded with varactor diodes.

<sup>19</sup>For the designed structure, the transmission zero in the vicinity of 5 GHz is of interest for the elimination of WLAN radio signals following the IEEE 802.11a or Hiperlan/2 standards (data rates up to 54 Mbps in a regulated frequency spectrum around 5 GHz).

<sup>20</sup>Although UWBPf filters with better performance have been designed and fabricated [48], the device of Figure 4.30 has been chosen to illustrate the possibility of etching the smaller CSRRs (responsible for the upper stopband) inside the larger CSRRs.

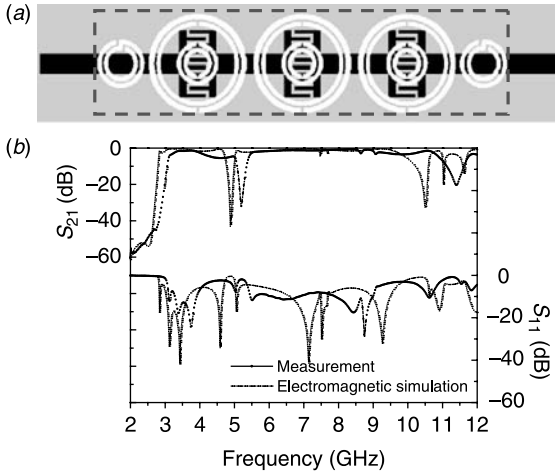


**FIGURE 4.30** Layout of the fabricated UWBPF (a) and frequency response (b). Dimensions of the smaller CSRRs are  $c = 0.17$  mm,  $d = 0.11$  mm and  $r_{\text{ext}} = 0.89$  mm (those CSRRs of the extremes are slightly larger to improve the upper stopband, as is explained in the text). CSRRs have been tuned to provide a transmission zero at 5 GHz ( $c = 0.17$  mm,  $d = 0.11$  mm and  $r_{\text{ext}} = 1.01$  mm). Dimensions of the larger CSRRs are  $r_{\text{ext}} = 2.10$  mm,  $d = 0.11$  mm,  $c = 0.22$  mm, and  $c = 0.16$  mm for the external and internal ring, respectively. The area of the device (dashed rectangle) is  $A = 1.77$  cm  $\times$  0.41 cm. CSRRs and CSRs are printed in the ground plane (in gray). The Rogers RO3010 substrate with thickness  $h = 635$   $\mu$ m and dielectric constant  $\epsilon_r = 10.2$  has been used.

Though not exclusive, one possibility of achieving tunability is managed by adding the varactor diodes to the resonant elements (SRRs). The result is the varactor-loaded split rings resonator (VLSRR), which was introduced by Gil et al. [52]. By loading a transmission line with VLSRRs and biasing the varactors at different voltages, the transmission characteristics of the structure can be tailored.

**4.2.6.1 Topology of the VLSRR and Equivalent-Circuit Model** The original topology (layout) of the VLSRRs proposed by Gil et al. [52] is depicted in Figure 4.31a. It is similar to the topology originally proposed by Pendry [53]

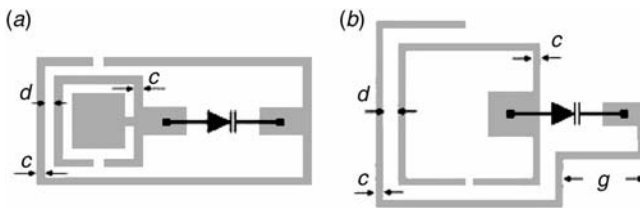


**FIGURE 4.31** Topologies of the tunable VLSRR (a) and VLSRR with improved geometry (b). The relevant dimensions are indicated. (Source: Reprinted with permission from [54]; copyright 2006, IEEE.)

(Chapter 2), although the separation between rings,  $d$ , is no longer uniform in order to connect the diode varactor between the internal and external conductors. A metal pad is added in the center of the particle to ease diode biasing, and rectangular rings have been considered to enhance line-to-rings coupling. With this configuration, the electromagnetic behavior of the VLSRRs does not substantially differ from that of the SRR, except in the fact that certain electronic control of the resonance frequency is possible thanks to the varactors, which are connected between the inner and outer conductors and dominate over the edge capacitance corresponding to the right half of the structure. Another difference between SRRs and VLSRRs concerns their excitation, or the generation of current loops at resonance. In the former, these currents are mainly induced by the magnetic field flowing into the inner ring, whereas in VLSRRs, rings excitation is mainly achieved by the magnetic field penetrating the inter-rings region where the varactors are allocated. Alternatively, the topology presented in Figure 4.31*b*, can also be considered to achieve tuning [54]. As compared to the structure of Figure 4.31*a*, the right-hand arm of the outer ring has been shortened because no appreciable current flows through it (this has been corroborated by electromagnetic simulation). In other words, the electric current is mostly absorbed by the varactor diode, preventing it from circulating across the portion of the external ring between the diode junction and the slit.

The lumped-element equivalent-circuit model of a biased VLSRR coupled to a microstrip transmission line is depicted in Figure 4.32 [54]. Diode varactors are modeled by a variable capacitance,  $C_{VAR}$ , and a series resistance,  $R_s$ , which takes into account not only the intrinsic losses of the diode,  $R_D$ , but also the resistance associated with the varactor-metal junctions,  $R_{VM}$ .  $C_R$  (which is neglected due to the shunt connection of  $C_{VAR}$  to it) and  $C_L$  are the edge capacitances corresponding to the right and left halves, respectively, of the VLSRR, and  $L_r$  and  $C_{pad}$  model the equivalent inductance of the VLSRRs and the pad-to-ground capacitance, respectively. Diode biasing is applied through a variable voltage source,  $V_{bias}$ , which has

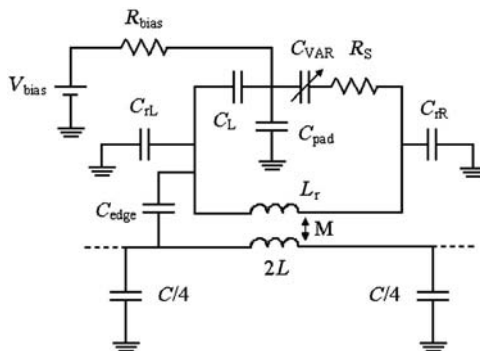


**FIGURE 4.32** Lumped-element equivalent-circuit model for the elemental cell of a biased VLSRR coupled to a microstrip transmission line.  $L$  and  $C$  are the per-section inductance and capacitance of the line. Due to symmetry, the magnetic wall concept has been used. (Source: Reprinted with permission from [54]; copyright 2006, IEEE.)



an equivalent output resistance termed  $R_{\text{bias}}$ . Concerning line-to-VLSRRs coupling, we *a priori* assume that VLSRRs can be driven either by the axial magnetic field generated by the line (inductive coupling) or by the electric field present between the line and the external ring (capacitive coupling). Both couplings have been properly modeled by means of a mutual inductance,  $M$  (magnetic coupling), and the edge capacitance between the line and the external ring,  $C_{\text{edge}}$  (electric coupling). The capacitances  $C_{\text{rL}}$  and  $C_{\text{rR}}$  are the rings-to-ground capacitances of the left and right halves, respectively.

**4.2.6.2 Validation of the Model** The previous model is validated by comparing the frequency response measured on a fabricated VLSRR-loaded microstrip line with that obtained through electrical simulation of the lumped-element equivalent circuit. To this end, a two-stage device has been fabricated (Fig. 4.33a). BB833-Infineon Technologies silicon tuning diodes have been used as nonlinear capacitances (the capacitance window for these diodes is 0.75–9 pF for voltages varying in the interval 0–30 V). As expected, a stopband (due to the negative effective permeability of the structure) with tuning capability is obtained (Fig. 4.33b). The device has been fabricated on a Rogers RO3010 substrate (dielectric constant  $\epsilon_r = 10.2$ , thickness  $h = 1.27$  mm,  $\tan \delta = 0.0023$ ). Except the mutual inductance,  $M$ , and the varactor–metal junction resistance,  $R_{\text{VM}}$ , which have been used as fitting parameters, the other element values have been estimated either through geometrical considerations or with the help of the commercial software *Agilent ADS* (see [54] for details). The frequency responses depicted in Figure 4.33c have been obtained by setting  $M = 2.4$  nH and  $R_{\text{VM}} = 3 \Omega$  (the other parameters are indicated in the caption of Fig. 4.33), and are those that have optimally fitted the experiment over the considered tuning interval. The good agreement between theory and experiment supports the validity of the model.

As it is, the equivalent-circuit model includes both magnetic and electric coupling between the host line and the VLSRRs. However, if the electric coupling is switched off by removing the coupling capacitance  $C_{\text{edge}}$ , no appreciable differences in the simulated frequency responses (over the tuning interval considered) come up. Moreover, no appreciable changes arise if  $C_{\text{pad}}$  is removed. Hence, the electric coupling can be neglected and the equivalent circuit model of the VLSRR-loaded microstrip line can be simplified to that shown in Figure 4.34a, where inductive excitation of the VLSRRs is the single coupling mechanism (the simulated frequency response with  $C_{\text{edge}}$  and  $C_{\text{pad}}$  removed is shown in Fig. 4.34b for comparison purposes). Indeed, this circuit can be further simplified to the circuit of Figure 3.23b, with  $C'_s$  replaced by  $C_{\text{eq}} = C_{\text{L}}C_{\text{VAR}}/(C_{\text{L}} + C_{\text{VAR}})$  (see details in Chapter 3).<sup>21</sup>

**4.2.6.3 Some Illustrative Results: Tunable Notch Filters and Stopband Filters** VLSRRs coupled to microstrip lines can be applied to the synthesis of

<sup>21</sup>The circuit is simplified by neglecting  $C_{\text{rL}}$  and  $C_{\text{rR}}$ , which are small. Thus,  $R_{\text{bias}}$  merely acts as a polarization path for the diodes (i.e., irrelevant for signal analysis).

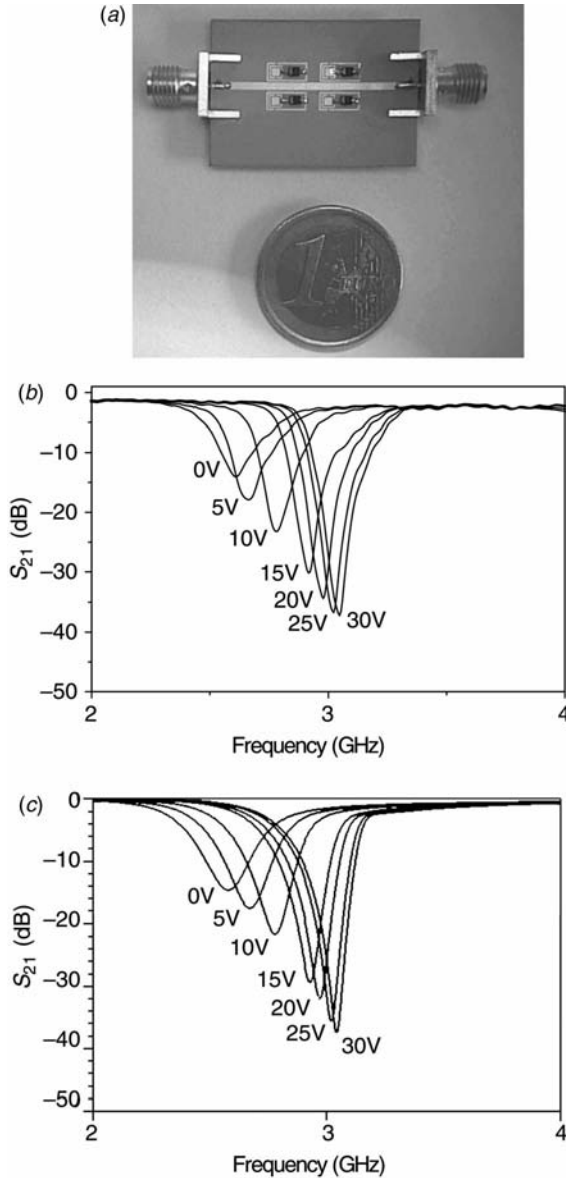


**FIGURE 4.33** Photograph of a two-stage VLSRR-loaded microstrip line (a), measured insertion losses for different diode polarizations (b) and frequency responses obtained by electrical simulation of the equivalent-circuit model shown in Figure 4.32. Relevant dimensions are  $c = d = 0.2$  mm, separation between line and external rings is 0.2 mm, and length and width of VLSRRs are 6.2 mm and 2.8 mm, respectively. Element values are  $L_r = 3$  nH,  $C_L = 1.4$  pF,  $C_{\text{edge}} = 1$  fF,  $C_{rL} = 0.1$  pF,  $C_{\text{pad}} = 0.44$  pF,  $C_{rR} = 0.89$  pF,  $L = 3.3$  nH,  $C = 1.3$  pF,  $R_S = 4.8 \Omega$ , (i.e.,  $R_D = 1.8 \Omega$  and  $R_{VM} = 3.0 \Omega$ ),  $R_{\text{bias}} = 50 \Omega$ ,  $M = 2.4$  nH and  $1 \text{ pF} \leq C_{\text{VAR}} \leq 9 \text{ pF}$ . (Source: Reprinted with permission from [54]; copyright 2006, IEEE.)

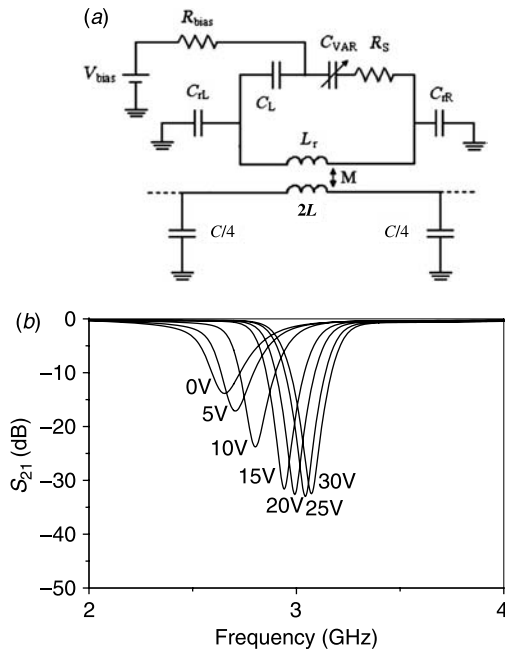


**FIGURE 4.34** Equivalent-circuit model of the VLSRR-loaded microstrip line with electric coupling removed (a), and electrical simulations for different diode polarizations (b). (Source: Reprinted with permission from [54]; copyright 2006, IEEE.)

tunable notch and stopband filters [52,54]. Indeed, the structure of Figure 4.33a is an example of a tunable notch filter, where the notch frequency is bias-controlled.<sup>22</sup> Rejection can be improved by adding VLSRR stages (see a four-stage device in Figure 4.35a and the corresponding response in Fig. 4.35b). By biasing the diodes at different voltage levels, it is possible to widen and to tailor filter bandwidth, as Figure 4.35c and d illustrate.<sup>23</sup>

By adding inductive vias to the previous structures, tunable bandpass filters exhibiting left-handedness are obtained [54]. However, due to varactor diode losses, the performance of these devices is very limited. To synthesize tunable bandpass filters with good performance, low-loss tuning elements such as RF-MEMS are required. The combination of these elements with SRRs or CSRR is very promising.

To summarize Section 4.2, it has been shown that metamaterial transmission lines based on SRRs and CSRRs are useful for the design of microwave filters in planar technology. Stopband filters and bandpass filters with narrow and widebands can

<sup>22</sup>Rejection level and bandwidth also change with tuning. This is explained by the variation in  $Q$  factor that results when the notch frequency is tuned (see Problem 4.2).

<sup>23</sup>Another possible solution to produce wide stopbands in stopband filters is to design the VLSRR stages having slightly different dimensions (closed resonances are obtained) and to apply the same varying bias voltage to the devices.

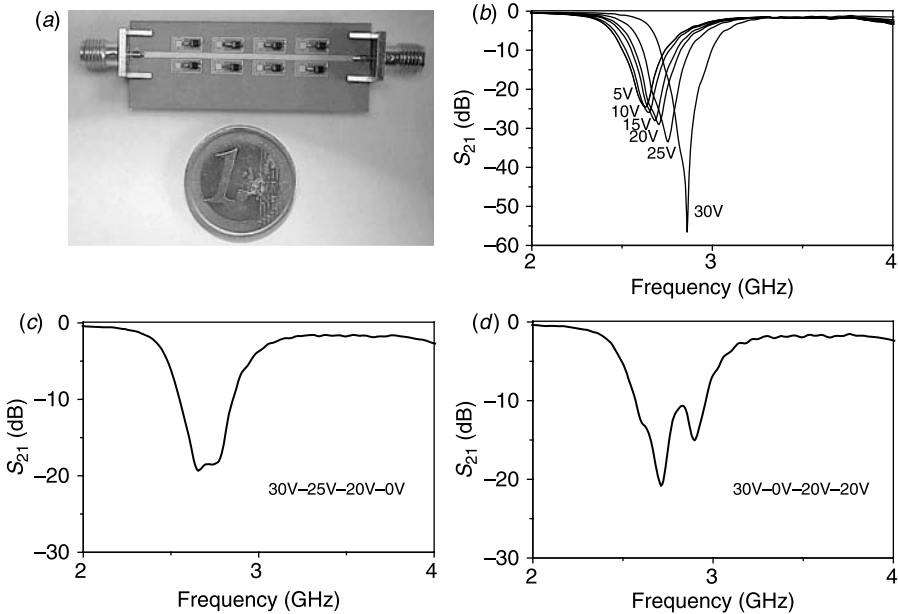


**FIGURE 4.35** Fabricated four-stage VLSRR microstrip line (a) and measured frequency response for identical bias voltage applied to the diode varactors (b). In (c) and (d) are depicted the measured transmission characteristics of the structure by applying the indicated voltages to the different VLSRR stages. Dimensions are identical to those of Figure 4.33a. (Source: Reprinted with permission from [54]; copyright 2006, IEEE.)

be synthesized, and a systematic design methodology has been proposed that allows us to design filters subject to specifications, or following standard approximations. Miniaturization, optimization of device performance through elimination of spurious frequencies, as well as the possibility to control filter bandwidth over wide margins are key issues. In the opinion of the authors, one of the domains where resonant-type one-dimensional metamaterials, or structures based (or inspired) on them, can find more practical applications is in the field of filters. However, the small dimensions of the unit cells, as well as their unusual electromagnetic properties, make resonant-type metamaterials very promising in other microwave applications, as will be explored in the next sections.

### 4.3 SYNTHESIS OF METAMATERIAL TRANSMISSION LINES WITH CONTROLLABLE CHARACTERISTICS AND APPLICATIONS

It has been pointed out at the beginning of this chapter that the most outstanding property of metamaterial transmission lines is the controllability of their electrical characteristics (impedance and phase). In these artificial lines there are more parameters to tailor, compared to conventional transmission lines. This means that the number of

degrees of freedom is larger and hence it is possible to synthesize transmission lines with a combination of characteristics and dimensions not easily achievable through conventional implementations. By engineering these lines it is also possible to design microwave components with superior performance as compared to existing devices, or to obtain microwave devices based on new functionalities, such as dual-band components. In this section we will review these aspects. Section 4.3.1 is devoted to the miniaturization of microwave components, Section 4.3.2 is focused on the synthesis of enhanced bandwidth devices, in Section 4.3.3 we will discuss the principles for the design of dual-band components, and, finally, Section 4.3.4 will be devoted to coupled-line couplers based on metamaterials.

### 4.3.1 Miniaturization of Microwave Components

The size reduction of microwave components is based on two features: (1) the small dimensions of the constitutive unit cells of metamaterial transmission lines and (2) the control of the electrical length of such lines, which covers a wide margin with a single-unit cell, as was pointed out in Chapter 3.<sup>24</sup> Planar microwave circuits based on the distributed approach consist of combinations of transmission lines and stubs with certain characteristic impedance,  $Z_B$ , and electrical length,  $\phi$ . Conventional transmission lines and stubs can thus be substituted by their metamaterial counterparts with the possibility of significantly reducing dimensions. Obviously, the most favorable solution in terms of dimensions is achieved if only one unit cell is used.<sup>25</sup>

The synthesis of metamaterial transmission lines consists of the determination of the parameters of the circuit model of such lines from the required values of characteristic impedance  $Z_n = Z_B(f_n)$  and electrical length  $\phi_n = \phi(f_n)$  at the operating (design) frequency,  $f_n$ . As the example given later is based on the resonant-type approach (using CSRR-based left-handed lines), the considered model to infer the reactive parameters from transmission line parameters is that depicted in Figure 3.38, where the line inductance has been neglected as it is assumed that the series impedance is dominated by the gap capacitance (this aspect was discussed in Chapter 3). From equations (3.1) and (3.2), the capacitance value of the series gap can be easily inferred as

$$C_g = \frac{1}{2\omega_n Z_n} \sqrt{\frac{1 + \cos \phi_n}{1 - \cos \phi_n}} \quad (4.20)$$

<sup>24</sup>According to the typical dispersion diagrams of left-handed and CRLH lines, the phase of the unit cell varies between  $-\pi$  and 0 along the left-handed band.

<sup>25</sup>At this point we would like to mention that although the commonly accepted definition of metamaterial transmission line refers to an effectively homogeneous periodic structure (i.e., with period much smaller than guided wavelength) with controllable characteristics, we will be flexible and we will adopt under this term also those structures not satisfying the former requirement (homogeneity), including structures with a single-unit cell. The reason is that for microwave circuit design the aim is to achieve the required electrical characteristics at the design frequency, rather than synthesizing an effective medium.

where  $\omega_n = 2\pi f_n$ . To obtain the other parameters of the equivalent-circuit model, inversion of equations (3.1), (3.2), (3.56), and (3.57) is necessary. This involves a tedious calculation. The final results are (see Problem 4.3 and [55])

$$L_c = \frac{Z_n}{2} \sqrt{\frac{1 + \cos \phi_n}{1 - \cos \phi_n}} \frac{\omega_n (\omega_H^2 - \omega_L^2)(\omega_H^2 - \omega_n^2)}{\omega_H^4 (\omega_n^2 - \omega_L^2)}, \tag{4.21}$$

$$C_c = \frac{1}{L_c \omega_H^2}, \tag{4.22}$$

and

$$C = \frac{2\omega_H^2(\omega_n^2 - \omega_L^2)\sqrt{1 - \cos^2(\phi_n)}}{Z_n \omega_n [\omega_n^2(1 + \cos \phi_n)(\omega_H^2 - \omega_L^2) - 2\omega_H^2(\omega_n^2 - \omega_L^2)]}, \tag{4.23}$$

where  $\omega_L = 2\pi f_L$  and  $\omega_H = 2\pi f_H$  ( $f_L$  and  $f_H$  being the lower and upper limit of the left-handed band, given by expressions 3.56 and 3.57). Inspection of equations (4.20)–(4.23) reveals that  $C_g$ ,  $L_c$ , and  $C_c$  are always positive provided  $\omega_L < \omega_n < \omega_H$ . However, depending on the relative values of these angular frequencies,  $C$  may be negative. Therefore, the operative bandwidth of the device is limited by the value of  $C$ , which must be a real positive number.<sup>26</sup>

To illustrate the achievable size reduction by using resonant-type left-handed lines, a Y-junction power divider is designed. In such power dividers, two 90° line admittance inverters are used (see the schematic in Fig. 4.36). In order to achieve

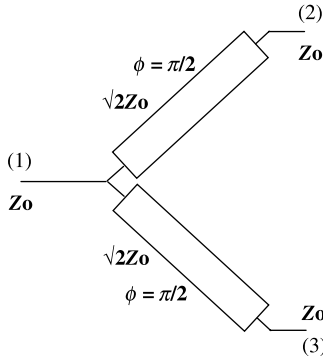


**FIGURE 4.36** Schematic of a Y-junction power divider implemented by means of 90° impedance inverters.

<sup>26</sup>Although  $f_L$  and  $f_H$  are not actually design parameters, device bandwidth increases as the separation between these frequencies is higher. More details on the limited bandwidth of these structures is given in [55].

impedance matching for the input port, the characteristic impedance of such  $90^\circ$  transmission lines must be set to  $1.41Z_o$ , where  $Z_o$  is the reference impedance of the ports (normally  $50\ \Omega$ ). The metamaterial power divider can be implemented by means of CSRR-based left-handed lines with the required electrical parameters ( $Z_n = 1.41Z_o = 70.7\ \Omega$  and  $\phi_n = -90^\circ$ )<sup>27</sup> at the operating frequency (which has been set to  $f_n = 1.5\ \text{GHz}$ ). From these parameters and frequency, the elements of the equivalent-circuit model have been obtained (following the procedure described above). To this end, the frequencies delimiting the allowed left-handed band have been set to  $f_L = 1.38\ \text{GHz}$  and  $f_H = 1.68\ \text{GHz}$ . With these delimiting frequencies, the element values are found to be reasonable (i.e.,  $C_g = 0.75\ \text{pF}$ ,  $C = 14.9\ \text{pF}$ ,  $L_c = 1.76\ \text{nH}$ , and  $C_c = 5.08\ \text{pF}$ ). Once the element values have been inferred, the layout of the inverter can be obtained (optimization and the parameter extraction method described in Chapter 3 are used). The layout of the CSRR-based power divider is depicted in Figure 4.37 and compared to that corresponding to a conventional implementation (photographs of the fabricated device are also depicted in this figure). Significant size reduction (50% as compared to conventional implementation) is achieved through the use of metamaterial admittance inverters. The measured and simulated frequency responses of the designed metamaterial power divider are depicted in Figure 4.38 ( $S_{31}$  is roughly identical to  $S_{21}$  and is not represented in the figure). The measured insertion losses at the design frequency ( $\text{dB}(S_{21}) = -3.2\ \text{dB}$ ), are close to the value corresponding to an ideal lossless device, and measured return losses are better than 20 dB. Thus, device miniaturization is achieved, maintaining device performance at the design frequency. Although not represented, the frequency response of the conventional device exhibits a wider operative bandwidth. However, this does not mean that in general the operative bandwidth of metamaterial-based devices is smaller than that achievable through conventional implementations. On the contrary, it will be shown in the next section that it is possible to design enhanced bandwidth devices by using metamaterial transmission lines in their designs.

### 4.3.2 Compact Broadband Devices

Let us now try to explain the principle for the design of compact broadband microwave components. The limited bandwidth of microwave components is due to the phase shift experienced by transmission lines and stubs when frequency is varied from the nominal operating value. Let us assume that at this frequency,  $\omega_n$ , the phase shift is  $\phi(\omega_n) = \phi_n$ . This phase shift is related to the phase velocity,  $v_p$ , of the line according to the following expression:

$$\phi_n = \beta l = \frac{l}{v_p} \omega_n, \quad (4.24)$$

<sup>27</sup>The negative sign of the phase of the left-handed admittance inverters is irrelevant for device operation.

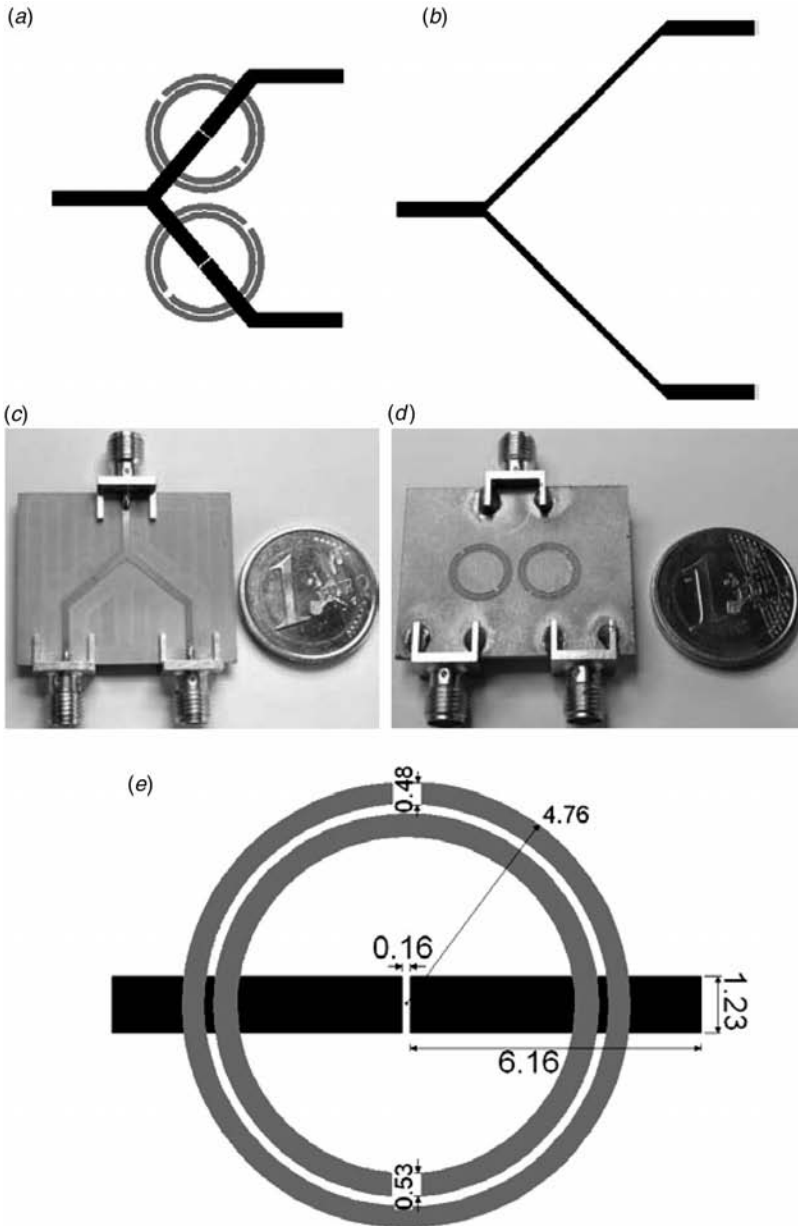


**FIGURE 4.37** Layout (a) and photographs of the top (c) and bottom (d) faces of the CSRR-based power divider implemented by following the schematic of Figure 4.36. For comparison, the layout of a conventional power divider designed by considering an identical substrate is also depicted (b). The dimensions (in mm) of the two impedance inverters forming the device are those indicated in (e). In (e), the upper metal strip is depicted in black, whereas the slot of the CSRR is depicted in gray. (Source: Reprinted with permission from [55].)



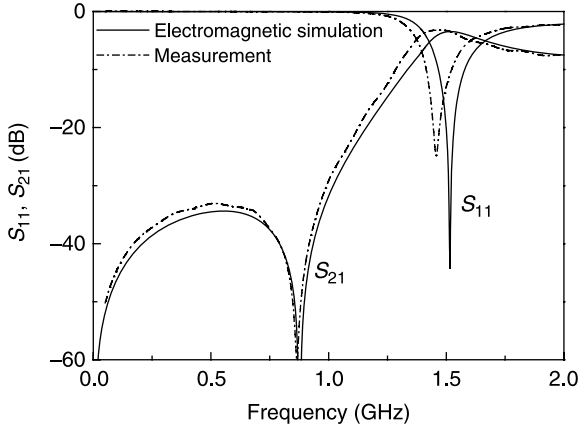


**FIGURE 4.38** Simulated and measured frequency responses for the power divider shown in Figure 4.37. (Source: Reprinted with permission from [55].)

where  $l$  is the length of the line. The bandwidth of any transmission-line-based device is given by the frequency interval where the variation of  $\phi$ , namely  $\Delta\phi = \phi - \phi_n$ , is lower than a certain predetermined value. Hence, bandwidth is intimately related to the derivative of  $\phi$  with frequency, also known as group delay. In view of expression (4.24), this derivative increases with the length of the line and therefore we obtain the well-known conclusion that bandwidth decreases with the phase shift (proportional to  $l$ ) of the line. To enhance bandwidth it is therefore necessary to reduce  $l$ . However, in practical situations, one needs a certain value of the phase shift and this procedure is not useful. However, by using metamaterial transmission lines, we can take advantage of certain control over the dispersion diagram of the line. This means that it is potentially possible to design a transmission line with the required phase shift at the operating frequency, and smaller group delay than that of a conventional line. To illustrate this, let us consider for instance the design of a transmission line with in-phase input and output signals, which can be of interest for instance to feed an array of antennas (where in-phase signals at either radiating element may be required). By using a conventional transmission line, the length of the line must be chosen according to equation (4.24) in order to obtain a phase shift between the input and output ports of  $\phi_n = 2\pi N$ , where  $N$  is an integer. Due to the reasons already explained at the beginning of this subsection, the optimum bandwidth is obtained when  $N = 1$ , which corresponds to the shorter line. Alternatively, a balanced CRLH line operating at the transition frequency can be designed to actually achieve zero phase shift at that frequency. The group delay for the conventional line is  $\tau_C = 2\pi/\omega_n$ . Therefore, to enhance bandwidth by means of the CRLH line, it is necessary that the group delay at the transition frequency satisfies  $\tau_{\text{CRLH}} < \tau_C$ . In reference to LC-loaded balanced CRLH lines, the phase shift in the vicinity of the transition frequency can be inferred by forcing  $\omega_s = \omega_p$  in equation (3.29). This gives

$$\beta l = \omega\sqrt{L_R C_R} - \frac{1}{\omega\sqrt{L_L C_L}}. \tag{4.25}$$

The first derivative with frequency gives  $\tau_{\text{CRLH}}$ , and by forcing it to be smaller than  $\tau_{\text{C}}$ , the following inequality results:

$$\omega_n \sqrt{L_R C_R} + \frac{1}{\omega_n \sqrt{L_L C_L}} < 2\pi. \quad (4.26)$$

Two additional equations arise from the balance condition and the required characteristic impedance,  $Z_o$ , of the line:

$$Z_o = \sqrt{\frac{L_R}{C_R}} = \sqrt{\frac{L_L}{C_L}}. \quad (4.27)$$

To satisfy inequality (4.26), and to obtain a significant bandwidth enhancement,  $\omega_R$  (equation 3.23) must be chosen as high as possible<sup>28</sup> and  $\omega_L$  (equation 3.24) as low as possible. This is consistent with the fact that to obtain a small variation of  $Z_o$  in the vicinity of the operating frequency,  $\omega_n = \omega_o$ ,  $L_R$  must be small (see equation 3.22).

Following the previous idea, bandwidth improvement has been experimentally demonstrated in a 1:4 series power divider, where zero-degree metamaterial phase-shifting lines have been used instead of  $360^\circ$  lines [56]. Namely, in-phase signals at the input of either divider branch are achieved though zero-degree designed metamaterial transmission lines, which are placed between the different output branches of the divider. As compared to the conventional device, the metamaterial-based power divider exhibits an improved bandwidth. The conventional and metamaterial power dividers are depicted in Figure 4.39 with their corresponding electrical characteristics. Another significant aspect of the metamaterial power divider is area reduction, because the metamaterial transmission lines are substantially shorter than the conventional  $\lambda$  lines.

Bandwidth enhancement can be achieved by using metamaterial transmission lines in devices based on the difference of phases between certain transmission lines. The idea is very simple. Let us consider that at the operating frequency,  $\omega_n$ , the required phases of two transmission lines in such device are  $\phi_1$  and  $\phi_2$ , respectively. Bandwidth depends in this case on the derivative of the phase difference with angular frequency, which is proportional to the difference in the length of such lines (expression 4.24). The larger the phase difference, the lower the bandwidth becomes. However, by replacing one of these lines with a metamaterial transmission line, it is possible to tailor the dispersion diagram of this line to be roughly parallel to that of the conventional line at the frequency of interest, and hence obtain a wider bandwidth. This situation is illustrated in Figure 4.40.

By using the previous idea, several devices have been implemented. For instance rat race hybrid couplers have been proposed, where the phase balance for the  $\Delta$  and  $\Sigma$  ports exhibit broader bandwidths than those obtained in the conventional implementations. The topology of the conventional rat race hybrid coupler is depicted in Figure 4.41a. It is essentially a four-port device consisting of a  $1.5 \lambda$  ring structure

<sup>28</sup>To obtain a high value of  $\omega_R$ , it suffices to implement the structure with a short host line.

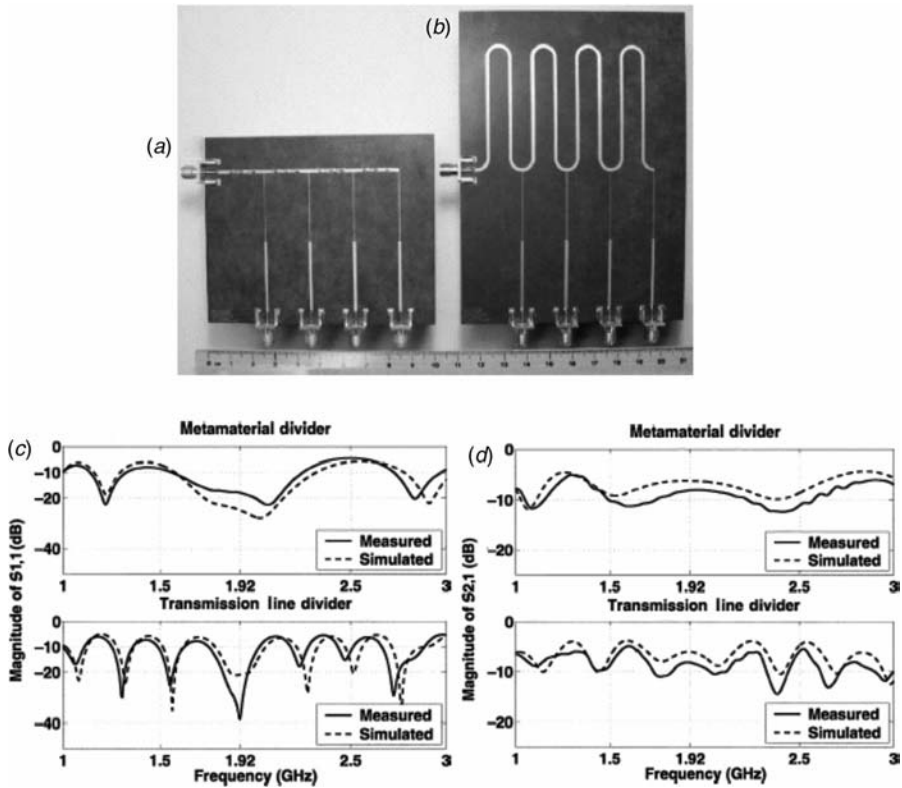


**FIGURE 4.39** Metamaterial-based (a) and conventional (b) 1:4 power dividers with their corresponding measured and simulated frequency responses (only  $S_{11}$  (c) and  $S_{21}$  (d) are depicted). (Source: Reprinted with permission from [56]; copyright 2005, IEEE.)

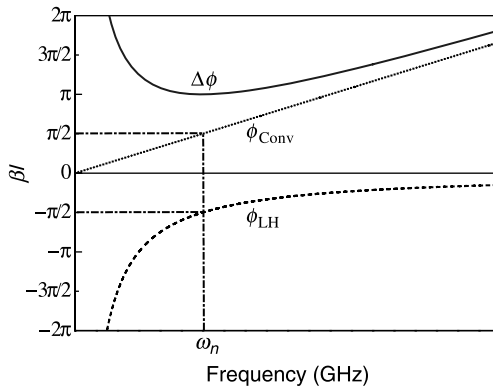


**FIGURE 4.40** Illustration of bandwidth enhancement by using a conventional and a left-handed transmission line. At the design frequency,  $\omega_n$ , the phase difference,  $\Delta\phi$ , between the two lines is  $\pi$ , and this difference is roughly preserved in a wide band.

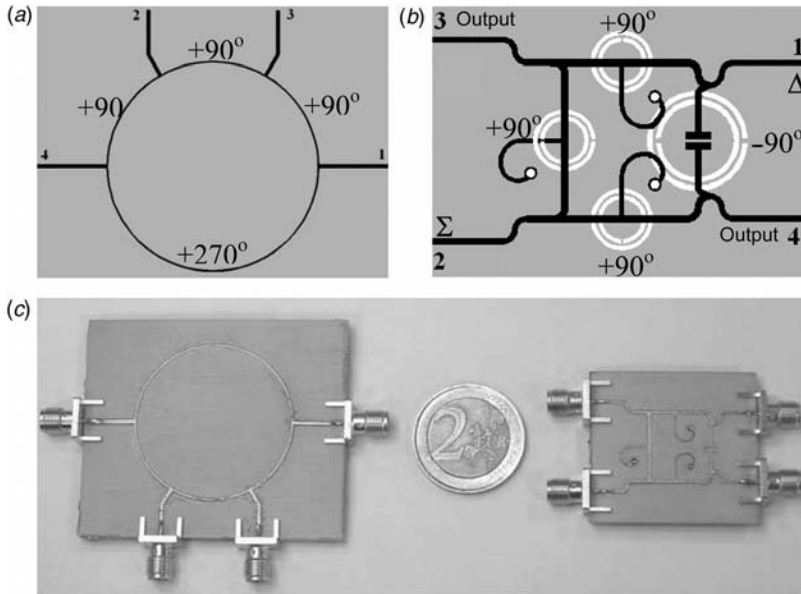


**FIGURE 4.41** Layout of the conventional (a) and metamaterial (b) rat race hybrid couplers. A comparative photograph of both devices can be seen in (c). The devices were fabricated on the Rogers RO3010 substrate with dielectric constant  $\epsilon_r = 10.2$  and thickness  $h = 635 \mu\text{m}$ . The active area (excluding access lines) of the CSRR-based hybrid coupler is  $3.62 \text{ cm}^2$ , whereas the conventional one occupies an area of  $10.33 \text{ cm}^2$ . (Source: Reprinted with permission from [58], copyright 2007, IEEE.)

(where  $\lambda$  is the guided wavelength at the design frequency,  $\omega_n$ ) with the ports equally spaced in the upper half of the ring. The metamaterial counterpart of this coupler can be implemented by substituting the  $270^\circ$  ( $0.75 \lambda$ ) line section by a  $-90^\circ$  left-handed line designed to provide the required characteristic impedance ( $70.7 \Omega$ ) and phase ( $-90^\circ$ ) at the operating frequency. This was done by Okabe et al. [57] by using the dual-transmission-line approach, where a host line was loaded with lumped inductors and capacitors in shunt and series connection, respectively. The performance and size of the device is good, with a wide bandwidth for the coupling coefficient and phase balance (see [57] for more details).

Alternatively, the metamaterial rat race hybrid coupler can be implemented by means of the resonant-type approach [58]. In this case, not only is the  $270^\circ$  line replaced by an artificial  $-90^\circ$  left-handed line, but the three  $90^\circ$  (right-handed) transmission lines are also implemented as artificial lines based on CSRRs<sup>29</sup> (the characteristic impedance of these artificial lines is  $70.7 \Omega$ ). This allows us to achieve a further controllability of the frequency dependence of phase in the lines, with the result of excellent performance in terms of phase balance. The topology of this

<sup>29</sup>As was described in Section 4.2.3.2, these lines consist of a combination of shunt stubs and CSRRs, and they can be described by the circuit model given in Figure 4.14.

implementation is depicted in Figure 4.41 (also included are photographs of conventional and metamaterial rat race hybrid couplers, designed to operate at 1.6 GHz, in order to appreciate the achievable size reduction obtained by using metamaterial transmission lines). The simulated and measured impedance matching, coupling and isolation for both structures are depicted in Figure 4.42. In Figure 4.43 is depicted the phase balance for the  $\Sigma$  and  $\Delta$  ports, namely  $\phi(S_{42}) - \phi(S_{32})$  and  $\phi(S_{41}) - \phi(S_{31})$ , respectively. The CSRR-based coupler exhibits good isolation, coupling, and matching. These magnitudes are comparable to those of the conventional device. Specifically, measured power splitting between ports 3 and 4 (considering

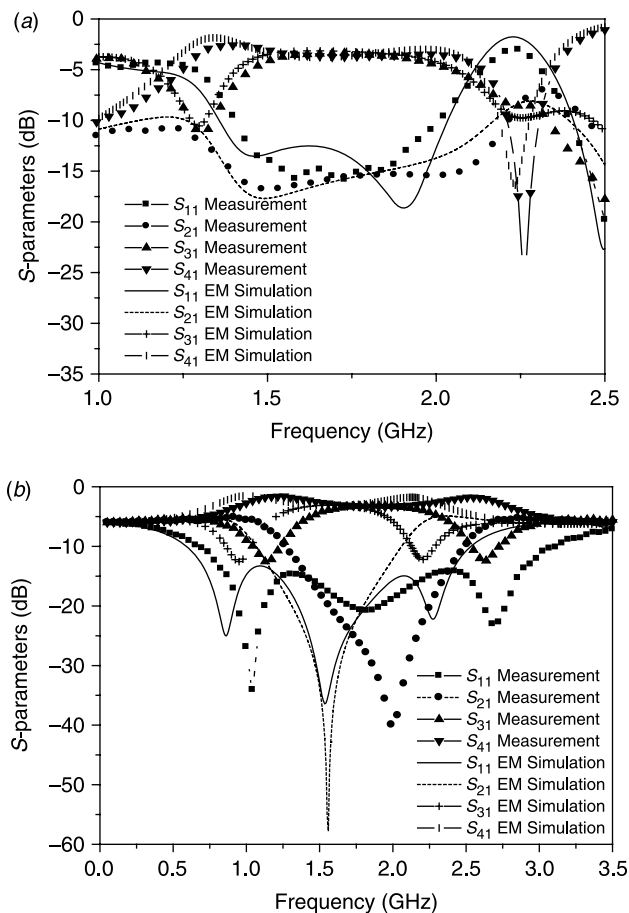


**FIGURE 4.42** Impedance matching ( $S_{11}$ ), coupling ( $S_{31}$ ,  $S_{41}$ ) and isolation ( $S_{21}$ ) for the CSRR-based hybrid coupler (a) and conventional coupler (b). The slight discrepancies between simulation and measurement in the conventional coupler are attributed to fabrication-related tolerances. (Source: Reprinted with permission from [58]; copyright 2007, IEEE.)

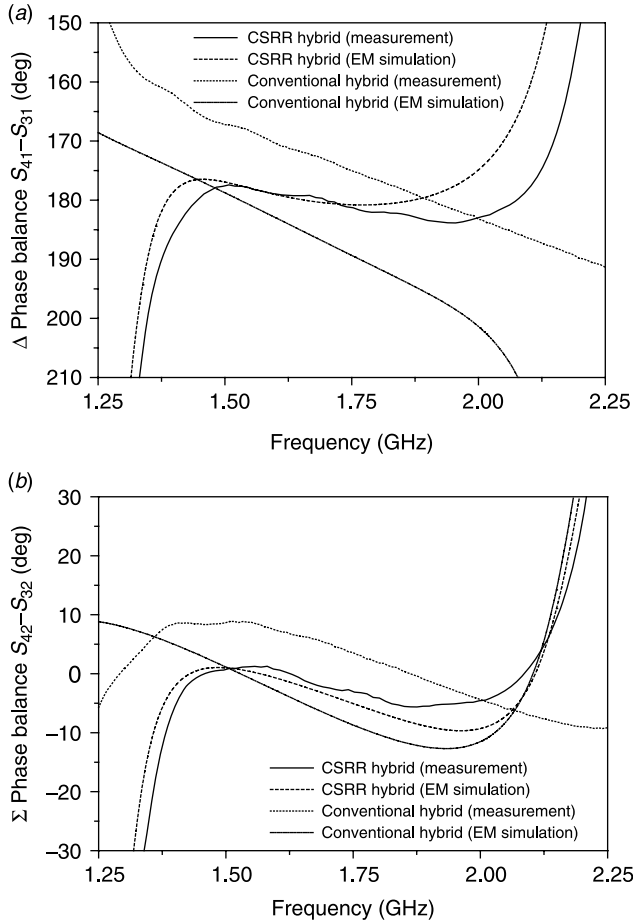


**FIGURE 4.43** Phase balance for the  $\Delta$  (a) and  $\Sigma$  (b) ports. (Source: Reprinted with permission from [58], copyright 2007, IEEE.)

port 1 as the input port) exhibits similar characteristics in terms of flatness. Measured isolation and matching are comparable in both devices at the operating frequency ( $f_0 = 1.6$  GHz). However, phase balance in the CSRR-based rat race is clearly superior to that obtained in the conventional hybrid, in particular for the  $\Delta$  input (Fig. 4.43). Namely, the phase balance variation with frequency is smaller in the new CSRR-based hybrid and hence the operating bandwidth is enhanced. This has been achieved thanks to an accurate control of the phase response of the individual artificial lines forming the proposed coupler. The design is fully compatible with planar technology, because no lumped elements are used. With the proposed design, size reduction by a factor of 3 is achieved as compared to conventional implementation.

The technique for bandwidth enhancement described in this section has been applied to other microwave components, such as phase shifters [59], where it has been demonstrated in operation over one octave bandwidth.

### 4.3.3 Dual-Band Components

Dual-band (DB) components are devices that exhibit a certain functionality at two different frequencies,  $f_1$  and  $f_2$ . Such devices are of interest for modern microwave and wireless communication systems because they make possible operation at two different bands without the need to design two different mono-band (MB) circuits. Contrary to conventional (right-handed) transmission lines, which are intrinsically MB structures, CRLH transmission lines exhibit a DB behavior. To demonstrate that a conventional transmission line is a MB structure, we simply have to have in mind that the number of electrical parameters of a conventional line, namely the per-unit length inductance,  $L'$  and capacitance,  $C'$ , coincide with the number of parameters given by the specifications at a given frequency,  $\omega_1$ , that is, the characteristic impedance,  $Z_1$ , and the electrical length,  $\beta_1 l$ , where  $l$  is the physical length of the transmission line. As is well known, the relationships between these parameters are given by

$$\beta_1 = \omega_1 \sqrt{L'C'} \quad (4.28)$$

and

$$Z_1 = \sqrt{\frac{L'}{C'}}. \quad (4.29)$$

From these equations, it is clear that we cannot obtain any arbitrary desired combination of values,  $Z_2$  and  $\beta_2 l$ , at the second operating frequency,  $\omega_2$ . Therefore, we cannot design DB components by means of conventional transmission lines. However, the situation changes if the number of electrical parameters that characterize the line increases. This is exactly the case for the artificial CRLH transmission lines, which are described by means of four independent parameters in  $LC$ -loaded lines or through five reactive elements in resonant-type structures. Therefore, from an analytical point of view, the previous limitation vanishes and CRLH lines are appropriate for the design and synthesis of DB components. Essentially, to design a DB component means tailoring the dispersion diagram and/or the characteristic impedance in order to achieve the required values of impedance and phase at the desired operating frequencies, and this can be done by means of CRLH transmission lines. To clarify this, we will give an example. The idea is to achieve by means of a single CRLH line cell described by the model of Figure 3.3, a DB  $\lambda/4$  impedance inverter (with normalized characteristic impedance  $K = 1$ ), operative at frequencies  $f_1 = 1$  GHz and  $f_2 = 2$  GHz. To achieve this, we can take benefit of the left-handed and right-handed behavior of the CRLH cell. To simplify the calculation, we will consider the balanced case. The idea behind this design is to set the transition frequency,  $\omega_0 = \omega_s = \omega_p$ , between the operating frequencies,  $\omega_1$  and  $\omega_2$ , and determine the line

parameters so that at  $\omega_1$  and  $\omega_2$  the electrical length of the line is  $\beta_1 l = -\pi/2$  and  $\beta_2 l = +\pi/2$ , respectively, with the characteristic impedance being  $Z_o = 50 \Omega$  at both frequencies. To this end, equations (3.21) and (3.22) are solved subject to the balanced case and to the previous specifications. The resulting electrical parameters of the line are  $C_L = 0.796$  pF,  $L_L = 3.98$  nH,  $C_R = 3.18$  pF, and  $L_R = 15.92$  nH. In Figure 4.44 are depicted the dispersion relation of the structure, and the dependence of the characteristic impedance on frequency. The required values for both  $\beta l$  and  $Z_o$  have been obtained at the operating frequencies. As the sign of the phase shift is irrelevant for impedance inversion, this is clearly a good example of the DB behavior of CRLH transmission lines. Other combinations of phase shifts (all being a positive or negative multiple of  $\pi/2$ ) at the desired frequencies are also possible. Depending on the required phase variation, more than one cell might be necessary.

Dual-band prototype components based on the CRLH transmission line concept have been developed by Lin et al. [60]. To illustrate the possibilities of the approach, Figure 4.45 includes a DB branch line coupler, and its measured frequency response. At the operating frequencies, the required impedance inverters have been designed to

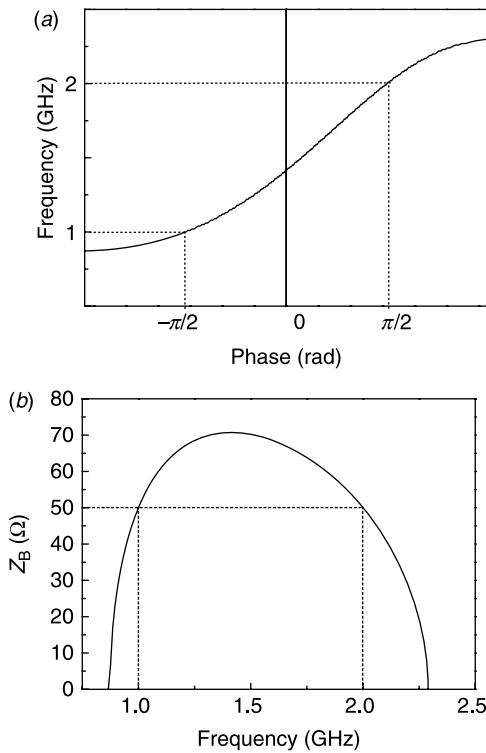


**FIGURE 4.44** Dispersion diagram (a) and characteristic impedance (b) for the CRLH model designed to achieve dual-band operation according to the frequencies and requirements explained in the text.



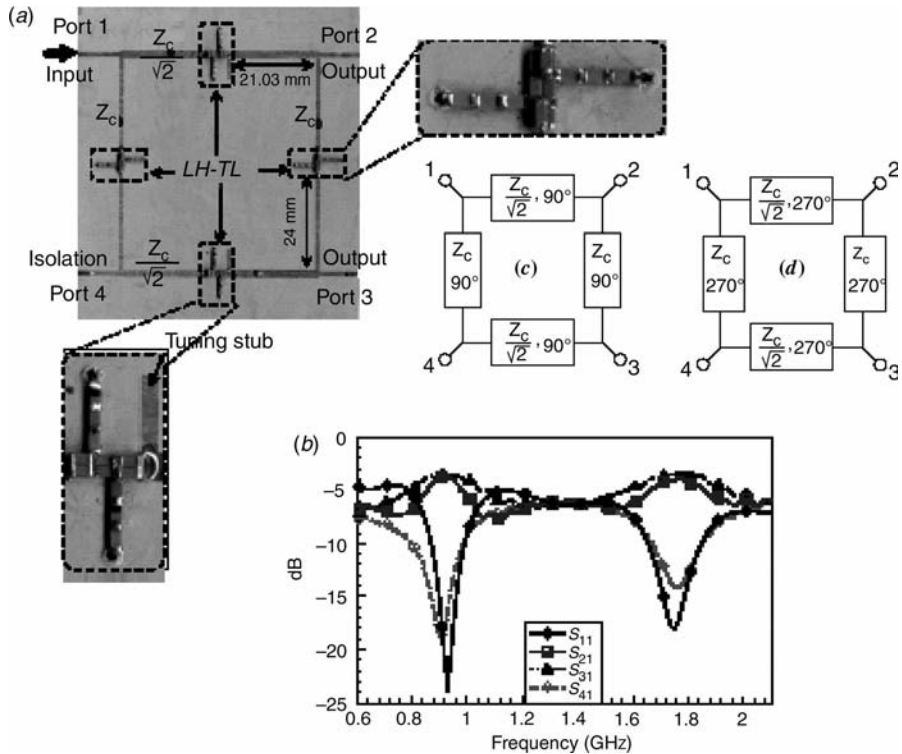


**FIGURE 4.45** DB branch line coupler (a), measured frequency response (b) and schematics of the coupler for the two operating frequencies (c)  $f_1$  and (d)  $f_2$ . (Source: Reprinted with permission from [60]; copyright 2004, IEEE.)

exhibit phase shifts of  $+90^\circ$  and  $+270^\circ$ , as indicated in the schematic. The circuit has been implemented by cascading purely right-handed (PRH) lines (implemented through conventional microstrip sections) and purely left-handed (PLH) lines (realized by means of SMT chip components) for either branch of the coupler. Operation at the design frequencies ( $f_1 = 930$  MHz and  $f_2 = 1780$  MHz) is clearly achieved, with near 3 dB transmission between the input port and both the coupled and through ports.

### 4.3.4 Coupled-Line Couplers

Metamaterial transmission lines can be also applied to the optimisation of coupled-line couplers. These are four-port devices consisting of a pair of coupled lines, as indicated in Figure 4.46, with diverging access lines for each port. Although topologically identical, there are two types of coupled-line couplers, namely the backward coupler and the forward coupler (Fig. 4.46). The principle of operation of such couplers has been exhaustively described elsewhere [61], but it is concisely

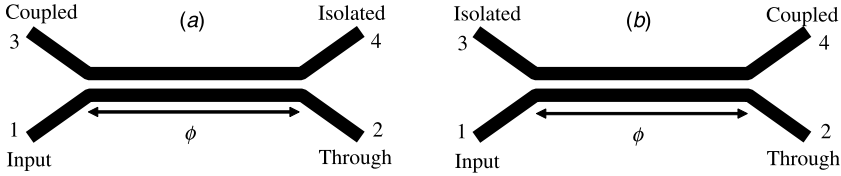


**FIGURE 4.46** Topology of the backward (a) and forward (b) wave couplers with indication of port designations.

reproduced here to understand the main limitations of these type of couplers and the advantages of metamaterial-based implementations of them.

In the backward wave coupler, the coupled port is that port sharing the same reference plane as the input port, whereas the isolated port is the crossing port (in reference to the input port). Under the assumption of a symmetric structure, even and odd mode analysis lead us to the coefficients of the  $S$ -matrix. The condition to obtain perfect matching at the input port is given by

$$Z_o = \sqrt{Z_{oe}Z_{oo}} \quad (4.30)$$

where  $Z_{oe}$  and  $Z_{oo}$  are the characteristic impedance for the even and odd modes, respectively, and  $Z_o$  is the reference impedance of the port. Under these conditions, the following results are obtained:

$$S_{11} = 0, \quad (4.31a)$$

$$S_{21} = \frac{\sqrt{1-k^2}}{\sqrt{1-k^2 \cos \phi + j \sin \phi}}, \quad (4.31b)$$

$$S_{31} = \frac{jk \sin \phi}{\sqrt{1-k^2 \cos \phi + j \sin \phi}}, \quad (4.31c)$$

and

$$S_{41} = 0, \quad (4.31d)$$

where it is assumed that the phase shift  $\phi$  (or the phase velocity) for the even and odd modes is roughly the same (which is in turn an assumption valid for quasi-TEM wave propagation). Coupling (i.e.,  $S_{31}$ ) depends on the electrical length of the coupled lines and on the coupling factor,  $k$ , given by

$$k = \frac{Z_{oe} - Z_{oo}}{Z_{oe} + Z_{oo}}. \quad (4.32)$$

The optimum coupling is obtained for  $\phi = \pi/2$ . In this case, coupling is  $C = |S_{31}| = k$ . Thus, in these backward wave couplers, maximum coupling depends on the difference between the characteristic impedance for the even and the odd modes. In practice, to achieve significant coupling levels, a high contrast between these impedances is required, and this is difficult to achieve in edge-coupled couplers, because too small distances between the coupled lines are required for this purpose. In other words, the coupling levels achievable with these couplers are very limited. This is the main drawback of these type of couplers. However, they are relatively small, because  $90^\circ$  lines (or shorter, depending on the required coupling) are used, and bandwidth is reasonably good.

Let us now briefly consider the forward wave couplers. In these devices, the distance between the coupled lines is deliberately large (i.e.,  $Z_{oe} \approx Z_{oo}$  and  $k \approx 0$ ). This means that signal is not transmitted to the so-called coupled port of the backward wave coupler (which is now the isolated port). Indeed, according to equations (4.31) and (4.32), all the input power should be collected in the through port. This trivial situation may change, however, if the phase velocities for the even and the odd modes are not identical, which is what actually occurs in real structures, that is, exhibiting quasi-TEM, rather than TEM, wave propagation. In this case, the scattering parameters are

$$S_{11} = 0, \quad (4.33a)$$

$$S_{21} = \exp\left(\frac{-j(\beta_e + \beta_o)l}{2}\right) \cos\left(\frac{(\beta_e - \beta_o)l}{2}\right), \quad (4.33b)$$

$$S_{31} = 0, \quad (4.33c)$$

and

$$S_{41} = -j \exp\left(\frac{-j(\beta_e + \beta_o)l}{2}\right) \sin\left(\frac{(\beta_e - \beta_o)l}{2}\right), \quad (4.33d)$$

where  $\beta_e$  and  $\beta_o$  are the phase constants for the even and odd modes, respectively, and  $l$  is the length of the coupled lines. The coupled port is the crossing port and coupling is now given by  $C = |S_{41}|$ . Hence, forward coupling is obtained, which justifies the name given to the device. According to equation (4.33d), coupling depends on the length of the device, and optimum coupling is obtained for the coherence length,  $l_c$ , given by

$$l_c = \frac{\pi}{|\beta_e - \beta_o|}. \quad (4.34)$$

Due to the comparable phase velocities for the even and the odd modes, the coherence length (or the typical length to achieve substantial couplings) is too long for

practical applications, this being the main limitation of this type of coupler. In the case of asymmetric forward wave couplers, the analysis is more complicated, but the same conclusion concerning device length is inferred (expression 4.34 holds but with the phase constants modified following  $\beta_c \rightarrow \beta_c$  and  $\beta_o \rightarrow \beta_\pi$  to account for the  $c$  and  $\pi$  modes of the asymmetric structure [61,62]).

Let us now analyze how the previous limitative aspects can be improved through the use of metamaterial transmission lines. With regard to forward couplers, the idea is to replace the coupled lines (or eventually only one of the coupled lines) by left-handed lines [63,64]. If both lines are backward lines, power is coupled forward (i.e., between port 1 and 4 in Fig. 4.46), although due to the left-handed nature of the coupled lines, wave propagation is backward. If only one of the coupled lines is backward, and it corresponds to that line connecting the input and through ports (line 1–2 according to Fig. 4.46), injected power into port 1 propagates towards port 2. However, due to left-handedness, waves propagate backward towards port 1. As coupling in this kind of couplers preserves the phase direction at both lines (coupling occurs through evanescent waves), it follows that phase and power in line 3–4 propagates to port 3, which is now the coupled port. Thus, power is coupled backward, rather than forward. This is a fundamental difference with the conventional (symmetric or asymmetric) forward wave coupler and with the forward coupler implemented by means of two coupled left-handed lines.<sup>30</sup> However, the coupling mechanism is identical. The key advantage of using left-handed lines in these couplers is the possibility of designing devices of small size and with enhanced coupling (compared to conventional forward wave couplers). The reason is the unusual dispersion diagram of left-handed lines. For couplers with identical left-handed coupled lines (symmetric coupler), an analysis similar to that shown above for conventional forward couplers leads us to the conclusion that coupling increases by decreasing frequency<sup>31</sup> (in contrast to conventional couplers, where high frequencies or long coupled lines are required to achieve maximum coupling). In asymmetric couplers implemented by a conventional and a left-handed line, the phase constants of expression (4.34) can be replaced with the phase constants of the conventional and left-handed lines [64].<sup>32</sup> As the phase constant of the left-handed line is negative, the sign in the denominator is positive and the coherence length is thus reduced. Alternatively, size reduction and high coupling in these type of couplers have been interpreted on the basis of coupled-mode theory [66]. To this end, the coupled-mode dispersion diagram for the coupled-line coupler has been inferred, and it has been concluded that operation in the stop-band for the coupled-mode system leads to continuous power leakage from one line to the other [66].

As an example, Figure 4.47 illustrates a fabricated prototype device corresponding to a mixed conventional/left-handed asymmetric coupler, where the left-handed line

<sup>30</sup>To avoid the incoherence of calling forward couplers to those metamaterial-based couplers implemented by means of only one left-handed line (where power is actually coupled backwards), Caloz and Itoh have termed these devices *phase couplers* in their textbook [65].

<sup>31</sup>This is due to the frequency dependence of the phase constant in left-handed lines.

<sup>32</sup>This is valid for very weak coupling between the lines.

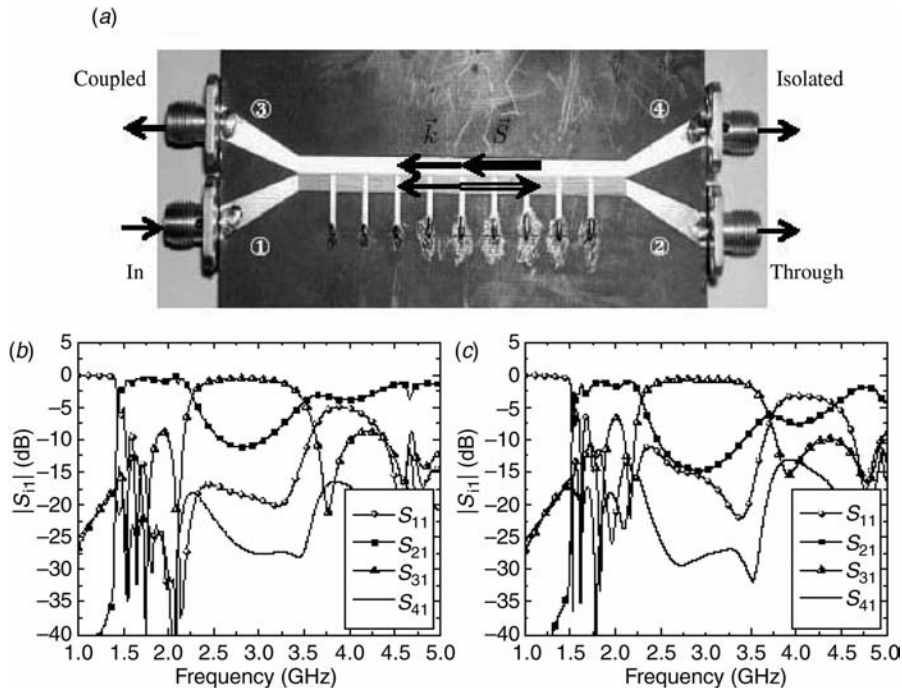


**FIGURE 4.47** Mixed conventional/left-handed coupled-line coupler (a), simulated (b), and measured frequency responses (c). (Source: Reprinted with permission from [64]; copyright 2004, IEEE.)

is implemented by *LC* loading a microstrip line. Near 0 dB backward coupling in a broad fractional bandwidth of roughly 50% is obtained in this coupler [64] (see Fig. 4.47). Alternatively, these mixed couplers have been implemented by loading the left-handed line with CSRRs and series gaps (Fig. 4.48) [67]. Simulation of electric field propagation (Fig. 4.49) indicates that power is coupled backward, as expected. The measured *S*-parameters for the coupler of Figure 4.48 are depicted in Figure 4.50, where they are compared with the simulated *S*-parameters of a conventional (backward)  $90^\circ$  parallel coupled-line coupler with identical distance between the coupled lines and substrate. For the metamaterial-based coupler, the coupling level at the design frequency, 4.3 GHz, is in the vicinity of  $-4$  dB, whereas it is lower than  $-20$  dB in the conventional backward coupler. It is also possible to design DB mixed conventional/left-handed couplers by loading the left-handed line of the coupler with two sets of CSRRs of different dimensions, as Figure 4.51 illustrates [67].

With regard to the improvement of the conventional backward wave coupler presented above, this is relatively complex and it has been considered in detail in [65,68]. The considered coupler, composed of two identical left-handed balanced lines, is symmetric and even/odd analysis is thus applicable in this case. Operation of the coupler in the stopband for either mode (even/odd) leads to enhanced bandwidth

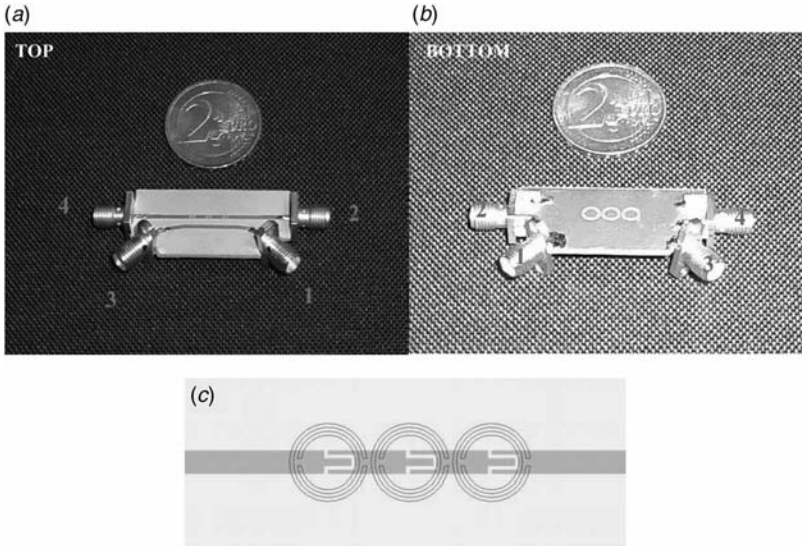


**FIGURE 4.48** Top (a) and bottom (b) photographs of the fabricated CSRR-based coupler. The device consists of a conventional line and a three-cell CSRR/gap loaded left-handed line. To further appreciate the details of the topology, the layout of the three-cell left-handed lines is depicted in (c). The device has been fabricated in the Rogers RO3010 substrate (dielectric constant  $\epsilon_r = 10.2$ , thickness,  $h = 1.27$  mm). CSRR dimensions are external radius,  $r_{\text{ext}} = 2$  mm, width,  $c = 0.2$  mm and separation,  $d = 0.2$  mm. Gap distance is 0.2 mm and the period of the structure is 4.2 mm. (Source: Reprinted with permission from [67]; copyright 2006, John Wiley & Sons.)

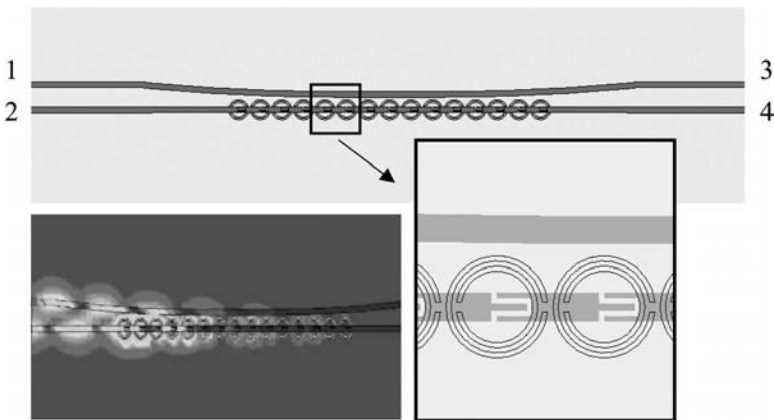


**FIGURE 4.49** Simulation of the electric field propagation in a 15-cell mixed conventional/left-handed coupler based on CSRRs. CSRR dimensions and separation are identical to those values of Figure 4.48.

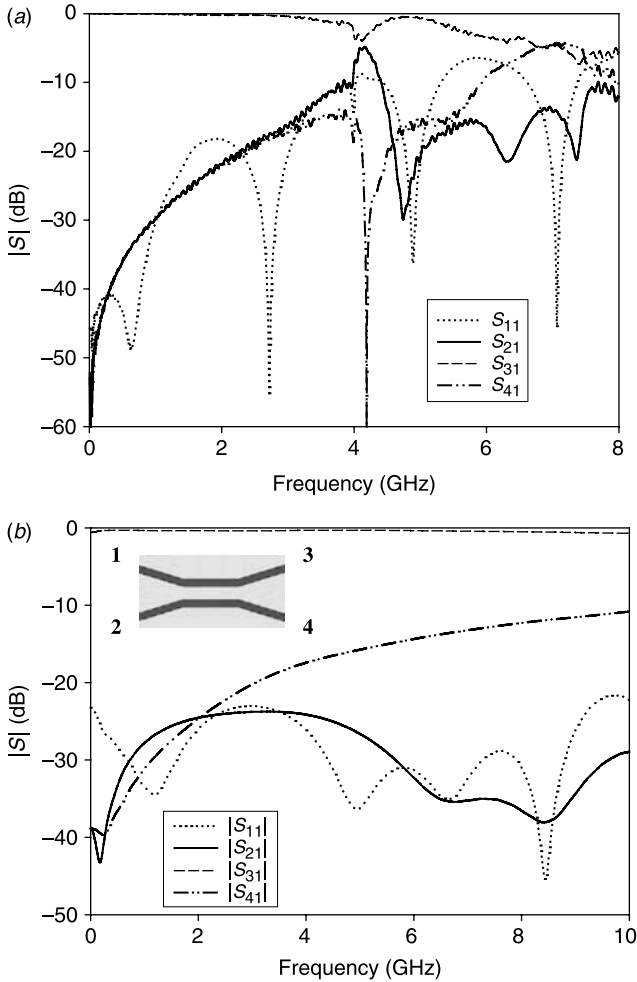


**FIGURE 4.50** Measured  $S$ -parameters of the CSRR-based coupler of Figure 4.48 (a) and simulated  $S$ -parameters for a  $90^\circ$  parallel coupled-line coupler with similar dimensions (b). (Source: Reprinted with permission from [67]; copyright 2006, John Wiley & Sons.)

and high coupling. As pointed out in [65], any arbitrary level of coupling can be achieved with these couplers, even with a large distance between the coupled lines. The detailed analysis of this type of couplers is outside the scope of this book, but the authors recommend reference [65] to the interested reader.

#### 4.4 ANTENNA APPLICATIONS

Antennas have become one of the most exciting applications of metamaterials due to the possibility of significantly improving their performance. Indeed, many

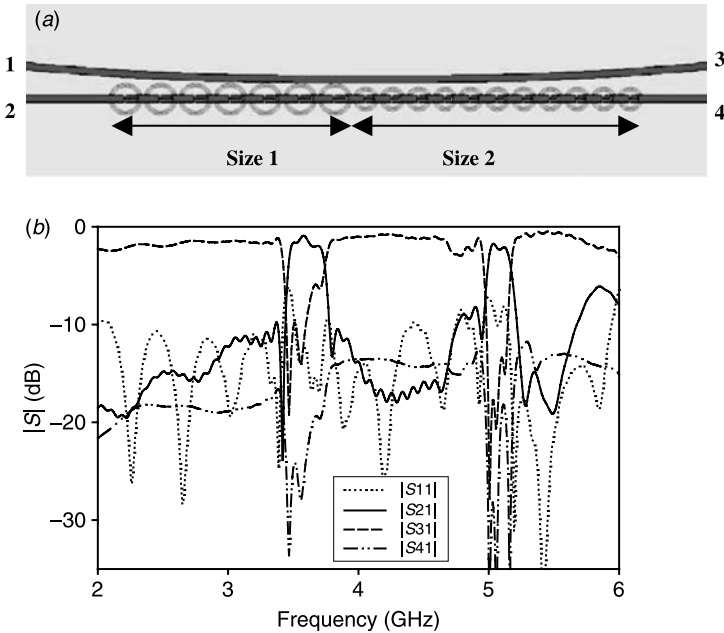


**FIGURE 4.51** Topology of the dual CSRR-based coupler (a) and simulated  $S$ -parameters (b). (Source: Reprinted with permission from [67]; copyright 2006, John Wiley & Sons.)

papers have been published since the boom of metamaterials in 2000. We will start by describing some pioneering work that focuses on the elemental properties of antennas and, later, we will continue with antenna applications of metamaterials.

It has been well established that pairs of media with positive and negative refraction indexes are analogous to reactive impedances of opposite sign, in that they are able to resonate. Alternatively, similar responses can be achieved by means of pairs of media exhibiting positive or negative permittivity or permeability [69]. Therefore, it follows that metamaterial structures can be useful to introduce changes in antenna impedance and, consequently, to obtain an improvement in antenna response. This was proposed in [70], where the authors show that it is possible to match an electrically small dipole to the free-space impedance thanks to the use of a metamaterial spherical cover with negative index of refraction. Further details concerning the expressions of the radiated fields, radiated power, lumped-element equivalent-circuit models, quality factor, and other properties of such elemental antennas when enclosed in right-handed or left-handed media, are presented in [70]. An interesting tunnel-effect interpretation of this impedance-matching phenomenon and a reciprocal scattering description are presented in [69]. Another surprising consequence of the structure proposed in [70] is that an important increase in the radiated power and a reduction of the reactance are simultaneously possible, thus allowing circumvention of the  $Q$  radiation limit of Chu [70].



A paper dealing with the study of the radiation properties of a traveling wave at the interface between a left-handed and a right-handed medium was published by Alú and Engheta [71], where the electromagnetic field distribution and the wavevector and Poynting vector orientation in both left-handed and right-handed half-spaces were calculated. Further analysis of metamaterial radiating structures can be found in [72].

The increasing effect on radiated power has encouraged research in antenna applications of metamaterials. For example, in [73] it is proposed to use an annular left-handed material ring inside a microstrip patch resonator antenna, where the resonance frequency can be decreased by proper design of ring dimensions relative to the rest of the patch antenna. This suggests, at least in theory, the possibility of very compact antenna design for relatively low frequencies. A theoretical study of patch antenna, including a left-handed medium, is presented in [74], and the use of SRRs as a magneto-dielectric substrate for patch antennas is proposed in [75].

The first experimental results of radiation in left-handed media were motivated by the demonstration of reversed Cerenkov radiation as predicted by Veselago [1]. In this regard, two simultaneous contributions appeared in 2002 [76,77], where backward, leaky wave radiation in dual transmission lines, analogous to reversed Cerenkov radiation, was experimentally demonstrated. Indeed, backfire-to-endfire radiation in these structures can be achieved by properly engineering the dispersion diagram.<sup>33</sup> A very interesting property of these leaky-wave antennas is their operation in the fundamental mode.<sup>34</sup> This reduces the feeding structure complexity and allows for broadside radiation, thanks to the nonzero group velocity (traveling wave). Moreover, continuous backfire-to-endfire radiation can be electronically achieved, which is very interesting for the design of electronically scanned antennas [78–83] (see Fig. 4.52). Backward leaky waves can also be achieved in SRR-based left-handed structures [84].

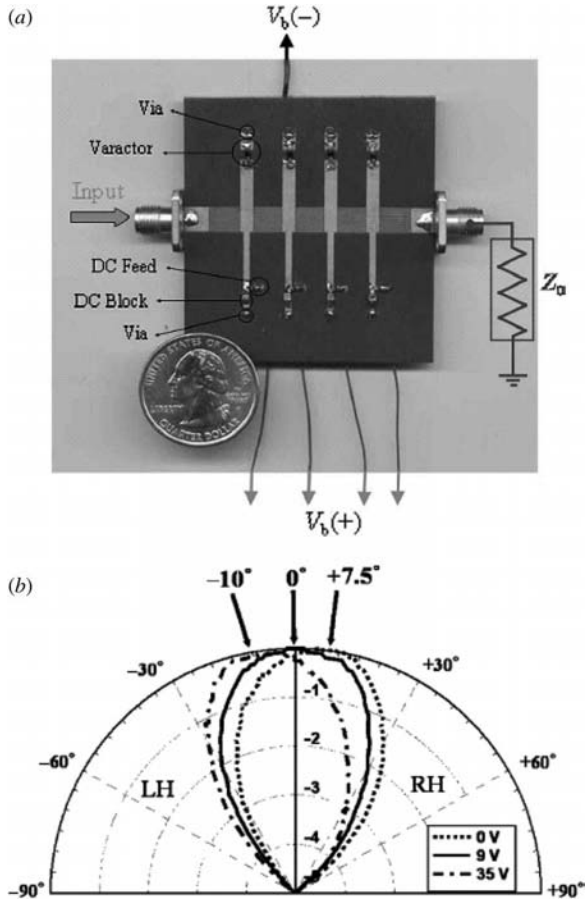
Through leaky wave analysis, the study of the radiation characteristics of left-handed (or CRLH) lines (including resonant and nonresonant structures) is possible. Indeed this analysis can also be extended to other periodic structures based on metamaterials not necessarily providing backward leaky waves. Comparison between the phase constant,  $\beta$ , and the free-space wavenumber,  $k_0$ , can be used to predict the frequency bands where these structures can radiate. Specifically, if  $|\beta| < k_0$ , then radiation may occur; and the angle,  $\theta$ , between the radiation beam and the propagation axis can be calculated as

$$\cos \theta = \frac{\beta}{k_0}, \quad (4.35)$$

where this angle can be positive or negative, depending on the sign of the phase constant. According to this, backward leaky wave radiation is expected if  $|\beta| < k_0$  and

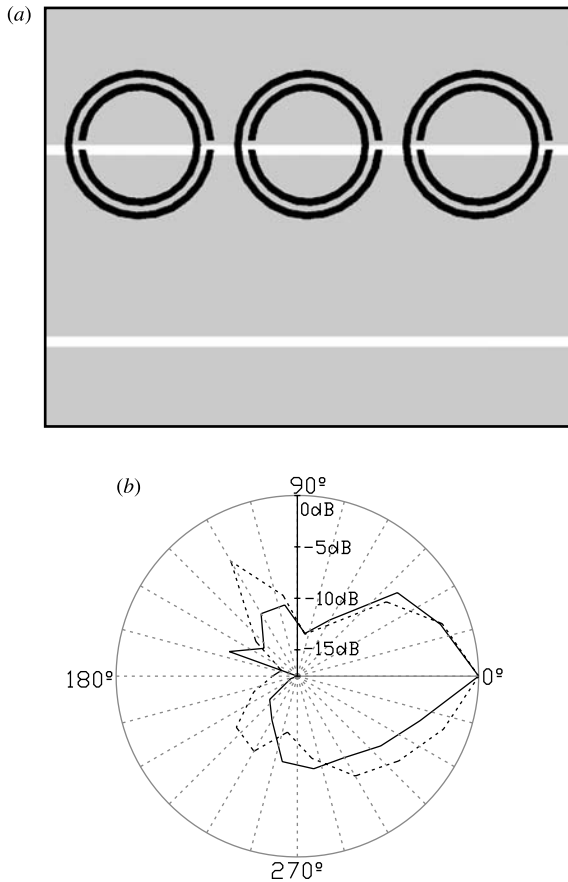
<sup>33</sup>Infact, the dual transmission lines exhibit a CRLH behavior that makes it possible to achieve backward or forward leaky waves.

<sup>34</sup>Conversely, operation of conventional periodic-type leaky-wave structures is based on spatial harmonics.



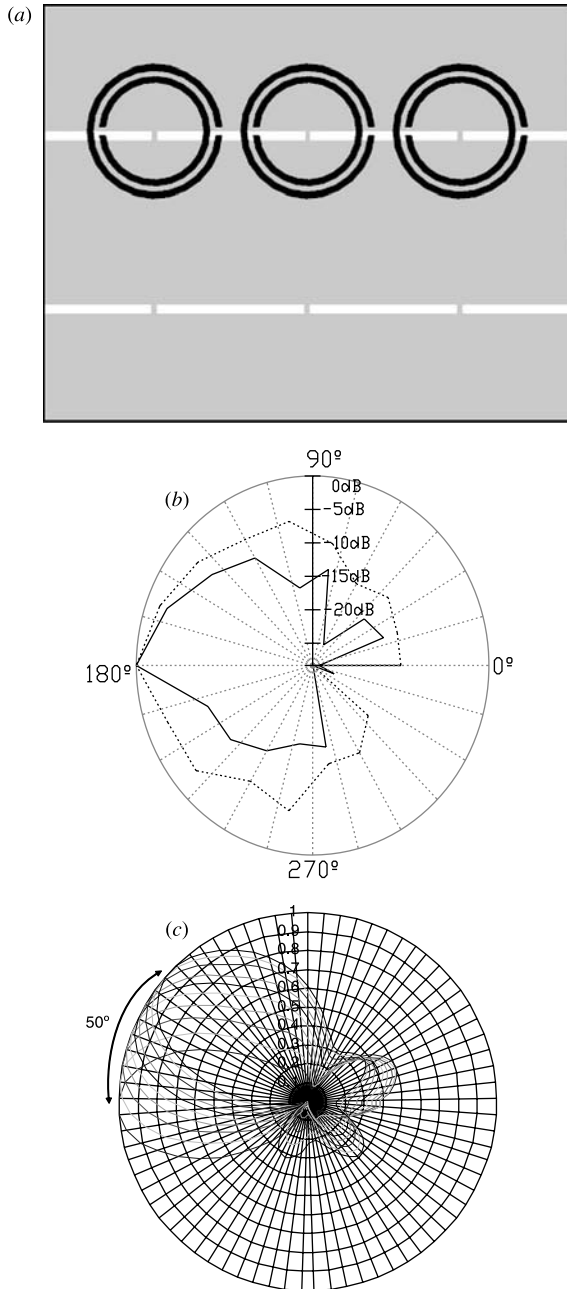
**FIGURE 4.52** Prototype of electronically scanned CRLH microstrip leaky-wave antenna (a) and measured radiation patterns at different bias voltages (b). (Source: Reprinted with permission from [83]; copyright 2004, IEEE.)

$\beta < 0$ , whereas forward leaky wave radiation will occur if  $|\beta| < k_0$  but  $\beta > 0$ . It has been demonstrated that CPW structures simply loaded with SRRs are able to produce forward leaky waves (Fig. 4.53) [84]. Conversely, if shunt-connected strips are added to the structure, a left-handed pass band results above the resonance frequency of the SRRs, and the radiation is backward (Fig. 4.54) [84]. The dispersion characteristics of these structures are depicted in Figure 4.55. In Figure 4.55a, the existence of a left-handed band for the structure shown in Figure 4.54 is verified. It corresponds to the zone of the dispersion diagram where the phase constant and its derivative with frequency have opposite signs (antiparallel group and phase velocities). The attenuation constant is small in most of this region. The upper part of such a band lies within the radiation region ( $|\beta| < k_0$ ), hence predicting the existence of a frequency range where the Bloch mode becomes leaky. As has been explained, the left-handed



**FIGURE 4.53** Layout of a forward leaky-wave structure consisting of a CPW loaded with SRRs in the back substrate side (a) and measured far-field radiation pattern (b). E-plane (continuous line) and H-plane (dashed line). (Source: Reprinted with permission from [84].)

behavior of the structure will result in a reversal of the direction predicted for the leaky wave radiation. The phase-matching condition along the interface between the left-handed structure and the medium where the energy is radiated (free space, and therefore a right-handed medium) implies that the radiated energy will necessarily have to propagate in the opposite direction. This can also be explained by means of equation (4.35), as  $\beta$  is negative for waves propagating energy from left to right (which is the usual convention), and therefore  $\theta$  will be included in the second quadrant, that is, corresponding to radiation from broadside ( $\theta = 90^\circ$ ) to back-fire ( $\theta = 180^\circ$ ) direction. This phenomenon can be seen as analogous to the reversal of Cerenkov radiation in left-handed materials, as predicted by Veselago in his seminal work [1].



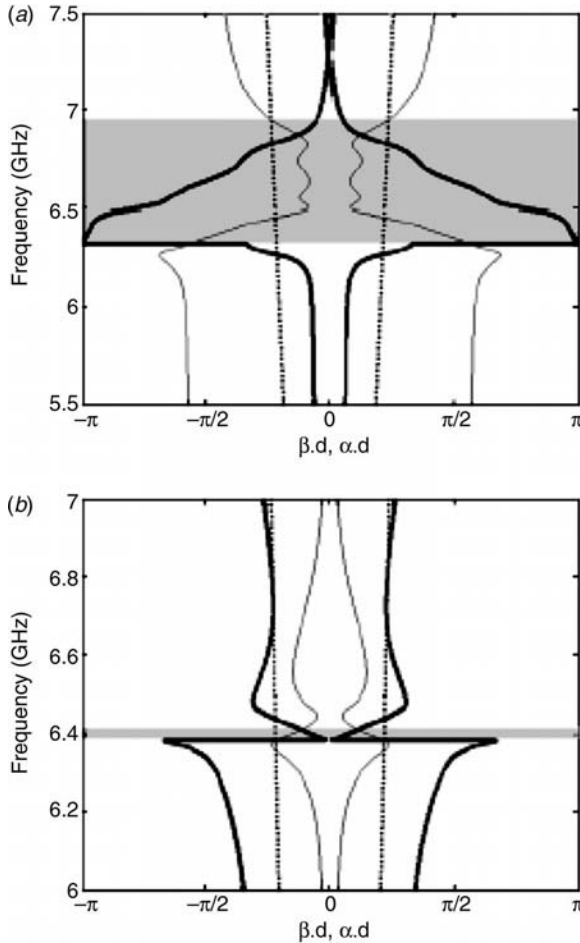
**FIGURE 4.54** Layout of a backward leaky-wave structure consisting of a CPW loaded with SRRs in the back substrate side and shunt-connected strips in the upper side (a) and measured far-field radiation pattern (b). E-plane (continuous line) and H-plane (dashed line). In (c) a CST Microwave Studio simulation of the E-plane pattern as frequency changes is depicted. (Source: Reprinted with permission from [84].)

Figure 4.55*b* shows the dispersion diagram for the CPW structure loaded only with SRRs (Fig. 4.53). In this case, there is a frequency band where strong rejection occurs due to the negative value that magnetic permeability exhibits in that band. In that region the attenuation constant is much larger than the phase constant. Both the rejection band and the lower part of the second pass band are included in the radiation region ( $|\beta| < k_0$ ). However, the high attenuation constant present in the stop-band prevents the structure from radiating, making the leakage almost completely reactive at these frequencies [84]. On the other hand, in the low-frequency region of the second pass band, the structure radiates (small attenuation constant), and because it is right-handed (parallel phase and group velocities), the radiation beam will be contained in the first quadrant, from broadside to endfire direction (positive value for  $\beta$ ).

Several envisaged applications of metamaterial-based leaky-wave structures include tunable antennas using distributed thin-film ferro-electric and ferro/i-magnetic materials, anisotropic minimum-impedance-path metamaterials for beam-forming structures, full-space scanning 2D leaky-wave antennas for a possibly inexpensive alternative to complex conventional phased arrays, compact-range wave generation and measurements, or endfire antennas. More details of these possible applications are described in [79,80].

## PROBLEMS

- 4.1. Synthesis of filters based on the hybrid model.** Under the approximation that the series reactance of the circuit model of Figure 4.18*b* is constant along the left-handed passband, demonstrate that the shunt impedance is  $Z_p = jZ_0/2$  and infinity, respectively, at the  $-3$  dB frequencies ( $\omega_1$  and  $\omega_2$ ) of the structure. From this, infer expressions (4.9) and (4.10).
- 4.2. Tunable notch filters based on VLSRRs.** In reference to Figure 4.33, explain the variations in the frequency response (gap width and rejection level) that result under different bias polarizations. Hint: Express the simplified circuit model of Figure 4.34 as that depicted in Figure 3.23*b* (by taking into account the parallel resistance of the resonant tank) and obtain the  $Q$ -factor of this tank.
- 4.3. Synthesis of left-handed lines based on CSRRs.** As was discussed in Chapter 3, the left-handed transmission lines based on the dual and resonant-type approach can be considered as artificial transmission lines, where impedance and phase can be tailored over a wide margin at a given operating frequency within the band. Specifically, for the circuit depicted in Figure 3.38 (which models a CSRR-based left-handed line), the phase varies in the interval  $(-\pi, 0)$  in the backward wave band, whereas the characteristic impedance is zero at the onset of the left-handed band, then increases progressively, and (ideally) tends to infinity at the upper edge of the band. Demonstrate that it occurs if the resonance frequency of the series branch is higher than the resonance frequency of the CSRRs (i.e., the series capacitance dominates over the



**FIGURE 4.55** Phase (bold line) and attenuation constant (thin line) for the structures of Figure 4.54 (a) and 4.53 (b). The radiation region is shown with dotted lines. (Source: Reproduced with permission from [84].)

series inductance in the backward wave band). Under these conditions (i.e., neglect the series inductance  $L$ ), obtain the equations that univocally determine the circuit parameters  $C_g$ ,  $C$ ,  $L_c$ , and  $C_c$  from the required impedance,  $Z_n$ , and phase  $\phi_n$  at the operating frequency  $f_n$ . The two additional inputs to solve this problem are the limits of the backward wave band,  $f_L$  and  $f_H$ .

**4.4. Bandwidth enhancement in metamaterial transmission line based devices.**

It was demonstrated in Section 4.3.2 that metamaterial transmission lines can be used for the design of enhanced-bandwidth components, and several prototype device examples are provided in that section. One of the devices is a 1 : 4 power divider, where the  $360^\circ$  transmission lines that are used in the

conventional implementation to achieve in-phase signals, are substituted by zero-degree artificial lines in the metamaterial counterpart. Discuss if it is always possible to improve the bandwidth of conventional lines through metamaterial transmission lines regardless of the electrical length of such lines.

## REFERENCES

1. V. G. Veselago "The electrodynamics of substances with simultaneously negative values of  $\epsilon$  and  $\mu$ ." *Sov. Phys. Usp.*, vol. 10, pp. 509–514 (1968).
2. F. Falcone, F. Martín, J. Bonache, R. Marqués, and M. Sorolla "Coplanar waveguide structures loaded with split ring resonators." *Microwave Opt. Tech. Lett.*, vol. 40, pp. 3–6, January 2004.
3. F. Falcone, T. Lopetegi, J. D. Baena, R. Marqués, F. Martín, and M. Sorolla "Effective negative- $\epsilon$  stop-band microstrip lines based on complementary split ring resonators." *IEEE Microwave Wirel. Comp. Lett.*, vol. 14, pp. 280–282, June 2004.
4. F. Martín, F. Falcone, J. Bonache, R. Marqués, and M. Sorolla "Split ring resonator based left handed coplanar waveguide." *Appl. Phys. Lett.*, vol. 83, pp. 4652–4654, December 2003.
5. F. Falcone, T. Lopetegi, M. A. G. Laso, J. D. Baena, J. Bonache, R. Marqués, F. Martín, and M. Sorolla "Babinet principle applied to the design of metasurfaces and metamaterials." *Phys. Rev. Lett.*, vol. 93, pp. 197401, November 2004.
6. F. Martín, F. Falcone, J. Bonache, T. Lopetegi, R. Marqués, and M. Sorolla "Miniaturized CPW stop band filters based on multiple tuned split ring resonators." *IEEE Microwave Wirel. Comp. Lett.*, vol. 13, pp. 511–513, December 2003.
7. J. García-García, J. Bonache, I. Gil, F. Martín, R. Marqués, F. Falcone, T. Lopetegi, M. A. G. Laso, and M. Sorolla "Comparison of electromagnetic bandgap and split rings resonator microstrip lines as stop band structures." *Microwave Opt. Tech. Lett.*, vol. 44, pp. 376–379, February 2005.
8. J. García-García, F. Martín, E. Amat, F. Falcone, J. Bonache, I. Gil, T. Lopetegi, Miguel A. G. Laso, A. Marcotegui, M. Sorolla, and R. Marqués "Microwave filters with improved stop band based on sub-wavelength resonators." *IEEE Trans. Microwave Theory Tech.*, vol. 53, pp. 1997–2006, June 2005.
9. J. D. Joannopoulos, R. D. Meade, and J. N. Winn *Photonic Crystals: Molding the Flow of Light*. Princeton University Press, Princeton, NJ, 1995.
10. E. Yablonovitch "Photonic bandgap structures." *J. Opt. Soc. Am. B*, vol. 10, pp. 283–295, February 1993.
11. F. R. Yang, K. P. Ma, Y. Qian, and T. Itoh "A uniplanar compact photonic-bandgap structure and its applications for microwave circuits." *IEEE Trans. Microwave Theory Tech.*, vol. 47, pp. 1509–1514, August 1999.
12. T. Lopetegi, M. A. G. Laso, J. Hernández, M. Bacaicoa, D. Benito, M. J. Garde, M. Sorolla, and M. Guglielmi "New microstrip wiggly-line filters with spurious passband suppression." *IEEE Trans. Microwave Theory Tech.*, vol. 49, pp. 1593–1598, September 2001.
13. F. Falcone, T. Lopetegi, and M. Sorolla "1-D and 2-D photonic bandgap microstrip structures." *Microwave Opt. Tech. Lett.*, vol. 22, pp. 376–379, February 2005.

14. J. Sor, Y. Qian, and T. Itoh "Miniature low loss CPW periodic structure for filter applications." *IEEE Trans. Microwave Theory Tech.*, vol. 49, pp. 411–412, September 1999.
15. F. Martín, F. Falcone, J. Bonache, T. Lopetegui, M. A. G. Laso, and M. Sorolla "New periodic-loaded photonic bandgap coplanar waveguide with complete spurious passband suppression." *IEEE Microwave Wirel. Comp. Lett.*, vol. 12 (11), pp. 435–437, November 2002.
16. F. Martín, F. Falcone, J. Bonache, T. Lopetegui, M. A. G. Laso, M. Coderch, and M. Sorolla "Periodic-loaded sinusoidal patterned electromagnetic bandgap coplanar waveguides." *Microwave Opt. Tech. Lett.*, vol. 36 (3), pp. 181–184, February 2003.
17. F. Martín, F. Falcone, J. Bonache, M. A. G. Laso, T. Lopetegui, and M. Sorolla "Dual electromagnetic bandgap CPW structures for filter applications." *IEEE Microwave Wirel. Comp. Lett.*, vol. 13, pp. 393–395, September 2003.
18. D. M. Pozar *Microwave Engineering*. Addison-Wesley, Reading, MA, 1990.
19. C. Person, A. Sheta, J. Ocupes, and S. Toutain "Design of high performance band pass filters by using multilayer thick film technology." *Proc. 24th European Microwave Conf.*, Cannes, France, September 1994, vol. 1, pp. 446–471.
20. J. T. Kuo and M. Jiang "Suppression of spurious resonance for microstrip band pass filters via substrate suppression." *Asia Pacific Microwave Conf.*, Kyoto, Japan, 2002, pp. 497–500.
21. M. Le Roy, A. Perennec, S. Toutain, L. C. Calvez "Continuously varying coupled transmission lines applied to design bandpass filters." *Int. J. RF Microwave Computer Aided Eng.*, vol. 12, pp. 288–295, May 2002.
22. J. T. Kuo and W. Hsu "Parallel coupled microstrip filters with suppression of harmonic response." *IEEE Microwave Wirel. Comp. Lett.*, vol. 12, pp. 383–385, October 2002.
23. T. Lopetegui, M. A. G. Laso, F. Falcone, F. Martín, J. Bonache, L. Pérez-Cuevas, and M. Sorolla, "Microstrip wiggly line band pass filters with multispurious rejection." *IEEE Microwave Wirel. Comp. Lett.*, vol. 14, pp. 531–533, November 2004.
24. V. Radisic, Y. Qian, and T. Itoh "Broad-band power amplifier using dielectric photonic bandgap structures." *IEEE Microwave Guided Wave Lett.*, vol. 8, pp. 13–15, January 1998.
25. M. A. G. Laso, T. Lopetegui, M. J. Erro, D. Benito, M. J. Garde, and M. Sorolla "Novel wideband photonic bandgap microstrip structures." *Microwave Opt. Tech. Lett.*, vol. 24, pp. 357–360, March 2000.
26. J. García-García, F. Martín, F. Falcone, J. Bonache, I. Gil, T. Lopetegui, M. A. G. Laso, M. Sorolla, and R. Marqués "Spurious passband suppression in microstrip coupled line band pass filters by means of split ring resonators." *IEEE Microwave Wirel. Comp. Lett.*, vol. 14, pp. 416–418, September 2004.
27. J. García-García, J. Bonache, F. Falcone, I. Gil, J. D. Baena, T. Lopetegui, M. A. G. Laso, F. Martín, R. Marqués, A. Marcotegui, and M. Sorolla "Spurious pass band suppression in microwave filters by means of sub-wavelength resonant structures." *34th European Microwave Conference Digest*, Amsterdam, Holland, October 2004, vol. II, pp. 577–580.
28. E. Rius, G. Prigent, H. Happy, G. Dambrine, S. Boret, and A. Cappy "Wide- and narrow-band bandpass coplanar filters in the W-frequency band." *IEEE Trans. Microwave Theory Tech.*, vol. 51, pp. 784–791, March 2003.



29. J. García-García, J. Bonache, F. Falcone, J. D. Baena, F. Martín, I. Gil, T. Lopetegi, M. A. G. Laso, A. Marcotegui, R. Marqués, and M. Sorolla "New stepped-impedance low pass filters with spurious passband suppression." *Electron. Lett.*, vol. 40, pp. 881–883, 2004.
30. J. Bonache, F. Martín, F. Falcone, J. García, I. Gil, T. Lopetegi, M. A. G. Laso, R. Marqués, F. Medina, and M. Sorolla "Super compact split ring resonators CPW band pass filters." *IEEE-MTT-S International Microwave Symposium Digest*, Fort Worth, TX, pp. 1483–1486, June 2004.
31. R. Marqués, F. Mesa, J. Martel, and F. Medina "Comparative analysis of edge and broad-side coupled split ring resonators for metamaterial design. Theory and experiment." *IEEE Trans. Antennas Propag.*, vol. 51, pp. 2572–2581, October 2003.
32. J. Bonache, F. Martín, F. Falcone, J. García-García, I. Gil, T. Lopetegi, M. A. G. Laso, R. Marqués, F. Medina, and M. Sorolla "Compact CPW band pass filter at S-band." *Microwave Opt. Tech. Lett.*, vol. 46, pp. 33–35, July 2005.
33. J. Bonache, F. Falcone, J. D. Baena, T. Lopetegi, J. García-García, M. A. G. Laso, I. Gil, A. Marcotegui, R. Marqués, F. Martín, and M. Sorolla "Application of complementary split rings resonators to the design of compact narrow band pass structures in microstrip technology." *Microwave Opt. Tech. Lett.*, vol. 46, pp. 508–512, September 2005.
34. J. Bonache, I. Gil, J. García-García, and F. Martín "Complementary split rings resonator for microstrip diplexer design." *Electron. Lett.*, vol. 41, pp. 810–811, July 2005.
35. J.-S. Hong and M. J. Lancaster, *Microstrip Filters for RF/Microwave Applications*. Wiley, New York, 2001.
36. G. L. Mathaei, L. Young, and E. M. T. Jones, *Microwave Filters Impedance-Matching Networks, and Coupling Structures*. Artech House, Norwood, MA, 1980.
37. J. Bonache, I. Gil, J. García-García, and F. Martín "Novel microstrip bandpass filters based on complementary split rings resonators." *IEEE Trans. Microwave Theory Tech.*, vol. 54, pp. 265–271, January 2006.
38. J. Bonache, M. Gil, I. Gil, J. García-García, and F. Martín "Limitations and solutions of resonant-type metamaterial transmission lines for filter applications: the hybrid approach." *2006 IEEE MTT-S International Microwave Symposium Digest*, pp. 939–942, San Francisco, CA, June 2006.
39. J. D. Baena, J. Bonache, F. Martín, R. Marqués, F. Falcone, T. Lopetegi, M. A. G. Laso, J. García, I. Gil, and M. Sorolla "Equivalent circuit models for split ring resonators and complementary split rings resonators coupled to planar transmission lines." *IEEE Trans. Microwave Theory Tech.*, vol. 53, pp. 1451–1461, April 2005.
40. J. Bonache, F. Martín, J. García-García, I. Gil, R. Marqués, and M. Sorolla "Ultra wide band pass filters (UWBPF) based on complementary split rings resonators." *Microwave Opt. Tech. Lett.*, vol. 46, pp. 283–286, August 2005.
41. J. Bonache, F. Martín, I. Gil, J. García-García, R. Marqués, and M. Sorolla "Microstrip bandpass filters with wide bandwidth and compact dimensions." *Microwave Opt. Tech. Lett.*, vol. 46, pp. 343–346, August 2005.
42. J. Bonache, I. Gil, J. García-García, and F. Martín "Complementary split rings resonators (CSRRs): towards the miniaturization of microwave device design." *Comput. Electron.*, vol. 5, pp. 193–197, May 2006.
43. J. Martel, R. Marqués, F. Falcone, J. D. Baena, F. Medina F. Martín, and M. Sorolla "A new LC series element for compact band pass filter design." *IEEE Microwave Wirel. Comp. Lett.*, vol. 14, pp. 210–212, May 2004.

44. J. Martel, J. Bonache, R. Marqués, F. Martín, and F. Medina "Design of wide-band semi-lumped bandpass filters using open split ring resonators." *IEEE Microwave Wirel. Comp. Lett.*, vol. 17, pp. 28–30, January 2007.
45. M. Gil, J. Bonache, J. García-García, J. Martel, and F. Martín "Composite right/left handed (CRLH) metamaterial transmission lines based on complementary split rings resonators (CSRRs) and their applications to very wide band and compact filter design." *IEEE Trans. Microwave Theory Tech.*, vol. 55, pp. 1296–1304, June 2007.
46. W. Menzel and P. Feil "Ultra-wide band (UWB) filter with WLAN notch." *Proc. 36th European Microwave Conf.*, pp. 595–598, Manchester, UK, September 2006.
47. K. Li, D. Kurita, and T. Matsui "UWB band pass filters with multi notched bands." *Proc. 36th European Microwave Conf.*, pp. 591–594A, Manchester, UK, September 2006.
48. M. Gil, J. Bonache, and F. Martín "Metamaterial filters with attenuation poles in the pass band for ultra wide band applications." *Microwave Opt. Tech. Lett.*, vol. 49, pp. 2909–2913, December 2007.
49. H. V. Nguyen and C. Caloz "Broadband highly selective bandpass filter based on a tapered coupled-resonator (TCR) CRLH structure." *Proc. European Microwave Association*, vol. 2, pp. 44–51, March 2006.
50. G. Rebeiz, *RF MEMS Theory, Design and Technology*. Wiley, New York, 2003.
51. I. Gil, J. Bonache, J. García-García, and F. Martín "Application of active electromagnetic bandgaps to the design of tunable resonators in CPW technology." *Microwave Opt. Tech. Lett.*, vol. 45, pp. 229–232, May 2005.
52. I. Gil, J. García-García, J. Bonache, F. Martín, M. Sorolla, and R. Marqués "Varactor-loaded split rings resonators for tuneable notch filters at microwave frequencies." *Electron. Lett.*, vol. 40, pp. 1347–1348, October 2004.
53. J. B. Pendry, A. J. Holden, D. J. Robbins, and W. J. Stewart "Magnetism from conductors and enhanced nonlinear phenomena." *IEEE Trans. Microwave Theory Tech.*, vol. 47, pp. 2075–2084, November 1999.
54. I. Gil, J. Bonache, J. García-García, and F. Martín "Tunable metamaterial transmission lines based on varactor loaded split rings resonators." *IEEE Trans. Microwave Theory Tech.*, vol. 54, pp. 2665–2674, June 2006.
55. M. Gil, J. Bonache, I. Gil, J. García-García, and F. Martín "Miniaturization of planar microwave circuits by using resonant-type left handed transmission lines." *IET Microwaves Antennas Propag.*, vol. 1, pp. 73–79, February 2007.
56. M. A. Antoniades and G. V. Eleftheriades "A broadband series power divider using zero-degree metamaterial phase shifting lines." *IEEE Microwave Wirel. Comp. Lett.*, vol. 15, pp. 808–810, November 2005.
57. H. Okabe, C. Caloz, and T. Itoh "A compact enhanced bandwidth hybrid ring using an artificial lumped element left handed transmission line section." *IEEE Trans. Microwave Theory Tech.*, vol. 52, pp. 798–804, March 2004.
58. G. Sisó, J. Bonache, M. Gil, J. García-García, and F. Martín "Compact rat-race hybrid coupler implemented through artificial left handed and right handed lines." *IEEE MTT-S Int'l Microwave Symposium Digest*, Honolulu, pp. 25–28, June 2007.
59. I. B. Vendik, O. G. Vendik, D. V. Kholodnyak, E. V. Serebryakova, and P. V. Kapitanova "Digital phase shifters based on right- and left-handed transmission lines." *Proc. European Microwave Assoc.*, vol. 2, pp. 30–37, March 2006.

60. I. H. Lin, M. De Vincentis, C. Caloz, and T. Itoh "Arbitrary dual-band components using composite right/left-handed transmission lines." *IEEE Trans. Microwave Theory Tech.*, vol. 52, pp. 1142–1149, April 2004.
61. R. Mongia, I. Bahl, P. Bhartia, and J. Hong, *RF and Microwave Coupled Line Circuits*. 2nd ed. Artech House, Norwood, MA, 2007.
62. P. K. Ikalainen and G. L. Matthaei "Wide-band, forward coupling microstrip hybrids with high directivity." *IEEE Trans. Microwave Theory Tech.*, vol. MTT-35, pp. 719–725, August 1987.
63. L. Liu, C. Caloz, C-C. Chang, and T. Itoh "Forward coupling phenomena between artificial left handed transmission lines." *J. Appl. Phys.*, vol. 92, pp. 5560–5565, November 2002.
64. C. Caloz and T. Itoh "A novel mixed conventional microstrip and composite right/left handed backward wave directional coupler with broadband and tight coupling characteristics." *IEEE Microwave Wirel. Comp. Lett.*, vol. 14, pp. 31–33, January 2004.
65. C. Caloz and T. Itoh, *Electromagnetic Metamaterials: Transmission Line Theory and Microwave Applications*. Wiley, Hoboken, NJ, 2006.
66. R. Islam, F. Elek, and G. V. Eleftheriades "Coupled line metamaterial coupler having codirectional phase but contra-directional power flow." *Electron. Lett.*, vol. 40 (5), pp. 315–317, March 2004.
67. E. Jarauta, M. A. G. Laso, T. Lopetegi, F. Falcone, M. Beruete, J. D. Baena, A. Marcotegui, J. Bonache, J. García-García, R. Marqués, and F. Martín "Novel microstrip backward coupler with metamaterial cells for fully planar fabrication techniques." *Microwave Opt. Tech. Lett.*, vol. 48, pp. 1205–1209, June 2006.
68. C. Caloz, A. Sanada, and T. Itoh "A novel composite right/left handed coupled-line directional coupler with arbitrary coupling level and broad bandwidth." *IEEE Trans. Microwave Theory Tech.*, vol. 52, pp. 980–992, March 2004.
69. N. Engheta and R. W. Ziolkowski "A positive future for double-negative metamaterials." *IEEE Trans. Microwave Theory Tech.*, vol. 53, No. 4, pp. 1535–1556, April 2005.
70. R. W. Ziolkowski, and A. D. Kipple "Application of double negative materials to increase the power radiated by electrically small antennas." *IEEE Trans. Antennas Propag.*, vol. 51, No. 10, pp. 2626–2640, October 2003.
71. A. Alú and N. Engheta "Radiation from a traveling-wave current sheet at the interface between a conventional material and a metamaterial with negative permittivity and permeability." *Microwave Opt. Tech. Lett.*, vol. 35, pp. 460–463, December 2002.
72. J. Sun, W. Sun, T. Jiang, and Y. Feng "Directive electromagnetic radiation of a line source scattered by a conducting cylinder coated with left-handed metamaterial." *Microwave Opt. Tech. Lett.*, vol. 47, pp. 274–279, November 2005.
73. S. F. Mahmoud "A new miniaturized annular ring patch resonator partially loaded by a metamaterial ring with negative permeability and permittivity." *IEEE Antennas Wirel. Propag. Lett.*, vol. 3, pp. 19–22, 2004.
74. S. N. Burokur, M. Latrach, and S. Toutain "Theoretical investigation of a circular patch antenna in the presence of a left-handed medium." *IEEE Antennas Wirel. Propag. Lett.*, vol. 4, pp. 183–186, 2005.
75. M. Kärkkäinen and P. Ikonen "Patch antenna with stacked split-ring resonators as an artificial magneto-dielectric substrate." *Microwave Opt. Tech. Lett.*, vol. 46, pp. 554–556, September 2005.

76. A. Grbic and G. V. Eleftheriades “Experimental verification of backward-wave radiation from a negative refractive index metamaterial.” *J. Appl. Phys.*, vol. 92, pp. 5930–5935, November 2002.
77. L. Liu, C. Caloz, and T. Itoh “Dominant mode (DM) leaky wave antenna with backfire-to-endfire scanning capability.” *Electron. Lett.*, vol. 38, pp. 1414–1416, November 2002.
78. S. Lim, C. Caloz, and T. Itoh “Metamaterial-based electronically-controlled transmission line structure as a novel leaky-wave antenna with tunable angle and beamwidth.” *IEEE Trans. Microwave Theory Tech.*, vol. 52, No. 12, pp. 2678–2690, December 2004.
79. C. Caloz and T. Itoh “Metamaterials for high-frequency electronics.” *Proc. IEEE*, vol. 93, pp. 1744–1752, October 2005.
80. A. Lai, C. Caloz, and T. Itoh “Composite right-/left-handed transmission line metamaterials.” *IEEE Microwave Mag.*, pp. 34–50, September 2004.
81. S. Lim, C. Caloz, and T. Itoh “A reflecto-directive system using a composite right-/left-handed (CRLH) leaky-wave antenna and heterodyne mixing.” *IEEE Microwave Wirel. Comp. Lett.*, vol. 14, pp. 183–185, April 2004.
82. C. Caloz and T. Itoh “Array factor approach of leaky-wave antennas and application to 1-D/2-D composite right/left-handed (CRLH) structures.” *IEEE Microwave Wirel. Comp. Lett.*, vol. 14, pp. 274–276, June 2004.
83. S. Lim, C. Caloz, and T. Itoh “Electronically scanned composite right/left handed microstrip leaky-wave antenna.” *IEEE Microwave Wirel. Comp. Lett.*, vol. 14, pp. 277–279, June 2004.
84. I. Arnedo, J. Illescas, M. Flores, T. Lopetegi, M. A. G. Laso, F. Falcone, J. Bonache, J. García-García, F. Martín, J. A. Marcotegui, R. Marqués, and M. Sorolla “Forward and backward leaky wave radiation in split ring resonator based metamaterials.” *IET Microwaves, Antennas Propag.*, vol. 1, pp. 65–68, February 2007.



# Advanced and Related Topics

---

## 5.1 INTRODUCTION

In previous chapters we have developed the central concepts of metamaterials science and its main technological applications as they are perceived by the authors. In addition, metamaterial concepts often act as shortcuts to many other concepts and applications that probably would not be developed (or would be developed in a different way) without the current interest in metamaterials. Some of these topics are described in this chapter. The choice is, of course, arbitrary, and has much to do with author's personal experience and taste. We have chosen those topics that, in our opinion, would likely give rise to practical applications in the near future. We hope that our intuition will not be too wrong.

The chapter begins with the analysis of admittance surfaces designed from SRRs and CSRRs (see Chapters 2 and 3), whose reflection and transmission properties can be related through Babinet principle. We hope that these structures may find application as frequency-selective surfaces, polarizers, and polarization converters. We also feel that the reported admittance surface approach could be useful for the analysis of two-dimensional micro- and nanostructured metal–dielectric surfaces with exotic electromagnetic properties (meta-surfaces).

Magneto-inductive waves—and the complementary electro-inductive waves—excited in one-, two-, and three-dimensional arrays of metamaterial elements are the next topic analyzed in this chapter. Magneto-inductive waves are of theoretical interest as a specific kind of waves that can be excited in metamaterial structures. They could find application in alternative waveguiding devices and systems, which may exploit their slow-wave characteristics. They could be also useful for near-field subdiffraction imaging.

Imaging is the last topic addressed in this chapter. Subdiffraction imaging is one of the most exciting applications of metamaterials. In this chapter, we will analyze

some subdiffraction imaging devices—other than the left-handed slab analyzed in Chapter 1—that provide similar results with a simpler design. These devices include plasmonic slabs, ferrite slabs, and coupled arrays of magnetic resonators. Finally, this last section also includes a brief report on some newly proposed imaging devices, based on light canalization.

## 5.2 SRR- AND CSRR-BASED ADMITTANCE SURFACES

Both SRRs and CSRRs are planar small resonators, which can be easily printed on a low-loss dielectric circuit board in order to configure resonant surface arrays with interesting electromagnetic properties. Duality [1] and the Babinet principle [2] impose that the behavior of SRR and CSRR surface arrays must be approximately dual (small deviations from this duality may arise from the effects of the dielectric substrate on which SRRs and CSRRs are printed). Moreover, as far as the electrical size of the elements and the periodicity can be considered small, the surface admittance concept appears a useful tool for the analysis of such configurations. Throughout this section, these concepts will be developed in order to provide a first approach to the behavior and applications of SRR and CSRR surface arrays.

### 5.2.1 Babinet Principle for a Single Split Ring Resonator

In the most general case, when it is illuminated by some external field  $\mathbf{E}^0, \mathbf{B}^0$ , a single edge-coupled SRR (EC-SRR) will show a set of polarizabilities given by (see Chapter 2)

$$m_z = \alpha_{zz}^{\text{mm}} B_z^0 - \alpha_{yz}^{\text{em}} E_y^0, \quad (5.1)$$

$$p_y = \alpha_{yy}^{\text{ee}} E_y^0 + \alpha_{yz}^{\text{em}} B_z^0, \quad (5.2)$$

and

$$p_x = \alpha_{xx}^{\text{ee}} E_x^0, \quad (5.3)$$

where, near the first EC-SRR resonance, the polarizabilities in expressions (5.1) and (5.2) take the general form

$$\alpha = \alpha_0 \left( \frac{\omega_0^2}{\omega^2} - 1 \right)^{-1}, \quad (5.4)$$

where  $\alpha_0$  is a geometrical factor (the remaining polarizability  $\alpha_{xx}^{\text{ee}}$  has a nonresonant behavior at  $\omega = \omega_0$ ). The effect of an incident electromagnetic field on a single EC-SRR is illustrated in Figure 5.1a. The magnetic and electric dipolar moments (5.1)–(5.3) are generated in the SRR, and, in the long wavelength approximation, determine the scattered fields  $\mathbf{E}'$  and  $\mathbf{B}'$ . The total fields are the superposition of the incident and the scattered fields. Let us now consider the complementary

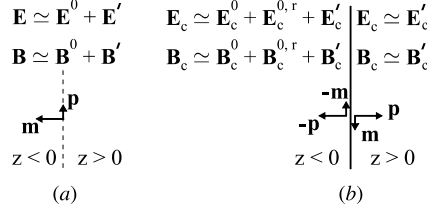


**FIGURE 5.1** Illustration of the behavior of an SRR (a) and a CSRR (b) when they are illuminated by an external field  $\mathbf{E}^0$ ;  $\mathbf{B}^0$  (a) or  $\mathbf{E}_c^0 = c\mathbf{B}^0$ ;  $\mathbf{B}_c^0 = -(1/c)\mathbf{E}^0$  (b) coming from  $z < 0$ .

screen, that is, the complementary resonator (CSRR). If the screen is a perfect conductor of negligible thickness, and the effects of the dielectric substrate are ignored (or it has a negligible dielectric susceptibility), the behavior of this CSRR can be deduced from classical diffraction theory and the Babinet principle [2]. The CSRR behavior when it is illuminated by the complementary fields

$$\mathbf{E}_c^0 = c\mathbf{B}^0; \quad \mathbf{B}_c^0 = -(1/c)\mathbf{E}^0 \quad (5.5)$$

( $c$  is the velocity of light in vacuum), incident from the left ( $z < 0$ ), is illustrated in Figure 5.1*b*. At the right-hand side of the screen ( $z > 0$ ), the fields are those produced by the electric and magnetic dipoles  $\mathbf{m}$  and  $\mathbf{p}$ . These electric and magnetic dipoles are given by

$$p_z = \beta_{zz}^{ee} E_z^0 - \beta_{yz}^{em} B_y^0, \quad (5.6)$$

$$m_y = \beta_{yy}^{mm} B_y^0 + \beta_{yz}^{em} E_z^0, \quad (5.7)$$

and

$$m_x = \beta_{xx}^{mm} B_x^0, \quad (5.8)$$

where, from the Babinet principle [2] and the well-known expressions for the electromagnetic fields of the electric and magnetic dipoles, it follows that [4]

$$\beta_{xx}^{mm} = -c^2 \alpha_{xx}^{ee}; \quad \beta_{yy}^{mm} = -c^2 \alpha_{yy}^{ee}; \quad \beta_{yz}^{em} = -\alpha_{yz}^{em}; \quad \beta_{zz}^{ee} = -\frac{1}{c^2} \alpha_{zz}^{mm}. \quad (5.9)$$

According to diffraction theory [2], the fields at the left-hand side of the screen ( $z < 0$ ) are the superposition of the incident field (5.5), the field that would be reflected by a perfect metallic screen at  $z = 0$  ( $\mathbf{E}_c^{0,r}$ ,  $\mathbf{B}_c^{0,r}$ ), and the field created by some magnetic and electric dipoles, which are the opposite of equations (5.6)–(5.8). Note that this change of sign for the induced dipoles at the right- and left-hand sides of the screen ensures that both the total magnetic polarization perpendicular to the screen and the total electric polarization parallel to the screen vanish, as must be for a plane screen.



### 5.2.2 Surface Admittance Approach for SRR Planar Arrays

Let us now consider the behavior of a plane array of EC-SRRs. For simplicity, a square array of periodicity  $a$  will be considered (see Fig. 5.2). The considered incident field will be a plane wave of arbitrary polarization, incident on this array from the left-hand side ( $z < 0$ ). As far as the size of the SRRs can be considered small with regard to the wavelength, the far field produced by the surface currents on the array can be approximated by the field created by the average currents on it. Such average currents arise from the mean surface electric  $\mathbf{P}_s$  and magnetic  $\mathbf{M}_s$  polarizations generated in the SRR array. Such polarizations are generated from the electric and magnetic fields

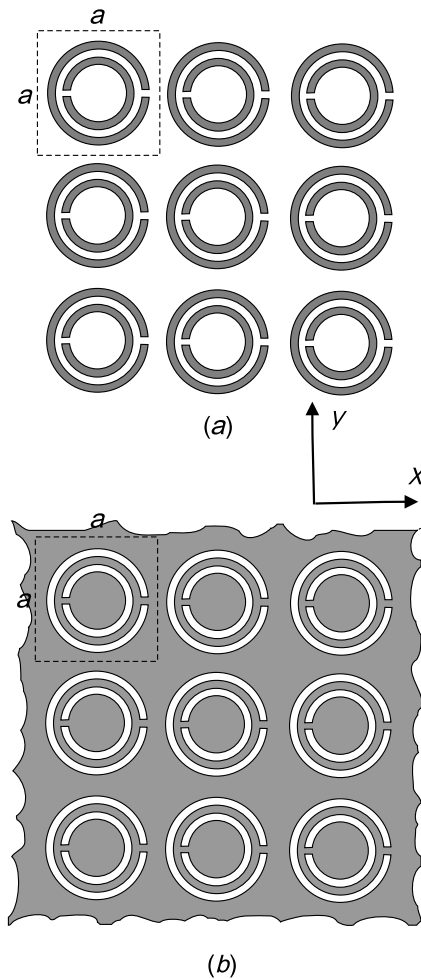


**FIGURE 5.2** A planar square array of EC-SRRs (a), and its complementary screen, a planar array of CSRRs (b). In the calculations both arrays are supposed to extend to infinity at both sides.

incident upon each SRR through expressions (5.1)–(5.3). Therefore, there is a linear relation between the mean surface currents and the average fields on the array of the kind [5]

$$\begin{pmatrix} J_{s,x} \\ J_{s,y} \end{pmatrix} = \begin{pmatrix} Y_{xx} & Y_{xy} \\ Y_{yx} & Y_{yy} \end{pmatrix} \cdot \begin{pmatrix} E_x \\ E_y \end{pmatrix}. \quad (5.10)$$

The surface current density  $\mathbf{J}_s$  comes from the surface polarization  $\mathbf{P}_s = p_y a^{-2} \hat{\mathbf{y}}$ , and the surface magnetization  $\mathbf{M}_s = m_z a^{-2} \hat{\mathbf{z}}$  through [6]

$$\mathbf{J}_s = j\omega\mathbf{P}_s - \hat{\mathbf{z}} \times \nabla\mathbf{M}_{s,z}, \quad (5.11)$$

where the last term comes from the identity  $\nabla \times \mathbf{M}_s \equiv -\hat{\mathbf{z}} \times \nabla\mathbf{M}_{s,z}$ . The surface admittances  $Y_{i,j}$ ;  $i, j \equiv x, y$ , can be deduced from the SRR polarizations (5.6)–(5.8) through the appropriate homogenization procedure.

The more simple homogenization procedure equates the local field seen by each SRR with the average field in equation (5.10).<sup>1</sup> In such a approximation—which is strictly valid only for very sparse arrays—the dipolar moments  $p_x$ ,  $p_y$ , and  $m_z$  are given by expressions (5.1)–(5.3) with  $\mathbf{E}^0 = \mathbf{E}$  and  $\mathbf{B}^0 = \mathbf{B}$ . Taking into account Faraday's law ( $\nabla \times \mathbf{E} = -j\omega\mathbf{B}$ ) and equation (5.11), the averaged surface current density on the SRR array can be expressed as

$$J_{s,x} = j\omega \frac{\alpha_{xx}^{ee}}{a^2} E_x - \frac{\alpha_{yz}^{em}}{a^2} \frac{\partial E_y}{\partial y} + j \frac{\alpha_{zz}^{mm}}{\omega a^2} \left\{ \frac{\partial^2 E_y}{\partial x \partial y} - \frac{\partial^2 E_x}{\partial y^2} \right\}, \quad (5.12)$$

and

$$J_{s,y} = j\omega \frac{\alpha_{yy}^{ee}}{a^2} E_y + \frac{\alpha_{yz}^{em}}{a^2} \frac{\partial E_x}{\partial y} - j \frac{\alpha_{zz}^{mm}}{\omega a^2} \left\{ \frac{\partial^2 E_y}{\partial x^2} - \frac{\partial^2 E_x}{\partial x \partial y} \right\}, \quad (5.13)$$

which, for the particular case of an incident plane wave ( $\mathbf{E}^0 \propto \exp(j\omega t - j\mathbf{k}\mathbf{r})$ ) reduces to [5]

$$Y_{xx} = j\omega \left\{ \frac{\alpha_{xx}^{ee}}{a^2} + \frac{k_y^2 \alpha_{zz}^{mm}}{\omega^2 a^2} \right\}, \quad (5.14)$$

$$Y_{yy} = j\omega \left\{ \frac{\alpha_{yy}^{ee}}{a^2} + \frac{k_x^2 \alpha_{zz}^{mm}}{\omega^2 a^2} \right\}, \quad (5.15)$$

$$Y_{xy} = j\omega \left\{ \frac{\alpha_{yz}^{em} k_y}{\omega a^2} - \frac{k_x k_y \alpha_{zz}^{mm}}{\omega^2 a^2} \right\}, \quad (5.16)$$

<sup>1</sup>An example of another—and more accurate—homogenization procedure is developed in the next section for the analysis of magneto-inductive surfaces. In this section, however, we will use this simpler homogenization, because we are mainly interested in a qualitative description of the most important physical effects associated with this kind of meta-surface.

and

$$Y_{yx} = j\omega \left\{ -\frac{\alpha_{yz}^{\text{em}} k_y}{\omega a^2} - \frac{k_x k_y \alpha_{zz}^{\text{mm}}}{\omega^2 a^2} \right\}, \quad (5.17)$$

where  $k_x$  and  $k_y$  are the transverse components of the wave vectors of the incident field. It is worth noting that, for loss-less SRRs,  $\alpha_{yz}^{\text{em}}$  is imaginary, whereas  $\alpha_{yy}^{\text{ee}}$  and  $\alpha_{zz}^{\text{mm}}$  are real numbers (see Chapter 2). Therefore  $Y_{yx} = -Y_{xy}^*$ , as is imposed by energy conservation.

It should be kept in mind that expressions (5.14)–(5.17) were obtained from the simplest approximation, only valid for sparse arrays of weakly coupled SRRs. However, (equation 5.10) is completely general, provided the long wavelength approximation is assumed. From this expression, provided the surface admittance matrix is known, the reflection and transmission coefficients of the array can be obtained (see Sections 5.2.4 and 5.2.5) for any angle of incidence.

### 5.2.3 Babinet Principle for CSRR Planar Arrays

Let us now consider the complementary array of Figure 5.2*b*. It is possible, in principle, to develop an admittance approach for this planar array, similar to that developed in the previous paragraphs. However, if the effects of the screen thickness and conductivity, as well as the dielectric board polarizability, are neglected, the transmission and reflection coefficients of such an array can be obtained directly from those of the SRR array by applying the Babinet principle.

Let us consider the complementary incident field (5.5) on the CSRR array. The Babinet principle [2] states that the total magnetic field of the SRR array,  $\mathbf{B}$ , and the total electric field of the CSRR array,  $\mathbf{E}_c$ , at the shadowed region ( $z > 0$ ) are related by

$$c\mathbf{B} + \mathbf{E}_c = c\mathbf{B}^0. \quad (5.18)$$

Therefore, the transmission coefficient for the CSRR array illuminated by the complementary wave (5.5),  $t_c$ , is related to the transmission coefficient for the SRR array,  $t$ , by

$$t + t_c = 1. \quad (5.19)$$

Therefore,

$$t_c = -r \quad \text{and} \quad r_c = -t, \quad (5.20)$$

where  $r$  and  $r_c$  are the reflection coefficients for the SRR array and for the CSRR array (illuminated by the complementary wave), respectively. Therefore, as is expected, the transmission and reflection coefficients for the SRR and the CSRR array interchange their roles when the CSRR array is illuminated by the complementary incident wave.

The aforementioned results are valid for the copolarized components of the reflected and transmitted waves (i.e., for the reflected and transmitted waves having

the same polarization as the incident one). However, because the admittance matrix in expression (5.10) may not be diagonal, cross-polarized reflected and transmitted waves can be generated at the SRR and CSRR arrays. If the cross-polarization transmission coefficients,  $t'$  and  $t'_c$ , are considered, from expression (5.18) it follows that  $t' + t'_c = 0$ . And, as it must be that  $r' + t' = 0$  for the cross-polarization coefficients, we finally obtain

$$t' = -r' = -t'_c = r'_c. \quad (5.21)$$

As has already been mentioned at the beginning of this section, the above results are strictly valid for perfectly conducting screens of negligible thickness, and for substrates of negligible polarizability. In practice, these results must be considered as a first approximation. For realistic structures, the most important deviations from the above results come from the ohmic losses in the screens, and from the deviations in the frequency of resonance between the SRR and CSRR arrays, due to the effect of the substrate. This last effect can be approximately taken into account by introducing the CSRR frequency of resonance in place of  $\omega_0$  in equations (5.1)–(5.3).

#### 5.2.4 Behavior at Normal Incidence

For normal incidence  $k_x = k_y = 0$  and the admittance matrix in equation (5.10) is diagonal. Therefore, no cross-polarization effects appear. That is, for the two orthogonal polarizations ( $\mathbf{E}^0 = E^0 \hat{\mathbf{x}}$ , and  $\mathbf{E}^0 = E^0 \hat{\mathbf{y}}$ ), the transmitted and reflected waves have the same polarization as the incident wave. As  $\alpha_{yy}^{ee}$  is resonant and  $\alpha_{xx}^{ee}$  is not, the behavior of the SRR array for both orthogonal polarizations is quite different. For waves polarized with the electric field along the  $x$ -axis, the SRR array is almost transparent. Of more interest is the behavior for waves polarized along the  $y$ -axis. A strong reflectivity can be expected for such waves near the SRR frequency of resonance. Therefore, near such frequency, the SRR array acts as a polarizer, which is transparent for  $x$ -polarization and opaque for  $y$ -polarization.

Let us now analyze in detail the behavior for the most interesting polarization of the incident wave:  $\mathbf{E}^0 = E^0 \hat{\mathbf{y}} \exp(j\omega t - kz)$ . In such a case, from equations (5.10) and (5.14)–(5.17), it follows that the SRR array is characterized by a surface admittance  $Y_s$  given by

$$\mathbf{J}_s = Y_s \mathbf{E}; \quad Y_s = j\omega \frac{\alpha_{yy}^{ee}}{a^2}. \quad (5.22)$$

The transmission and reflection coefficients for the SRR array can now be obtained from equation (5.22) and the appropriate boundary conditions for the tangential components of the electric and magnetic fields at the screen. The final result is [5]

$$t = 1 + r = \frac{2}{Y_s \eta_0 + 2}, \quad (5.23)$$

where  $\eta_0 = \sqrt{\mu_0/\epsilon_0}$  is the free-space impedance. This equation predicts a total reflection peak when  $Y_s \rightarrow \infty$ , that is, at the frequency of resonance of the SRRs. It also predicts a total transmission frequency point when  $Y_s \eta_0 = 0$ . According to the expression for  $\alpha_{yy}^{ee}$  given in Chapter 1, this point must be located above the frequency of resonance of the SRRs.

The behavior of the complementary CSRR array for complementary excitation, that is, for a plane incident wave polarized along the  $x$ -axis, can be deduced from the above equations and from equation (5.20): a strong transmission peak is predicted at the CSRR frequency of resonance, as well as a total reflection peak just above this frequency. These results are exact only for the very strict conditions mentioned at the end of Section 5.2.3.<sup>2</sup> However, they still describe most of the physics of the analyzed devices. In practice, deviations from Babinet correspondence (5.20) can be expected as a consequence of substrate effects and ohmic losses. In addition, deviations of the aforementioned SRR-reflection and CSRR-transmission peaks frequencies from the resonant frequencies of the SRR and CSRR must be expected as a consequence of the coupling between array elements (which were ignored in equations 5.14–5.17).

An experimental confirmation of the behavior described in the previous paragraph is shown in Figure 5.3, where the aforementioned strong SRR-reflection and CSRR-transmission peaks can be clearly appreciated. As was already mentioned, the frequency shift between these peaks can be attributed to the presence of the dielectric substrate, and the deviation from total transmission in the CSRR array to ohmic losses. It may be worth mentioning here that the presence of such extraordinary transmission/reflection peaks at normal incidence is a consequence of the cross-polarization effects in the EC-SRR, already analyzed in Chapter 2. In fact, these effects would disappear if nonbianisotropic elements—such as the NB-SRRs or BC-SRRs reported in Chapter 2—were used. Finally, it may be worth noting (in order to judge the accuracy of the proposed models) that the frequency of resonance of the SRRs considered in Figure 5.3, predicted by the model reported in Chapter 2, is  $\omega_0 = 2\pi \times 4.41$  GHz, and the frequency of resonance of the CSRRs, predicted by the model reported in Chapter 3, is  $\omega_0 = 2\pi \times 4.65$  GHz.

### 5.2.5 Behavior at General Incidence

In order to obtain the transmission and reflection coefficients for an arbitrary angle of incidence, the boundary conditions on the surface  $z = 0$ ,

$$J_{s,x} = H_y^i + H_y^r - H_y^t, \quad (5.24)$$

$$J_{s,y} = -H_x^i - H_x^r + H_x^t, \quad (5.25)$$

$$0 = E_x^i + E_x^r - E_x^t, \quad (5.26)$$

<sup>2</sup>And, because the particular homogenization procedure has a limited scope, only for weakly coupled SRRs/CSRRs arrays.

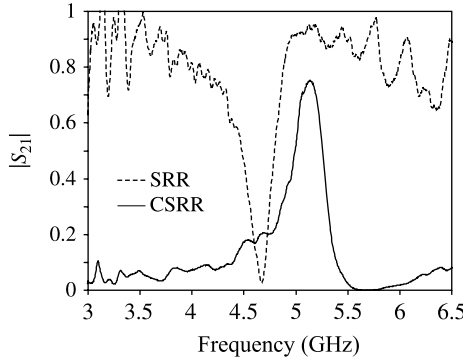


**FIGURE 5.3** Measured transmission coefficient through a CSRR (solid line) and an SRR (dashed line) square planar array. The CSRRs and SRRs are etched on a commercial low-loss microwave circuit board with permittivity  $\epsilon = 2.43\epsilon_0$ , thickness  $h = 0.49$  mm, and metallizations of copper with a thickness  $t = 35$   $\mu\text{m}$ . The CSRR and SRR parameters are  $r_{\text{ext}} = 3.5$  mm,  $c = 0.4$  mm, and  $d = 0.4$  mm. The CSRRs and SRRs are arranged in a cubic lattice with periodicity  $a = 8$  mm. The characteristics of the incident waves are described in the text. (Source: Reprinted with permission from [3]; copyright 2004, the American Physical Society.)

and

$$0 = E_y^i + E_y^r - E_y^t, \quad (5.27)$$

must be substituted in equation (5.10). Using Faraday's law, expressions (5.24) and (5.25) can be expressed in terms of the derivatives of the electric fields on the SRR array. Then, after some manipulations, the following equations are obtained for the electric fields of the reflected and transmitted waves at  $z = 0$ :

$$\begin{pmatrix} E_x \\ E_y \end{pmatrix}^r = \begin{pmatrix} A - Y_{xx} & B - Y_{xy} \\ B - Y_{yx} & C - Y_{yy} \end{pmatrix}^{-1} \cdot \begin{pmatrix} Y_{xx} & Y_{xy} \\ Y_{yx} & Y_{yy} \end{pmatrix} \cdot \begin{pmatrix} E_x \\ E_y \end{pmatrix}^i \quad (5.28)$$

$$\begin{pmatrix} E_x \\ E_y \end{pmatrix}^t = \begin{pmatrix} A - Y_{xx} & B - Y_{xy} \\ B - Y_{yx} & C - Y_{yy} \end{pmatrix}^{-1} \cdot \begin{pmatrix} A & B \\ B & C \end{pmatrix} \cdot \begin{pmatrix} E_x \\ E_y \end{pmatrix}^i, \quad (5.29)$$

where  $A$ ,  $B$ , and  $C$  are given by

$$A = -\frac{2}{\omega\mu_0} \frac{k_x^2 + k_z^2}{k_z}, \quad (5.30)$$

$$B = -\frac{2}{\omega\mu_0} \frac{k_x k_y}{k_0}; \quad k_0 = \omega\sqrt{\epsilon_0\mu_0}, \quad (5.31)$$

and

$$C = -\frac{2}{\omega\mu_0} \frac{k_y^2 + k_z^2}{k_z}, \quad (5.32)$$

with

$$k_x = k_x^i = k_x^r = k_x^t \quad (5.33)$$

$$k_y = k_y^i = k_y^r = k_y^t \quad (5.34)$$

and

$$k_z = k_z^i = -k_z^r = k_z^t. \quad (5.35)$$

From equations (5.28) and (5.29), the transmission and reflection coefficients for the co- and cross-polarization components can be obtained for any polarization and angle of incidence,  $\theta_i = \tan^{-1} \left\{ \sqrt{(k_x^2 + k_y^2)/k_z^2} \right\}$ , of the incoming wave.

The main effects that appear for oblique incidence are analyzed in [4], where an experimental confirmation of these effects is also provided. From equations (5.28)–(5.35), it follows that strong reflections peaks will appear in the SRR arrays (for the appropriate polarization of the incident waves) near the frequency of resonance of the SRRs. This independence of the surface resonances of the angle of incidence is a remarkable property of the analyzed SRR/CSRR arrays. Regarding cross-polarization effects, from equations (5.28)–(5.35) it follows that cross-polarization effects are present in general. However, for the two orthogonal main planes of incidence (i.e., the  $x-z$  and the  $y-z$  planes), from equations (5.28)–(5.35) it follows that cross-polarization only occurs if  $Y_{yx}$  or  $Y_{xy}$  are nonzero. That is, cross-polarization effects do not appear for incidence in the  $x-z$  plane. The experimental results for transmittance through the SRR array already considered in Figure 5.3, corresponding to a TE wave with this kind of incidence (or TE<sub>y</sub> wave<sup>3</sup>), are shown for several angles of incidence in Figure 5.4a (the transmittance for a TM<sub>y</sub> wave is, as expected, near unity for all angles of incidence). The experimental results confirm the absence of cross-polarization effects, as well as the presence of a high reflectivity around the frequency of resonance of the SRRs. From the Babinet principle, a complementary behavior is expected for TM<sub>y</sub> waves incident upon a CSRR array. This behavior is shown in Figure 5.4b.

For incidence not in the  $x-z$  plane, cross-polarization effects are unavoidable. This effect can be seen in Figure 5.5a, where the measured transmittances for plane TM<sub>x</sub> waves incident upon the same SRR array are shown. These experimental results confirms the presence of strong cross-polarization effects near the SRR resonance. The same effect can be observed in Figure 5.5b, where the transmittance for the

<sup>3</sup>In our notation, the subindex,  $x$  or  $y$ , indicates the polarization of the main field component (electric for TE waves and magnetic for TM waves), which should also be perpendicular to the plane of incidence.

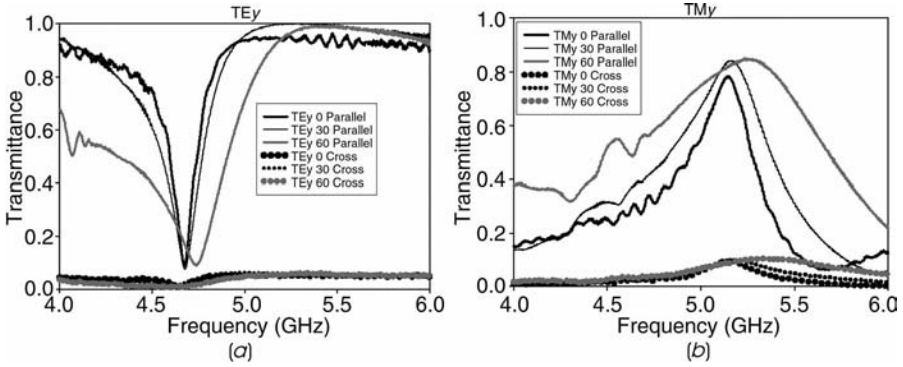


**FIGURE 5.4** Measured transmittance through the SRR (a) and the CSRR (b) arrays of Figure 5.3 for incidence in the  $x-z$  plane at several angles. Incident waves are  $TE_y$  for the SRR array and  $TM_y$  for the CSRR array. (Source: Reproduced with permission from [4]; copyright 2006, Taylor & Francis Group, LLC.)

complementary  $TE_x$  waves incident upon the CSRR array are shown. From the general form of the cross-polarization  $\alpha_{yz}^{em}$ , it follows that for loss-less arrays  $Y_{xy}$  is imaginary, and  $Y_{xx}, Y_{yy}$  are real quantities. Therefore, from equations (5.28)–(5.35), it follows that the co- and cross-polarized transmitted (or reflected) waves must be in quadrature.<sup>4</sup> That is, when cross-polarization is present, the transmitted and reflected waves are elliptically polarized. When both components are of equal magnitude, the transmitted or reflected wave is circularly polarized. This possibility is confirmed by the experimental results shown in Figure 5.5 for both arrays.

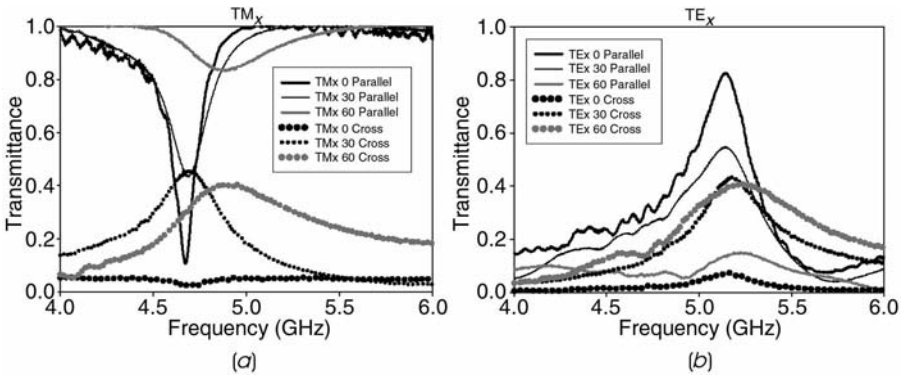


**FIGURE 5.5** Measured transmittance through the SRR (a) and the CSRR (b) arrays of Figure 5.3 for incidence in the  $y-z$  plane at several angles. Incident waves are  $TM_x$  for the SRR array and  $TE_x$  for the CSRR array. (Source: Reproduced with permission from [4]; copyright 2006, Taylor & Francis Group, LLC.)

<sup>4</sup>Note that for this incidence  $B = 0$ .



SRR and CSRR arrays belong to a family of planar devices presenting enhanced transmission and/or reflection in some frequency band. As has already been mentioned, the transmission and reflection properties of SRR/CSRR arrays do not crucially depend on periodicity. Therefore their behavior is closer to a *frequency-selective* surface than to a diffraction screen. In addition, their transmission and reflection properties—which, in some cases, may include polarization conversion—strongly depend on the polarization of the incident wave. Such a high variety of effects present in SRR/CSRR surface arrays may find application in devices such as artificial impedance and/or frequency-selective surfaces, as well as polarizers and/or polarization converters. As it will be shown in Section 5.4, they may also find application in the design of microwave lenses with enhanced resolution.

### 5.3 MAGNETO- AND ELECTRO-INDUCTIVE WAVES

Although some historical precedents can be found (see [7] and references therein) magneto-inductive waves (MIWs) were first reported and systematically studied in the frame of metamaterial science in [8,9], and subsequent works from the same group. Magneto-inductive waves were first reported in one-, two-, and three-dimensional arrays of capacitively loaded metallic rings. After such seminal works, MIWs were soon reported in arrays of swiss rolls [11]<sup>5</sup> and SRRs [10]. Magneto-inductive waves are quasimagnetostatic waves, where the field behavior is mainly governed by Ampère’s and Faraday’s laws. Therefore, the effects of the displacement current—for instance, retardation—are ignored. As usual in quasistatic waves,<sup>6</sup> this approach is only valid in the short wavelength limit ( $\mathbf{k} \gg \mathbf{k}_0 \equiv \omega\sqrt{\varepsilon_0\mu_0}$ ). Therefore, MIWs are slow waves, with phase and group velocity usually much smaller than the velocity of light in free space. In bulk (three-dimensional) SRR arrays, MIWs can be considered as a special kind of magnetostatic wave, arising when the internal wavelength is of the same order as the interspacing between the SRRs. In fact, if the bianisotropic effects are ignored (or nonbianisotropic elements, such as BC-SRRs or NB-SRRs, are used) and the internal wavelength is of the same order as the SRRs’ interspacing, it can be expected that interactions between nearest neighbors through Faraday’s law dominate. In such case we are in the realm of the magneto-inductive approximation. Thus, we can distinguish between three kinds of waves in three-dimensional SRR arrays:

- Electromagnetic waves, where the internal wavelength is large with regard to SRR interspacing and of the same order as the free-space wavelength;

<sup>5</sup>Swiss rolls were introduced as a mechanism to obtain magnetic flux channelization in the megahertz range [12] (see also Section 5.4).

<sup>6</sup>Other examples of quasistatic waves are surface plasmons in metallic interfaces [13] or magnetostatic waves in ferrite samples [14,15].

- Conventional magnetostatic waves (see Problem 2.10), where the internal wavelength is large with regard to SRR interspacing, but short with regard to the free-space wavelength;<sup>7</sup> and
- MIWs, where the internal wavelength is of the same order as SRR interspacing, and short with regard to the free-space wavelength.<sup>8</sup>

Electro-inductive waves (EIWs) can be considered as the quasiolelectrostatic counterpart of magnetoinductive waves. In such a case, the wave equation is dominated by the quasiolelectrostatic interaction (Coulomb's law) between the elements of the structure. Electro-inductive waves in chains of metallic resonators have been known for a long time [16]. More recently, the interest in this kind of quasiolelectrostatic waves has been renewed in connection with the problem of the generation and guidance of electromagnetic slow waves at optical frequencies [17,18]. In this section, we will restrict our analysis to the electro-inductive waves guided by one- and two-dimensional arrays of CSRRs [19]. Such specific EIWs can be considered as the dual counterpart of the aforementioned magneto-inductive waves in SRR arrays.

### 5.3.1 The Magneto-Inductive Wave Equation

Let us consider the one-dimensional chains of conducting NB-SRRs<sup>9</sup> shown in Figure 5.6. Considering loss-less rings and neglecting other than nearest-neighbor interactions, the current on the  $n$ th NB-SRR,  $I_n$ , is given by

$$\left\{ j\omega L + \frac{1}{j\omega C} \right\} I_n = -j\omega M(I_{n-1} + I_{n+1}), \quad (5.36)$$

where  $L$  and  $M$  are the self and mutual inductances of the NB-SRRs, and  $C$  is the NB-SRR total capacitance.<sup>10</sup> The dispersion equation for MIWs propagating along the chain is computed from equation (5.36) assuming a current dependence of the kind  $I_n = \exp\{-jk(m-n)a\}I_m$ , where  $k$  is the propagation constant and  $a$  the

<sup>7</sup>In fact, in many practical SRR arrays, where the electrical size of the elements is  $\sim 1/10$  of the free-space wavelength, this region may be very small or irrelevant.

<sup>8</sup>Therefore, the magneto-inductive approach can be very useful for the analysis of waves propagating in bulk SRR-based metamaterials in the short wavelength region (see Section 2.4.3 of Chapter 2).

<sup>9</sup>This particular configuration has been chosen for simplicity. However, a similar analysis will hold for other SRR designs such as BC-SRRs or EC-SRRs (provided cross-polarization effects are not present, or can be neglected), as well as for similar arrays of capacitively loaded rings, metallic swiss-rolls, and other similar elements.

<sup>10</sup>That is,  $C = \pi r C_{\text{pul}}/2$ , where  $C_{\text{pul}}$  is the per-unit-length capacitance in the slot between the rings, and  $r$  is the average radius of the NB-SRR (see Chapter 2).

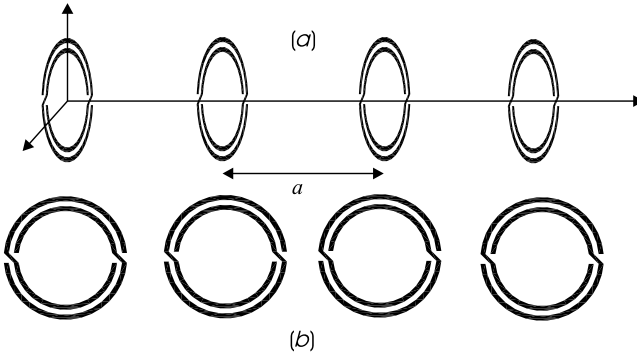


**FIGURE 5.6** One-dimensional chain of NB-SRRs of periodicity  $a$ . Axial configuration (a) and coplanar configuration (b).

periodicity of the array. The final result is [9]

$$\frac{\omega_0^2}{\omega^2} = 1 + \frac{2M}{L} \cos(ka), \quad (5.37)$$

where  $\omega_0$  is the frequency of resonance of the isolated NB-SRR

$$\omega_0^2 = \frac{1}{LC} = \frac{2}{\pi r C_{\text{pul}}}. \quad (5.38)$$

The parameters  $L$  and  $C$  appearing in equation (5.37) can be calculated following the procedure developed in Section 2.3.1. The mutual inductance is more difficult to evaluate in a closed form, because it depends on the specific disposition of the NB-SRRs. Losses in magneto-inductive waveguides are mainly related to ohmic losses in the resonators. They can be easily taken into account (see Problem 5.4) by including the ring ohmic resistance in the current equation (5.36).

The group velocity associated with the dispersion relation (5.37) is

$$v_g \equiv \frac{\partial \omega}{\partial k} = \frac{M}{L} \omega_0 a \sin(ka) \left( 1 + 2 \frac{M}{L} \cos(ka) \right)^{-3/2}. \quad (5.39)$$

It can be easily realized by inspection that the mutual inductance,  $M$ , is positive in the axial configuration and negative in the coplanar configuration of Figure 5.6. Therefore, MIW propagation is forward in the axial configuration, and backward in the co-planar configuration. The bandwidth for the excitation of MIWs can also be deduced from equation (5.37). Assuming, as usual, that  $|M/L| \ll 1$ , it is easily deduced from equation (5.37) that MIWs can be excited in the frequency

interval  $\omega_0 - \delta\omega < \omega < \omega_0 + \delta\omega$ , with

$$\delta\omega = \omega_0 \frac{|M|}{L}. \quad (5.40)$$

The dispersion equation (5.37) can be easily generalized to two- and three-dimensional arrays of SRRs and similar elements. For a three-dimensional cubic array of NB-SRRs, similar to that shown in Figure 2.12, considering only interactions between nearest neighbors, the dispersion relation is

$$\frac{\omega_0^2}{\omega^2} = 1 + \frac{2M_c}{L} (\cos(k_x a) + \cos(k_y a)) + \frac{2M_a}{L} \cos(k_z a), \quad (5.41)$$

where  $M_c$  and  $M_a$  are the mutual inductances in the coplanar and axial configurations, respectively. The magneto-inductive wave equation can also be generalized to the case when the nearest-neighbor approximation is not enough to characterize the system. If the interactions between all the elements are taken into account, the magneto-inductive wave equation (5.41) becomes

$$\frac{\omega_0^2}{\omega^2} = 1 + \sum_l \sum_n \sum_m \frac{2M_{lmn}}{L} \cos\{a(lk_x + nk_y + mk_z)\}, \quad (5.42)$$

where the notation is rather obvious. Regarding the usefulness of the nearest-neighbor approximation, it becomes less and less accurate when the dimensionality of the system increases. In fact, for rings located beyond some critical distance, the dipolar approximation must be valid. For such rings the mutual inductances decay as  $1/d^3$ , where  $d$  is the distance to these rings. However, the number of rings located at such a distance varies as 1,  $d$ , and  $d^2$  for one-, two-, and three-dimensional configurations, respectively. Therefore, the influence of the rings located far away from a given ring substantially increases with the dimensionality of the configuration. The usefulness of the nearest-neighbor approximation also depends on the specific characteristics of the elements.<sup>11</sup>

The coupling between magneto-inductive and electromagnetic waves in a composite including SRRs has also been investigated [20]. In this analysis such coupling is modeled as the coupling between a chain of SRRs and a transmission line. The equivalent circuit proposed in [20] is similar to the circuit model reported in Figure 3.23, but also including the magnetic coupling between nearest SRRs through a mutual inductance. As this circuit model implies a nearest-neighbor approximation, the accuracy of the reported model is higher for shorter internal wavelengths. Thus, for left-handed composites, the model is expected to provide better accuracy at the lower end of the left-handed pass band. For the same reason, better accuracy is expected for low-dimensional structures (one- and two-dimensional structures).

<sup>11</sup>For instance, it is not appropriate for one-dimensional chains of swiss rolls [11].

### 5.3.2 Magneto-Inductive Surfaces

Two-dimensional square planar arrays of NB-SRRs and similar configurations support magneto-inductive waves, which, in the nearest-neighbor approximation, satisfy the equation

$$\frac{\omega_0^2}{\omega^2} = 1 + \frac{2M_c}{L} (\cos(k_x a) + \cos(k_y a)). \quad (5.43)$$

When the incidence of plane waves on the array is analyzed, solutions to equation (5.43) must appear as poles of the transmission and reflection coefficients for imaginary values of the transverse wavevector  $k_z$  (see Chapter 1). This effect cannot be taken into account by the simple homogenization procedure used in Section 5.2.2. Throughout this section, we will develop a modification of such homogenization, which takes into account the excitation of MIWs in the surface array. This modified formalism is based on the analysis developed in [22] for plane arrays of coupled resonators.

For simplicity, a plane array of NB-SRRs will be considered. Therefore, cross-polarization effects are not present, a fact that substantially simplifies the analysis. The size of the NB-SRRs, as well as the periodicity of the array will be assumed electrically small. Therefore, the admittance approximation (5.10) holds. However, because the NB-SRRs do not exhibit cross-polarization effects, the array is isotropic in the  $x$ - $y$  plane. Therefore, equation (5.10) is substituted by the simpler equation

$$\mathbf{J}_s = \frac{1}{Z_a} \mathbf{E}_{\parallel}, \quad (5.44)$$

where  $Z_a$  is the array impedance and  $\mathbf{E}_{\parallel}$  is the component of the average electric field parallel to the array. A cell impedance,  $Z_c$ , is now defined. This impedance relates the surface current on the array with the field of the incident wave

$$\mathbf{J}_s = \frac{1}{Z_c} \mathbf{E}_{\parallel}^i, \quad (5.45)$$

where  $\mathbf{E}_{\parallel}^i$  is the component of the incident field parallel to the array. The average field  $\mathbf{E}_{\parallel}$  is related to the incident field by

$$\mathbf{E}_{\parallel} = \mathbf{E}_{\parallel}^i - \frac{1}{2} Z_0 \mathbf{J}_s, \quad (5.46)$$

where the second term accounts for the electric field of the TE wave created by the surface currents on the array. In this equation  $Z_0$  is simply the wave impedance for TE waves,

$$Z_0 = \frac{\omega \mu_0}{k_z}; \quad k_z = \sqrt{\omega^2 \varepsilon_0 \mu_0 - k_x^2 - k_y^2} \quad (5.47)$$

with  $\text{Im}(k_z) < 0$ . In the quasistatic approximation, this expression reduces to

$$Z_0 = \frac{j\omega\mu_0}{\left| \sqrt{k_x^2 + k_y^2} \right|}. \quad (5.48)$$

Equations (5.46)–(5.48) are the basis for the new homogenization procedure. The cell impedance  $Z_c$  can be calculated from the NB-SRR polarizabilities as will be shown later, and the array impedance is obtained from equations (5.44)–(5.46):

$$Z_a = Z_c - \frac{1}{2}Z_0. \quad (5.49)$$

The average surface current on the array can be obtained from equation (5.11) with  $\mathbf{P}_s = 0$  (cross-polarization effects are not present) and  $\mathbf{M}_s = m_z a^{-2} \hat{\mathbf{z}}$ , where  $m_z$  is the magnetic moment induced in the NB-SRRs. This magnetic moment can be obtained from the external magnetic field,  $\mathbf{B}^{\text{ext}} = j\nabla \times \mathbf{E}^{\text{ext}}/\omega$ , seen by each NB-SRR through (see Chapter 2)

$$m_z = \alpha B_z^{\text{ext}}; \quad \alpha = \frac{\pi^2 r^4}{L} \left( \frac{\omega_0^2}{\omega^2} - 1 \right)^{-1}, \quad (5.50)$$

where  $r$  is the mean radius of the NB-SRR. In the nearest-neighbor approximation, this external magnetic field can be expressed as

$$B_z^{\text{ext}} = B_z^i + \frac{2M}{\pi^2 r^4} (\cos(k_x a) + \cos(k_y a)) m_z. \quad (5.51)$$

In this equation,  $B_z^i$  is the magnetic field of the incident wave, and the last term accounts for the magnetic flux through the NB-SRR due to its four nearest neighbors. Putting all this together, the cell impedance (5.45) is found as

$$Z_c = \frac{j\omega\mu_0 a^2}{k_x^2 + k_y^2} \left( \frac{1}{\mu_0 \alpha} - \beta \right), \quad (5.52)$$

where

$$\beta = \frac{M}{2\mu_0 \pi^2 r^4} (\cos(k_x a) + \cos(k_y a)). \quad (5.53)$$

It can be realized from this expression that the MIWs supported by the array (5.43) correspond to the zeroes of the cell impedance  $Z_c$ . That is, they correspond to a situation on which, according to equation (5.45), there is a nonvanishing surface current

on the array in the absence of any incident wave. Finally, from equations (5.49) and (5.52), it is concluded that the surface impedance of the considered array of NB-SRRs is

$$Z_a = \frac{j\omega\mu_0 a^2}{k_x^2 + k_y^2} \left( \frac{1}{\mu_0 \alpha} - \beta \right) - \frac{1}{2} Z_0. \quad (5.54)$$

The transverse transmission matrix of the NB-SRR array can be defined as in Chapter 1,

$$\begin{pmatrix} E_1^+ \\ E_1^- \end{pmatrix} \equiv \bar{T} \cdot \begin{pmatrix} E_2^+ \\ E_2^- \end{pmatrix} = \begin{pmatrix} T_{11} & T_{12} \\ T_{21} & T_{22} \end{pmatrix} \cdot \begin{pmatrix} E_2^+ \\ E_2^- \end{pmatrix}, \quad (5.55)$$

where  $E_1^\pm$  ( $E_2^\pm$ ) is the electric field for the positive/negative waves at the left-(right-) hand side of the array (see Chapter 1 for more details on the notation). This matrix can be obtained from the boundary conditions at both sides of the array (continuity of the tangential electric field and Ampère's law for the magnetic field), and from equation (5.44). The final result is<sup>12</sup>

$$\bar{T} = \frac{1}{2} \begin{pmatrix} 2 + Z_0/Z_a & Z_0/Z_a \\ -Z_0/Z_a & 2 - Z_0/Z_a \end{pmatrix}. \quad (5.56)$$

Magneto-inductive waves correspond to solutions of equation (5.55) with  $E_1^+ = E_2^- = 0$ . That is,  $T_{11} = 0$  or  $Z_a = -Z_0/2$ . From equation (5.54) it can be easily realized that this condition is actually fulfilled by MIWs with the dispersion relation (5.43).

Although the above analysis has been carried out for a particular kind of element (the NB-SRRs), it is also valid for any array of magneto-inductive rings, provided cross-polarization effects can be neglected and the nearest-neighbor approximation can be considered valid. In fact, the extension of this analysis to situations where the aforementioned conditions are not fulfilled is cumbersome but straightforward.

### 5.3.3 Electro-Inductive Waves in CSRR Arrays

As has already been mentioned, propagation of electromagnetic waves through chains of electrically coupled resonators has long been known at microwave frequencies [16], and more recently at optical frequencies [17,18]. In this section we will address the propagation of such types of waves in chains of CSRRs. For simplicity, it will be assumed that cross-polarization effects are not present or can be neglected. Figure 5.7a shows an example of such a kind of chain, whose unit cell is a complementary NB-SRR (C-NB-SRR) etched on a metallic plate. As was shown in Chapter 3, these resonators behave as an *LC* circuit, presenting a strong electric polarizability at resonance. Therefore, the coupling between the elements of the

<sup>12</sup>There is a small difference regarding the expression reported in [22] due to the different definitions for the transmission matrix.

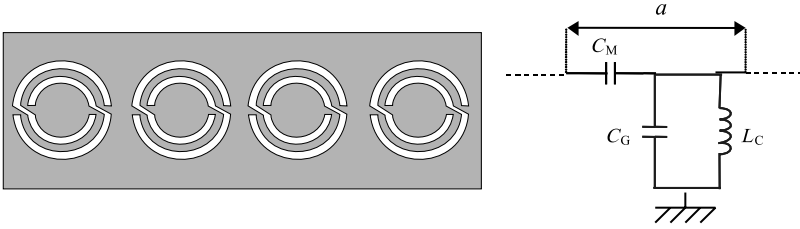


**FIGURE 5.7** Chain of complementary NB-SRRs (C-NB-SRRs) etched on a metallic plate (left) and equivalent circuit for the unit cell (right).

chain is capacitive. The equivalent circuit for the unit cell is shown in Figure 5.7*b*, where  $C_G$  is the capacitance to ground of the internal disk of the C-NB-SRR, and  $L_C$  the self-inductance of the resonator.<sup>13</sup> The mutual capacitance  $C_M$  is the capacitance between the inner disks of two consecutive C-NB-SRRs. Considering an infinite chain, the dispersion equation arising from this equivalent circuit is [19]

$$\frac{\omega^2}{\omega_0^2} = 1 + 2\omega^2 C_M L_C \cos(ka), \quad (5.57)$$

where

$$\omega_0^2 = \frac{1}{(C_G + 2C_M)L_C}. \quad (5.58)$$

As  $C_G + 2C_M = C_C$  is approximately the total capacitance between the inner disk of an isolated C-NB-SRR and the ground, this  $\omega_0$  is approximately the frequency of resonance of an isolated C-NB-SRR. The C-NB-SRR chain is, in fact, the dual of the coplanar NB-SRR chain shown in Figure 5.6*b*. Therefore, the dispersion relation must be the same for both configurations (see Problem 5.6).

The same considerations made in Section 5.3.1 for two-dimensional arrays of NB-SRRs (it is apparent that three-dimensional arrays of C-NB-SRRs cannot be made) can be extended to two-dimensional arrays of C-NB-SRRs (see Problem 5.7). The coupling between CSRRs and transmission lines, taking into account the mutual capacitive couplings between the nearest CSRRs, has been studied in [23]. This analysis can be considered as the dual counterpart of the analysis developed in [20].

### 5.3.4 Applications of Magneto- and Electro-Inductive Waves

Magneto-inductive waves have potential applications in radio-frequency (RF), microwave, and millimeter-wave applications, that is, from the megahertz to the terahertz range. Such applications may take advantage of the versatility and simplicity of MIW devices, as well as from its relatively easy mathematical analysis. Magneto-inductive waveguides and devices, including bends, power dividers, couplers, and phase shifters,

<sup>13</sup>As was shown in Chapter 3, this self-inductance comes from the connection in parallel of the inductances of the co-planar waveguide formed between the inner disk of the C-NB-SRR and the ground.



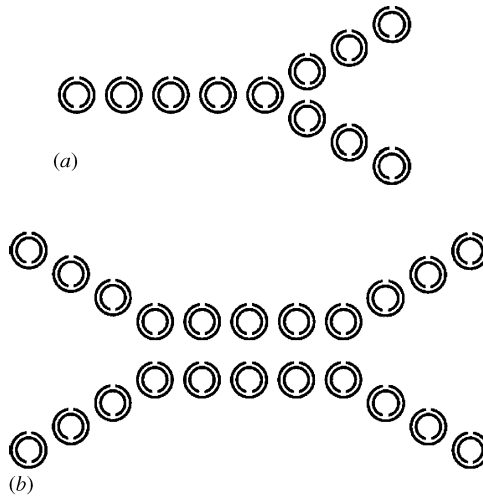


**FIGURE 5.8** Schematic of a power divider (a) and a coupler (b) in planar magneto-inductive waveguide technology. (Source: Reprinted with permission from [7], copyright 2006, Elsevier.)

have been demonstrated and described in [24] and [25] among others (see also [7] and references therein). As an example, Figure 5.8 reproduces the design of a power divider and a backward-wave coupler in MIW technology.

Applications of MIWs in conventional microstrip microwave technology have also been proposed. Transduction from conventional microstrip to planar magneto-inductive waveguides is possible by simply etching the magneto-inductive waveguide on the microstrip dielectric substrate [10].<sup>14</sup> A five-step microstrip MIW transducer is shown in Figure 5.9. This device provides a transmission coefficient of  $-5$  dB between the input and output microstrips, with a bandwidth of 0.5 GHz centered at 4.5 GHz. As has already been mentioned, MIWs are slow waves, which can be excited in a narrow frequency band. Such properties strongly suggest the usefulness of the reported MIW transducers as microwave filters and/or delay lines. Specifically, they have potential interest as an alternative to surface acoustic wave and/or ferrite delay lines. The time delay provided by the microstrip MIW transducer of Figure 5.9 is also shown in the figure. It corresponds to a slow-wave factor  $c/v_g \approx 100$ . This value, although high, is still smaller than those provided by conventional surface acoustic or ferrite delay lines. However, MIW transducers have a much simpler design and, due to the scalability of the SRRs, they can be designed over a much wider bandwidth (from RF to terahertz). Electro-inductive wave transducers in microstrip technology, with performances quite similar to the aforementioned microstrip MIW transducers, have also been reported [19].

<sup>14</sup>Care must be taken, however, in placing the transition from the microstrip to the magneto-inductive waveguide near the region where current in the microstrip has a maximum, and in such a way that the magnetic flux lines are properly coupled to the magneto-inductive elements. This configuration can be seen in Figure 5.9, where the first SRR is placed at a quarter-wavelength from the microstrip open circuit.

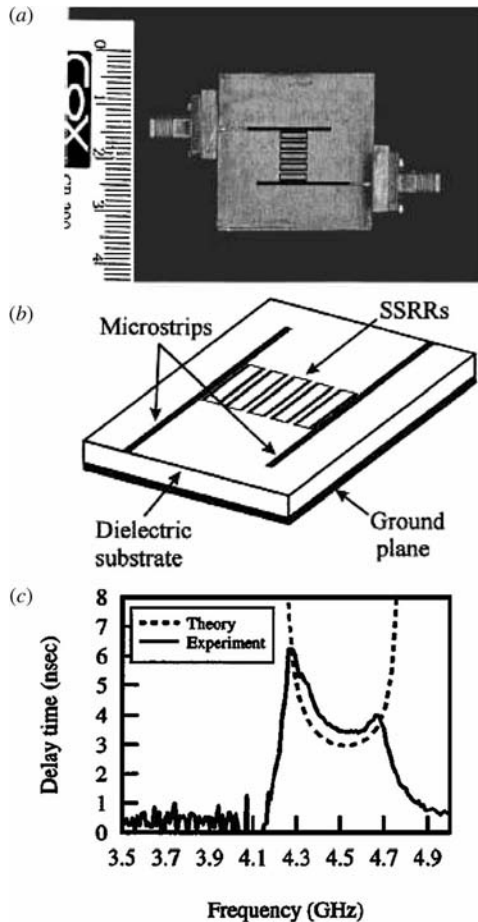


**FIGURE 5.9** Photograph (a), sketch (b), and delay time (c) provided by the planar MIW transducer proposed in [10]. The input and output ports are conventional microstrip lines, and MIWs are guided by a chain of modified NB-SRRs of rectangular shape (in order to enhance mutual inductance) etched on the dielectric substrate. (*Source:* Reprinted with permission from [10], copyright 2004, American Institute of Physics.)

Finally, magneto-inductive devices may also find interesting applications in RF and microwave imaging devices [12,26,27]. We will return to this topic in the next section.

## 5.4 SUBDIFFRACTION IMAGING DEVICES

After the seminal paper of Pendry [28] on the ability of left-handed slabs to overcome the diffraction limit for lens resolution (see Chapter 1), this issue became one of the

most active research topics in metamaterial science. It was already noted by Pendry in his seminal paper that, for near-field subdiffraction imaging, it is not necessary to have a left-handed slab, but simply a slab with only negative permittivity (for TM polarization). This was the first proposal of a device different from the left-handed perfect lens (see Chapter 1) able to produce subdiffraction imaging. Other proposals came soon after, such as imaging by planar circuit arrays [29], imaging by anisotropic media with negative parameters or indefinite media [30], ferrite slabs [31], coupled arrays of weakly coupled electric resonators [22], coupled magneto-inductive surfaces [27], and plane slabs of two- and three-dimensional photonic crystals [32,33]. Although this list is probably incomplete, it gives an idea of the intense research activity on this topic. Among the motivations of such proposals was the desire to find more practical devices, easier to manufacture than a left-handed slab. In this section, we will examine some such proposals, with emphasis on potential practical advantages. However, before developing this analysis, some general characteristics of any subdiffraction imaging device will be analyzed.

In addition to the above devices, which can create subdiffraction images of sources located at some distance from the lens, some metamaterial structures can produce pixel-to-pixel image translation between front- and back-side interfaces. Some examples of such devices are the hexagonal swiss-roll structure proposed in [12], the wire media proposed in [34], and the photonic band gap collimation effect analyzed in [35]. This image translation is based on mechanisms quite different from that described in Chapter 1 for Pendry's super-lens. Such devices, which can be more properly termed as canalization devices, will be briefly analyzed at the end of this section.

#### 5.4.1 Some Universal Features of Subdiffraction Imaging Devices

The main characteristics of subdiffraction imaging by left-handed slabs have already been reported in Chapter 1, and include

1. Field decay at the backward side of the lens, which implies that there is no focusing of energy in spots of subdiffraction size;
2. Matching capabilities, which imply that some apparent three-dimensional focuses may appear in the image detection process, as a consequence of the tunneling of power between the source and the detector;
3. High sensitivity to material losses, which restricts the usefulness of such devices to near-field imaging.

Although the analysis in Chapter 1 was mainly focused on left-handed slabs, it can be shown that the above properties are actually independent of the specific nature of the lens, thus being general characteristics of any subdiffraction imaging device [36]. In fact, regarding the first property, this comes directly from the fact that the transfer function in free space for any evanescent spatial Fourier harmonic must be an exponential decaying function, regardless of the specific nature of the lens. Therefore, the restoration of evanescent spatial Fourier harmonics at some distance from the

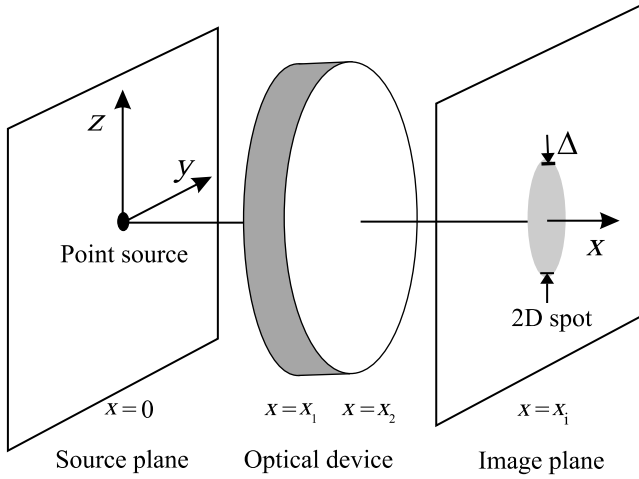


**FIGURE 5.10** Illustration of the image formation by an optical device. A point excitation is located at  $z = 0$ , creating the excitation field  $\psi_e(0, y, z) = (2\pi)^2 \delta(y, z)$  at such a plane. The imaging device, located between  $x = x_1$  and  $x = x_2$ , restores the excitation field at the image plane with a resolution  $\Delta$ . As a result, a two-dimensional spot of size  $\sim \Delta$  is created at the image plane. Outside this spot, the field rapidly vanishes in the  $x = x_1$  plane.

back-side interface of the lens, implies necessarily the presence of fields decaying from this interface towards the image.

In order to illustrate such an effect, let us consider a hypothetical optical system (see Fig. 5.10) able to reproduce some time-harmonic excitation field imposed at some plane (the source plane at  $x = 0$  in Fig. 5.10) at some other plane (the image plane, at  $x = x_i$  in Fig. 5.10) with a resolution  $\Delta$ . Such an optical system is located between  $x_1$  and  $x_2$  ( $0 < x_1 < x_2 < x_i$ ). For simplicity, the excitation field will be assumed to be a delta function in the  $x = 0$  plane

$$\psi_e(0, y, z) = (2\pi)^2 \delta(y, z), \quad (5.59)$$

where  $\psi_e$  is some component of the electric/magnetic field tangential to the plane  $x = 0$  (for simplicity, the remaining tangential component of the excitation field is supposed to vanish at  $x = 0$ ). The total field for  $x > 0$  will be the superposition of the excitation field and the scattered field created by the optical system. For  $x > 0$  the excitation field can be expanded as a Fourier integral of plane waves:

$$\psi_e(x, y, z) = \int_{-\infty}^{\infty} dk_y \int_{-\infty}^{\infty} dk_z e^{-jk_x x - jk_y y - jk_z z + j\omega t}, \quad (5.60)$$

where  $k_x = \sqrt{\omega^2 \varepsilon_0 \mu_0 - k_y^2 - k_z^2}$ . In order to have physical fields, the sign of the square root has to be chosen with  $\text{Re}(k_x) > 0$ ,  $\text{Im}(k_x) = 0$  for propagative waves,

and with  $\text{Re}(k_x) = 0$ ,  $\text{Im}(k_x) < 0$  for evanescent waves. Because the optical system is supposed to reproduce the excitation field at  $x = x_1$  with a resolution  $\Delta$ , the *total* field at  $x = x_1$  must be

$$\psi(x_1, y, z) \approx \int_{-k_{\max}}^{k_{\max}} dk_y \int_{-k_{\max}}^{k_{\max}} dk_z e^{-jk_y y - jk_z z + j\omega t}, \quad (5.61)$$

where the resolution  $\Delta$  is given by

$$k_{\max} = 2\pi/\Delta. \quad (5.62)$$

As there are no sources for  $x > x_2$ , the total field for  $x_2 < x < \infty$  is the analytical continuation of equation (5.61); that is

$$\psi(x, y, z) \approx \int_{-k_{\max}}^{k_{\max}} dk_y \int_{-k_{\max}}^{k_{\max}} dk_z e^{-jk_y y - jk_z z - jk_x(x-x_1) + j\omega t}. \quad (5.63)$$

If  $\Delta < \lambda = 2\pi/k_0$ , some of the plane waves included in equation (5.63) are evanescent, decaying from  $x = x_2$  towards  $x \rightarrow \infty$ . Figure 5.11 shows several field distributions around  $x = x_1$ , corresponding to some values for the resolution  $\Delta$ . The field distribution is calculated from equation (5.63) with  $k_{\max}$  given by equation (5.62). The focusing of energy in a three-dimensional spot at the image can be clearly seen when  $\Delta > \lambda$ . However, a field decay from the lens towards the image can be clearly observed when  $\Delta < \lambda$ . Such field decay is compatible with image formation at the image plane ( $x = x_1$ ) with a resolution  $\Delta$ , according to equation (5.61).

Regarding the second characteristic of the above list, this comes directly from the fact that evanescent electromagnetic waves do not carry power. Therefore, any detection process, which actually implies some amount of power transmitted between the source and the detector, must imply a substantial perturbation of the field created by the source in the presence of the lens alone. This detection process was actually analyzed in Sections 1.9.2 and 1.9.4, and the main conclusions of such an analysis can be extended without modification to other subdiffraction imaging devices. Therefore, care must be taken in any image measurement in order to avoid artifacts arising from the matching capabilities of such devices [37,38]. The presence of apparent three-dimensional focusing in imaging measurements can be one such artifact [39]. To avoid them, probes that do not substantially affect the field at the back side of the lens must be used. Small electric dipoles and/or magnetic loops, as well as resistive loads in the receiving antenna can be used for this purpose [36,39]. On the other hand, future practical applications based on such matching capabilities of subdiffraction imaging devices can also be envisaged.

The high sensitivity of subdiffraction imaging devices to material losses also comes from the exponential decay of the field at the back side of the lens. This

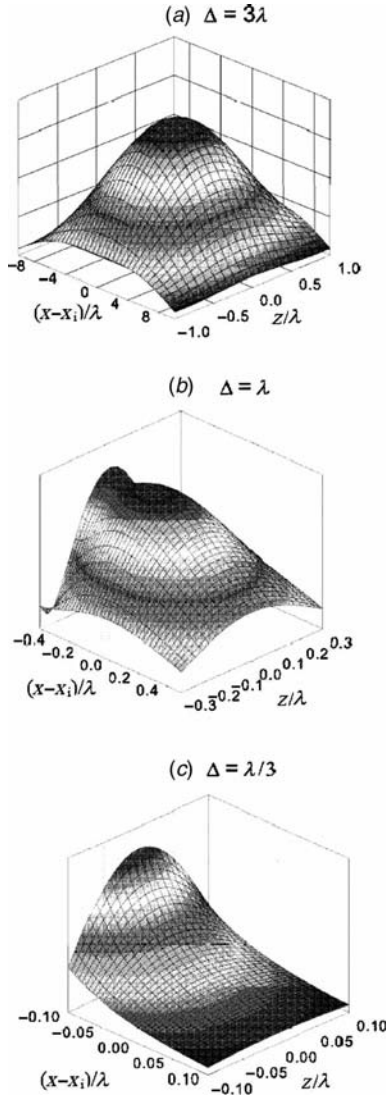


**FIGURE 5.11** The total field intensity  $|\psi(x, y, z)|$  obtained from equation (5.63) at both sides of the image plane  $x = x_i$ , for several values of the resolution  $\Delta$ : (a)  $\Delta = 3\lambda$ ; (b)  $\Delta = \lambda$ ; (c)  $\Delta = \lambda/3$ . (Source: Reprinted with permission from [36], copyright 2006, American Institute of Physics.)

field decay implies that, in order to have a good image at some distance from the back interface of the lens, very high densities of energy must be present just at this interface. As material losses are proportional to the field intensity, this behavior implies very high losses inside the lens (see also Section 1.10). In order to avoid such

losses, it is better to place the lens in such a way that the image is formed near its back interface.<sup>15</sup> Due to this high sensitivity to losses, subdiffraction imaging devices are, in practice, near-field devices. To overcome losses in such devices, multilayer configurations have been proposed [41,42]. However, it must be clarified that such proposals, although enlarging the distance between the source and the image, do not enlarge the available distances between the image (or the source) and the lens.

#### 5.4.2 Imaging in the Quasielectrostatic Limit: Role of Surface Plasmons

Because metamaterial super-lenses are near-field devices, it may be of interest that the analysis of quasistatic devices is able to produce similar effects. In fact, quasistatic approaches are approximately valid when the scale of the spatial variations of the field is small with regard to the free-space wavelength, which is, indeed, the main characteristic of near-field devices. In the quasielectrostatic limit  $\mathbf{E} = -\nabla\phi$ , where  $\phi$  is the quasielectrostatic potential. Quasielectrostatic plane waves are TM waves, which, in a homogeneous and isotropic medium, satisfy Laplace's equation  $\nabla^2\phi = 0$ . Surface plasmons (see Chapter 1, Problems 1.2 and 1.3) are examples of such waves. In order to develop our analysis, it will be of interest to determine the quasielectrostatic transverse transmission matrix (see Sections 1.7 and 1.8) for an air–dielectric interface, and for a dielectric slab in air. According to the definitions of Chapter 1, TM quasielectrostatic positive/negative waves of the form  $\phi^\pm = \phi_0 \exp\{-jkz \mp \alpha x\}$  will be considered, where, from Laplace's equation,

$$\alpha = |k|. \quad (5.64)$$

The transverse transmission matrix for a dielectric interface perpendicular to the  $x$ -axis is defined as

$$\begin{pmatrix} \phi_1^+ \\ \phi_1^- \end{pmatrix} \equiv \bar{T} \cdot \begin{pmatrix} \phi_2^+ \\ \phi_2^- \end{pmatrix} = \begin{pmatrix} T_{11} & T_{12} \\ T_{21} & T_{22} \end{pmatrix} \cdot \begin{pmatrix} \phi_2^+ \\ \phi_2^- \end{pmatrix}, \quad (5.65)$$

where  $\phi_1^\pm$  ( $\phi_2^\pm$ ) stand for the potentials at the left-(right-)hand side of the interface. This matrix is readily calculated from the boundary conditions at the dielectric interface: continuity of the quasistatic potential  $\phi = \phi^+ + \phi^-$  and continuity of the normal component of the field displacement vector  $D_x = \varepsilon(\alpha\phi^+ - \alpha\phi^-)$ . The result is

$$\bar{T}_d = \frac{1}{2\varepsilon_1} \begin{pmatrix} \varepsilon_1 + \varepsilon_2 & \varepsilon_1 - \varepsilon_2 \\ \varepsilon_1 - \varepsilon_2 & \varepsilon_1 + \varepsilon_2 \end{pmatrix}, \quad (5.66)$$

<sup>15</sup>In fact, it has been reported that the best resolution is obtained when the image is formed just on this interface [40].

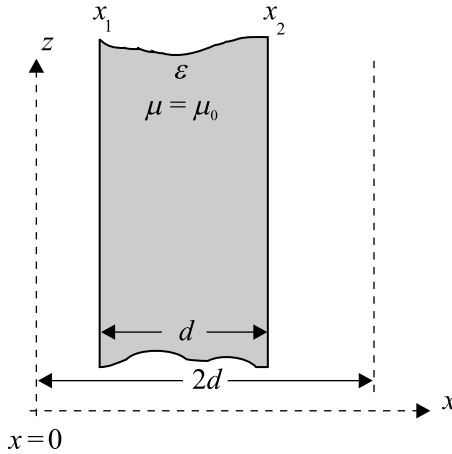


FIGURE 5.12 A slab of nonmagnetic medium of width  $d$ .

where  $\epsilon_1(\epsilon_2)$  is the dielectric constant at the left-(right-)hand side of the interface. From this result, the transverse transmission matrix for the dielectric slab of Figure 5.12 (from  $x_1$  to  $x_2$ ) can be easily found:

$$\bar{\bar{T}}_s = \frac{1}{4\epsilon_0\epsilon} \begin{pmatrix} \epsilon_0 + \epsilon & \epsilon_0 - \epsilon \\ \epsilon_0 - \epsilon & \epsilon_0 + \epsilon \end{pmatrix} \cdot \begin{pmatrix} e^{|k|d} & 0 \\ 0 & e^{-|k|d} \end{pmatrix} \cdot \begin{pmatrix} \epsilon + \epsilon_0 & \epsilon - \epsilon_0 \\ \epsilon - \epsilon_0 & \epsilon + \epsilon_0 \end{pmatrix}. \quad (5.67)$$

For the specific case when  $\epsilon = -\epsilon_0$ , which corresponds to the condition for excitation of surface plasmons at an air-slab interface (see Chapter 1, Problem 1.2), this matrix becomes

$$\bar{\bar{T}}_s = \begin{pmatrix} e^{-|k|d} & 0 \\ 0 & e^{|k|d} \end{pmatrix}. \quad (5.68)$$

Thus, the quasistatic transverse transmission matrix between  $x=0$  and  $x=2d$  in Figure 5.12 is the identity

$$\bar{\bar{T}}_{0 \rightarrow 2d} = \begin{pmatrix} 1 & 0 \\ 0 & 1 \end{pmatrix}. \quad (5.69)$$

That is, there is perfect matching, as well as amplitude and phase compensation for all the TM quasiolestatic waves between  $x=0$  and  $x=2d$ . Therefore, for  $\epsilon = -\epsilon_0$  the quasiolestatic field at  $x=0$  is reproduced at  $x=2d$ , which is the condition for perfect lens behavior. Moreover, from equations (5.67)–(5.69), it follows that the amplitude of the quasiolestatic potential has the decaying-growing-decaying behavior shown in Figure 5.13, just as in the left-handed perfect lens analyzed in Chapter 1. However, it must be taken into account that the quasiolestatic analysis developed in this section is approximate, and valid only for  $|k| \gg k_0 \equiv \omega\sqrt{\epsilon_0\mu_0}$ .



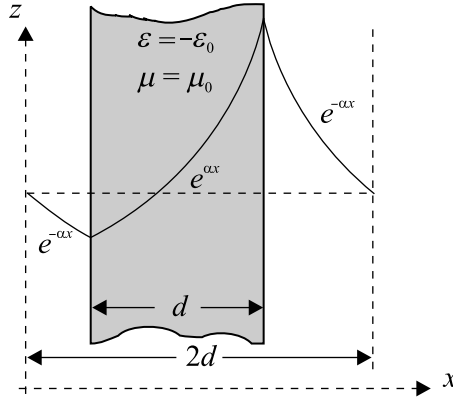


**FIGURE 5.13** Variation along the lens of the amplitude of the quasielectrostatic potential in a quasielectrostatic quasiperfect lens.

As has already been mentioned, quasistatic subdiffraction imaging by negative permittivity media was first proposed in [28] as a useful alternative to left-handed perfect lenses at infrared and optical frequencies. In fact, the complex permittivity of metals is mostly real and negative at such frequencies [2]. Experimental confirmation of such an effect in thin silver slabs has been provided in [43] and in [44].

As the above analysis find its main application in imaging by thin metallic slabs, a deeper analysis of the transfer function when the slab is made of a medium that satisfies a Drude model for its permittivity is of interest. The lens transfer function is defined as the transmission coefficient between  $x = 0$  and  $x = 2d$  of Figure 5.12, which can be deduced from equation (5.67) as

$$T(|k|, \omega) = \frac{e^{-\alpha d}}{[T_s]_{11}} = \frac{4\varepsilon_0 \varepsilon e^{-|k|d}}{(\varepsilon + \varepsilon_0)^2 e^{|k|d} - (\varepsilon - \varepsilon_0)^2 e^{-|k|d}}, \quad (5.70)$$

which takes the desired value of  $T = 1$  when  $\varepsilon = -\varepsilon_0$ . For our purposes it is convenient to rewrite this transfer function, as well as the complex permittivity of the slab (Eq. 2.78 of Chapter 2), in terms of the dimensionless variables  $k' = |k|d$  and  $\omega' = \omega/\omega_p$ , and the dimensionless parameter  $f' = f_c/\omega_p$ :

$$T(k', \omega') = \frac{4\varepsilon_0 \varepsilon e^{-k'}}{(\varepsilon + \varepsilon_0)^2 e^{k'} - (\varepsilon - \varepsilon_0)^2 e^{-k'}}, \quad (5.71)$$

where

$$\varepsilon = \varepsilon_0 \left( 1 - \frac{1}{\omega'(\omega' - jf')} \right). \quad (5.72)$$

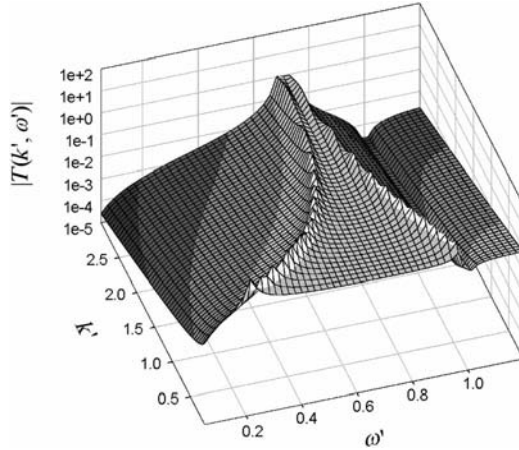


**FIGURE 5.14** Plot of the transfer function (5.71) as a function of the dimensionless variables  $k'$  and  $\omega'$ , for  $f' = 10^{-2}$ . The values for  $\omega'$  are centered around  $\omega' = 1/\sqrt{2}$  which correspond to  $\text{Re}(\varepsilon) \simeq -1$ .

A plot of  $T(k', \omega')$  for  $f' = 10^{-2}$  (which can be considered a typical value for good conductors) is shown in Figure 5.14. The two crests that appear in this plot correspond to the surface plasmons supported by the slab (see Chapter 1). Between these crests there is a region where the transfer function is flat and approximately equal to unity. This is the region of the  $(\omega', k')$  plane for which the restoration of spatial Fourier harmonics takes place. Maximum values of  $k'$  inside this region (i.e., better resolution) are obtained for  $\omega' = 1/\sqrt{2}$ , which corresponds to the frequency of excitation for the quasistatic surface plasmons at the interface of a semi-infinite slab. As resolution is limited by the maximum value of  $k$  for which  $T \approx 1$ , it is clear from Figure 5.14 that resolution is better for thinner slabs ( $k = k'/d$  reaches higher values for thinner slabs). However, it is also clear from the figure that, for very high values of  $k' = kd$ , the bandwidth of both surface plasmons collapses to a single band, and the transfer function cannot reach values near unity. Thus, it can be concluded that super-resolution in plasmonic super-lenses is limited to that region of the  $(\omega, k)$  plane where two different surface plasmons can be clearly identified in the slab, and disappears when the bandwidth of both surface plasmons collapse to a single frequency band.

### 5.4.3 Imaging in the Quasimagnetostatic Limit: Role of Magnetostatic Surface Waves

Quasimagnetostatics, like quasioelectrostatics, can also be applied to the analysis and design of near-field devices. It is apparent, from duality, that a slab with  $\varepsilon = \varepsilon_0$  and  $\mu = -\mu_0$ , (which could be made from an appropriate array of small size SRRs) can also produce subdiffraction imaging. However, this possibility does not have too much practical interest because—unlike negative- $\varepsilon$  media—such

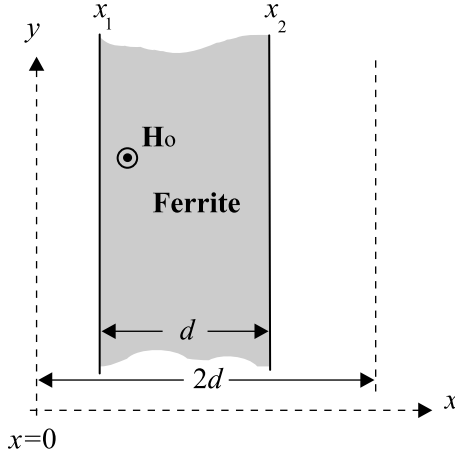


**FIGURE 5.15** Near-field quasimagnetostatic ferrite lens made of a ferrite slab magnetized along the direction parallel to the slab.

kinds of materials are not directly available in nature. Of much more interest is finding and analyzing quasimagnetostatic subdiffraction imaging devices that can be made from available materials. Because ferrites exhibit regions of negative permeability at microwave frequencies (see Chapter 2), they are good candidates for such a purpose. Moreover, from the role played by surface plasmons in quasistatic imaging devices, and the similarities between surface plasmons and magnetostatic surface waves (MSSWs), it can be guessed that such waves can play a similar role in quasimagnetostatic subdiffraction imaging. Therefore, we will analyze the transmission of quasimagnetostatic waves through the ferrite slab of Figure 5.15, which has the proper magnetization for the excitation of MSSWs propagating along the  $y$ -axis at each interface (see Problems 2.11–2.13 of Chapter 2). In the quasimagnetostatic approximation  $\mathbf{H} = -\nabla\psi$ , where  $\psi$  is the quasimagnetostatic potential, which satisfies the magnetostatic wave equation (see Chapter 2)

$$\nabla \cdot \bar{\bar{\mu}} \cdot \nabla \psi = 0, \tag{5.73}$$

where  $\bar{\bar{\mu}}$  is the Polder tensor,

$$\bar{\bar{\mu}} = \mu_0 \begin{pmatrix} \bar{\mu}_t & 0 \\ 0 & \mu_z \end{pmatrix} = \mu_0 \begin{pmatrix} \mu & j\kappa & 0 \\ -j\kappa & \mu & 0 \\ 0 & 0 & 1 \end{pmatrix}, \tag{5.74}$$

where the external magnetic field is assumed along the  $z$ -axis,  $\mathbf{H}_0 = H_0 \hat{\mathbf{z}}$ , and

$$\mu = 1 + \frac{\omega_M \omega_H}{\omega_H^2 - \omega^2} \tag{5.75}$$

$$\kappa = \frac{\omega \omega_M}{\omega_H^2 - \omega^2} \tag{5.76}$$

(see Chapter 2 for more details on these definitions).

As in Chapter 1, we will classify the magnetostatic waves into positive and negative plane waves, with the field dependence  $\psi^\pm = \psi_0 \exp\{-jky \mp \alpha x\}$ , where, from equation (5.73),  $\alpha$  and  $k$  are related through

$$\alpha = |k|. \quad (5.77)$$

The transverse transmission matrix for such waves can be obtained from the boundary conditions at the air–ferrite interfaces of Figure 5.15. Such boundary conditions are as follows: continuity of  $\psi = \psi^+ + \psi^-$  and continuity of  $B_x = \mu H_x + j\kappa H_y$ . When this last condition is put in terms of the quasimagnetostatic potential, it takes the form

$$\psi_1^+ - \psi_1^- = (\mu + \xi\kappa)\psi_2^+ - (\mu - \xi\kappa)\psi_2^-, \quad (5.78)$$

where  $\xi = \mp 1$  for  $k \geq 0$ . This equation is valid for the air  $\rightarrow$  ferrite interface of Figure 5.15 (at  $x = x_1$ ) and, as in the previous section,  $\psi_1^\pm / \psi_2^\pm$  stands for potentials at the left-/right-hand side of the interface. From such boundary conditions, the quasimagnetostatic transverse transmission matrix for an air  $\rightarrow$  ferrite interface is obtained as

$$\bar{\bar{T}}_{a \rightarrow f} = \frac{1}{2} \begin{pmatrix} 1 + \mu + \xi\kappa & 1 - \mu + \xi\kappa \\ 1 - \mu - \xi\kappa & 1 + \mu - \xi\kappa \end{pmatrix}. \quad (5.79)$$

The dependence on the sign of  $k$  of this matrix is closely related to the nonreciprocity of ferrites [15], and with the fact that MSSWs—which correspond to the zeroes of  $[T_{a \rightarrow f}]_{11}$ —can only be excited at an air–ferrite interface for a specific sign of  $k$  (see Problem 2.13 of Chapter 2). The quasimagnetostatic transverse transmission matrix for the ferrite  $\rightarrow$  air interface of Figure 5.15 (at  $x = x_2$ ) is

$$\bar{\bar{T}}_{f \rightarrow a} = \left\{ \bar{\bar{T}}_{a \rightarrow f} \right\}^{-1} = \frac{1}{2\mu} \begin{pmatrix} 1 + \mu - \xi\kappa & -1 + \mu - \xi\kappa \\ -1 + \mu + \xi\kappa & 1 + \mu + \xi\kappa \end{pmatrix}. \quad (5.80)$$

Finally, from equations (5.79) and (5.80), the transverse transmission matrix for the ferrite slab of Figure 5.15 (between  $x = x_1$  and  $x = x_2$ ) can be found from

$$\bar{\bar{T}} = \bar{\bar{T}}_{a \rightarrow f} \cdot \begin{pmatrix} e^{k|d} & 0 \\ 0 & e^{-|k|d} \end{pmatrix} \cdot \bar{\bar{T}}_{f \rightarrow a}. \quad (5.81)$$

The frequency of excitation of MSSWs at an isolated ferrite  $\rightarrow$  air interface magnetized as the right-hand side interface of the ferrite slab (i.e., such as the interface located at  $x = x_2$  in Fig. 5.15) can be obtained from  $[T_{f \rightarrow a}]_{11} = 0$ . This equation has two positive frequency solutions. For  $k < 0$  (i.e., for  $\xi = 1$ ), the solution is  $\omega = \omega_H$ , which is not a practical solution because it corresponds to the ferrimagnetic

resonance. However, for  $k > 0$  (i.e., for  $\xi = -1$ ), equation  $[T_{f \rightarrow a}]_{11} = 0$  becomes

$$1 + \mu + \kappa = 0, \quad (5.82)$$

which corresponds to the frequency

$$\omega = \omega_H + \omega_M/2. \quad (5.83)$$

At this frequency, the ferrite slab transverse transmission matrix (5.81) becomes

$$\bar{T}_+ = \begin{pmatrix} e^{-|k|d} & -2\frac{1+\mu}{\mu}\sinh(|k|d) \\ 0 & e^{|k|d} \end{pmatrix}, \quad (5.84)$$

for  $k > 0$  (or  $\xi = -1$ ). For  $k < 0$  (or  $\xi = 1$ ) it is

$$\bar{T}_- = \begin{pmatrix} e^{-|k|d} & 0 \\ 2\frac{1+\mu}{\mu}\sinh(|k|d) & e^{|k|d} \end{pmatrix}. \quad (5.85)$$

In both cases the transmission coefficient is

$$t = 1/[T_{\pm}]_{11} = e^{|k|d}, \quad (5.86)$$

which corresponds to the condition for the restoration at the image plane ( $x = 2d$ ) of the amplitude of the *incident* quasimagnetostatic wave at  $x = 0$ . This result, which is valid for any value of  $k$ , shows that a properly magnetized ferrite slab can reproduce the incident quasimagnetostatic field at the source plane ( $x = 0$  in Fig. 5.15) at the image plane ( $x = 2d$  in Fig. 5.15).

The main difference between quasimagnetostatic subdiffraction imaging by magnetized ferrite slabs, and the quasioleostatic imaging analyzed in the previous section is the nondiagonal form of the transverse transmission matrices (5.84) and (5.85) for ferrites. This nondiagonal form introduces some key differences. In fact, for  $k > 0$  the reflection coefficient  $r = [T_+]_{12}/[T_+]_{11}$  vanishes.<sup>16</sup> However, if  $k < 0$ , the reflection coefficient  $r = [T_-]_{12}/[T_-]_{11}$  is not zero. Because a general field distribution at  $x = 0$  must incorporate Fourier harmonics with positive and negative values of  $k$ , it is clear that, in general, the ferrite slab will not reproduce at the image the whole field at the source plane (which is the sum of the *incident* field and the *reflected* field), in spite of the fact that it reproduces the incident field (i.e., the field created by the source alone). This behavior makes a substantial difference with previously reported subdiffraction imaging devices, which are *matched* to free

<sup>16</sup>That is, in general, for  $\mathbf{k} \propto \mathbf{H}_0 \times \mathbf{n}$ , where  $\mathbf{n}$  is the outward normal of the back-side lens interface.

space (i.e., do not produce *reflected* fields). As other obvious difference is the anisotropy of the device, which is only able to reproduce two-dimensional sources, of (practically) infinite extent in the  $z$ -direction (i.e., the direction of magnetization). The main advantage of near-field subdiffraction imaging by ferrite slabs is tunability. In fact, the frequency of operation of such devices can be tuned by changing the value of the external magnetization  $\mathbf{H}_0$ . This can be a crucial advantage, because all subdiffraction imaging devices reported to date are intrinsically very narrow-band devices. Quasistatic subdiffraction imaging by ferrite slabs was first reported in [31]. In this paper, the relation between the *whole* fields at the image and source planes was analyzed. It was shown that the field at the image plane is a combination of the field at the source plane and its Hilbert transform.

#### 5.4.4 Imaging by Resonant Impedance Surfaces: Magneto-Inductive Lenses

Let us consider an arbitrary surface, characterized by some transverse transmission matrix

$$\begin{pmatrix} E_1^+ \\ E_1^- \end{pmatrix} \equiv \bar{T}_1 \cdot \begin{pmatrix} E_2^+ \\ E_2^- \end{pmatrix} = \begin{pmatrix} a & b \\ c & d \end{pmatrix} \cdot \begin{pmatrix} E_2^+ \\ E_2^- \end{pmatrix}. \quad (5.87)$$

The corresponding transverse transmission matrix for a pair of identical coupled surfaces, separated by a distance  $d$  (see Fig. 5.16) will be

$$\bar{T}_2 = \begin{pmatrix} a & b \\ c & d \end{pmatrix} \cdot \begin{pmatrix} e^{\alpha d} & 0 \\ 0 & e^{-\alpha d} \end{pmatrix} \cdot \begin{pmatrix} a & b \\ c & d \end{pmatrix} \quad (5.88)$$

or

$$\bar{T}_2 = \begin{pmatrix} a^2 e^{\alpha d} + bc e^{-\alpha d} & ab e^{\alpha d} + bd e^{-\alpha d} \\ ac e^{\alpha d} + c^2 e^{-\alpha d} & cb e^{\alpha d} + d^2 e^{-\alpha d} \end{pmatrix}, \quad (5.89)$$

where only evanescent waves in the transverse direction are considered, and  $\alpha(\omega)$  is the attenuation constant of such waves.<sup>17</sup> It is clear that, in order to have the proper transmission coefficient for evanescent wave amplification through the device, ( $t = 1/T_{11} \propto \exp\{\alpha d\}$ ) it must be that

$$a = 0 \quad \text{and} \quad bc = \text{constant}. \quad (5.90)$$

<sup>17</sup>In the quasistatic limit, where the effects of the displacement current are neglected,  $\alpha = |k|$ , where  $k$  is the propagation constant of the considered surface wave.

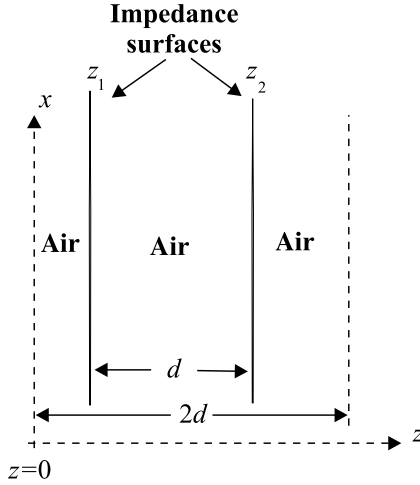


**FIGURE 5.16** Two coupled impedance surfaces, separated by a distance  $d$ .

It can be easily realized that the first condition corresponds to the excitation of surface waves in a single impedance surface (allowing for solutions to equation 5.87 with  $E_1^+ = E_2^- = 0$ ). However, it must be taken into account that, in order to have an imaging device, the above condition must be simultaneously satisfied for all values of the propagation constant  $k$ . In practice, this means that the dispersion relation for such surface waves must be very flat, so that all the wavevectors are excited in a small frequency band. If this condition is fulfilled, the goal is to obtain

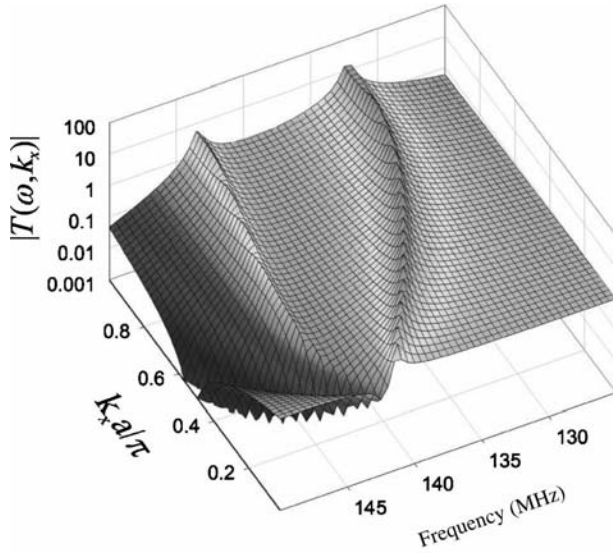
$$a(\omega, k) \approx 0 \quad \text{and} \quad b(\omega, k)c(\omega, k) \approx \text{constant}, \tag{5.91}$$

for a wide region of the  $(\omega, k)$  plane.

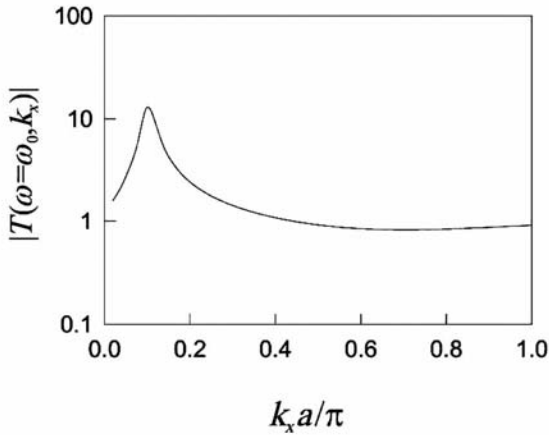
As has already been mentioned, the key concepts of subdiffraction imaging devices made of a pair of coupled arrays of resonators were first proposed in [22]. Subsequently, this approach has been applied in [45] to the analysis of the magneto-inductive lens previously reported in [27]. As was shown in Section 5.3.2, a two-dimensional array of magnetic resonators—such as SRRs or capacitively loaded metallic rings—can support MIWs whose dispersion relation is given (in the nearest-neighbor approximation) by equation (5.43). Such surface MIWs can be excited in the interval  $|\omega - \omega_0| \leq \delta\omega$ , where

$$\delta\omega = 2\omega_0 \frac{M}{L}. \tag{5.92}$$

Except for very close rings,  $M/L \lesssim 0.1$ , which implies that a pair of coupled magneto-inductive surfaces can be a good candidate for the design of subdiffraction imaging devices. The transfer function for such devices is the transmission coefficient



(a)



(b)

**FIGURE 5.17** (a) Three-dimensional plot of the transfer function  $T(k_x, k_y = 0, \omega)$  for a magneto-inductive lens such as that shown in Figure 5.16 when the surfaces at  $x = x_1, x_2$  are square arrays of capacitively coupled rings. The transfer function is calculated for the following parameters: distance  $d = 4.5$  mm, periodicity  $a = 12.5$  mm, ring resistance  $R = 0.04 \Omega$ , ring capacitance  $C = 82$  pF, ring inductance  $L = 16.3$  nH, frequency of resonance of the rings  $\omega_0 = 2\pi \times 137.5$  MHz, and ring inductance  $M = -0.015L$ . The average radius of the rings is  $r = 4.5$  mm. (b) Two-dimensional plot of the transfer function  $T(k_x, k_y = 0, \omega)$  at  $\omega = 2\pi \times 140$  MHz. (Source: Data reproduced with permission from [45], copyright 2006, American Institute of Physics.)



between  $x = 0$  and  $x = 2d$  in Figure 5.16

$$T(|k|, \omega) = \frac{e^{-ad}}{[T_2]_{11}} = \frac{e^{-|k|d}}{a^2 e^{|k|d} + bc e^{-|k|d}}; \quad |k| = +\sqrt{k_x^2 + k_y^2}, \quad (5.93)$$

where, from equation (5.56)

$$\begin{pmatrix} a & b \\ c & d \end{pmatrix} = \frac{1}{2} \begin{pmatrix} 2 + Z_0/Z_a & Z_0/Z_a \\ -Z_0/Z_a & 2 - Z_0/Z_a \end{pmatrix}, \quad (5.94)$$

with  $Z_0$  and  $Z_a$  given by equations (5.48) and (5.54), respectively. If  $a = 2 + Z_0/Z_a \approx 0$ , then  $bc \approx -1$ , and equation (5.91) is satisfied. Figure 5.17 shows a three-dimensional plot of the transfer function (5.93) for two coupled square arrays of capacitively coupled rings of periodicity  $a$ , separated a distance  $d$ . The plot is shown in the first Brillouin zone  $0 < k < \pi/a$ . As can be seen, a flat transfer function with  $|T(|k|, \omega)| \approx 1$  is obtained at frequencies around the frequency of resonance of the rings, which is also the center of the bandwidth for the excitation of MIWs in a single array. Such a flat transfer function frequency region is limited by two crests, which corresponds to the two MIWs that can be excited in the pair of coupled magneto-inductive arrays. As has already been mentioned, this behavior is typical of a subdiffraction imaging device. It can also be seen from equations (5.89) and (5.90) that the reported magneto-inductive lens (as well as any other similar lens made from two *identical* resonant impedance surfaces) is not matched to free space. That is, it produces *reflected* fields that can affect the source field. However, by using two different surfaces, it is possible—at least theoretically—to obtain a *matched* lens [22] (see Problem 5.10). An extensive analysis of magneto-inductive lenses, including experiments, has been reported in [45].

### 5.4.5 Canalization Devices

Canalization devices are devices that are able to translate a field distribution, pixel to pixel, from one interface to another. There can be many designs allowing such image translation, and probably the simpler one is the wire media lens proposed in [46] and subsequently demonstrated in [34]. The device is sketched in Figure 5.18, and is made from a square array of conducting wires of periodicity  $a \ll \lambda$  and length  $l = n\lambda/2$ , where  $\lambda$  is the free-space wavelength at the operation frequency. The device can reproduce at the exit interface any quasioleostatic field distribution imposed at the input interface, with a resolution that is limited by the array periodicity  $a$ . This behavior has been explained as a consequence of the specific properties of the homogenized wire media [47]. In this paragraph we will give an alternative and perhaps even simpler explanation. The wire array can be seen as a multiconductor TEM transmission line that supports  $N - 1$  orthogonal

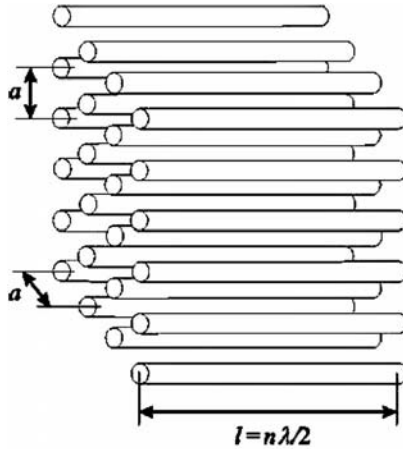


**FIGURE 5.18** Sketch of the wire lens proposed in [46]. (Source: Reprinted with permission from [46], copyright 2005, American Physical Society.)

degenerate TEM modes ( $N$  is the total number of wires), all of them propagating with the vacuum phase constant  $k = \omega\sqrt{\epsilon_0\mu_0}$ .<sup>18</sup> If the condition  $l = n\lambda/2$  is imposed on the total length of the device, it becomes a Fabry–Perot resonator, which can support standing waves corresponding to any combination of the aforementioned TEM modes, bouncing back and forth between both ends of the device. These resonator modes, which can have an arbitrary voltage distribution on the wires, have zero currents and maximum voltages on each wire end. When a given quasielectrostatic voltage distribution is imposed at the input interface ( $l = 0$ ), it excites the resonator mode that most closely matches this voltage distribution, which is reproduced at the output interface ( $l = n\lambda/2$ ) with the aforementioned resolution  $a$ . In fact, it can be easily realized that the transfer function of the device is  $T = \pm 1$ , where the  $\pm$  sign applies to *even/odd* values of  $n$ .

The wire lens described above operates in the quasielectrostatic limit; that is, it can canalize only TM field distributions, being almost insensitive to TE incident fields. One quasimagnetostatic canalization device, able to reproduce TE incident fields, is the swiss-roll hexagonal array proposed in [12] for operation at radio frequencies.<sup>19</sup> Canalization of light seems also to be the main mechanism for imaging in some recently reported photonic crystal devices [35,46].

<sup>18</sup>It is clear that the simpler choice for this set of orthogonal modes is to define the  $i$ th mode by  $V_i \propto e^{\pm jkz}$  on the  $i$ th wire and  $V = 0$  on the remaining ones.

<sup>19</sup>The mechanism of operation of such device has been further analyzed in [26], where the effect of magneto-inductive waves excited in the array was also studied.

## PROBLEMS

- 5.1. Polarizabilities of the CSRR.** Using the Babinet principle (5.18), deduce equations (5.6)–(5.8) for a CSRR etched on a perfect conducting plate.
- 5.2. Circular polarization in SRR arrays.** Consider a plane wave incident upon a loss-less SRR array. The incident wavevector is in the  $y$ – $z$  plane, forming an angle  $\theta$  with the normal to the surface (i.e., with the  $z$ -axis). The incident wave is polarized with the magnetic field perpendicular to the plane of incidence (p-polarization). Find, as a function of the SRR polarizabilities, the angle of incidence for which the transmitted wave is circularly polarized.
- 5.3. Circular polarization in CSRR arrays.** Consider the plane wave incident upon a loss-less CSRR array. Discuss, as a function of the CSRR polarizabilities, the angle of incidence and polarization for which the transmitted wave is circularly polarized.
- 5.4. Lossy magnetoinductive waves.** By including the ohmic resistance of the rings in the equation for the current

$$\left\{ j\omega L + \frac{1}{j\omega C} + R \right\} I_n = M(I_{n-1} + I_{n+1}), \quad (5.95)$$

find the attenuation constant of MIWs propagating on one-, two-, and three-dimensional arrays of NB-SRRs. Assume that the nearest-neighbor approximation is valid.

- 5.5. MIWs in sparse arrays of SRRs.** By using the dipole approximation (each SRR is assumed to be equivalent to an elemental dipole), find closed expressions for the dispersion relation of a magneto-inductive waveguide formed by a one-dimensional coplanar array of capacitively loaded rings. Use

$$L = \mu_0 r \left[ \ln \left( \frac{16r}{d} \right) - 2 \right], \quad (5.96)$$

where  $r$  and  $d$  are the ring radius and the wire diameter, respectively, as an approximation of the ring inductance. Discuss the conditions for the validity of this approach.

- 5.6. Duality between MIWs/EIW in NB-SRR/C-NB-SRRs arrays.** Taking duality into account, find the relations between the capacitance and the inductance of the equivalent circuit of an NB-SRR (see Chapter 2) and those of the equivalent circuit of its complementary, the C-NB-SRR (see Chapter 3). From this result show that, in the limit  $|M|/L \ll 1$ , the dispersion equation (5.57) for

the C-NB-SRR chain of Figure 5.7a is approximately given by

$$\frac{\omega^2}{\omega_0^2} \approx 1 - \frac{2M}{L} \cos(ka), \quad (5.97)$$

where  $L$  and  $M$  are the self- and mutual-inductances of the dual chain of NB-SRRs. It is clear that, in the limit  $|M|/L \ll 1$ , this expression coincides with (5.37). This limit is a natural condition for the validity of the assumed nearest-neighbor-approach.

- 5.7. EIWs in two-dimensional CSRR arrays.** Find, in terms of the NB-SRR polarizabilities (see Chapter 1) the dispersion relation for EIWs propagating on a two-dimensional sparse square array of C-NB-SRRs of periodicity  $a$ .
- 5.8. Surface plasmons in a slab of negative permittivity.** Find, from equation (5.67), the dispersion relation  $k(\varepsilon; d)$  for the quasistatic surface plasmons supported by a metallic slab of width  $d$ . Assume a Drude–Lorentz model for the permittivity of the metal.
- 5.9. MSSWs in a ferrite slab.** Find from equation (5.81) the dispersion equation for MSSWs in a ferrite slab with an external magnetization parallel to the slab.
- 5.10. Matched impedance-surface lens.** Consider two distinct parallel coupled surface impedances separated by a distance  $d$ , as in Figure 5.16. Find the conditions that must satisfy its respective array impedances  $Z_a$  and  $Z'_a$  in order to obtain a perfectly matched lens ( $t \propto e^{jk|d}$ ;  $r = 0$ ) from such configuration (see [22]).

## REFERENCES

1. R. F. Harrington *Time-Harmonic Electromagnetic Fields*. McGraw-Hill, New York, 1961.
2. J. D. Jackson *Classical Electrodynamics*. Wiley, New York, 1999 (3rd. ed.).
3. F. Falcone, T. Lopetegi, M. A. G. Laso, J. D. Baena, J. Bonache, M. Beruete, R. Marqués, F. Martín, and M. Sorolla “Babinet principle applied to metasurface and metamaterial design.” *Phys. Rev. Lett.*, vol. 93, paper 197401, 2004.
4. M. Beruete, M. Sorolla, R. Marqués, J. D. Baena, and M. Freire “Resonance and cross-polarization effects in conventional and complementary split ring resonator periodic screens.” *Electromagnetics*, vol. 26, pp. 247–260, 2006.
5. R. Marqués, J. D. Baena, M. Beruete, F. Falcone, T. Lopetegi, M. Sorolla, F. Martín, and J. García “*Ab initio* analysis of frequency selective surfaces based on conventional and complementary split ring resonators.” *J. Optics A*, vol. 7, pp. S38–S43, 2005.
6. R. E. Collin *Field Theory of Guided Waves*. IEEE Press, New York, 1990 (2nd. ed.).
7. E. Shamonina and L. Solymar “Properties of magnetically coupled metamaterial elements.” *J. Magnetism and Magnetic Materials*, vol. 300, pp. 38–43, 2006.
8. E. Shamonina, V. A. Kalinin, K. H. Ringhofer, and L. Solymar “Magneto-inductive waveguide.” *Electron. Lett.*, vol. 38, pp. 371–373, 2002.

9. E. Shamonina, V. A. Kalinin, K. H. Ringhofer, and L. Solymar “Magneto-inductive waves in one, two and three dimensions.” *J. Appl. Phys.*, vol. 92, pp. 6252–6261, 2002.
10. M. J. Freire, R. Marqués, F. Medina, M. A. G. Laso, and F. Martin “Planar magnetoinductive wave transducers: Theory and applications.” *Appl. Phys. Lett.*, vol. 85, pp. 4439–4441, 2004.
11. M. C. K. Wiltshire, E. Shamonina, I. R. Young, and L. Solymar “Experimental and theoretical study of magneto-inductive waves supported by one-dimensional arrays of swiss-rolls.” *J. Appl. Phys.*, vol. 95, pp. 4490–4493, 2004.
12. M. C. K. Wiltshire, J. B. Pendry, I. R. Young, D. J. Larkman, D. J. Gilderdale, and J. V. Hajnal “Microstructured magnetic materials for RF flux guides in magnetic resonance imaging.” *Science*, vol. 291, pp. 849–851, 2001.
13. H. Raether, *Excitation of Plasmons and Interband Transitions by Electrons*. Springer, Berlin, 1980.
14. M. S. Sodha and N. C. Shrivastava, *Microwave Propagation in Ferrimagnetics*. Plenum Press, New York, 1981.
15. A. G. Gurevich and G. A. Melkov, *Magnetization Oscillations and Waves*. CRC Press, Boca Raton, FL 1996.
16. J. Shefer “Periodic cylinder arrays as transmission lines.” *IEEE Trans. Microwave Theory Tech.*, vol. 11, pp. 55, 1963.
17. M. L. Brongersma, J. W. Hartmann, and H. A. Artwater “Electromagnetic energy transfer and switching in nanoparticle chain arrays below the diffraction limit.” *Phys. Rev. B*, vol. 62, pp. R16356–R16359, 2000.
18. W. H. Weber and G. W. Ford “Propagation of optical excitations by dipolar interactions in metal nanoparticle chains.” *Phys. Rev. B*, vol. 70, paper 125429, 2004.
19. M. Beruete, F. Falcone, M. J. Freire, R. Marqués, and J. D. Baena “Electroinductive waves in chains of complementary metamaterial elements.” *Appl. Phys. Lett.*, vol. 88, paper. 083503, 2006.
20. R. R. A. Syms, E. Shamonina, V. Kalinin, and L. Solymar “A theory of metamaterials based on periodically loaded transmission lines: Interaction between magnetoinductive and electromagnetic waves.” *J. Appl. Phys.*, vol. 97, paper 064909, 2005.
21. F. Martin, J. Bonache, F. Falcone, M. Sorolla, and R. Marqués “Split ring resonator-based left-handed coplanar waveguide.” *Appl. Phys. Lett.*, vol. 83, pp. 4652–4654, 2003.
22. S. Maslowski, S. Tretyakov, and P. Alitalo “Near-field enhancement and imaging in double planar polariton-resonant structures.” *J. Appl. Phys.*, vol. 96, pp. 1293–1300, 2004.
23. I. Gil, J. Bonache, M. Gil, J. García-García, F. Martin, and R. Marques “Accurate circuit analysis of resonant-type left handed transmission lines with inter-resonator’s coupling.” *J. Appl. Phys.*, vol. 100, paper 074908, 2006.
24. M. C. K. Wiltshire, E. Shamonina, I. R. Young, and L. Solymar “Dispersion characteristics of magneto-inductive waves: comparison between theory and experiment.” *Electron. Lett.*, vol. 39, pp. 215–217, 2003.
25. E. Shamonina and L. Solymar “Magneto-inductive waves supported by metamaterials elements: components for a one-dimensional waveguide.” *J. Phys. D: Appl. Phys.*, vol. 37, pp. 362–367, 2004.
26. O. Zhuromskyy, E. Shamonina, and L. Solymar “2D metamaterials with hexagonal structure: spatial resonances and near field imaging.” *Opt. Express*, vol. 13, pp. 9299–9309, 2005.

27. M. J. Freire and R. Marqués “Planar magnetoinductive lens for three-dimensional sub-wavelength imaging.” *Appl. Phys. Lett.*, vol. 86, paper 182505, 2005.
28. J. B. Pendry “Negative refraction makes perfect lens.” *Phys. Rev. Lett.*, vol. 85, pp. 3966–3969, 2000.
29. A. Grbic and G. Eleftheriades “Overcoming diffraction limit with a planar left-handed transmission line lens.” *Phys. Rev. Lett.*, vol. 92, paper 117403, 2004.
30. D. R. Smith and D. Schurig “Electromagnetic wave propagation in media with indefinite permittivity and permeability tensors.” *Phys. Rev. Lett.*, vol. 90, paper 077405, 2003.
31. R. Marques, F. Mesa, and F. Medina “Near-field enhanced imaging by a metamaterial magnetized ferrite slab.” *Appl. Phys. Lett.*, vol. 86, paper 023505, 2005.
32. P. V. Parimi, W. T. Lu, P. Vodo, and S. Sridhar “Imaging by flat lens using negative refraction.” *Nature*, vol. 426, pp. 404, 2003.
33. Z. Lu, J. A. Murakowski, C. A. Schuetz, S. Shi, G. J. Schneider, and D. W. Prather “Three-dimensional subwavelength imaging by a photonic crystal flat lens using negative refraction at microwave frequencies.” *Phys. Rev. Lett.*, vol. 95, paper 153901 (2005).
34. P. A. Belov, Y. Hao, and S. Sudhakaran “Subwavelength microwave imaging using an array of parallel conducting wires as a lens.” *Phys. Rev. B*, vol. 73, paper 033108, 2006.
35. J. L. Garcia-Pomar and M. Nieto-Vesperinas “Waveguiding, collimation and sub-wavelength concentration in photonic crystals.” *Opt. Express*, vol. 13, pp. 7997–8007, 2005.
36. R. Marqués, M. J. Freire, and J. D. Baena “Theory of three-dimensional subdiffraction imaging.” *Appl. Phys. Lett.*, vol. 89, paper 211113, 2006.
37. V. G. Veselago “Some remarks regarding electrodynamics of materials with negative refraction.” *Appl. Phys. B*, vol. 81, pp. 403–407, 2005.
38. V. Veselago “Superlens as a matching device.” <http://xxx.lanl.gov/ftp/cond-mat/papers/0501/0501438.pdf>.
39. F. Mesa, R. Marques, M. Freire, and J. D. Baena “Three dimensional super-resolution in metamaterial slab lenses.” *Phys. Rev. B*, vol. 72, paper 235117, 2005.
40. V. A. Podolskiy and N. A. Kuhta “Optimizing the superlens: Manipulating geometry to enhance the resolution.” *Appl. Phys. Lett.*, vol. 87, 231113, 2005.
41. E. Shamonina, V. A. Kalinin, K. H. Ringhofer, and L. Solymar “Imaging, compression and Poynting vector streamlines with negative permittivity materials.” *Electron. Lett.*, vol. 37, pp. 1243–1244, 2001.
42. S. A. Ramakrishna, J. B. Pendry, M. C. K. Wiltshire, and W. J. Stewart “Imaging the near field.” *J. Mod. Opt.*, vol. 50, pp. 1419–1430, 2003.
43. N. Fang, H. Lee, C. Sun, and X. Zhang “Sub-diffraction-limited optical imaging with a silver superlens.” *Science*, vol. 308, pp. 534–537, 2005.
44. R. J. Blaikie and D. O. S. Melville “Imaging through planar silver lenses in the optical near field.” *J. Opt. A*, vol. 7, pp. S176–S183, 2005.
45. M. J. Freire and R. Marqués “Near-field imaging in the megahertz range by strongly coupled magnetoinductive surfaces: Experiment and ab initio analysis.” *J. Appl. Phys.*, vol. 100, paper 063105, 2006.
46. P. A. Belov, C. R. Simowski, and P. Ikonen “Canalization of subwavelength images by electromagnetic crystals.” *Phys. Rev. B*, vol. 71, paper 193105, 2005.
47. P. A. Belov and M. G. Silveirinha “Resolution of subwavelength transmission devices formed by a wire medium.” *Phys. Rev. E*, vol. 73, paper 056607, 2006.



---

# INDEX

---

- Admittance surfaces, 268–278
- All angle negative refraction, 8
- Alternate right-handed/left-handed (ARLH) sections, 199–207
- bandpass filters and, 203–207
- complementary split ring resonators, 203–207
- diplexers and, 203–207
- S-band filter, 202
- split ring resonators, 199–203
- Amplification of evanescent modes, 20–21, 288–292
- Antenna applications, 252–258
- angle of main radiation lobe, 254
- electronically scanned antennas, 254–258
- leaky-wave antenna, 254–258
- left-handed media, 254–258
- media pairs, 253
- radiation limit of Chu for Q, 254
- radiated power, 254
- Anti-symmetric resonances, 71
- ARLH. *See* alternate right-handed/left-handed.
- Babinet principle, 268–269, 272–273
- complementary split ring resonator
- planar arrays, 272–273
- Backward leaky modes, 19–20, 254–259
- Backward media, 2, 3
- Backward transmission line, 120–128
- backward wave, 120–121
- characteristic impedance, 120
- constitutive parameters, 123–124
- design and fabrication, 128
- dispersion of, 123
- forward wave, 121
- implementation of, 124–125, 128–131
- composite right-/left-handed (CRLH), 124–128
- left-handed structure, 120–121
- right-handed structure, 121
- transverse electromagnetic (TEM) mode propagation, 123–124
- Backward wave, 120–121
- Backward wave coupler, 246–248
- Backward-wave propagation, 2–4, 9–12
- Cerenkov radiation, 10–11
- inverse Doppler effect, 10
- negative Goos–Hanchen shift, 12
- Balanced composite right-/left-handed (CRLH) transmission lines, 127–128
- Bandpass filters, 198–227
- admittance inverters, 208
- alternate right-handed/left-handed (ARLH) sections, 199–207
- design methodology, 210



- Bandpass filters (*Continued*)  
 hybrid approach, 210  
 hybrid model, 210  
 right-handed section implementation, 218–225  
 ultra-wide, 219–227
- Bandwidth, enhancement of, 236–244  
 phase shifters, 244  
 rat race hybrid couplers, 239–243
- BC-SRR. *See* broadside-coupled split-ring resonator design.
- Bianisotropy, 65–69
- Bloch impedance, 120, 152, 155
- Bloch impedance. *See* Characteristic impedance
- Broadband device components, 236–244
- Broadside-coupled split-ring resonator design (BC-SRR), 60–62
- Bulk metamaterials  
 alternative designs, 102–107  
 chiral, 97–102  
 ferrite, 92–97  
 infrared frequencies, at, 79–80  
 optical frequencies, at, 79–80, 106–107  
 split ring resonators (SRRs) based, 65–70, 80–88
- Canalization devices, 302–303
- Cerenkov radiation, 10–11
- Characteristic (Bloch) impedance, 120
- Chiral media, 97–102  
 backward-wave propagation, 98–99  
 chiral nihility, 102  
 racemic mixture, 97
- Chiral metamaterials, 97–102
- Chiral nihility, 102
- Circuit analysis approach, 44
- Circuit model comparisons, 175–180  
 dual left-handed lines vs. resonant types, 175–180
- Coefficients, transmission and reflection, 13–15, 17
- Compact broadband device components, 236–244
- Complementary split ring resonators (CSRR), 119, 155–163  
 admittance surfaces, 268–278  
 alternate right-handed/left-handed (ARLH) sections, 203–207  
 electromagnetic properties of, 156–160  
 electro-inductive waves, 284–287  
 equivalent circuit models, 156–160, 166–170  
 filters, characteristics of, 207–224  
 frequency-selective surface, 278  
 left-handed transmission lines, 163–166  
 metamaterial transmission line synthesis and, 163–175  
 negative permittivity, 163–166  
 numerical calculation, 160–163  
 parameter extraction technique, 170–172  
 planar arrays, 272–273
- Complex waves, 19–20
- Composite right-/left-handed (CRLH) transmission lines, 124–128  
 balanced, 127–128  
 coplanar waveguide (CPW)  
 configuration, 129  
 host propagating medium, 129  
 distributed components, 129  
 lumped elements, 129  
 leaky-wave antennas, 254–255  
 microstrip structure, 129
- Constitutive parameters  
 backward transmission line and, 123–124  
 bulk split-ring metamaterials, 65–70
- Coplanar waveguide (CPW), 129, 136
- Couplers in planar technology, 246–252  
 backward wave, 246–248  
 forward wave, 248–249  
 improvements to, 249–252
- CPW. *See* Coplanar waveguide
- CRLH. *See* Composite right-/left-handed transmission lines
- Cross-polarization effects, 54–59, 99–100, 276–278
- CSRR. *See* Complementary split ring resonators
- Diplexers, 188–189  
 alternate right-handed/left-handed (ARLH) sections, 206–207
- Dispersion relations  
 of bulk metamaterials, 69, 83–87, 90–92

- of transmission-line metamaterials, 120–128
- of resonant type transmission-line metamaterials, 151, 167
- Distributed components, 129
- Double-negative media, 2
- Double-split split-ring resonator (2-SRR), 62
- Dual left-handed lines, resonant types vs., 175–180
- Dual transmission line. *See* backward transmission line.
- Dual transmission line. *See* purely left-handed transmission line.
- Dual-band components, 244–246
- Duality, 155, 272–273, 285
- Dynamic resonances, 71
  
- EBGs. *See* Electromagnetic band gaps
- EC-SRR. *See* Edge-coupled split ring resonator
- Edge-coupled split ring resonator (EC-SRR), 52–59
- EIWs. *See* Electro-inductive waves
- Electric resonances, 71
- Electro-inductive waves
  - applications of, 287
  - complementary split ring resonators, 284–287
- Electrodynamics of left-handed media, 1–35
- Electromagnetic band gap (EBG), 194, 227
  - transmission line, 191–192
- Energy density, 4–6
- Equivalent circuit models
  - of composite right/left handed (CRLH) transmission lines, 124–125
  - of complementary split ring resonators (CSRRs), 156–160
  - of complementary split ring resonators (CSRRs) loaded transmission lines, 166
  - of purely right/left handed (PRH and PLH) transmission lines, 121
  - of split ring resonators (SRRs), 52–65
  - of split ring resonators (SRRs) loaded transmission lines, 146
- Evanescent Fourier harmonics, 25–27, 289–290
- Evanescent mode amplification. *See* Amplification of evanescent modes
  
- Fermat principle, 9
- Ferrite lens, 296
- Ferrite metamaterials, 92–97
  - left-handed circularly polarized (LCP) wave, 93
  - magnetostatic surface waves (MSSWs), 95
  - right-handed circularly polarized (RCP) wave, 93
- Ferrites, low-loss cubic, 92
- Filters, 188–189
  - complementary split ring resonators (CSRR), 207–224
  - high-pass, 225–227
  - narrow bandpass, 198–207
  - planar, 193–198
  - S-band, 203
  - tunable, 227–233
  - ultra-wide bandpass, 225–227
- Forward leaky modes, 254–259
- Forward transmission line, phase velocity calculation, 122
- Forward wave coupler, 248–249
- Forward wave, 121
- Fourier harmonics, 26–27
- Frequency-selective surface, 278
  
- Goos–Hanchen shift, negative, 12
- Group velocity, 4–6
  - calculation of, 122
- Guided waves, 17–19
  
- Higher-order resonances, 70–73
- High-pass filters (HPFs), 225–227
- HPFs. *See* High-pass filters
  
- In vacuo* capacitance, 57, 100
- Indefinite media, 34–35
- Infrared frequencies, SRRs at, 75–80
- Inverse Doppler effect, 10
- Isotropic split-ring resonators, 73–75

- LCP. *See* Left-handed circularly polarized wave
- Leaky backward waves, 19–20
- Left-handed circularly polarized (LCP) wave, 93
- Left-handed media
- antenna applications and, 252–258
  - energy density, 4–6
  - Fermat principle, 9
  - group velocity, 4–6
  - impedance, 9, 14, 17, 20, 23, 29
  - impedance matrix, 30
  - left-handed
    - slabs, 16–20
    - triplet, 3
  - losses and dispersions, 32–34
  - negative refraction, 6–9
  - other effects, 9–12
  - Poynting vector, 3–6, 36, 41
  - slabs,  $\epsilon/\epsilon_0 \rightarrow -1$  and  $\mu/\mu_0 \rightarrow -1$ , 20–32
  - wave fronts, 3–5, 10–11
  - wave numbers, 4, 19, 34
  - wave propagation, 2–4
  - wave vector, 6, 8, 12–15, 19, 35
- Left-handed metamaterials
- chiral bulk, 97–102
  - ferrite bulk, 92–97
  - split ring resonators (SRRs) bulk, 65–70, 80–88
  - planar transmission-line, 120–180
  - resonant type planar transmission line, 135–175
  - resonant/nonresonant planar transmission line (comparison), 175–180
- Left-handed slabs
- guided waves, 17–19
  - leaky waves, 19–20
  - reflection coefficients, 17
  - transmission coefficients, 17
  - with  $\epsilon/\epsilon_0 \rightarrow -1$  and  $\mu/\mu_0 \rightarrow -1$ , 20–32
- Left-handed transmission lines, equivalent circuit models, 146–155
- Left-handed transmission line design, split ring resonators, 135–146
- coplanar waveguide, 136
  - CPW technology, 139–143
  - microstrip line, 136, 139–143
  - negative permeability transmission lines, 136–138
  - resonant-type approach, 135
  - size reduction, 144–146
- Left-handed triplet, 3
- Left-handed waves
- backward leaky modes, 19–20
  - complex waves, 19–20
  - guided waves, 17–19
  - surface waves, 15–16, 18
  - TEM waves, 3
- Longitudinal section electric (LSE), 13
- Longitudinal section magnetic (LSM) waves. *See* P-polarized waves
- Losses and dispersions, 32–34
- Pendry's perfect lens, 32
  - super-lens, 33–34
  - Veselago analysis, 32
- Low-loss cubic ferrites, 92
- yttrium iron garnets, 92
- Low-loss plasmas, 1
- LSE. *See* Longitudinal section electric
- LSM waves. *See* P-polarized waves
- Magnetic plasma, 105
- Magnetic resonances, 71
- Magneto-inductive lenses, 299–302
- Magneto-inductive waves (MIWs), 278–284
- applications of, 285–287
  - equation, 279–281
  - surfaces, 282–284
- Magnetostatic surface waves (MSSWs), 95, 295–299
- Matching device, perfect lens and, 29–32
- MB. *See* Mono-band
- Media pairs, 253
- Metallic plates, 44–46
- two-dimensional plasmas, 44–46
- Metallic waveguides, 44–46
- magnetic plasma, 105
  - one-dimensional plasmas, 44–46
- Metamaterials, left-handed, 80–91
- Metamaterial transmission lines, balanced
- composite right-/left-handed, 225–227
- Metamaterial transmission line synthesis

- compact broadband devices, 236–244
- complementary split ring resonators, 163–175
  - equivalent circuit models, 166–170
  - frequency response, 172–175
  - left-handed transmission lines, 163–166
  - negative permittivity, 163–166
  - parameter extraction, 170–172
- coupled-line couplers, 246–252
- dual-band components, 244–246
- microwave component miniaturization, 234–236
- Microstrip, 139–143
- Microwave applications, 187–258
- Microwave filters, 188–233
- MIWs. *See* Magneto inductive waves
- Mono-band (MB) circuits, 244
- MSSWs. *See* Magnetostatic surface waves
- Multi-tuning, stop-band filters and, 190–191
  
- Narrow bandpass filter, 198–207
- NB-SRR. *See* Nonbianisotropic split ring resonator
- Negative Goos–Hanchen shift, 12
- Negative magnetic permeability
  - bulk split-ring resonator metamaterials, 65–70
  - edge-coupled SSR, 52–59
  - split-ring resonator designs, 59–65
  - synthesis of, 51–80
- Negative permeability transmission lines, 136–138
- Negative permittivity transmission lines, 163–166
- Negative refraction, 6–9
  - all-angle, 8
- Negative  $\epsilon$  and  $\mu$ . *See* Left-handed
- Negative-permittivity, 44–50
  - spatial dispersion, 49–50
- Negative refractive media. *See* Left-handed media
- Nonbianisotropic split-ring resonator (NB-SRR), 62
  
- Non-resonant circuit analysis
  - approach, 44
- Notch tunable filters, 230–233
  
- One-dimensional plasmas
  - metallic waveguides and, 44–46
- One-dimensional split-ring resonator based
  - left-handed metamaterials, 81–85
- Optical frequencies, 75–80, 106–107
- Open EC-SRR, 111
  
- Parameter extraction technique, 170–172
- Pendry's perfect lens, 27–29, 32
- Perfect lens, 25–32
  - evanescent Fourier harmonics, 26–27
  - tunneling/matching device, 29–32
- Perfect tunneling, 21–25
- Phase compensation, 20–21
- Phase shifters, 244
- Phase velocity, calculation of, 122
- Planar arrays
  - complementary split ring resonator, 272–273
  - split ring resonator, 270–272
- Planar filters, 188–233
- Planar technology metamaterials, 119–180
  - backward transmission line, 120–128
  - circuit model comparison, 175–180
  - complementary split rings resonator (CSRR), 119
  - left-handed transmission lines, 135–146
  - three dimensional metamaterials, 132
  - two-dimensional (2D), 131–134
- Plates, metallic, two dimensional plasmas, 44–46
- PLH. *See* Purely left-handed transmission line
- P-polarized waves. *See* Longitudinal section magnetic (LSM) or transverse magnetic (TM) waves, 13
- PRH. *See* Purely right-handed transmission line
- Purely left-handed (PLH) transmission line, 125, 246
  - dual, 125
- Purely right-handed (PRH) transmission line, 125, 246

- Quasielectrostatic limit imaging, 292–295  
 surface plasmons, 292–295
- Quasimagnetostatic limit imaging, 295–299  
 magnetostatic surface waves, 295–299
- Quasistatic resonance, 70
- Racemic mixture, 97, 99
- Radiated power, 254
- Rat race hybrid couplers, 239–243
- RCP. *See* Right-handed circularly polarized wave
- Reflection coefficients, 17  
 transmission coefficients and, 13–15
- Resonances, higher order, 70–73
- Resonant impedance surface imaging, 299–302  
 magneto-inductive lenses, 299–302
- Resonant-type approach, 135
- Resonant-type balanced composite right/left-handed metamaterial transmission lines, 225–227
- Resonant-type transmission lines, dual left-handed vs., 175–180
- Right handed sections, bandpass filters and, 218–225
- Right-handed circularly polarized (RCP) wave, 93
- Scaling plasmas at microwave frequencies, 44–50  
 metallic plates, 44–46  
 metallic waveguides, 44–46  
 wire media, 47–50
- Silver lens, 294
- Simultaneously negative  $\epsilon$  and  $\mu$ . *See* Left-handed
- Single split ring resonators, 268–269  
 Babinet principle, 268–269
- Size reduction, split ring resonators and, 144–146
- Slabs,  $\epsilon/\epsilon_0 \rightarrow -1$  and  $\mu/\mu_0 \rightarrow -1$ , 19–32  
 perfect lens, 25–32  
 perfect tunneling, 21–25
- Spatial dispersion, wire media and, 49–50
- Spirals, 62–65  
 two-turns spiral resonator (2-SR), 62
- Split-ring resonator based left-handed metamaterials, 80–91  
 continuous-medium approach, 87–88  
 modeling and numerical accuracy of, 90–91  
 one-dimensional, 81–84  
 superposition hypothesis, 88–90  
 three-dimensional, 85–87  
 two-dimensional, 85–87
- Split-ring resonator metamaterials, bulk, 65–70
- Split-ring resonator designs, 59–65  
 broadside-coupled, 60–62  
 chiral, 99–100  
 double-split, 62  
 nonbianisotropic, 62  
 spirals, 62–65
- Split-ring resonator planar arrays, 270–272
- Split-ring resonators (SRRs), 43  
 admittance surfaces, 268–278  
 alternate right-handed/left-handed (ARLH) sections and, 199–203  
 Babinet principle for, 268–269  
 complementary, 155–163  
 duality, 155–163  
 edge-coupled, 52–59  
 equivalent circuit models, 52–65, 146–155  
 higher-order resonances, 70–73  
 isotropic, 73–75  
 left-handed transmission line design and, 135–146  
 negative permeability transmission lines, 136–138  
 resonant-type approach, 135  
 scaling down of, 75–80  
 infrared frequencies, 75–80  
 optical frequencies, 75–80  
 size reduction, 144–146
- S-polarized waves, 13. *See* Longitudinal section electric (LSE); Transverse electric (TE)
- Spurious frequency bands, 193–197
- SRRs. *See* Split ring resonators
- Stop-band filters, 189–193  
 electromagnetic band gap (EBG) transmission line, 191–192  
 multi-tuning, 190–191

- Subdiffraction imaging devices, 287–303
  - canalization devices, 302–303
  - features of, 288–292
  - ferrite lens, 296
  - magnetostatic waves, 295–297
  - resonant impedance surfaces, 299–302
  - silver lens, 294
  - surface plasmons, 292–295
- Super-lens, 33–34
  - Veselago, 34
- Superposition hypothesis, 88–90
- Surface plasmons, 16, 292–295
- Surface waves, 15–16, 18
  - magnetostatic, 295–299
  - s-polarized, 16
- Symmetric resonances, 71
- Synthesis of negative magnetic permeability, 51–80
- Synthesis, bulk metamaterials, 43–109
  
- TEM. *See* Transverse electromagnetic mode propagation
- Three-dimensional SRR-based left-handed metamaterials, 85–87
- TM waves. *See* P-polarized waves
- Transmission coefficients, 17
- Transmission, reflection coefficients and, 13–15
- Transmission lines, negative permeability, 136–138
- Transverse electric (TE) waves, 13
- Transverse electromagnetic (TEM) mode propagation, 123–124
- Transverse magnetic (TM) waves. *See* P-polarized waves
- Tunable filters, 227–233
  - notch type, 230–233
  - varactor-loaded split rings resonators (VLSRRs), 227–233
- Tunneling
  - perfect, 21–25
  - perfect lens and, 29–32
- 2-SR. *See* Two-turns spiral resonator
- 2-SRR. *See* Double-split split ring resonator
- Two dimensional left handed structure, lumped elements and, 131–132
  
- Two dimensional metamaterials
  - bulk SRR based, 85–87
  - planar technology, 131–135
- Two dimensional plasma
  - metallic plates and, 44–46
- Two-turns spiral resonator (2-SR), 62
  
- Ultra-wide bandpass filter (UWBPF), 219–222, 225–227
  - resonant-type balanced composite right/left-handed metamaterial transmission lines, 225–227
- UWBPF. *See* Ultra-wide bandpass filters
  
- Varactor-loaded split rings resonators (VLSRRs), 227–233
  - equivalent circuit model, 228–230
  - model validation, 230
  - topology of, 228–230
- Veselago
  - analysis, 32
  - lens, 34
  - media, 2
- VLSRRs. *See* Varactor-loaded split rings resonators
  
- Wave impedance, 14
- Wave propagation, 2–4
- Wave transmission and guidance, left-handed slabs and, 16–20
- Waveguides, metallic
  - as one dimensional magnetic plasmas, 105
  - as one dimensional plasmas, 44–46
- Waves at interfaces, 13–16
  - surface, 15–16
  - transmission and reflection coefficients, 13–15
- Wire media, 47–50
  - spatial dispersion in, 49–50
  
- YIG. *See* Yttrium iron garnets
- Yttrium iron garnets (YIG), 92